UNIVERSITAT DE BARCELONA

Multiproperty materials: luminescent and/or magnetic coordination compounds containing *f*-block elements. Chirality

Ànnia Tubau Ribot

ADVERTIMENT. La consulta d'aquesta tesi queda condicionada a l'acceptació de les següents condicions d'ús: La difusió d'aquesta tesi per mitjà del servei TDX (**www.tdx.cat**) i a través del Dipòsit Digital de la UB (**diposit.ub.edu**) ha estat autoritzada pels titulars dels drets de propietat intel·lectual únicament per a usos privats emmarcats en activitats d'investigació i docència. No s'autoritza la seva reproducció amb finalitats de lucre ni la seva difusió i posada a disposició des d'un lloc aliè al servei TDX ni al Dipòsit Digital de la UB. No s'autoritza la presentació del seu contingut en una finestra o marc aliè a TDX o al Dipòsit Digital de la UB (framing). Aquesta reserva de drets afecta tant al resum de presentació de la tesi com als seus continguts. En la utilització o cita de parts de la tesi és obligat indicar el nom de la persona autora.

ADVERTENCIA. La consulta de esta tesis queda condicionada a la aceptación de las siguientes condiciones de uso: La difusión de esta tesis por medio del servicio TDR (**www.tdx.cat**) y a través del Repositorio Digital de la UB (**diposit.ub.edu**) ha sido autorizada por los titulares de los derechos de propiedad intelectual únicamente para usos privados enmarcados en actividades de investigación y docencia. No se autoriza su reproducción con finalidades de lucro ni su difusión y puesta a disposición desde un sitio ajeno al servicio TDR o al Repositorio Digital de la UB. No se autoriza la presentación de su contenido en una ventana o marco ajeno a TDR o al Repositorio Digital de la UB (framing). Esta reserva de derechos afecta tanto al resumen de presentación de la tesis como a sus contenidos. En la utilización o cita de partes de la tesis es obligado indicar el nombre de la persona autora.

WARNING. On having consulted this thesis you're accepting the following use conditions: Spreading this thesis by the TDX (**www.tdx.cat**) service and by the UB Digital Repository (**diposit.ub.edu**) has been authorized by the titular of the intellectual property rights only for private uses placed in investigation and teaching activities. Reproduction with lucrative aims is not authorized nor its spreading and availability from a site foreign to the TDX service or to the UB Digital Repository. Introducing its content in a window or frame foreign to the TDX service or to the UB Digital Repository is not authorized (framing). Those rights affect to the presentation summary of the thesis as well as to its contents. In the using or citation of parts of the thesis it's obliged to indicate the name of the author.

Multiproperty materials: luminescent and/or magnetic coordination compounds containing f-block elements. Chirality.

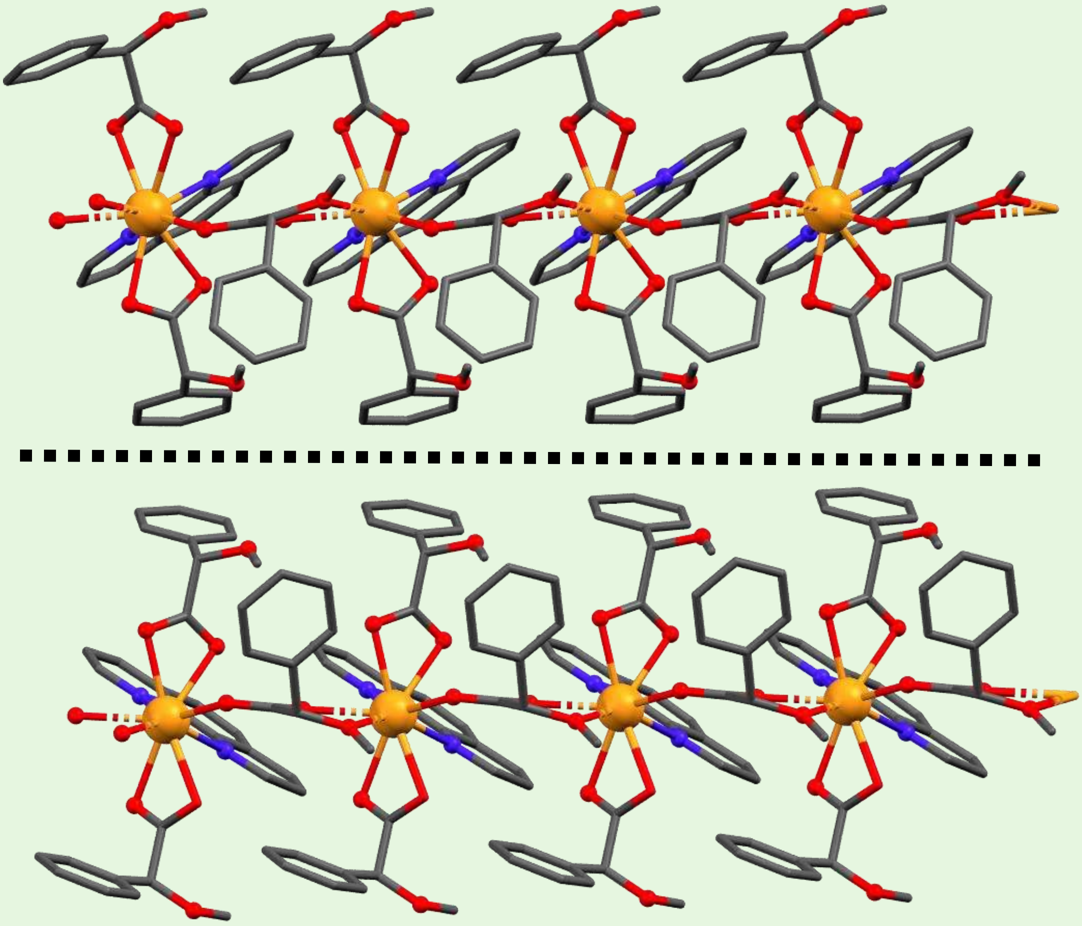

Ànnia Tubau Ribot

UNIVERSITAT DE BARCELONA

“Multiproperty materials: luminescent and/or magnetic coordination compounds containing *f*-block elements. Chirality.”

Programa de Doctorat de Nanociències

Autora: Ànnia Tubau Ribot

Director: Ramon Vicente Castillo

Tutor: Ramon Vicente Catillo

Departament de Química Inorgànica i Orgànica,

Secció de Química Inorgànica,

Facultat de Química

UNIVERSITAT DE BARCELONA

Als meus pares

“Lanthanum has only one important oxidation state in aqueous solution, the +3 state. With few exceptions, this tells the whole boring story about the other 14 Lanthanides”

G. C. Pimentel and R. D. Spratley, Understanding Chemistry,

Holden-Day, San Francisco, 1971

Agraïments

Inicialment m'agradaria agrair al Ramón Vicente Castillo qui m'ha dirigit la Tesi doctoral al llarg d'aquests quatre anys. Gràcies per escoltar les meves proposicions i donar-me llibertat de decisió així com ajudar-me cada vegada que ho he necessitat, tant a nivell professional com a també personal. A més a més, vull agrair a la resta de professors del grup de Magnetisme Molecular, Albert Escuer, Mohamed Salah i sobretot a la professora Júlia Mayans per totes les consultes sobre magnetisme i per estar disposada a ajudar-me en qualsevol moment. També vull donar gràcies a la professora Laura Rodríguez per les consultes sobre luminescència i per deixar-me mesurar els rendiments quàntics amb el Quantaurus i gràcies a la resta del grup de SuNS, especialment a la Araceli per les mil preguntes que he li he fet i que no ha dubtat en ajudar-me.

Gràcies a tots el professors amb els que he compartit hores de docència durant aquests quatre anys i dels que he pogut aprendre moltíssim sobre aquesta dedicada professió.

Als meus companys de Magmol i del departament Evangelos, Ernesto, Joan, Sergio, Joan petit i Manto per estar allà tant per resoldre mil dubtes com per treure'm un somriure cada dia. Gràcies a la Jeanette, la última incorporació al grup i una de les millors persones que conec. Joan i Jeanette, gràcies per ajudar-me a treure el virus del meu ordinador el dia que per poc em moro en veure que perdia tota la feina. Thank you Evangelos, specially these last months for helping me on all my doubts about the Thesis work and for asking me how I was doing every day.

Mil gràcies als meus amics de química física: Santi, Dr. Ignasi, Olga, Joshua (bueno tu eres de física però da igual) i Joel. Així com a tota la gent meravellosa que ha passat per aquest grup al llarg dels anys, Jonay, Xavi, Elle i els mil estudiants d'Erasmus que el Santi ens ha anat presentant. Tinc la gran sort de conèixer-vos i haver compartit bons i no tan bons moments amb vosaltres. Gràcies per tots els atacs de riure i els moments de desconnexió alhora de dinar. You are all wonderful people.

Vull agrair a tota la meva família la qual han fet qui sóc avui. Especialment, un enorme gràcies a la meva mare i al meu pare, sense els quals hagués pogut fer aquesta Tesi doctoral. Gràcies per totes les oportunitats que m'heu donat i en educar-me en la cultura de l'esforç i el treball i gràcies per les classes d'anglès i de mecanografia. Gràcies a la Júlia, la meva germana, i a *las primas i primos*, Andrea, Clara, Mar, Alba, Marc i Marius als que estimo moltíssim i estic molt orgullosa de poder dir que formo part d'un grup tant bonic.

Mil, mil gràcies a les dones de la meva vida, Julia, Marta i Maria. Per tot el suport que ens em donat des de que èrem petites, perquè si fos per vosaltres seguiria sent la millor científica del món encara que les pròximes 400 pàgines estiguessin en blanc. Gràcies per els últims 26 anys que hem sigut amigues i per tots els que ens esperen, ara amb més disponibilitat per part meva perquè ja no estaré fent Tesi ni corregint informes els caps de setmana.

Gràcies als meus gats (Meicu i Diemen) i tots els animalons amb els que he compartit part de la meva vida.

Per últim, gràcies al Sergi, al qui no li calen paraules per saber que haver-te conegut em fa molt feliç.

Table of Contents

Acronyms / Abbreviations / Symbols

2,6-HF2Bz: 2,6-difluorobenzoic acid

2-HFBz: 2-fluorobenzoic acid

4,4’-dinonyl-2,2’-bipyridine: 4,4’-dinonyl-2,2’-bipy

Ac: alternating current

ATR-IR: Attenuated total reflection Infra-Red

Bathophen: 4,7-Diphenyl-1,10-phenanthroline

Bipy: 2,2’-bipyridil

Btfa: 4,4,4-trifluoro-1-phenyl-1,3-butanedionate

CD: Circular Dichroism

CIE: Commission Internationale de l’éclairage.

CPL: Circular Polarized Luminescence

CShM: Continuous Shape Measurement

Dc: direct current

DCM: dichloromethane

EL: electroluminescence

HBtfa: 4,4,4-trifluoro-1-phenyl-1,3-butanedione

KD: Kramer doublet

NTSC: standard television systems committee.

PDRX: Powder X-Ray Diffraction

Phen: 1,10-phenanthroline

QTM: Quantum Tunneling of Magnetization

***R*/*S*-2-HPhBut**: *R*/*S*-2-phenylbutanoic acid

***R*/*S*-HMPA:** *R*/*S*-α-methoxyphenylacetic acid

SCPDRX: Single Crystal Powder X-Ray Diffraction

SIM: Single Ion Magnet

SMM: Single Molecular Magnet

Terpy: 2,2';6',2"-terpyridine

TGA: Thermogravimetric analysis

List of Compounds

Chapter 2.2

(**1-H_2O**) [Ce(Btfa)(H_2O)$_2$]

(**2-phen**) [Ce(Btfa)(phen)]

(**3-bpy**) [Ce(Btfa)(bpy)]

(**4-terpy**) [Ce(Btfa)(terpy)]

(**5-bathophen**) [Ce(Btfa)(Bphen)]

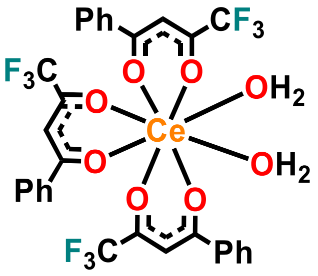

1-H_2O

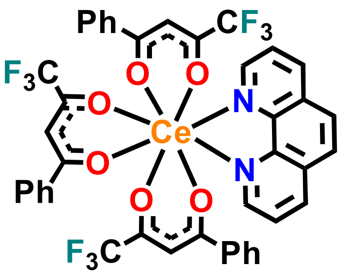

2-phen

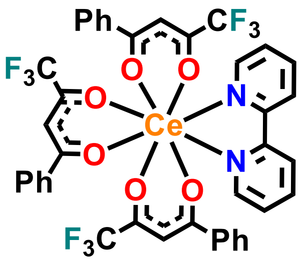

3-bipy

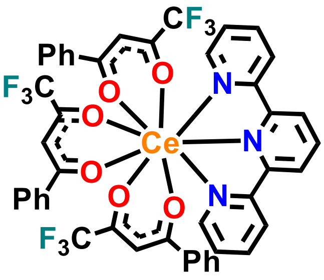

4-terpy

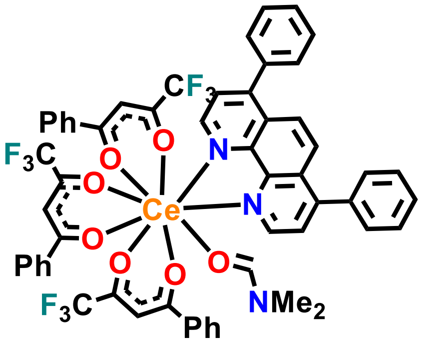

5-bathophen

Chapter 2.3

(**1-Sm**) [Sm(Btfa)$_3$(4,4’-dinonyl-bipy)]

(**2-Eu**) [Eu(Btfa)$_3$(4,4’-dinonyl-bipy)]

(**3-Tb**) [Tb(Btfa)$_3$(4,4’-dinonyl-bipy)]

(**4-Dy**) [Dy(Btfa)$_3$(4,4’-dinonyl-bipy)]

(**5-Er**) [Er(Btfa)$_3$(4,4’-dinonyl-bipy)]

(**6-Yb**) [Yb(Btfa)$_3$(4,4’-dinonyl-bipy)]

(**7-Gd**) [Gd(Btfa)$_3$(4,4’-dinonyl-bipy)]

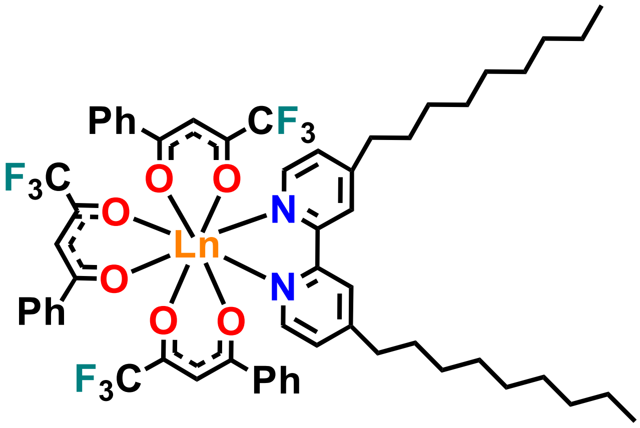

1-Sm, 2-Eu, 3-Tb, 4-Dy, 5-Er, 6-Yb, 7-Gd

Chapter 3.1.1

(**8-Ce**) $[Ce_2(\mu\text{-}2FBz)_4(2FBz)_2(H_2O)_4]_n$

(**9-Sm**) $[Sm_2(\mu\text{-}2FBz)_4(2FBz)_2(H\text{-}2FBz)_2(H_2O)_2]$

(**10-Eu**) $[Eu_2(\mu\text{-}2FBz)_4(2FBz)_2(H\text{-}2FBz)_2(H_2O)_2]$

(**11-Gd**) $[Gd_2(\mu\text{-}2FBz)_4(2FBz)_2(H\text{-}2FBz)_2(H_2O)_2]$

(**12-Tb**) $[Tb_2(\mu\text{-}2FBz)_4(2FBz)_2(H\text{-}2FBz)_2(H_2O)_2]$

(**13-Dy**) $[Dy_2(\mu\text{-}2FBz)_4(2FBz)_2(H\text{-}2FBz)_2(H_2O)_2]$

(**14-Er**) $[Er_2(\mu\text{-}2FBz)_4(2FBz)_2(H\text{-}2FBz)_2(H_2O)_2]$

(**15-Yb**) $[Yb_2(\mu\text{-}2FBz)_4(2FBz)_2(H\text{-}2FBz)_2(H_2O)_2]$

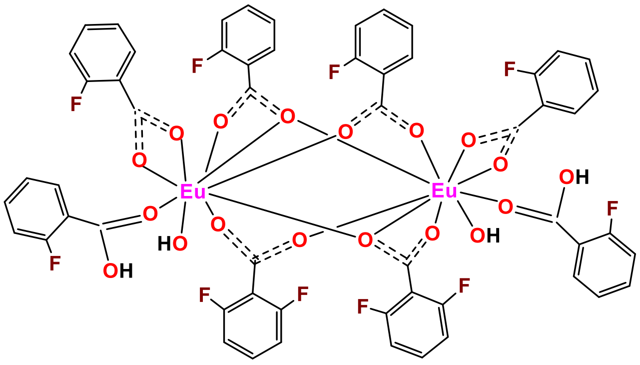

9-Sm to **15-Yb**

Chapter 3.1.2

(16-Ce) $(PPh_4)_2[Ce_2(\mu\text{-}2\text{-}FBz)_2(2\text{-}FBz)_6(H_2O)_2]\cdot H_2O$

(17-Eu) $(PPh_4)_2[Eu_2(\mu\text{-}2\text{-}FBz)_2(2\text{-}FBz)_6(H_2O)_2]$

(**18-Tb**) $(PPh_4)_2[Tb_2(\mu\text{-}2\text{-}FBz)_2(2\text{-}FBz)_6(H_2O)_2]$

(19-Dy) $(PPh_4)_2[Dy_2(\mu\text{-}2\text{-}FBz)_2(2\text{-}FBz)_6(H_2O)_2]$

(20-Er) $(PPh_4)_2[Er_2(\mu\text{-}2\text{-}FBz)_2(2\text{-}FBz)_6(H_2O)_2]$

(21-Yb) $(PPh_4)_2[Yb_2(\mu\text{-}2\text{-}FBz)_2(2\text{-}FBz)_6(H_2O)_2]$

(**22-Sm**) Chemical formula unknown

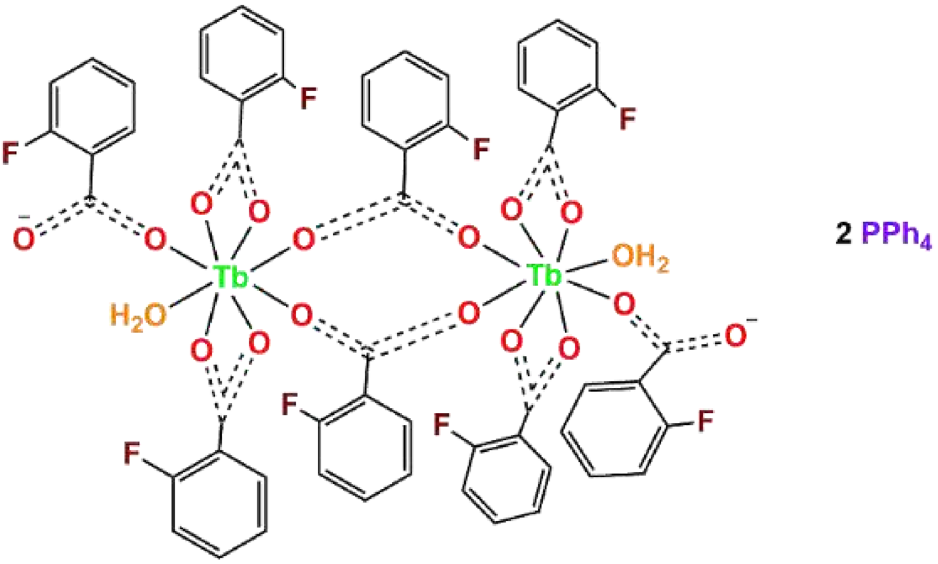

16-Ce to **21-Yb**

Chapter 3.2.1

(**23-Eu**) (HPy)$_2$[Eu$_2$(μ-2,6-F2Bz)$_4$(NO$_3$)$_4$]

(**24-Tb**) (HPy)$_2$[Tb$_2$(μ-2,6-F2Bz)$_4$(NO$_3$)$_4$]

(**25-Dy**) (HPy)$_2$[Dy$_2$(μ-2,6-F2Bz)$_4$(NO$_3$)$_4$]

(**26-Nd**) (HPy)$_2$[Nd$_2$(μ-2,6-F2Bz)$_4$(NO$_3$)$_4$]

(**27-Yb**) (HPy)$_2$[Yb$_2$(μ-2,6-F2Bz)$_4$(NO$_3$)$_4$]

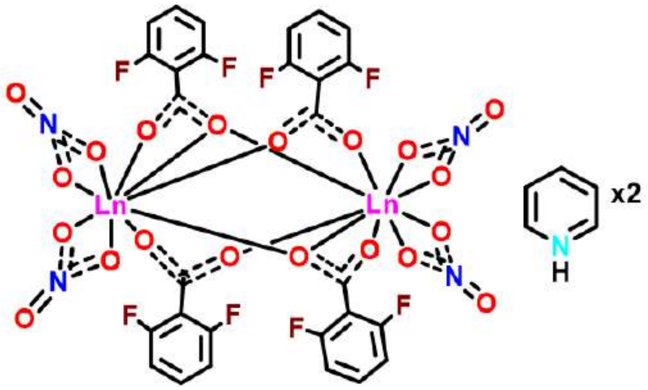

23-Eu to **27-Yb**

Chapter 3.2.2

(28-Eu) (HPy)$_2$[Eu$_2$(μ-2,6-F2Bz)$_4$(2,6-F2Bz)$_4$]

(29-Tb) (HPy)$_2$[Tb$_2$(μ-2,6-F2Bz)$_4$(2,6-F2Bz)$_4$]

(30-Dy) (HPy)$_2$[Dy$_2$(μ-2,6-F2Bz)$_4$(2,6-F2Bz)$_4$]

(31-Nd) Chemical formula unknown

(32-Gd) (HPy)$_2$[Gd$_2$(μ-2,6-F2Bz)$_4$(2,6-F2Bz)$_4$]

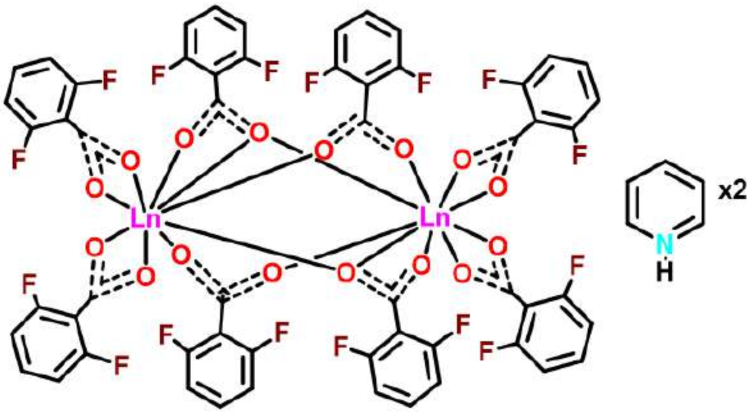

28-Eu to **32-Gd**

Chapter 4.1

(*R*-33-Ce) [Ce(μ-*R*-MPA)(*R*-MPA)$_2$(phen)]$_n$

(*S*-34-Ce) [Ce(μ-*S*-MPA)(*S*-MPA)$_2$(phen)]$_n$

(*R*-35-Nd) [Nd(μ-*R*-MPA)(*R*-MPA)$_2$(phen)]$_n$

(*S*-36-Nd) [Nd(μ-*S*-MPA)(*S*-MPA)$_2$(phen)]$_n$

(*R*-37-Eu) [Eu(μ-*R*-MPA)(*R*-MPA)$_2$(phen)]$_n$

(*S*-38-Eu) [Eu(μ-*S*-MPA)(*S*-MPA)$_2$(phen)]$_n$

(*R*-39-Tb) [Tb(μ-*R*-MPA)(*R*-MPA)$_2$(phen)]$_n$

(*S*-40-Tb) [Tb(μ-*S*-MPA)(*S*-MPA)$_2$(phen)]$_n$

(*R*-41-Dy) [Dy(μ-*R*-MPA)(*R*-MPA)$_2$(phen)]$_n$

(*S*-42-Dy) [Dy(μ-*S*-MPA)(*S*-MPA)$_2$(phen)]$_n$

(*R*-43-Sm) [Sm(μ-*R*-MPA)(*R*-MPA)$_2$(phen)]$_n$

(*S*-44-Sm) [Sm(μ-*S*-MPA)(*S*-MPA)$_2$(phen)]$_n$

(*R*-45-Er) [Er(μ-*R*-MPA)(*R*-MPA)$_2$(phen)]$_n$

(*S*-46-Er) [Er(μ-*S*-MPA)(*S*-MPA)$_2$(phen)]$_n$

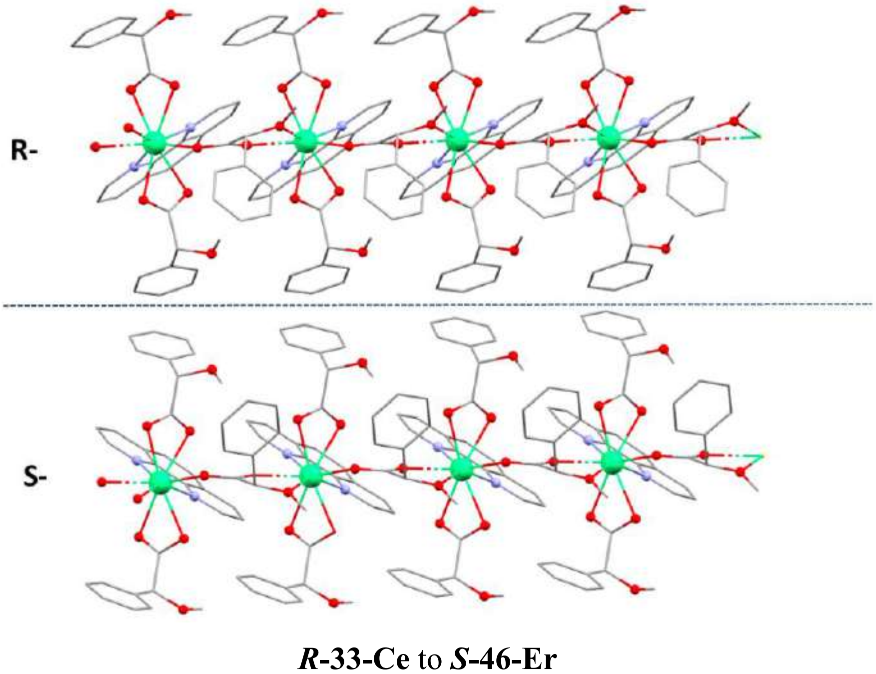

***R*-33-Ce** to ***S*-46-Er**

Chapter 4.2

(*R*-47-Nd-a) [Nd$_2$(μ-*R*-2-PhBut)$_4$(*R*-2PhBut)$_2$(bathophen)$_2$]

(*S*-48-Nd-a) [Nd$_2$(μ-*S*-2-PhBut)$_4$(*S*-2PhBut)$_2$(bathophen)$_2$]

(***R*-49-Sm-a)** [Sm$_2$(μ-*R*-2-PhBut)$_4$(*R*-2PhBut)$_2$(bathophen)$_2$]

(*S*-50-Sm-a) [Sm$_2$(μ-*S*-2-PhBut)$_4$(*S*-2PhBut)$_2$(bathophen)$_2$]

(***R*-51-Eu-a)** [Eu$_2$(μ-*R*-2-PhBut)$_4$(*R*-2PhBut)$_2$(bathophen)$_2$]

(*S*-52-Eu-a) [Eu$_2$(μ-*S*-2-PhBut)$_4$(*S*-2PhBut)$_2$(bathophen)$_2$]

(***R*-53-Tb-a)** [Tb$_2$(μ-*R*-2-PhBut)$_4$(*R*-2PhBut)$_2$(bathophen)$_2$]

(***S*-54-Tb-a**) [Tb$_2$(μ-*S*-2-PhBut)$_4$(*S*-2PhBut)$_2$(bathophen)$_2$]

(*R*-55-Tb-b) [Tb$_2$(μ-*R*-2-PhBut)$_4$(*R*-2PhBut)$_2$(bathophen)$_2$]

(***S*-56-Tb-b**) [Tb$_2$(μ-*S*-2-PhBut)$_4$(*S*-2PhBut)$_2$(bathophen)$_2$]

(***R*-57-Dy-a)** [Dy$_2$(μ-*R*-2-PhBut)$_4$(*R*-2PhBut)$_2$(bathophen)$_2$]

(*S*-58-Dy-a) [Dy$_2$(μ-*S*-2-PhBut)$_4$(*S*-2PhBut)$_2$(bathophen)$_2$]

(*R*-59-Dy-b) [Dy$_2$(μ-*R*-2-PhBut)$_4$(*R*-2PhBut)$_2$(bathophen)$_2$]

(*S*-60-Dy-b) [Dy$_2$(μ-*S*-2-PhBut)$_4$(*S*-2PhBut)$_2$(bathophen)$_2$]

(***R*-61-Tm-b)** [Tm$_2$(μ-*R*-2-PhBut)$_4$(*R*-2PhBut)$_2$(bathophen)$_2$]

(*S*-62-Tm-b) [Tm$_2$(μ-*S*-2-PhBut)$_4$(*S*-2PhBut)$_2$(bathophen)$_2$]

(***R*-63-Yb-b)** [Tm$_2$(μ-*R*-2-PhBut)$_4$(*R*-2PhBut)$_2$(bathophen)$_2$]

(*S*-64-Yb-b) [Yb$_2$(μ-*S*-2-PhBut)$_4$(*S*-2PhBut)$_2$(bathophen)$_2$]

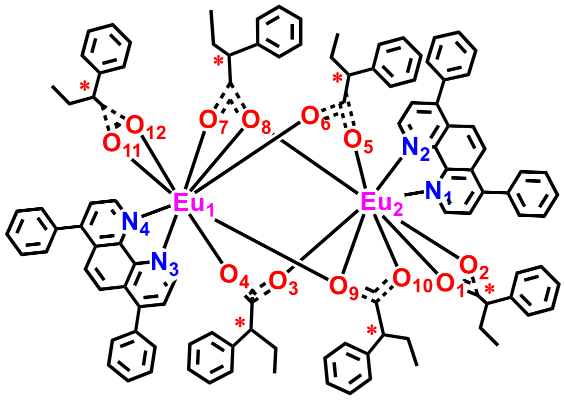

***R/S*-XX-Ln-a**

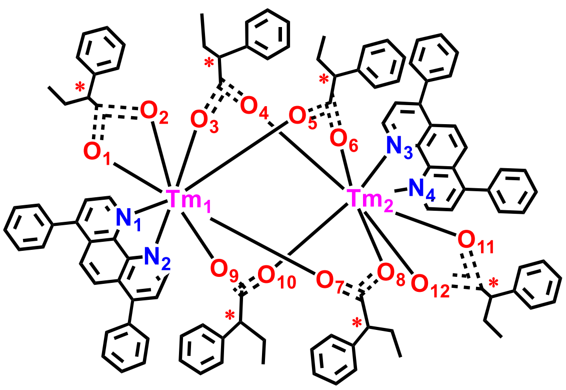

***R/S*-XX-Ln-b**

1. Introduction

1. Introduction

1.1 The so-called rare earth elements

As stated by the International Union of Pure and Applied Chemistry, the well-known IUPAC, the rare earth elements (RE) are a group of seventeen elements comprised between the fifteen metallic group Lanthanum(57) to Lutecium(71) series as well as Yttrium(39) and Scandium(21).[1a] The lanthanoids (more often used the term lanthanides) comprise the elements between La to Lu. The lanthanide elements are inserted between Barium(56) and Hafnium(72) in the periodic table, with Scandium(21), Yttrium(39) and Lutecium(71) forming the column in the third group.

The most common oxidation state in which lanthanides (Ln) are found is +III with an $[Xe]4f^n$ electronic configuration. According to the n value, they are classified as the lighter and the heavier rare earth elements. The lighter RE comprises the ones with no paired electrons in the 4*f* shell (with n=0-7) and they correspond from the La to Gd. The considered heavier RE are the ones bearing n=8-14 with at least two paired electrons in the 4*f* orbital. Moreover, Y has similar chemical properties to Dy and Ho elements, so it is included as a heavy RE element. Geochemical and chemical characteristics of Sc are comparable to the lanthanides in aqueous medium (reason why it is found in the RE group), however in solid state its properties are rather different from the other rare earth, and it is not included into this classification.

These elements are highly electropositive, being a challenge to obtain their metallic forms unless specialized reduction techniques are used. However, these reduction techniques were not always accessible by the time the new RE elements were being separated and identified. Consequently, the RE elements were gradually discovered in their oxide forms rather than in their elemental state.

For the Rare Earths, the term ‘rare’ is somehow not accurate. Some RE elements are more abundant in the Earth’s crust than other metals commonly used in technology like Silver or Indium and are found in quantities equivalent to the Lead metal. For instance, the abundance of Cerium in the Earth's crust is comparable to that of Copper. The term 'rare' arises because, despite having a relatively high concentration in certain minerals (about 35% to 75%), these elements are typically dispersed and mixed within the rocks or sand where they are found, making its extraction more challenging. RE deposits have been identified in approximately 34 different countries. The estimated worldwide RE reserves are calculated to be 130 million tons, with China and Brazil holding about the 42.3% and 16.9% of these reserves, respectively. During the latter twentieth century the majority of RE were extracted from USA deposits, nonetheless, the extraction and exportation of RE elements as well as production of materials containing these elements (for instance the strong Neodymium magnets) is now governed by China. Rare earth elements are believed to play a crucial role in materials for the new technologies for energy transition. For instance, RE are necessary in the strong magnets that electric cars and wind turbines contain. As the demand for these materials increase, dependence of Europe on other countries becomes a significant concern. Recently,[1c] in 2024, what is believed to be the largest rare earth deposit in Europe was discovered in Norway, in a deposit called Fensfeltet, which it might contain about 8.8 million tons of resources. The extraction in this Norwegian deposit is believed to start in 2030.[1c]

Although it is said that more than 270 minerals may contain RE, two specific minerals have been crucial in the discovery of the 4*f* elements. On one hand there is the Gadolinite, $RE_2FeBe_2Si_2O_{10}$ which contains Y and the heavier RE, Eu to Lu. On the other hand, a silicate complex with the $(Ca,Ce)_{10}(Fe^{3+})(SiO_4)_6(OH,F)_5$ composition which is mainly composed of La, Ce, Nd and fewer quantities of Sm and Eu.

The different RE elements were gradually differentiated and isolated along the eighteenth to twentieth centuries. The first isolated RE element was Ce in 1751 followed by Y in 1797 whereas the last one was the radioactive Pm in 1945 found in fission products of Uranium. The RE show similar chemical properties though it was possible to isolate and identify them, mainly employing fractional crystallization and precipitation methods (for instance with the addition of oxalates, a method used until today) with further help of spectroscopic techniques.[2]

1.1.1 Electronic configuration of lanthanides

Focusing on the lanthanides, the electronic configuration of these elements shares the same core which corresponds to [Xe]=$1s^2$, $2s^2$, $2p^6$, $3s^2$, $3p^6$, $3d^{10}$, $4s^2$, $4p^6$, $4d^{10}$, $5s^2$, $5p^6$. The valence electrons of the Ln series are placed into the 6*s* and 4*f* orbitals since the energy difference between the 4*f* and 5*d* orbitals is rather large (ΔE around 32,000 cm^{-1}) with [Xe]$4f^n6s^2$. La, Gd and Lu are exceptions to this, since filling with one electron the 5*d* orbital lead to a favourable empty $4f^0$ orbital (for La), half-filled $4f^7$ orbital (for Gd) and fully occupied $4f^{14}$ orbital (for Lu), thus they follow [Xe]$4f^{n-1}5d^16s^2$. On the other hand, the valence electrons found in the 4*f* shell are highly localized due to the shielding of fully occupied 5*s* and 5*p* orbitals which are higher in energy. The atomic radius of the lanthanide (both in the elemental state and in higher oxidation states) decreases on increasing the atomic number. This is a consequence of the shielding of the 4*f* electrons. As the number of electrons in the 4*f* orbitals increase from La to Lu, they are drawn closer to the nucleus due to an increase of the attraction Coulombic force between the nucleus and the electrons, thereby decreasing the ionic radius. This phenomenon is called lanthanide contraction and significantly influences in the chemistry characteristics as well as the spectroscopic and magnetic properties of these elements.[3]

As already commented, the most common oxidation state is +III because it leads to a favourable [Xe]$4f^n$ electronic configuration where n=0 for La^{3+} and n=14 for Lu^{3+}. Nonetheless, Europium and Ytterbium can stabilize the +II oxidation state. Since this configuration leads to half-filled *f* orbitals for Eu^{2+} ion ([Xe]$4f^7$) and fully occupied *f* orbital for the Yb^{2+} ion ([Xe]$4f^{14}$). Owing to the same reasoning, Cerium and Terbium lanthanides can also be found in the +IV oxidation state due to stabilization of empty and half-filled 4*f* orbitals, respectively, with electronic configuration of [Xe]$4f^0$ for Ce^{4+} and of [Xe]$4f^7$ for Tb^{4+}. It is worth remarking that due to the shielded quality of the 4*f* electrons, the chemical bond of a Ln^{3+} ion with adjacent atoms, once it is placed in a chemical environment (for instance in a coordination compound) is of electrostatic nature.[4]

1.1.2 4*f* electrons and the Ground state

Pauli exclusion principle states that an electron of an atom must have its unique quantum state defined by the four n, ℓ, m_ℓ and m_s quantum numbers, where n is the principal quantum number, ℓ is the azimuthal quantum number (ℓ = 0, 1, …, n-1) which is represented by the letters ℓ = s, p, d, f, g, h, *etc.* corresponding to ℓ = 0, 1, 2, 3, 4, *etc*. and m_ℓ accounts to the magnetic quantum number which is comprised between m_ℓ =- ℓ, - ℓ +1, …, 0, …, ℓ -1, ℓ. The n, ℓ and m_ℓ quantum numbers define the size, the shape and the direction in space, respectively, of the Atomic Orbital in which the specific electron is set. Moreover, the spin quantum number (S) which define the intrinsic angular momentum of the electron is an intrinsic property of the electron and its quantized projections are represented as spin-up and spin-down by m_s=-1/2, +1/2.

For an electron found in the 4*f* orbitals of a lanthanide atom, the n quantum number is 4 and ℓ is 3. Then the electron will be defined by one of the magnetic quantum numbers m_ℓ =-3, -2, -1, 0, +1, +2, +3. The orientation of the spin, given by the m_s quantum number, will be one of the ±1/2 values.

For a Ln^{3+} ion with a $4f^n$ electron configuration, the degenerated ground state is split into $^{2S+1}\Gamma$ spectroscopic terms due to electronic repulsion, where S is the overall spin momentum ($S = \sum_i s_i$) and $2S$+1 is the spin multiplicity of the subshell. The overall orbital quantum number ($L = \sum_i \ell_i$) is represented as capital letters Γ = S, P, D, F, G, H, etc. corresponding to the values of L = 0, 1, 2, 3, 4, 5, etc. Then the spectroscopic term can be defined as ^{2S+1}L. The interelectronic repulsion is large because the wave functions of the 4*f* electrons are contracted. The spin and orbital multiplicities provide the degeneracy of the spectroscopic term which is given by $(2\cdot S+1)(2\cdot L+1)$. Hence, the ^{2S+1}L spectroscopic terms are further split into J states due to the spin-orbit coupling giving $^{2S+1}L_J$ spectroscopic levels, where J is the overall angular momentum quantum number. The J value in the ground state is $J = L-S$ if the f shell is less than half filled (f^1-f^6) and $J = L+S$ if the f shell is half or more than half filled (f^7-f^{14}) and the ^{2S+1}L term is split on as many states as $|L-S| \leq J \leq L+S$ can give. Finally, the ligand field perturbation caused by the chemical environment surrounding the Ln^{3+} ion splits the spectroscopic levels into sublevels. The $^{2S+1}L_J$ level can split into $2J$+1 sublevels generating the ±m_j Kramer doublets. Depending on the symmetry produced by the crystal field, the 2J+1 sublevels will be totally covered or not. The only method to reveal all 2J+1 sublevels, for any metal ion, is to apply an external magnetic field, Figure 1. 1 a). As can be observed, due to the unquenched L that lanthanides present, spin-orbit coupling splitting is more energetic (about 10^4 cm^{-1}) than the crystal field splitting (10^2 cm^{-1}) in contrast to transition metal ions.

Let's take the example of Eu^{3+} to determine the ground state of a subshell. The electronic configuration of Eu^{3+} is [Xe]4f^6, Figure 1. 1 b). According to the first Hund's rule, the lowest energy state will be the one with largest spin multiplicity, then for a Eu^{3+}, $S = \sum_i s_i = \frac{1}{2} \cdot 6 = 3$ and 2S+1 is 7. The second Hund's rule implies that the lower energy level should present the higher orbital angular momentum thus, $L = \sum_i \ell_i = |-3| + |-2| + |-1| + 0 + 1 + 2 + 3 = |-3| = 3$. Hence, the ground spectroscopic term of an Eu^{3+} ion is ^7F. Due to spin-orbit coupling the ^7F states are further split into ^7F_J spectroscopic levels with J=0, 2, 3, 4, 5 and 6. The third Hund's rule states that the lower energy sublevel will be the one with $J = L-S$ (J lowest value) if the f shell is less than half filled or $J = L+S$ (J highest value) if the f shell is half or more than half filled. The 4f^6 shell in the Eu^{3+} ion is less than half filled therefore the ground state correspond to the one with $J = L-S$ = 3-3 = 0. In conclusion, the ground state of a Eu^{3+} ion is $^7F_0$, Figure 1. 1 c).[4,5]

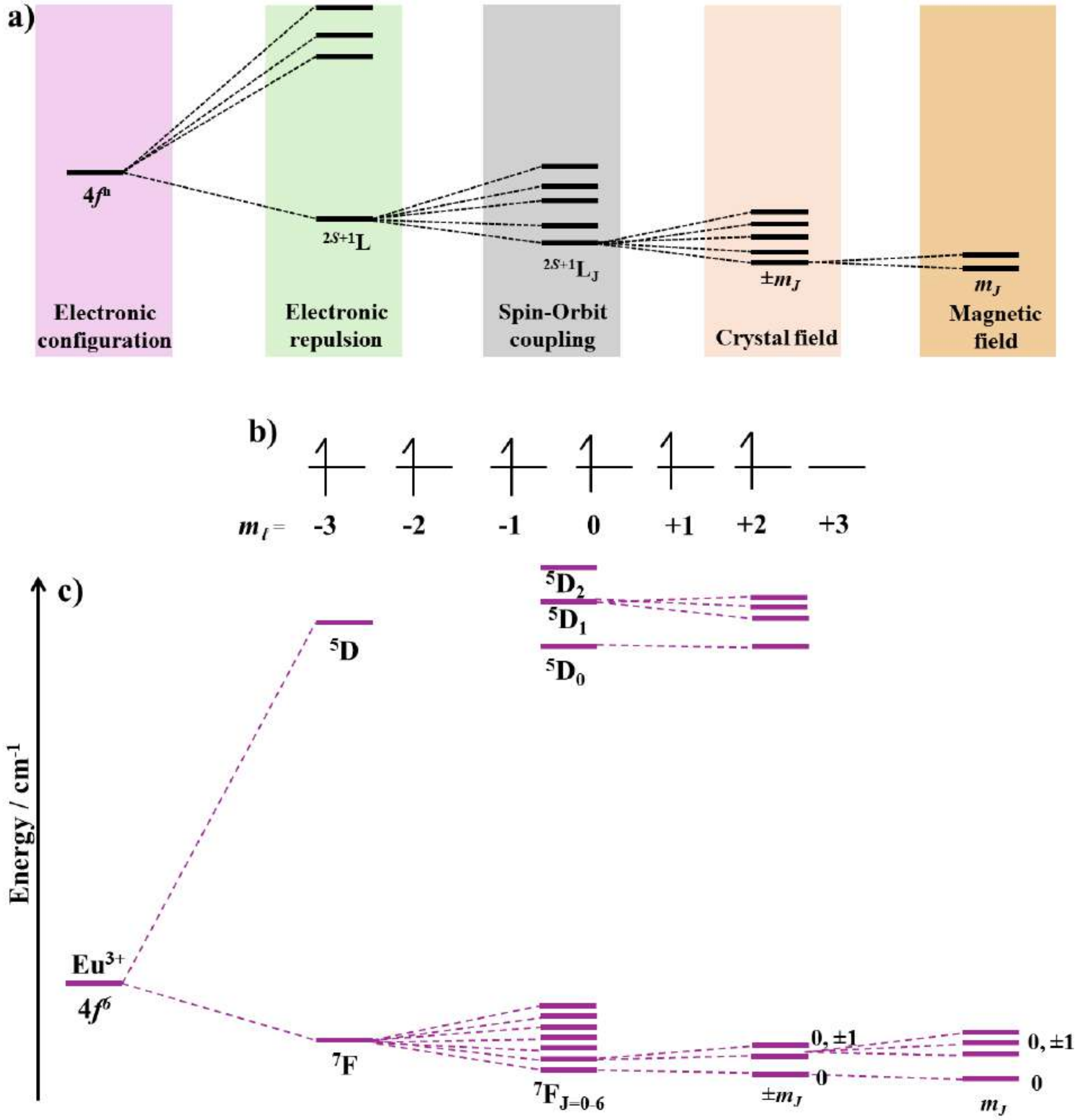

Figure 1. 1 a) Energy splitting Scheme produced by the different perturbation for a $4f^n$ electronic configuration of a Ln^{3+} ion b) electronic configuration of Eu^{3+} ion and c) energy splitting Scheme of an Eu^{3+} ion.

1. 2 Luminescence properties

1.2.1 Luminescence and selection rules

Given two electronic states with different energy, an electron found in the lowest energy state such as the ground state, can absorb energy in a certain wavelength from the light and promote to the higher energy state, called excited state. This process may take place if the incident light coincides with the energy difference between the ground and excited states. Once the system is found in the excited state the molecule can either use this energy to react with the surrounding molecules as in a photochemistry process or, ultimately, it can relax to find the first situation where it was laying in the lowest energy state.

Relaxation processes can be of different nature, non-radiative in which there is no photon emission or, on the other hand, radiative were photon emission takes place. Non-radiative deactivation involves different mechanisms. For instance, collision between particles that diminish the energy from the system or the process called internal conversion that transforms an electronic excitation into a vibrational excitation to decay to an excited vibrational sublevel within the ground electronic state (hot electronic lower state). Moreover, non-radiative transitions also can take place through quenching processes due to overlapping of the electronic states from another atom or molecule, the quencher.

On the other hand, the radiative deactivation can take place via processes such as luminescence which encompasses fluorescence and phosphorescence. Let’s take the example of an organic chromophore molecule which absorbs light in the UV-visible range. In these molecules, the absorption of photons occurs throughout the molecular orbitals, particularly from the HOMO (Highest Occupied Molecular Orbital) to the higher in energy LUMO (Lowest Unoccupied Molecular Orbital). After absorption, the electronic configuration of the excited state of the chromophore presents an electron in its HOMO (π) and an electron in the LUMO (π^*). In the excited state picture, the state can present singlet (S_1) or triplet (T_1) multiplicity. The triplet state, T_1 is generated due to the inversion of the electron spin, through an intersystem crossing (ISC) process. Now if the deactivation of this excited state is through a radiative process, fluorescence is produced when the deactivation take place through the excited state, S_1 to a S_0 ground state, whereas phosphorescence takes place when the radiative deactivation occurs via the T_1 excited state to the S_0 ground state. The $T_1 \rightarrow S_0$ deactivation in phosphorescence phenomena accounts for a spin forbidden transition since it requires a change on the total spin, therefore it is a slower process (microsecond to second scale) compared to the $S_1 \rightarrow S_0$ allowed transition occurring in fluorescence which is quicker and comprised in the nanosecond time scale. In many cases, the spin-forbidden nature of the phosphorescence process allows radiative deactivation to continue even after the excitation light has been removed, Figure 1. 2.

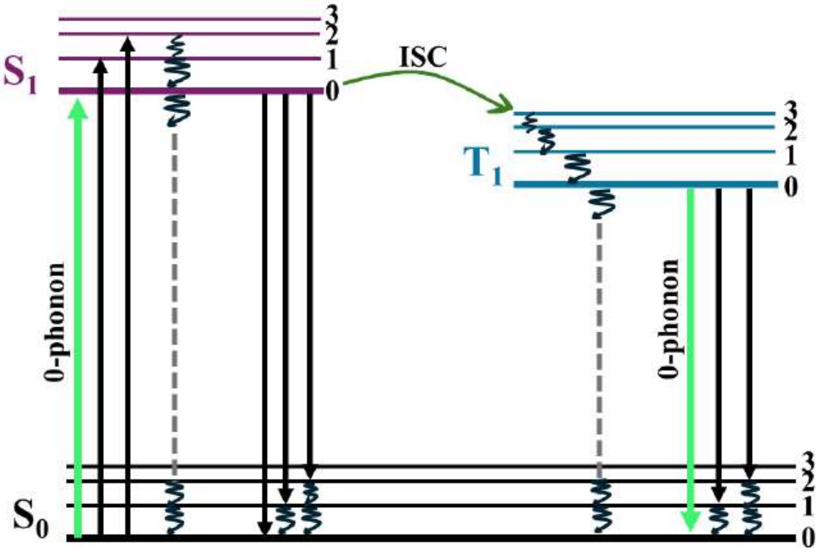

Figure 1. 2 Jablonski diagram of an organic chromophore molecule showing the Singlet ground state (S_0) Singlet excited state (S_1) and Triplet excited state (T_1). The light-green and black arrows represent radiative transitions, grey dotted line and wavy arrows represent non-radiative deactivation and dark-green horizontal arrow represent Intersystem crossing from S_1 to T_1 excited states.

Moreover, the electronic absorption of organic molecules displays broad bands due to significant vibronic coupling, known as the Franck-Condon principle, which is related to the movement of the chemical bonds of the excited species compared to the species found in the ground state.

Regarding luminescence of trivalent lanthanide cations, they present intriguing luminescence properties that range from the Visible to the Infra-Red range. One notable aspect about Ln^{3+} luminescence is that each ion presents a unique emission spectrum, which can serve as a distinctive fingerprint for each cation. Given the fact that Ln^{3+} cations show similar chemical properties, their distinct luminescence characteristics were crucial in the extraction and characterization of each lanthanide cation.[4] The unique emission spectrum that each lanthanide ion presents is due to the intraconfigurational nature of lanthanide transitions which occur between the 4*f* orbitals. The partially filled 4*f* orbitals of the lanthanide(III) cations are shielded by the closed $5s^2$ and $5p^6$ shells, causing the energies of the lanthanide electronic states to be relatively independent of the Ln^{3+} chemical environment. Thus, there is no relevant shift in the emission wavelength when comparing the bands of emission spectra of two different luminescent coordination compounds containing the same Ln^{3+} cation. Moreover, they exhibit large Stokes shifts, so the absorption bands corresponding to the Ln^{3+} intrinsic *f*-*f* transitions appear at wavelengths significantly higher in energy compared to the respective emission transitions in contrast of a chromophore organic molecule in which generally the absorption and emission band overlap. Besides, in coordination compounds encompassing lanthanide ions, the Franck-Condon effect is almost negligible due to the low-energy vibrations between Ln^{3+} ions and the donor atoms of the ligand molecule. Consequently, the emission from the Ln^{3+} ions is characterized by narrow bands, in contrast to the broader bands observed in organic chromophore molecules. The lanthanide(III) ions have no vibrational structure as understood for an organic molecule, thus radiationless deactivation is not produced because of internal conversion. However, different chemical species acting as quenchers can reduce or even cancel the luminescence characteristics of the lanthanide coordination compounds (see below). The quenching effect are of relevant importance in emissive lanthanides presenting lower energy separation between the emitting excited state and the ground state such as the near Infra-red (nIR) emitters: Nd^{3+}, Er^{3+} and Yb^{3+}.[6]

The probability or strength of a transition is governed by several selection rules, including the spin selection rule (the most critical), the symmetry selection rule and the vibrational selection rule or Franck-Condon principle (particularly relevant in chromophore organic systems, though less important in Ln-based systems).

Further to that, selection rules affect the intensity of the bands related to both, emission and absorption processes. For instance, to consider an allowed transition, the promoted electron cannot change its spin multiplicity during the transition, thus those transitions occurring between the triplet excited state to the singlet ground state $T_1 \rightarrow S_0$, in organic chromophore molecules, are forbidden. Additionally, transitions within the same subshell or within orbitals of same symmetry, such as the intraconfigurational *f-f* in lanthanide cations, are also not allowed as they do not accomplish Laporte's rule (they are forbidden by symmetry).

On the other hand, the π→π* transitions in organic systems of $S_1 \rightarrow S_0$ nature are allowed by both, the Spin and Laporte selection rules. Because these transitions are allowed, they exhibit greater intensity and probability. Consequently, the bands higher in energy in a chromophore molecule are attributed to these transitions as can be seen in the Jablonski diagram in Figure 1. 2. However, in practical scenarios these selection rules are not absolute, and coupling between the wavefunctions of the energy levels can cause forbidden transitions happen. Nevertheless, they will remain slower, weaker and of lower probability compared to the allowed ones.

As pointed out before, phosphorescence phenomena account to a Spin-forbidden transition ($T_1 \rightarrow S_0$). Firsts Hund's rule stablishes that an energy state with higher spin multiplicity resides at a lower energy level than states with lower spin multiplicity, therefore $T_1 \rightarrow S_0$ transition will be less energetic than $S_1 \rightarrow S_0$ transition.

For lanthanide ions, the *f-f* transitions with energy in the visible range overcome a change in Spin multiplicity ($2S$+1) whereas the *f-f* transitions with energy in the nIR do not change the spin. For instance, the characteristic emission of a Eu^{3+} ion takes place from the $^5D_0$ emitting state to the $^7F_{J=0-6}$ ground state. Spin multiplicity changes from 5 in the excited state to 7 in the ground state, thus emission transitions of Europium(III) are Spin forbidden. On the other hand, the nIR emission seen for a Yb^{3+} ion arise from $^2F_{5/2} \rightarrow {}^2F_{7/2}$, were there is no change in Spin multiplicity: it accounts to a Spin allowed transition. It is common for several lanthanides to show emission from the Visible to the IR range and so forth, to present both mechanisms. That is why is best referring to luminescence when it comes to lanthanide absorption and emission transitions rather than just fluorescence or phosphorescence. Moreover, depending on the excitation method, different types of luminescence may be considered. Emission after excitation by exposure to an electromagnetic radiation leads to photoluminescence, emission produced by recombination of electrons and holes under the influence of an electric field refers to electroluminescence, the non-thermal production of light by a chemical reaction will lead to chemiluminescence whereas the emission observed by applying mechanical stress by fracture of the sample crystals may produce the intriguing property of triboluminescence.

The symmetry forbidden character of the intraconfigurational *f-f* transitions is partially overcomed when the Ln^{3+} ions are set in a coordination compound. The distortion produced by the chemical environment around the ion modifies the symmetry of the *f* orbitals by mixing of the electronic states with states of the ligand field, or by coupling of 4*f* and 5*d* orbitals wavefunctions, leading to less forbidden *f-f* transitions. Because of their forbidden character (by Spin and Laporte in case of the Visible emitters), the *f-f* transitions are slower and the lanthanide luminescence tends to present longer lifetimes of the excited state (up to the ms scale) for those emitting in the Visible range.[4,5]

On the other hand, the electronic transitions can be of different nature depending on the interaction between the incident light with the electric and magnetic dipoles of the molecules. An electric dipole (ED) transition is induced due to the interaction between the electric dipoles of the molecule with the oscillating electric field of light. Moreover, the electrons in the atomic orbitals and by extension in the molecular orbitals within a molecule also have magnetic dipole moments. Hence, the magnetic dipole transitions (MD) are those induced from the interaction of the magnetic dipole moments in the molecule with the oscillating magnetic field of an electromagnetic radiation. In organic chromophores, only electric dipole transitions are observed whereas in Ln^{3+} *f-f* luminescence both, ED and MD transitions are present.

Electric dipole and magnetic dipole transitions are differentiated on the nature of their associated movements of charge, when interacting with the electromagnetic radiation and in their selection rules. ED transitions involve a linear movement of charge (ED operator transforms as x, y and z), reversing its direction under inversion, which gives them odd parity. On the other hand, MD transitions involve rotating movement of charge (MD operator transforms as R_x, R_y and R_z), which remains unaltered under inversion, giving them even parity. Hence, MD transitions are allowed within inner subshells, such as *f-f* intraconfigurational transitions though they are still weaker in intensity compared to the ED transitions. This is because MD transitions result from the electron's rotational movement caused by the magnetic component of light, which changes the symmetry selection rules compared to the straight-line movement in ED transitions. In MD the ΔJ=0, ±1 (but no 0↔0) selection rule is followed so few magnetic dipole transitions such as $^5D_0 \rightarrow {}^7F_1$ from Eu^{3+} are known. Conversely, in ED transitions the ΔJ≤6 (2,4 or 6 if J or J'=0) selection rule is followed. As a result, MD transition intensities are practically unaffected by the chemical environment in which the Ln^{3+} cation is found. For instance, in Ln^{3+} ions within higher symmetry coordination environments, the intensity of ED transitions will diminish and consequently the MD will gain significance in the spectra. If the lanthanide cation is set around a coordination geometry with lower symmetry, the ED transition will increase its intensity.[5]

In terms of luminescence efficiency of a compound it will depend on the kinetics of its deactivation processes, specifically the relation between radiative and non-radiative processes. If the radiative deactivation processes are faster than the non-radiative ones, the compound will exhibit efficient luminescence.

1.2.2 Sensitized luminescence, the antenna effect

For a luminescent trivalent lanthanide cation found in a coordination compound, the molar absorption coefficients (ε) resulting from the intrinsic *f-f* transitions are low (smaller than 10 M^{-1} cm^{-1}) due to its forbidden character.[4,5] Only a very limited amount of radiation is absorbed by direct excitation from the 4*f* levels. Thus, it is essential to excite the lanthanide(III) cation in a more efficient way.

The photosensitization effect (or just sensitization or antenna effect) is mainly based on using a molecule with higher molar absorption coefficient compared to the Ln^{3+} ion itself, generally a chromophore organic molecule acting as a ligand. Then the absorbed energy by the organic moiety will be transferred to the lanthanide excited emitting state, resulting in enhanced metal-centred luminescence. The chromophore molecule is provided as the ligand in the lanthanide coordination compound, and it acquires the role of the antenna (or sensitizer). In addition to provide an efficient path for the excitation of lanthanide ions, the sensitization process also presents the advantage of conferring larger apparent “Stokes shift” to the final system, which allows an easy spectral separation between the absorption of the compound and luminescence emission from the metal ion. Alternative sensitization pathways other than using a chromophore organic ligand are found in the literature, for instance sensitization of the lanthanide ion throughout d-metals[7] or other lanthanides with a higher energy gap between the ground and emitting state compared to the sensitized Ln^{3+}.[8]

The sensitization mechanism first involves excitation of the ligand from the S_0 ground state to a singlet excited level (S_2). Then the excited S_2 state will decay to its first singlet excited level (S_1) through internal conversion (IC). The excited ligand can deactivate through non-radiative processes ($k_{nr}^{L(S)}$) or by radiative processes involving fluorescence (k_f^L). In Figure 1. 3, decay pathways are indicated by their rate constants. In presence of a lanthanide(III) cation, the singlet states S_1 and S_2 can undergo spin-forbidden transitions known as the Intersystem Crossing (ISC) to populate the lowest energy triplet state (T_1). Then the T_1 excited state can deactivate non-radiatively ($k_{nr}^{L(T)}$) or radiatively through phosphorescence (k_{ph}^L) to the S_0 ground state. Ultimately, energy transfer (ET) to the lanthanide excited state from the T_1 can take place through either Dexter or Förster mechanisms, exposed hereafter. After population of the lanthanide upper states, deactivation may proceed newly through non-radiative transitions of the metal (k_{nr}^{Ln}) or alternatively via the desired radiative transitions by means of luminescence (k_{rad}^{Ln}).

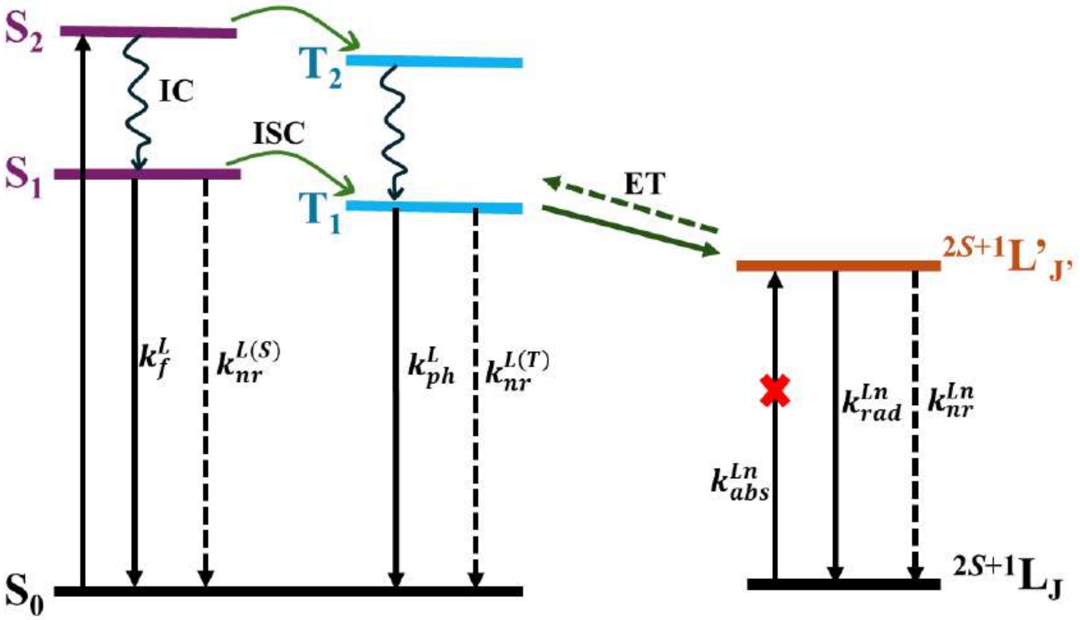

Figure 1. 3 Scheme of the sensitization effect (or the antenna effect) with a simplified Jablonski diagram. IC, ISC and ET stands for internal conversion, intersystem crossing and energy transfer respectively. In order to simplify the Scheme, only the lowest vibrational state of each S_0, S_1, S_2, T_1, T_2, $^{2S+1}L'_{J'}$ and $^{2S+1}L_J$ electronic state is considered. However, the higher in energy vibrational states of each electronic state must not be forgotten when considering the sensitization mechanism as in Figure 1.2.

A mechanism of direct sensitization of the lanthanide cation from the excited singlet state of the ligand was proposed by Weissman in 1942 whom reported the first description of lanthanide sensitized luminescence through intermolecular energy transfer from an organic fluorophore.[9] Thereafter, Dexter[10] and Crosby[11] introduced the role of the triplet state into the sensitization mechanism, although it was not until the later 1980 when Sabbatini and Lehn referred to the phenomenon as the antenna effect.[12,13]

It is important to note that the ligand triplet states should be utilized in the emission processes of lanthanide complexes as it is evident by their long emission lifetimes compared to the singlet state. Actually, in the sensitization process, the lowest triplet state from the ligand is typically involved to improve energy transfer efficiency because it minimizes energy loss through internal conversion.[14] However, the significance of alternative $S_1 \rightarrow {}^{(2S+1)}L'_{J'}$ routes have also gained recognition after being considered less important. Reports highlighting the relevance of multiple donor states, or even a dominant singlet energy transfer have increased significantly, and several systems are now well-characterized.[15,16,17]

As above mentioned, once the triplet state is populated, the energy transfer (ET) to the lanthanide (III) excited state may proceed by two different mechanisms. The Förster resonance energy transfer (FRET)[18] and the Dexter electron transfer.[19] Both mechanisms describe the ET from a donor (D) to an acceptor (A). The FRET mechanism relies on the Coulombic interactions and a dipole-dipole coupling. In this mechanism an electron from the A molecule found in the ground state is promoted to its excited state (A*). Then the electron from the excited donor molecule (D*) returns to the ground state releasing a virtual photon, Figure 1. 4, top. On the other hand, the Dexter mechanism involves an exchange of electrons between the excited and ground state of the D* and A molecules. The excited D* transfers an excited electron to the A which at the same time transfers an electron found in A ground state to the D ground state, Figure 1. 4 bottom.

Both mechanisms depend on the overlap of the Donor and Acceptor energy levels and the distance between them. However, they differ in how the energy transfer rate decreases with distance. In Dexter mechanism, the energy transfer rate decreases exponentially with increasing distance (r) between D and A, whereas the FRET mechanism's efficiency decreases with $1/r^6$. Consequently, the FRET mechanism does not require the donor and acceptor to be in close contact, they only need to be within a sufficient distance for energy transfer to occur.

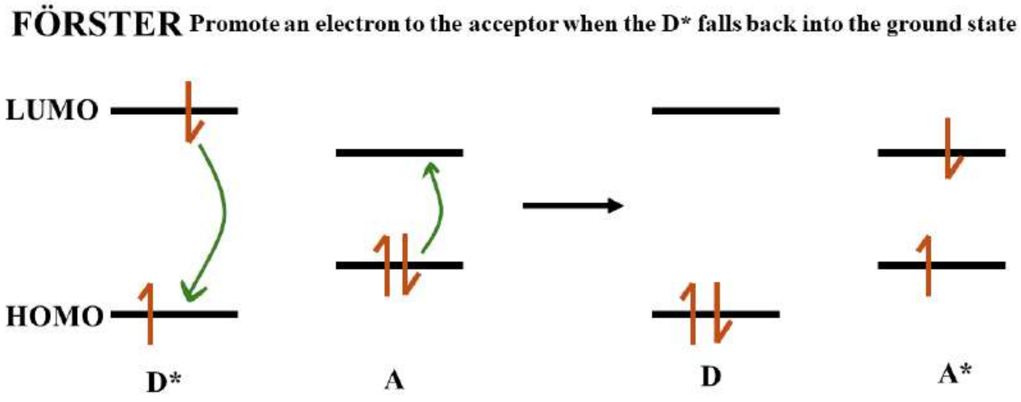

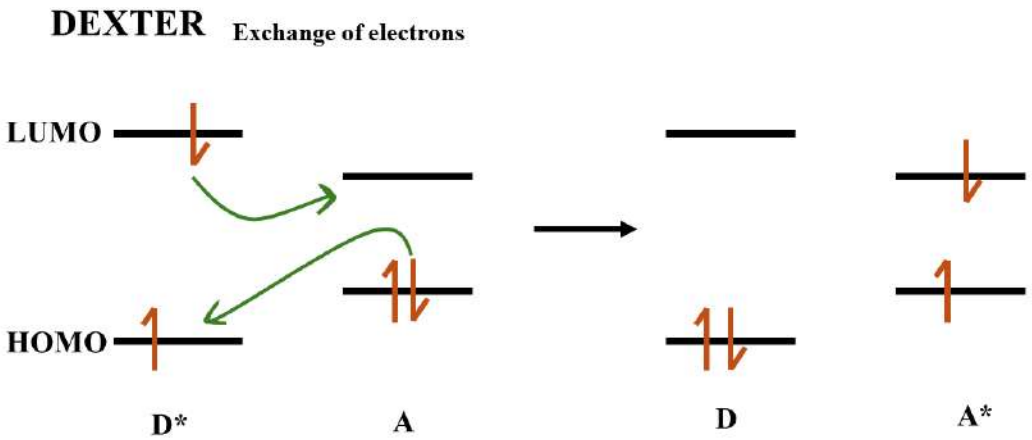

Figure 1. 4 Top, Dexter mechanism and bottom, Förster energy transfer mechanism.

Furthermore, in certain cases, a charge transfer can take place between the ligand (acting as the sensitizer) and the acceptor (trivalent lanthanide cation) in lanthanide complexes, termed a ligand-to-metal charge transfer (LMCT) transition. Conversely, metal-to-ligand charge transfer (MLCT) is less frequent due to the high ionization energies of the Ln^{3+} metals. Usually, the reduced lanthanide ion is re-oxidized by transferring an electron back to the oxidized ligand, similar to the Dexter mechanism. Moreover, in solid polycrystalline samples, ligands commonly interact via π-stacking, hydrogen bonding and other Van der Waals forces, inducing ligand-to-ligand charge transfer (LLCT) transitions. These transitions, including LLCT, LMCT and MLCT, typically have lower energies than intraligand absorption. LLCT is particularly relevant for lanthanide ions coordinated to organic chromophores and is favoured in solid state, whereas some cases of LMCT are reported in the literature due to the easily reducible character of Eu^{3+} and Yb^{3+} ions to Eu^{2+} and Yb^{2+}, respectively.[20,21]

Moreover, the spin forbidden ISC transition between $S_1 \rightarrow T_1$ energy states (as well as $T_1 \rightarrow S_1$ phosphorescence transition, which it can also be a drawback) can be favoured by the presence of heavy atoms in the so-called heavy atom effect. Adding the heavy atom may increase the spin-orbit coupling within the atom and the nearby atoms. This enhancement in coupling improves the mixing of singlet and triplet states that will lead in a less strict spin selection rule making the $S_1 \rightarrow T_1$ transition more effective. This effect occurs not only with lanthanide atoms but also in presence of other heavy metals.[22] However, it should be taken into account that the presence of a heavy atom increases $S_1 \rightarrow T_1$ efficiency as well as $T_1 \rightarrow S_0$ phosphorescence which can be a drawback in terms of sensitization.

Finally, in luminescent lanthanide coordination complexes, two kinds of chromophore ligands are generally employed to carry out the role of the sensitizer. First, organic molecules in which the chromophore is directly coordinated to the lanthanide such as aza-aromatic compounds (2,2'-bipyridine, 1,10-phenantroline, terpyridine, etc.) or phenolate ligands. The proximity of the chromophore group to the emitting lanthanide centre makes this design effective. Besides, sensitized luminescence can also occur if the chromophore is not directly coordinated to the lanthanide cation but is found as part of the ligand. For example, a coordinating unit such as diethylenetriamine pentaacetate or a cyclen moiety in which one or more positions are substituted by a chromophore group. However, the increased distance between the chromophore and the Ln^{3+} may reduce sensitization efficiency. Nonetheless, this ligand design offers greater versatility in choosing the chromophore of the lanthanide coordination compound.[4,23]

1.2.3 Quenching phenomena

Back transfer energy

As seen in the sensitization mechanism, the lanthanide ion can be de-excited via nonradiative deactivations just like any chromophore system. If the excited states of the sensitizer are too close in energy with the excited emitting level of the lanthanide(III), an energy transfer from the lanthanide ion back to the sensitizer might also be possible. Thus, the sensitizer can partially function as a quencher, along with solvent molecules or any other compounds close to the lanthanide ion. Hence, the emissive performance of the resulting lanthanide compound depends on the sensitization capacity and excited energy levels of the organic ligand. Latva *et al.*[24] proposed that the optimal energy difference between the lowest lying triplet state and Eu^{3+} emitting level ($^5D_0$: 17,267 cm^{-1}) for an efficient $S_1 \rightarrow T_1 \rightarrow {}^5D_0$ energy transfer should be in the range of 2,500-5,500 cm^{-1}. While for a Tb^{3+} compound the energy difference between T_1 and $^5D_4$ emitting state (20,400 cm^{-1}) should be at least 1,850 cm^{-1} to avoid back energy transfer. These are known as the Latva's rules, which are based on empirical statistics results. However, Latva's rules can only be considered in sensitization of Eu^{3+} and Tb^{3+} lanthanide coordination compounds.

Quenching of the ligand triplet state

Preventing the quenching of the triplet state in the sensitizing ligand is crucial for efficient energy transfer to the trivalent lanthanide cation. The triplet state, which has longer lifetimes than the singlet state, can be quenched by molecular oxygen through a triplet-triplet annihilation process. This process involves a collision where there is an energy transfer between the excited triplet state of the ligand to the triplet ground state of the oxygen. Consequently, the ligand returns to the ground singlet state (S_0) while the oxygen is excited to its singlet state. Moreover, the rate at which triplet oxygen quenches the triplet states of organic molecules and the amount of singlet oxygen produced after quenching, depend on several factors. These include the energy of the organic molecule triplet state as well as the nature of its excited state, the redox potential of the excited state and the polarity of the solvent where the molecules are dissolved.[25]

The triplet state quenching of the oxygen can occur, but it is usually reduced if the energy transfer from the ligand's triplet state to the lanthanide is rather quick and efficient. If quenching by triplet oxygen becomes a problem in luminescence of our lanthanide system, removing the oxygen from the environment can effectively prevent this issue.

Presence of high energy oscillators (multiphonon relaxation)

The presence of high energy oscillators C-H, N-H and especially O-H from the ligands and/or from coordinating solvent molecules can effectively quench the lanthanide luminescence. Quenching is achieved through several vibrational quanta from the bound molecules (solvent or surrounding ligand) and/or through overtones of the implied vibrations.

For the visible emitters Tb^{3+} and Eu^{3+}, quenching of the luminescence due to high energy bond oscillations is mainly affected by quenching through the O-H oscillators in presence of coordinating H_2O molecules or when dissolved in aqueous medium. In case of the Tb^{3+}, it is less sensitive to quenching through O-H oscillations than other lanthanide ions because of its larger energy gap. Whereas the third harmonic (ν_3) of the O-H stretching vibration effectively quenches the $^5D_0$ emitting state of Eu^{3+} (ν_1 of water is 3,657 cm^{-1}). The energy difference between $^7F_6$ from the $^7F_{J=0-6}$ ground and the $^5D_0$ excited state of Eu^{3+} is 12,297 cm^{-1}.[23] Interestingly, reports found in the literature have demonstrated that the quenching ability of the O-H vibrations are considerably attenuated when the water molecules coordinated to the lanthanide(III) are involved in strong intra or inter-molecular H-bonding within the crystal lattice.[26]

Moreover, luminescence of the nIR emitting lanthanides among them Nd^{3+}, Er^{3+} and Yb^{3+}, is also significantly quenched by multiphonon relaxation due to vibronic coupling with O-H vibrations as well as C-H and N-H. The emission quantum yields and luminescence lifetimes of these nIR cations are lower compared to the Eu^{3+} and Tb^{3+} ones, due to the lower energy gap between the emitting excited state and the ground state that confers more probability to non-radiative deactivation. Hence, these lanthanides with lower energy gaps are more susceptible to the O-H, C-H and N-H vibrations, because the energy at which these bonds oscillate is in resonance with the energy from the nIR emitting states. For instance, the second order C-H stretching vibration (ν_2) oscillates at an energy close to the energy gap between $^4I_{13/2}$ excited state and $^4I_{15/2}$ ground state of Erbium(III). Similarly, the O-H stretching vibration (ν_3~10.971 cm^{-1}) effectively deactivates ytterbium's emitting state because its energy is close to the gap between the $^7F_{5/2}$ (~10,288 cm^{-1}) excited state and the $^7F_{7/2}$ ground state. These bonds are common in organic chromophores used as sensitizers and so they can become a problem in the obtaintion of efficient nIR emission from the lanthanides.

A solution to reduce the quenching effect produced by the presence of high energy oscillators is deuteration of the sample. Furthermore, a more effective solution is fluorination of the C-H bonds of the organic moiety, or at least, fluorination of the C-H bonds closer to the lanthanide. C-D and especially C-F oscillate at lower frequencies, reducing this way the impact of quenching of the lanthanide emitting state due to multiphonon relaxation. Additionally, encapsulating lanthanides in confined inorganic cavities, such as zeolites, has been shown to improve Er^{3+} luminescence. This improvement is due to the reduction of non-radiative deactivation due to the absence of C-H bonds near the lanthanide cation.[6,27]

Finally, the non-radiative deactivation through multiphonon relaxation due to O-H, C-H and N-H bonds is temperature dependent. Thus, this quenching phenomenon should be effectively reduced at lower temperatures.[23] If the luminescent properties do not improve with varying temperature, it suggests that multiphonon relaxation is not an important contribution of the quenching effect in the measured system.

1.2.4 Emission Quantum Yield and luminescence lifetimes

The emission efficiency of a compound is generally quantified by the emission quantum yield (Φ_{em}). It considers the relationship between the absorbed photons (N_{abs}) and the emitted photons (N_{em}) of the luminescent compound as shown in Equation1.1. A Φ_{em} yielding the unity value would indicate that all the absorbed photons are then emitted through radiative deactivation from the excited state whereas a value of 0 would indicate that deactivation of the excited state is taking place through non-radiative processes.

$$\phi_{em} = \frac{N_{em}}{N_{abs}} \quad \textbf{Equation 1.1}$$

In a luminescent lanthanide coordination compound where luminescence takes place via the sensitization effect, the overall quantum yield (Φ_{Ln}^{L}) is defined as the result of multiplying the intrinsic quantum yield (ϕ_{Ln}^{Ln}) by the sensitization efficiency (η_{sens}) as follows in Equation 1.2.

$$\Phi_{Ln}^{L} = \eta_{sens} \cdot \Phi_{Ln}^{Ln} \quad \textbf{Equation 1.2}$$

The sensitization efficiency (η_{sens}) accounts to the percentage of photons absorbed by the ligand transferred to the excited state of the lanthanide ion and it comprises the relative efficiencies of both, the intersystem crossing (η_{ISC}) and energy transfer (η_{ET}) mechanisms, Equation 1. 3.

$$\eta_{sens} = \eta_{ISC} \cdot \eta_{ET} \quad \textbf{Equation 1.3}$$

The other step that elucidates the ϕ_{Ln}^{L} is the intrinsic quantum yield (ϕ_{Ln}^{Ln}) that refers to the quantum yield once the emitting level of the Ln^{3+} ion is populated, and it can be expressed as the radiative decay (k_{rad}) from the excited lanthanide to the non-radiative decay ($k_{non-rad}$) as in Equation 1.4.[4,28]

$$\phi_{Ln}^{Ln} = \frac{k_{rad}}{k_{rad}+k_{non-rad}} \quad \textbf{Equation 1.4}$$

Furthermore, in luminescent compounds, the time-resolved luminescence reveals that emission intensity diminishes as a function of time after exposure of a pulsed excitation. Generally, the emission decreases following a monoexponential law with time. This emission decay corresponds to the observed deactivation rate constant of the excited state (k_{obs}). This constant is defined by the sum of the radiative rate constant and the non-radiative rate constant, Equation 1.5.

$$k_{obs} = k_{rad} + k_{non-rad} \quad \textbf{Equation 1.5}$$

Moreover, the deactivation rate constant can be expressed as lifetime, Equation 1.6.

$$\tau_{obs} = 1/k_{obs} \quad \textbf{Equation 1.6}$$

Then, by combining Equations 1.4, 1.5 and 1.6, the relation of the intrinsic quantum yield with the observed and radiative lifetimes can be expressed as in Equation 1.7.

$$\phi_{Ln}^{Ln} = \frac{\tau_{obs}}{\tau_{rad}} \quad \textbf{Equation 1.7}$$

For a luminescent lanthanide coordination compound, the overall quantum yield can be measured experimentally by means of a method that uses a well characterized reference. This method is time consuming, it needs a reference emitting in a similar range as the studied compound and it can only be measured in solution.[29] The use of an integrating sphere equipped with a multichannel spectrometer permits the measurement of the quantum yield based in an absolute method.[30] On the other hand, luminescence lifetimes can be measured with the time-resolved phosphorescence mode exciting the sample with a pulsed lamp. With this equipment luminescence lifetimes lower than around 9 microseconds are not able to measure. To measure lifetimes lower than 9 microseconds other instrumentation equipped with single phonon counting spectrometer with microsecond pulse lamp as the excitation is needed.[31]

The sensitization efficiency as well as the intrinsic quantum yield and the radiative lifetime may be more difficult to estimate. However, for the special case of Eu^{3+}, τ_{rad} can be calculated through a simpler equation presented by Werst *et al.*[32] and experimentally validated by other researchers.[29,33,34] Due to the rare property of the pure magnetic dipole transition of the Eu^{3+} ion ($^5D_0 \rightarrow {}^7F_1$) which intensity is practically independent of the chemical environment, τ_{rad} can be calculated with Equation 1.8. Then only the corrected emission spectrum of the europium compound is needed. It is important to use the corrected spectrum to take into account the sensitivity function of the detector.

$$\frac{1}{t_{rad}} = A_{MD,0} \cdot n^3 \cdot \left(\frac{I_{TOT}}{I_{MD}}\right) \quad \textbf{Equation 1.8}$$

In Equation 1.8, $A_{MD,0}$ is a constant (14.65 cm^{-1}), n is the refractive index and $\frac{I_{TOT}}{I_{MD}}$ is the ratio between the total integrated area measured from the corrected Eu^{3+} emission spectrum (I_{TOT}) to the integrated area of the pure magnetic dipole transition $^5D_0 \rightarrow {}^7F_1$ (I_{MD}). Once the τ_{rad} value is obtained, the intrinsic quantum yield as well as the sensitization efficiency of the particular Eu^{3+} coordination compound is calculated.

1.2.5 Emission of the trivalent lanthanide ions

One of the most interesting features about trivalent lanthanide ions is that their emission is comprised in a wide spectral range of energies from the Visible to the near Infrared (nIR) range and as already commented, their characteristic narrow bands make each lanthanide's spectrum unique. The trivalent lanthanide cations that can show luminescence are Ce^{3+}, Pr^{3+}, Nd^{3+}, Sm^{3+}, Eu^{3+}, Tb^{3+}, Dy^{3+}, Ho^{3+}, Er^{3+}, Tm^{3+} and Yb^{3+}. The La^{3+} and Lu^{3+} cations don't show luminescence due to their electronic configuration. The La^{3+} doesn't have electron occupation in the *f* orbital whereas it is fully occupied in Lu^{3+}. Moreover, Gd^{3+} with a half-filled 4*f* configuration, shows the highest energy gap between the excited state ($^6P_{7/2}$ ~32,500 cm^{-1}) and the ground state ($^8S_{7/2}$) among all the lanthanide(III). Sensitization of Gd^{3+} through organic chromophores does not take place because the excited state of the ligand molecules is usually found in an energy level lower than the $^6P_{7/2}$ gadolinium's$^+$ excited state.

Compounds with Ce^{3+} can show strong emission in the blue range. In contrast to the rest of Ln^{3+} ions, this observed fluorescence is due to a transition between the 5*d* to the 4*f* orbital. Due to its symmetry allowed character, emission assigned to this transition is rather intense and because of the 5*d* participation in this emission, its appearance strongly depends on the coordination environment.[35]

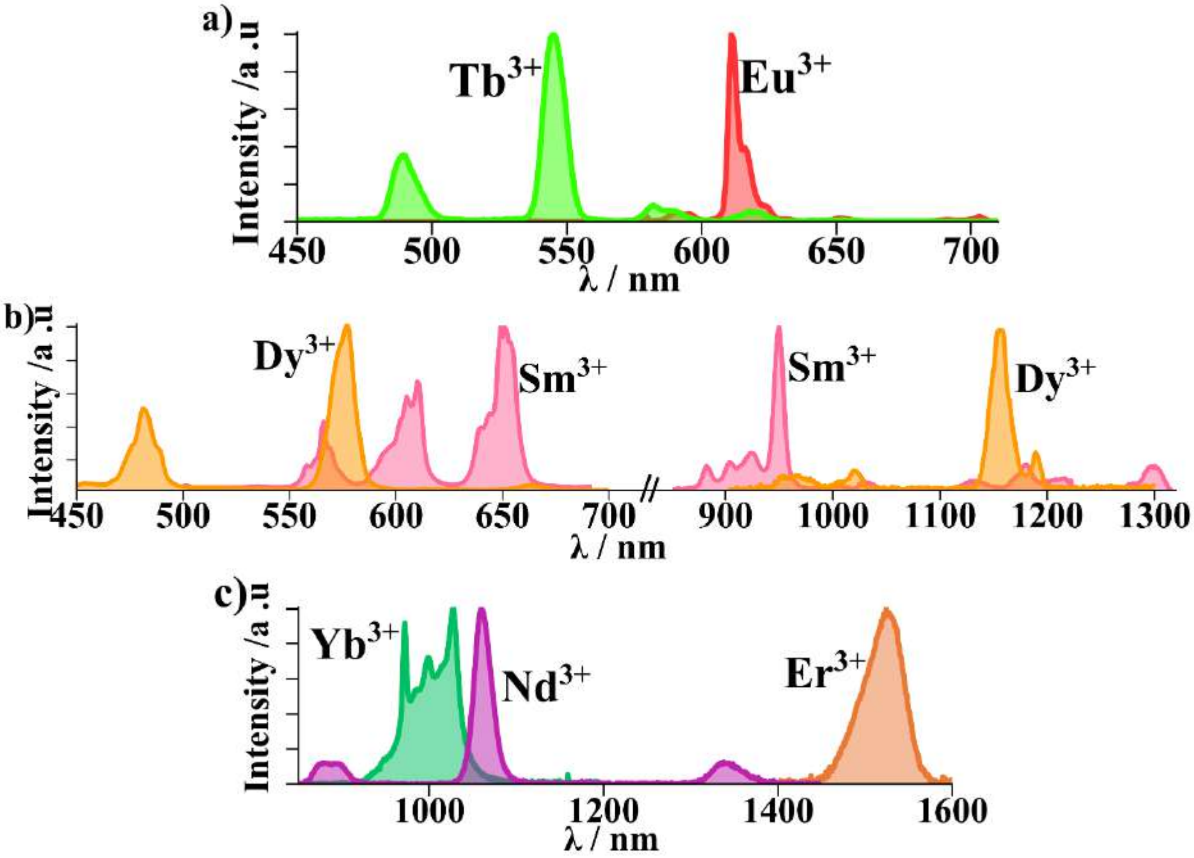

Figure 1. 5 Emission spectra of a) Tb^{3+} and Eu^{3+} in the visible range b) Dy^{3+} and Sm^{3+} in both, Visible and nIR range and c) Yb^{3+}, Nd^{3+} and Er^{3+} in the nIR range. All the emission spectra have been obtained from compounds presented in this *Thesis* work.

On the other hand, Tb^{3+} and Eu^{3+} cations are the lanthanides showing emission purely in the Visible range leading to green and red emission, respectively, Figure 1. 5a). Moreover, emission of Pr^{3+}, Sm^{3+}, Dy^{3+}, Ho^{3+} and Tm^{3+} can occur both, in the Visible and in the nIR range. Emission spectra of Dy^{3+} and Sm^{3+} are shown in Figure 1. 5b). However, the emission of Pr^{3+} and Tm^{3+} is rather weak. To obtain luminescence spectra from these cations, first, the chromophore ligands as well as the coordination environment, must be well design. On the other hand, Nd^{3+}, Er^{3+} and Yb^{3+}, emit in the nIR range, Figure 1. 5c).[4,5]

The highest emission quantum yields are presented by Tb^{3+} and Eu^{3+} coordination compounds while concerning emission in the nIR, Yb^{3+} is the one showing better performance.[23]

If the emission spectra are recorded at low temperatures, the hyperfine structure can be observed for each emission band and $2J+1$ components generated due to crystal field perturbation (all of them or some of them depending on the symmetry point group around the Ln^{3+} centre) can be well discerned and structural information from the spectroscopic measurements can be obtained.

Interestingly, coordination compounds containing the Gd^{3+} cation can be used to extract information about the excited energies of the chromophore ligands. Due to the heavy atom effect, the ISC between the S_1 and T_1 states of the ligand is favoured, making them easier to be observed. Then from the edge of the absorption spectrum of the Gd^{3+} compound, the energy of the lowest singlet S_1 state can be extracted. Whereas the lowest lying triplet state T_1 can be measured from the phosphorescence spectrum of the same Gd^{3+} sample at low temperatures (at liquid nitrogen, 77 K or lower). The 0-phonon transition in the phosphorescence spectrum is assigned to the T_1 state, Figure 1. 2. By characterizing the S_1 and T_1 states of our system, we could know about the ISC effectiveness. Also, knowing the T_1 state can provide information about back energy transfer as well as get insights into the sensitization mechanism of the considered system. These analyses can also be performed for the La^{3+} and Lu^{3+} or even Y^{3+} analogues. However, the difference on the ionic radius of La^{3+} and Lu^{3+}, which are at each extreme of the lanthanide series, may induce different structural motifs compared to the coordination system in which we want to study the sensitization mechanism.[16,36]

The rather long luminescence lifetimes as well as the narrow emission bands presented by Ln^{3+} coordination compounds, makes them good candidates to be used as biomedical sensors for biomedical imaging and sensitization, in bioanalytical applications, in electroluminescence devices, in photovoltaics, in telecommunications or in inks and security markings, among other.[23,37-40]

1.2.6 Chirality in lanthanide systems

Chiral molecules exist as a pair of non-superimposable mirror-image isomers, also known as enantiomers. Usually, enantiomers possess identical physical and chemical properties except for how each enantiomer interacts with polarized light of other chiral molecules. Characterization of chirality is of great relevance in pharmaceutic industry.[41] When it comes to characterize one enantiomeric compound, single crystal X-Ray diffraction is the absolute method to know the structure. Chiroptical spectroscopies such as Circular Dichroism (CD) and Circularly Polarized Luminescence (CPL) are convenient tools to study the compound's optical activity.

CD consists of a differential absorption (ΔA) of the left- and right-handed circularly polarized light. According to Beer's law, ΔA can be expressed as in Equation 1.9.

$$\Delta A = \Delta\varepsilon \cdot l \cdot C_x \quad \textbf{Equation 1.9}$$

Where $\Delta\varepsilon$ is the molar extinction coefficient, C_x is the concentration of the measured sample and l is the path length. A positive CD signal denotes that left-handed circularly polarized light is absorbed to a greater extent than the opposite and vice versa. A racemic sample shows no CD signal. CD spectroscopy gives chiroptical information on the ground state of the chiral sample. This spectroscopic technique allows the analysing of the secondary structure or the specific conformation of macromolecules such as proteins upon changes in the molecular environment, pH or temperature. Each chiral compound has its own chiral fingerprint.

On the other hand, CPL spectroscopy is the emission analogue to CD as fluorescence is to absorption. It is a more sensitive chiroptical technique as it is able to reflect the changes in the proximal environment of the local chiral structure. It probes the excited-state properties of a chiral luminescent system by measuring the difference in emission intensities of the left and right-handed circularly polarized light emitted by the luminescent chiral sample. In the CD technique, it is necessary for the chiral compound to absorb at some wavelength within the UV-Visible range. However, to measure CPL properties, the compound must not only induce chirality to the structure but also it must be luminescent. This implies designing chiral lanthanide coordination compounds showing efficient sensitization effect that can lead to Ln^{3+} emission.[42]

CPL properties are characterized by means of the dissymmetry factor (g_{lum}) with Equation 1.10.

$$g_{\mathrm{lum}} = 2\frac{I_L - I_R}{I_L + I_R} = 2\frac{\Delta I}{I} \quad \textbf{Equation 1.10}$$

Where I_L and I_R are the left- and right- handed intensities of the circularly polarized light of the chiral luminescent sample. A g_{lum} of 0 indicates no circular polarized emission while the maximum value of g_{lum} yields 2.

Furthermore, the sign and magnitude of CPL optical activity is governed by the rotatory strength (R_{ij}) of an *i*→*j* transition, Equation 1.11.

$$R_{ij} = |\mu_{ij}||m_{ij}|cos\theta_{ij} \quad \textbf{Equation 1.11}$$

Where μ_{ij} and m_{ij} are the electric-dipole (ED) and magnetic-dipole (MD) transition vectors, respectively, and θ_{ij} is the angle between μ_{ij} and m_{ij} vectors.

Now, as mentioned before (*Section 1.2.1*), *f-f* transitions are electrical dipole forbidden transitions resulting in R_{ij}=0. However, the ED transitions become less prohibited due to coupling mechanism when an asymmetric environment is applied around the emitting Ln^{3+} ion. When the Ln^{3+} is coordinated to ligand molecules conferring a distorted crystal field, the interconfigurational mixing of the 4*f* and 5*d* orbitals provides odd-parity interactions leading to the lanthanide transitions less prohibited, therefore R_{ij} would become non-zero. Let remember that the majority of Ln^{3+} emission transitions are predominantly of ED nature except of $^5D_0 \rightarrow {}^7F_1$ transition of the Eu^{3+} cation which is of purely MD nature.

The relationship between R_{ij} and g_{lum} of a *i*→*j* transition can be represented by Equation 1.12.

$$g_{\mathrm{lum}} = 4\frac{R_{ij}}{D_{ij}} = 4\frac{|\mu_{ij}||m_{ij}|}{|\mu_{ij}|^2 + |m_{ij}|^2}cos\theta_{ij} = 4\frac{|m_{ij}|}{|\mu_{ij}|}cos\theta_{ij} \quad \textbf{Equation 1.12}$$

D_{ij} accounts for the dipole strength of the transition which is defined as $D_{ij} = |\mu_{ij}|^2 + |m_{ij}|^2$. Assuming that the total CPL intensities are attributed to transitions with predominantly electric dipole interaction mechanisms, we could do the approximation of D_{ij} to $|\mu_{ij}|^2$.[43]

Consequently, the mathematical expression of g_{lum} implies that transitions allowed by magnetic dipole but forbidden by electric dipole will result in larger values of g_{lum}. This is the case of chiral Eu^{3+} compounds presenting CPL properties, where the highest g_{lum} value is generally assigned to the MD $^5D_0 \rightarrow {}^7F_1$ transition. Whereas transitions allowed by both magnetic and electric dipole mechanisms are likely to generate high CPL intensities.

Most chiral organic fluorophores have high fluorescence quantum yields, however they generally exhibit low g_{lum} ($<10^{-2}$) values because emission in those systems is governed by ED transitions.[44] Whereas for europium(III) compounds, g_{lum} up to +1.38 (in chloroform solution) has been observed for the MD $^5D_0 \rightarrow {}^7F_1$ transition.[45]

In lanthanide coordination compounds the highest g_{lum} values are observed for the Eu^{3+} compounds but CPL properties are also studied for compounds containing Sm^{3+}, Tb^{3+} and Dy^{3+}.[46-48] Moreover, CPL properties have been measured in solution for the Yb^{3+} nIR emitter in the 900-1040 nm range and the highest $|g_{\mathrm{lum}}|$ values reported in the literature are 0.38 and 0.31 for an Yb^{3+} enantiomeric pair with formula $[CsYb((+/-)\text{-hfbc})_4]$, where hfbc is the 3-heptafluorobutylyryl camphorate.[49]

Moreover, in CPL spectroscopy just as in luminescence spectra, the splitting of each *J* level due to crystal field perturbation can be differentiated. For instance, in CPL spectrum of a chiral Eu^{3+} coordination compound, the band assigned to $^5D_0 \rightarrow {}^7F_1$ transition can split into a maximum of $2J+1$ components (-1, 0, +1). If the three components are differentiated in such compounds, each one might present opposite sign. This feature make luminescence chiral compounds very interesting for application as sensors in molecular recognition[50] In addition, chiral lanthanide(III) coordination compounds are of great current interest for other applications such as Circularly Polarized organic light-emitting diodes (CP-OLEDs)[51] and anti-counterfeiting devices.[52]

Generally, the obtention of these chiral coordination compounds, can be achieved through several synthetic strategies in coordination chemistry:

i) Disruption of Symmetry: Chirality can be induced by disrupting the symmetry of the coordination complex. This can be achieved by using asymmetric ligands or creating steric hindrance, leading to a non-symmetric arrangement around the metal center.

ii) Chiral Induction: Chiral induction involves using a chiral environment, such as chiral solvents or catalysts, to influence the formation of a chiral complex. The chiral surroundings guide the complex to favor one enantiomer over the other through non-covalent interactions.

iii) Addition of a Chiral Ligand: The most straightforward method to induce chirality is by incorporating chiral ligands into the coordination sphere of the metal center. Chiral ligands are molecules that possess inherent chirality, such as those with asymmetric carbon atoms or chiral centers. When these ligands coordinate to the metal, they induce their chirality to the entire complex. Examples of chiral ligands include chiral phosphines, amines, and carboxylates. This synthetic strategy is the one considered in the presented work, specifically using chiral carboxylates as ligands. Moreover, to increase and ensure good luminescence properties, an extra non-chiral chromophore ligand can be added to the final system. It will provide with good sensitization efficiency to the emitting trivalent lanthanide ion.

Finally, the vast majority of CPL reports of lanthanide compounds are measured for mononuclear Eu^{3+} complexes, while it is more rarely investigated for complexes with higher nuclearity, such as binuclear helicates[53] or trinuclear,[54] heptanuclear[55] as well as in polymeric[56] systems. Most of these measurements are found in solution while CPL properties measured in the polycrystalline samples remain rare. However, for these compounds to be used in chiral materials or as part of OLED devices, the CPL properties should remain in the solid state.

1.2.7 Organic Light-Emitting diode (OLED) devices

A very interesting application of luminescent lanthanide compounds is to use their characteristic luminescence properties into the emissive layers of Organic Light-Emitting diode (OLED) devices. An OLED device is a display that emits light after the application of a potential difference thus it is based in the electroluminescence phenomenon. This emission light comes from an organic light-emitting material that is packed between the two electrodes (anode and cathode). The research on highly emissive compounds for OLED devices has been focused on pure organic dyes and transition-metal complexes owing to the suitable emission properties for optoelectronic modulation. However, emission spectra of these organic dyes and transition metal complexes present broad bands due to their complex electronic transitions. The broader nature of the emission bands excludes most of these complexes into the research of high-definition displays with narrow emission bands and high color purity. Nevertheless, luminescence compounds containing trivalent lanthanide cations are well characterized by its sharp bands from the *f-f* transitions and so, phosphors with high color purity emission can be obtained.[23]

To improve charge carrier transport, additional layers are added to the emissive layer. The components resulting in an OLED device are depicted in Figure 1. 6. The different layers are comprised between the anode (bottom) and the cathode (top). The bias voltage is applied between the anode and cathode, then holes are injected from the anode and transported in the hole transport layer (HTL) whereas electrons are provided in the cathode and transported in the electron transport layer (ETL). The charge carriers (electrons and holes) meet at the emissive layer and recombine, exciting the emissive layer material leading to electroluminescence. Moreover, a hole injection layer (HIL) between the anode substrate and the HTL, and an electron injection layer (EIL) between the cathode substrate and the ETL can be added to improve hole and electron injection. At least one electrode should be transparent for visible light. In most cases, indium tin oxide (ITO) is used as transparent anode. Generally, the layers are added one on top of the other to mount the device, by thermal evaporation or spin coating. In thermal evaporation, the material should be thermally stable and volatile while in spin coating, solubility of the compound is more important.

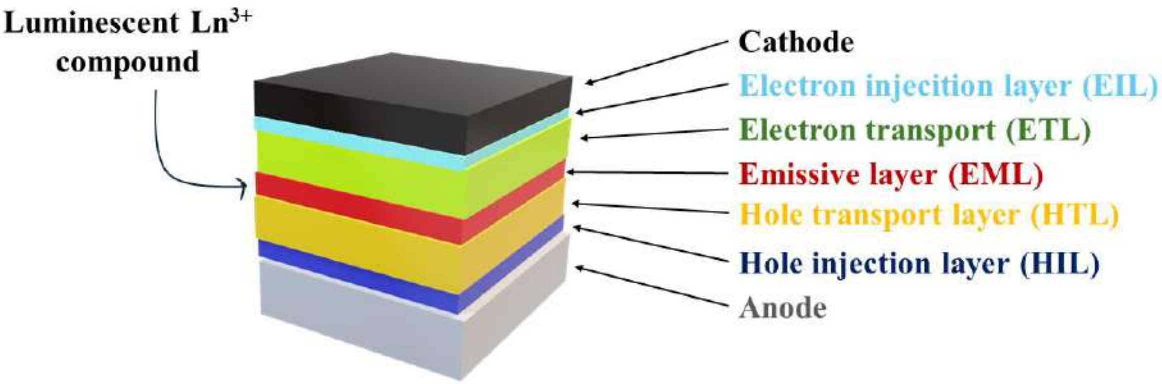

Figure 1. 6 Layer sequence in an OLED device

In *Section 2.3* of *Chapter 2* of this work, two OLED devices are prepared from two different lanthanide coordination compounds containing Europium and Ytterbium respectively.

The OLED's optoelectrical characteristics are measured by three basic parameters:

i) Drive voltage (V) which is the threshold voltage at a luminance of 1 cd m^{-2}. It is commonly defined as the turn-on voltage which is the voltage applied to the OLED device to power them.

ii) Current density (mA cm^{-2})

iii) Luminance (cd m^{-2}): which is defined as the intensity of light emitted from a surface per unit area in each direction. Thus, luminance is an indicator of how bright the surface will appear. For computer screens and fluorescent lamps, 100 and 1000 cd m^{-2} are regarded as suitable levels of luminance for practical display and lighting, respectively.

Then the electro-optical conversion efficiency of OLEDs is determined by:

i) Current efficiency (CE, η_A) defined as the ratio of luminance to current.

ii) Power efficiency (PE, η_P) defined as the ratio of luminance to electrical power.

iii) External quantum efficiency (EQE, η_E) defined as the ratio of photons out of the device to the number of injected electrons.[57]

1.3 Molecular magnetism

1.3.1 Magnetism and Curie Law

Molecular magnetism studies how a molecule (for instance a radical or a metal) interacts with an external magnetic field to generate the sates described by the Zeeman Hamiltonian.[58] The applied magnetic field in which researchers work to study the molecular magnetism properties of a substance is low, of the order of cm^{-1}, therefore only the states derived from the electronic ground term are studied. The ground state population closely depends on temperature and Boltzmann distribution.

When an external magnetic field ($\vec{H}$) is applied to a substance containing unpaired electrons, the magnetic field measured inside the sample is different from the free magnetic field. This is known as magnetic induction ($\vec{B}$), Equation 1.13:

$$\vec{B} = \vec{H} + \Delta\vec{H} \quad \textbf{Equation 1.13}$$

The variation in the $\vec{H}$ is produced because of the magnetization ($\vec{M}$) of the sample which accounts to the magnetic moment density (μ) oriented with $\vec{H}$. The complete orientation of the magnetic moments of the molecule, in some cases, can be observed at low temperatures. At higher temperatures, the thermal energy tends to oppose the coherence between the orientations of the magnetic moments, Equation 1.14.

$$\vec{B} = \vec{H} + 4\pi\vec{M} \quad \textbf{Equation 1.14}$$

A diamagnetic compound where all electrons (of the inner and valence shell) are paired will repel the external magnetic field whereas a paramagnetic compound, which contains unpaired electrons in the valence shell, will be attracted by the external magnetic field. In the paramagnetic sample, the unpaired electrons will align parallel to and in the same direction as $\vec{H}$ making $\vec{B}>\vec{H}$.

In molecular magnetism, the magnetic susceptibility parameter (χ) is commonly used. It relates the variation of the magnetization of the sample with the applied magnetic field. Under conditions of rather low magnetic fields and low temperatures, χ can be defined as in Equation 1.15.

$$\chi = \frac{\vec{M}}{\vec{H}}$$ **Equation 1.15**

In molecular magnetism, the molar magnetic susceptibility (χ_M) is commonly used, and it is defined as in Equation 1.16:

$$\chi_M = \chi \frac{W_M}{\rho}$$ **Equation 1.16**

Where W_M is the molecular weight of the sample (g·mol^{-1}) and ρ accounts to the density in (g·cm^{-3}). Thus, the χ_M units are cm^{3}mol^{-1}.

Furthermore, due to the unpaired electrons found in the inner shell of the atoms, a sample with unpaired electrons always will exhibit a certain diamagnetic character. Thus, the total measured susceptibility corresponds to the sum of both, diamagnetic and paramagnetic contributions. The diamagnetic contribution always has a negative value, whereas the paramagnetic contribution implies positive values. Therefore, when the susceptibility of a paramagnetic sample is calculated, the diamagnetic contribution is neglected, Equation 1.17.

$$\chi_{Para} = \chi_{Meas} - \chi_{Dia}$$ **Equation 1.17**

Diamagnetic of each atom contained in the measured sample can be calculated from the Pascal tables[59] though it is a time-consuming process. Otherwise, an approximation can be obtained with Equation 1.18.[58]

$$\chi_{Dia} = -\frac{W_M}{2} 10^{-6}$$ **Equation 1.18**

Following to that, Curie's law describes magnetic susceptibility values for a considered isolated metal under the external magnetic field application ($\vec{H}$) and at relatively high temperatures. Curie's law defines magnetic susceptibility as in Equation 1.19:

$$\chi = \frac{M}{H} = \frac{N\,g^2\,\mu_\beta^2}{4k_BT}$$ **Equation 1.19**

Thus, molar magnetic susceptibility can be described as in Equation 1.20:

$$\chi_M = \frac{M}{H} = \frac{N\,g^2\,\mu_\beta^2}{4k_BT} \cdot \frac{W_M}{\rho}$$ **Equation 1.20**

Where N refers to Avogadro's number, μ_B is the absolute value of the magnetic moment of the *z*-component of a free ion (Bohr magneton) and k_B is the Boltzmann constant equal to 0.695 $cm^{-1}K^{-1}$.

It is of a common practice among researchers in the field of molecular magnetism to represent the temperature dependence of χ_M as the product of $\chi_M T$, therefore Curie's law is described as in Equation 1.21:

$$\chi_M T = \frac{N\,g^2\,\mu_\beta^2}{4k_B} \cdot \frac{W_M}{\rho}$$ **Equation 1.21**

The above value of $\chi_M T$ can be applied, using the Brillouin formula for magnetization, to compounds with transition metals that have an energy term with a zero-orbital component (L=0). For these compounds the magnetic moment is then described by the molecule's spin moment (S), Equation 1.22.

$$\chi_M T = \frac{N\,g^2\,\mu_\beta^2}{3k_B} \cdot \frac{W_M}{\rho} \cdot S(S+1)$$ **Equation 1.22**

In contrast, due to the non-quenched L moment of lanthanide ions, magnetism of these ions is influenced by both, the spin magnetic moment (S) and the orbital magnetic moment ($L\neq0$). Hence, for a free Ln^{3+} ion, the Curie law takes the following form, Equation 1.23:

$$\chi_M T = \frac{N\,g_J^2\,\mu_\beta^2}{3k_B} \cdot \frac{W_M}{\rho} \cdot J(J+1)$$ **Equation 1.23**

Where Landé's g-factor is described as in Equation 1.24:

$$g_J = \frac{3}{2} + \frac{S(S+1)-L(L+1)}{2J(J+1)} \quad \textbf{Equation 1.24}$$

Then, by using the above Equations (Equation 1.23 and Equation1.24), the values of $\chi_M T$ and g_J can be obtained and they are listed in Table 1. 1 for all lanthanide(III) cations. As already discussed, in Ln^{3+} ions the Spin-Orbit coupling effect is more important than the ligand field effect to determine the electronic configuration. Hence, the impact of ligand field on the static magnetic properties in lanthanide compounds is noticeable only at low temperatures, down to 2 K. At low temperatures, the thermal energy is reduced and the excited states (m_j) are not populated. Besides, at room temperature, the experimental $\chi_M T$ values of coordination compounds typically match the tabulated ones. This is because the excited m_j states are populated, then the Ln^{3+} is allowed to be treated as if it was isolated from the coordinating ligands.[60] The comparison of experimental $\chi_M T$ values to the calculated ones can confirm the Ln^{3+} composition of the studied sample, such as oxidation state, presence of other spin carriers, number of spin carriers, etc.

As seen in Table 1. 1, the experimental $\chi_M T$ values for the Eu^{3+} ion are higher than the 0 value expected for a free ion. This is because Eu^{3+} has a rather small spin-orbit coupling parameter (λ) (around 300 cm^{-1}) between the $^7F_{(0-1)}$ states. Then, at room temperature the higher energy ^7F_J states closer to the ground state are thermally populated (mainly the $^7F_1$ state) leading to a $\chi_M T$ value different from 0. A similar effect happens to the Sm^{3+} cation for which the experimental $\chi_M T$ value at room temperature is higher than the 0.09 $cm^3mol^{-1}K$ calculated for a free ion. For a Sm^{3+} ion, the ^6H ground state is split due to spin-orbit coupling by $^6H_{J=5/2-15/2}$ with a λ parameter around 200 cm^{-1}. Therefore, at room temperature, the excited ^6H_J states are also thermally populated leading to a higher value of $\chi_M T$.[61]

Table 1. 1 Compilation of electronic configuration, spectroscopic ground term, g_J and calculated and experimental room temperature magnetic susceptibility for isolated trivalent lanthanide ions.

Ln^{3+}	Configuration	Ground state	g_J	χT_{calc} (emu mol^{-1}K)	χT_{exp} (emu mol^{-1}K)
Ce	f^1	$^2F_{5/2}$	6/7	0.8	0.66–0.78
Pr	f^2	$^3H_4$	4/5	1.6	1.45–1.62
Nd	f^3	$^4I_{9/2}$	8/11	1.64	1.45–1.53
Pm	f^4	$^5I_4$	3/5	0.9	1.05
Sm	f^5	$^6H_{5/2}$	2/7	0.09	0.32
Eu	f^6	$^7F_0$	—	—	1.53
Gd	f^7	$^8S_{7/2}$	2	7.88	7.61–7.80
Tb	f^8	$^7F_6$	3/2	11.82	11.76–12.01
Dy	f^9	$^6H_{15/2}$	4/3	14.17	13.01–14.05
Ho	f^{10}	$^5I_8$	5/4	14.07	13.26–13.78
Er	f^{11}	$^4I_{15/2}$	6/5	11.48	11.05–11.28
Tm	f^{12}	$^3H_6$	7/6	7.15	7.03
Yb	f^{13}	$^2F_{7/2}$	8.7	2.57	2.53

1.3.2 Single Molecule Magnets (SMMs)

A Single Molecule Magnet (SMM) is an isolated molecule system that below a certain temperature is able to keep the magnetization, temporally. Under application of the oscillating magnetic field, the ground state magnetic moment aligns into one of the possible directions: α or β (up-spin state or down-spin state). These are bistable states of equal energy but to switch the magnetic moment from one direction to the other, the systems need to surpass an energy barrier (ΔE). The value of ΔE corresponds to the energy difference between the excited and ground states. For a SMM molecule found at a low enough temperature, the magnetic moment will retain its orientation (for a concrete period of time) once the applied magnetic field is removed, due to the energy barrier. The energy barrier prevents reorientation towards the other bistable state and thus forces the spin to relax slower to the equilibrium state presenting slow relaxation of the magnetization, Figure 1. 7. It is crucial to understand that the SMM behaviour is an intrinsic property of the molecule itself, therefore each molecule unit can be considered as one magnet.[60] Moreover, the SMM behaviour is only present below a certain temperature called the blocking temperature (T_B). This temperature is defined as the highest temperature at which the system presents a hysteresis cycle, in plots of magnetization *vs* magnetic field. Thus, for a SMM system, a saturation magnetization and coercive field (H_c), in principle, should be also described. Open hysteresis loops up to 80 K had been reported for a Dy^{3+} compound[62] with a molecular formula of $[(Cp^{iPr5})Dy(Cp^*)]^+$, where Cp^{iPr5} is penta-iso-propylcyclopentadienyl and Cp* is pentamethylcyclopentadienyl. However, the large predominance of Quantum Tunnelling effect (presented hereafter) in most Ln-SMM systems lead to butterfly-shaped hysteresis cycles.[63] Additionally, it has been observed that T_B strongly depends on the sweep rate of the magnetic field when measuring the hysteresis loop. Consequently, T_B and H_c are generally less used to characterize Ln based SMM systems.[64]

SMM compounds are of significant interest for their potential applications in quantum computing[65], high-density memory storage[66] and spintronics,[67] among other fields, because a single molecule can act as one bit. However, due to their low temperatures and fast time scale in which slow relaxation is observed for these SMM systems, its applications are actually rather limited.

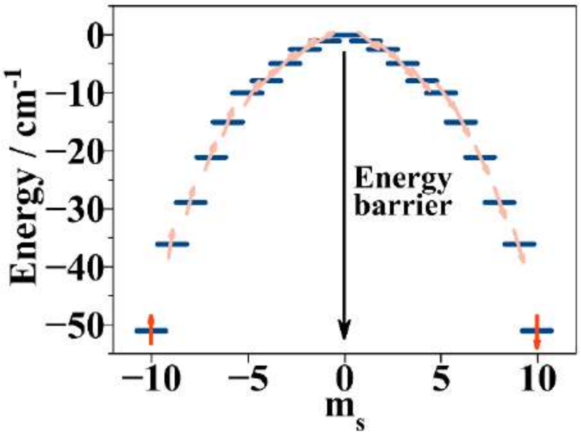

Figure 1. 7 Graphical approximation of potential energy as a function of the m_s quantum number of the Mn_{12} system.[68] The red arrow represents spin of the magnetic moment.

For a molecule containing transition metals two criteria are necessary to present a significant energy barrier between the two ground state spin configurations (α and β) and, consequently, to show SMM behaviour. First, the molecule should present a large overall ground spin state (*S*), which in transition metal compounds the *S* value can be increased by designing compounds with ferromagnetically coupled metal centres. The second requisite is to present axial magnetic anisotropy which can be provided by inducing the adequate ligand field geometry around the transition metal centres. The latter is represented with the zero-field splitting parameter (D). In this context, the energy barrier can be calculated from Equations 1.25 for an integer and Equation 1.26 for a non-integer S value.

$$\Delta E = |D|S^2 \quad \textbf{Equation 1.25}$$

$$\Delta E = |D|(S^2 - 1/2) \quad \textbf{Equation 1.26}$$

The first molecular system in which SMM behaviour was observed is a mixed valence dodecanuclear manganese (Mn^{3+} and Mn^{4+}) cluster with formula $[Mn_{12}O_{12}(CH_3COO)_{16}(H_2O)_4]$ reported in 1993[68] and previously synthesized in 1980.[69] This system is well known in the molecular magnetism community as Mn_{12} or Mn_{12}acac. Mn_{12} presented an energy barrier between the $S=\pm10$ ground state ($M_s=2S+1$) of 51 cm^{-1} and a zero-field splitting parameter of D=-0.51. With this starting point, over the last three decades, the research for new molecules with SMM properties has expanded. Numerous complexes with SMM behaviour, based on other transition metals such as Vanadium, Iron, Cobalt and Nickel ions have been discovered, along with other numerous complexes containing Manganese cations.[70]

In contrast to transition metal compounds, the 4f orbitals in trivalent lanthanide ions exhibit strong angular dependence because the 4f electrons are shielded by the full occupied $5s^2$ and $5p^6$ orbitals, hence the interaction between the lanthanide ion and the donor atoms can be considered as electrostatic in nature. Consequently, Ln^{3+} ions (with the exception of Gd^{3+}, $4f^7$ and Lu^{3+}, $4f^{14}$) display significant unquenched orbital angular momentum ($L\neq0$) and strong spin-orbit coupling in a ligand field. This results in strong single-ion anisotropies, leading to Single Molecule Magnet behaviour in mononuclear Ln^{3+} coordination complexes, known as Single Ion Magnets (SIM).[71]

The first Ln-based SIM was isolated by N. Ishikawa *et al.*[72] who designed a mononuclear phthalocyaninato-based double-decker complex of formula $[TbPc_2]^-$ (Pc=phthalocyanine) in 2003. Since then, the most studied trivalent lanthanide ions showing SMM behaviour, within the 4f series, are complexes containing Tb^{3+}, Dy^{3+} and Er^{3+} due to the large ground state magnetic moment and magnetic anisotropy that these cations present.[4,73-76] However, other less studied lanthanides such as Ce^{3+}, Nd^{3+}, Ho^{3+}, Tm^{3+} and Yb^{3+} are gaining importance and the slow relaxation of the magnetization of these compounds is also under study.[77,78]

Experimentally, SMM behaviour at low temperatures can be observed through various measurement techniques. One is in zero-field-cooled (ZFC) and field-cooled (FC) magnetization measurements. Divergence between the measured curves might indicate slow relaxation of the magnetization. Additionally, the presence of hysteresis loop in magnetization response to an external magnetic field should be necessary to have a real SMM. Furthermore, SMM also exhibit frequency and temperature dependence of the in-phase (χ_M') and out-of-phase (χ_M'') components of magnetic susceptibility measured under an alternating current (ac) magnetic field. At low temperatures, magnetization of a SMM molecule cannot remain in phase with the oscillating magnetic field, then response of the χ_M'' with temperature and frequency is observed. The latter method is the most usual when studying slow relaxation of the magnetization in a molecule, and the measurements are performed with a SQUID (Superconducting Quantum Interference Device) instrument which can measure magnetization and magnetic susceptibility from room temperature down to liquid helium (2 K) temperature.

1.3.3 Alternating current magnetic susceptibility studies

Alternating current (ac) magnetic susceptibility studies provide us information about the spin dynamics of the sample under an alternating magnetic field. With the appropriate treatment of magnetic data, information about relaxation of the magnetization of the molecule showing SMM behaviour can be extracted. This measurement consists of applying an alternating magnetic field at different oscillating frequencies in the specific temperature range. If a compound exhibits slow relaxation of the magnetization within a certain temperature range, the rate at which the spin transitions from the α to the β state, will be comparable to or match the oscillating frequency of the ac magnetic field. When this happens, the out-of-phase component of the magnetic susceptibility (χ_M'') will show a maximum. This maximum corresponds to the frequency at which the spin is no longer able to follow the oscillations of the ac field because it is being retained in a particular state due to its magnet characteristics. The maximum move to higher temperatures on increasing the frequency, Figure 1. 8b). On the contrary, at this point, there will be fewer spins following the oscillating magnetic field, and therefore the in-phase component

(χ_M’) of the magnetic susceptibility should decline at the temperatures in which maxima of χ_M’’ appear, Figure 1. 8a).

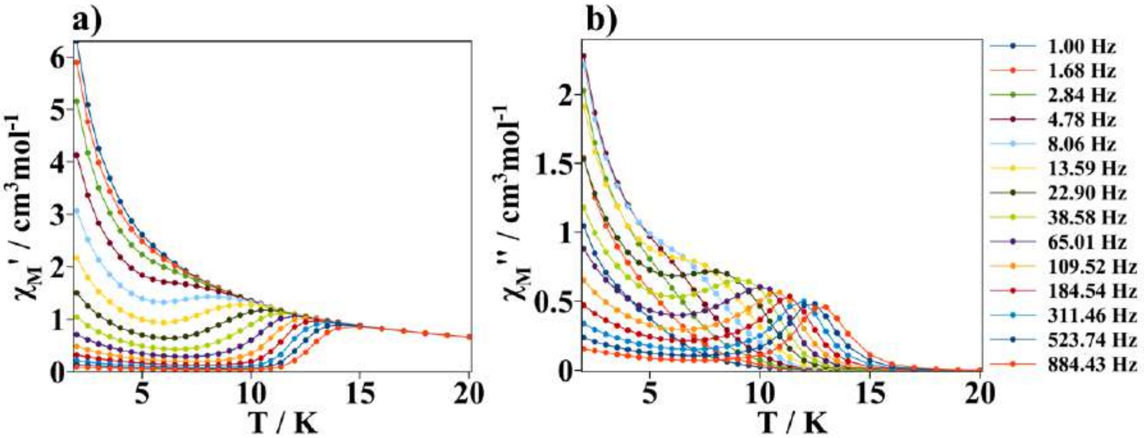

Figure 1. 8 In phase (a) and out-of-phase (b) magnetic susceptibility components with Temperature plotsof a Dy^{3+} SMM. The measurements are from compound **4-Dy** presented in *Chapter 2.*

When a magnet molecule is subjected to an oscillating magnetic field, it can undergo various relaxation mechanisms to return to the equilibrium state. The magnetic moment can relax via energy exchanges between the magnetic moment of the electrons in the paramagnetic ions and the vibrations of the structural lattice in which they are placed, known as spin-lattice relaxation. To understand this interaction, it is important to recognize that the magnetic system comprises two components, the spin system which is formed by the magnetic moments of the electrons and the lattice system, which refers to the vibrational energy of the lattice, described as phonon radiation. These two systems are typically in thermal equilibrium. When an oscillating magnetic field is applied to the sample, the equilibrium is disturbed. This causes energy exchanges between the spin system and the lattice system. This energy transfer may proceed through different mechanism with different relaxation times of the magnetization (τ).[79] The relaxation processes are presented below and a simplified Scheme describing these mechanisms is depicted in Figure 1. 9.

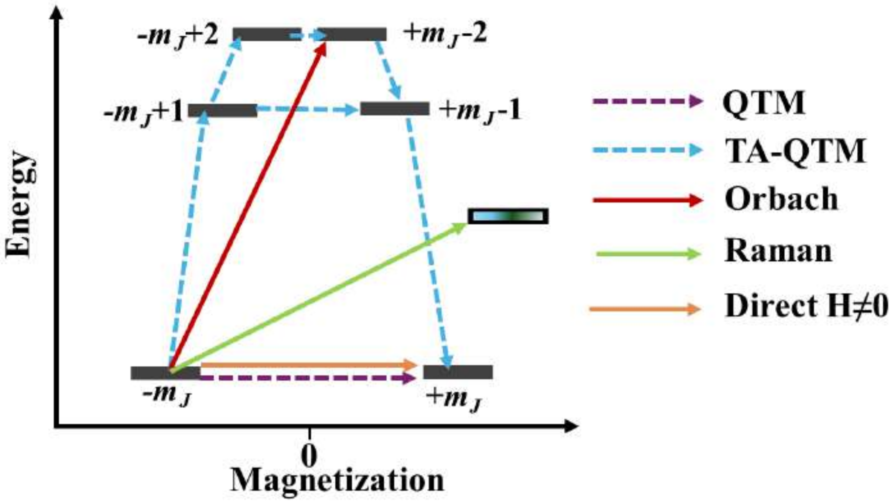

Figure 1. 9 Scheme representing the relaxation of the magnetization mechanisms between ±m_j states of a Ln^{3+} ground state

The Orbach mechanism describes relaxation of the magnetization through the entire energy barrier from one of the ±m_j ground states passing through the highest in energy excited m_j state and relaxing to either of the ground ±m_j states. It involves absorption and emission of two phonons. This process is described with Equation 1.27. It follows an Arrhenius law, from which the anisotropy barrier (*ΔE*) (representing the energy required for the spin to reorient to its equilibrium state) can be determined. Since the spin must overcome this energy barrier to pass from the ground state to the excited state, it needs sufficient energy for this process to occur. Consequently, the Orbach mechanism predominates at higher temperatures. Traditionally, relaxation of the magnetization times dependence with temperature is represented as ln(τ) *vs* T^{-1} semi-log curves. This is because on applying the logarithmic function in the obtained τ values, Equation 1.27 is linearized. Thus, a system relaxing through the Orbach process should follow a linear trend of ln(τ) *vs* T^{-1} along all the temperature range. However, a lack of axial symmetry around the lanthanide ion can add rhombic contributions to the ground and excited ±m_j states, leading to mixed states. Moreover, hyperfine coupling between the electronic spin and the nuclear spin as well as intermolecular interactions can also generate admixed states. The lack of pure m_j states along with lack of well differentiated energy between the ground and excited m_j levels may produce relaxation of the magnetization occur through underbarrier processes. In the ln(τ) *vs* T^{-1} plots, this is observed as a deviation of the linearity, generally on cooling the sample.

In Ln^{3+} based SMMs this deviation in the linear trend accounts to QTM (explained hereafter) when the $\ln(\tau)$ *vs* T^{-1} curve reaches a plateau. In other cases, τ clearly show dependence with T, nonetheless the linear trend is somehow followed in few experimental points. Moreover, in this second case the extracted ΔE values become very low. This suggests that relaxation of the magnetization in the system is not dominated by the Orbach process, and other mechanisms should be considered.[80]

$$\tau^{-1} = \tau_0^{-1}\exp\left(\frac{\Delta E}{k_B}\right) \quad \textbf{Equation 1.27}$$

In the Direct process, the spin system emits or absorbs a single lattice phonon that has the same energy as the energy between the α and β states, allowing the spin to change its configuration without needing to surpass the energy barrier between the states. This process takes place when an external direct current (dc) magnetic field is applied to the sample and breaks the degeneracy between the $\pm m_j$ doublets. The relaxation time rate derived from this mechanism depend on the applied dc field (H) and the temperature (T) as in Equation 1.28.

$$\tau^{-1} = AH^mT \quad \textbf{Equation 1.28}$$

A is an adjustable parameter whereas m equals 2 for non-Kramer ions (even number of unpaired electrons in the valence shell) or 4 for Kramer ions (odd number of unpaired electrons in the valence shell).

The Raman process, which strongly depends on temperature, is a mechanism that involves two phonons. However, phonon absorption and emission doesn’t take place through a real m_j excited state as in the Orbach mechanism, but it involves a virtual excited state with energy smaller than the Debye temperature. A virtual state is understood as a spin state which no longer is an eigenstate of the total system, including spin and phonons. In this scenario, external perturbations, such as phonons, can cause slight mixing of all $\pm m_j$ doublets of the system.[81] If relaxation of the magnetization takes place via the Raman mechanism, τ will follow Equation 1.29.

$$\tau^{-1} = CT^n \quad \textbf{Equation 1.29}$$

Where C is and adjustable parameter and n corresponds to 7 for non-Kramer ions and 9 for Kramer ions. However, experimentally the n parameter is also used as an adjustable parameter. Given that magnetization relaxation is taking place at very low temperatures, it is possible that in the spin-lattice exchange there is contribution of lower-energy phonons. In such cases, there may not be enough phonons available with the matching energies to effectively exchange with the spin. In these situations, the n value may yield smaller values, in the range of 1-6.[81]

Moreover, another proposed spin-lattice relaxation mechanism is the Local mode, referred to a thermally dependent process which considers that the spin relaxation goes through a higher energy state that is a local vibration from the same m_j ground state. The Local mode mechanism follows Equation 1.30 where Δ_{loc} can be extracted and is referred to the local mode energy (discrete vibrations of the molecule) (cm^{-1}).[82] A_{loc} is a constant that is related to the amplitude of the mode that is activated in the relaxation process. Moreover, Δ_{loc} can be experimentally assigned from vibrational spectroscopic techniques.[83,84]

$$\tau^{-1} = A_{loc}\left(\frac{e^{-\frac{\Delta_{loc}}{k_B T}}}{\left(e^{-\frac{\Delta_{loc}}{k_B T}}-1\right)^2}\right) \qquad \textbf{Equation 1.30}$$

It is important to consider that significant care must be taken when fitting τ *vs* T data with the different relaxation of the magnetization mechanisms due to over parametrization when using such equations.

On the other hand, after exposure of the oscillating magnetic field, the magnetic moment of a molecular magnet can also relax trough a mechanism of a quantum nature, the Quantum Tunnelling of Magnetization (QTM). This mechanism takes place between the ground state $\pm m_j$ doublets. This relaxation process is fast and temperature independent, thus diminish relaxation of the magnetization times. It only shows dependence with an applied dc magnetic field. Therefore, reduction of this effect can be directed when applying an external dc magnetic field because it slightly perturbs the energy of the degenerate $\pm m_j$ doublets. As mentioned before, this mechanism might appear because of transverse anisotropy caused by distortions of the axial symmetry around the ion. In addition, the presence of hyperfine interactions between 4*f* electrons and the nuclear spin and the dipole-dipole interactions between different molecules also contributes to facilitate an efficient QTM relaxation path. Moreover, QTM relaxation mechanism can also occur between non-ground states of equal energy. Then this process is known as Thermally Activated Quantum Tunnelling of Magnetization (TA-QTM).[73] This mechanism is quite common in Ln^{3+} complexes in contrast to polynuclear transition metal compounds where is less dominating due to the strong magnetic exchange coupling interactions between the metal centres.

Generally, Direct, Raman and QTM mechanism become more prominent at lower temperatures and oppose to the Orbach mechanism. This effect may lead to a considerable reduction of the effective energy barrier of the orientation inversion of the magnetic moment. Therefore, to achieve compounds presenting good SMM properties with large energy barriers, the QTM, in principle, should be suppressed. Reduction of the underbarrier mechanism, especially the fast QTM, could be acquired by providing the Ln^{3+} ion with the suitable ligand field to stabilize the $\pm m_j$ doublet with the highest value as the ground state. A high magnetic moment is maintained at temperatures where only the ground state is significantly populated when the highest value of $\pm m_j$ ground state is populated. Additionally, the application of an external dc magnetic field and diluting the sample by co-crystallizing the diamagnetic analogues (Zn^{2+}, Y^{3+} or La^{3+}) might reduce quenching of slow relaxation of the magnetization by the QTM process.[85]

1.3.4 Trivalent lanthanide Magnetism and Ligand Field

Rinehard and Long *et al*.[71] proposed a model to predict which ligand design around the metal would generate stronger magnetic anisotropy for a series of trivalent lanthanide ions, thus obtaining Ln^{3+} compounds with improved SMM performance. The $\pm m_j$ ground state should possess a well-defined state with the highest possible absolute value. Moreover, the energetic separation between $\pm m_j$ and $\pm m_{j\pm1}$ states need to be as high as possible to obtain high ΔE values. The axiality of the Ln^{3+} ions can be potentiated taking into account the charge distribution in the J ground state of the free ion which can be of oblate, prolate or spherical shape, based on their quadrupole moment.

The lanthanides with oblate electron distribution in the ground state are Ce^{3+}, Pr^{3+}, Nd^{3+}, Tb^{3+}, Dy^{3+} and Ho^{3+}. Whereas the lanthanide cations exhibiting prolate charge distribution are Pm^{3+}, Sm^{3+}, Eu^{3+}, Er^{3+}, Tm^{3+} and Yb^{3+}. Designing a magnet molecule, predicting the necessary crystal field that would lead to stronger easy-axis anisotropy, it can be easier if the shape of the *J* ground state charge cloud in the Ln^{3+} cation is considered.

The ligand distribution should be designed in order to minimize the repulsive contacts between 4*f* electron charge cloud and the electron density from the ligand donor atoms. In an oblate distribution, the negative charge is concentrated in the equatorial plane while the negative charge cloud is distributed along the axial plane for a prolate charge distribution, Figure 1. 10a).

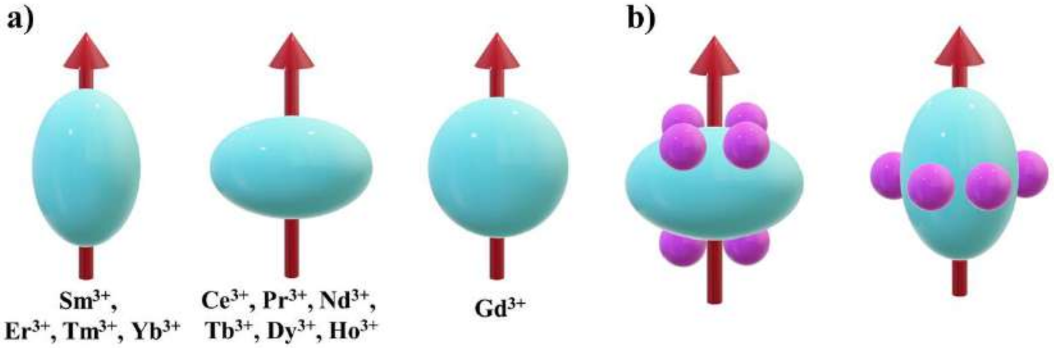

Figure 1. 10 a) Quadrupole approximation of the 4*f* electron distribution of *J* ground state of the Ln^{3+} series. Europium(III) is not depicted due to its *J*=0 ground state b) Scheme of the low-energy configuration of the *f* orbital electron density with respect to the crystal field environment for a 4*f* ion with oblate (right) and prolate (left) charge distribution in the ground *J* state.

Therefore, to provide with stronger magnetic anisotropy in a Ln^{3+} with oblate ground state, the donor atoms from the ligand, with greatest electronic density should coordinate in the axial positions. Generally, the atoms with higher electron density will form shorter Ln-X bond distances, where X is the donor atom. The anisotropy axis will point to the donor atoms with higher electron density. Whereas, for a Ln^{3+} with prolate ground state, the donor atoms from the ligand showing greatest electron density should coordinate at equatorial positions to achieve axial anisotropy. In the latter case, the anisotropy axis lies perpendicular to the plane where the donor atoms with greatest electron density are located, Figure 1. 10b).[71]

However, control of the coordination geometry and coordination number of Ln^{3+} might become a difficult task. Due to the relatively large electronic radius that trivalent lanthanides present, the coordination compounds derived from these metals exhibit large coordination numbers (generally higher than 8).

1.3.5 Treatment of alternating current (ac) magnetic data

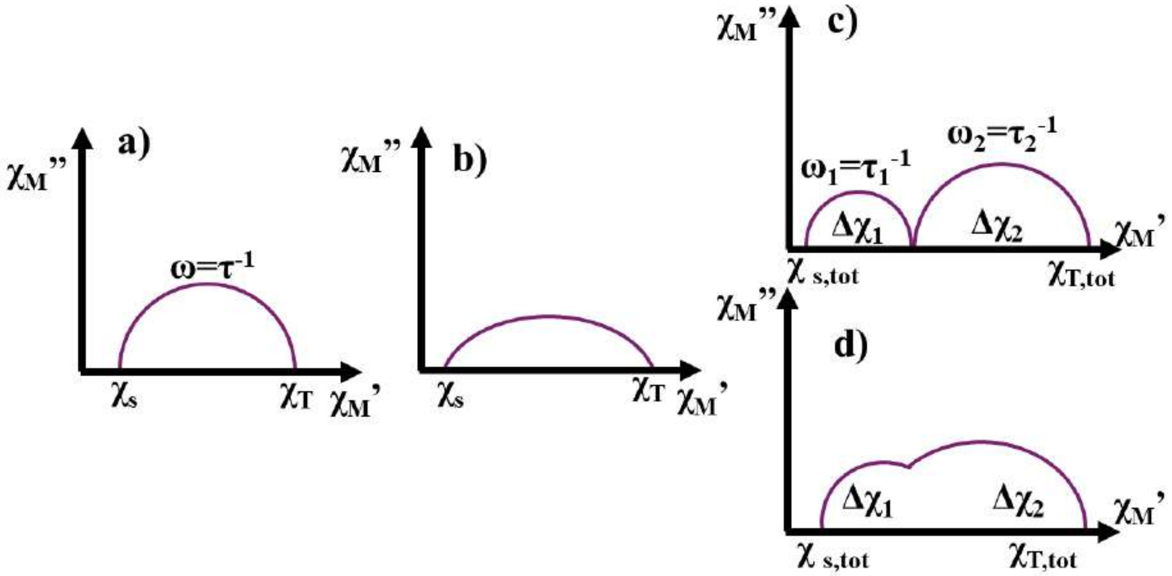

Figure 1. 11 Scheme of a Cole-Cole plot for a) a single relaxation of the magnetization process with one time constant b) with distribution of relaxation of the magnetization times c) with two processes with two times constants for each process and d) two processes with distribution of relaxation times.

Alternating current magnetic data, χ_M' and χ_M'' with temperature and frequency generally are treated with the Debye model. This model allows the study of ac magnetic susceptibility (χ_{AC}) as a function of the oscillating frequency. If a molecule relaxes by a single relaxation process with a single relaxation time, for fixed values of magnetic field (H) and temperature (T), χ_{AC} is described in the Generalized Debye model as in Equation 1.31.

$$\chi_{AC}(\omega) = \chi_S + \frac{\chi_T - \chi_S}{1 + i\omega\tau} \quad \textbf{Equation 1.31}$$

In this equation, χ_S and χ_T are the adiabatic and isothermal magnetic susceptibilities respectively, τ is the relaxation of the magnetization time and ω is the angular frequency of the ac field (ω=2πν). χ_T is the susceptibility in the limit of the lowest field frequencies where the thermal equilibrium of the system is observed. On the contrary, χ_S (lower than the χ_T) is observed when the oscillations of the ac field are fast compared to the time constant, τ, and the magnetic system remains isolated from its environment.[73]

With the so-called Cole-Cole plots (or Argand plots), it is possible to study the dependence of ac magnetic susceptibility components as a function of the oscillating frequency and temperature. In these plots, χ_{AC} magnetic data as a function of frequency are represented by decomposing into the imaginary or out-of-phase component (χ_M'') in the *y* axis and the real or in-phase component (χ_M') on the *x* axis for fixed values of H and T. Therefore, each curve represents χ_{AC} at a constant T and H and at variable frequencies which increase along the *x* axis. These representations are useful for quantifying the relaxation times of each curve.

If the relaxation of the magnetization of the studied system relaxes through a single relaxation process via a single relaxation time, then the Cole-Cole plot shows a perfectly semicircle with the centre on the χ_M' axis. Then the relaxation time ($\omega = \tau^{-1}$) is determined by the angular frequency of the ac field in which χ_{AC} has its maximum [$\chi_{max}=1/2(\chi_{T-}\,\chi_S)$], Figure 1. 11a).

On the other way, if the Cole-Cole plot show flattened, asymmetrical or uncompleted semicircles (which happens in most cases), it is an indication that there is a distribution of the relaxation of magnetization times, Figure 1. 11b). In this case, the χ_{AC} is better described in a modified Generalized Debye model described with the Casimir-Du Pré function as in Equation 1.32.[86]

$$\chi_{AC}(\omega) = \chi_S + \frac{\chi_T - \chi_S}{1+(i\omega\tau)^{1-\alpha}} \quad \textbf{Equation 1.32}$$

Where the α parameter quantifies the width of the τ distribution of each curve and it ranges from 0 to 1. The wider the distribution, α acquires a larger value. Whereas a value of α = 0 indicates that relaxation of the magnetization takes place through a single mechanism described by a single τ, and we would have the case of Equation 1.31.

Moreover, in some molecules the relaxation of the magnetization can take place through more than one process. In the case of two processes, they can be well differentiated if relaxation of the magnetization times are separated enough, one respect to the other. Then, in the Cole-Cole plot, two well separated semicircles accounting to two relaxation processes are observed in case that relaxation of the magnetization of one process is significantly slower than the other. In contrast, if there are two processes with similar relaxation of the magnetization rates, the two merged semicircles appear in the Cole-Cole plot each one assigned to the two different relaxations, Figure 1. 11c) and d). In any case, if the two processes are well differentiated, then a two-step relaxation model is described by the sum of two modified Debye functions, Equation 1.33.[87,88]

$$\chi_{AC}(\omega) = \chi_{S1} + \chi_{S2} + \frac{\chi_{T1}-\chi_{S1}}{1+(i\omega\tau_1)^{1-\alpha_1}} + \frac{\chi_{T2}-\chi_{S2}}{1+(i\omega\tau_2)^{1-\alpha_2}}$$ **Equation 1.33**

χ_{S1} and χ_{S2} of each process cannot be determined therefore, $\chi_{S,TOT}$ is defined as:

$$\chi_{S,TOT} = \chi_{S1} + \chi_{S2}$$ **Equation 1.34**

$\chi_{S,TOT}$ represents the adiabatic susceptibility of both relaxation processes, then the difference of isothermal and adiabatic susceptibility of each process $\Delta\chi_1$ and $\Delta\chi_2$ can described as:

$$\Delta\chi_1 = \chi_{T1} + \chi_{S1}$$ **Equation 1.35**

$$\Delta\chi_2 = \chi_{T2} + \chi_{S2}$$ **Equation 1.36**

Taking into consideration Equations 1. 34, 1.35 and 1.36, the two steps relaxation model can also be depicted with Equation 1.37.

$$\chi_{AC}(\omega) = \chi_{S,TOT} + \frac{\Delta\chi_1}{1+(i\omega\tau_1)^{1-\alpha_1}} + \frac{\Delta\chi_2}{1+(i\omega\tau_2)^{1-\alpha_2}}$$ **Equation 1.37**

Each $\chi_{AC}(\omega)$ equation split into their real ($\chi'(\omega)$) and imaginary ($\chi''(\omega)$) components and the respective equations are found in APXII. The exact cause of the two distinct relaxation processes is often unclear and can vary between different cases. One possible explanation is the presence of two crystallographically independent compounds within the same structure.[87] However, several compounds with a single paramagnetic ion in their crystal structure have also been observed to exhibit two sets of maxima. When two thermally activated processes are present in the case of a single ion, it has been suggested that these are either direct processes originating from the multi-level system (caused by the existence on an external magnetic field) or due to interactions between molecules.[89]

1.4 Multiproperty lanthanide compounds

Until here, we have presented both, luminescence and magnetic properties of trivalent lanthanide systems, separately. However, compounds containing Ln^{3+} can show SMM and luminescence properties at the same time, thus presenting multiproperty character. The first metal coordination compound in which multiproperty characteristics was highlighted, was in a manganese $\{Mn_2^{2+}Mn_2^{3+}\}$ cluster reported by Hendrickson *et al*.[90] which showed ligand-based fluorescence as well as SMM performance. Since then, compounds exhibiting multiple properties simultaneously have been sought after. Coordination compounds derived from trivalent lanthanides are good candidates for achieving multiproperty characteristics, particularly with good luminescence and magnetic responses.

In the design for obtaining Ln^{3+} systems that present both optimized characteristics, an important factor should be taken into consideration. For enhancing an axial magnetic anisotropy and thus minimize the contribution of the QTM, a high order around the oblate or prolate ion with a high symmetry coordination sphere is demanded. On the other hand, to make the *f-f* emission transitions less prohibited, a more distorted thus, asymmetric, coordination environment is beneficial. Then, to obtain a molecular system showing both, magnetic and luminescence properties, a compromise point should be directed. Moreover, selection of the appropriate Ln^{3+} is important. Luminescent SMMs are presented in the literature based on few different trivalent Ln ions, including the visible emitters Sm^{3+}, Dy^{3+} and Tb^{3+}, or the nIR emitters Nd^{3+}, Er^{3+} and Yb^{3+}. Due to the outstanding SMM and luminescence properties shown separately for these compounds, further insights into their magneto-optical correlations as well as the switching of their emission using a magnetic field have been presented.[69,91]

Correlation between luminescence and magnetic properties can be derived from multiproperty Ln^{3+}-systems. From the luminescence spectrum, information about the crystal-field energy splitting of the ground multiplet can be obtained. Accordingly, if a well resolved luminescence spectrum (normally measured at low temperatures) is obtained, crystal field components ($\pm m_j$) can be differentiated, thus the energy difference between the $\pm m_j$ states of the J ground state can be extracted. Then if the calculated energy barrier from the ac magnetic data coincides with the $\pm m_j$ doublets separation from spectroscopic data, the Orbach mechanism is taking place.

Otherwise, if the obtained *ΔE* from the ac magnetic measurements is way lower than the one obtained in the luminescence spectrum, then a shortcut mechanism is taking place in the relaxation of the magnetization.[92] Hence, magneto-optical correlation of multiproperty Ln^{3+}-systems affords insights into spin dynamics in the relaxation of the magnetization process. This analysis is performed for compound **4-Dy** in *Chapter 2.3* of this *Thesis* work.

On the other hand, application of a magnetic field to the lanthanide sample might have an impact into the alignment of the Ln^{3+} magnetic moment, thereby altering the electronic transitions responsible for luminescence. In luminescent lanthanide SMM, the research carried out has observed notable shifts and splitting in emission bands when the compound is exposed to a magnetic field.[93a] This observation shows the capacity to manipulate or adjust emission characteristics of these materials by simply varying the intensity and direction of the applied magnetic field, this way obtaining luminescent switches. Application of magnetic fields to control luminescence of lanthanide SMMs not only highlights their intriguing magneto-optical characteristics but also introduces interesting applications comprised between optoelectronics and information processing.[93]

Another interesting application of luminescence Ln-based SMMs would be in the luminescence thermometry field. As already seen, SMM behaviour strongly depends on temperature, whether in its relaxation pathways as much as the temperature in which the magnet performance is manifested (T_B). Control of the temperature in which the system is found is crucial, however conventional thermometers are rather useless to accomplish this task. An SMM lanthanide system showing luminescence thermometry properties could work as a contactless and more precise thermometer. If the SMM compound is luminescent with emission properties (emission colour, band intensity and lifetime) significantly changing on varying temperature, it could also act as a luminescent thermometer. The important requisite for these systems, however difficult to acquire, is that both properties must overlap at the same temperature range.[94]

Finally, further induction of chirality to the final luminescent lanthanide SMM molecule can lead to interesting functionalization of the compound. Incorporation of chirality to the system may lead to additional optical and magneto-optical properties. For instance, Magneto-Chiral Dichroism (MChD), which consists of the manipulation of unpolarized absorbed light of the chiral molecule. The dependence of the absorbed light would depend on the direction of a magnetic field generated from the chiral magnetized system. Therefore, MChD doesn't demand a circularly polarized source as opposed to other chiroptical techniques such as CPL. Compounds with MChD effect might present potential applications in advanced optical data processing using unpolarized light. However, compounds showing MChD are rather scarce due to the challenge it presents both, at the instrumental level to detect the phenomenon and at the design and synthesis of the compounds level to exhibit this characteristic.[28] Alternatively, as presented before in this *Thesis* work, luminescent lanthanide compounds embedded in a chiral environment can present Circularly Polarized Luminescence (CPL). The CPL property is sensitive to external stimuli such as temperature, magnetic fields or the chemical environment. Therefore, CPL properties of new Chiral luminescent lanthanide SMM compounds could be manipulated by external magnetic fields and find potential applications as optical output magnetic data storage devices.[91a]

1.5 Research Objectives and Thesis organization

With the main objective of obtaining multiproperty molecular materials, different lanthanide coordination compounds are synthetized and characterized in this *Thesis* work.

In all the synthetized coordination compounds +III oxidation number is expected for all the lanthanide cations, as the starting salt used in all cases contain the Ln^{3+} ion. Mainly the luminescence and molecular magnetism properties will be investigated in this work. The new compounds will be principally synthetized from Ce, Nd, Sm, Eu, Tb, Dy, Er and Yb due to the interesting luminescent and magnetic properties that they can show.

Different molecules will be used as ligands to achieve a range of nuclearities in the synthetized compounds. Additionally, some of these ligands will serve as sensitizers due to their potential chromophore properties. The molecules used to prepare the anionic forms of the main ligands along this *Thesis* work are 4,4,4-Trifluoro-1-phenyl-1,3-butanedione (HBtfa), 2-fluorobenzoic acid (2-HFBz), 2,6-difluorobenzoic acid (2,6-HF2Bz) and the chiral *R*- and *S*-α-methoxyphenylacetic acid (*R*- and *S*-HMPA) and *R* and *S*-2-phenylbutanoic acid (*R* and *S*-2-HPhBut), Scheme 1.1 a)-e). All syntheses are conducted in basic medium to deprotonate the ligands and facilitate their coordination to the lanthanide ion. Moreover, the molecules used as auxiliary ligands will be 4,4’-dinonyl-2,2’-bipyridine (4,4,’-dinonyl-bipy), 1,10-phenanthroline (phen), 2,2’-bipyridil (bipy), 2,2';6',2"-terpyridine (terpy) and 4,7-Diphenyl-1,10-phenanthroline (bathophen), Scheme 1.1 f)-j).

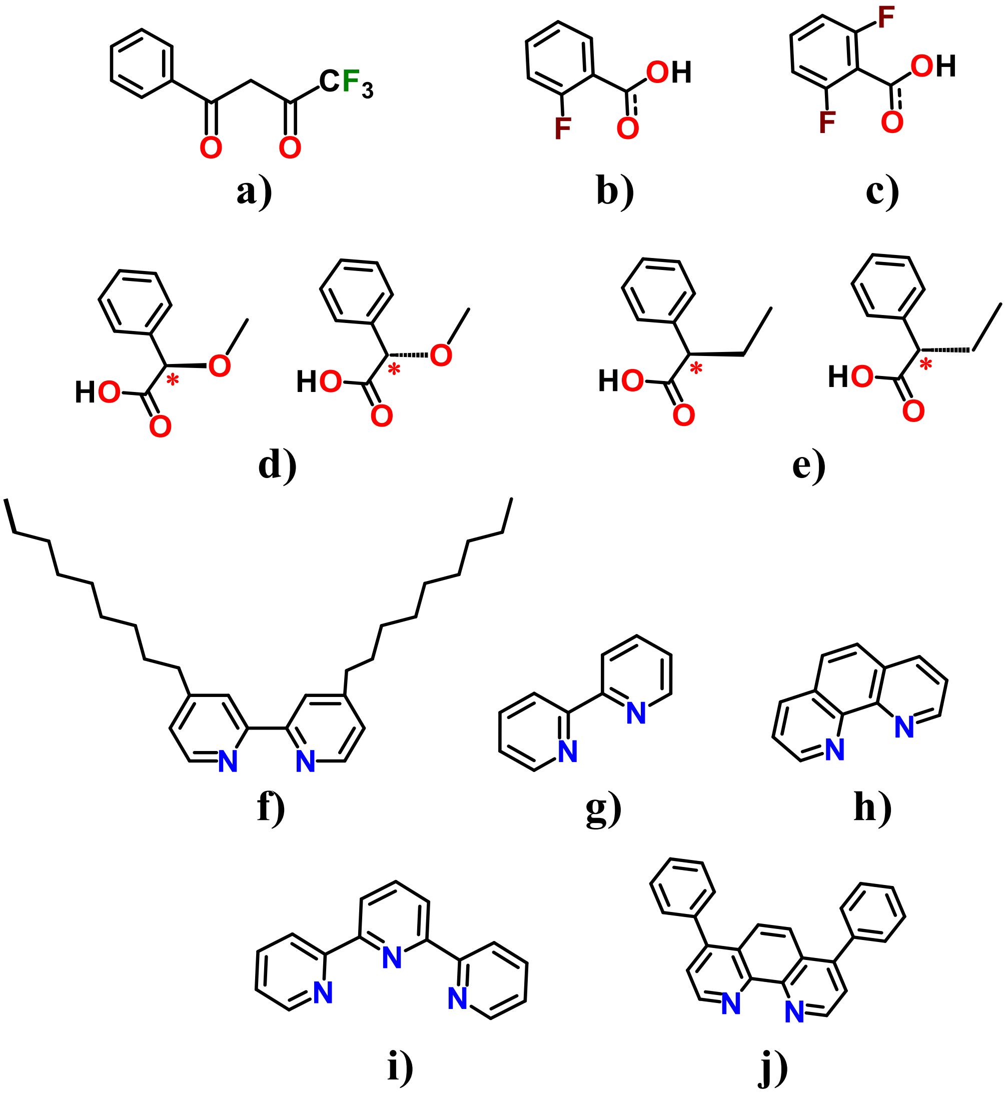

Scheme 1.1 a) 4,4,4-Trifluoro-1-phenyl-1,3-butanedione (HBtfa), b) 2-fluorobenzoic acid (2-HFBz), c) 2,6-difluorobenzoic acid (2,6-HF2Bz), d) *R*- and *S*-α-methoxyphenylacetic acid (*R*- and *S*-HMPA), e) *R* and *S*-2-phenylbutanoic acid (*R* and *S*-2-HPhBut), f) 4,4’-dinonyl-2,2’-bipyridine (4,4,’-dinonyl-2,2’-bipy), g) 2,2’-bipyridil (bipy), h) 1,10-phenanthroline (phen), i) 2,2';6',2''-terpyridine (terpy) and j) **4,7-**Diphenyl-1,10-phenanthroline (bathophen).

Compounds derived from the β-diketonate ligand 4,4,4-Trifluoro-1-phenyl-1,3-butanedionate (Btfa) are presented in *Chapter 2.* Mononuclear compounds are expected by using this ligand. Two different families are synthetized. First, using only the Ce^{3+} cation and the different N,N- and N,N,N-polypyridyl ligands. In this family the magnetic properties are studied, to expand the knowledge about the slow relaxation of magnetization behaviour of cerium(III) which is rather scarce in the literature. Moreover, a different approach of the magnetic data processing of the cerium(III) family is presented in comparison to the magnetic data of the rest of the compounds showing slow relaxation of the magnetization in this work. On the other hand, with Btfa and the chromophore 4,4’-dinonyl-2,2’-bipy ligand, lanthanide(III) compounds showing both, luminescence and magnetic properties are expected. The thermal stability of the Eu and Yb derivatives will be analysed to use these materials as the emissive layer of two different Organic Light Emitting Diode (OLED) devices.

With the 2-fluorobenzoate (2-FBz) and 2,6-difluorobenzoate (2,6-F2Bz) derived lanthanide compounds, presented in *Chapter 3*, the main goal is to increase emission quantum yields of the Eu and Tb derivatives by designing new synthetic routes in order to remove completely the coordinating H_2O molecules from the Ln^{3+} chemical environment. Due to the high coordination numbers and the oxyphilic character of Ln^{3+} cations, this task is not trivial. Moreover, by synthetizing the Ce, Nd, Sm, Dy, Gd, Er and Yb analogues, multiproperty compounds are expected.

Finally, a third property is added to the lanthanide compounds presented in *Chapter 4* by using the chiral carboxylates *R/S*-MPA and *R/S*-PhBut as ligands. With the complementation of the auxiliary chromophore ligands, 1,10-phenantroline and bathophenantroline, the luminescence, molecular magnetism and chiroptical properties will be studied for these two enantiopure lanthanide families. The chiroptical properties will be studied in terms of Circular Dichroism (CD) and Circular Polarized Luminescence (CPL).

The study of all the synthetized lanthanide coordination compounds will be conducted, systematically, as follows. First, the crystal structure of at least one analogue of each family will be measured from a monocrystal from the sample. To confirm phase purity along all the obtained product, Powder X-Ray diffraction, ATR Infrared spectroscopy as well as elemental analysis will be performed in all the samples of this work. Moreover, to study the luminescence properties, excitation and emission spectra of solid samples are measured in the fluorimeter. For the compounds showing stability in solution, luminescence properties as well as absorption spectra will be also measured in this medium. Emission quantum yield and luminescence lifetimes will be measured for those compounds showing best luminescence properties (generally the Eu^{3+} and Tb^{3+} analogues). For the magnetic properties, the direct current magnetic susceptibility from 2 K to Room Temperature will be measured for all compounds in the SQUID instrument. For those compounds that might present relaxation of the magnetization under an oscillating magnetic field, alternating current measurements will be also performed. A detailed description of the measurements performed along this *Thesis* work is depicted in APX.II.

1.6 References

[1] a) International Union of Pure and Applied Chemistry (2005). *Nomenclature of Inorganic Chemistry* (IUPAC Recommendations 2005). Cambridge (UK): RSC–IUPAC, p. 51 b) N. Dushyantha, N. Batapola, I. Ilankoon, S. Rohitha, R. Premasiri, B. Abeysinghe, N. Ratnayake, K. Dissanayake. The story of rare earth elements (REEs): Occurrences, global distribution, genesis, geology, mineralogy and global production. *Ore Geology Reviews* 2020, **122**, 103521 c) Joan Lluís Ferrer, Descubierto el mayor yacimiento de tierras raras de Europa. El Periódico de España, June 9th, 2024.

[2] R. Pöttgen, T. Jünstel, C. A. Strassert Eds. *Rare Earth Chemistry,* 2020 Walter De Gruyter GmbH.

[3] S. G. Wang, W. H. E. Schwarz, Lanthanide Diatomics and Lanthanide Contractions, *J. Phys. Chem*. 1995, **99**, 11687-11695.

[4] D.A. Atwood, Ed., The Rare Earth Elements: Fundamentals and Applications, John Wiley & Sons Ltd, 2005.

[5] *Luminescence of Lanthanide Ions in Coordination Compounds and Nanomaterials,* ed. A. de Bettencourt-Dias, John Wiley & Sons Ltd, 2014

[6] B. Chen, Y. Yang, F. Zapata, G. Qian, Y. Luo, J. Zhang, E.B. Lobkovsky, Enhanced Near-Infrared-Luminescence in an Erbium Tetrafluoroterephthalate Framework, *Inorg. Chem*, 2006, **45**, 8882-8886.

[7] A. Baschieri, S. Muzzioli, E. Matteucci, S. Stagni, M. Massi, L. Sambri, New heterometallic Ir(III)2-Eu(III) complexes: white light emission from a single molecule. *Dalton Trans.* 2015, **44**, 37–40

[8] X. Rao, T. Song, J. Gao, Y. Cui, Y. Yang, C. Wu, B. Chen, G. Qian, A highly sensitive mixed lanthanide metal-organic framework self-calibrated luminescent thermometer, *J. Am. Chem. Soc*. 2013, **135**, 15559–15564

[9] S.I. Weissman, Intramolecular Energy Transfer The Fluorescence of Complexes of Europium, *J. Chem. Phys.*, 1942, **10**, 214-217.

[10] D. L. Dexter, A Theory of Sensitized Luminescence in Solids, *J. Chem. Phys.*, 1953, **21**, 836-850

[11] G.A. Crosby, R.E. Whan, R.M. Alire, Intramolecular energy transfer in rare earth chelates. Role of the triplet state, *J. Chem Phys*. 1961, **34**, 743-748.

[12] N. Sabbatini, S. Perathoner, V. Balzani, B. Alpha, J.-M. Lehn, in Supramol. Photochem. (Ed.: V. Balzani), Springer Netherlands, Dordrecht, 1987, 187–206

[13] J.-M. Lehn, Perspectives in Supramolecular Chemistry- From Molecular recognition towards Molecular Information Processing and Self-Organization, *Angew. Chem. Int. Ed.* 1990, **29,** 1304–1319.

[14] H. Xu, Q. Sun, Z. An, Y. Wei, X. Liu, Electroluminescence from europium(III) complexes, *Coord. Chem. Rev*., 2015, **293**, 228-249.

[15] M. Kleinerman, Energy migration in lanthanide chelates, *J. Chem. Phys*., 1969, **51**, 2370-2381

[16] L.E.N. Aquino, G.A. Barbosa, J.L. Ramos, S.O.K. Giese, F.S. Santana, D.L. Hughes, G.G. Nunes, L. Fu, M. Fang, G. Poneti, A. N. Carneiro Neto, R. T. Moura Jr, R. A. S. Ferreira, L. D. Carlos, A. G. Macedo and J. F. Soares, Seven-Coordinate Tb^{3+} complexes with 90% Quantum Yields: High-Performance Examples of Combined Singlet- and Triplet-to-Tb^{3+} Energy- Transfer Pathways, *Inorg. Chem*. 2021, **60**, 892-907.

[17] a) D. Kovacs, X. Lu, L.S. Meszaros, M. Ott, J. Andres, K.E. Borbas, Photophysics of coumarin and carbostyril-sensitized luminescent lanthanide complexes: implications for complex design in multiplex detection, *J. Am. Chem. Soc*. 2017, **139**, 5756-5767 b) V. F Plyusnin, A. S. Kupryakov, V. P. Grivin, A. H. Shelton, I. V. Sazanovich, A. J. H. M Meijer, J. A. Weinstein, M. D. Ward, Photophysics of 1,8-Naphthalimide/Ln(Iii) Dyads (Ln = Eu, Gd): Naphthalimide → Eu(iii) Energy-Transfer from Both Singlet and Triplet States. *Photochem. Photobiol. Sci*. 2013, **12**, 1666−1679 c) A. K. R. Junker, T. J. Sørensen, Shining Light on the Excited State Energy Cascade in Kinetically Inert Ln(iii) Complexes of a Coumarin-Appended Do3a Ligand. *Dalton Trans*. 2019, **48**, 964− 970.

[18] T. Förster, Zwischenmolekulare energiewanderung und fluoreszenz, *Annalen der Physik*. 1948, **437**, 55–75

[19] D. L. Dexter, A theory of Sensitized Luminescence in Solids, *J. Chem. Phys*. 1953, **21**, 836–850.

[20] L. Prodi, M. Maestri, R. Ziessel, V. Balzani, Luminescent Eu^{3+}, Tb^{3+} and Gd^{3+} complexes of a branched-triazacyclononane ligand containing three 2,2'-bipyridine units, *Inorg. Chem*., **30**, 1991, 3798-3802.

[21] Y. Zhong, L. Si, H. He, A.G. Sykes, BODIPY chromophores as efficient green light sensitizers for lanthanide-induced near-infrared emission, *Dalton Trans.*, 2011, **40**, 11389-11395.

[22] F. J. Steemers, W. Verboom, D. N. Reinhoudt, E. B. van der Tol, J. W. Verhoeven, New sensitizer-modified calix [4] arenes enabling near-UV excitation of complexed luminescent lanthanide ions, *J. Am. Chem. Soc*. 1995, **117**, 9408–9414.

[23] J.C.G. Bünzli, On the design of highly luminescent lanthanide complexes, *Coord. Chem. Rev.*, 2015, **293,** 19-47

[24] M. Latva, H. Takalo, V.M. Mukkala, C. Matachescu, J.C. Rodríguez-Ubis, J. Kankare, Correlation between the lowest triplet state energy level of the ligand and lanthanide(III) luminescence quantum yield. *Journal of Luminescence,* 1997, **75**, 149-169.

[25] a) F. Wilkinson and A.A. Abdel-Shafi, Mechanism of Quenching of Triplet States by Oxygen; Biphenyl Derivatives in Acetonitrile, *J. Phys. Chem. A* 1997, **101**, 5509-5516 b) C. Schweitzer, Z. Mehrdad, F. Shafii, R. Schmidt, Charge transfer induced quenching of triplet sensitizers by ground state oxygen and of singlet oxygen by ground state sensitizers: A common deactivation channel, *Phys. Chem Chem. Phys,* 2001, **3**, 3095-3101.

[26] P. Wang, J.P. Ma, Y.B. Dong, Guest-Driven Luminescence: Lanthanide-Based Host-Guest System with Bimodal Emissive Properties Based on a Guest-Driven Approach, *Chem. Eur. J*. 2009, **15**, 10432-10445

[27] S. Kishimoto, T. Nakagawa, T. Kawai, Y. Hasegawa, Enhanced Near-Infrared Luminescence of Yb(III) complexes with Phosphine Oxide and Hexafluoroacetylacetone Ligands, *Bull. Chem. Soc. Jpn*. 2011, **84**, 148–154

[28] M. Atxori, G. L. J. A. Rikken, C. Train, Magneto-Chiral Dichroism: A Playground for Molecular Chemists, *Chem. Eur. J.*, 2020, **26**, 9784-9791.

[29] A. Aebischer, F. Gumy, and J. C. G. Bünzli, Intrinsic quantum yields and radiative lifetimes of lanthanide tris (dipicolinates), *Phys. Chem. Chem. Phys.*, 2009, **11**, 1346–1353.

[30] a) D. Rönnow, A. Roos, Correction factors for reflectance and transmittance measurements of scattering samples in focusing Coblentz spheres and integrating spheres, *Rev. Sci. Instrum.*, 1995, **66**, 2411-2422 b) J. C. de Mello, H. Felix Wittmann, R. H. Friend, An Improved Experimental Determination of External Photoluminescence Quantum Efficiency, *Adv. Mater.*, 1997, **9**, 230-232 c) M. S. Wrighton, D. S. Ginley, D. L. Morse, A Technique for the Determination of Absolute Emission Quantum Yields of Powdered Samples, *The Journal of Physical Chemistry*, 1974, **78**, 2229-2233.

[31] H. Ishida, S. Tobita, Y. Hasegawa, R. Katoh, K. Nozaki, Recent advances in instrumentation for absolute emission quantum yield measurements, *Coord. Chem. Rev.*, 2010, **254**, 2449-2458.

[32] M. H. V. Werts, R. T. F. Jukes, and J. W. Verhoeven, The emission spectrum and the radiative lifetime of Eu^{3+} in luminescent lanthanide complexes, *Phys. Chem. Chem. Phys.*, 2002, **4**, 1542–1548.

[33] Binnemans, Interpretation of europium(III) spectra, *Coord. Chem. Rev.*, 2015, **295**, 1–45

[34] S. Petoud, S. M. Cohen, J.-C. G. Bünzli, and K. N. Raymond, Stable Lanthanide Luminescence Agents Highly Emissive in Aqueous Solution: Multidentate 2-Hydroxyisophthalamide Complexes of Sm^{3+}, Eu^{3+}, Tb^{3+}, Dy^{3+}, *J. Am. Chem. Soc.* 2003, **125**, 13324–13325

[35] J.C. Rybak, L.V. Meyer, J. Wagenhöfer, G. Sextl, K. Müller-Buschbaum, Homoleptic Lanthanide 1,2,3-Triazolates ${}_{\infty}2–3[\mathrm{Ln}(\mathrm{Tz}^*)_3]$ and Their Diversified Photoluminescence Properties, *Inorg. Chem*. 2012, **51**, 13204-13213.

[36] a) C. Wei, B. Sun, Z. Cai, Z. Zhao, Y. Tan, W. Yan, H. Wei, Z. Liu, Z. Bian, C. Huang, Quantum yields over 80% achieved in luminescent europium complexes by employing diphenylphosphoryl tridentate ligand, *Inorg. Chem.* 2018, **57**, 7512-7515.

[37] C.P. Montgomery, B.S. Murray, E.J. New, R. Pal, D. Parker, Cell-Penetrating Metall Complex Optical Proves: targeted and responsive systems based on Lanthanide Luminescence, *Acc. Chem. Res*., 2009, **42**, 925-937.

[38] M.D. McGehee, T. Bergstedt, C. Zhang, A.P. Saab, M.B. O'Regan, G.C. Bazan, V.I. Srdanov, A. J. Heeger, Narrow Bandwidth Luminescence from Blends with Energy Transfer from Semiconducting Conjugated Polymers to Europium Complexes, *Adv. Mater*. 1999, **11**, 1349-1354

[39] R.C. Evans, P. Douglas, C.J. Winscom, Coordination complexes exhibiting room-temperature phosphorescence: Evaluation of their suitability as triplet emitters in organic light emitting diodes, *Coord. Chem. Rev*. 2006, **250**, 2093-2126

[40] E. Klampaftis, D. Ross, K.R. McIntosh, B.S. Richards, Enhancing the performance of solar cells vial luminescent down-shifting of the incident spectrum: A review, *Sol. Energy Mater. Sol. Cells* 2009, **93**, 1182-1194.

[41] G. Muller, Luminescent chiral lanthanide(III) complexes as potential molecular probes, *Dalton Trans*., 2009, **44**, 9692-9707.

[42] M. Górecki, L. Carpita, L. Arrico, F. Zinna, L. Di Bari, Chiroptical methods in a wide wavelength range for obtaining Ln^{3+} complexes with circularly polarized luminescence of practical interest, *Dalton Trans*., 2018, **47**, 7166-7177.

[43] F.S. Richardson, Selection rules for lanthanide optical activity, *Inorg. Chem.*, 1980, **19**, 2806-2812.

[44] a) E.M. Sánchez-Carnerero, A.R. Agarrabeitia, F. Moreno, B.L. Maroto, G. Muller, M.J. Ortiz, S. de la Moya, Circularly Polarized luminescence from Simple Organic Molecules, *Chem. Eur. J.,* 2015, **21**, 13488-13500 b) J. Roose, B.Z. Tang, K.S. Wong. Circularly-polarized luminescence (CPL) from chiral AIE molecules and macrostructures, *Small*, 2016, **12**, 6495-6512.

[45] J.L. Lunkley, D. Shirotani, K. Yamanari, S. Kaizaki, G. Muller, Extrordinary Circularly Polarized Luminescence Activity Exhibited by Cesium Tetrakis(3-heptafluoro-butylryl-(+)-camphorato) Eu(III) complexes in EtOH and $CHCl_3$, *J. Am. Chem. Soc*. 2008, 130, **42**, 13814-13815.

[46] S. Petoud, G. Muller, E.G. Moore, J. Xu, J. Sokolnicki, J.P. Riehl, U.N. Le, S.M. Cohen, K.N. Raymond, Brilliant Sm, Eu, Tb and Dy Chiral Lanthanide Complexes with Strong Circularly Polarized Luminescence, *J. Am. Chem. Soc*. 2007, **129**, 77-83.

[47] J.L. Lunkley, D. Shirotani, K. Yamanari, S. Kaizaki, G. Muller, Chriptical Spectra of a Series of Tetrakis((+)-3-heptafluorobutylyrylcamphorato)lanthanide(III) with an Encapsulated Alkali Metal Ion: Circularly Polarized Luminescence and Absolute Cheral Structures for the Eu^{3+} and Sm^{3+} Complexes, *Inorg. Chem*. 2011, **50**, 12724-12732.

[48] M. Seitz, E.G. Moore, A.J. Ingram, G. Muller, K.N. Raymond, Enantiopure, octadentate ligands as sensitizers for europium and terbium circularly polarized luminescence in aqueous solution, *J. Am. Chem. Soc*. 2007, **129**, 50, 15468-15470.

[49] O. G. Willis, F. Zinna, G. Pescitelli, C. Micheletti, L. Di Bari, Remarkable near-infrared chiroptical properties of chiral Yb, Tm and Er complexes, *Dalton Trans*., 2022, **51**, 518-523.

[50] a) M. Leonzio, A. Melchior, G. Faura, M. Tolazzi, M. Bettinelli, F. Zinna, L. Arrico, L. Di Bari and F. Piccinelli, A chiral lactate reported based on total and circularly polarized Tb(III) luminescence, *New J. Chem*., 2018, **42**, 7931-7939 b) J. Yuasa, T. Ohno, H. Tsumatori, R. Shiba, H. Kamikubo, M. Kataoka, Y. Hasegawa and T. Kawai, Fingerprint signatures of lanthanide circularly polarized luminescence from proteins covalently labelled with a β-diketonate europium(III) chelate, *Chem. Commun*., 2013, **49**, 4604-4606 c) K. M. Ayers, N. D. Schley and G. Ung, Circularly Polarized Luminescence from Enantiopure C_2-Symmetrical Tetrakis(2-

pyridylmethyl)-1,2-diaminocyclohexane Lanthanide Complexes *Inorg. Chem*., 2020, **59**, 7657-7665; d) J. Gong and X. Zang, Coordination-based circularly polarized luminescence emitters: Design strategy and application in sensing, *Coord. Chem. Rev*., 2022, **453**, 214329 e) N. F. M. Mukthar, N. D. Schley and G. Ung, Strong circularly polarized luminescence at 1550 nm from enantiopure molecular erbium complexes, *J. Am. Chem. Soc*., 2022, **144**, 6148-6153 f) P. Stachelek, L. MacKenzie, D. Parker and R. Pal, Circularly polarised luminescence laser scanning confocal microscopy to study live cell chiral molecular interactions, *Nat. Commun*., 2022, **13**, 553 g) A. T. Frawley, R. Pal and D. Parker, Very bright, enantiopure europium (III) complexes allow time-gated chiral contrast imaging. *Chem. Commun*., 2016, **52**, 13349-13352.

[51] a) F. Zinna, U. Giovanella and L. Di Bari, Highly circularly polarized electroluminescence form a chiral europium complex, *Adv. Mater*., 2015, **27**, 1791-1795 b) F. Zinna, M. Pasini, F. Galeotti, C. Botta, L. Di Bari and U. Giovanella, Design of lanthanide-based oleds with remarkable circularly polarized electroluminescence, *Adv. Funct. Mater*., 2017, **27**, 1603719 c) F. Zinna, L. Arrico, T. Funaioli, L. di Bari, M. Pasini, C. Botta and U. Giovanella, Modular chiral Eu(III) complexes for efficient circularly polarized OLEDs, *J. Mater. Chem. C*, 2022, **10**, 463-468.

[52] a) M. Górecki, L. Carpita, L. Arrico, F. Zinna and L. Di Bari, Chiroptical methods in a wide wavelength range for obtaining Ln^{3+} complexes with circularly polarized luminescence of practical interest, *Dalton Trans*., 2018, **47**, 7166-7177, b) L. E. MacKenzie and R. Pal, Circularly polarized lanthanide luminescence for advanced security inkis, *Nat. Rev. Chem.*, 2021, **5**, 109–124.

[53]. a) M. Cantuel, G. Bernardinelli, G. Muller, J. P. Riehl and C. Piguet, The first enantiomerically pure helical noncovalent tripod for assembling nine-coordinate lanthanide(III) podates, *Inorg. Chem*., 2004, **43**, 1840-1849 b) F. Stomeo, C. Lincheneau, J. P. Leonard, J. E. Obrien, R. D. Peacock, C. P. McCoy and T. Gunnlaugsson, Metal-Directed Synthesis of Enantiomerically Pure Dimetallic Lanthanide Luminescent Triple-Stranded Helicates, *J. Am. Chem. Soc.*, 2009, **31**, 9636-9637.

[54] a) O. Mamula, M. Lama, S. G. Telfer, A. Nakamura, R. Kuroda, H. Stoeckli-Evans and R. Scopelitti, A trinuclear EuIII Array within a diastereoselectively self-assembled helix formed by chiral bipyridine-carboxylate ligands, *Angew. Chem.*, 2005, **117**, 2583-2587.

[55] G. Bozoklu, C. Gateau, D. Imbert, J. Pecaut, K. Robeyns, Y. Filinchuk, F. Memon, G. Muller and M. Mazzanti, Metal-controlled diastereoselective self-assemby and circularly polarized luminescence of a chiral heptanuclear europium wheel, *J. Am. Chem. Soc.*, 2012, **134**, 8372-8375.

[56] À. Tubau, F. Zinna, L. Di Bari, M. Font-Bardía. R. Vicente, Luminescence, CPL and magnetic properties of 1D enantiopure Ln^{3+} complexes with (S-) and (R-) α-methoxyphenylacetate ligand, *Dalton Trans.*, 2023, **52**, 1122-1132.

[57] a) H. Xu, Q. Sun, Z. An, Y. Wei, X. Lui, Electroluminescence form europium(III) complexes, *Coord. Chem. Rev.*, 2015, **293**, 228-249 b) W. G. Quirino, C. Legnani, M. Cremona, P. P. Lima, S. A. Junior, O. L. Malta, *Thin Solid Films*, White OLEDS using β-diketones rare earth binuclear complex as emitting layer, 2006, **494**, 23–27 c) G.-L. Law, K.-L. Wong, H.-L. Tam, K.-W. Cheah, W.-T. Wong, White OLED with a single-component europium complex, *Inorg. Chem*. 2009, **48**, 10492–10494 d) E. V Baranov, G. K. Fukin, T. V Balashova, A. P. Pushkarev, I. D. Grishin, M. N. Bochkarev, 8-Quinolinolate complexes of yttrium and ytterbium: molecular arrangement and fragmentation under laser impact, *Dalton Trans*. 2013, **42**, 15699–15705 e) M. A. Katkova, A. P. Pushkarev, T. V. Balashova, A. N. Konev, G. K. Fukin, S. Y. Ketkov, M. N. Bochkarev, Near-infrared electroluminescent lanthanide [Pr (III), Nd (III), Ho (III), Er (III), Tm (III), and Yb (III)] N, O-chelated complexes for organic light-emitting devices *J. Mater. Chem*. 2011, **21**, 16611–16620 f) H. Wei, G. Yu, Z. Zhao, Z. Liu, Z. Bian, C. Huang, Constructing lanthanide [Nd (III), Er (III) and Yb (III)] complexes using a tridentate N, N, O-ligand for near-infrared organic light-emitting diodes, *Dalton Trans*. 2013, **42**, 8951–8960 g) J. P. Martins, P. Martín-Ramos, C. Coya, A. L. Álvarez, L. C. Pereira, R. Díaz, J. Martín-Gil, M. Ramos Silva, Lanthanide tetrakis-β-diketonate dimers for solution-processed OLEDs, *Mater. Chem. Phys.* 2014, **147**, 1157– 1164, h) P. Martín-Ramos, C. Coya, V. Lavín, I. R. Martín, M. R. Silva, P. S. P. Silva, M. García-Vélez, A. L. Álvarez, J. Martín-Gil, Active layer solution-processed NIR-OLEDs based on ternary erbium (III) complexes with 1, 1, 1-trifluoro-2, 4-

pentanedione and different N, N-donors, *Dalton Trans.* 2014, **43**, 18087–18096 i) R. Ilmi, M.S. Khan, Z. Li, L. Zhou, W.Y. Wong, F. Marken, P.R. Raithby, Utilization of ternary europium complex for organic electroluminescent devices and as a sensitizer to improve electroluminescence of red-emitting iridium complex, *Inorg. Chem.*, 2019, **58**, 8316-8331 and j) M.A. Katkova, M.N. Bochkarev, New trends in design of electroluminescent rare earth metallo-complexes for OLEDs, *Dalton Trans*., 2010, **39**, 6599–6612.

[58] J. Ribas, *Coordination Chemistry,* Wiley-VCH, 2008.

[59] G. A. Bain, J. F. Berry, Diamagnetic corrections and Pascal's constants, J. *Chem. Educ*. 2008, **85**, 532

[60] C. Benelli, D. Gatteschi, Introduction to Molecular Magnetism from Transition Metals to Lanthanides, Wiley-VCH, 2015.

[61] a) M. Andruh, E. Bakalbassis, O. Kahn, J. C. Trombe and P. Porcher, *Inorg. Chem.* 1993, **32**, 1616 b) O. Kahn, *Molecular Magnetism*, VHC Publishers, Inc., USA, 1993.

[62] a) C.A.P. Goodwin, F. Ortu, D. Reta, N.F. Chilton, D.P. Mills, Molecular magnetic hysteresis at 60 kelvin in dysprosocenium, *Nature*, 2017, **548**, 439-442 b) F.S. Guo, B.M. Day, Y.C. Chen, M.L. Tong, A. Mansikkamäki, R. A. Layfield, Magnetic hysteresis up to 80 kelvin in a dysprosium metallocene single-molecule magnet, *Science*, 2018, **362**, 1400-1403.

[63] F. Pointillart, K. Bernot, S. Golhen, B. Le Guennic, T. Guizouarn, L. Ouahab, O. Cador, Magnetic memory in an isotopically enriched and magnetically isolated mononuclear dysprosium complex, *Angew. Chem. Int. Ed*., 2015, **54**, 1504-1507.

[64] D.N. Woodruff, R.E.P. Winpenny, R.A. Layfield, Lanthanide Single Molecule Magnets, *Chem. Rev*. 2013, **113**, 5110-5148.

[65] D. Aguilà, L.A. Barrios, V. Velasco, O. Roubeau, A. Repollés, P.J. Alonso, J. Sesé, S.J. Teat, F. Luis, G. Aromí, Heterodimetallic [LnLn'] Lanthanide Complexes: Toward a Chemical Design of Two-Qubit Molecular Spin Quantum Gates, *J. Am. Chem. Soc.*, 2014, **40**, 14215-14222.

[66] M Affronte, Molecular nanomagnets for information technologies, *J. Mater. Chem.*, 2009, **19**, 1731-1737

[67] L Bogani, W Wernsdorfer, Molecular spintronics using single-molecule magnets, *Nat. Mater.*, 2008, **7**, 179-186.

[68] R. Sessoli, D. Gatteschi, A. Caneschi and M. A. Novak, Magnetic bistability in metal-ion cluster, *Nature*, 1993, **365**, 141–143.

[69] T. Lis, Preparation, Structure, and Magnetic Properties of a Dodecanuelear Mixed-Valence Manganese Carboxylate, *Acta Crystallogr., Sect. B: Struct. Crystallogr. Cryst. Chem.,* 1980, **36**, 2042–2046

[70] G. A. Craig, M. Murrie, 3d single-ion magnets, *Chem. Soc. Rev*., 2015, **44**, 2135-2147

[71] J.D. Rinehart, J.R. Long, Exploiting single-ion anisotropy in the design of f-element single-molecule magnets, *Chem. Sci.*, 2011, **2**, 2078-2085.

[72] N. Ishikawa, M. Sugita, T. Ishikawa, S.-Y. Koshihara and Y. Kaizu, Lanthanide Double-Decker Complexes Functioning as Magnets at the Single-Molecular Level, *J. Am. Chem. Soc.*, 2003, **125**, 8694–8695.

[73] J. Tang, P. Zhang, *Lanthanide Single Molecule Magnets*, Springer Berlin Heidelberg, Berlin, Heidelberg, 2015.

[74] S. T. Liddle, J. van Slageren, Improving f-element single molecule magnets, *Chem. Soc. Rev*., 2015, **44**, 6655.

[75] A. Zabala-Lekuona, J. M. Seco, E. Colacio, Single-Molecule Magnets: From Mn12-ac to dysprosium metallocenes, a travel in time, *Coord. Chem. Rev.*, 2021, **441**, 213984.

[76] D. N. Woodruff, R. E. P. Winpenny, R. A. Layfield, Lanthanide Single-Molecule Magnets, *Chem. Rev.* 2013, **113**, 5110-5148.

[77] a) F. Pointillart, O. Cador, B. Le Guennic, L. Ouahab, Uncommon lanthanide ions in purely 4f Single Molecule Magnetis, *Coord. Chem. Rev*., 2017, **346**, 150-175 b) A. Borah, R.

Murugavel, Magnetic relaxation in single-ion magnets formed by less-studied lanthanide ions Ce(III), Nd(III), Gd(III), Ho(III), Tm(II/III) and Yb(III), *Coord. Chem Rev.*, 2002, **453**, 214288.

[78] F. A. Mautner, F. Bierbaumer, R. C. Fischer, À. Tubau, S. Speed, E. Ruiz, S. S. Massoud, R. Vicente, S. Gómez-Coca, Insights into the Spin Dynamics of Mononuclear Cerium(III) Single-Molecule Magnets, *Inorg. Chem.*, 2022, **61**, 11124-11136.

[79] K. N. Shrivastava, Theory of Spin-Lattice Relaxation, *Phys. Stat. Sol. (b)*, 1983, **117**, 437-458.

[80] K.S. Pedersen, J. Dreiser, H. Weihe, R. Sibille, H.V. Johannesen, M.A. Sørensen, B.E. Nielsen, M. Sigrist, H. Mutka, S. Rols, J. Bendix, S. Piligkos, *Inorg. Chem.* 2015, **54**, 7600-7606

[81] M. Briganti, F. Santanni, L. Tesi, F. Totti, R. Sessoli**,** A. Lunghi, A Complete Ab Initio View of Orbach and Raman Spin-Lattice Relaxation in a Dysprosium Coordination Compound, *J. Am. Chem. Soc*., 2021, **143**, 13633-13645

[82] a) P.G. Klemens, Anharmonic attenuation of localized lattice vibrations, *Phys. Rev.*, 1961, **122**, 443. b) D. W. Feldman, J. G. Castle, J. Murphy, spin relaxation of atomic hydrogen in CaF_2-evidence for local mode, *Phys. Rev.*,1965, **138**, A1208-A1216. c) Y. Zhou, B. E. Bowler, G. R. Eaton, S. S. Eaton, Electron Spin Lattice Relaxation Rates for S = 12 Molecular Species in Glassy Matrices or Magnetically Dilute Solids at Temperatures between 10 and 300 K, *J. Magn. Reson.*, 1999, **139**, 165-174.

[83] C. B. Harris, R. M. Shelby, P. A. Cornelius, Effects of Energy Exchange on Vibrational Dephasing Times in Raman Scattering, *Phys. Rev. Lett.*, 1977, **38**, 1415-1419.

[84] N. V. Vugman and M. Rothier Amaral, Jr., Influence of localized anharmonic vibrations on electron paramagnetic resonance spectroscopy, *Phys. Rev. B* 1990, **42**, 9837-9872.

[85] D. Gatteschi, R. Sessoli, Quantum Tunneling of Magnetization and Related Phenomena in Molecular Materials, *Angew. Chem. Int*., 2003, **42**, 268-297.

[86] H.B.G. Casimir, D. Bijl, F.K. Du Pré, Measurememts on paramagnetic relaxation in chromium potassium alum, *Physica*, **1941**, 8, 449-460.

[87] Y.N. Guo, G.F. Xu, P. Gamez, L. Zhao, S.Y. Lin, R. Deng, J. Tang, H.J. Zhang, Two-step relaxation in a linear tetranuclear dysprosium(III) aggregate showing single-molecule magnet behavior. *J. Am. Chem. Soc.***132**, 8538–8539.

[88] Y.N. Guo, G.F. Xu, Y. Guo, J. Tang, Relaxation dynamics of dysprosium(III) single molecule magnets. *Dalton. Trans.* **40**, 9953–9963.

[89] a) J. Ruiz, A.J. Mota, A. Rodríguez-Diéguez, S. Titos, J.M. Herrera, E. Ruiz, E. Cremades, J.P. Costes, E. Colacio, Field and dilution effects on the slow relaxation of a luminescent DyO_9 low-symmetry single-ion magnet, *Chem. Commun*., 2012, **48**, 7916-7918 b) A. Arauzo, A. Lazarescu, S. Shova, E. Bartolomé, R. Cases, J. Luzón, J. Bartolomé, C. Turta, Structural and magnetic properties of some lanthanide (Ln=Eu(III), Gd(III) and Nd(III)) cyanoacetate polymers: field-induced slow magnetic relaxation in the Gd and Nd substitutions, *Dalton Trans*., 2014, **43**, 12342–12356

[90] C. C. Beedle, C. J. Stephenson, K. J. Heroux, W. Wernsdorfer and D. N. Hendrickson, Photoluminescent Mn_4 Single-Molecule Magnet, *Inorg. Chem*., 2008, **47**, 10798–10800.

[91] a) R. Jankowski, M. Wyczesany, S. Chorazy, Multifunctionality of luminescent molecular nanomagnets based on lanthanide complexes, *Chem. Commun*., 2023, **59**, 5961-5986 b) J.-H. Jia, Q.-W- Li, Y.-C. Chen, J.-L. Liu, M.-L. Tong, Luminescent single-molecule magnets based on lanthanides: Design strategies, recent advances and magneto-luminescent studies, *Coord. Chem. Rev*., 2019, **378**, 365-381.

[92] G. Cucinotta, M. Perfetti, J. Luzon, M. Etienne, P.-E. Car, A. Caneschi, G. Calvez, K. Bernot and R. Sessoli, Magnetic anisotropy in a dysprosium/DOTA single-molecule magnet: beyond simple magneto-structural correlations. *Angew. Chem., Int. Ed*., 2012, **51**, 1606–1610

[93] a) Y.C. Chen, J.L. Liu, Y. Lan, Z.Q. Zhong, A. Mansikkamaki, L. Ungur, Q.W. Li, J.H. Jia, L. F. Chibotaru, J.-B. Han, W. Wernsdorfer, X.-M. Chen and M.-L. Tong, Dynamic Magnetic and Optical Insight into a High Performance Pentagonal Bipyramidal Dy^{3+} Single-Ion Magnet, *Chem. Eur. J.*, 2017, **23**, 5708–5715 b) D. Errulat, R. Marin, D. A. Galico, K. L. M. Harriman, A. Pialat, B. Gabidullin, F. Iikawa, O. D. D. Couto Jr., J. O. Moilanen, E. Hemmer, F. A. Sigoli and M. Murugesu, A Luminescent Thermometer Exhibiting Slow Relaxation of the

Magnetization: Toward Self-Monitored Building blocks for Next-Generation Optomagnetic Devices, *ACS Cent. Sci.*, 2019, **5**, 1187–1198.

[94] a) J. Wang, J. J. Zakrzewski, M. Heczko, M. Zychowicz, K. Nakagawa, K. Nakabayashi, B. Sieklucka, S. Chorazy and S. Ohkoshi, Proton Conductive Luminescent Thermometer Based on Near-Infrared Emissive $YbCo_2$ Molecular Nanomagnets, *J. Am. Chem. Soc.*, 2020, **142**, 3970–3979 b) J. Corredoira-Vazquez, C. Gonzalez-Barreira, M. Fondo, A. M. Garcia-Deibe, J. Sanmartin-Matalobos, M. A. Hernandez Rodriguez and L. D. Carlos, Luminescent thermometry in a Dy4 single molecule magnet, *Dalton Trans.*, 2022, **51**, 15593–15600

2. Compounds derived from the 4,4,4-Trifluoro-1-phenyl-butanedione (HBtfa)

2. Compounds derived from the 4,4,4-Trifluoro-1-phenyl-butanedione (HBtfa):

2.1 Introduction

1,3-Diketones, more commonly called β-diketones, are widely used in the field of coordination chemistry due to the great synthetic flexibility they present and the wide range of interesting properties that the resulting compounds may exhibit in different areas such as luminescence and magnetism.[1,2,3] Coordination compounds derived from β-diketones have shown potential applications ranging from material science (Solar concentrators, Lasers, Sensors, OLEDs, etc) to biomedical analysis.[4,5] β-diketone molecules exhibit a structural arrangement where two carbonyl groups are separated by one carbon atom (the α-carbon). This particular arrangement gives distinct chemical properties to the β-diketones differentiating them from other compounds containing carbonyl groups. The general structural formula of a β-diketone is as shown in Scheme 2.1 a), where R_1, R_2 represent organic substituents. Generally, the substituent on the α-carbon is a hydrogen atom, though it can also be provided with an organic functionalized group[6]. Acetylacetone (Hacac) is the simplest and extensively used β-diketone where the R substituents consist of two methyl groups. Hacac was first synthetized from acetone and ethyl acetate through a base-catalyzed condensation reaction, now well known as the Claisen condensation, named after the scientific who first described its preparation more than 100 years ago, Rainer Ludwing Claisen[7] From then, multiple synthetic routes using different reactants, have been formulated. Otherwise, the R substituents can go from a methyl group to functionalized and more voluminous organic groups such as polypyridyl rings, groups with multiple aromatic rings, long alkyl chains etc., adjusting in this way the physicochemical properties of the final coordination compound.

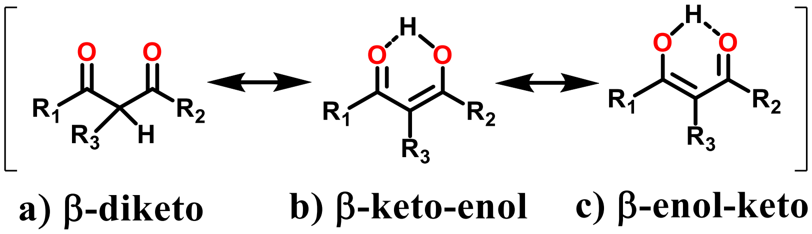

Scheme 2.1. β-diketone tautomerism

1,3-diketones usually present keto-enol tautomerism, Scheme 2.1. The characteristics of the prototropic tautomerism showing the double-single and single-double bonds in the keto-enol and enol-keto forms of free β-diketones are consolidated through coordination to the metal ion. Moreover, an interesting facility showed by these systems is that they can be easily deprotonated in basic medium. The resulting deprotonated β-diketonate can act as an anionic bidentate ligand which added to the Lewis acid character of the Ln^{3+} confers stable metal coordination compounds, even in solution.[8] Generally, the most common ligand arrangement is in the chelating coordination mode, forming a six-membered chelate ring with the metal ion, Scheme2.2 a). Other coordination modes such as μ and μ_3 are found in other metal complexes extending from mononuclear to polynuclear coordination metal structures, Scheme2.2 b).[9]β-diketonate systems widespread from mono-β-diketonate to poly-β-diketonate molecules, thus opening up a whole range of possibilities from mononuclear to self-assembled metallo-supramolecular coordination compounds.[9]

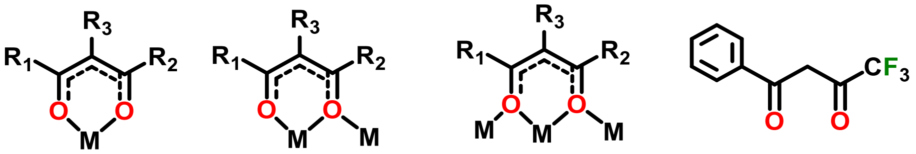

a) **b)** **c)**

Scheme 2.2 Coordination modes of β-diketonate ligands. a) Chelating coordination mode b) chelating bridging η_1:η_2:μ and η_1:η_1:η_2:μ_3 coordination mode respectively c) 4.4.4-Trifluoro-1-phenyl-1,3-butanedione (HBtfa)

4.4.4-Trifluoro-1-phenyl-1,3-butanedione (HBtfa), Scheme 2.2c) is a mono-β-diketone ligand which R_1 group is substituted by a phenyl group and the R_2 group by a fluorinated -CF_3. The α-carbon stays bonded to a hydrogen atom. Fluorination of C-H bonds reduce the degree of higher oscillator C-H vibrational quenching which may improve thermal stability, volatility and photoluminescence properties of the final lanthanide compound. In addition, the presence of an electron withdrawing group (-CF_3), results in a more acidic β-diketone since -CF_3 stabilizes better the negative charge left in the β-diketonate.[10]

In this regard, HBtfa has been used in this work to obtain mononuclear lanthanide compounds in which the luminescence and single molecule magnetic properties will be studied. After deprotonation of HBtfa in basic medium, the 4.4.4-Trifluoro-1-phenyl-1,3-

butanedionate anion (Btfa) coordinates to the lanthanide ion in the chelating coordination mode. To obtain neutral mononuclear compounds the 1:3 ratio lanthanide(III) to Btfa is used. Due to the high coordination numbers that Ln^{3+} ions can reach, we will add also ancillary ligands to occupy two or more coordinating positions and provide to the final compound with additional luminescent or magnetic properties. To accomplish this goal, the ancillary ligands used in the presented work are N,N- and N,N,N-donor polypyridyl ligands, presented hereafter. They confer additional stability to the final compound since they also coordinate in a chelating coordination mode. Moreover, all of them present aromatic rings which, due to the delocalized electron density, could provide with good optical properties.

2.2 Compounds derived from Cerium(III) and 4,4,4-Trifluoro-1-phenyl-butanedione (HBtfa).

In the Single Molecular Magnets (SMM) field bearing lanthanide(III) coordination compounds, the most studied complexes, till date, are the ones containing Dy^{3+}, Tb^{3+} and Er^{3+} ions with the dysprosium ones usually showing the most promising results. The above mentioned lanthanide atoms possess large number of unpaired electrons that lead to larger angular momentum ($J=L+S$) and large magnetic anisotropy which can also be improved by the adequate ligand field, as remarked in the *Introduction Chapter*. Cerium(III) compounds, together with those of Ho^{3+}, Tm^{3+}, Yb^{3+} and Nd^{3+}, are less studied in this field. In any case, the few compounds studied exhibit quite interesting magnetic properties.[11]

In this Chapter we focus on the lighter Ce^{3+} lanthanide cation. Cerium is one of the most abundant in nature and inexpensive rare earth element, its natural isotopes do not possess nuclear spin and it has been added as a dopant to one of the currently strongest permanent magnet, $Nd_2Fe_{14}B$, replacing dysprosium.[12] Its electronic configuration is $4f^1$ with a $^2F_{5/2}$ ground state. Though having only one unpaired electron in the f orbital, relaxation of the magnetization of Ce^{3+} can be observed because the spin-orbit effect of the $4f^1$ electron creates non-negligible magnetic anisotropy. When the Ce^{3+} ion is set in a coordination complex, the spin-orbit coupling component (J) splits, due to crystal field, into ($2J$+1) $\pm m_j$ states: +J, +J-1 ,.., -J+1, -J: ±5/2, ±3/2 and ±1/2. With the aim to improve the SMM character in Ce^{3+} compounds we can try to choose the ideal coordination environment around the lanthanide ion to stress an axial geometry that would stabilize the m_j=±5/2 Kramer Doublet (KD) with an oblate *4f*-shell electron density distribution as the ground state and destabilize the prolate electron distribution in m_j=±1/2 and ±3/2 states. Such systems would lead to a reduced Quantum Tunneling of Magnetization (QTM) effect with anisotropic barriers higher in energy (reduce m_j mixing) and, in principle, improve the SMM performance.[13, 14, 15]

Regarding β-diketonate systems, two series of mononuclear Ce^{3+} β-diketonate complexes with N-donor auxiliary ligands are found in the literature, Table 2.1. First, the 1,1,1-trifluoro-5,5-dimethyl-2,4-hexadione (Hfdh) led to the $[Ce(fdh)_3(bpy)]$ compound with a D_4d symmetry~~.~~[16] Moreover, with another β-diketonate ligand named 4,4,4-trifluoruro-1-(naphthalene-2-yl)butane-1,3-dionato (ntfa), a new series of Ce^{3+} compounds were published showing slow relaxation of the magnetization under applied H_{dc} field with formulae $[Ce(ntfa)_3(MeOH)_2]$, $[Ce(ntfa)_3(5,5'\text{-}Me_2bipy)]$ and $[Ce(ntfa)_3(bipy)_2]$ and with D_2d, D_2d and C_2v point group symmetry respectively.[3] For these mononuclear Ce^{3+} β-diketonate complexes, the ab-initio calculations at zero field on the electron gyromagnetic ratio (g-tensor) for each m_j states were described. Easy axial anisotropy was found (g_{xx} and $g_{yy} < g_{zz}$) through the calculations which demonstrated that the effective g tensor of the ground doublet shows considerable transverse contributions (g_{xx} and g_{yy}) that led to the ground state wave function |±5/2〉 mixed with the |±1/2〉 and |±3/2〉 from the other excited m_j doublets.

Otherwise, the only Ce^{3+} compound showing SMM behavior till date is the trinuclear Zn-Ce-Zn compound prepared from an *o*-vanillin Schiff base based ligand.[17] For this heterometallic compound, the g_{zz} yielded 4.06 from ab-initio calculations which is close to the theoretical value of 4.28 for a pure m_j=±5/2 Kramer Doublet, $g_{zz}= 2g_jm_j$.[18] From the measured High-field Electron Paramagnetic Resonance (HF-EPR) spectrum, g_{zz} yielded 3.27 which is assigned to the ground state of m_j=5/2 KD with slight mixing of the m_j=1/2 pair. Nevertheless, two mononuclear metallocene Ce^{3+} compounds with the formulae $[Ce(Cp^{ttt})_2\{(C_6F_5\text{-}k^1\text{-}F)B(C_6F_5)_3\}]$ and $[Ce(Cp^{ttt})_2Cl]$ (where Cp^{ttt} is $C_5H_2tBu_3$-1,2,4) are found in the literature where the g_{zz} axial component obtained by multiconfigurational analysis shows even higher values than the trinuclear Zn-Ce-Zn SMM compound (4.16 and 4.22 respectively) and a ground state wavefunction of 100% |±5/2〉 for the first compound.[19] The two Cp^{ttt} groups placed in the axial positions of the lanthanide cation and the low equatorial interactions of the $[B(C_6F_5)_4]^-$ and Cl^- anions, led the Ce^{3+} centers in an axial stressed symmetry. Furthermore, for these organometallic compounds, the EPR measurements were performed and the experimental g^{eff} values were close to the computed ones. However, despite the calculated g_{zz} values near 4.28, these compounds only showed slow relaxation of the magnetization when applying an external magnetic field of 0.1 T. The rest of the previous mononuclear Cerium(III) compounds found in the literature showing slow relaxation of the magnetization under an external H_{dc} with performed ab-initio calculations resulted of axial symmetry but with considerable rhombic contribution in the ground state. Their magnetic properties are compiled in Tables 2.1 and 2.2,[20-24] Similar result was found in the dinuclear Ce^{3+} compound of formula $[Ce_2(RR\text{-}L)_2(\mu\text{-}Cl)_6]$, where L is 1,4,7,10-tetrakis(2-pyridylmethyl)-1,4,7,10-tetraaza-cyclododecane, Table 2.3[25] In addition, as previously mentioned, the natural isotopes of Ce^{3+} don't have nuclear spin resulting in a more clarifying and interpretative EPR spectra. Interestingly, in the published studies where EPR is also measured for the Ce^{3+} compounds, the g_{xx}, g_{yy} and g_{zz} experimental values are in good agreement with the computational experiments.[17,19,20,25] At the moment, pure Ising type axial anisotropy (g_z=4.28) hasn't been found in the computational calculations nor in EPR measurements for any of the Ce^{3+} compounds found in the literature. It is worth to note that slow relaxation of the magnetization under relatively small H_{dc} fields was measured for some Ce^{3+} coordination complexes were multiconfigurational CASSCF calculations indicated easy plane magnetic anisotropy that led to larger contributions of the $|\pm1/2\rangle$ and $|\pm3/2\rangle$ wavefunctions in the ground state $\pm m_j$ KD.[20-24] Despite the existence of transverse contribution in the ground state, these compounds showed similar magnetic behavior as the ones showing more axial strained coordination geometries. Magnetic characteristics of the previous Ce^{3+} coordination compounds found in the literature are compiled in Tables 2.1-2.5.

To further understand spin relaxation dynamics of Ce^{3+} coordination compounds, deep study of more examples of these complexes are needed. This way we could control and manipulate the synthesis of these compounds to be able to design Cerium based systems with enhanced magnetic properties and SMM performance.

Table 2.1. β-diketonate Ce^{3+} mononuclear compounds

	H (Oe)	Orbach		QTM	Raman		Direct	Local Mode		ΔE_{calc} (cm^{-1})	Calculated g_{xx}, g_{yy}, g_{zz}	Wavefunction analysis of the ground doublet state	Ref
		U_{eff} (cm^{-1})	τ_0 (s)	τ_{QTM} (s)	C ($s^{-1}K^{-n}$)	n	D ($s^{-1}K^{-1}$)	C_{LOC} (s^{-1})	ω (cm^{-1})				
[Ce(fdh)$_3$(bpy)]	**2000**	**23.14**	**$1.8*10^{-7}$**							**339.6**	**0.18, 0.46, 3.79**	**0,92|±5/2〉 +0.014|±3/2〉 +0.066|±1/2〉**	**16**
					0.40	**6.0**							
[Ce(ntfa)$_3$(MeOH)$_2$]	**200**	**Around 20-30**		**0.006$^{(c)}$**	**24.82**	**2.98**	**0.00045$^{(c)}$**	**$1.23*10^9$**	**32.2**	**319**	**1.06, 1.30, 3.16**	**|±5/2〉 with contribution of |±3/2〉**	**3**
[Ce(ntfa)$_3$(5,5'-Me$_2$bipy)]	**200**	**Around 20-30**		**0.06$^{(c)}$**	**0.86**	**8.01**	**0.0006$^{(c)}$**	**$2.83*10^5$**	**9.5**	**258**	**0.22, 0.37, 3.32**	**|±5/2〉 with contribution of |±3/2〉**	
[Ce(ntfa)$_3$(bipy)$_2$]	**200**	**Around 20-30**		**0.04$^{(c)}$**	**131.39**	**1.28**	**0.0002$^{(c)}$**	**$6.20*10^5$**	**15.7**	**325**	**0.09, 0.44, 3.91**	**|±5/2〉 with contribution of |±3/2〉**	

fdh: 1,1,1-fluoro-5,5-dimethyl-hexa-2,4-dione
ntfa:4,4,4-trifluoro-1-(naphthalen-2-yl)butane-1,3-dionato
$^{(c)}$To be able to compare, τ_{QTM} and D have been calculated applying the corresponding equation to the values obtained from the fit of the dependence with field (B_1 and B_2 for the QTM parameter τ_{QTM} and $A*H^4$ for the Direct parameter D and dT^n, e and f for the Raman C constant).

Table 2.2. Mononuclear Ce^{3+} compounds

Compound[(a)]	H (Oe)	Orbach		QTM	Raman		Direct	ΔE_{calc} (cm^{-1})	Calculated g_{xx}, g_{yy}, g_{zz}	Wavefunction analysis of the ground doublet state	Ref
		U_{eff} (cm^{-1})	τ_0 (s)	τ_{QTM} (s)	C (s^{-1}K^{-n})	n	D (s^{-1}K^{-1})				
$\mathrm{Li(DME)_3[Ce(COT)_2]}$	400	20.85	$1.2*10^{-6}$	0.058				503	2.43, 2.43, 1.03	$\|\pm1/2\rangle$	35, 18
$\mathrm{[Ce(NO_3)_3(18\text{-}crown\text{-}6)]}$	1000	21.82	$1.7*10^{-7}$								41
		21.06	$2.2*10^{-7}$		0.108	5(fixed)					
		17.79	$9*10^{-7}$		1.5×10^{-3}	9(fixed)					
$\mathrm{[Ce(NO_3)_3(1,10\text{-}diaza\text{-}18\text{-}crown\text{-}6)]}$	1000	30.58	$2.3*10^{-8}$								
		31.28	$2.6*10^{-8}$		0.52	5(fixed)					
		15.99	$6*10^{-6}$		22	9(fixed)					
$\mathrm{[Ce(NO_3)_3(HL_3)]}$	3000	26.06	$2.76*10^{-8}$	0.076	0.154	7.36		348	0.06, 0.69, 3.82	0.94 $\|\pm5/2\rangle$	21
$\mathrm{[Ce(18\text{-}crown\text{-}6)(Cl_4Cat)(NO_3)]\cdot MeCN}$	1500				1.22	5(fixed)	31.9	443	0.26 0.40 3.84 [(b)]<0.5(not visible), 0.81, 3.59	$0.99\|\pm5/2\rangle$ $+0.004\|\pm3/2\rangle$ $+0.001\|\pm1/2\rangle$	20
$\mathrm{[Ce(18\text{-}crown\text{-}6)(Br_4Cat)(NO_3)]\cdot MeCN}$	800				1.87	5(fixed)	45.4	-	-	-	
$\mathrm{[Ce(NO_3)_3L^5{}_3]}$	200	14.94	$2.7*10^{-7}$					220	1.90, 1.67, 0.26	Mixed m_j states	36
					1.44	6.8	99.5				
$\mathrm{[Ce_{0.29}La_{0.71}(NO_3)_3L^5{}_3]}$	30				0.8	7.55	306.5	220	1.98 1.68 0.01	Mixed m_j states	
$\mathrm{[Ce(Cp^{ttt})_2\{(C_6F_5\text{-}k^1\text{-}F)B(C_6F_5)_3\}]}$	1000				0.03	5.37		787	0.1 0.1 4.16 [(b)]4.22(g_z)	$1\|\pm5/2\rangle$	19
$\mathrm{[Ce(Cp^{ttt})_2Cl]}$					0.005	6.48		353	0.10 0.14 4.09 [(b)]4.19(g_z)	$0.97\|\pm5/2\rangle$ $+0.3\|\pm1/2\rangle$	
$\mathrm{[Ce(Fcterpy)(NO_3)_3(H_2O)]}$	2000	13.9	$1.8*10^{-11}$		They used Orbach +Raman functions for the fitting. But the parameters for Raman aren't published.						45
$\mathrm{[Ce(L^6)(NO_3)_3(MeOH)]}$	2000	11.82	$3.9*10^{-8}$								39
$\mathrm{[CeL^7F](CF_3SO_3)\cdot 2H_2O}$	1200	26.2						503	1.24 1.34 3.30	$0{,}86\|\pm5/2\rangle$ $+0.12\|\pm3/2\rangle$	22
					0.049	6.56					
$\mathrm{[Ce(dppbO_2)Cl_3]}$	100	38			31	3.4		291	0.08, 0.82, 2.86	$0.53\|\pm5/2\rangle$ $+0.27\|\pm3/2\rangle$ $+0.20\|\pm1/2\rangle$	23
$\mathrm{[Ce(L^8)(NO_3)_3]}$	1500	20.16	$2.0*10^{-10}$	$2.69*10^{-4}$							47

[(a)]Ligand abbreviations:
COT: bis(trimethylsilyl)cyclooctatetraenyl dianion.
18-crown-6: 1,4,7,10,13,16-hexanoxacyclooctadecane.
1,10-diaza-18-crown-6: 1,4,10,13-tetraoxa-7,16-diazacyclooctadecane
HL: 2-methoxy-6-[(E)-phenyliminomethyl]phenol
L^5: $\mathrm{tBuPO(NH^iPr)_2}$:*tert*-butyl-phosphonic-di(isopropyl)amide
Fcterpy: Fcterpy = 4′-ferrocenyl-2,2′:6′,2′′-terpyridine
L^6: N,N'-bis(pyridine-2-ylmethylene)cyclohexane-1,2-diamine.
L^7: 1,4,7,10-tetrakis(2-pyridylmethyl)-1,4,7,10-tetraaza-cyclododecane)
[(b)] Values obtained from EPR spectra recorded in the X-band (9.4 Hz).
$\mathrm{dppbO_2}$: 1,2-bis(diphenylphosphino) benzenedioxide
L^8: macrocyclic Schiff base ligand derived from a template reaction of o-phenylene diamine and pyridine-2,6-biscarboxyaldehide.

Table 2.3. Dinuclear Ce^{3+} compounds

Compound$^{(a)}$	**H (Oe)**	**Orbach**		**QTM**	**Raman**		**Direct**	**ΔE_{calc} (cm^{-1})**	**Calculated g_{xx}, g_{yy}, g_{zz}**	**Wavefunction analysis of the ground doublet state**	**Ref**
		U_{eff} (cm^{-1})	**τ_0 (s)**	**τ_{QTM} (s)**	**C ($s^{-1}K^{-n}$)**	**n**	**D ($s^{-1}K^{-1}$)**				
$[Ce_2(RR\text{-}L^4)_2(\mu\text{-}Cl)_6]$	**3000**	**-**	**-**		**The τ vs. T magnetic data was best reproduced with Raman+Direct function combination**			**$^{(g)}$Ce1:348 Ce2:320**	**Ce1: 0.53 0.90 3.06 Ce2: 0.27 0.62 3.07 $^{(e)}$<0.5, 0.71, 3**	**Ce1:0.65|±5/2〉 +0.05|±3/2〉 +0.3|±1/2 〉 Ce2:0.67|±5/2〉 +0.07|±3/2〉 +0.26|±1/2**	**25**

$^{(a)}$Ligand abbreviations:

L^4: N,N’-bis((2,2-diphenyl-(pyridine-2-yl)methylene)-(R,R/S,S)-ethane-1,2-diamine)

$^{(g)}$ Dinuclear compound with two cristallographically different Ce^{3+} atoms.

$^{(e)}$ Values obtained from EPR spectra recorded in the X-band (9.4 Hz).

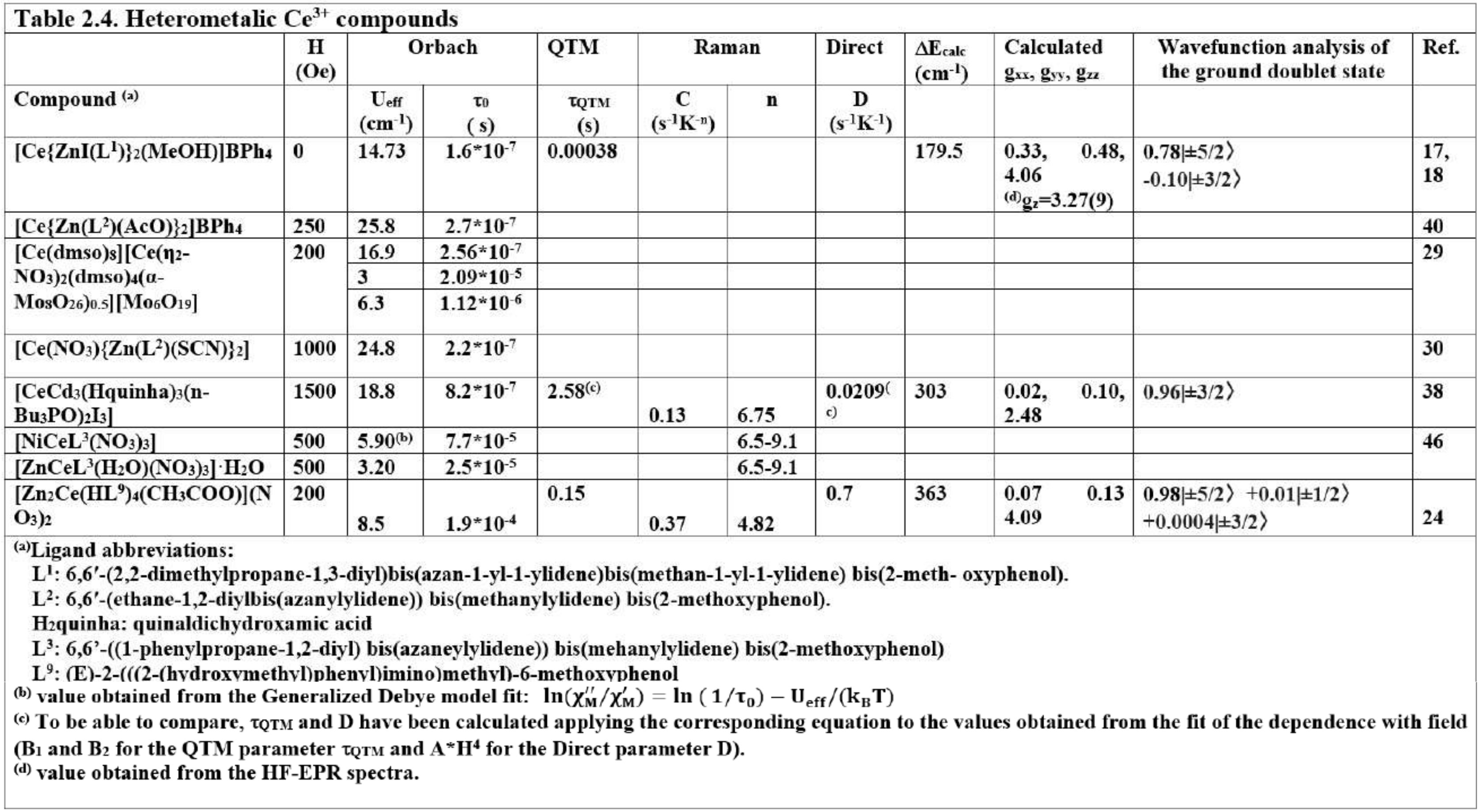

Table 2.4. Heterometalic Ce^{3+} compounds

	H (Oe)	Orbach		QTM	Raman		Direct	ΔE_{calc} (cm^{-1})	Calculated g_{xx}, g_{yy}, g_{zz}	Wavefunction analysis of the ground doublet state	Ref.
Compound [(a)]		U_{eff} (cm^{-1})	τ_0 (s)	τ_{QTM} (s)	C ($s^{-1}K^{-n}$)	n	D ($s^{-1}K^{-1}$)				
$[Ce\{ZnI(L^1)\}_2(MeOH)]BPh_4$	0	14.73	$1.6*10^{-7}$	0.00038				179.5	0.33, 0.48, 4.06 $^{(d)}g_z$=3.27(9)	$0.78\|\pm5/2\rangle$ $-0.10\|\pm3/2\rangle$	17, 18
$[Ce\{Zn(L^2)(AcO)\}_2]BPh_4$	250	25.8	$2.7*10^{-7}$								40
$[Ce(dmso)_8][Ce(\eta_2\text{-}NO_3)_2(dmso)_4(\alpha\text{-}Mo_8O_{26})_{0.5}][Mo_6O_{19}]$	200	16.9	$2.56*10^{-7}$								29
		3	$2.09*10^{-5}$								
		6.3	$1.12*10^{-6}$								
$[Ce(NO_3)\{Zn(L^2)(SCN)\}_2]$	1000	24.8	$2.2*10^{-7}$								30
$[CeCd_3(Hquinha)_3(n\text{-}Bu_3PO)_2I_3]$	1500	18.8	$8.2*10^{-7}$	2.58[(c)]	0.13	6.75	0.0209[(c)]	303	0.02, 0.10, 2.48	$0.96\|\pm3/2\rangle$	38
$[NiCeL^3(NO_3)_3]$	500	5.90[(b)]	$7.7*10^{-5}$			6.5-9.1					46
$[ZnCeL^3(H_2O)(NO_3)_3]\cdot H_2O$	500	3.20	$2.5*10^{-5}$			6.5-9.1					
$[Zn_2Ce(HL^9)_4(CH_3COO)](NO_3)_2$	200	8.5	$1.9*10^{-4}$	0.15	0.37	4.82	0.7	363	0.07 0.13 4.09	$0.98\|\pm5/2\rangle$ $+0.01\|\pm1/2\rangle$ $+0.0004\|\pm3/2\rangle$	24

[(a)] Ligand abbreviations:

L^1: 6,6′-(2,2-dimethylpropane-1,3-diyl)bis(azan-1-yl-1-ylidene)bis(methan-1-yl-1-ylidene) bis(2-meth- oxyphenol).

L^2: 6,6′-(ethane-1,2-diylbis(azanylylidene)) bis(methanylylidene) bis(2-methoxyphenol).

H_2quinha: quinaldichydroxamic acid

L^3: 6,6’-((1-phenylpropane-1,2-diyl) bis(azaneylylidene)) bis(mehanylylidene) bis(2-methoxyphenol)

L^9: (E)-2-(((2-(hydroxymethyl)phenyl)imino)methyl)-6-methoxyphenol

[(b)] value obtained from the Generalized Debye model fit: $\ln(\chi''_M/\chi'_M) = \ln(1/\tau_0) - U_{eff}/(k_BT)$

[(c)] To be able to compare, τ_{QTM} and D have been calculated applying the corresponding equation to the values obtained from the fit of the dependence with field (B_1 and B_2 for the QTM parameter τ_{QTM} and $A*H^4$ for the Direct parameter D).

[(d)] value obtained from the HF-EPR spectra.

Table 2.5. Ce^{3+} Frameworks

Compound [(a)]	**H (Oe)**	**Orbach**		**QTM**	**Raman**		**Direct**	**ΔE_{calc} (cm^{-1})**	**Calculated g_{xx}, g_{yy}, g_{zz}**	**Wavefunction analysis of the ground doublet state**	**Ref**
		U_{eff} (cm^{-1})	**τ_0 (s)**	**τ_{QTM} (s)**	**C ($s^{-1}K^{-n}$)**	**n**	**D ($s^{-1}K^{-1}$)**				
$\{[Ce_2(2,5\text{-}pzdc)_3(H_2O)_4]\}\cdot H_2O$	**2000**	**12.0**	**99.8*10^{-8}**		**3285**	**9 (fixed)**	**18.6*10^{-3}**	**303**	**3.59, 2.91, 2.03**[(b)]	**|±1/2⟩** [(b)]	**37a**
	1000	**10.5**	**65.3*10^{-8}**		**3411**	**9 (fixed)**	**19.2*10^{-3}**				
$[Ce_2Zn_3(oda)_6(H_2O)_6]\cdot 12H_2O$	**2000**	**13**						**326.6**	**1.37, 1.37, 1.16**	**0.41|±5/2⟩ +0.58|±1/2⟩**	**37b**
	2000				**631**	**2.6**					
	1000				**501**	**2.7**					

(a) Ligand abbreviations:
pzdc: 2,5-pyrazinedicarboxylate dianion.
oda: oxydiacetate
(b) Values obtained from Q-band EPR spectra.

To provide with new insights into the understanding of the Cerium(III) spin relaxation in coordination compounds, five new β-diketonate Ce^{3+} complexes are presented. They derive from the β-diketonate ligand Btfa = 4,4,4-trifluoro-1-phenyl-1,3-butanedionate and polypyridyl molecules as ancillary ligands. The polypyridyl ligands used are 1,10-phenanthroline (phen), 2,2'-bipyridyl (bipy), 2,2′:6′,2″-terpyridine (terpy) and 4,7-Diphenyl-1,10-phenanthroline (bathophen), Scheme 2.3 b), c), d), e) respectively. With this purpose, the nitrogen donor N,N-L and N,N,N-L auxiliary ligands could be placed in the equatorial positions of the Ce^{3+} metallic center while the β-diketonates can be fixed in the axial positions, stressing in this way an axial geometry. The five new compounds have been structurally and magnetically characterized and a thorough investigation along the experimental magnetic data and ab initio calculations has been conducted to gain deeper insights into the spin dynamics involved in the relaxation of magnetization of these compounds.

2.1.1 Experimental procedure

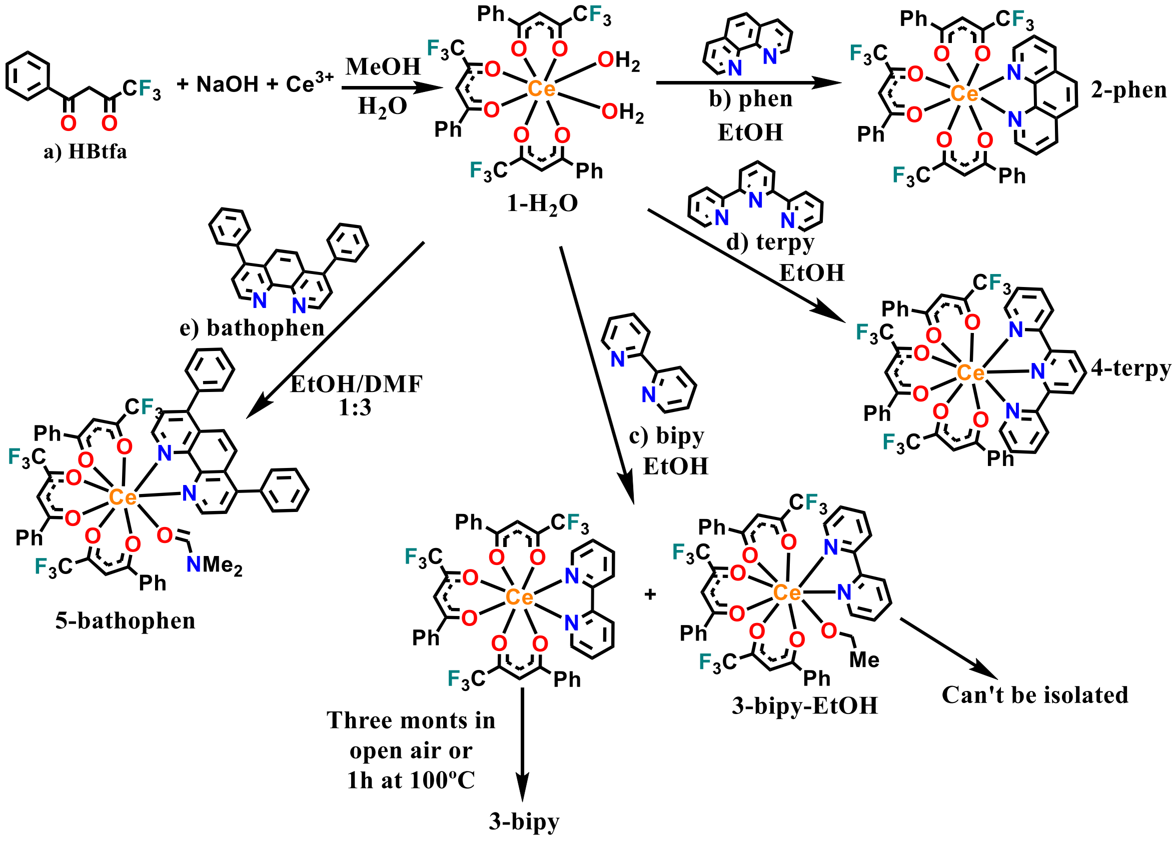

Scheme 2.3. Synthetic routes to obtain the presented Cerium(III) compounds. Molecular representations of compounds **1-H$_2$O** to **5-bathophen** and of a) 4,4,4-trifluoro-1-phenyl-1,3-butanedionate (HBtfa), b) 1,10-phenanthroline (phen), c) 2,2’-bipyridil (bipy), d) 2,2';6',2"-terpyridine (terpy) and e) bathophenanthroline (bathophen).

A schematic representation of obtention of the compounds from **1-H$_2$O** to **5-bathophen** with the molecular representation of the compounds and the ligands we have used is shown in Scheme 2.3. First, compound **1-H$_2$O** with formula [Ce(Btfa)$_3$(H$_2$O)$_2$] was synthetized and used as the precursor in the subsequent reactions. Synthesis of **1-H$_2$O** was carried out as follows: a methanol solution (5 mL) containing CeCl$_3$·6H$_2$O (2 mmol, 0.745 mg) was added to a previous mixed methanol solution (10 mL) composed of NaOH (6 mmol, 240 mg) and HBtfa (6 mmol, 1296.96 mg). The solution was stirred for 1 hour at room temperature. Then 80 mL of deionized water were added to the reaction mixture, and it was allowed to stir overnight. The obtained orange precipitate was filtrated, cleaned with deionized water and dried under vacuum. Compound 1-H2O was obtained in a 82%

yield. Then, 0.125 mmol of **1-H_2O** powder were dissolved in 15 mL of ethanol to obtain single crystals by slow evaporation at room temperature. Orange block crystals suitable for X-Ray diffraction analysis were obtained in one week.

Subsequently, compounds **2-phen**, **3-bipy-EtOH**, **4-terpy** and **5-bathophen** were obtained in a displacement reaction of the H_2O molecules of **1-H_2O** by the different polypyridyl ligands. The auxiliar molecules used for this family of Cerium(III) compounds were: 1,10-phenanthroline (phen), 2,2’-bipyridil (bipy), 2,2';6',2"-terpyridine (terpy) and 4,7-Diphenyl-1,10-phenanthroline (bathophen) to obtain compounds **2-phen**, **3-bipy**, **4-terpy** and **5-bathophen** respectively.

Reaction of 1mmol of **1-H_2O** compound with the chelating N,N-L and N,N,N-L ligands in a 1:1 ratio led to the mononuclear Ce^{3+} coordination complexes of formula $[Ce(Btfa)_3(phen)]$ (**2-phen**), $[Ce(Btfa)_3(bipy)(EtOH)]$ (**3-bipy-EtOH**), $[Ce(Btfa)_3(terpy)]$ (**4-terpy**) and $[Ce(Btfa)_3(bathophen)(DMF)]$ (**5-bathophen**). The solvent used in each synthesis was ethanol for the obtention of compounds **2-phen**, **3-bipy** and **4-terpy** and a mixture of dimethylformamide (DMF)/ethanol (1:3) in the case of **5-bathophen**. Orange block single crystals of all compounds were obtained by slow evaporation at room temperature of the respective solutions. All of the above compounds crystallized in a week except compound **5-bathophen** which needed a month, probably because of DMF which has a higher evaporation temperature. The compounds were obtained with high yields, all of them above 70%.

In the case of the synthesis after the reaction of **1-H_2O** with the bipy ligand in ethanol, structural determination from single crystal X-ray diffraction by using one chosen crystal from the bulk product, indicated that the compound had the molecular formula $[Ce(Btfa)_3(bipy)(EtOH)]$. We will label this product as **3-bipy-EtOH**. By comparing **3-bipy** and **3-bipy-EtOH**, the difference is that in **3-bipy-EtOH** an ethanol molecule from the reaction solvent has entered into the Ce^{3+} coordination environment increasing by one the metal coordination number. Powder X-Ray Diffraction (PXRD) of the whole powder sample, indicated the presence of more than one phase (PXRD of all products are presented in the following Section). After various recrystallization processes of the product, the PXRD spectra was still the same. At that point, by choosing another single crystal of the bulk compound, the SCXRD afforded a different structure of formula [Ce(Btfa)$_3$(bipy)], **3-bipy.** Therefore, the one pot reaction of **1-H$_2$O** and bipy in a 1:1 ratio, afforded crystals containing the mononuclear Ce^{3+} coordination compounds with both crystal structures, **3-bipy-EtOH** and **3-bipy**, co-crystalizing at the same time, Scheme 2.3.

From this mix of structures, complex **3-bipy** can be isolated by removing all the coordinated EtOH molecules of [Ce(Btfa)$_3$(bipy)(EtOH)] (**3-bipy-EtOH**) present in the bulk product. We found out two different pathways to do so. First, by leaving the obtained solid after the reaction in open air for 3 months. The second method was to keep the obtained product in the oven for 1h at 100ºC. Moreover, thermogravimetric analysis (TGA) measurements were performed on a freshly prepared product**.** As can be observed in Figure 2.1, between 29.6 ºC and 175.2 ºC there is a weight decrease corresponding to the loss of 4.9% of the sample content. This percentage coincides to the loss of one EtOH molecule. Then complex **3-bipy** is formed and it is stable until approximately 300 ºC. However, compound **3-bipy-EtOH** could not be isolated.

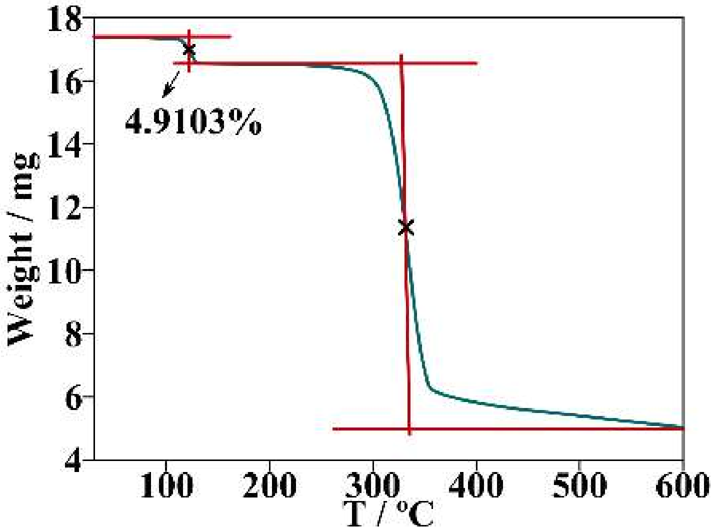

Figure 2.1. TGA on a freshly prepared sample containing a mix of **3-bipy-EtOH** and **3-bipy**.

For all compounds elemental analysis of C, H and N and the most characteristic bands obtained in Infra-red spectroscopy are depicted in Tables 2.6 and 2.7.

Table 2.6. Elemental analysis calculated and found, of compounds **1-H_2O** to **5-bathophen**.

	Calculated			**Found**		
Compound	**%C**	**%H**	**%N**	**%C**	**%H**	**%N**
1-H_2O **$C_{30}H_{22}CeF_9O_8$, 821.6 g/mol**	43.8	2.7	-	43.2	2.7	-
2-phen **$C_{42}H_{26}CeF_9N_2O_6$, 965.8 g/mol**	52.2	2.7	2.9	52	2.6	2.9
3-bipy **$C_{40}H_{26}CeF_9N_2O_6$, 941.8 g/mol**	51.0	2.8	2.9	51.2	2.8	2.8
4-terpy **$C_{45}H_{29}CeF_9N_3O_6$, 1018.8 g/mol**	53.0	2.9	4.1	52.6	2.6	4.0
5-bathophen **$C_{57}H_{41}CeF_9N_2O_7$, 1191.1 g/mol**	57.4	3.5	3.5	57.1	3.4	3.5

Table 2.7 Selected bands (cm^{-1}) of **1-H_2O** to **5-bathophen** (s=strong, m=medium and w=weak, br=broad) obtained in ATR-IR spectroscopy.

1-H_2O	3648(m), 3363(br), 1608(s), 1571(s), 1530(m), 1483(m), 1457(m), 1308(m), 1281(s), 1243(m), 1182(m), 1133(s), 1075(m), 943(m), 771(m), 700(m), 629(m)
2-phen	1609(s), 1576(s), 1521(s),1486(m), 1470(m9, 1320(m), 1287(s), 1241(m), 1180(s), 1133(s), 945(m), 844(m), 746(s), 699(s), 628(m), 578(m)
Bulk crystal containing both, 3-bipy and 3-bipy-EtOH	3054(m, broad), 1635(m), 1606(s, split), 1572(s), 1523(m),1483(m), 1466(m), 1433(m), 1313(m, split), 1280(s), 1240(m), 1170(m), 1123(s, split), 1071(s), 1011(m), 941(m), 755(s, split), 699(s), 626(s), 573(s)

3-bipy	1635(m), 1606(s, split), 1572(s), 1523(m),1483(m), 1466(m), 1433(m), 1313(m, split), 1280(s), 1240(m), 1170(m), 1123(s, split), 1071(s), 1011(m), 941(m), 755(s, split), 699(s), 626(s), 573(s)
4-terpy	1609(s, split), 1576(s), 1526(m), 1469(s), 1439(m), 1313(m), 1277(s), 1237(m), 1170(s), 1123(s), 1071(m), 1004(m), 938(m), 759(s), 716(s), 696(s), 652(m), 629(s), 573(m).
5-bathophen	1662(w), 1612(s, split), 1572(m), 1526(m), 1466(m), 1433(w), 1310(m), 1277(s), 1234(m), 1180(s), 1123(s), 1067(m), 1021(m), 938(m), 762(s, split), 696(s), 669(m), 626(s), 573(s).

2.1.2 Structural characterization

The structures of compound **1-H$_2$O** to **5-bathophen** and **3-bipy-EtOH** were obtained by Single Cristal X-Ray diffraction (SCXRD), and they are presented hereunder. Selected bond distances compilation and information about the single crystal measurement are depicted in Tables 2.8 and Tables APX.III.1 and APX.III.2.

Table 2.8. Selected bond lengths (Å) of compounds **1-H_2O** to **5-bathophen**.

	1-H_2O	**1-H_2O r.t.**	**2-phen**	**3-bipy-EtOH**	**3-bipy**	**4-terpy**	**5-bathophen**
Ce-O1	2.455(3)	2.438(7)	2.453(2)	2.443(3)	2.421(2)	2.450(2)	2.448(3)
Ce-O2	2.427(4)	2.474(6)	2.467(2)	2.481(2)	2.467(1)	2.454(2)	2.461(3)
Ce-O3	2.505(3)	2.522(6)	2.425(2)	2.460(3)	2.405(2)	2.531(2)	2.511(4)
Ce-O4	2.390(3)	2.379(7)	2.419(1)	2.496(3)	2.459(2)	2.490(2)	2.470(3)
Ce-O5	2.471(3)	2.422(7)	2.434(2)	2.464(3)	2.417(2)	2.428(2)	2.476(3)
Ce-O6	2.402(4)	2.473(7)	2.416(2)	2.490(2)	2.446(2)	2.461(2)	2.479(3)
Ce-O7	2.535(4)	2.509(7)	-	2.570(3)	-	-	2.541(3)
Ce-O8	2.520(3)	2.553(7)	-	-	-	-	
Ce-N1	-		2.659(2)	2.713(3)	2.660(2)	2.688(3)	2.701(4)
Ce-N2	-		2.697(2)	2.730(3)	2.668(2)	2.717(2)	2.701(4)
Ce-N3	-		-	-	-	2.680(3)	-
Shortest Ce---Ce	6.105(4)	6.109(9)	8.806(1)	8.057(7)	8.647(6)	10.563(7)	10.770(6)

[Ce(Btfa)$_3$(H_2O)$_2$] 1-H_2O:

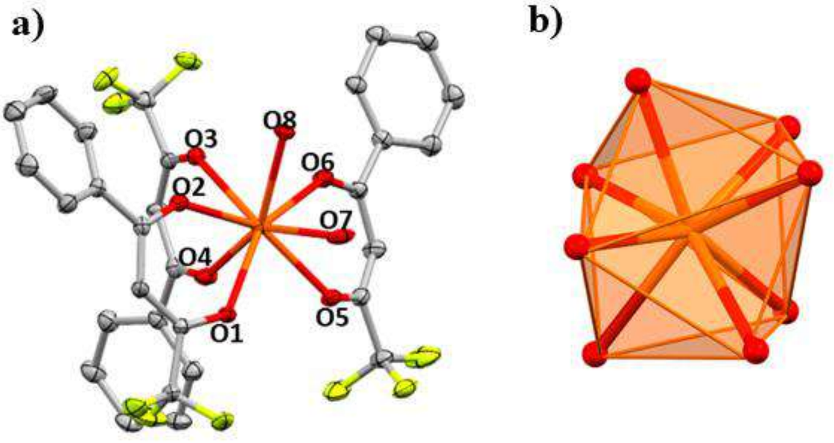

Figure 2.2. a) Partially labelled structure of **1-H_2O** where hydrogen atoms have been omitted for clarity. b) Idealized coordination polyhedron (triangular dodecahedron, TDD-8, D_2d) compared with the real positions of the coordinating atoms of compound **1-H_2O**.Complex **1-H_2O,** with formula [Ce(Btfa)$_3$(H_2O)$_2$], crystallizes in an orthorhombic crystal system, $P2_12_12_1$ space group. The structure consists of mononuclear molecules in which each Ce^{3+} ion is octa-

coordinated with a CeO_8 coordination environment, Figure.2.2 a). The central ion is coordinated to six oxygen atoms from three different Btfa ligands, with Ce-O distances in the 2.390-2.505 Å range. In addition, the other two coordination sites around the central atom are occupied by the O7 and O8 atoms of two water molecules, with Ce-O(water) bond distances of 2.535 and 2.520 Å, respectively. The estimation of the distortion coefficients of the CeO_8 coordination polyhedron for **1-H_2O** from the ideal eight vertex reference polyhedron was performed by employing the continuous shape measures theory and SHAPE software,[26] as for all the other compounds presented herein, showing that the CeO_8 disposition in **1-H_2O** is intermediate between different coordination polyhedra. The best SHAPE estimation led to triangular dodecahedron (TDD-8, D_2d) geometry with a Continuous Shape Measurement (CShM) value of 0.416, Figure.2.2 b).

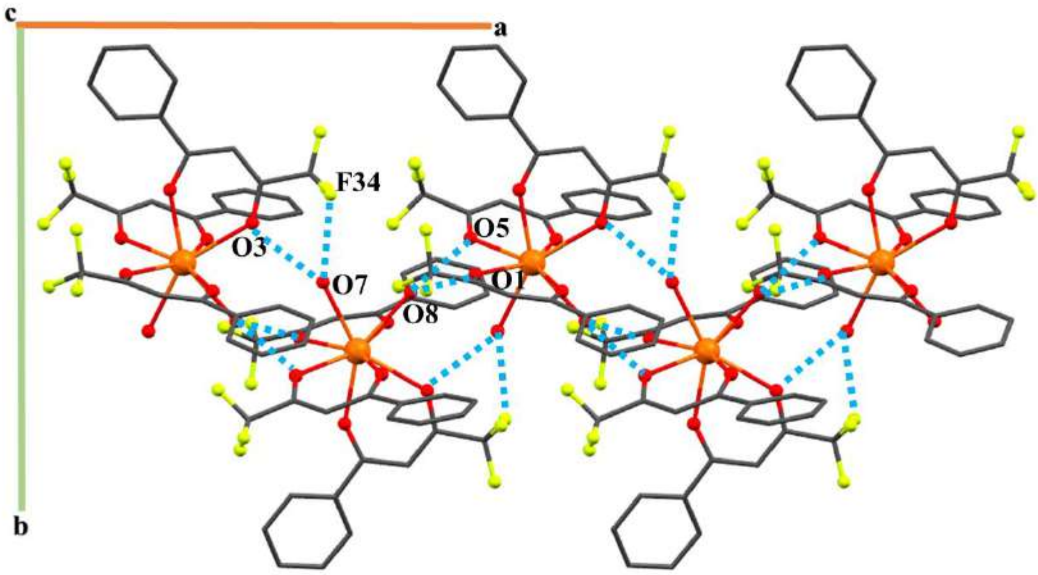

Figure 2.3. Intermolecular interactions of compound **1-H_2O**. The H-bond interactions are represented by the blue dotted lines.

Molecules in **1-H_2O** are arranged in space through hydrogen bonds forming an infinite 1D chain in the [1 0 0] direction, Figure 2.3. The atoms contributing to these intermolecular interactions are the hydrogens from the two water molecules coordinated to the Cerium(III) atoms. On the one hand, the H atoms from O8 interact with O1 and O5 from two different β-diketonates of the neighboring coordination complex with Donor(D)---Acceptor(A) distances of 2.777 and 2.761 Å respectively. On the other hand, the H atoms from the other O7 water molecule are connected through H-bonds with the

O3 and F34 atoms from the nearby complex with D---A distances of 2.868 and 3.026 Å respectively. The shortest Ce---Ce intermolecular distance is 6.105 Å.

To verify that all the polycrystalline product is the same as the structure obtained through single crystal X-Ray diffraction, in other words, to check phase purity, PXRD of **1-H_2O** was obtained and the resulting diffractogram was compared with the calculated one from the single crystal measured at 100 K, Figure 2.4. However, the peaks don't match. Not even after several recrystallizations of the product. Note that PXRD measurement is set at room temperature (294 K) as default.

Then, one single crystal was measured by SCXRD at room temperature (300 K). The calculated pattern from this new structural determination matches the powder diffractogram measured at 294 K, as observed in Figure 2.4. Comparing the crystallographic data of **1-H_2O** at 100 K and at room temperature (Table APX.III.1) we can see that, on diminishing the temperature, there is a slight structural change. The Crystal System and Space group are still the same (Orthorhombic, $\alpha = \beta = \gamma = 90º$ and $P2_12_12_1$), but the cell parameters change from a = 10.854, b = 13.219 and c = 23.317 Å at room temperature to a =10.809, b = 14.77 and c = 21.079 Å at 100 K. The structure at room temperature (294 K) shows Ce-O distances and angles that are slightly different from the measurement at 100 K. At room temperature, the coordination polyhedron geometry is still close to an ideal Triangular Dodecahedron (TDD-8, D_2d) with a CShM value of 0.327 whereas the CShM value for **1-H_2O** at 100 K was 0.416.

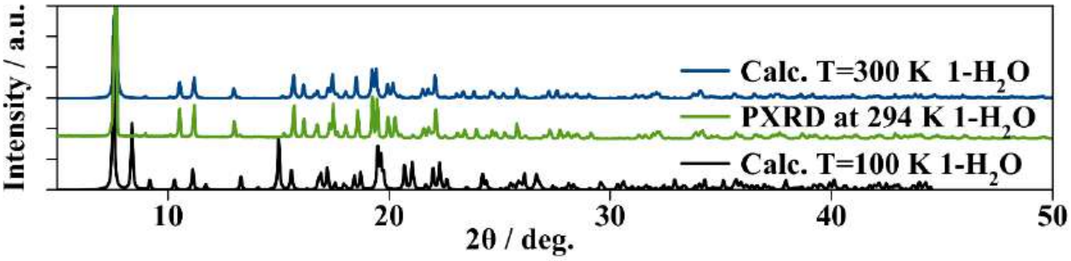

Figure 2.4. Powder XRD spectra of compound **1-H_2O** (green), calculated spectra from the crystal structure measured at 100K (black) and at 300K (blue).

In Figure 2.5 the structures obtained at 300 K and 100 K are superimposed. The slight difference between the bond distances and angles is enough to change significantly the cell parameters when cooling down the single crystal resulting in different PXRD patterns.

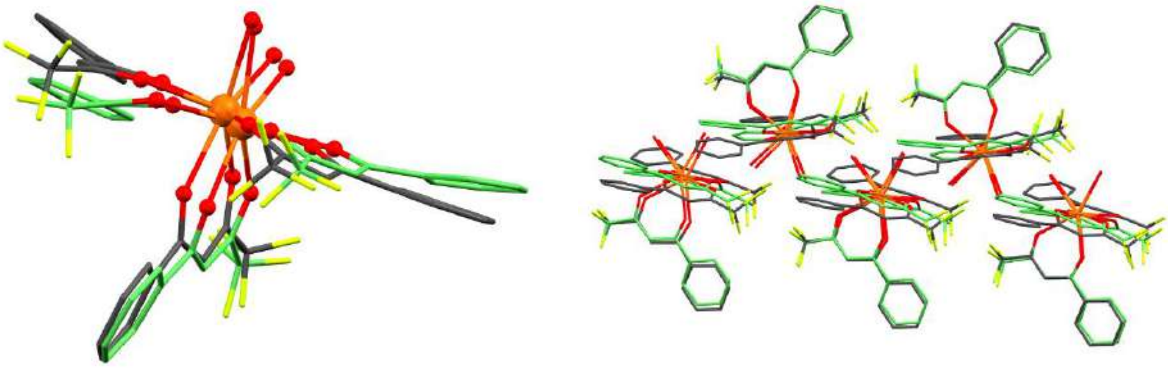

Figure 2.5 Superimposed crystal structures of compound **1-H_2O** obtained by Single Crystal XRD. The structure in the default colours is the structure measured at 100 K and in green is the structure measured at 294 K.

[Ce(Btfa)$_3$(phen)] (2-phen)

Complex **2-phen** of formula [Ce(Btfa)$_3$(phen)] crystallizes in the monoclinic crystal system and $P2_1/c$ space group. In **2-phen** each Ce^{3+} ion is octacoordinated with a CeN_2O_6 coordination environment formed by one phen and three Btfa ligands, Figure 2.6. Two of the coordination sites around the central Ce^{3+} ion are occupied by the N1 and N2 atoms of the phen ligand, with Ce-N bond distances of 2.659 and 2.697 Å, respectively. In addition, the Ce^{3+} ion is also coordinated to six oxygen atoms from three different Btfa chelating ligands, with Ce-O distances in the 2.416-2.467 Å range.

The CeN_2O_6 disposition for **2-phen** is intermediate between different coordination polyhedra. The lowest CShM values for **2-phen** correspond to triangular dodecahedron (TDD-8, D_{2d}) and square antiprism (SAPR-8, D_{4d}) geometries with CShM values of 1.700 and 1.835, respectively, Figures. 2.6 b) and c). The PXRD diffractogram of a **2-phen** polycrystalline sample compared to the calculated one from the single crystal structure match perfectly indicating the purity of the bulk product, Figure 2.7.

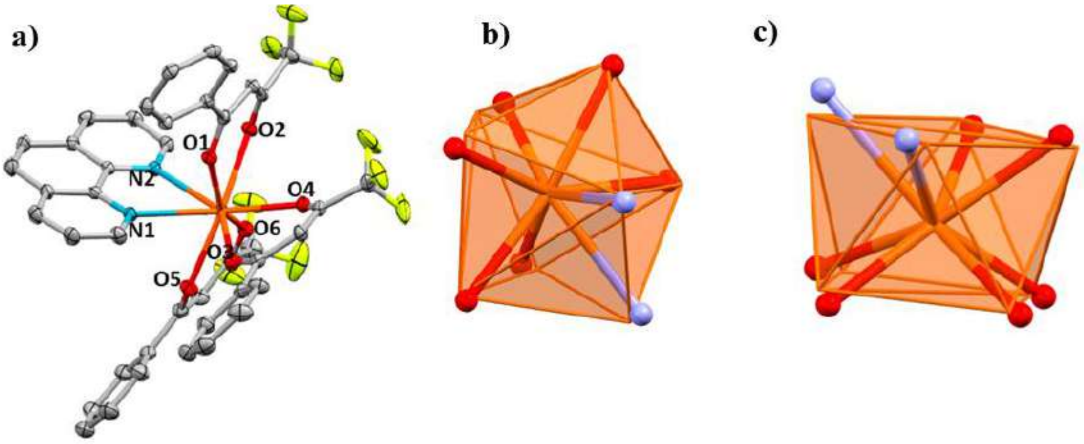

Figure 2.6. a) Partially labelled structure of **2-phen**. The hydrogen atoms have been omitted for clarity. b) Idealized coordination polyhedron (triangular dodecahedron TDD-8, D_{2d}) compared with the real positions of the coordinating atoms of **2-phen**. c) Idealized coordination polyhedron (square antiprism SAPR-8, D_{4d}) compared with the real positions of the coordinating atoms of **2-phen.**

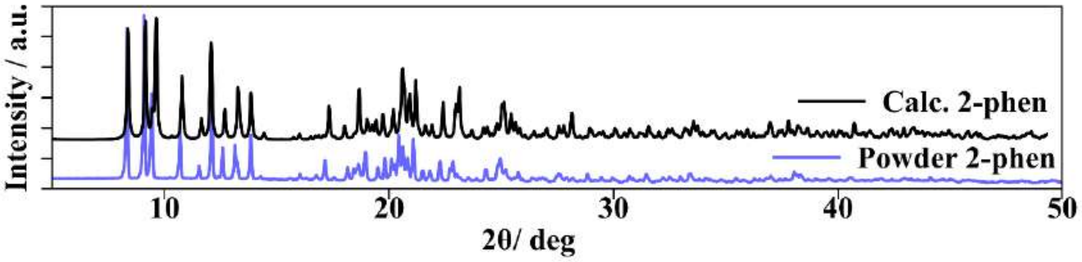

Figure 2.7. Calculated pattern from the crystal structure (black) compared to the PXRD diffractogram of compound **2-phen** (purple).

The [Ce(Btfa)$_3$(phen)] molecules are arranged in the crystal lattice through π---π stacking interactions between the ring formed by C5 to C10 from one Btfa ligand (Cg3) and the three rings with delocalized electron density from the phen ligand (Cg9). The distance between the two centroids (Cg3---Cg9) is 3.921 Å and the interaction grow along the [0 0 1] base vector as an infinite 1D-Chain Figure 2.8. The shortest Ce---Ce intermolecular distance is 8.806 Å.

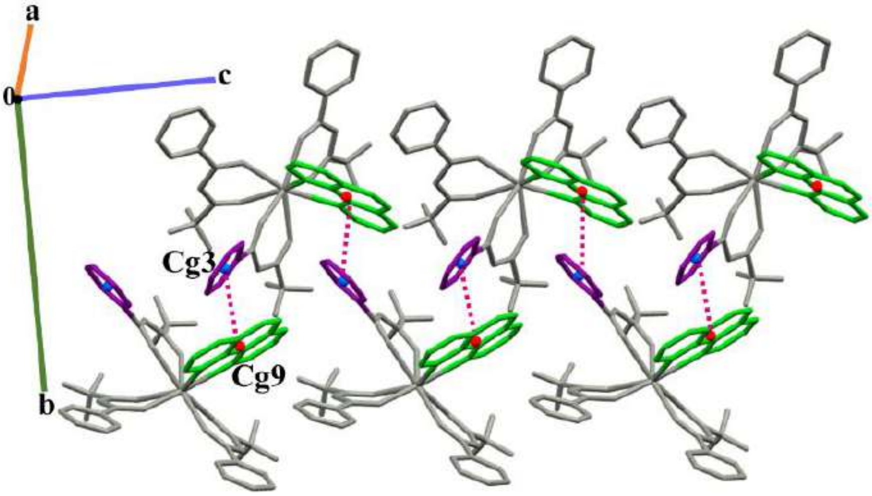

Figure 2.8. Intermolecular interactions in compound **2-phen**. The π-π stacking interactions are represented by the pink dotted lines.

[Ce(Btfa)$_3$(bipy)(EtOH)] (**3-bipy-EtOH**)

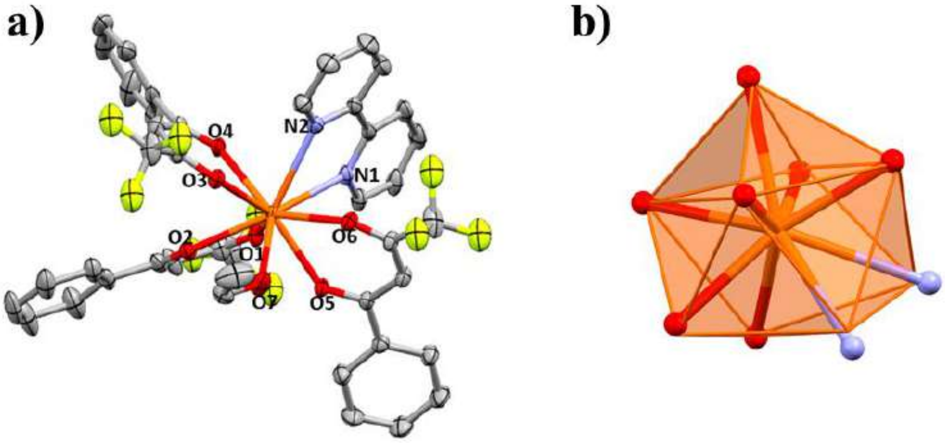

Figure 1.9 a) Partially labelled structure of **3-bipy-EtOH** where hydrogen atoms have been omitted for clarity. b) Idealized coordination polyhedron (Tricapped trigonal prism TCTPR-9, D_{3h}) compared with the real positions of the coordinating atoms of compound **3-bipy-EtOH**.

Complex [Ce(Btfa)$_3$(bipy)(EtOH)], **3-bipy-EtOH** crystallizes in the triclinic crystal system, P-1 space group, Figure 2.9 a). Crystal structure of **3-bipy-EtOH** consists of mononuclear molecules in which each Ce^{3+} ion is nonacoordinated with a CeN_2O_7 coordination environment formed by six O atoms from the three deprotonated β-diketonate ligands with Ce-O distances in the 2.496-2.443 Å range, two N atoms from the bipy ancillary ligand with Ce-N distances of 2.713 and 2.730 Å and the O atom from the ethanol molecule with a Ce-O distance of 2.570 Å. The fluorine atoms from the -CF_3 group of the substituted β-diketone molecule show disorder. The CeN_2O_7 coordination polyhedron has a coordination geometry close to a Tricapped trigonal prism (TCTPR-9, D_3h), Figure 2.9 b), with a CShM value of 0.562.

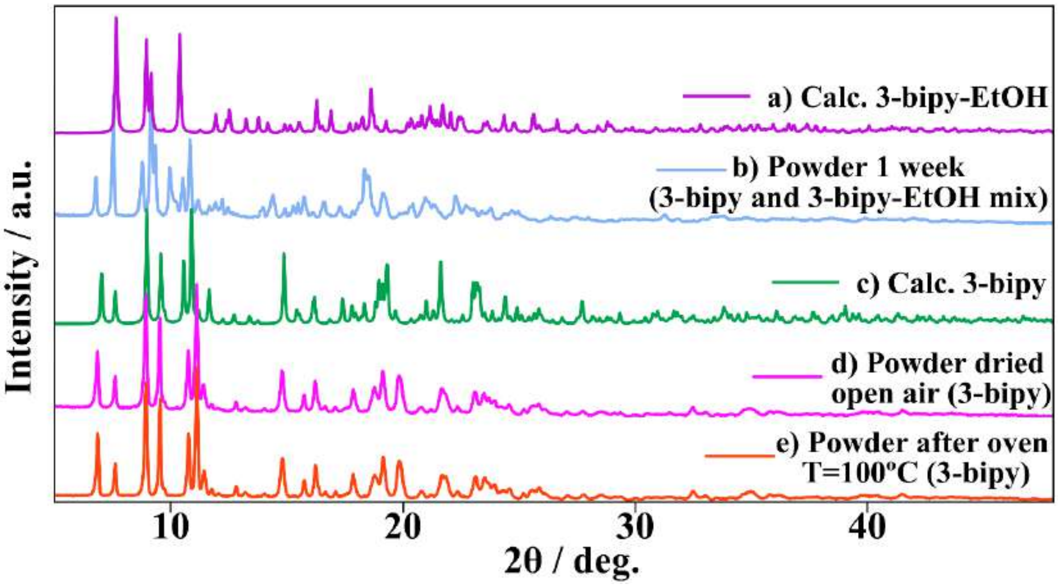

Figure 2.10. Powder X-Ray Diffraction of compounds **3-bipy-EtOH** and **3-bipy.** a) and c) are the calculated PDRX spectra from the structure obtained in Single Crystal XRD of **3-bipy-EtOH** and **3-bipy** respectively, b) PDRX of the powder 1 week later after obtention, d) PDRX spectra dried in the open air for 1 month and e) PDRX spectra after leaving the obtained powder in the oven at 100ºC for an hour.

Powder X-Ray Diffraction was performed and compared with the calculated PXRD pattern from the single crystal structure of **3-bipy-EtOH**, but the peaks did not match properly Figure 2.10 a). As mentioned before, this is because after addition of bipy to the [$Ce(Btfa)_3(H_2O)_2$] (**1-H$_2$O**) precursor, a mix of the structures [$Ce(Btfa)_3$(bipy)(EtOH)] (**3-bipy-EtOH**) and [$Ce(Btfa)_3$(bipy)] (**3-bipy**) co-crystallize. Unlike **3-bipy**, compound **3-bipy-EtOH** could not be to isolate as pure compound in solid.

[Ce(Btfa)$_3$(bipy)] (3-bipy)

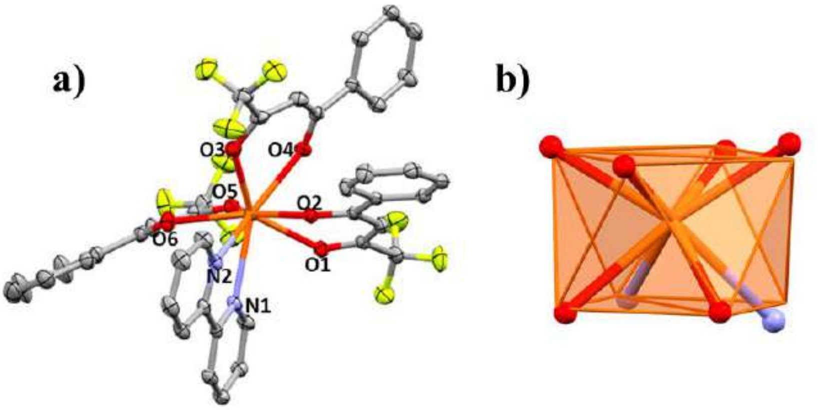

Figure 2.11. a) Partially labelled structure of **3-bipy** where hydrogen atoms have been omitted for clarity. b) Idealized coordination polyhedron (square antiprism SAPR-8, D_{4d}) compared with the real positions of the coordinating atoms of compound **3-bipy**.

Complex [Ce(Btfa)$_3$(bipy)] (**3-bipy**) crystallizes in the monoclinic crystal system, $P2_1/n$ space group. **3-bipy** structure consists of molecules in which each Ce^{3+} ion is octacoordinated with a CeO_6N_2 coordination environment formed by six O atoms from the three Btfa molecules with Ce-O bond distances in the range of 2.467-2.405 Å and by two N atoms from the bipy ligand with Ce-N distances of 2.660 and 2.668 Å, Figure 2.11 a). In this mononuclear complex the Ce-O and Ce-N bond distances are slightly shorter compared to the ones found in [Ce(Btfa)$_3$(bipy)(EtOH)] **3-bipy-EtOH** structure. The CeO_6N_2 octacoordinated polyhedron has a coordination geometry that is close to an ideal Square antiprism (SAPR-8, D_4d) with a CShM value of 1.058, Figure 2.11 b). As explained in the General Syntheses section, compound **3-bipy** can be isolated from the mixture of **3-bipy-EtOH** and **3-bipy** that is obtained after the reaction by letting the powder dry at the open air or by heating the sample in the oven for 1h at 100ºC. Through both methods powder containing only structure **3-bipy** is obtained as verified in the PXRD diffractograms, Figure 2.10.

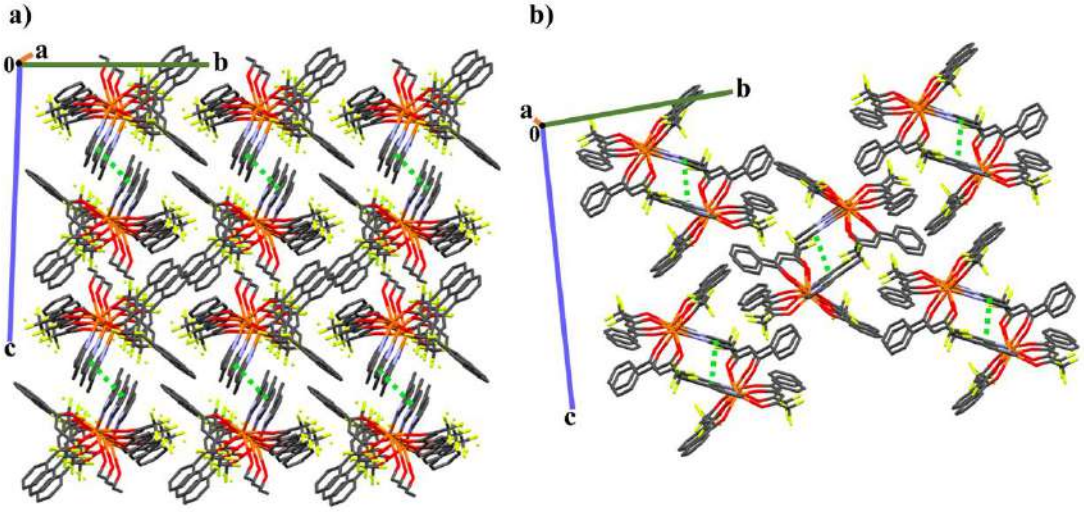

Figure 2.12. Intermolecular interactions of single crystal structures of a) **3-bipy-EtOH** and b) **3-bipy**. The π---π stacking interactions are represented by the green dotted lines.

Intermolecular interactions to consider for **3-bipy** and also for structure **3-bipy-EtOH**, are the π---π stacking interactions between the rings from the bipy ligands with Cg1---Cg2 distances of 3.687 Å for **3-bipy-EtOH** and of 3.999 Å for **3-bipy**. Moreover, other weak intermolecular interactions such as π---H build up a three-dimensional supramolecular structure, Figures 2.12 a) and b) for **3-bipy-EtOH** and **3-bipy** packing respectively. The shortest Ce---Ce intermolecular distances are 8.058 Å for **3-bipy-EtOH** and 8.647 Å for **3-bipy.**

[Ce(Btfa)$_3$(terpy)] (**4-terpy**)

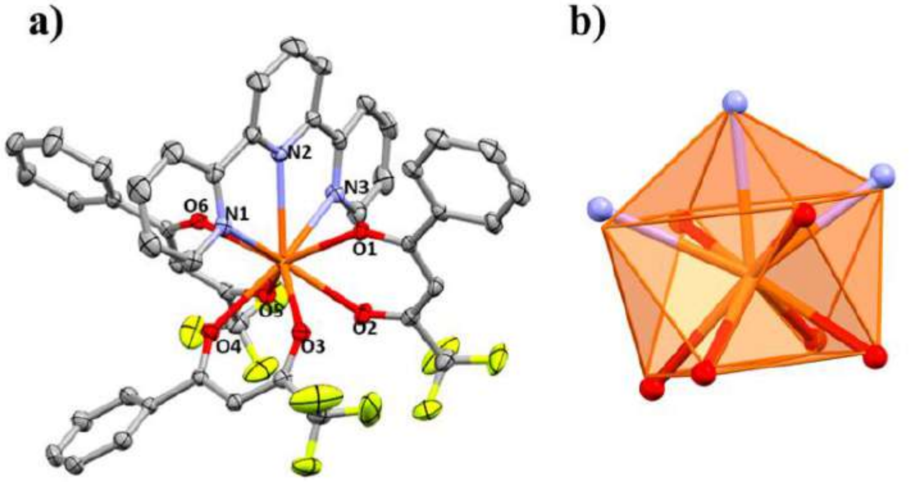

Figure 2.13. a) Partially labelled structure of **4-terpy** where hydrogen atoms have been omitted for clarity. b) Idealized coordination polyhedron (Capped square antiprism CSAPR-9, C_{4v}) compared with the real positions of the coordinating atoms of compound **4-terpy**.

Complex **4-terpy** crystallizes in a tetragonal crystal system in a Sohncke $P4_3$ space group. The Sohncke space groups are formed by 65 space groups which contain only the rotation and translation symmetry operations (operations of the first kind) and where the reflexion, glide reflexion, rotoinversion and inversion mirror operations are restricted. Some of the molecular structures containing these non-enantiogenic space groups, 22 out of 65, result in chiral crystal structures (which are different from chiral molecules). For example, proteins generally crystallize in Sohncke space groups.[27] **4-terpy** structure consists in molecules in which each Ce^{3+} ion is nonacoordinated with a CeO_6N_3 coordination environment. The CeO_6N_3 coordination sphere is generated by six O atoms from the three Btfa ligands with Ce-O distances ranging from 2.428 to 2.531 Å and the three N atoms from the terpy ligand with Ce-N distances ranging from 2.680 to 2.717 Å. The CeN_3O_6 nine coordination polyhedron has a coordination geometry close to an ideal Capped square antiprism (CSAPR-9, C_4v) with a CShM value of 0.751, Figure 2.13 b).

Each asymmetric unit is formed by one mononuclear entity. For **4-terpy**, the asymmetric unit grows in space forming a laevorotatory 4_3-helical chain through the *c* axis (left-handed chain) and, therefore, it is induced a propeller's homo-chiral packing in the crystal.

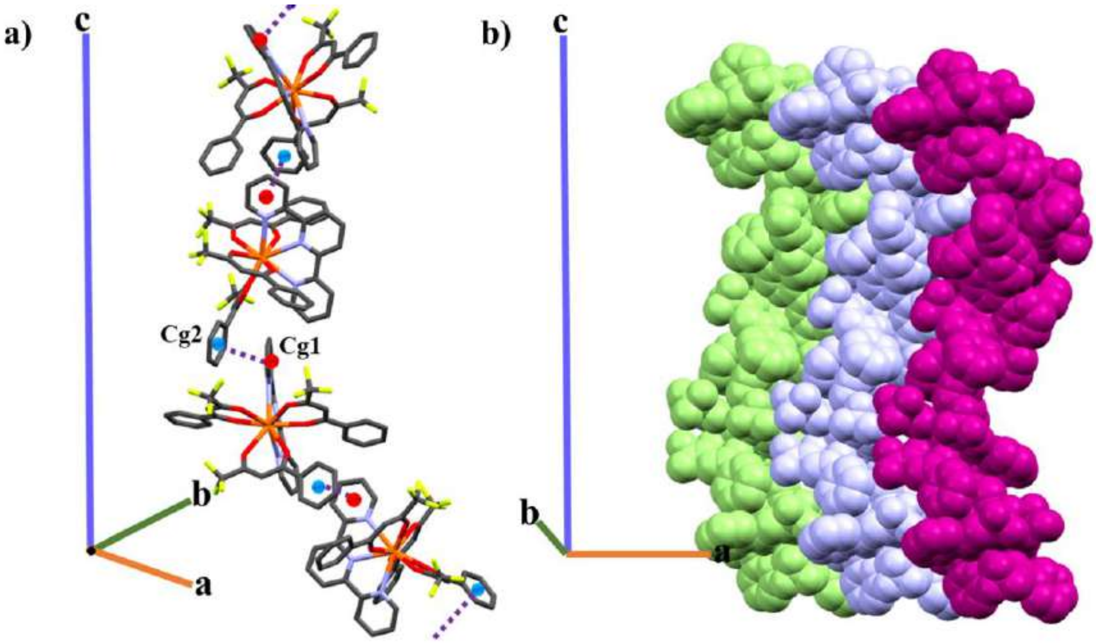

Figure 2.14. a) Helical chain formed by the intermolecular interactions of compound **4-terpy**. The π-π stacking interactions are represented by the purple dotted lines and b) helical chains along the 4_3 screw axe.

The helix is formed around the crystallographic 4_3 screw axis via the π---π stacking interaction between two different rings with delocalized electron density, one from the terpy ligand (Cg1) and the other from one β-diketonate ligand (Cg2) with an interligand distance of 3.767 Å, Figure 2.14 a). The helices stand along the *a* and *b* axis by weak Van der Waals interactions forming the chiral crystal, Figure 2.14 b). The shortest Ce---Ce intermolecular distance is 10.563 Å.

The enantiomeric pair for this Sohncke space group is the $P4_1$ in which the helix would be dextrorotatory. To try to find a crystal with the enantiomeric $P4_1$ Sohncke space group, a second single crystal was measured. For this second measurement, the same $P4_3$ space group was found. Though both measured crystals presented the same chirality, we cannot assert that the final product is entirely chiral and neglect the idea that it could be a racemic mixture. The PXRD presented in Figure 2.15 supports one single phase for the whole powder product of **4-terpy**.

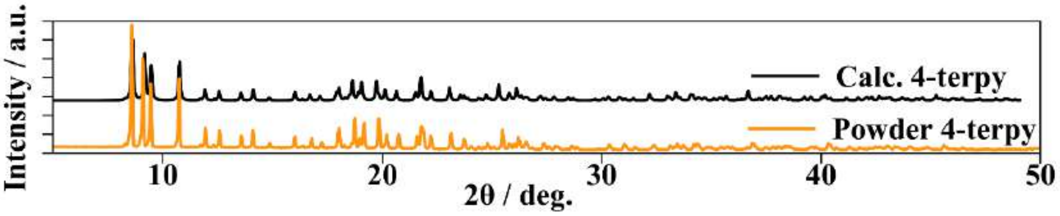

Figure 2.15. Calculated powder XRD patter from the crystal structure (black) compared with the powder XRD diffractogram of compound **4-terpy** (yellow).

[Ce(Btfa)$_3$(bathophen)(DMF)] (5-bathophen)

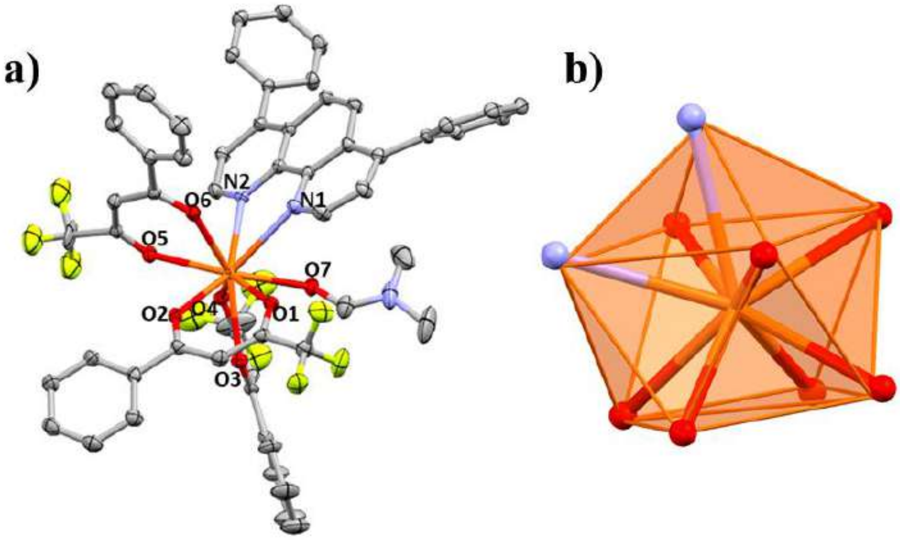

Figure 2.16 a) Partially labelled structure of **5-bathophen** where hydrogen atoms have been omitted for clarity. b) Idealized coordination polyhedron (Capped square antiprism CSAPR-9, C_{4v}) compared with the real positions of the coordinating atoms of compound **5-bathophen**.

Complex [Ce(Btfa)$_3$(bathophen)(DMF)], **5-bathophen,** crystallizes in the monoclinic crystal system, $P2_1/c$ space group. Structure of **5-bathophen** consists of mononuclear molecules in which each Ce^{3+} ion is nonacoordinated with a CeN_2O_7 coordination environment, Figure 2.16 a). The coordination sphere encompasses six O atoms from three Btfa ligands with Ce-O bond distances in the 2.448 to 2.511Å range, two N atoms from the bathophen ligand with Ce-N distances of 2.724 and 2.701 Å and a DMF molecule through the O atom with a Ce-O bond distance of 2.541 Å. The N_2O_7 vertices are stablished around the Ce^{3+} metal in a polyhedron geometry that is close to an ideal Capped square antiprism (CSAPR-9, C_4v) with a CShM value of 0.316, Figure 2.16 b).

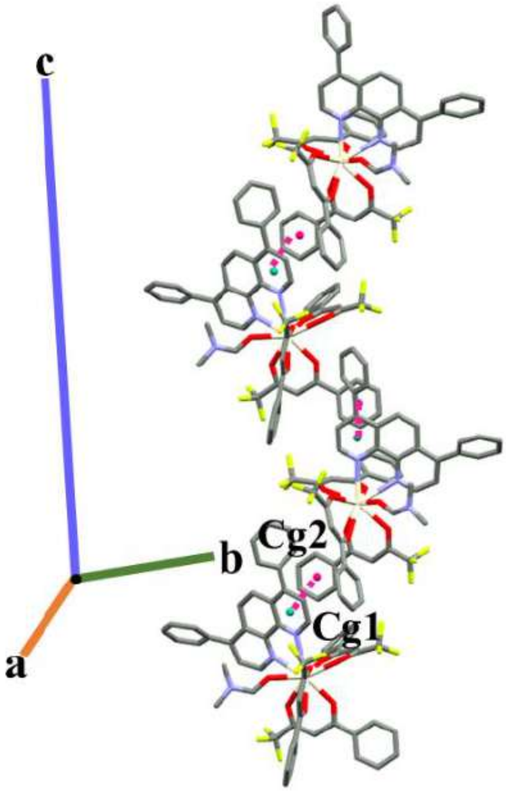

Figure 2.17. Intermolecular interactions representation of compound **5-bathophen**. The π---π stacking interactions are represented by the pink dotted lines

The mononuclear complexes are arranged in the space through π---π stacking interactions between one of the aromatic rings from the bathophen ligand (Cg1) and one phenyl ring from a Btfa ligand, Cg(2). The Cg(1)---Cg(2) intermolecular distance is 3.818 Å and it grows along the *c* axis as shown in Figure 2.17. The shortest Ce---Ce intermolecular distance is 10.770 Å. Moreover, PXRD measurements were performed on the powder product. The calculated PXRD pattern from the single crystal structure was compared with the experimental one affirming a single phase through all the sample Figure 2.18.

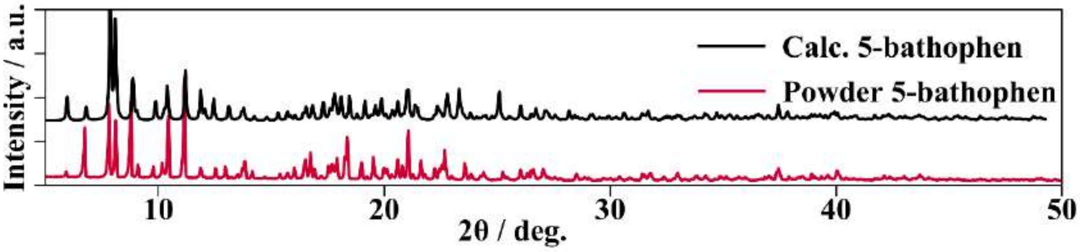

Figure 2.18. Calculated spectra from the crystal structure (black) compared with the powder XRD spectra of compound **5-bathophen** (maroon).

2.1.3 Magnetic characterization

Static magnetic properties

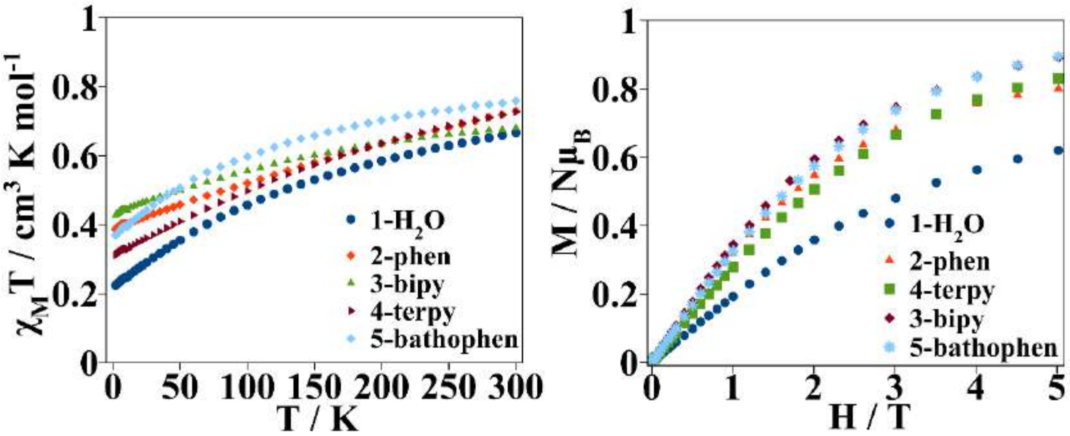

Figure 2.19. $\chi_M T$ *vs* T plot (left) and M *vs* the magnetic field plot (right) for compounds **1-H$_2$O** to **5-bathophen**.

Direct current (dc) magnetic susceptibility and magnetization measurements were performed on polycrystalline samples of compounds **1-H$_2$O** to **5-bathophen**. Since compound **3-bipy-EtOH** could not be isolated as pure compound, the magnetic study was not performed for this sample. The $\chi_M T$ *vs* T plots in the 2-300 K temperature range under a dc magnetic field of 0.3 T are shown in Figure 2.19 (*left*). At room temperature (300 K) the $\chi_M T$ values for compounds **1-H$_2$O** to **5-bathophen** are 0.67, 0.73, 0.68, 0.73 and 0.76 cm^{3}mol^{-1}K respectively. These $\chi_M T$ values are close to the calculated value for an isolated Ce^{3+} cation in the ground state $^2F_{5/2}$ (S=1/2, L=3, J=5/2, g_J = 6/7) which is 0.8 cm^{3}mol^{-1}K.[28] On cooling the samples, the $\chi_M T$ values decrease gradually due to the progressive thermal depopulation of the m_j states to finite values at 2 K of 0.23, 0.40, 0.44, 0.32 and 0.38 cm^{3}mol^{-1}K for **1-H$_2$O** to **5-bathophen** respectively. Other mononuclear Ce^{3+} coordination compounds show similar $\chi_M T$ *vs* T curves.[3,29,30] Field dependence of the magnetization (M) recorded at 2 K is depicted in Figure 2.19 *(right)*. On increasing the external magnetic field up to 5 T, the magnetization values increase to 0.62, 0.84, 0.89, 0.83 and 0.89 N$_A\mu_B$ for **1-H$_2$O** to **5-bathophen,** respectively, without stabilization of the M values, showing no evidence of saturation of the magnetization ($g_J \cdot J = \frac{6}{7} \cdot 3 = 2.6$). Similar behavior is found for other Ce^{3+} compounds showing significant magnetic anisotropy.[11,3,25]

Dynamic magnetic properties

No frequency dependence of the out-of-phase magnetic susceptibility component (χ_M'') was found under a 0 T external magnetic dc field for complexes **1-H$_2$O** to **5-bathophen** **(**Figure APXIII.1), suggesting that the lack of pure axial Ising type geometry, that sets the m_j=±5/2 as the ground doublet, makes that the reorientation of the magnetization occurs through the fast Quantum Tunneling of Magnetization (QTM) mechanism preventing the SMM behavior.[28] Nevertheless, by applying a small direct current magnetic field (H$_{dc}$), the QTM was suppressed enough so that all the above compounds showed slow relaxation of the magnetization.

To decide which external dc magnetic field was the optimal for each compound, ac measurements were performed at a constant temperature of 2.5 K for **1-H$_2$O**, **3-bipy** and **5-bathophen**, of 3.5 K for **2-phen**, and of 2.0 K for **4-terpy** at oscillating frequencies between 1-1488 Hz and different H$_{dc}$ fields. The measurements of χ_M'' with frequency (ν) plots, at a constant temperature, are depicted in Figure 2.20 for samples **1-H$_2$O** to **5-bathophen**. When applying a low H$_{dc}$ (0.002-0.01 T), the χ_M'' shows maximum values at higher frequencies. On increasing H$_{dc}$, the peaks increase on intensity reaching their maximum values and shifting to the 96-177 Hz frequency zone staying constant until higher H$_{dc}$ are applied. Then χ_M'' shifts again to higher frequencies diminishing its intensity. The optimal H$_{dc}$ resulted of 0.1 T for **1-H$_2$O** and **3-bipy**, 0.05 T for **2-phen** and 0.02 T for **4-terpy** and **5-bathophen**, (Figure APX.III.2). Given to the shorter Ce---Ce intermolecular distance of 6.105 Å, compound **1-H$_2$O** might require a greater external

H_{dc}.[13] The shortest Ce---Ce intermolecular distances found for structures of **2-phen** to **5-bathophen** are 8.806, 8.647, 10.563 and 10.770 Å respectively.

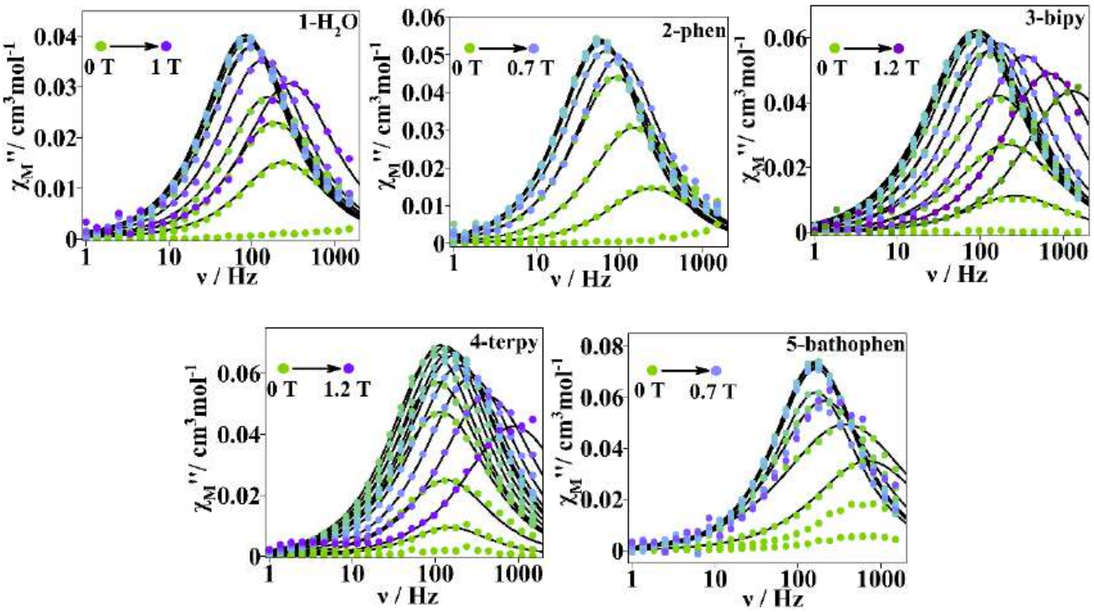

Figure.2.20. χ_M'' component with frequency plots of compounds **1-H$_2$O** to **5-bathophen**. The alternating current measurements were recorded at different external direct current magnetic fields and at a constant temperature of 2.5 K for **1-H$_2$O**, **3-bipy** and **5-bathophen**, of 3.5 K for **2-phen** and 2 K for **4-terpy.** Ac data dependent on the magnetic field were measured in the H_{dc} range of 0-1 T for **1-H$_2$O**, of 0-0.7 T for **2-phen** and **5-bathophen** and of 0-1.2 T for **3-bipy** and **4-terpy.** Continuous black lines correspond to the fitting with the Generalized Debye model. The χ_M'' *vs* ν curves measured at H_{dc} = 0 T, for **1-H$_2$O** to **4-terpy** and at H_{dc} ç = 0 and 0.002 G for **5-bathophen** could not be fitted to the Debye model due to the lack of χ_M'' maxima.

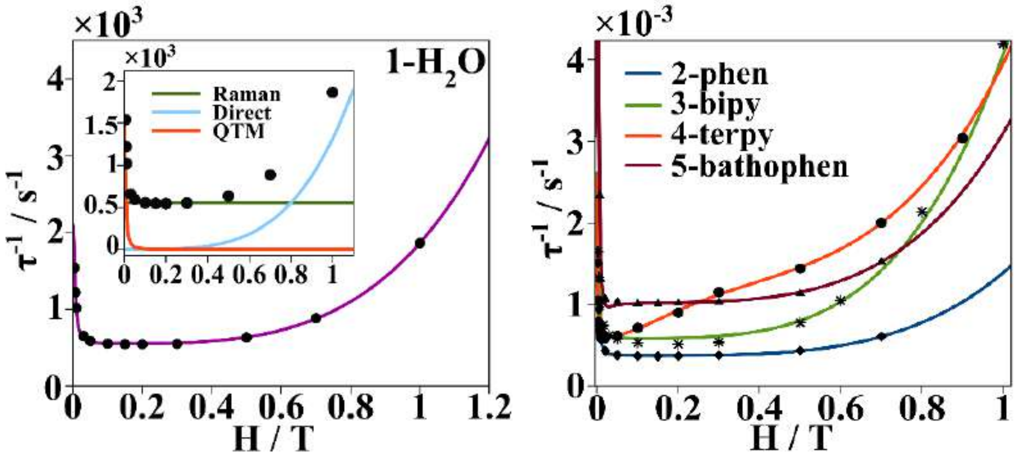

Figure 2.21. Left**,** dependence of τ^{-1} on a static magnetic field (black dots) of compound **1-H$_2$O**, continuous purple line accounts for the fitting using the field dependent Equation 2.1. Inset shows the contribution of Raman, Direct and QTM mechanism to the τ^{-1} *vs* H of compound **1-H$_2$O**. Right, dependence of τ^{-1} on a static magnetic field of compounds **2-phen** to **5-bathophen**. The continuous blue, green, orange and red lines correspond to the fitting with Equation 2.1 of the experimental magnetic data (discrete dots) of compounds **2-phen** to **5-bathophen** respectively.

This behavior is represented as τ^{-1} *vs* the H$_{dc}$ plots, Figure 2.21. At low magnetic fields, τ^{-1} values decrease corresponding to the suppression of the QTM mechanism by the external magnetic field. After 0.3 T for **1-H$_2$O** to **3-bipy** and **5-bathophen**, the τ^{-1} values remain almost constant, accounting for the predominancy of Raman and the other thermally dependent relaxation processes. For compound **4-terpy**, the constant trend at intermediate H$_{dc}$ is rather poor and it is not well differentiated as in the rest of the compounds. When surpassing the specific H$_{dc}$, this constant tendency is broken, and τ^{-1} values increase exponentially following the H^4 power law showing that the Direct process is taking place at higher magnetic fields. ($\tau^{-1} = AH^4T$ for the relaxation of the magnetization with a Direct Process)

Under the chosen dc external magnetic field, dynamic measurements were performed under an oscillating ac field of 4·10^{-4} T in the 1-1488 Hz frequency range for **1-H$_2$O**, **3-bipy** and **5-bathophen,** and in the 10-1488 Hz frequency range for **2-phen** and **4-terpy**. Maximum values of the out of phase magnetic susceptibility component can be seen below 5 K for **1-H$_2$O** to **5-bathophen**, Figure APX.III.3. All the samples show slow relaxation of the magnetization in a similar temperature range, being compound **2-phen** the one in which the χ_M*''* dependence extends to higher temperature (5.7 K).

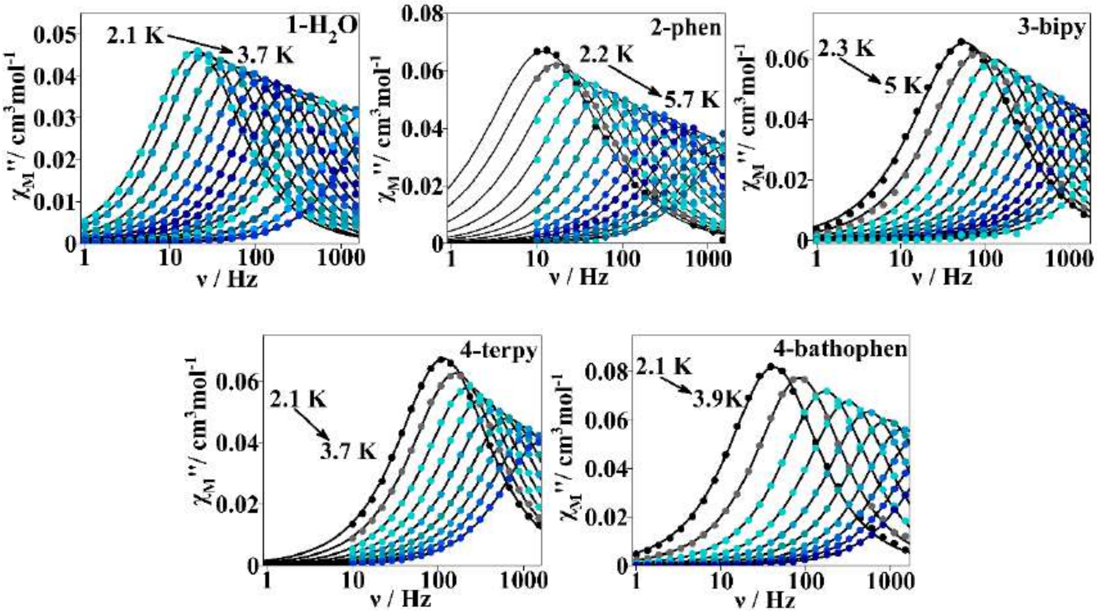

Figure 2.22. χ_M'' *vs* frequency plots for compound **1-H$_2$O** to **5-bathophen** measured at an oscillating ac field of $4 \cdot 10^{-4}$ T, and at a H_{dc} of 0.1 T for **1-H$_2$O** to **3-terpy,** and of 0.02 T for **4-terpy** and **5-bathophen.** The continuous lines correspond to the fitting with the Generalized Debye model.

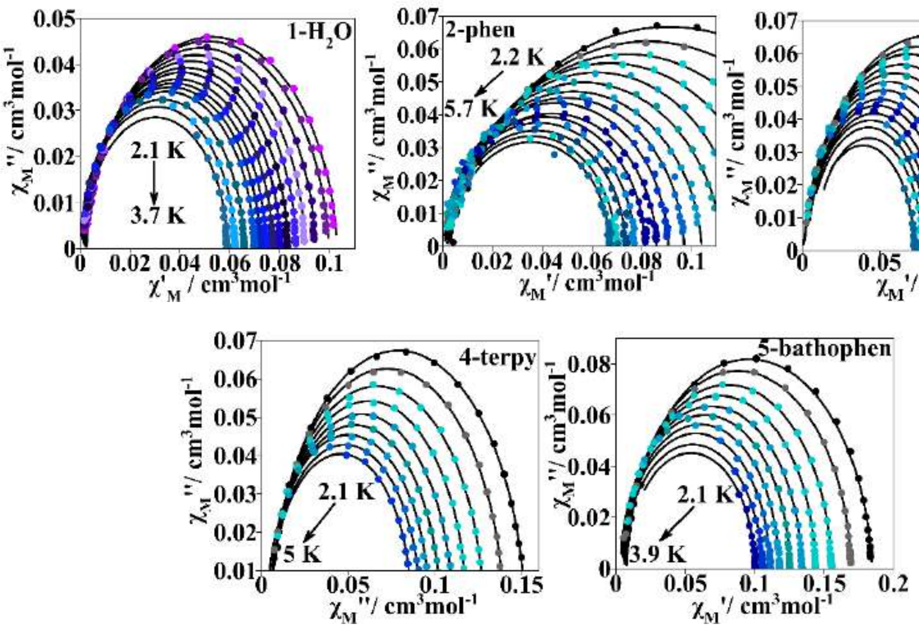

Figure 2.23. Cole-Cole plots of **1-H$_2$O** to **5-bathophen** from the temperature dependent ac magnetic data measured at a H$_{dc}$ of 0.1 T for **1-H$_2$O** to **3-terpy** and of 0.02 T for **4-terpy** and **5-bathophen.** The continuous lines correspond to the fitting with the Generalized Debye model.

The χ_M'' *vs* oscillating frequency plots at different temperatures are depicted in Figure 2.22. For complexes **1-H$_2$O** to **5-bathophen**, the χ_M'' peaks shift progressively to higher frequencies as the temperature increases showing thermal dependence of the relaxation of the magnetization. Therefore, we could assume that the QTM relaxation process is considerably reduced after the application of an external dc magnetic field.[31] When comparing compounds **1-H$_2$O** to **5-bathophen**, **2-phen** is the one showing χ_M'' dependence with T at lower frequencies whereas **3-bipy** at higher ones.

The Cole-Cole plots for **1-H$_2$O** to **5-bathophen** (Figure 2.23) are not perfectly symmetrical semicircles. The curves could be fitted using the Generalized Debye model described with the Casimir-Du Pré function (Equation 1.32, *Introduction Section*)[32] from which the relaxation times of the magnetization can be extracted. The distribution of the relaxation times (α) is narrow for the presented compounds mostly for **1-H$_2$O**, **4-terpy** and **5-bathophen** in which α values are comprised between 0.077-0.0041, 0.0529-0.0031 and 0.05-0.0118 respectively while for **2-bipy** and **3-terpy** α values are comprised in a slightly wider range of 0.1804-0.0018 and 0.1335-0.0146 respectively.

For a spin system, the relaxation of the magnetization can occur through different relaxation mechanisms. The dependence of τ with temperature (T) and the applied external magnetic field (H) is expressed as in Equation 2.1.

$$\tau^{-1} = aH^4T + d\left(\frac{1+eH^2}{1+fH^2}\right)T^n + \frac{B_1}{1+B_2H^2} + \tau_0^{-1}\exp\left(\frac{-\Delta E}{k_BT}\right) \qquad \text{Equation 2.1}$$

The first term is the field dependent Direct process which involves one phonon, the second term refers to the Raman process that occurs through a virtual state involving two phonons. Here it is represented as a field dependent term using the Brons-Van Vleck equation which has a coefficient field dependent and the exponential dependence with temperature. The d parameter represents zero-field relaxation, e is related with the paramagnetic center concentration and the f parameter reports the effect of the external field in suppressing the spin relaxation. The third term of Equation 2.1 describes the fast QTM and, finally, the last term relates to the so called thermally assisted relaxation process: the Orbach process. It follows an Arrhenius law and experimentally, when Orbach takes place, a linear trend of log(τ) with temperature is expected. The Orbach spin-lattice mechanism involves two phonons, and the relaxation occurs through an effective energy barrier from the ground state $\pm m_j$ through a real excited state. Normally, the Orbach process takes place at the higher temperature range since the system needs enough energy to surpass the whole energy barrier between the $\pm m_j$ ground states.[33, 34]

For the titled compounds a linear slope seems to be followed in the higher temperature range. We have fitted the experimental τ values of **1-H$_2$O** to **5-bathophen** using the Arrhenius law, and the obtained values of the activation energy barrier are in the range of 12.2-19.8 cm^{-1} with τ_0 values comprised between 10^{-7} and 10^{-8} s, Figure APX.III.4 and Table 2.9.

Table 2.9. Values obtained from the fitting of ln(τ) *vs* T^{-1} curves using the Arrhenius law that describe the Orbach mechanism.

Arrhenius	1-H_2O	2-phen	3-bipy	4-terpy	5-bathophen
ΔE/cm^{-1}	19.8	18.1	16.4	12.2	16.6
τ_0 /s	2.6e-8	9.7e-7	3.2e-7	8.5e-7	8.3e-8

This linear trend could indicate that the relaxation of magnetization is taking place through an over-barrier Orbach mechanism for **1-H_2O** to **5-bathophen** or a thermally assisted tunneling process through the first $\pm m_j$ excited state**.** Nevertheless, for the Cerium(III) compounds found in the literature where the ab initio calculations were performed, the energy differences between the $\pm m_\mathrm{j}$ ground Kramer Doublet (KD) and the first excited $\pm m_\mathrm{j}$ KD are in the range of 258-339 cm^{-1} for mononuclear Ce^{3+}-β-diketonate complexes,[3,16] 220-787 cm^{-1} for other Ce^{3+}-mononuclear compounds,[18-23, 35, 36] 303-348 cm^{-1} for Ce^{3+}-polynuclear compounds[25,37] and 180-303 cm^{-1} for Ce^{3+}-heterometallic compounds.[18,24,38,39] Interestingly, the activation energy barrier calculated from the experimental data (ΔE_{exp}), with the Arrhenius law, considering an Orbach mechanism, led to very similar values for all the previous Ce^{3+} compounds. The maximum value reported is 38 cm^{-1},[23] but the ΔE_{exp} value for the vast majority of the published Ce^{3+} complexes lie in the 20-30 cm^{-1} range and there is no difference with the ones showing easy axial or easy plane symmetry.[3,16,21,22,24,30,35,38,40,41] Besides, ab initio calculations (see below computational results) of the former Cerium (III) systems result in an energy difference between the ground and first excited m_j states much higher in energy (151.9-372.6 cm^{-1}, see Table 2.13) than the energy barriers obtained from the experimental data using the Arrhenius law that describes the Orbach process.

The lack of a linear trend in the log(τ) *vs T* plots along all the temperature range could be explained by considering the presence of other relaxation of the magnetization mechanisms occurring at the same time as the Orbach or taking into consideration that the Orbach process is not taking place at all, as comparison of experimental data with ab initio calculations appears to indicate. Furthermore, hyperfine interactions between the electronic spin with the nuclear spin of a lanthanide ion can split the electronic doublet into different manifolds making in this way new pathways of the relaxation of the magnetization that could explain the linear trend with the temperature. But the natural isotopes of cerium don't possess nuclear spin. Another proposed spin-lattice relaxation mechanism is the Local mode, and it is referred to a thermally dependent process which considers that the spin relaxation goes through a higher energy state that is a local vibration from the same m_j ground state following Equation 2.2. Then Δ_{loc} can be extracted and is referred to the local mode energy (cm^{-1}).[42] Δ_{loc} could be experimentally assigned from vibrational spectroscopic techniques.[43,44]

$$\tau^{-1} = A_{loc}\left(\frac{e^{-\frac{\Delta_{loc}}{k_B T}}}{\left(e^{-\frac{\Delta_{loc}}{k_B T}}-1\right)^2}\right) \qquad \text{Equation 2.2}$$

With the above exposed considerations, we tried to fit the magnetic data with the thermally dependent components of Equation 2.1 and adding the Local mode function instead of the Orbach one. Given that for **1-H$_2$O** to **5-bathophen**, the temperature ranges in which there is magnetic response are small and the risk of over-parametrization when many parameters are used in the equation, we first proceed to fit the τ^{-1} with the magnetic field so in this way we can extract the parameters from the equations that are field dependent: dT^n, e and f for Raman, B_1 and B_2 for the QTM and a for Direct process (Equation 2.3) and then the parameters corresponding to these equations can be fixed in the temperature dependent function.

The Cole-Cole plots from the field dependent experimental magnetic data measured at a constant temperature were fitted using the Generalized Debye model, Figure APX.III.5. The field dependent magnetic data could be fitted following Equation 2.3 for all the compounds**.** Since in the τ^{-1} in front of H the different tendencies from the predominant mechanism QTM, Raman and Direct are well differentiated, first, each part was fitted independently with the corresponding mechanism and the fitted parameters were used as the starting point of the whole set, Figure 2.21. The obtained parameters from the field dependent fitting of compounds **1-H$_2$O** to **5-bathophen** are compiled in Table 2.10 a). Inset Figure 2.21 and Figure APX.III.6 show the contribution of each relaxation mechanism to the magnetization relaxation along the applied magnetic field of compounds **1-H_2O** to **5-bathophen**. When looking at the dependence of τ^{-1} with magnetic field, for all compounds, at low external bias dc magnetic fields, the QTM mechanism is the one dominating the relaxation of the magnetization. While at high external dc fields for **1-H_2O** and **3-bipy** Direct is the dominant process whereas, for **2-phen**, **4-terpy** and **5-bathophen** the Raman is still relevant.

$$\tau^{-1} = aH^4T + \frac{B_1}{1+B_2H^2} + d\left(\frac{1+eH^2}{1+fH^2}\right)T^n + K(T) \qquad \text{Equation 2.3}$$

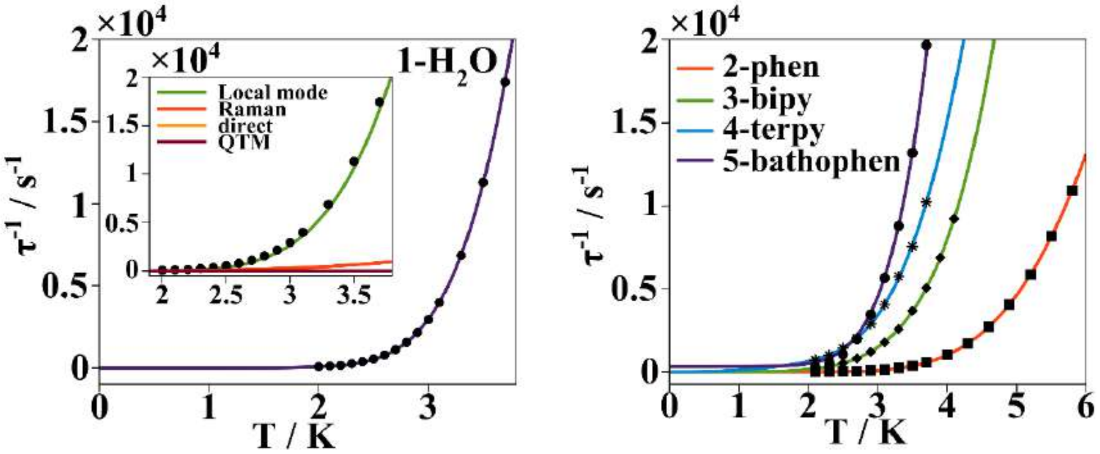

Figure 2.24. Dependence of τ^{-1} with temperature obtained from the experimental magnetic data measured at an external magnetic field of 0.1 T for **1-H_2O** and **3-bipy**, of 0.05 T for **2-phen** and of 0.02 T for **4-terpy** and **5-bathophen**. Left, plot of compound **1-H_2O**. Inset shows the contribution of each relaxation of the magnetization mechanisms separately. Right, plots of compounds **2-phen** to **5-bathophen**.

Then the temperature dependent experimental magnetic data were fitted with Equation 2.4 and the parameters n from Raman and A_{loc} and ω from Local Mode spin relaxation mechanisms were obtained for **1-H_2O** to **5-bathophen**. The τ^{-1} dependence with T plots are depicted in Figure 2.24 and the obtained parameters from the best fit are compiled in Table 2.10 b). The contribution of each relaxation mechanism for τ^{-1} with Temperature magnetic data is shown in Inset of Figure 2.24 for **1-H_2O** and in Figure APX.III.7.

$$\tau^{-1} = A(H)T + K(H) + D(H)T^{n} + A_{loc}\left(\frac{e^{-\frac{\Delta_{loc}}{k_B T}}}{\left(e^{-\frac{\Delta_{loc}}{k_B T}}-1\right)^{2}}\right) \qquad \text{Equation 2.4}$$

From the global fit, the obtained Local Mode energy values for the different compounds are in the range of 11.5-20.9 cm^{-1} (16.6-30.1 K). With this approach, spin relaxation of compound **1-H$_2$O** appears to be governed by the Local mode mechanism, Figure 2.24 inset. While for **2-phen**, **4-terpy** and **5-bathophen** spin relaxation along the temperature range is best described by both, Raman and Local Mode mechanisms, Figure APX.III.7. In fact, for compound **4-terpy** it is well discerned that Raman prevails in the lower temperature range while Local mode takes an important role at the higher temperature range, Figure APX.III.7(**4-terpy**). Moreover, compound **3-bipy** shows smaller contribution of the local mode (ω is the smallest for the presented compounds with a value of 11.5 cm^{-1} /16.6 K) but higher contribution of the *n* parameter from the Raman process (*n* = 8.2) and the Direct mechanism (it has the highest A(H) value). These values suggest that for **3-bipy**, the spin relaxation is mostly taking place through the Raman and Direct processes.

On the other hand, the temperature dependence of τ could also be fit with only the Raman term as the ln(τ) *vs* ln(T) plots lead to straight lines of the magnetic data for all compounds, Figure APX.III.8. A fit of these plots taking into account just Raman relaxation of the magnetization mechanism described by the $\ln(\tau) = -n \cdot \ln(T) + \ln(C)$ equation lead to good values of n and C with n = 8.9 and C = 5.9 for **1-H$_2$O**, n = 7.0 and C = 17.8 for **2-phen**, n = 5.7 and C = 0.3 for **3-bipy**, n = 4.7 and C = 0.0519 for **4-terpy** and n = 7.5 and C = 0.9 for **5-bathophen**. This leads us to considerate that Raman may actually be the relevant mechanism in the magnetic relaxation of these Cerium(III) compounds. However, a fit of temperature dependent data with Equation 2.4 without considering the Local mode but taking into account the contribution of all the field dependent terms, lead to unsuccessful fit of the data, Figure APX.III.9. Therefore, two different approaches are presented to explain spin dynamics of **1-H$_2$O** to **5-bathophen**.

The first considers that the contributions of QTM and Direct processes in magnetic relaxation leads to overparametrization, then the parameters of those mechanisms are first obtained from the field dependent magnetic data and fixed in the temperature dependent fit. In this approach, Local mode needs to be considered to obtain a good fitting of relaxation of the magnetization times with temperature since only considering Raman lead to unsuccessful fit. The second approach is just considering Raman relaxation mechanism and neglect the contribution that Direct and QTM may have into spin relaxation, which also lead to reasonable results. Still the intervention of QTM and Direct mechanism into spin relaxation shouldn't be overlooked, especially Direct mechanism if an external magnetic field is applied to measure the alternating current magnetic susceptibility. The second approach is actually a first approximation. The field dependent parameters are only calculated for the measurements at one constant T. Similarly, the temperature dependent parameters are calculated from the ac measurements at one constant H_{dc} field. However, in reality these parameters will change from one constant T and from one constant H_{dc} field. For instance, B_1 and B_2 parameters will slightly change when calculating them from the τ *vs* H curve measured at 2 K and from the same curve measured at 3 K. Similarly, the n parameter from Raman relaxation will not be exactly the same when calculated from the τ *vs* T curve at H_{dc} = 0.01T compared to the same curve obtained at H_{dc} = 0.02 T. Therefore, field dependent measurements should be performed at different constant T and temperature dependent measurements should be performed at different constant H_{dc} fields. This way we could obtain several τ *vs* H curves and different τ *vs* T curves. Then the field and temperature dependent parameters could be fitted from a tensor constructed from all these experimental data. These would lead to more accurate values of all the parameters. However, to realize this approach a large quantity of magnetic measurements are needed in addition to extensive knowledge in mathematics and programs for solving complex equations, therefore this has not been carried out in this *Thesis* work.

The existence of multiple potential explanations to describe the spin dynamics phenomenon of compounds **1-H_2O** to **5-bathophen**, once again, highlights the need for continued investigation into the magnetic behavior, at the molecular level, of Ce^{3+} coordination compounds.

Moreover, the geometry optimization and calculation of the DFT vibrational frequencies was performed for **1-H$_2$O**, **2-phen** and **4-terpy**. The analysis of the frequencies shows a large amount of low energy vibrational frequencies (Table APX.III.3) that can contribute to the spin relaxation through the Local mode process, however a spin-phonon calculation of those frequencies to verify their contribution is out of the scope of this *Thesis* work.

Table 2.10. a) Values obtained from the fitting of the τ^{-1} *vs* H curves with the field dependent curve function: $\boldsymbol{\tau^{-1} = AH^4T + \frac{B_1}{1+B_2H^2} + d\left(\frac{1+eH^2}{1+fH^2}\right)T^n}$+K(T)

	Raman			Direct	QTM	
	dT^n (s^{-1})	e (T^{-2})	f (T^{-2})	a (s^{-1} T^{-4})	B_1 (s^{-1})	B_2 (T^{-2})
1-H$_2$O	549.21	82.78	22760.23	526.71	1549.17	22760.21
2-phen	370.07	214.49	77778.39	291.57	1691.25	77778.40
3-bipy	575.89	1279.27	87007.58	1394.18	2054.14	87010.40
4-terpy	585.82	23.25	15.40	1270.65	2055.59	556254.6
5-bathophen	197.48	14891.10	3561.34	832.12	5754.71	42402.08

Table 2.10 b) Values obtained from the fitting of the τ^{-1} *vs* H curves with the field dependent curve function: $\boldsymbol{\tau^{-1} = A_{loc}\left(\frac{e^{-\frac{\omega}{T}}}{(e^{-\frac{\omega}{T}}-1)^2}\right)T^n + D(H)T^n + A(H)T + K(H)}$

	Raman	Local Mode	
	n	A_{loc} (s^{-1})	ω (cm^{-1}) / (K)
1-H$_2$O	4.82	$4.03\cdot10^7$	19.95 / 28.71
2-phen	7.20	$1.7\cdot10^7$	20.89 / 30.07
3-bipy	8.27	$3.16\cdot10^5$	11.55 / 16.61
4-terpy	2.40	$3.05\cdot10^6$	15.42 / 22.19
5-bathophen	6.16	$1.20\cdot10^7$	17.70 / 25.47

2.1.4 Computational results

Ab initio calculations were performed on the crystallographic structures (See APX.II for the computational details). Complete Active Space Self-Consistent Field (CASSCF) calculations incorporating spin-orbit effects via the Restricted Active Space State Interaction (RASSI) approach were conducted to investigate the magnetic characteristics of compounds **1-H$_2$O** to **5-bathophen** in detail. Cerium(III) complexes exhibit a $4f^1$ configuration and a $^2F_{5/2}$ ground state. The simulated magnetic susceptibility and magnetization profiles are similar to the experimentally observed curves, see Figures

APX.III.10 and APX.III.11, indicating a good agreement between theoretical predictions and actual experimental results.

Table 2.11. Calculated components of the g tensor and wavefunction analysis of the ground Kramer doublet state at CASSCF-RASSI level.

Compound	g_x	g_y	g_z	Wavefunction
1-H$_2$O	0.563	1.391	2.392	0.28|±5/2〉 +0.42|±3/2〉 +0.30|±1/2〉
2-phen	0.108	0.481	3.754	0.90|±5/2〉 +0.005|±3/2〉 +0.09|±1/2〉
3-bipy	0.460	0.940	3.600	0.87|±5/2〉 +0.04|±3/2〉 +0.09|±1/2〉
4-terpy	0.775	1.255	3.379	0.89|±5/2〉 +0.08|±3/2〉 +0.03|±1/2〉
5-bathophen	0.501	1.500	3.350	0.82|±5/2〉 +0.04|±3/2〉 +0.14|±1/2〉

Except compound **1-H$_2$O**, the rest of the studied systems show larger g_z component, see Table 2.11, indicating larger axial anisotropy. The values are similar to other previously reported Ce^{3+} systems (Table 2.1-2.5). However, for a perfectly axial Ce^{3+} complex the g_z value should be 4.19 (30/7). Compounds **2-phen** to **5-bathophen** with values in the range of 3.3 – 3.8 are consistent with a $m_J = \pm5/2$ ground state with a contribution of $m_J = \pm3/2$ states. The orientation of the calculated g_z is quite different depending on the compound, Figure 2.24. In the case of a $m_J = \pm5/2$ ground state it is expected an oblate *f* electron density, with a perpendicular g_z orientation. The g_z would be oriented in a way that the metal-ligand electrostatic repulsion is reduced. It can be achieved by: *i)* the alignment of g_z with the shortest Ce-O bond distances, in a way that the *f* electron density disc stays perpendicular to that direction or *ii*) the location of the *f* electron density disc in the plane containing the longest Ce-L bond distances. In this family of compounds in general g_z is located in a way that it is not pointing to any ligand and the electron density disc tries to avoid all the ligands. This happens for **1-H$_2$O**, **2-phen**, **4-terpy** and **5-bathophen**. However, for **3-bipy** it is mainly oriented with one of the Ce-O bonds (Ce1-O5, which is the second shortest Ce-O bond distance in **3-bipy**) and with the *f* electron density disc oriented close to the Ce-N bonds. In the case of **4-terpy** g_z is oriented in a way that *f* electron density disc avoids most of the ligands but being in the same plane than some of the Ce-N bonds of the terpyridine ligand.

The analysis of the decomposition of the RASSI wavefunction of the ground Kramer doublet can be found at Table 2.13. It shows, as expected, a different contribution for **1-H$_2$O**, where a large mixture of the three components is observed, which correlates with smaller g_z and larger g_x and g_y components. For the other compounds a larger contribution of the wave function |±5/2〉 (80-90 %) mixed with the |±1/2〉 and |±3/2〉 from the other excited m_j doublets is found, explaining also the larger anisotropy of this Ce^{3+} complexes.

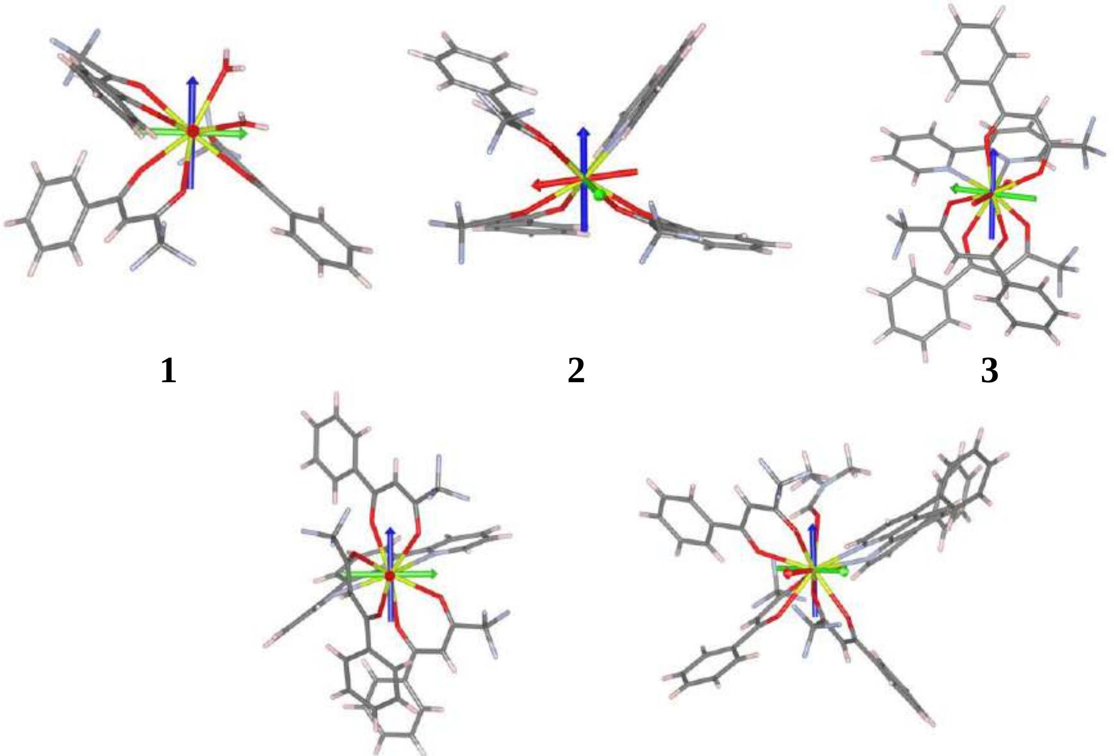

1 **2** **3**

4 **5**

Figure 2.24. Calculated orientations of the g tensor of the ground Kramers doublet, where g_z, g_y and g_x components are represented by blue, green and red arrows, respectively. Cerium, fluor, oxygen, nitrogen, carbon and hydrogen are represented in yellow, light blue, red, blue, gray and pink respectively.

The energy of the Kramer doublet and transition probabilities between the states were calculated, Figure 2.25. The first excited Kramer doublet is around 150 cm^{-1} in **1-H$_2$O** and **5-bathophen** and around 300 cm^{-1} or more for the other complexes. In all cases, as commented before, the energy difference is much larger than the energy barrier that could be obtained from the fit of the dependence of relaxation times with temperature to an Arrhenius equation, 12-20 cm^{-1}. All complexes show large tunnelling probability in the ground state, having complex **2-phen** the smallest one, but practically 0.1. This agrees with the need of applying an external dc field to show out-of-phase magnetic susceptibility signal. Besides **2-phen** having the smallest tunnelling probability in this family of compounds the optimal field needed is not the smallest one (0.1 T for **1-H$_2$O** and **3-bipy**, of 0.05 T for **2-phen** and of 0.02 T for **4-terpy** and **5-bathophen)**. This could also be related to the shorter Ce---Ce distance in **2-phen** in comparison with **4-terpy** and **5-bathophen**.

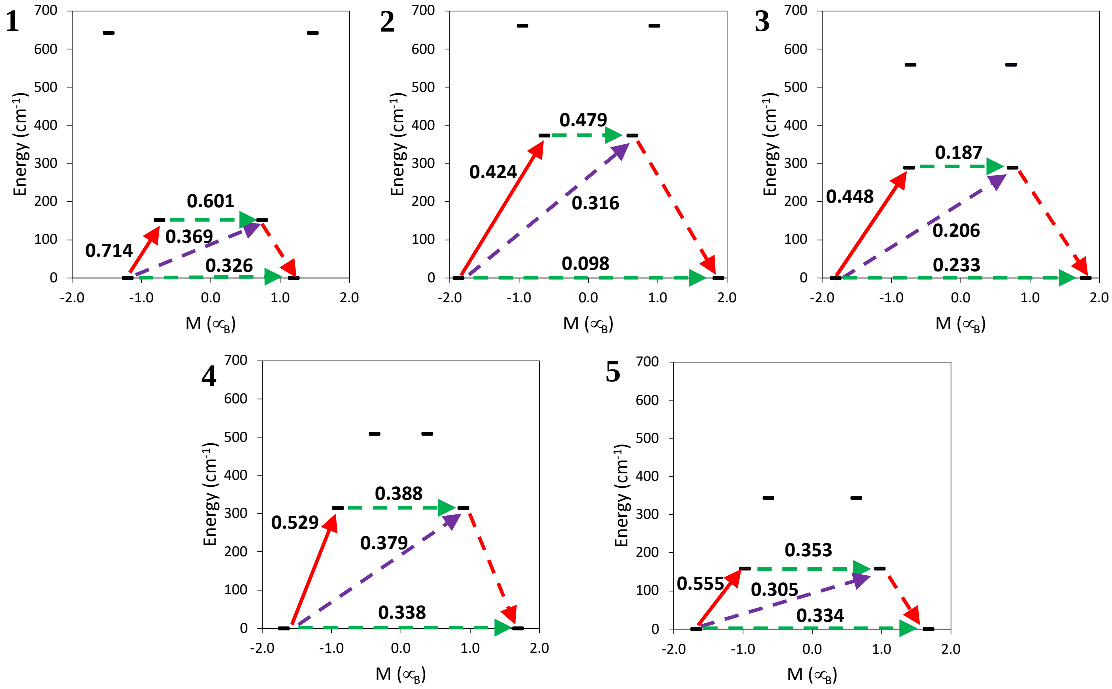

Figure 2.25. Calculated states energies as a function of their magnetic moment, Mz, along the main anisotropy axis. The arrows correspond to the quantum tunneling mechanism of ground and first excited states (green), the hypothetical Orbach relaxation process (purple) and the transition between the ground and first Kramer's doublet (red). The values close to the arrows indicate the matrix elements of the transition magnetic moments (efficient spin relaxation mechanism is expected above 0.1).

Table 2.13. Calculated energy (in cm^{-1}) of the three lowest Kramer doublets and their wavefunction analysis

Compound	**KDs**	**E (cm^{-1})**	**Wavefunction**
1-H$_2$O	GS	0	0.28|±5/2〉 +0.42|±3/2〉 +0.30|±1/2
	1st ES	151.9	0.23|±5/2〉 +0.24|±3/2〉 +0.53|±1/2
	2nd ES	641.7	0.49|±5/2〉 +0.34|±3/2〉 +0.17|±1/2
2-phen	GS	0	0.90|±5/2〉 +0.005|±3/2〉 +0.09|±1/2〉
	1st ES	372.6	0.06|±5/2〉 +0.27|±3/2〉 +0.67|±1/2〉
	2nd ES	661.3	0.04|±5/2〉 +0.72|±3/2〉 +0.24|±1/2〉
3-bipy	GS	0	0.87|±5/2〉 +0.04|±3/2〉 +0.09|±1/2〉
	1st ES	289.2	0.06|±5/2〉 +0.42|±3/2〉 +0.52|±1/2〉
	2nd ES	558.1	0.07|±5/2〉 +0.54|±3/2〉 +0.39|±1/2〉
4-terpy	GS	0	0.89|±5/2〉 +0.08|±3/2〉 +0.03|±1/2〉
	1st ES	313.9	0.08|±5/2〉 +0.90|±3/2〉 +0.02|±1/2〉
	2nd ES	509.02	0.03|±5/2〉 +0.02|±3/2〉 +0.95|±1/2〉
5-bathophen	GS	0	0.82|±5/2〉 +0.04|±3/2〉 +0.14|±1/2〉
	1st ES	158.0	0.07|±5/2〉 +0.78|±3/2〉 +0.15|±1/2〉
	2nd ES	344.1	0.11|±5/2〉 +0.18|±3/2〉 +0.71|±1/2〉

2.3 Compounds derived from lanthanide(III), 4,4,4-Trifluoro-1-phenyl-butanedione (HBtfa) and 4,4’-dinonyl-2,2’-bipyridine. OLED preparation.

As already Illustrated in *Chapter 1.*, choosing a ligand that acts as an efficient sensitizer is key to enhance luminescence intensity of lanthanide coordination compounds. Added to their versatility and great stability in solid and solution state, β-diketonates are among the most important lanthanide sensitizers owing to the following merits: *i*) they show intense absorption from their conjugated π→π* transitions within a wide wavelength range, *ii*) they show efficient $S_1 \rightarrow T_1$ intersystem crossing, *iii*) several β-diketonate systems have shown to exhibit optimal triplet state energy, above the emitting level of the lanthanide ion, therefore providing adequate sensitization of the central atom, specially to Eu^{3+} and nIR emitters lanthanide(III) ions such as Yb^{3+}, Er^{3+} and Nd^{3+}.[48]

On the other hand, Organic Light-Emitting Diode (OLED) devices are widely used in displays and lighting systems in modern technology because of their outstanding color quality, ease of construction, affordability, low impact on the environment and energy-saving qualities. Kido et al.[49a] reported in 1994 a ternary Eu^{3+} complex of formula [Eu(DMB)$_3$phen] where DMB and phen stands for 1,3-diphenylpropane-1,3-dionate and 1,10-phenantroline respectively. The β-diketonate europium system was studied as the red emitter in an OLED device showing maximum luminance of 460 cd m^{-2}. Since then β-diketonate derivatives have become the most popular anionic ligands for preparing electroluminescent europium(III) complexes. Owing to their characteristic *f-f* transitions, the emission of the lanthanide-based compounds leads to narrow and high colour purity bands which are essential for developing phosphors for OLED applications. Regarding the europium β-diketonate based systems, they show outstanding luminescence and, due to the rather high quantum yields, red color purity, thermal stability and great sensitization effect of the β-diketonate to the Eu^{3+}: they are good candidates in OLED devices for multiple potential applications compressed between optical communications and lasers.[49b,c] Similarly, Yb^{3+} complexes displaying photoluminescence at ~1000 nm are ideal candidates for use in nIR-OLEDs which are far less studied compared with OLEDs emitting in the visible range. Interesting application of nIR-OLEDS are compressed in biomedical and biosensing applications owing to the fact that the 700-1000 nm window matches with the biological tissue semitransparency window.[50] Additionally, nIR-OLED devices show potential applications in telecommunications for data transmission and in night-vision readable displays for low-light environments.[51a]

Despite their ability to produce nearly monochromatic emission, lanthanide compounds have a disadvantage when it comes to electroactivity, compared to organic dyes. One of the drawbacks is associated with high turn on voltages and lower efficiencies. Adding functional groups like heterocyclic rings or electron-donating and electron-withdrawing atoms may be a practical way to enhance the electrical characteristics of hole and electron injection and transportation of these compounds.

In this regard 4,4,4-trifluoro-1-phenyl-1,3-butanedionate (Btfa), may be a good candidate to obtain ternary lanthanide(III) systems with good electroluminescence properties thanks to both, the phenyl group (electron-donating) found in one α-carbon and the -CF_3 (electron-withdrawing) group located at the other α-carbon. The phenyl group will increase electron delocalization of the anionic β-diketonate improving its molar absorptivity coefficient. Meanwhile, the introduction of C-F bonds, instead of higher energy frequency oscillator C-H bond, near the emitting lanthanide(III) center reduces non-radiative deactivation. Since the C-F bond oscillating energy is much lower than the C-H bond oscillating energy, radiative deactivation of the emissive energy levels of the lanthanide ion will be less quenched leading to an enhanced emission intensity of the final compound, especially for the nIR emitters. Also, by providing an asymmetric ligand such as Btfa which adds more distortion to the coordination environment of the lanthanide ion will make the *f-f* transitions less prohibited. This is especially important for the Eu^{3+} ion, since an asymmetry around its coordination environment will enhance the hypersensitive $^5D_0 \rightarrow {}^7F_2$ band intensity leading, essentially, to monochromatic single-band red emission at around 612 nm.[52]

Our aim in this *Chapter* section is to achieve two main objectives: *i)* the obtention of multiproperty lanthanide coordination compounds in which, fundamentally, the optical and magnetic properties will be studied and *ii)* the obtention of compounds showing good electroluminescence properties and great thermal stability to be thermally deposited in neat films of the emissive layer of OLED devices. To try to accomplish the above-mentioned targets, the auxiliary neutral ligand chosen is the 4,4'-dinonyl-2,2'-bipyridine (4,4'-dinonyl-bipy), Scheme 2.4 a). The addition of the Lewis base N-donor polypyridyl ligand reinforces the fluorescence emission of the final compound and also completes the coordination sphere of the lanthanide(III) ion preventing, this way, coordination of undesired H_2O or EtOH molecules from the solvent reaction. Moreover, the fluorinated Btfa and the long alkyl tails provided by the 4,4'-dinonyl-bipy may enhance the thermal stability and increase the volatility of the final complexes which is of significant relevance to build the OLED device by vacuum deposition.[53]

The obtained coordination complexes show the [Ln(Btfa)$_3$(4,4'-dinonyl-bipy)] formula were Ln^{3+} is Sm^{3+} (**1-Sm**), Eu^{3+} (**2-Eu**), Tb^{3+} (**3-Tb**), Dy^{3+} (4-**Dy**), Er^{3+} (**5-Er**), Yb^{3+} (**6-Yb**) and Gd^{3+} (**7-Gd**). The synthesized compounds were structurally analyzed and their photoluminescent and static and dynamic magnetic properties were studied. Due to the promising luminescence properties that the Eu^{3+} and Yb^{3+} analogues presented; the complexes were used in the emissive layer material of five different OLED devices which were properly characterized.

2.3.1 Experimental procedure

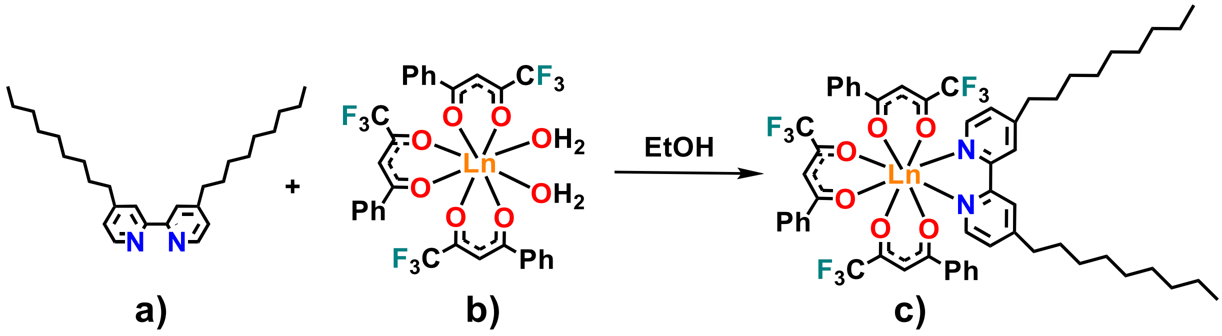

Scheme 2.4. Synthetic route to obtain compounds **1-Sm** to **7-Gd**. Molecular representations of a) 4,4'-dinonyl-2,2'-bipyridine (4,4'-dinonyl-bipy) b) precursor lanthanide compound [Ln(Btfa)$_3$(H$_2$O)$_2$] and c) compounds **1-Sm** to **7-Gd**.

Compounds **1-Sm** to **7-Gd**, with [Ln(Btfa)$_3$(4,4'-dinonyl-bipy)] formula, were obtained in a straightforward room temperature reaction from the β-diketonate precursor and the neutral 4,4'-dinonyl-bipy ligand in a 1:1 ratio, Scheme 2.4. The β-diketonate precursor was the Sm^{3+}, Eu^{3+}, Tb^{3+}, Dy^{3+}, Er^{3+}, Yb^{3+} and Gd^{3+} analogues of compound **1-H$_2$O** *(Chapter 2 Section 2.2)*. The synthesis procedure to obtain each precursor was the same as for **1-H$_2$O**, explained in section *2.2.1 Experimental procedure*, but changing the $CeCl_3·6H_2O$ reactant to the respective lanthanide salts. The obtained pale powders (light pink for the Er^{3+} analogue) yielded around 70-80%.

The synthesis of compounds **1-Sm** to **7-Gd** proceed as follows: an ethanol solution (15 mL) containing 4,4'-dinonyl-bipy (1 mmol, 408.7 mg) was added to another ethanol solution (15 mL) containing the corresponding $[Ln(Btfa)_3(H_2O)_2]$ compound (1 mmol). The solution was stirred for 30 minutes and then it was left to stand at room temperature. Block like, single crystals suitable for X-Ray diffraction were obtained within a week (yield: 60-70%).

TGA measurements were performed in the temperature range between 30 and 600 °C for **2-Eu** and **6-Yb**. The sample weight stays steady up until 250-300º C where it loses 75.2% (**2-Eu**) and 74.7% (**6-Yb**) of its weight, Figure 2.26. Decomposition of the compounds is observed at temperatures above 300 °C. One step decomposition at rather high temperatures is a promising indication that these compounds can potentially be used for vacuum vapor deposition.

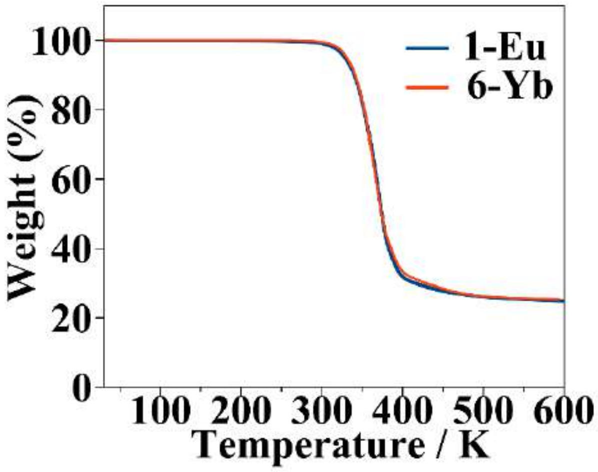

Figure 2.26. TGA analysis of compounds **1-Eu** and **6-Yb**.

For all compounds elemental analysis of C, H and N and the most characteristic bands obtained in Infra-red spectroscopy are depicted in Tables 2.14 and 2.15, respectively.

Table 2.14. Elemental analysis calculated and found, for compounds **1-Sm** to **6-Yb**.

	Calculated			**Found**		
Compound $\mathbf{C_{58}H_{62}F_9N_2O_6Ln}$	**%C**	**%N**	**%H**	**%C**	**%N**	**%H**
1-Sm 1204.48 g/mol	57.8	2.3	5.2	58.0	2.3	5.4
2-Eu 1206.1 g/mol	57.8	2.3	5.2	58.0	2.3	5.4
3-Tb 1213.0 g/mol	57.4	2.3	5.2	57.6	2.3	5.3
4-Dy 1216.6 g/mol	57.3	2.3	5.1	57.0	2.3	5.2
5-Er 1221.4 g/mol	57.0	2.3	5.1	57.4	2.4	5.3
6-Yb 1227.2 g/mol	56.8	2.3	5.5	59.0	2.4	5.4
7-Gd 1211.4 g/mol	57.5	2.3	5.2	58.1	2.2	5.0

Table 2.15 Selected bands (cm^{-1}) of compounds **1-Sm** to **7-Gd** compounds s=strong, m=medium and w=weak, br=broad obtained in ATR-IR spectroscopy.

1-Sm	2928.6(m), 2858.5(m), 1608.5(s), 1573.4(m, split), 1522.4(m, split), 1318.3(m), 1292.8(s), 1241.8(m), 1184.4(s), 1133.4(s), 1076.0(m), 1015.4(m), 945.3(m), 763.5(s), 702.9(s), 632(m), 578.57(m)
2-Eu	2924.0(m), 2847.6(m), 1612.2.5(s), 1569,0(m, split), 1525.8(m, split), 1472.7(m), 1293.4(s), 1246.9(l), 1183.8(s), 1133.4(s), 1120.7(s), 1015.4(m), 1070.9(l), 781.9(s), 679.0(s), 562.7(m).
3-Tb	2924.0(m), 2854.2(m), 1605.5(s), 1572.3(m), 1519.2(m), 1476.0(m), 1286.7(s), 1183.8(s), 1124.0(s), 1074.2(m), 1076.0(m), 762.0(m), 945.3(m), 692.3(m), 702.9(s), 625.8(m), 576.0(m).
4-Dy	2924.0(m), 2850.9(m), 1608.9(s), 1572.3(m), 1522.5(m, split), 1483.0(m, split), 1293.4(s), 1236.9(m), 1183.7(s), 1133.9(s),

	1067.5(m), 1014.4(m), 945.3(m), 938.0(m), 758.7(s), 695.6(m), 629.2(m), 576.0(m).
5-Er	2920.6(m), 2854.2(m), 1605.5(s), 1572.3(m), 1522.5(m, split), 1479.3(m, split), 1290.0(s), 1240.2(m), 1183.8(s), 1127.3(s), 1067.5(m), 1007.7(l), 762.0(m), 695.6(m), 625.8(m), 695.6(m), 576.0(m).
6-Yb	2927.3(m), 2850.9(m), 1605.5(s), 1569.0(m), 1519.2(m, split), 1486.0(m, split), 1290.0(s), 1240.2(m), 1177.1(s), 1127.3(s), 1070.9(m), 1011.1(l), 944.7(l), 758.7(s), 695.6(s), 625.8(m), 576.0(m).
7-Gd	2927.3(m), 2850.9(m), 1605.5(s), 1575.6(m), 1522.5(m, split), 1479.3(m, split), 1286.7(s), 1236.9(m), 1177.1(s), 1184.7(s), 1130.6(s), 1074.2(l), 1011.0(l), 941.3(s), 758.6(s), 698.9(s), 625.8(m), 579.3(m), 509.6(l), 463.1(l).

2.3.2 Structural characteristics

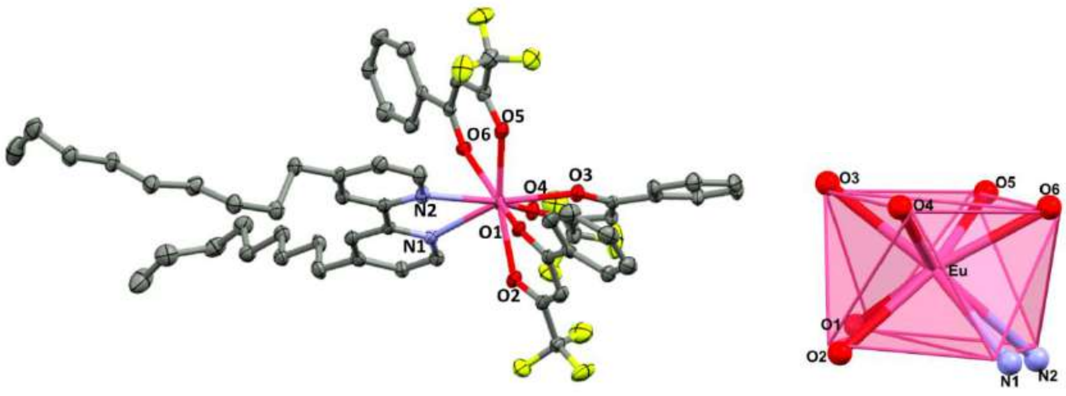

Figure 2.27 *Left*, crystal structure of complex **2-Eu**. Only the atoms coordinating the central ion are labeled. Hydrogen atoms have been omitted for clarity. *Right*, ideal coordination polyhedron superimposed on the coordination sphere around the Eu^{3+} ion.

Single crystal X-Ray diffraction was measured at 100 K on single crystals of compounds **2-Eu**, **4-Dy** and **6-Yb.** Crystallographic details from the measurement and selected bond distances and angles are compiled in Table APX.IV.1 and Table 2.16 respectively. The three compounds **2-Eu**, **4-Dy** and **6-Yb** are isostructural, therefore only the structure of compound **2-Eu** will be described, Figure. 2.27 (*left*).

Compound **2-Eu** crystallizes in a triclinic crystal system and a P-1 space group. The Eu^{3+} ion is octacoordinated and the EuO_6N_2 polyhedron is made up of six O atoms from three β-diketonate ligands with Eu-O bond distances in the range 2.343-2.389 Å and two N atoms from one polypyridyl ancillary ligand with Eu-N distances of 2.559 and 2.575 Å. The closest Eu---Eu intermolecular distance is 8.968 Å. The six oxygen and two nitrogen atoms are gathered around the Eu^{3+} central ion, forming a geometrical polyhedron that is close to an ideal square antiprism (SAPR-8, D_4d symmetry) Figure 2.28 (*right*). One of the basal planes is made up of the O1, O2, N1 and N2 atoms and the other one of O3, O4, O5 and O6. The geometry has been calculated with the SHAPE program.[26] For compound **2-Eu** the deviation from the optimal polyhedron accounted by the Continuous Shape Measurement (CShM) values for the SAPR-8 geometry is 1.040. For compounds **4-Dy** and **6-Yb** the CShM values for the SAPR-8 geometry are 0.902 and 0.790 respectively.

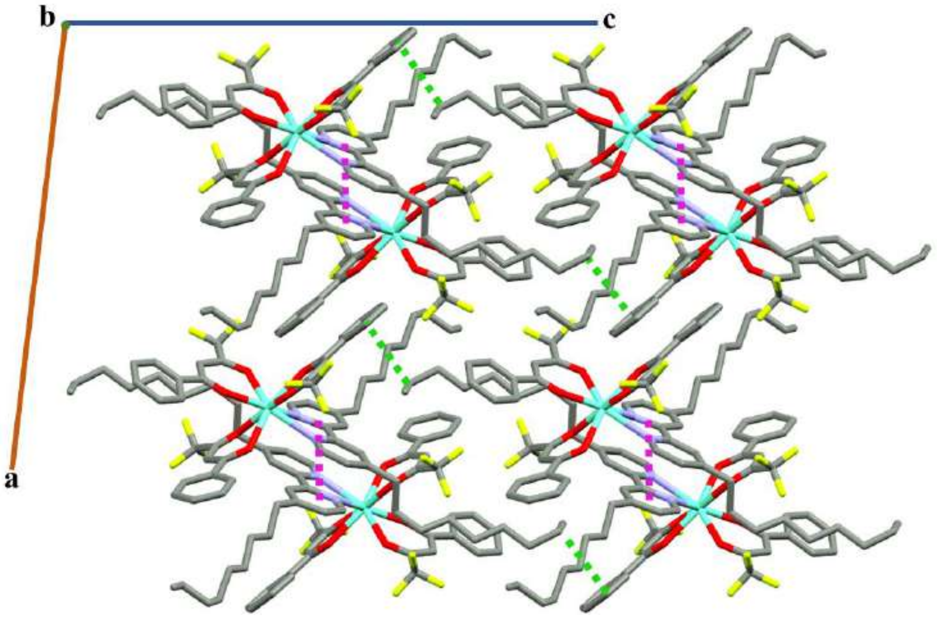

Figure. 2.28 Crystal packing of compound **2-Eu.**

The crystal packing in **2-Eu** is built up through weak intermolecular interactions. Figure 2.28. The shortest Cg---Cg distance is 3.938 Å from the pyridine ring constituted by N1, C31, C32, C33 C34, C35 atoms. The shortest H---π interaction is 2.7 Å from the ring of one β-diketone molecule and one hydrogen from the alkyl chain. All in all, the distances of the intermolecular interactions are large enough (longer than 3.35 Å for Cg---Cg interaction and 2.5 Å for Cg---H interaction) to consider isolated mononuclear systems packed in the crystal lattice.

Table 2.16. Selected bond distances (Å) for **2-Eu**, **4-Dy** and **6-Yb**.

	2-Eu	**4-Dy**	**6-Yb**
Ln-O1	2.389(2)	2.333(3)	2.283(2)
Ln-O2	2.362(2)	2.311(3)	2.268(19)
Ln-O3	2.343(2)	2.320(3)	2.292(2)
Ln-O4	2.351(2)	2.311(3)	2.270(18)
Ln-O5	2.364(2)	2.320(3)	2.278(2)
Ln-O6	2.353(2)	2.355(3)	2.315(19)
Ln-N1	2.559(3)	2.527(3)	2.488(2)
Ln-N2	2.575(3)	2.540(3)	2.489(2)
Shortest Ln---Ln	8.9668	8.921	8.920

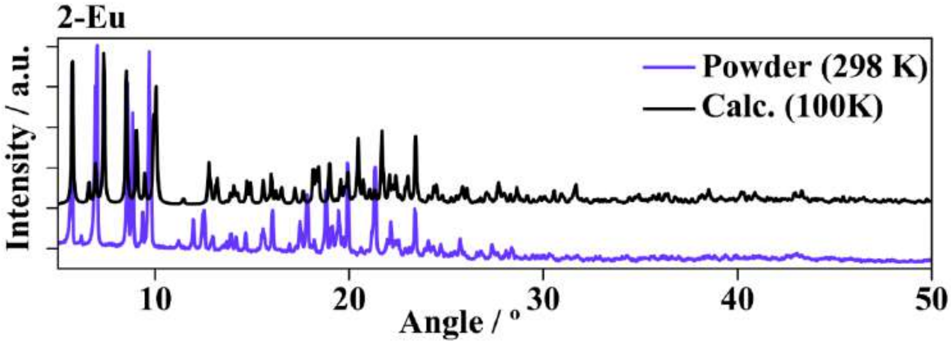

Figure 2.29 Powder X-Ray Diffraction pattern of the powder sample of **2-Eu** compared to the pattern calculated from the Single Crystal structure. Powder X-Ray Diffraction is measured at room temperature (298 K) and the Single crystal structure is measured at 100 K.

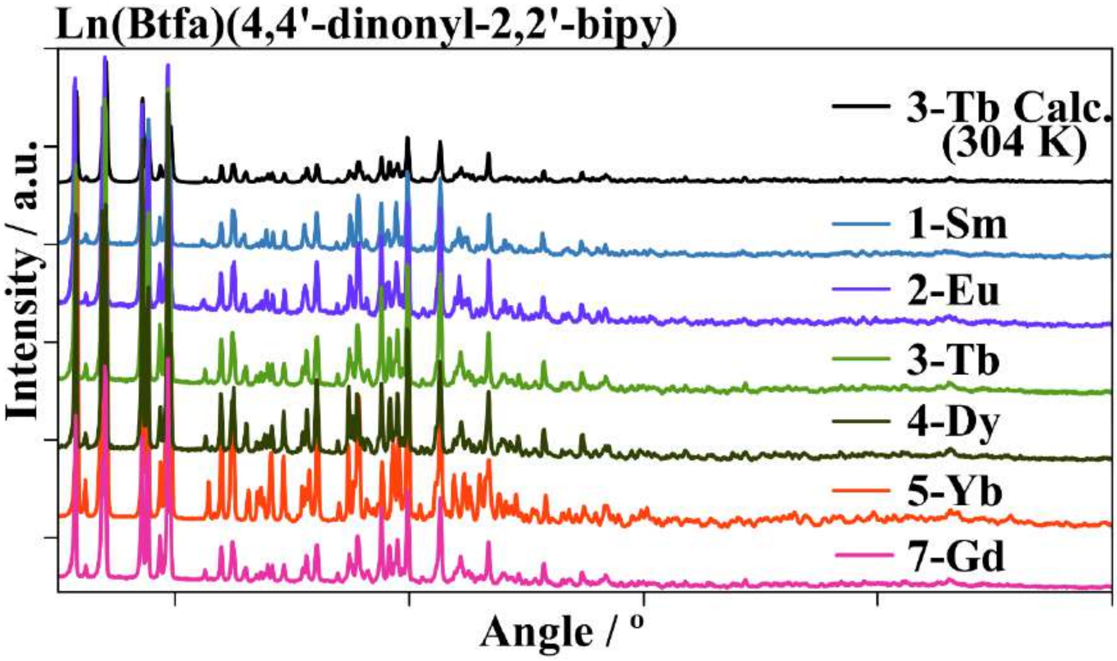

Figure 2.30. Powder X-Ray Diffraction pattern of samples **1-Sm** to **7-Gd** measured at room temperature (298K) compared to the pattern calculated from the Single Crystal structure measured at 304 K.

To verify the crystallinity and phase purity in bulk, Powder X-Ray Diffraction (PXRD) was recorded at room temperature for **1-Sm** to **7-Gd** complexes. The PXRD were compared to the calculated patterns obtained from the single crystal structure of **2-Eu**, **4-Dy** and **6-Yb** recorded at 100 K, Figure 2.29. Interestingly, we observed that the experimental and calculated diffractograms did not match. Then, we performed a single crystal measurement at room temperature (304 K) using **3-Tb** crystals (Figure 2.30 *first spectrum*). The calculated powder spectrum obtained from this measurement is in good match with the powder diffractograms of the other complexes Figure 2.30. From these results we conclude that upon changing the temperature from 300 K to 100 K, there is a slight change in the atomic coordinates of the crystals which results in a noticeable difference in some cell parameters (*i.e.* parameter b is greater compared to the 100 K measurements, Table APXIV.1), thus leading to a different PXRD pattern, but the crystal cell and space group remain the same, Figure 2.31.

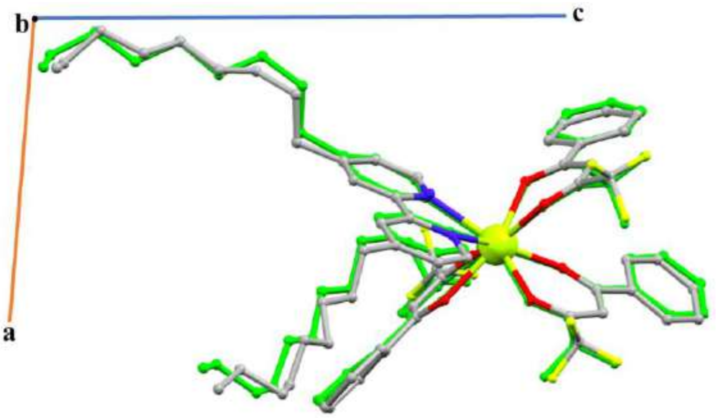

Figure 2.31. Single crystal structure overlay of compound **1-Eu** measured at 77K (green) and compound **3-Tb** measured at 304 K (default colors).

2.3.3 Luminescence properties

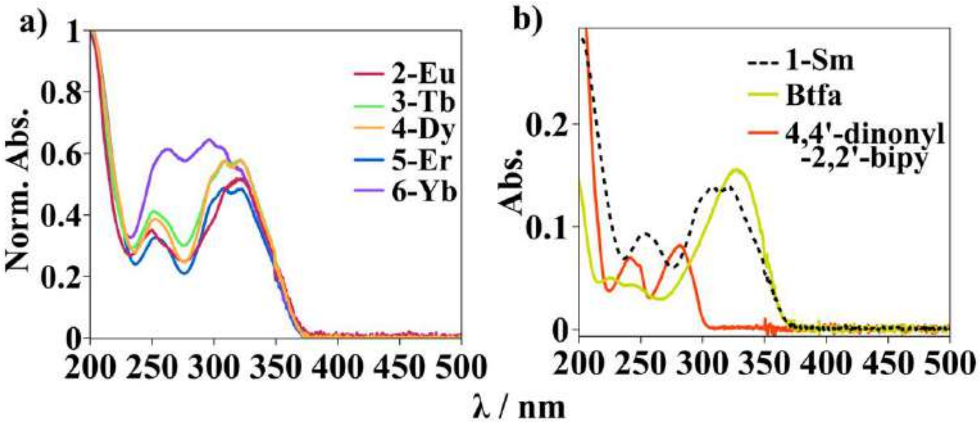

Figure 2.32. Absorption spectra of a) the Ln^{3+} compounds in chloroform solutions c = 10^{-6} M; and b) Spectra of the free 4,4’-dinonyl-2,2’-bipy ligand in $CHCl_3$ solution and spectra of Btfa salt in a 1mM NaOH, $CHCl_3$ solution. The free ligand absorption spectrum has been superimposed onto **1-Sm** for sake of wavelength shift comparison.

Absorption spectra were recorded for all complexes in chloroform solutions (c= 10^{-6} M), Figure 2.32 a). Spectra of complexes **1-Sm** to **6-Yb** show similar absorption pattern in the 235-370 nm range. As a means of assigning the absorption bands shown by the coordination complexes, absorption spectra were also recorded for the free ligands separately. The 4,4’-dinonyl-bipy ligand was diluted in chloroform solution (c= 10^{-6} M) and HBtfa was diluted in a 1 mM NaOH chloroform solution to measure absorption of the β-diketonate salt, Figure 2.32 b). Absorption spectrum of the free 4,4'-dinonyl-bipy show two bands at 242 and 282 nm while Btfa shows an intense band at 325 nm and less intense bands at 220-248 nm corresponding to the π→π* and n→π* singlet state transitions. The UV-Vis absorption spectra of **1-Sm** to **6-Yb** correlate with those of the constituent ligands. The band corresponding to coordinated Btfa absorption appears slightly blue shifted, compared to the free ligand, about 6 nm. Whereas the absorption bands of 4,4'-dinonyl-bipy were red-shifted, compared to the free ligand, about 25 nm upon coordination. The band appearing at 282 nm in the free 4,4'-dinonyl-bipy spectrum appears as a shoulder around 310 nm in the spectra of the complexes, superimposing to the Btfa associated absorption band. This may explain the intense and broader band appearing at 277-370 nm. Similar UV-Vis absorption spectra are obtained for previous published [Ln(β-diketonate)$_3$(L)] systems, where L is an ancillary ligand based on N,N-donor polypyridyl molecules.[54]

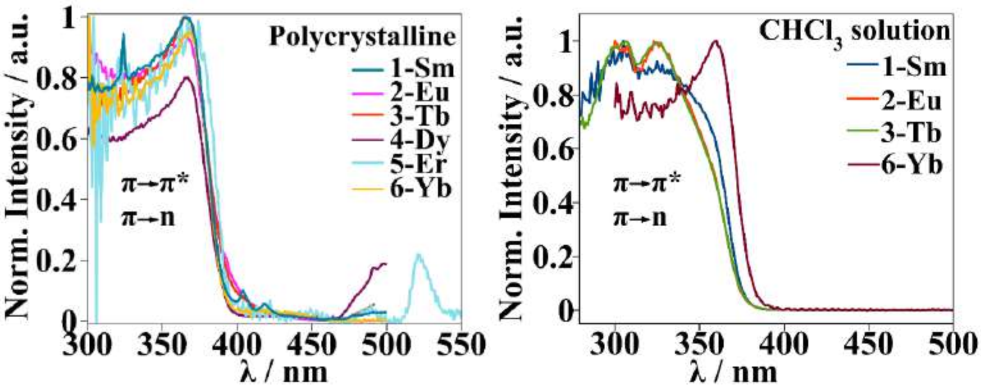

Figure 2.33. Excitation spectra of the polycrystalline samples (left) and CHCl$_3$ solutions (right) of compounds **1-Sm** to **6-Yb.**

Excitation spectra of both, polycrystalline samples and CHCl$_3$ solutions, were measured at the emission wavelength (λ_{em}) of 650 nm ($^4G_{5/2}\rightarrow{}^6H_{9/2}$) for **1-Sm**, at 614 nm ($^5D_0\rightarrow{}^7F_2$) for **2-Eu**, at 546 nm ($^5D_4\rightarrow{}^7F_5$) for **3-Tb**, at 577 nm ($^7F_{9/2}\rightarrow{}^6H_{13/2}$) for **4-Dy**, at 1526 nm ($^4I_{13/2}\rightarrow{}^4I_{15/2}$) for **5-Er** and at 1027 nm ($^5F_{5/2}\rightarrow{}^2F_{7/2}$) for **6-Yb**, Figure 2.33 *left* and *right*. The narrow peak appearing at 325 nm in the solid state excitation spectra of **1-Sm** corresponds to a harmonic signal of the lamp replica (614/2=307 nm). Reliably excitation spectra could not be obtained for the 10^{-6} M chloroform solutions containing compounds

4-Dy and **5-Er** because of the poor luminescence properties that these complexes showed in solution. The $CHCl_3$ solutions spectra of **1-Sm, 2-Eu** and **3-Tb** show similar profile with a broad band showing two peaks maxima. This is very similar to the absorption spectra obtained for those compounds, meanwhile, compound **6-Yb** shows a band with a solely peak appearing at longer wavelengths. This may indicate that while sensitization of compounds **1-Sm**, **2-Eu** and **3-Tb** take place through both ligands, Btfa and 4,4'-dinonyl-bipy (lower wavelength peak), sensitization of **6-Yb** takes place through only the Btfa ligand. β-diketonate singlet state is less energetic than the polypyridyl N,N-donor ligand as was seen in the absorption measurements. Since the emitting level of the Yb^{3+} ion is of lower energy, Btfa might play a more important role in **6-Yb** sensitization effect.

Emission spectra of all complexes in the series **1-Sm** to **6-Yb** were recorded in $CHCl_3$ (c = 10^{-6} M) solution and in polycrystalline samples. To measure the emission spectra, samples were excited at the excitation wavelength (λ_{exc}) of 306 nm for **1-Sm** and **2-Eu**, of 320 nm for **3-Tb** and of 360 nm for **6-Yb**, for solution samples. Solution samples **4-Dy** and **5-Er** were excited at 320 nm according to the absorption spectra since no reliably excitation spectra could be obtained. Polycrystalline samples were excited at the λ_{exc} of 359 nm for **1-Sm** to **6-Yb**. After excitation of **1-Sm** to **6-Yb** in solution and solid state, the emission profiles shown in Figure 2.24 were obtained in the visible (400-700 nm) and nIR range (800-1600 nm).

The expected emission profiles are recorded in all cases (with slightly better resolution in the polycrystalline samples) except for **4-Dy** and **6-Er** where no significant emission was observed in solution. Emission bands displayed by the aforementioned lanthanide compounds are assigned in Figure 2.24 and a compilation of the obtained wavelengths with the assignation of each transition can be found in Table 2.17. The characteristic red, green, and yellowish photoluminescence emission color of the **1-Sm**, **2-Eu**, **3-Tb** and **4-Dy** samples in solid state and in solution, were sufficiently intense to be observed with the naked eye, Figsure 2.25. Color coordinates were calculated based on the measured emission spectra (in the visible range) recorded in solid and solution state and are shown in the Comission Internationale de l'éclairage (CIE) chromaticity diagram 1931 in Figure APX.IV.1.[55] Compound **2-Eu** showed CIE chromaticity coordinates of (0.667, 0.332) in solid and of (0.664, 0.335) in solution. These values are very close to the National

Television System Committee (NTSC) standard CIE values for red (x=0.67, y=0.33) denoting the high color purity red emission showed by **2-Eu**.

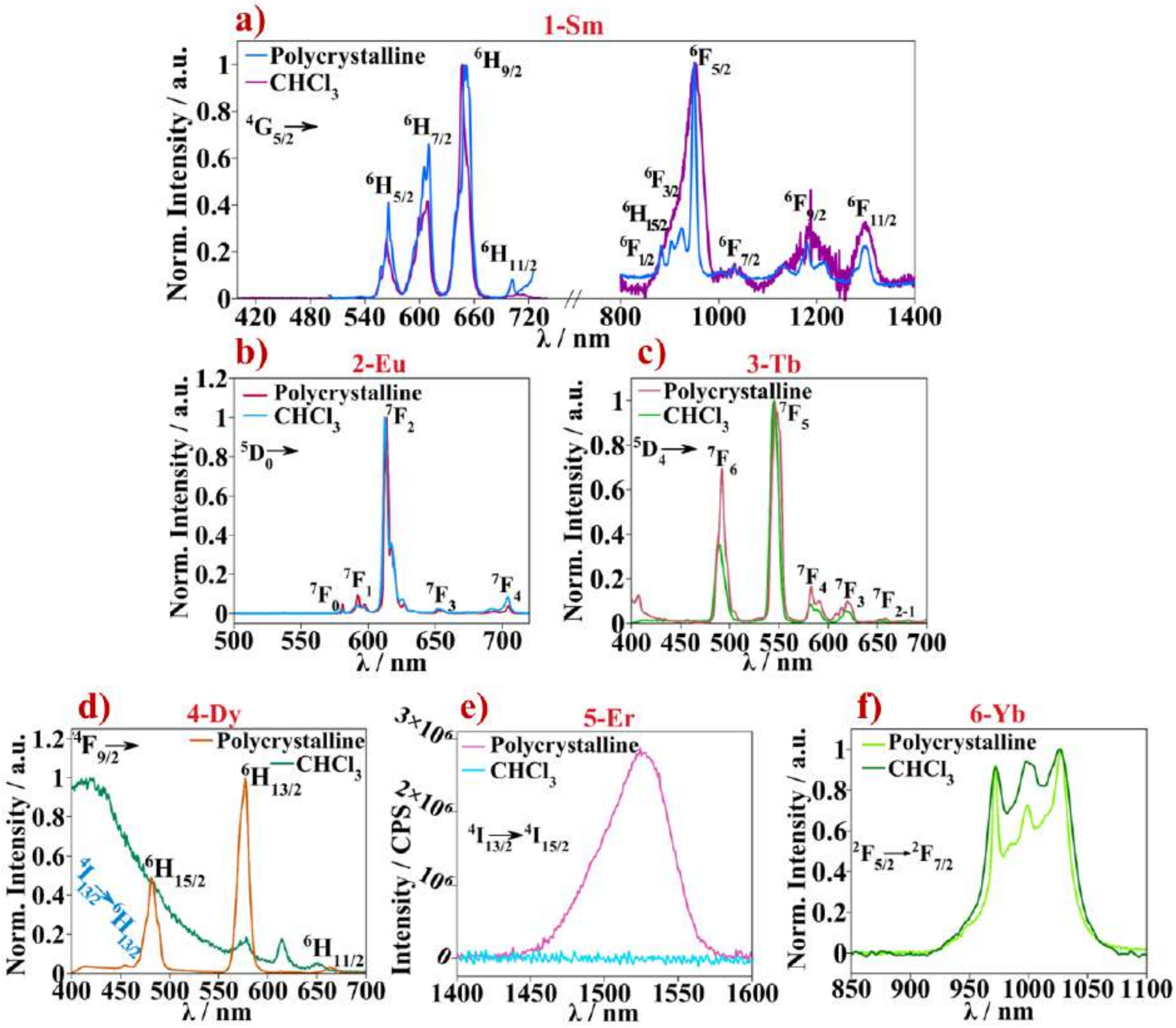

Figure. 2.24. Luminescence emission spectra of compounds **1-Sm** to **6-Yb** measured in polycrystalline samples and in a $1\cdot10^{-6}$ M $CHCl_3$ solution.

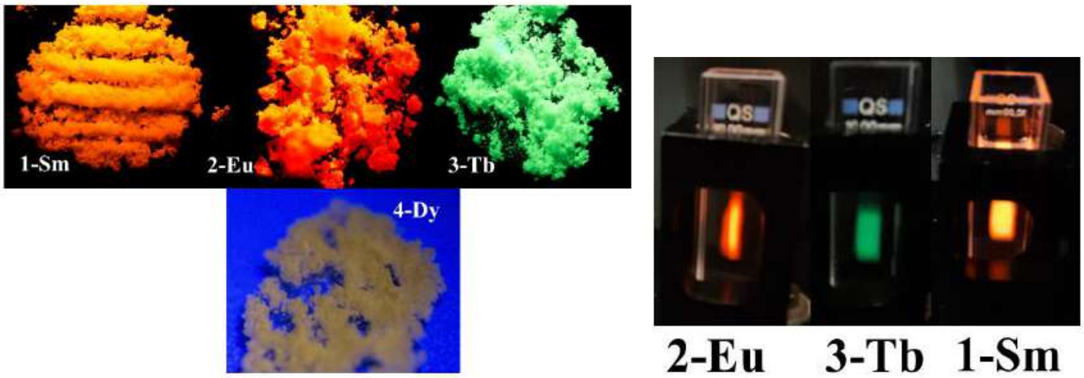

Figure 2.25. Emission color observed by the naked eye of *left*, **1-Sm**, **2-Eu, 3-Tb** and **4-Dy** polycrystalline samples and *right*, **1-Sm**, **2-Eu, 3-Tb** CHCl3 samples under the radiation 365 nm of a laboratory UV lamp.

Table 2.17 Wavelength assigned to the emission transitions observed in the emission spectra of the compounds **1-Sm** to **6-Yb**.

1-Sm
Polycrystalline: $^4G_{5/2}\rightarrow{}^6H_{5/2}$ at 566 nm, $^4G_{5/2}\rightarrow{}^6H_{7/2}$ at 609 nm, $^4G_{5/2}\rightarrow{}^6H_{9/2}$ at 651 nm and $^4G_{5/2}\rightarrow{}^6H_{11/2}$ at 702 nm. **$1\cdot10^{-6}$M $CHCl_3$ solution**: $^4G_{5/2}\rightarrow{}^6H_{5/2}$ at 564 nm, $^4G_{5/2}\rightarrow{}^6H_{7/2}$ at 609 nm, $^4G_{5/2}\rightarrow{}^6H_{9/2}$ at 647 nm and $^4G_{5/2}\rightarrow{}^6H_{11/2}$ at 709 nm.
2-Eu
Polycrystalline: $^5D_0\rightarrow{}^7F_0$ at 581 nm, $^5D_0\rightarrow{}^7F_1$ at 592 nm, $^5D_0\rightarrow{}^7F_2$ at 614 nm, $^5D_0\rightarrow{}^7F_3$ at 653 nm and $^5D_0\rightarrow{}^7F_4$ at 707 nm. **$1\cdot10^{-6}$M $CHCl_3$ solution**: $^5D_0\rightarrow{}^7F_0$ at 579 nm, $^5D_0\rightarrow{}^7F_1$ at 591 nm, $^5D_0\rightarrow{}^7F_2$ at 611 nm, $^5D_0\rightarrow{}^7F_3$ at 651 nm and $^5D_0\rightarrow{}^7F_4$ at 703 nm.
3-Tb
Polycrystalline: $^5D_4\rightarrow{}^7F_6$ at 492 nm, $^5D_4\rightarrow{}^7F_5$ at 546 nm, $^5D_4\rightarrow{}^7F_4$ at 583 nm, $^5D_4\rightarrow{}^7F_3$ at 619 nm and $^5D_4\rightarrow{}^7F_{2-1}$ at 658 and 681 nm. **$1\cdot10^{-6}$M $CHCl_3$ solution:** $^5D_4\rightarrow{}^7F_6$ at 489 nm, $^5D_4\rightarrow{}^7F_5$ at 545 nm, $^5D_4\rightarrow{}^7F_4$ at 582 nm, $^5D_4\rightarrow{}^7F_3$ at 618 nm and $^5D_4\rightarrow{}^7F_{2-1}$ at 658 and 681 nm.
4-Dy
Polycrystalline: $^4F_{9/2}\rightarrow{}^6H_{15/2}$ at 481 nm, $^4F_{9/2}\rightarrow{}^6H_{13/2}$ at 577 nm and $^4F_{9/2}\rightarrow{}^6H_{11/2}$ at 664 nm
5-Yb
Polycrystalline: $^7F_{5/2}\rightarrow{}^2F_{7/2}$ at 998 nm **$1\cdot10^{-6}$M $CHCl_3$ solution:** $^7F_{5/2}\rightarrow{}^2F_{7/2}$ at 999 nm
6-Er
Polycrystalline: $^4I_{13/2}\rightarrow{}^4I_{15/2}$ at 1524 nm

The characteristic emission originated from the *f-f* transitions of each lanthanide ion can be observed for **1-Sm**, **2-Eu**, **3-Tb**, and **5-Yb** with no residual emission of the ligand in the 300-500 nm range. This indicates an efficient energy transfer from the excited state of the ligand to the lanthanide emitting energy levels, the so-called antenna effect. This is also confirmed by the corresponding excitation spectra which shows the broad and intense band corresponding to the ligand while excitation transitions corresponding to the *f-f* lanthanide (III) ions are not observed.[56] The emission bands at 564, 608, 647 and 707 nm found in the **1-Sm** spectrum are assigned to the transitions from the $^4G_{5/2}$ energy level to the $^6H_{5/2}$, $^6H_{7/2}$, $^6H_{9/2}$ and $^6H_{11/2}$ ground state ^6H_J level respectively, Figure 2.24 a). Additional bands are found at 953 nm in the nIR range, assigned to the $^4G_{5/2}\rightarrow{}^6F_{5/2}$ transition, overlapped with the $^4G_{5/2}\rightarrow{}^6F_{1/2}$, $^4G_{5/2}\rightarrow{}^6H_{15/2}$ and $^4G_{5/2}\rightarrow{}^6F_{3/2}$ transitions. The less intense bands found at 1033, 1188 and 1300 nm are assigned to $^4G_{5/2}\rightarrow{}^6F_{7/2}$, $^4G_{5/2}\rightarrow{}^6F_{9/2}$ and $^4G_{5/2}\rightarrow{}^6F_{11/2}$ transitions respectively. A better defined nIR emission spectrum was observed for **1-Sm** polycrystalline sample than in $CHCl_3$ solution.[57]

The emission spectrum of **2-Eu** displays several bands at 579, 592 and 611 nm (most intense) that are assigned to the $^5D_0\rightarrow{}^7F_0$ (ΔJ=0), $^5D_0\rightarrow{}^7F_1$ (split due to the crystal field) and $^5D_0\rightarrow{}^7F_2$ transitions respectively, Figure 2.24 b). While the band at 592 nm is a pure magnetic dipole transition in which the intensity is practically independent of the Eu^{3+} environment, the signal at 611 nm is assigned to the hypersensitive band since it accounts for an electric dipole transition. From the latter, the structure of the band with at least three components, ascribed to the $^5D_0\rightarrow{}^7F_2$ transition, can be discerned. Differentiation of $^5D_0\rightarrow{}^7F_2$ components may indicate that the Eu^{3+} ion is not occupying an inversion symmetry site inside the structure which agrees with the coordination geometry obtained from the SHAPE calculations (Square Antiprism, D_4d symmetry). The less intense bands at 651 and at 703 nm are assigned to $^5D_0\rightarrow{}^7F_3$ and $^5D_0\rightarrow{}^7F_4$ transitions, respectively.[52]

For compound **3-Tb**, the bands found at 489, 545, 581 and 619 nm are assigned to the transitions from the $^5D_4$ emissive state to the ground state $^7F_6$, $^7F_5$, $^7F_4$ and $^7F_3$ energy levels, respectively, Figure 2.24 c).

For **4-Dy**, the emission of the $CHCl_3$ solution is mainly dominated by the ligand in the 300-400 nm range instead of the transitions centered at the Dy^{3+} ion. For the polycrystalline sample, three intense emission bands originating from the dysprosium (III) $^4F_{9/2}$ emissive energy level are differentiated at 481, 577, and 664 nm, Figure 2.24 d). The bands are assigned to $^4F_{9/2}\rightarrow{}^6H_{15/2}$, $^4F_{9/2}\rightarrow{}^6H_{13/2}$ and $^4F_{9/2}\rightarrow{}^6H_{11/2}$ transitions, respectively. In addition, a very low intense signal at 454 nm is observed. This signal is assigned to the forbidden magnetic dipole transition (ΔJ=0) $^4I_{13/2}\rightarrow{}^6H_{13/2}$, such as in the case of $^5D_0\rightarrow{}^7F_0$ in the Eu^{3+} ion.[58]

Furthermore, for the nIR Er^{3+} emitter (**5-Er**), the emission is totally quenched when the compound is found in the $CHCl_3$ solution. However, in the solid-state sample, Er^{3+} centered emission is observed at 1526 nm which is assigned to the $^4I_{13/2}\rightarrow{}^4I_{15/2}$ transition, Figure 2.24 e).

Finally, **6-Yb** displays the expected Yb^{3+} band corresponding to the $^5F_{5/2}\rightarrow{}^2F_{7/2}$ transition appearing at 1000 nm, Figure 2.24 f). The band splitting due to crystal field effects is clearly visible. [52, 56]

Emission spectra of the polycrystalline samples were also recorded at 77 K, Figure. 2.25. Under these conditions, the crystal field splitting of the emission bands acquire better resolution in all the polycrystalline samples except for the **5-Er** compound (not shown) where the emission spectrum remains unchanged from the luminescence observed at room temperature. For compounds **1-Sm**, **4-Dy** and **6-Yb** the splitting into the degenerated $\pm m_j$ components (for Kramer ions) due to crystal field can be clearly observed. However, for compounds **2-Eu** and **3-Tb**, the $2J$+1 (non-Kramer ions) splitting of each emission band is not clearly resolved. Probably even lower temperatures than 77 K are necessary to obtain high-resolution spectra in this case.[56]

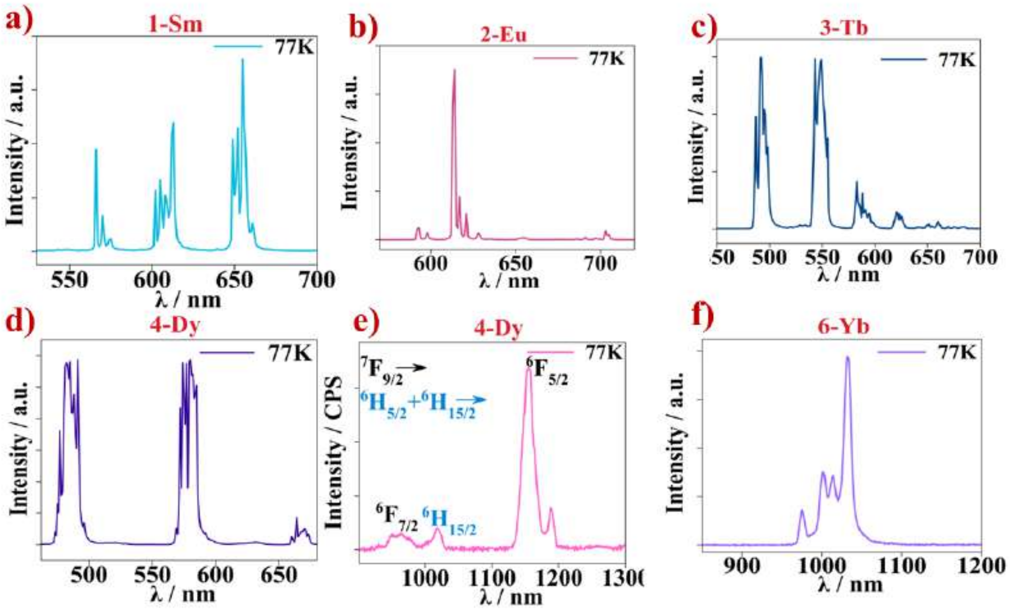

Figure 2.25. Emission spectra measured at 77 K of the compounds **1-Sm** to **6-Yb** in the Visible a), b), c), d) and in the nIR range e) and f).

nIR emission of compound **1-Sm** at 77 K didn't show any enhancement of its resolution therefore its spectrum is not shown. Interestingly, the nIR spectra of the **4-Dy** compound, for which emission has not been observed at room temperature, could be recorded at 77 K, Figure 2.25 e). Clear bands are now discerned at 964 and 1154 nm which are assigned to the $^4F_{9/2}\rightarrow{}^6F_{7/2}$ and $^4F_{9/2}\rightarrow{}^6F_{5/2}$, *f-f* Dy^{3+} transitions, respectively. Furthermore, the third band found at 1018 nm is attributed to the $^6H_{5/2}+{}^6F_{7/2}\rightarrow{}^6H_{15/2}$ transition.[59]

Luminescence quantum yield (ϕ_{Ln}^{L}) and luminescence decay time (τ_{obs})

Overall photoluminescence quantum yields (ϕ_{Ln}^{L}) and luminescence decay times (τ_{obs}) were measured in $CHCl_3$ solution and polycrystalline samples at room temperature, and the results are presented in Table 2.18.

Table 2.18 Overall quantum yields and luminescence lifetime of compounds **1-Sm** to **4-Dy** measured in polycrystalline samples (ϕ_{Ln}^{L} $_{\text{polycryst}}$ and $\tau_{\text{obs polycryst}}$) and $CHCl_3$ solutions (ϕ_{Ln}^{L} $_{\text{solution}}$ and $\tau_{\text{obs solution}}$). Samples were excited at the respective λ_{exc} found in the excitation spectra. [a] value not recorded due to limitations in the equipment.

	ϕ_{Ln}^{L} **polycryst**	ϕ_{Ln}^{L} **solution**	τ**obs polycryst (ms)**	τ**obs solution (ms)**
1-Sm	0.03	0.03	0.06	0.07
2-Eu	0.68	0.42	0.90	0.65
3-Tb	0.01	0.006	[a]	[a]
4-Dy	0.005	[a]	[a]	[a]

2-Eu is the complex showing the highest ϕ_{Ln}^{L} and longest luminescence lifetime that is at least one order of magnitude larger compared to the values recorded for the other compounds. The ϕ_{Ln}^{L} values recorded for **2-Eu**, **3-Tb** and **4-Dy** are about 2-fold higher in the polycrystalline samples than in chloroform solution. Lifetimes are in order of ~60-70 µs (**1-Sm**) to ~1 ms (**2-Eu**) while all samples display monoexponential luminescence lifetime curves, Figure 2.26. The presence of a single decay time component, τ_{obs}, for **1-Sm** and **2-Eu** suggest a single radiative deactivation process, both in the solid state and in solution.[52]

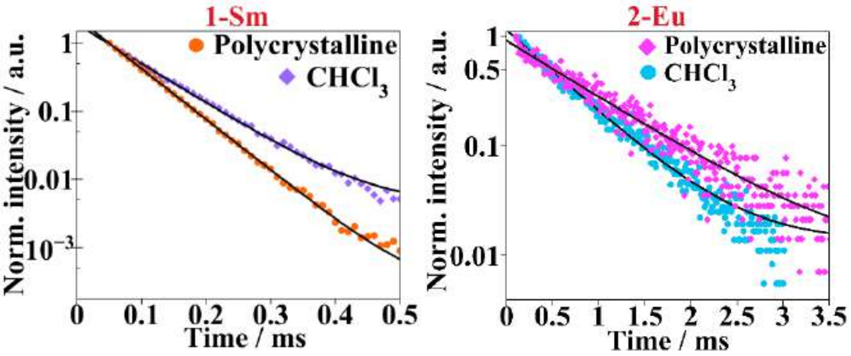

Figure 2.26. Luminescence lifetime curves are presented in semi-log plots for complexes **1-Sm** and **2-Eu**. The solid black lines represent the mono-exponential fit with

$$I(t) = I_0 e^{-\frac{t}{\tau_{obs}}} + C$$

The low ϕ_{Ln}^{L} values observed in **3-Tb** are consistent with other reported in the literature.[60] For these compounds, low luminescence ϕ_{Ln}^{L} values are related to back energy transfer due to the low energy gap between the lowest triplet state of the ligands and terbium (III) $^5D_4$ (20,400 cm^{-1}) emitting energy level. Latva *et al.*[61] concluded that the back transfer energy (studied for a large group of Tb^{3+} coordination compounds) usually occurs when this energy difference is below 1,850 cm^{-1}. This could explain the low ϕ_{Ln}^{L} that **3-Tb** presents. Nevertheless, in order to make this statement with certainty, computational calculations would be needed for our specific system since the lowest triplet state energy may be influenced by both ligands. In this regard, luminescence characteristics of **7-Gd** were studied. From the edge of the UV absorption spectrum the energy of the singlet state (S_1) was obtained, 27,137 cm^{-1} (376 nm), Figure 2.27 *left*. The triplet state energy can be deduced from the 0-phonon band of the Gd^{3+} analogue phosphorescence spectrum measured at 77 K which appeared at 21,229 cm^{-1} (471 nm), Figure 2.27 *right*. The energy separating the S_1 and T_1 states is 5908 cm^{-1}. Such small singlet-triplet energy difference (below 7,000 cm^{-1}) favors Intersystem Crossing ($S_1 \rightarrow T_1$) leaving behind other competitive processes such as deactivation back to the S_0 ground state. Moreover, the energy difference between the lowest triplet state and the emissive Tb^{3+} energy level, is 829 cm^{-1}. Thus, following Latva's rule, compound **3-Tb** shows a low quantum yield due to back energy transfer taking place as a result of the low energy difference between T_1 and terbium's $^5D_4$ emitting level.[60]

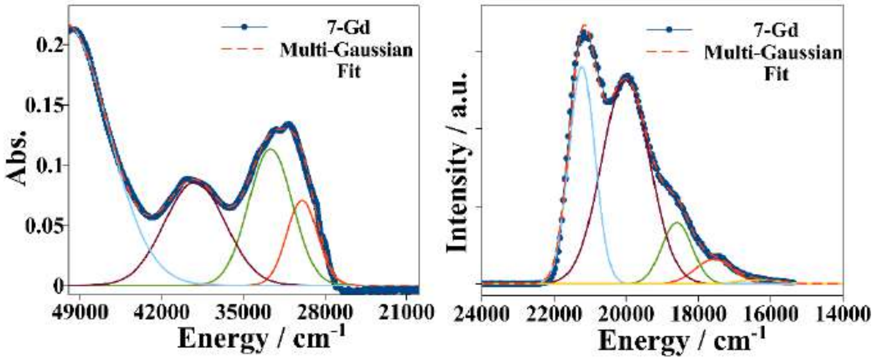

Figure 2.27 *Left*, UV-Vis absorbance spectrum of compound **7-Gd** measured on a 1mM $CHCl_3$ solution. Singlet state (S_1) is extracted from the edge of the Gaussian function form the multi-gaussian fit of the absorbance spectrum. *Right*, phosphorescence spectrum of 1 mM $CHCl_3$ solution containing **7-Gd** measured at λ_{exc} = 336 nm. The band, corresponding to the ligand phosphorescence, was fitted with a multi-gaussian fit. Lowest triplet state (T_1) is obtained from the barycenter of the gaussian function found in the highest energy range

Additionally, the narrow energy gap of the Sm^{3+} cation promotes nonradiative relaxation processes, which shortens luminescence decay and reduces luminescence efficiency. This also explains the low values of ϕ_{Ln}^{L} and τ_{obs} obtained for **1-Sm** which are common in other Sm-β-diketone systems.[57] For **5-Yb** and **6-Er** samples, the ϕ_{Ln}^{L} could not be measured as being too low to be recorded accurately.

Additional parameters regarding the sensitization mechanism of **2-Eu** system can be calculated. Owing to the pure magnetic dipole character of the $^5D_0\rightarrow{}^7F_1$ transition, the radiative lifetime (τ_{rad}) from the $^5D_0$ emissive level of the **2-Eu** compound can be calculated from the corrected emission spectrum with Equation 1.8.[62] (see section *1.2.4 of Introduction*). For the **2-Eu** polycrystalline sample τ_{rad} is 1.26 ms and 1.23 ms for the $CHCl_3$ solution. Then the intrinsic quantum yield (ϕ_{Ln}^{Ln}) is 0.71 and 0.53 for the solid and solution samples, respectively. Moreover, the amount of energy absorbed by the chromophore ligands that is transferred to the excited state of the lanthanide ion is known as the sensitization efficiency (η_{sens}), and it plays a significant role in the overall quantum yield, which is defined as: $\phi_{Ln}^{L} = \eta_{sens} \cdot \phi_{Ln}^{Ln}$. Thus, the η_{sens} values are 0.95 in polycrystalline powder and 0.79 in $CHCl_3$ solution, showing a nearly 100% efficient sensitization of the [$Eu_2(Btfa)_3$(4,4'-dinonyl-2,2'-bipy)] (**2-Eu**) system in solid state.[52, 61a]

Stability of the coordination sphere in $CHCl_3$ solutions

If the corresponding normalized emission profiles in $CHCl_3$ and polycrystalline samples are overlayed and observable changes are differentiated, a change in the lanthanide coordination environment due to solvation effects may be considered and therefore a lack of stability in solution of the coordination compound. However, emission spectra of the aforementioned compounds have similar shape, hinting that the coordination compound are still present in the $CHCl_3$ solution.

Moreover, spectroscopic-structure correlation (from solid state and $CHCl_3$ solution) can be derived from the corrected emission spectra of **1-Sm** and **2-Eu** compounds owing to the distinctive emission bands exhibited by these lanthanide ions. The crystal field splitting of the hypersensitive band ($^5D_0\rightarrow{}^7F_2$) recorded for Eu^{3+} compound is the same in both solid and solution. Also, the integrated area of the magnetic dipole transition ($^5D_0\rightarrow{}^7F_1$) to the electric dipole ratio ($0\rightarrow1/0\rightarrow2$) gives information about the asymmetry factor being 0.09 for the polycrystalline sample and 0.07 in chloroform. The ratio between these two bands is minor, evidencing that there is no significant change around the Eu^{3+} environment when dissolving the **2-Eu** sample into chloroform. Same reasoning can be done for the **1-Sm** compound since ${}^4G_{5/2}\rightarrow{}^6H_{9/2}$ transition also has a hypersensitive character (yet not as strong as in Eu^{3+}) and ${}^4G_{5/2}\rightarrow{}^6H_{5/2}$ is predominantly magnetic dipole in nature. Then for the polycrystalline sample the (5/2→5/2)/(5/2→9/2) ratio is 0.26 and for the $CHCl_3$ is 0.22. The difference of the asymmetric factor of **1-Sm** is similar on changing the phase from solid to solution as well, therefore, suggesting that structural changes in the Samarium(III) environment are the slightest due to solvating effects.[52, 57a]

By comparing the QY and η_{sens} values for the polycrystalline and solution samples we reach similar conclusions. Both diminish on dissolving the samples in $CHCl_3$. There are more degrees of freedom in solution media, that is vibrations and rotations, hence escalating the non-radiative decay. In this way, **4-Dy** and **5-Er** solution samples are virtually non-emissive.

2.3.4 Organic light-emitting diodes (OLEDs)

Despite their large molecular weight, complexes **2-Eu** and **6-Yb** sublime at relatively low temperatures, around 140-150 °C (significantly below the decomposition temperature at ~290 °C) at $\sim 10^{-6}$ mbar pressure. This may be due to their ball-like geometry and the peripheral alkyl and $-CF_3$ ligand groups that reduce intermolecular interactions and increase the volatility of the material. This type of design is highly desirable in materials used in the emissive layer of OLEDs. Vacuum-deposited devices were produced as a proof-of-concept with this group of luminescent materials. OLED electroluminescence and electrical characteristics are shown in Figure 2.28, Figure 2.29, Figure APX.IV.2 and Figure APX.IV.3 as well as in Table 2.19.

The complex **2-Eu** displays high photoluminescence quantum yield (PLQY) both in neat film and in powder, indicating that photoluminescence quenching is negligible in the solid state. As **2-Eu** can be used at higher loads in the emissive layer, OLEDs incorporating **2-Eu** at 20% load in the hole-transporting host mCP were produced {**Device 1**: ITO | HAT-CN (10 nm) | TSBPA (40 nm) | mCP (2 nm) | mCP co 20% **2-Eu** (20 nm) | PO-T2T (5 nm) | TPBi (40 nm) | LiF (0.8 nm) | Al (100 nm)} or in the blend host mCP:TPBi {**Device**

2: ITO | HAT-CN (10 nm) | TSBPA (40 nm) | mCP (2 nm) | mCP:TPBi (60:40) co 20% **2-Eu** (20 nm) | TPBi (50 nm) | LiF (0.8 nm) | Al (100 nm)}. As **2-Eu** does not significantly absorb light above 400 nm and its absorbance in the 350-400 nm region is limited, a non-negligible level of host luminescence contaminating the EL spectrum is observed. An alternative approach to **Devices 1** and **2** was to use a 5 nm thick neat emissive layer of **2-Eu** sandwiched between electron-blocking and hole-blocking materials {**Device 3**: ITO | HAT-CN (10 nm) | TSBPA (40 nm) | **2-Eu** (5 nm) | PO-T2T (20 nm) | TPBi (30 nm) | LiF (0.8 nm) | Al (100 nm)}. This strategy led to eliminate the host emission and to improve the color purity. However, the maximum luminance of this OLED was significantly reduced.

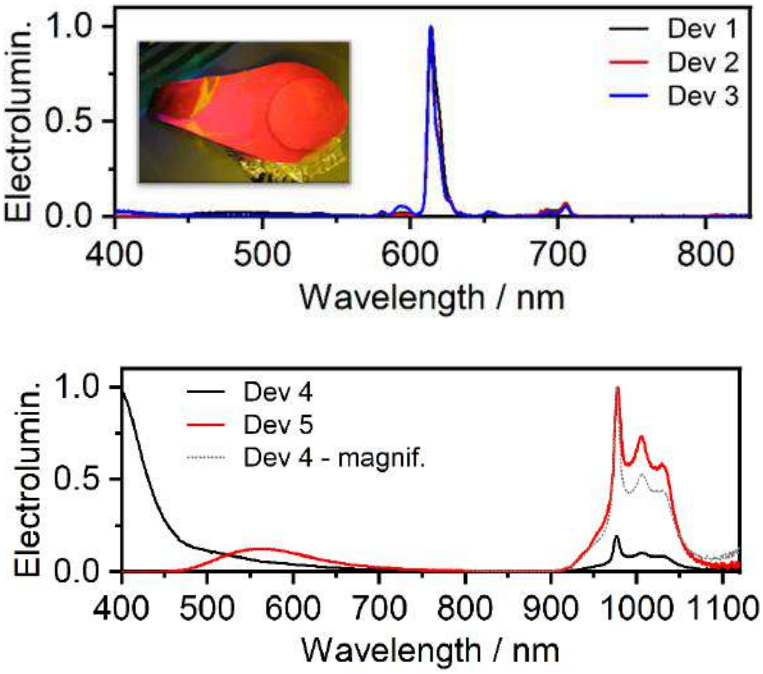

Figure. 2.28. Electroluminescence spectra of devices **1-5** from compounds **1-Eu** (Top) and **6-Yb** (Bottom). Inset top, photoluminescence from a film of **1-Eu** thermally deposited on aluminum foil (λ_{exc}=365 nm).

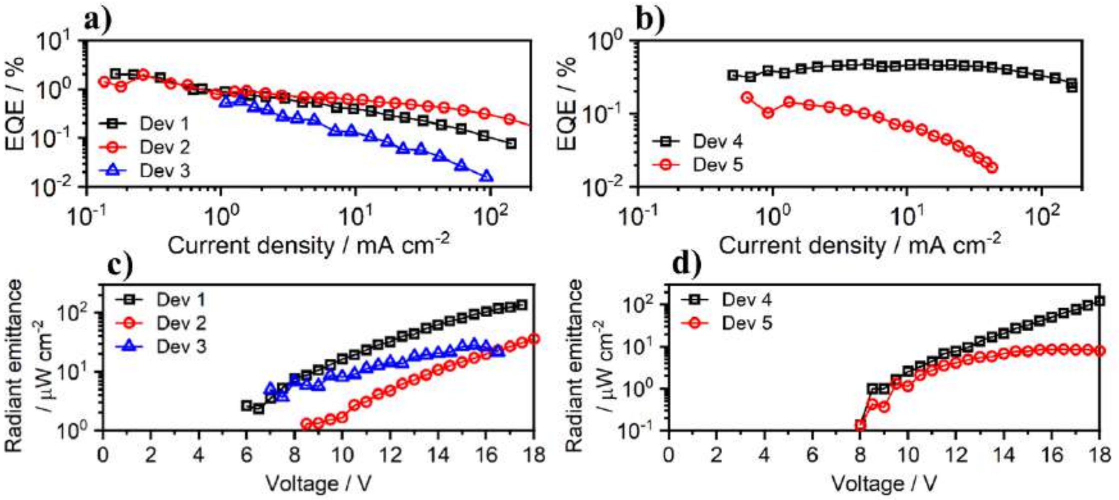

Figure 2.29. External quantum efficiency (EQE) *vs* current density characteristics of devices **1-5** from compounds a) **1-Eu** and b) **6-Yb**. Radiant emittance *vs* voltage bias for devices **1-5** from compounds c) **1-Eu** and d) **6-Yb**.

All three OLED structures (OLEDs **1-3**) display similar EL spectra typical of luminescence originating from Eu^{3+}complexes with visibly narrowband emission peak at 614 nm, Figure 2.28 *top*. Significantly less intense emission bands in the 530-710 nm region are also observed. These EL spectra are significantly narrowband with FWHM of 6-8 nm leading to high color purity, with potential for good color rendering in displays. The modest maximum external quantum efficiency (EQE) of 2.0-2.1 % and luminance ~200-600 cd m^{-2} is most likely a result of the long photoluminescence lifetime characteristic of Eu^{3+}complexes. Similar electroluminescent characteristics have been obtained for OLEDs containing Eu-Btfa systems as dopants in the emissive layer of the device.[49] Additionally, [Eu(Btfa)$_3$(bipy)] system used in a red emitting OLED device has been reported recently.[49e] Addition of the alkyl chains into the bipy ligand does not significantly affect the sublimation temperature (140-153 ºC for the reported [Eu(Btfa)$_3$(bipy)] system) nevertheless the maximum luminance is slightly increased in our system. For the presented [Eu(Btfa)$_3$(4,4'-dinonyl-bipy)] L$_{max}$ is 590 cd m^{-2} while for the reported [Eu(Btfa)$_3$(bipy)] system L$_{max}$ is 428 cd m^{-2}.

Similarly to **2-Eu**, complex **6-Yb** offers also attractive luminescent properties, but this time in the near infra-red region. OLEDs with the similar structure of **Device 2** but using **6-Yb** as the emitter were produced (**Device 4**). A significant electroluminescence contribution from the host material is visible in this device, mostly due to the relatively small PLQY of the **6-Yb** complex. However, the electroluminescence originating from the **6-Yb** emitter appears at relatively longer wavelengths in the near infra-red region, and hence is attractive for various practical potential applications,[50,51a] Figure 2.28 *bottom*. The ~1000 nm electroluminescence band on its own reaches a maximum radiant emittance of 121 μW cm^{-2} and 0.1% EQE, which is comparable with other emitters in this wavelength range. To eliminate the electroluminescence from the host material, we used complex **6-Yb** in neat film, reproducing the structure of **Device 3.** However, the thickness of 5 nm was found to be insufficient and a significant electroluminescence from a through-space TSBPA:PO-T2T exciplex was observed. Hence, **Device 5** features an emissive layer of 10 nm **6-Yb** neat film. This device produces a relatively strong near infra-red electroluminescence at ~1000 nm, but a weak contribution from the TSBPA:PO-T2T exciplex is still present. Other Yb-β-diketonate systems show comparable results.[51] As for compounds derived from Yb-Btfa, luminescence properties have been studied, nevertheless as far as we are concerned this is the first Yb-Btfa based system used to generate a nIR-OLED device.[63]

Table 2.19. Electroluminescent properties of OLED devices **1-5.**

	Dev 1	**Dev 2**	**Dev 3**	**Dev 4**	**Dev 5**
Emitter	**2-Eu**	**2-Eu**	**2-Eu**	**6-Yb**	**6-Yb**
V_{ON} / V [a]	4.5	5.0	4.0	4.0	4.5
L_{max} / cd m^{-2} [b]	210	590	20	477	4
R_{max} / µW cm^{-2} [c]	135*	36*	28*	121**	9**
λ_{EL} / nm [d]	581, 593, 614, 655, 694, 704*	581, 593, 614, 655, 694, 704*	581, 593, 614, 655, 694, 704*	977, 1005, 1031**	977, 1005, 1031**
CIE 1931 (x; y) [e]	(0.51; 0.30)	(0.52; 0.28)	(0.60; 0.30)	-	-
CE_{max} / cd A^{-1} [f]	2.6	2.6	0.4	-	-
EQE_{max} / % [g]	2.1	2.0	0.6	0.46 / 0.10**	0.17

[a] turn-on voltage at 10^{-2} mA cm^{-2}; [b] maximum luminance (visible spectrum); [c] maximum radiant emittance for the EL bands associated with the emitter; [d] EL maxima associated with the emitter emission; [e] colour coordinates of electroluminescence spectrum in colour space CIE 1931 as defined by the Commission Internationale de l'éclairage; [f] maximum current efficiency; [g] maximum external quantum efficiency. * For wavelength range $\lambda > 550$ nm; ** For wavelength range $\lambda > 900$ nm.

2.3.5 Magnetic properties

DC measurements

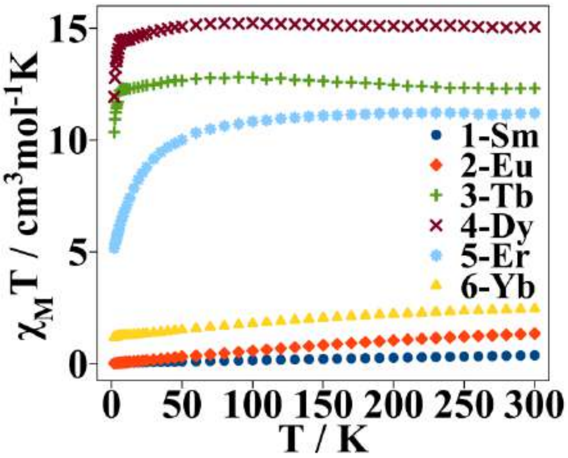

Figure 2.30. Temperature dependence of $\chi_M T$ measured at an external static field of 0.3 T, for compounds **1-Sm** to **6-Yb**.

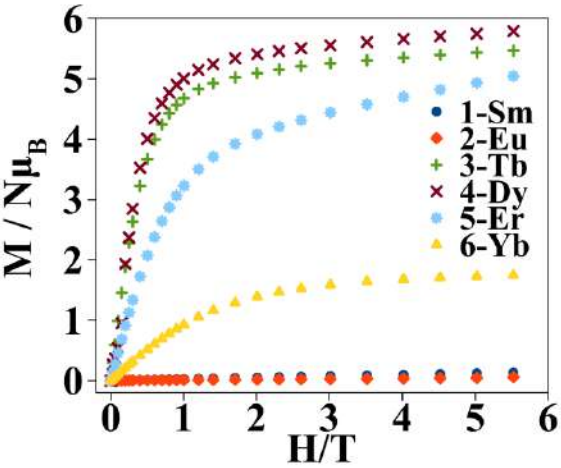

Figure 2.31. Magnetization dependence with an external magnetic field measured at 2 K for compounds **1-Sm** to **6-Yb**.

Direct current (dc) magnetic susceptibility (χ_M) and magnetization (M) measurements were performed on polycrystalline samples of **1-Sm** to **6-Yb**. The χ_M measurements were carried out under a dc field of 0.3 T in the 2-300 K temperature range. The temperature dependence of $\chi_M T$ is shown in Figure 2.30. $\chi_M T$ values at room temperature (300 K) are 0, 1.3, 11.8**,** 15.0, 11.2 and 2.6 cm^3 mol^{-1} K for **1-Sm**, **2-Eu**, **3-Tb**, **4-Dy, 5-Er**, and **6-Yb** respectively. For one isolated Ln^{3+} cation, the calculated $\chi_M T$ values are: 0.09 cm^{3}mol^{-1}K for Sm^{3+} ground state $^6H_{5/2}$ and g_j=2/7; 0 cm^3 mol^{-1} K for Eu^{3+} ground state $^7F_0$; 11.82 cm^3 mol^{-1} K for Tb^{3+} ground state $^7F_6$ and g_j=3/2; 14.17 cm^3 mol^{-1} K for Dy^{3+} ground state $^6H_{15/2}$ and g_j=4/3, 11.48 cm^3 mol^{-1} K for Er^{3+} ground state $^4I_{15/2}$ and g_j=6/5 and 2.57 cm^3 mol^{-1} K for Yb^{3+} ground state $^2F_{7/2}$ and g_j=8.7.[28]

Owing to the relatively small spin-orbit coupling parameter (λ) between the ^6H_J (for Sm^{3+}) and ^7F_J (for Eu^{3+}) states, the J states higher in energy are found to be electronically populated at room temperature. This may explain why room temperature $\chi_M T$ values of **1-Sm** and **2-Eu** determined experimentally are larger than the calculated values. Upon cooling both samples, $\chi_M T$ curves decrease due to thermal depopulation of the excited J states of Sm^{3+} and Eu^{3+} ions respectively.[64]

Room temperature $\chi_M T$ of **3-Tb**, **4-Dy**, **5-Er** and **6-Yb** agree with the calculated parameters for an isolated Ln^{3+} ion. Upon decreasing the temperature, the $\chi_M T$ curves of the four compounds remain nearly constant until ~50 K. Below this temperature, $\chi_M T$ values decrease suddenly to 10.3, 11.9, 5.1 and 1.2 $cm^3 mol^{-1} K$, for **3-Tb**, **4-Dy**, **5-Er** and **6-Yb** respectively, due to thermal depopulation of the crystal field m_j states. For the presented compounds, magnetic coupling between the lanthanide ions has not been considered due to *i)* the mononuclear nature of such compounds that lead to extensive Ln---Ln intermolecular distances and *ii)* the well shielded nature of electrons in the $4f^n$ orbitals.[31]

The curves of the magnetization dependence with an external magnetic field, measured at a constant temperature of 2 K, are depicted in Figure 2.31. None of the presented compounds show saturation of the magnetization at 5 T. ($g_J \cdot J$).[28]

Alternating current measurements

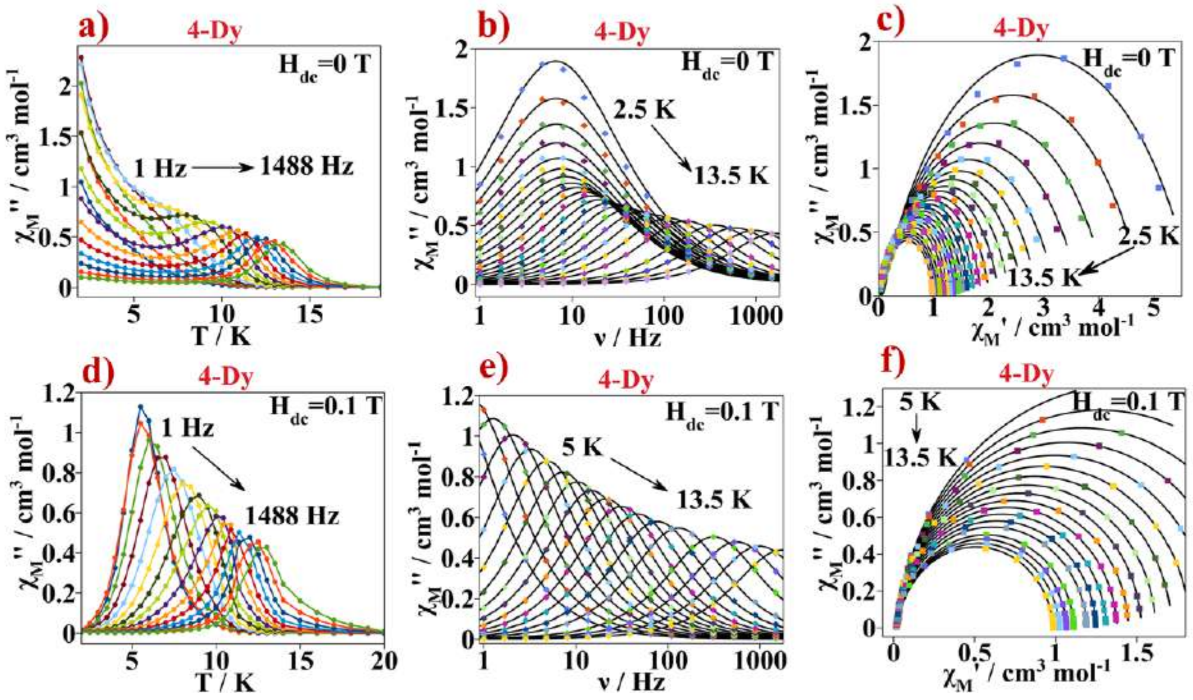

Fig. 2.32 a) χ_M" versus temperature plot obtained at a H_{dc} = 0 T for **4-Dy**. Continuous lines serve as an eye guide, b) χ_M'' versus Frequency plot obtained at a H_{dc} = 0 T for **4-Dy.** Continuous black lines correspond to the best fit according to the Generalized Debye model, c) Cole-Cole plot for **4-Dy** from the AC data recorded at a H_{dc} = 0 T. Continuous black line corresponds to the best fit according to the Generalized Debye model, d) χ_M" versus temperature plot obtained at a H_{dc} = 0.1 T for **4-Dy**. Continuous lines serve as an eye guide**,** e) χ_M" versus frequency plot obtained at a H_{dc} = 0.1 T for **4-Dy**. Continuous black line corresponds to the best fit according to the Generalized Debye model and f) Cole-Cole plot for **4-Dy** from the AC data measured at a H_{dc} = 0.1 T. Continuous black line corresponds to the best fit according to the Generalized Debye model.

Moreover, alternating current (ac) magnetic susceptibility measurements were performed for all lanthanide samples except for **1-Eu**. Under a direct current external magnetic field (H_{dc}) of 0 T, only **4-Dy** showed slow relaxation of the magnetization and therefore single ion magnet (SIM) behavior. Magnetic susceptibility imaginary component (χ_M") shows maxima in the 2-18 K temperature range Figure 2.32 a). When cooling the sample down to 2 K, the χ_M" values increase again, though a second peak is not observed. This is probably due to the Quantum Tunnelling of the Magnetization mechanism that is taking place at such low temperatures.[31] The ac magnetic data were measured under an oscillating magnetic field of $4\cdot10^{-4}$ T in the 1-1488 Hz frequency range Figure 2.32 b). χ_M'' maxima from the low temperature curves remain constant until a certain temperature where they move to higher frequencies upon heating the sample. This suggests that at low temperature the relaxation of the magnetization occurs via a temperature independent mechanism such as QTM whereas at the higher temperature range, thermally activated mechanisms, such as Orbach and/or Raman, are taking place.[65] In-phase and out-of-phase magnetic susceptibility representation (χ_M' *vs* χ_M'') in the so called Cole-Cole plot shows semicircles that are not perfectly symmetric, Figure 2.32 c).

The Cole-Cole plot can be fitted using the one component Generalized Debye model in the 2.5-13.5 K temperature range. The α parameter quantifies the width distribution of the relaxation times of magnetization. For **4-Dy** α varies from 0.24 at 2.5 K to 0.03 at 13.5 K. The α value remains near 0 throughout the whole temperature range, indicating no change in relaxation mechanism as temperature changes.

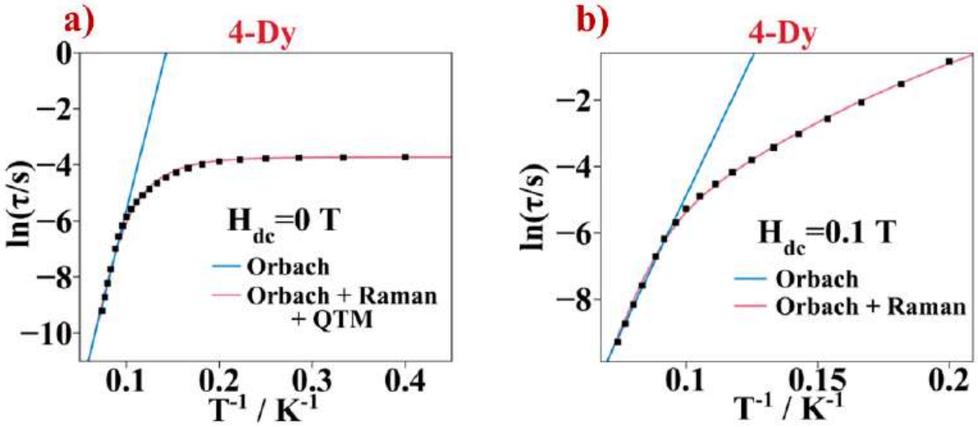

Figure.2.33 a) ln(τ) *vs* 1/T plot of **5-Dy** obtained in the $H_{dc} = 0$ T. b) ln(τ) *vs* 1/T plot of **5-Dy** obtained in the H_{dc}=0.1 T. In both Figures, continuous lines represent the best fit using the stated equations of the relaxation of magnetization mechanisms.

The semi-log representation of the relaxation of the magnetization times as function of temperature (ln(τ) *vs* T^{-1}) is depicted in Figure 2.33. In the high temperature range a clear linear trend is observed. The linear segment is fitted following an Arrhenius law. This mode describes the thermally assisted Orbach relaxation of the magnetization mechanism taking place between the degenerate ±m_j ground state levels via an energetically higher m_j excited state of the Dy^{3+} ion.

$$\tau^{-1} = \tau_0^{-1}\exp\left(\frac{-\Delta E}{k_B T}\right) \qquad \text{Equation 2.5}$$

By fitting the magnetic data in the 10-13.5 K temperature range with Equation 2.5, the effective energy barrier (ΔE) yielded 91.1 cm^{-1} and the pre-exponential factor (τ_0) was 7.2·10^{-9} s. However, the linear fashion is not followed along all the temperatures. This indicates the presence of another mechanism responsible for the relaxation of the magnetization under 13.5 K. On cooling the sample, the ln(τ) *vs* T^{-1} curve enters to a plateau region indicating that the spin of the lanthanide ion returns to the equilibrium phase via the faster QTM process. Consequently, the ln(τ) *vs* T^{-1} curve was fitted with Equation 2.6 considering the three relaxation mechanisms. The best fit was obtained with ΔE =103.7 cm^{-1} and τ_0 = 2.53×10^{-9} s for Orbach, C = 8.18×10^{-4} s^{-1} K^{-n} and n = 5.5 for Raman and τ_{QTM} = 0.03 s for the QTM processes.

$$\tau^{-1} = CT^n + \tau_0^{-1}\exp\left(\frac{-\Delta E}{k_B T}\right) + \tau_{QMT}^{-1} \qquad \text{Equation 2.6}$$

To remove the QTM in the relaxation of the magnetization process of **4-Dy**, an external magnetic field can be applied while measuring the ac magnetic susceptibility response. An external magnetic field breaks the degeneracy between the ±m_j states so the fast QTM between the m_j levels is reduced or even eliminated.[31]

To establish the optimal H$_{dc}$ for the Dy^{3+} sample, χ_M' and χ_M'' components were measured at constant temperature (11 K) by applying different external magnetic fields, from 0 to 1.8 T. A plot of τ *vs* H$_{dc}$ shows that the relaxation time is the greatest when the applied external magnetic field is 0.1 T. This dc field was found to be the optimal, Figure 2.34.

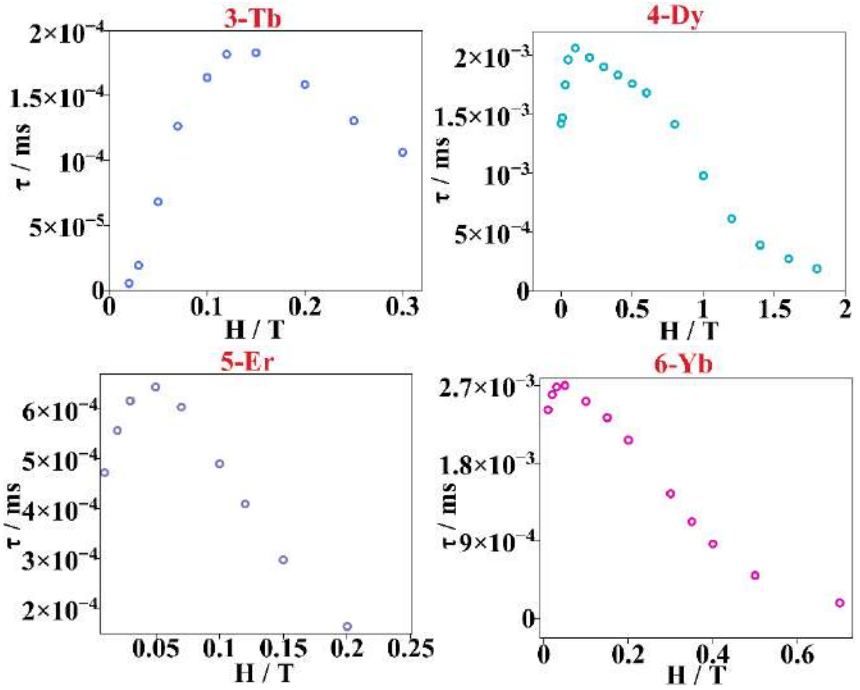

Figure 2.34 Relaxation times in front of different static magnetic fields measured at a constant temperature of 2 K for **3-Tb** and **5-Er**, 11 K for **4-Dy** and 2.7 K for **6-Yb** under an ac magnetic field of $4{\cdot}10^{-4}$ T oscillating between 1 to 1488 Hz.

Figures 2.32 d) and e) show the ac measurement of **4-Dy** at H_{dc} of 0.1 T. Now, on cooling the sample, no increase of the χ_M'' component with temperature is observed, suggesting that the fastest relaxation mechanism observed at lower temperatures in the $H_{dc} = 0$ experiments, QTM, is not present. The magnetic data were analyzed in the temperature range where the χ_M'' *vs* T peaks appear between 5 and 13.5 K. The χ_M'' versus the oscillating frequency relationship shows maxima that move progressively from lower frequency to higher frequency values as temperature increases, indicating a temperature dependent relaxation mechanism. The curves from the Cole-Cole plots, Figure 2.32 f), were fitted using the one component Generalized Debye model, and the obtained α values are in the range 0.02-0.05.

The ln(τ) *vs* T^{-1} plot obtained in the $H_{dc} = 0.1$ T measurement is shown in Figure 2.33 b). A linear trend appears in the high temperature range corresponding to the Orbach relaxation mechanism. The linear part was fitted using the Arrhenius law giving ΔE =109.3 cm^{-1} and $\tau_0 = 9.3{\cdot}10^{-10}$ s. The trend of the ln(τ) *vs* T^{-1} curve changes as the temperature decreases. Moreover, the plateau at low temperature seen in the ln(τ) *vs* T^{-1}

curve of the H_{dc} = 0 T measurement, corresponding to the QTM, is not seen anymore. Thus, the fitting was done taking out the QTM part of Equation 2.6. The best fit gave ΔE =140.5 cm^{-1} and $\tau_0 = 3.6\times10^{-11}$ s values for the Orbach mechanism and $C = 1.10\times10^{-4}$ $s^{-1}K^{-n}$ and $n = 6.2$ values for the Raman mechanism.

The magnetic behavior of the former compound is similar to other β-diketonate compounds with the DyO_6N_2 coordination environment. The ΔE value presented herein is similar to that obtained in other systems with the Btfa β-diketonate ligand found in the literature.[67] The mononuclear compound with formula [Dy(Btfa)(bipy)][67a] shows SIM behavior, but just a few maxima are found in the high frequency range. When applying an external magnetic field of 0.12 T, the QTM is reduced, and the SIM performance is improved with a ΔE of 62.9 cm^{-1}. Changing the polypyridyl ligand from bipy to 4,4'-dinonyl-bipy (**6-Dy**) in the presented work, the SIM performance improves with a ΔE of 91.1 cm^{-1} at a 0 T dc external magnetic field and it is enhanced to 109 cm^{-1} when a H_{dc} of 0.1 T is applied.

The magnetic anisotropy axis of the $m_j = \pm15/2$ state can be calculated using a simple electrostatic model presented by the *Chilton Group.*[68] To enhance the SMM behavior, the $\pm m_j$ state with the greatest value should be stabilized by the crystal field, as the ground state. In case of a Dy^{3+} ion with a $^6H_{15/2}$ ground state the highest m_j value would be the ±15/2 state, which has an oblate electron density. Therefore, to stabilize this m_j state, an axially stressed coordination environment should be induced. The more electron-rich atoms (O atoms from the β-diketone ligands in this case) should be in the axial positions. Generally, the atoms with highly electron-rich atoms will form the shortest Dy-donor atom bond distances. Therefore, by calculating the anisotropy axis, if it passes through the shortest Dy-O bond distances of the more electronegative atoms, this will indicate that the m_j ground state is of ±15/2 in its major contribution, thus the largest m_j value. To calculate the anisotropy axis from the crystallographic data, the Magellan program, which can only be used for Dy^{3+} ions, was employed. Figure 2.35 shows the magnetic axis in yellow, and it goes along the Dy-O bonds formed by Dy-O2 and Dy-O5 with the shortest bond distances of 2.311 and 2.320 Å, respectively. We can conclude that the stabilized m_j ground state of compound **4-Dy** has a major contribution of the ±15/2 state.

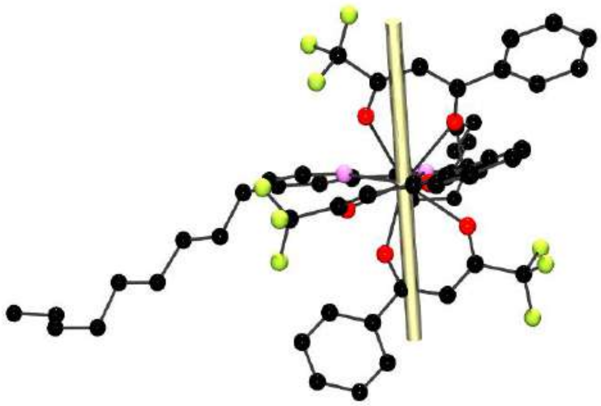

Figure 2.35. Orientation of the magnetic anisotropy axis of the m_j= ±15/2 state (yellow rod) of compound **4-Dy**

The remaining lanthanide compounds, **3-Tb**, **5-Er** and **6-Yb**, showed slow relaxation of the magnetization just when an external magnetic field was applied. The magnetic responses of such complexes were measured under the optimal H_{dc} = 0.1 T for **3-Tb** and **6-Yb** and 0.05 T for **5-Er**, Figure 2.34. The plots of the out-of-phase magnetic susceptibility components varying with temperature and frequency are depicted in Figure 2.36 for **3-Tb**, **5-Er** and **7-Yb**.

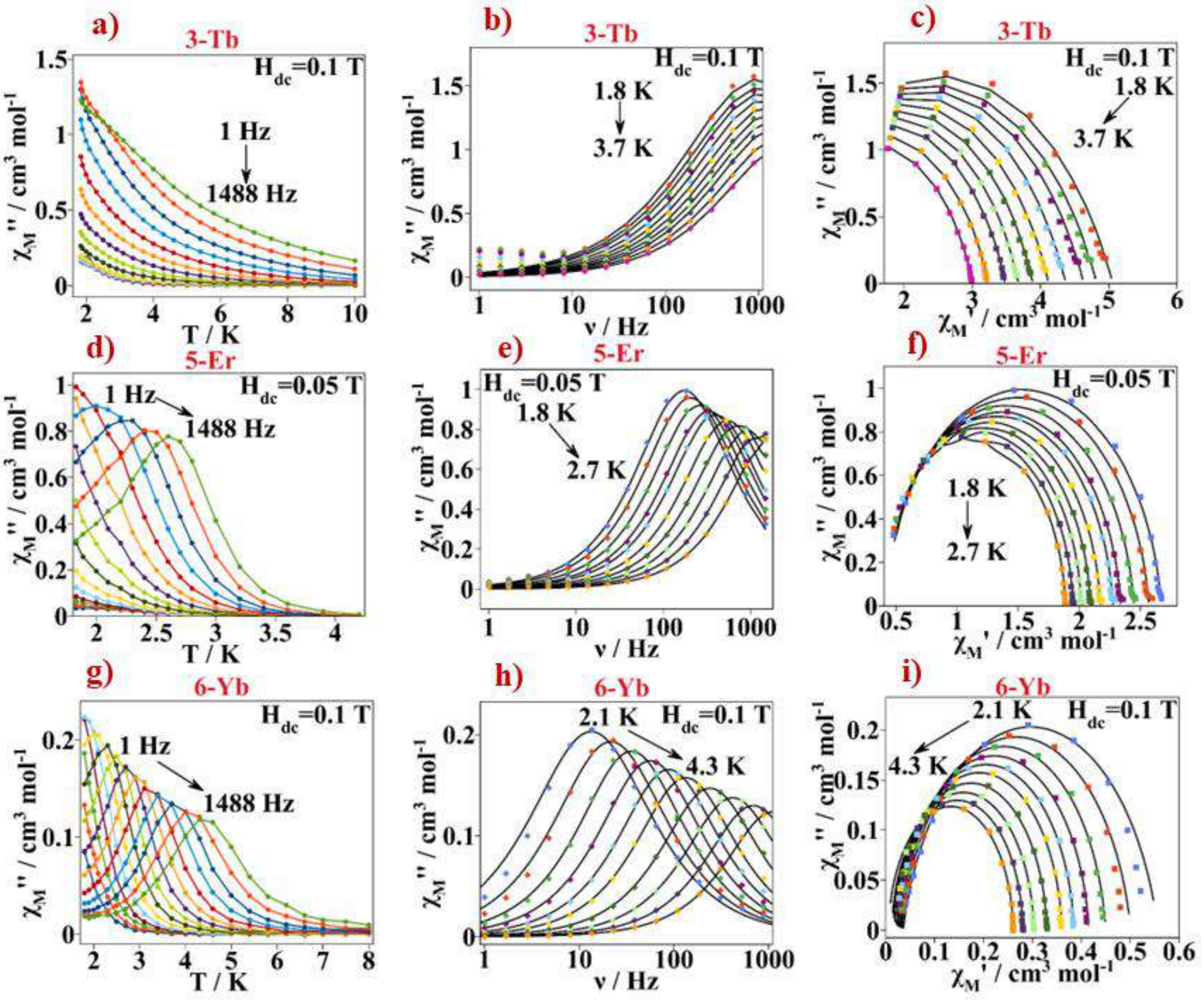

Figure 2.36 a), d) and g) temperature dependence of χ_M” for **3-Tb**, **5-Er** and **6-Yb** respectively. Continuous lines serve as an eye guide. b), e) and h) χ_M” *vs* frequency plots for **3-Tb**, **5-Er** and **6-Yb** respectively. Continuous black lines correspond to the best fit with the Generalized Debye model. c), f), i) Cole-Cole plots for compounds **3-Tb**, **5-Er** and **6-Yb** respectively. Continuous black lines correspond to the best fit with the Generalized Debye model. The ac data were recorded with H_{dc} = 0.1 T for **3-Tb** and **6-Yb** and 0.05 T for **5-Er.**

For **3-Tb**, the maximum values of χ_M*”* appear upon cooling the sample down to the liquid helium temperature and at high oscillating frequencies. Nevertheless, the Cole-Cole plots for **3-Tb** are uncompleted asymmetric semicircles that can be fitted using the one component Debye model with α values of 0.3 to 0.23 on increasing temperature. The ln(τ) *vs* T^{-1} plot is shown in Figure 2.37 a). No linear trend is followed along the temperature axis, indicating that the relaxation of the magnetization of the Tb^{3+} compound does not occur through the Orbach process. Clearly, a temperature dependence of the relaxation times is observed, therefore the Raman process can be considered. The best fit of the magnetic data of **3-Tb** is obtained when both, Raman and Direct mechanism, are considered with values of $C = 0.93$ s^{-1}K^{-n} and $n = 5.21$ for Raman and of $A = 3275.1$ s^{-1}K^{-1} for Direct process, Equation 2.7.

$$\tau^{-1} = CT^{n} + AT \qquad \text{Equation 2.7}$$

The Terbium(III) ion has a $^7F_6$ ground state. When the Tb^{3+} ion is coordinated to ligand molecules forming a coordination compound, J splits into $2J+1$ $\pm m_j$ states due to the crystal field effect. For J equal to 6, there may be13 m_j sublevels comprised between +6 to -6. Due to the non-Kramer nature of the Tb^{3+} ion, a certain crystal field can stabilize the m_j ground state with the lower value which in this case would be $m_j = 0$. If this occurred, then no relaxation of the magnetization nor SMM behavior could be seen at all. For a Tb^{3+} compound showing SMM behavior, the crystal field should optimize the oblate shaped electron density m_j state with larger value ($\pm m_{\mathrm{j}} = \pm 6$). Therefore, the crystal field of compound **3-Tb** stabilizes a ground state different than $m_j = 0$, though there is transverse contribution in the ground state wavefunction because of QTM presence at $H_{dc} = 0$ T and even applying an optimal external magnetic field, slow relaxation of the magnetization is recorded but in a low and very narrow temperature range.[69]

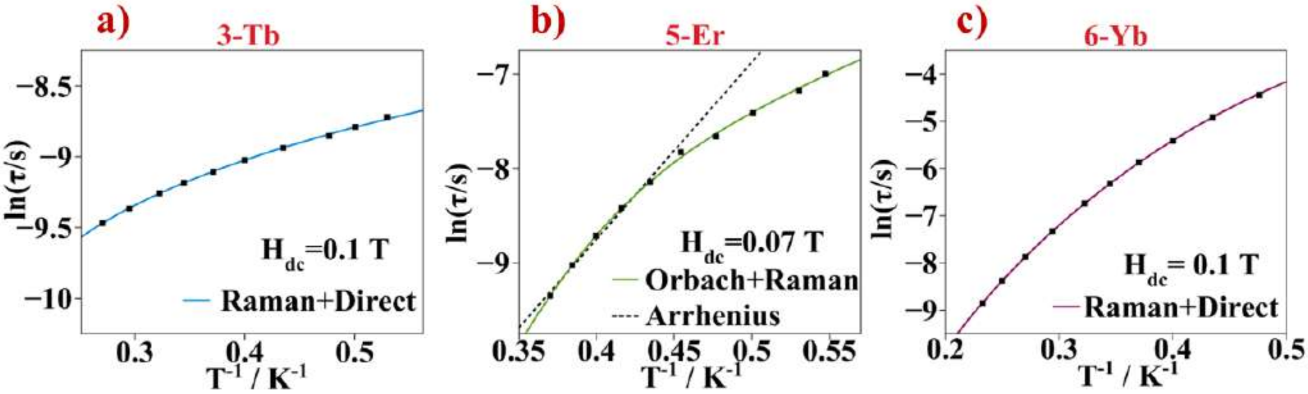

Figure 2.37 a) ln(τ) *vs* T^{-1} plot of a) **3-Tb**, b) **5-Er** and c) **6-Yb** obtained at the $H_{dc} = 0.1$, 0.07 and 0.1 T respectively. In the three figures, continuous lines represent the best fit using the stated equations of the relaxation of magnetization mechanisms. The black dotted line in Figure b) represents the fit in the high temperature range following an Arrhenius law.

Compounds **5-Er** and **6-Yb** show clear maxima of the χ_M'' component in a rather low temperature range (1.8-2.7 K for **5-Er** and of 2.1-4.3 K for **6-Yb**). For **5-Er** and **6-Yb**, in the plots of the out-of-phase magnetic susceptibility components with temperature and frequency, the χ_M'' peaks move progressively to higher frequencies upon increasing the temperature. The Cole-Cole plots show non-symmetric semicircles, Figures 2.36 c), f) and i). For **5-Er** and **6-Yb**, Cole-Cole curves could be fitted with the one component Generalized Debye model. The α values obtained from the fit are in the range of 0.08 to 0.03 (for **5-Er**) and of 0.16 to 0.02 (for **6-Yb**) on increasing temperature. Relaxation of magnetization times with temperature characteristics are plotted in Figures 2.37 b) and c).

For the **5-Er** compound, the Arrhenius law is used to fit the linear segment in the higher temperature range. The obtained effective energy barrier is 13.0 cm^{-1} and the pre-exponential factor is $8.75 \cdot 10^{-8}$ s. The linear trend is not followed along the curve, therefore a function with the equation including the Orbach and Raman relaxation mechanisms (first two components in Equation 2.6) gives the best fit. The obtained parameters are ΔE = 24.6 cm^{-1}, $\tau_0 = 8.75 \cdot 10^{-8}$ s, C = 96.1 $s^{-1}K^{-n}$ and n=4.05. Finally, for compound **6-Yb**, the magnetic data cannot be fitted using the Arrhenius law since there is no clear linear trend in the higher temperature range and therefore the relaxation of the magnetization by the Orbach process is excluded. The best fit of the ln(τ) *vs* T^{-1} curves is acquired when equations describing the Raman and Direct relaxation of the magnetization processes are considered, Equation 2.7, and the obtained parameters are C = 0.51 $s^{-1}K^{-n}$, n = 6.5 and A = 8.58 $s^{-1}K^{-1}$. Other Yb^{3+} coordination compounds where the slow relaxation of the magnetization process is dominated by Raman and Direct mechanisms rather than Orbach, are found in the literature.[70] A compilation of the fitting parameters of compounds **3-Tb**, **4-Dy**, **5-Er** and **6-Yb** is found in Table 2.20.

Table 2.20. Compilation of the fitted parameters from the relaxation of the magnetization mechanisms of compounds **3-Tb**, **4-Dy**, **5-Er** and **6-Yb**.

	H_{dc} (T)	**Orbach**		**QTM**	**Raman**		**Direct**
		ΔE (cm^{-1})	τ_0 (s)	τ_{QTM} (s)	C (s^{-1}K^{-n})	n	A (s^{-1}K^{-1})
3-Tb	0.1				0.93	5.2	3275.14
4-Dy	0	103.7	$2.53\cdot10^{-9}$	0.03	$8.18\cdot10^{-4}$	5.5	
	0.1	140.5	$3.6\cdot10^{-11}$		$1.10\cdot10^{-4}$	6.2	
5-Er	0.05	24.64	$8.75\cdot10^{-8}$		96.1	4.1	
6-Yb	0.05				0.51	6.5	8.58

Correlation between magnetic and spectroscopic data

The relaxation of magnetization energy barrier described by the Orbach mechanism of **4-Dy** calculated by means of the magnetic data can be compared with the energy barrier calculated through the spectroscopic data. The emission spectrum of **4-Dy** was obtained at T = 77 K configuring the experiment in a slower acquisition time measurement mode. By measuring the emission spectrum at such low temperature, the corresponding ±m_j energy levels formed by the crystal field splitting can be distinguished. Assuming that only the first m_j state of the $^4F_{9/2}$ emitting level is populated and that at such low temperature we can reduce, as much as possible, the presence of hot bands and vibronic side bands, the $^6H_{15/2}$ ground state of the Dy^{3+} Kramer ion splits due to the crystal field effect into J+1/2 degenerated doublets (2J+1 m_j states): ±m_j= ±15/2, ±13/2, ±11/2, ±9/2, ±7/2, ±5/2, ±3/2, ±1/2.

A multi-Gaussian function fit is performed for the $^4F_{9/2}\rightarrow{}^6H_{15/2}$ emission band, Figure 2.38. Different trials with more than eight Gaussian functions were performed to include the 'hot bands'. A good fit is obtained when 9 Gaussian functions are used. The ninth Gaussian function covers the small shoulder at the low energy range. This indicates that even at low temperatures the side emission bands such as the 'hot bands' are still present. They can appear even at lower temperatures as demonstrated in other published studies.[71] Thus, the first two bands that are higher in energy are assigned to the zero phonon 0'→0 and 0'→1 transitions. The energy difference between the peaks of the two first Gaussian functions is 93.8 cm^{-1}. Attending to the calculated ΔE value from the magnetic data (91 cm^{-1}), the Orbach relaxation process occurs only through the first ±m_J excited state. This could consider the fact that the thermally activated relaxation of the magnetization process (Orbach) does not take place through the whole energy barrier composed by all the ±m_J doublets of the Dy^{3+} ion but only via the first ±m_J excited state. Thus, suggesting that **4-Dy** relaxation of the magnetization takes place via thermal activated QTM.

In addition, the emission spectrum of the **6-Yb** compound measured at 77 K shows that the $^2F_{5/2} \rightarrow {}^2F_{7/2}$ emission transition is split due to crystal field into four well distinguished peaks, Figure 2.39. The Yb^{3+} $^2F_{7/2}$ ground state breaks the degeneracy due to crystal field splitting and should lead to four ±m_J doublets (±7/2, ±5/2, ±3/2, ±1/2). A multi-Gaussian fit of the emission spectra is performed successfully with four Gaussian functions. The splitting between the peaks is as follows: 25.1 (1st-2nd), 13.6 (2nd-3rd) and 17.7 cm^{-1} (3rd-4th). The dynamic magnetic data for **6-Yb** show that the magnetization does not relax through an effective energy barrier via the Orbach process.

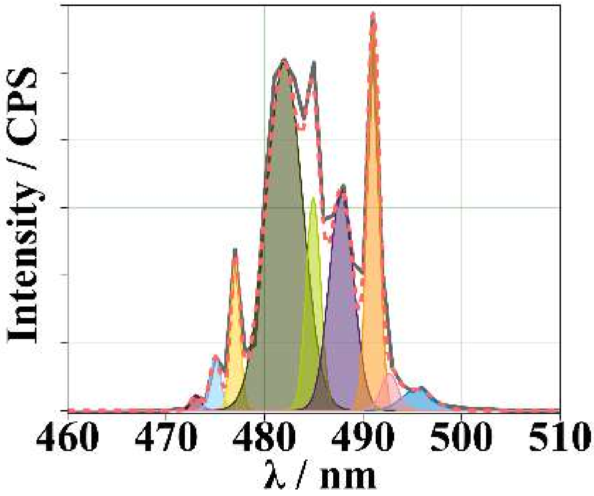

Figure 2.38 $^4F_{9/2} \rightarrow {}^6H_{15/2}$ emission band measured at 77 K of **4-Dy**. Grey continuous line is the experimental emission band. Scattered red line is the total multi-Gaussian fit.

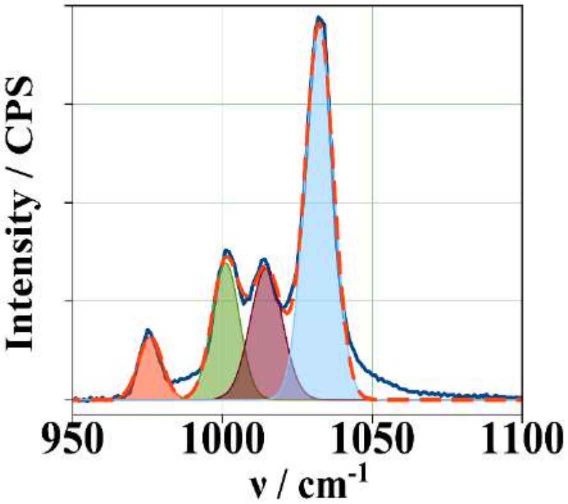

Figure 2.39 $^2F_{5/2} \rightarrow {}^2F_{7/2}$ emission band measured at 77 K of **6-Yb**. Blue continuous line is the experimental emission band. Scattered red line is the total multi-Gaussian fit.

2.3 Conclusions

β-diketonate mononuclear lanthanide coordination compounds derived from the 4,4,4-trifluoro-1-phenyl-1,3-butanedione (HBtfa), could be successfully synthetized by displacement reactions from the β-diketonate precursor of formula $[Ln(Btfa_3)(H_2O)_2]$ with the respective N,N- and N,N,N-polypyridyl ligands. Two different families of lanthanide compounds were synthetized in *Chapter 2* which are compiled in Table 2.21.

Table 2.21 Compilation of compounds synthetized in *Chapter 2*.

Formula	**Coordination number and coordination polyhedron**	**Identification code**
$[Ce(Btfa_3)(H_2O)_2]$	8 TDD-8, D_2d	**1-H_2O**
$[Ce(Btfa_3)(phen)]$	8 TDD-8, D_2d and SAPR-8, D_4d	**2-phen**
$[Ce(Btfa_3)(bipy)]$	8 SAPR-8, D_4d	**3-bipy**
$[Ce(Btfa_3)(terpy)]$	9 CSAPR-9, C_4v	**4-terpy**
$[Ce(Btfa_3)(bathophen)(DMF)]$	9 CSAPR-9, C_4v	**5-bathophen**
$[Ln(Btfa_3)$(4,4'-dinonyl-bipy)$]$	8 SAPR-8, D_4d	**1-Sm**, **2-Eu**, **3-Tb**, **4-Dy**, **5-Er**, **6-Yb** and **7-Gd**

First, with the aim to provide with new insights into the understanding of the Cerium(III) spin relaxation, five β-diketonate Ce^{3+} have been synthetized and structurally characterized. Moreover, the five compounds have been magnetically characterized and a meticulous study has been carried out to further understand the spin dynamics in the relaxation of the magnetization that they present under an external direct current magnetic field. Ab initio calculations were performed to support the experimental magnetic data. For all the compounds, the Orbach mechanism was disregarded in light of the published literature and the obtained ab initio results. Instead, the local mode mechanism was considered. The calculations also show the axiality of the compounds and corroborate the presence of low energy vibrational modes that could contribute to the spin relaxation through the Local mode. Finally, a compilation of the Cerium(III) coordination complexes found in the literature before 2023 and showing slow relaxation of the magnetization are presented in Tables 2.1-2.5. From the published experimental data and ab initio calculations can be extracted that the stabilization of the m_j with greatest value as the ground state, does not imply the presence of SMM behavior for the previously magnetically studied Ce^{3+} coordination compounds.

Secondly, with the aim of obtaining multiproperty lanthanide complexes, isostructural mononuclear compounds derived from the Btfa and the 4,4’-dinonyl-2,2’-bipyridine ancillary ligand have been isolated and structurally characterized. Photoluminescence studies were performed for all complexes in $CHCl_3$ solution and in solid state. Furthermore, the solid samples were also measured at the liquid nitrogen temperature (77 K). All polycrystalline samples show sensitized luminescence when exciting the samples at the ligand excitation band indicating an effective antenna effect. Luminescence quantum yield could be measured for the visible light emitters **1-Sm**, **2-Eu**, **3-Tb**, and **4-Dy** in chloroform solution and in solid state, with the europium analogue yielding the highest value of 0.68 in polycrystalline sample and of 0.42 in solution. Moreover, luminescence decay lifetime was measured for the **1-Sm** and **2-Eu** compounds with the **2-Eu** polycrystalline sample showing the greatest τ_{obs} = 0.90 ms.

Owing to the peripheral alkyl and $-CF_3$ groups of the 4,4’-dinonyl-2,2’-bipy and Btfa ligands, the **2-Eu** and **6-Yb** complexes showed a relatively low sublimation temperature, around 140-150 °C at $\sim 10^{-6}$ mbar, hence they are promising materials for the emissive layer of OLED devices. Considering the good luminescence properties of the **2-Eu** complex and **6-Yb** they were selected to produce vacuum deposited OLEDs. The **2-Eu** based OLED showed an external quantum efficiency of 2.0-2.1% and luminance in a range ~200-600 cd m^{-2}. Using **6-Yb** as the emitting material, gave a near infrared electroluminescence at ~1000 nm with an EQE of 0.1-0.17%.

Moreover, from the magnetic study of this series of compounds, dynamic magnetic measurements proved that **5-Dy** display Single Ion Magnet (SIM) behaviour at relatively high temperatures showing maximum values of the χ_M” component up to 14 K. The phonon lattice mechanism dominating in the high temperature range is the Orbach process with an effective energy barrier of 91.1 cm^{-1}. Moreover, at intermediate temperatures the Raman mechanism is present and the process of quantum nature, Quantum Tunneling of Magnetization (QTM), governs the relaxation of the magnetization at the low temperature range. By applying an optimal dc magnetic field of 0.1 T the QTM is removed, and the magnetic relaxation is still dominated by the Orbach process at high temperatures with a greater ΔE value of 109.3 cm^{-1} than that found at H_{dc} = 0 T. The Raman mechanism is involved while cooling the sample. Magnetic and spectroscopic correlation studies of **5-Dy** showed that the thermal activated relaxation of the magnetization process (Orbach) does not take place through the whole energy barrier composed of all the $\pm m_j$ states of the Dy^{3+} ion but only via the first $\pm m_j$ excited state. This may suggest that in reality, instead of the Orbach mechanism, a thermal activated QTM process is taking place.

In addition, **3-Tb**, **5-Er** and **6-Yb** show slow relaxation of the magnetization under an applied external magnetic field. The mechanisms that best describe the relaxation of the magnetization of these three compounds resulted in a combination of Raman and Direct for **3-Tb** and **6-Yb** and Orbach and Raman for the **5-Er** analogue.

2.4 References

[1] a) J.-C. G. Bünzli, On the design of highly luminescent lanthanide complexes, *Coord. Chem. Rev*., 2015, **293**, 19-47 b) K. Binnemans, Lanthanide-Based Luminescent Hybrid Materials, *Chem. Rev.* 2009, **109**, 4283-4374.

[2] a) R. Vicente, À. Tubau, F. A. Mautner, F. Bierbaumer, R. C. Fischer, S. S. Massoud, Slow magnetic relaxation and luminescence properties in neodymium(III)-4,4,4-trifluoro-1-(2-naphthyl)butane-1,3-dionato complexes incorporating bipyridyl ligands, *New J. Chem*., 2021, **45**, 14713-14723 b) G. Aromí, D. Aguilà, P. Gamez, F. Luis, O. Roubeau, Design of magnetic coordination complexes for quantum computing, *Chem. Soc. Rev*., 2012, **41**, 537-546.

[3] F. A. Mautner, F. Bierbaumer, R. C. Fischer, À. Tubau, S. Speed, E. Ruiz, S. S. Massoud, R, Vicente, S. Gómez-Coca. Insights into the Spin Dynamics of Mononuclear Cerium(III) Single-Molecule Magnets. *Inorg. Chem.*, 2022, **61**, 11124-11136.

[4] a) S. F. H. Correia, P. P Lima, P. S. André, M. Rute Sá Ferreira, L. A. Dias Carlos, High-efficiency luminescent solar concentrators for flexible waveguiding photovoltaics, Solar Energy Materials & Solar Cells, 2015, **138**, 51-57 b) M. L. Aulsebrook, B. Graham, M. R. Grace, K. L. Tuck, Lanthanide complexes for luminescence-based sensing of low molecular weight analytes, Coord. Chem. Rev., 2018, **375**, 191-220 c) H. Xu, Q. Sun, Z. An, Y. Wei, X. Liu, Electroluminescence from europium(III) complexes, *Coord. Chem. Rev*. 2015, **293**, 228-249 d) M. T. Meltin, D. O. Goryachii, D. F. Aminev, N. P. Datshevich, V. M. Korshunov, D. A. Metlina, A. A. Pavlov, L. V. Mikhalchenko, M. A. Kiskin, V. V. Garaeva, I. V. Taydakov, Bright Yb^{3+} complexes for efficient pure near-infrared OLEDs, *Dyes and Pigments*, 2021, 195, 109701.

[5] a) M. L. P. Reddy, V. Divya, R. Pavithran, Visible-light sensitized luminescent europium(III)-β-diketonate complexes: bioprobes for cellular imaging, *Dalton Trans.*, 2013, **42**, 15249-15262 b) C. Nie, Q. Zhang, H. Ding, B. Huang, X. Wang, X. Zhao, S. Li, H. Zhou, J. Wu, Y. Tian, Two novel six-coordinated Cadmium(II) and Zinc(II) complexes from carbazate β-diketonate: crystal structures, enhanced two-photon absorption and biological imaging application, *Dalton Trans*., 2014, **43**, 599-608.

[6] D. J. Bray, J.K. Clegg, L.F. Lindoy, D. Schilter, Self-assembled metallo-supramolecular systems incorporating β-diketone motifs as structural elements. *Advances in Inorganic Chemistry*, 2006, **59**, 1-37.

[7] L. Claisen, E. F. Ehrhardt, Ueber die Darstellung des Acetylacetons und seiner Homologen, *Chem. Ber*. 1889, **22**, 1009.

[8] a) Binnemans, K., Rare-earth beta-diketonates. *Handbook on the physics and chemistry of rare earth*, 2005, 35(5), 107-272 b) D. A. Atwood, Ed., β-diketonate. *The Rare Earth Elements: Fundamentals and Applications*, John Wiley & Sons Ltd, 2005, 249-261.

[9] (a) J. K. Clegg, F. Li, L. F. Lindoy. Oligo-β-diketones as versatile ligands for use in metallo-supramolecular chemistry: Recent progress and perspectives. *Coord. Chem. Rev*., 2022, **455**, 214355 (b) G. Aromí, P. Gamez. J. Reedijk, Poly beta-diketones: Prime ligands to generate supramolecular metalloclusters, *Coord. Chem. Rev*., **2008**, 252, 964-989 (c) A. Vigato, V. Peruzzo, S. Tamburini, The evolution of β-diketone or β-diketophenol ligands and related complexes, *Coord. Chem. Rev*. **2009**, 253, 1099-1201 d) Viktor I. Saloutin, Y. O. Edilova, Y. S. Kudyakova, Y. V. Burgart and Denis N. Bazhin, Heterometallic Molecular Architectures Based on Fluorinated β-Diketone Ligands, *Molecules*, **2022,** 27, 7894.

[10] S. Mishra, S. Daniele, Metal-Organic Derivatives with Fluorinated Ligands as Precursors for Inorganic Nanomaterials, *Chem. Rev*. 2015, **115**, 8379-8448.

[11] (a) F. Pointillart, O. Cador, B. Le Guennic, L. Ouahab, Uncommon lanthanide ions in purely 4f Single Molecule Magnets, *Coord. Chem. Rev.*, 2017, **346**, 150–175 (b) A. Borah, R. Murugavel, Magnetic Relaxation in Single-Ion Magnets Formed by Less-Studied Lanthanide Ions Ce(III), Nd(III), Gd(III), Ho(III), Tm(II/III) and Yb(III). *Coord. Chem. Rev.*, 2022, **453**, 214288.

[12] (a) S. M. McLennan, Geology, Geochemistry and Natural Abundances of the Rare Earth Elements. *The Rare Earth Elements: Fundamentals and Applications*, John Wiley & Sons Ltd, 2005, 249-261 (b) Pathak,A. K.; Khan,M.; Gschneidner,K. A.; McCallum,R. W.;Zhou,L.; Sun, K.; Dennis,K. W.; Zhou,C.; Pinkerton,F. E.; Kramer,M. J.;

Pecharsky,V. K. Cerium: Unlikely Replacement of Dysprosium in High Performance Nd-Fe-B Permanent Magnets. Adv. Mater. 2015, 27, 2663-2667.

[13] J. Rinehart, J. Long, Exploiting single-ion anisotropy in the design of f-element single-molecule magnets, *Chem. Sci.* 2011, **2**, 2078–2085.

[14] S. T. Liddle, J. van Slageren, Improving f-element single molecule magnets. *Chem. Soc. Rev.*, 2015, **44**, 6655-6669.

[15] J.-L. Liu, Y.-C. Chen, M.-L. Tong, Symmetry strategies for high performance lanthanide-based single-molecule magnets. *Chem. Soc. Rev.*, 2018, **47**, 2431-2453.

[16] M.-X. Xu, Y.-S. Meng, J. Xiong, B.-W. Wang, S.-D. Jiang, S. Gao, Magnetic anisotropy investigation on light lanthanide complexes. *Dalton Trans.*, 2018, **47**, 1966-1971.

[17] S. Hino, M. Maeda, K. Yamashita, Y. Kataoka, M. Nakano, T. Yamamura, H. Nojiri, M. Kofu, O. Yamamuro, T Kajiwara, Linear trinuclear Zn(II)-Ce(III)-Zn(II) complex which behaves as a single-molecule magnet. *Dalton Trans.*, 2013, **42**, 2683-2686.

[18] S. K. Singh, T. Gupta, L. Ungur, G. Rajaraman, Magnetic Relaxation in Single-Electron Single-Ion Cerium(III) Magnets: Insights from Ab Initio Calculations, *Chem. Eur. J.*, 2015, **21**, 13812-13819.

[19] J. Liu, D. Reta, J. A. Cleghorn, Y. X. Yeoh, F. Ortu, C. A. P. Goodwin, N. F. Chilton, D. P. Mills, Light lanthanide Metallocenium cations exhibiting weak equatorial anion Interactions. *Chem. Eur. J.*, 2019, **25**, 7749-7758.

[20] E. Rousset, M. Piccardo, M.-E. Boulon, R. W. Gable, A. Soncini, L. Sorace, C. Boskovic. Slow magnetic relaxation in Lanthanoid Crown Ether Complexes: interlay of Raman and Anomalous Phonon Bottleneck Process. *Chem. Eur. J.*, 2018, **24**, 14768-14785.

[21] A. Upadhyay, K. R. Vignesh, C. Das, S. K. Singh, G. Rajaraman, M. Shanmugam, Influence of the ligand field on the slow relaxation of magnetization of unsymmetrical

monomeric lanthanide complexes: synthesis and theoretical studies. *Inorg. Chem.*, 2017, **56**, 14260-14276.

[22] E. Regincós-Martí, A. B. Canaj, T. Sharma, A. Celmina, C. Wilson, G. Rajaraman, M. Murrie, Importance on an Axial LnIII-F Bond across the lanthanide series and Single-Molecule Magnet Behavior in the Ce and Nd analogues. *Inorg. Chem.*, 2022, **61**, 9906-9917.

[23] J.-D. Leng, Q.-Y. Hua, W.-T. Liu, Z.-X. Tao, N.-W. Tan, Y.-F. Wang, W.-Q. Lin, Slow magnetic relaxation of mononuclear complexes based on uncommon Kramers lanthanoide ions CeIII, SmIII and YbII. *Dalton, Trans.*, 2022, **51**, 12661-12669.

[24] N. Ahmed, K. U. Ansaria, Zero-field slow magnetic relaxation behavior of Zn2Dy in a family of trinuclear near-linear Zn2Ln complexes: synthesis, experimental and theoretical investigations. *Dalton Trans.*, 2022, **51**, 8766-8776.

[25] J. Mayans, L. Tesi, M. Briganti, M.-E. Boulon, M. Font-Bardía, A. Escuer, L. Sorace, Single-ion anisotropy and Intramolecular interactions in Ce^{3+} and Nd^{3+} dimers. *Inorg. Chem.*, 2021, **60**, 8692-8703.

[26] (a) M. Llunell, D. Casanova, J. Cirera, P. Alemany, S. Alvarez, Shape Program., version 2, Universitat de Barcelona, Barcelona, Spain, 2010; (b) P. Alemany, D. Casanova, S. Alvarez, C. Dryzum, D. Avnir, Continuous Symmetry Measures: A New Tool in Quantum Chemistry, *Rev. Comput. Chem.*, 2017, **30**, 289-352.

[27] a) C. Dryzum, D. Avnir, On the abundance of chiral crystals, *Chem. Commun.*, 2012, **48**, 5874-5876. b) K. Chulvi, A. M. Costero, L. E. ochando, P, Gaviña, Racemic Triarylmethanol Derivative Crystallizes as a Chiral Crystal Structure with Enantiomeric Disorder, in the Sohncke Space Group $P2_1$, *Cryst. Growth Des.* 2015, **15**, 3452-3456. c) M. Nespolo, M. I. Aroyo, B. Souvignier, Crystallographic shelves: space-group hierarchy explained, *J. Appl. Cryst.* 2018, **51**, 1481-1491.

[28] D. A. Atwood, Ed., Magnetism. *The Rare Earth Elements: Fundamentals and Applications*, John Wiley & Sons Ltd, 2005, 153-159.

[29] A. Ben Khélifa, M. S. Belkhiria, G. Huang, S. Freslon, O. Guillou, K. Bernot, Single-molecule magnet behavior in polynuclear assembly of trivalent cerium ions with polyoxomolybdates. *Dalton Trans.*, 2015, **44**, 16458-16464.

[30] C. Takehara, P. L. Then, Y. Kataoka, M. Nakano, T. Yamamura, T. Kajiwara Slow magnetic relaxation of light lanthanide-based linear LnZn2 trinuclear complexes. *Dalton Trans.*, 2015, **44**, 18276-18283.

[31] A. Zabala-Lekuona, J. M. Seco, E. Colacio, Single-Molecule Magnets: From Mn12-ac to dysprosium metallocenes, a travel in time *Coord. Chem. Rev.*, 2021, **441**, 213984.

[32] H.B.G. Casimir, D. Bijl, F.K. Du Pré, Measuremements on paramagnetic relaxation in chromium potassium alum, *Physica*, **1941**, 8, 449-460.

[33] C. E. Jackson, I. P. Moseley, R. Martinez, S. Sung, J. M. Zadrozny, A reaction-coordinate perspective of magnetic relaxation. *Chem. Soc. Rev.*, 2021, **50**, 6684-6699.

[34] D. Aravena, E. Ruiz, Spin dynamics in single-molecule magnets and molecular qubits. *Dalton Trans.*, 2020, **49**, 9916-9928.

[35] J. J. Le Roy, I. Korobkov, J. E. Kim, E. J. Schelter, Muralee Murugesu, Structural and magnetic conformation of cerocene [Ce(COT'')$_2$]$^-$ exhibiting a uniconfigurational f^1 ground state and slow-magnetic relaxation. *Dalton Trans.*, 2014, **43**, 2737-2740.

[36] S. K. Gupta, S. Shanmugan, T. Rajeshkumar, A. Borah, M. Damjanović, M. Schulze, W. Wernsdorfer, G. Rajaraman, R. Murugavel, A single-ion single-electron cerrous magnets. *Dalton Trans.*, 2019, **48**, 15928-15938.

[37] a) M. V. Marinho, D. O. Reis, W. X. C. Oliveira, L. F. Marques, H. O. Stumpf, M. Déniz, J. Pasán, C. Ruiz-Pérez, J. Cano, F. Lloret, M. Julve, Photoluminescent and Slow Magnetic Relaxation Studies on Lanthanide(III)-2,5-pyrazinedicarboxylate Frameworks. *Inorg. Chem.*, 2017, **56**, 2108-2123. b) A. López, C. Cruz, V. Paredes-García, V. Veiga, F. Lloret, J. Torres and R. Chiozzone, Field-induced magnetic relaxation in heteropolynuclear LnIII/ZnII metal organic frameworks: cerium and dysprosium cases, *New J. Chem.*, 2023, **47**, 21781-21789.

[38] Q.-W. Li, R.-C. Wan, Y.-C. Chen, J.-L. Liu, L.-F. Wang, J.-H. Jia, N. F. Chilton, M.-L. Tong, Unprecedent hexagonal bipyramidal single-ion magnets based on metallacrows. *Chem. Commun.*, 2016, **52**, 13365-13368.

[39] E. Pilichos, M. Font-Bardia, A. Escuer, J. Mayans, Structural and magnetic studies of mononuclear lanthanide complexes derived from N-rich chiral Schiff bases. *Dalton Trans.*, 2021, **50**, 1746-1753.

[40] S. Hiro, M. Maeda, Y. Kataoka, M. Nakano, T. Yamamura, T. Kajiwara, SMM behavior observed in Ce(III)Zn(II)2 linear trinuclear complex. *Chem. Lett.*, 2013, **42**, 1276-1278.

[41] H. Wada, S. Ooka, T. Yamamura, T. Kajiwara, Light lanthanide Complexes with crown ether and its aza derivative which show slow magnetic relaxation behaviors. *Inorg. Chem.*, 2017, **56**, 147-155

[42] a) P.G. Klemens, *Phys. Rev.*, 1961, **122**, 443. b) D. W. Feldman, J. G. Castle, J. Murphy, spin relaxation of atomic hydrogen in CaF2-evidence for local mode, *Phys. Rev.*,1965, **138**, A1208-A1216. c) Y. Zhou, B. E. Bowler, G. R. Eaton, S. S. Eaton, Electron Spin Lattice Relaxation Rates for S = 12 Molecular Species in Glassy Matrices or Magnetically Dilute Solids at Temperatures between 10 and 300 K, *J. Magn. Reson.*, 1999, **139**, 165-174.

[43] C. B. Harris, R. M. Shelby, P. A. Cornelius, Effects of Energy Exchange on Vibrational Dephasing Times in Raman Scattering, *Phys. Rev. Lett.*, 1977, **38**, 1415-1419.

[44] N. V. Vugman and M. Rothier Amaral, Jr., Influence of localized anharmonic vibrations on electron paramagnetic resonance spectroscopy, *Phys. Rev. B* 1990, **42**, 9837-9872.

[45] T. Shi, M.-X. Li, C.-M. Liu, E. N. Nfor, Z.-X. Wang, A 10-coordinate cerium(III) complex with a ferrocene-based terpyridine ligand exhibiting field-induced slow magnetic relaxation, *Polyhedron*, 2020, **188**, 114695.

[46] J. Mayans, Q. Saez, M. Font-Bardia, A. Escuer, Enhancement of magnetic relaxation properties with 3d diamagnetic cations in [$Zn^{II}Ln^{III}$] and [$Ni^{II}Ln^{II}I$], Ln^{III}=Kramers lanthanides, *Dalton Trans.*, 2019, **48**, 641-652.

[47] M. Wasim, K. Uddin Ansari, P. Kumar, B. Mallick and M. Shanmugam, A unique and discrete Ce(III) macrocyclic complex exhibits ferroelectric, dielectric and slow relaxation of magnetization properties, *Inorg. Chem. Front.*, 2022, 9, 2284.

[48] (a) Y. Ding, Y. Wang, H. Li, Z. Duan, H. Zhang, Y. Zheng, Photostable and efficient red-emitters based on zeolite L crystals *J. Mater. Chem.*, 2011, **21**, 14755-14759; (b) R. Ilmi, S. Kanslz, N. Dege, M. S. Khan, Synthesis, structure, Hirshfeld surface analysis and photophysical studies of red emitting europium acetylacetonate complex incorporating a phenanthroline derivative *J. Photochem. Photobiol., A*, 2019, **377**, 268-281; (c) P. P. F. da Rosa, Y. Kitagawa, Y. Hasegawa, Luminescent lanthanide complex with seven-coordination geometry *Coord. Chem. Rev.*, 2020, **406**, 213153; (d) Z. Ahmed, K. Iftikhar, Red, orange-red and near-infrared light emitting ternary lanthanide tris β-diketonate complexes with distorted C_{4v} geometrical structures *Dalton Trans.*, 2019, **48**, 4973-4986; (e) J. Li, H. Li, P. Yan, P. Chen, G. Hou, G. Li, Synthesis, Crystal Structure, and Luminescent Properties of 2-(2,2,2-Trifluoroethyl)-1-indone Lanthanide Complexes *Inorg. Chem.*, 2012, **51**, 5050-5057; (f) R. Ilmi, M. S. Khan, Z. Li, L. Zhou, W.-Y. Wong, F. Marken, P. R. Raithby, Utilization of Ternary Europium Complex for Organic Electroluminescent Devices and as a Sensitizer to Improve Electroluminescence of Red-Emitting Iridium Complex *Inorg. Chem.*, 2019, **58**, 8316-8331; g) D. Mara, F. Artizzu, P. F. Smet, A. M. Kaczmarek, K. Van Hecke and R. Van Deun, Vibrational Quenching in Near-Infrared Emitting Lanthanide Complexes: A Quantitative Experimental Study and Novel Insights, *Chem. Eur. J.* 2019, **25**, 15944-15956.

[49] (a) J. Kido, H. Hayase, K. Hongawa, K. Nagai, K. Okuyama, Bright red light-emitting organic electroluminescent devices having a europium complex as an emitter. *Appl. Phys. Lett.*, 1994, **65**, 2124-2126 (b) R. Ilmi, X. Li, N. K. Al Rasbi, L. Zhou, W. Y. Wong, P. R. Raithby and M. S. Khan, Two new red-emitting ternary europium(III) complexes with high photoluminescence quantum yields and exceptional performance in OLED devices, *Dalton Trans.*, 2023, **52**, 12885-12891 (c) H. Xu, Q. Sun, Z. An, Y. Wei, X. Liu,

Electroluminescence from europium(III) complexes, *Coord. Chem. Rev*. 2015, **293-294**, 228-249 (d) R. Ilmi, D. Zhang, J. D. L. Dutra, N. Dege, L. Zhou, W.-Y. Wong, P. R. Raithby, M. S. Khan, A tris β-diketonate europium(III) complex based OLED fabricated by thermal evaporation method displaying eficient bright red emission, *Organic Electronics*, 2021, **96**, 106216 (e) I. J. Al-Busaidi, R. Ilmi, D. Zhang, J. D.L. Dutra, W. F. Oliveira, N. K. Al Rasbi, L. Zhou, W.-Y. Wong, P. R. Raithby, M. S. Khan, *Dyes and Pigments*, 2022, **197**, 109879 (f) M. S. Khan, R. Ilmi, W. Sun, J. D. L. Dutra, W. F. Oliveira, L. Zhou, W.-Y. Wong and P. R. Raithby, Bright and efficient red emitting electroluminescent devices fabricated from ternaly europium complexes, *J. Mater. Chem. C*, 2020, **8**, 5600-5612

[50] A. M. Smith, M. C. Mancini and S. Nie, Second window for *in vivo* imaging, *Nat. Nanotechnol*. 2009, **4**, 710.

[51] (a) A. Zampetti, A. Minotto and F. Cacialli, Near-Infrared (NIR) Organic Light-Emitting Diodes (OLEDs): Challenges and Opportunities, *Adv. Funct. Mater*. 2019, **29**, 1807623 (b) Z. Ahmed, R. E. Aderne, J. Kai, H. I. P. Chavarria, M. Cremona, Ytterbium β-diketonate complexes for near infra-red organic light-emitting devices, *Thin Solid Films*, 2016, **620**, 34-42 (c) L. O. Tcelykh, A. A. Vashchenko, A. V. Medved'ko, L. Marciniak, A. E. Aleksandrov, A. S. Goloveshkin, L. S. Lepnev, E. V. Latipov, A. S. Burlov and V. V. Utochnikova, Ytterbium complexes with 2-(tosylamino)-benzylidene-N-(2-halobenzoyl)-hydrazones for solution-processable NIR OLEDs, *J. Mater. Chem. C*, 2022, **10**, 1371.

[52] K. Binnemans, Interpretation of europium (III) spectra. *Coord. Chem. Rev.*, 2015, **295**, 1.

[53] (a) S. Mishra, S. Daniele. Metal–organic derivatives with fluorinated ligands as precursors for inorganic nanomaterials. *Chem. Rev*. 2015, **115**, 8379–8448 (b) A. Devi, 'Old Chemistries' for new applications: Perspectives for development of precursors for MOCVD and ALD applications. *Coord. Chem. Rev*. 2013, **257**, 3332–3384

[54] a) R. Ishimatsu, E. Kunisawa, K. Nakano, C. Adachi and T. Imato, Electrogenerated Chemiluminescence and Electronic States of Several Organometallic Eu(III) and Tb(III) Complexes: Effects of the Ligands, *ChemistrySelect*, 2019, **4**, 2815-2831 b) L. Arrué, J. Santoyo-Flores, N. Pizarro, X. Zarate, D. Páez-Hernández and E. Scott, *Chem. Phys. Lett*. 2021, **773**, 138600.

[55] E. H. H. Hasabeldaim, H. C. Swart, and R. E. Kroon, Luminescence and stability of Tb doped CaF_2 nanoparticles, *RSC Adv.*, 2023, **13**, 5353-5366.

[56] (a) *Luminescence of Lanthanide Ions in Coordination Compounds and Nanomaterials,* ed. A. de Bettencourt-Dias, John Wiley & Sons Ltd, 2014 (b) J. Andres, A.-S Chauvin, Lanthanides: Luminescence Applications. *The Rare Earth Elements: Fundamentals and Applications,* John Wiley & Sons Ltd, 2005, 153-159.

[57] a) S. Biju, Y. K. Eom, J.-C. G. Bünzli, H. K. Kim, A new tetrakis β-diketone ligand for NIR emitting Ln III ions: Luminescent doped PMMA films and flexible resins for advanced photonic applications. *J. Mater. Chem. C* 2013, **1**, 6935–6944. b) J. Bolton, New NIR emission from Sm^{3+} in Yb^{3+}-Sm^{3+} co-doped tellurite glass. *J. Lumin.* 2021, **231**, 117717. c) H. F. Brito, O. L. Malta, M. C. F. C. Felinto, E. E. S. Teotonio, J. F. S. Menezes, C. F. B. Silva, C. S. Tomiyama, C. A. A. Carvalho, Luminescence investigation of the Sm(III)-β-diketonates with sulfoxides, phosphine oxides and amides ligands. *J. Alloy. Compd.* 2002, **344,** 293–297. d) L.-N. Sun, J.-B. Yu, H.-J. Zhang, Q.-G. Meng, E. Ma, C.-Y. Peng, K.-Y. Yang, Near-infrared luminescent mesoporous materials covalently bonded with ternary lanthanide [Er(III), Nd(III), Yb(III), Sm(III), Pr(III)] complexes. *Microporous Mesoporous Mater.* 2007, **98**, 156–165.

[58] C. M. Reddy, B. D. P. Raju, N. J. Sushma, N. S. Dhoble, S.J. Dhoble, *Renewable and Sustainable Energy Reviews*, 2015, **5**, 566-584.

[59] a) W. T. Carnall, P. R. Fields, K. Rajnak, Electronic Energy Levels in the Trivalent Lanthanide Aquo Ions. I. Pr^{3+}, Nd^{3+}, Pm^{3+}, Sm^{3+}, Dy^{3+}, Ho^{3+}, Er^{3+}, and Tm^{3+} *J. Chem. Phys.*, 1968, **49**, 4424-4442 b) X. Yu, J. Peng, Z. Shi, Y. Shen, Z. Zhang and G. Li, Tubular solids of lanthanide-doped polyoxometalates in micrometer-scale: synthesis and NIR-luminescent properties, *Journal of Luminescence*, 2015, **160**, 289-292, c) À. Tubau, F. Zinna, L. Di Bari, M. Font-Bardía, R. Vicente, Luminescence, CPL and magnetic properties of 1D enantiopure Ln^{3+} complexes with (S-) and (R-) α-methoxyphenylacetate ligand, Dalton Trans., 2023, 52, 1122–1132, d) J. Feng, L. Zhou, S.-Y. Song, A.-F. Li, W.-F. Li, W.-Q. Fan, L.-N. Sun, Y.-N. Yu and H.-J. Zhang, A study on the near-infrared luminescent properties of xerogel materials doped with dysprosium complexes, *Dalton Trans.*, 2009, 6593–6598 e) M. Pan, B.-B. Du, Y.-X. Zhu, M.-Q. Yue, Z.-W. Wei, C.-Y.

Su, Highly Efficient Visible-to-NIR Luminescence of Lanthanide(III) Complexes with Zwitterionic Ligands Bearing, Chem. Eur. J. 2016, **22**, 2440 – 2451 f) S. Biju, N. Gopakumar, J.-C. G. Bünzli, R. Scopelliti, H. K. Kim and M. L. P. Reddy, Brilliant Photoluminescence and Triboluminescence from Ternary Complexes of DyIII and TbIII with 3-Phenyl-4-propanol-5-isoxazolonate and a Bidentate Phosphine Oxide Coligand, Inorg. Chem. 2013, 52, 8750−8758.

[60] a) A. Aebischer, F. Gumy, J.-C. G. Bünzli, Intrinsic quantum yields and radiative lifetimes of lanthanide tris(dipicolinates). *Phys. Chem. Chem. Phys*., 2009, **11**, 1346-1353. b) S. Sato, M. Wada, Relations between Intramolecular Energy Transfer Efficiencies and Triplet State Energies in Rare Earth β-diketone Chelates. *Bull. Chem. Soc. Jpn.* 1970, **43**, 1955–1962. c) C. R. De Silva, J. Li, Z. Zheng, L. R. Corrales, Correlation of calculated excited-state energies and experimental quantum yields of luminescent Tb (III) β-diketonates. *J. Phys. Chem. A* 2008, **112**, 20, 4527-4530.

[61] M. Latva, H. Takalo, V.-M. Mukkala, C. Matachescu, J. C. Rodríguez-Ubis, J. Kankare., Correlation between the lowest triplet state energy level of the ligand and lanthanide(III) luminescence quantum yield. Journal of Luminescence, 1997, **75**, 149-169.

[62] M. H. V. Werts, R. T. F. Jukes, J. W. Verhoeven, The emission spectrum and the radiative lifetime of Eu^{3+} in luminescent lanthanide complexes. *Phys. Chem. Chem. Phys.*, 2002, **4**, 1542-1548.

[63] (a) D. Mara, F. Artizzu, P. F. Smet, A. M. Kaczmarek, K. Van Hecke, R. V. Deun, Vibrational Quenching in Near-Infrared Emitting Lanhtanide Complexes: A quantitative Experimental Study and Novel Insights, *Chem. Eur. J.* 2019, **25**, 15944-15956 (b) L Chen, Y Tan, H Xu, K Wang, ZH Chen, N Zheng, YQ Li, LR Lin, Enhanced E/Z-photoisomerization and luminescence of stilbene derivative co-coordinated in di-β-diketonate lanthanide complexes, *Dalton trans*., 2020, **49**, 16745-16761 (c) S. Kishimoto, T. Nakagawa, T. Kawai, Y. Hasegawa, Enhanced-Infrared Luminescence of Yb(III) Complexes with phosphine Oxide and Hexafluoroacetylacetonate Ligands, *Bull. Chem. Soc. Jpn.*, 2011, **84**(2), 148-154 (d) YG Wang, YQ Li, HH Tang, LR Lin, LH Ma, Near-infrared photoluminescence and reversible trans-to-cis photoisomerization of

mononuclear and binuclear ytterbium(III) complexes functionalized by Azobenzene Groups, *ACS Omega*, 2018, **3**, 5480-5490 (e) G. Brito-Santos, B. Gil-Hernández, I. R. Martín, R. Guerrero-Lemus, J. Sanchiz, Visible and NIR emitting Yb(III) and Er(III) complexes sensitized by β-diketonates and phenanthroline derivatives, *RSC Adv.*, 2020, **10**, 27815-27823 (f) X Yao, X Wang, Y Han, P Yan, Y Li, G Li, Structure, color-tunable luminescence, and UV-vis/NIR benzaldehyde detection of lanthanide coordination polymers based on two fluorinated ligands, *Cryst. Eng. Comm*., 2018, **20**, 3335-3343.

[64] (a) M. Andruh, E. Bakalbassis, O. Kahn, J. C. Trombe, P. Porcher, Structure, spectroscopic and magnetic properties of rare earth metal(III) derivatives with the 2-formyl-4-methyl-6-(N-(2-pyridylethyl)formimidoyl)phenol ligand. *Inorg. Chem.* 1993, **32**, 1616-1622 (b) O. Kahn, *Molecular Magnetism*, VHC Publishers, Inc., USA, 1993.

[65] a) K. N. Shrivastava, Theory of Spin–Lattice Relaxation.Physica status solidi (b), 1983, **117**, 437-458. b) R. Orbach, On the theory of spin-lattice relaxation in paramagnetic salts. Proc. Phys. Soc. **1961**, 77, 821-826. c) H. B. G. Casimir, F. K. Du Pré, Note on the thermodynamic interpretation of paramagnetic relaxation phenomena, Physica. 1938, **5**, 507-511.

[66] N. F. Chilton, CC-FIT, program/ https://www.nfchilton.com/ software.html, 2014.

[67] a) P. P. Cen, S. Zhang, X. Y. Liu, W. M. Song, Y. Q. Zhang, G. Xie, S. P. Chen, Electrostatic potential determined magnetic dynamics observed in two mononuclear β-diketone dysprosium (III) single-molecule magnets. *Inorg. Chem*. 2017, **56**, 3644-3656. b) Z. G. Wang, J. Lu, C. Y. Gao, C. Wang, J. L. Tian, W. Gu, X. Liu, S. P. Yan, Single-ion magnet behavior of a new mononuclear dysprosium complex. *Inorg. Chem. Commun.* 2013, **27**, 127-130. c) X. L. Li, A. Wang, M. Cui, C. Gao, X. Yu, B. Su, L. Zhou, C. M. Liu, H. P. Xiao**,** Y. Q. Zhang**,** Modulating Two Pairs of Chiral DyIII Enantiomers by Distinct β-Diketone Ligands to Show Giant Differences in Single-Ion Magnet Performance and Nonlinear Optical Response. I*norg. Chem.* 2022, **61**, 9283-9294. d) X. L. Li, C. Zhu, Q. Rong, J. Wei, R. Li, C. M. Liu, Xi-Li Li, Cancan Zhu, Qixiang Rong, Jiahao Wei, Ruixue Li and Cai-Ming Liu, A pair of mononuclear Dy(iii) enantiomers showing single-ion magnetic and ferroelectric properties *New J. Chem*., 2018, **42**, 10906-10911.

[68] N. F. Chilton, D. Collison, E. J. L. McInnes, R. E. P. Winpenny, A. Soncini, An electrostatic model for the determination of magnetic anisotropy in dysprosium complexes. Nat. Commun., 2013, 4:2551, doi: 10.1038/ncomms3551.

[69] S. Kapurwan, A. Mondal, P. K. Sahu, S. Konar, *Inorg. Chem*. 2022, **61**, 44, 17459-17468.

[70] a) F. Guégan, J. Jung, B. L. Guennic, F. Riobé, O. Maury, B. Gillon, J. F. Jacquot, Y. Guyot, C. Morell, D. Luneau, Evidencing under-barrier phenomena in a Yb(iii) SMM: a joint luminescence/neutron diffraction/SQUID study. *Inorg. Chem. Front.,* 2019, **6**, 3152-3157. b) K. S. Pedersen, J. Dreiser, H. Weihe, R. Sibille, H. V. Johannesen, M. A. Sørensen, B. E. Nielsen, M. Sigrist, H. Mutka, S. Rols, J. Bendix, S. Piligkos, Design of Single-Molecule Magnets: Insufficiency of the Anisotropy Barrier as the Sole Criterion *Inorg. Chem*., 2015, **54**, 7600-7606 c) D. Q. Wu, D. Shao, X. Q. Wei, F. X. Shen, L. Shi, Y. Q. Zhang, X. Y. Wang, Single-ion magnetism in seven-coordinate YbIII complexes with distorted D_{5h} coordination geometry. *Dalton Trans.,* 2017, **46**, 12884-12892. d) W. Zhao, H. Cui, X.-Y. Chen, G. Yi, L. Chen, A. Yuan, C. L. Luo, An eight-coordinate ytterbium complex with a hexagonal bipyramid geometry exhibiting fieldinduced single-ion magnet behaviour. *Dalton Trans*., 2019, **48**, 5621-5626.

[71] a) G. Cucinotta, J. Luzón, Magnetic anisotropy in a dysprosium/DOTA single-molecule magnet: Beyond simple magneto-structural correlations. *Angew. Chem. Int. Ed.,* 2012**, 51**, 1606-1610. b) ACS Cent. Sci. 2019, **5**, 1187-1198. c) J. Long, J. Rouquette, J.-M. Thibaud, R. A. S. Ferreira, L. D. Carlos, B. Donnadieu, V. Vieru, L. F. Chibotaru, L. Konczewicz, J. Haines, Y. Guari, J. Larionova, A High-Temperature Molecular Ferroelectric Zn/Dy Complex Exhibiting Single-Ion-Magnet Behavior and Lanthanide Luminescence. *Angew. Chem. Int. Ed*. 2015, **54**, 2236-2240. d) Y. Bi, C. Chen, Y.-F. Zhao, Y.-Q. Zhang, S.-D. Jiang, B.-W. Wang, J.-B. Han, J.-L. Sun, Z.-Q. Bian, Z.-M. Wanga, S. Gao, Thermostability and photoluminescence of Dy(III) single-molecule magnets under a magnetic field. *Chem. Sci*., 2016, **7**, 5020-5031.

3. Lanthanide Fluorobenzoates

3. Lanthanide Fluorobenzoates

In the syntheses of lanthanide(III) coordination compounds, the carboxylate anions have been widely used as ligands due to the strong interaction between the Ln^{3+} ions and the oxygen atoms from the carboxylate group. The lanthanide cations with a +3 oxidation state can be considered as a hard Lewis acids facilitating the coordination with hard Lewis bases such as the O atoms from a deprotonated carboxylic acid, providing high stability to the final coordination compound. The lanthanide ions in coordination compounds embedding carboxylate ligands present high coordination numbers up to eight or nine.[1] Moreover, the carboxylate ligands, can present multiple coordination modes enhancing coordination flexibility and tunability of the final compound. The diverse coordination geometries that the carboxylate group can show, allows obtaining a wide range of coordination complexes, from mononuclear to polynuclear heterometallic compounds. Generally, obtention of lower nuclearity compounds is favored when the ligand contains only one carboxylate group, and it is used in an excess. Whereas if an excess of the metal is used during the syntheses or if the ligand molecule contains two to more carboxylate groups, defined as a polycarboxylate ligand, the final compound will result of higher nuclearity even polymeric structures.[2-5] Some of the coordination modes that the carboxylate ligand can present are depicted in Scheme 3.1. Carboxylate coordinating geometries are diverse, from monodentate (a) to chelating (b) or to bridging coordination modes (c-g) or even bridging more than two metal centers (h and i). The bridging coordination mode leading to shorter Ln---Ln intramolecular distances is the bridging-chelating (η^2: η^1:μ_2) whereas the symmetric bridging *anti-anti* mode (η^1: η^1:μ_2) leads to larger Ln---Ln distances. Normally, the η^2: η^1: μ_2 coordination mode stabilizes better the Ln^{3+} cations with higher ionic radius such as Ce^{3+} or Nd^{3+} because it increases by one the coordination number of the metal compared to the η^1: η^1:μ_2 mode.[6] This trend of the coordination mode of the carboxylate ligand related with the ionic radius of the Ln^{3+} atom, because of lanthanide contraction, will be also reflected through this *Thesis* work. In addition, a number of lanthanide carboxylate compounds reported in the literature present remarkable characteristics including magnetic materials, optical sensors, Lewis acid catalysts and compounds where luminescence and single molecular magnet properties coexist.[7-10]

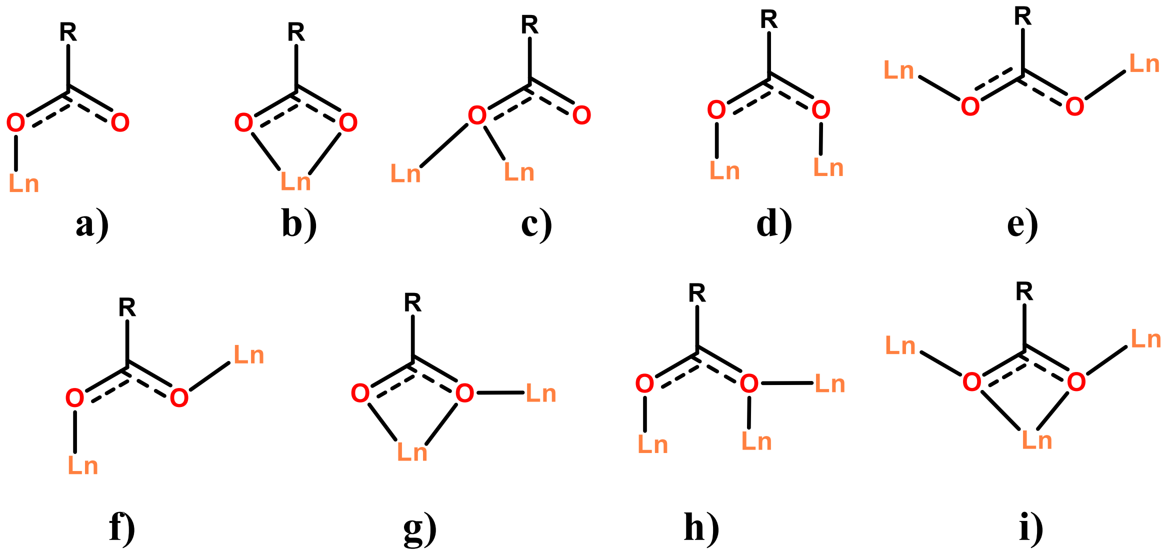

Scheme 3.1 Depiction of different coordination modes presented by carboxylate ligands: a) monodentate (η^1), b) chelating (η^1: η^1), c) o-bridging (η^2: μ_2), d) *syn-syn* bridging (η^1: η^1:μ_2), e) *anti-anti* bridging (η^1: η^1:μ_2), f) syn-anti bridging (η^1: η^1:μ_2), g) chelating-bridging (η^2: η^1:μ_2) h) triple bridging η^1: η^2:μ_3 and i) triple bridging η^2: η^2:μ_3.

Focusing now on the R- substituted benzoate ligands, the lanthanide coordination compounds derived from these molecules present interesting luminescence properties generated from the strong absorbing chromophore group of the organic fragment.[6] On substituting the H atoms in the benzoate moiety to F atoms, the luminescence quenching due to high energy C-H oscillator bonds decreases. Thus, enhancing radiative deactivation instead and improving the luminescence of the lanthanide compound.

One of the potential applications of the lanthanide fluorobenzoate coordination compounds is its use as bio-probes. The final compounds might accomplish some requisites to provide accurate imaging data in biological environments. Some of these requirements are water solubility, high thermodynamic stability, non-toxicity, high cell permeability as well as outstanding photoluminescent properties. Lanthanide coordination complexes, in particular derived from aromatic carboxylate ligands such as R-benzoates, efficiently fulfill these conditions. These may show high stability after exposition of UV radiation for a long time and they can show broad chemical modification possibilities. Because of their chemical structure, R-benzoates can be extensively modified to give researchers unique features for a variety of imaging applications and experimental requirements.[7, 11, 12]

Promising luminescence properties were observed in a study with R-benzoates presented by S. Bräse *et al.*[13a,b] who published a thorough study of lanthanide fluorobenzoate coordination compounds searching for the optimal lanthanide element and optimal ligand fluorination degree to obtain photo-stable, non-toxic and luminescent compounds suitable for their use as bio-probes. As a conclusion of the study, the europium and terbium 2-fluorobenzoate (2-FBz) dihydrate of formula $[Ln_2(\mu\text{-}2\text{-}FBz)_4(2\text{-}FBz)_2(H_2O)_4]$ combined the best properties with a luminescence quantum yield of 0.15 (over 1) for the europium and of 0.5 for the terbium polycrystalline analogues.

In this regard, *Chapter 3* of this *Thesis* work focuses on obtaining lanthanide fluorobenzoate compounds with high emission quantum yields. The use of the 2-fluorobenzoate (2-FBz) and 2,6-difluorobenzoate (2,6-F2Bz) as ligands, aims to synthetize multiproperty lanthanide coordination compounds, with special interest in high luminescent complexes emitting in the visible range. To increase the emission quantum yield, two strategies were considered. First, using the fluorobenzoate ligands to reduce C-H bonds with high energy oscillations, near the emissive lanthanide cation. Due to the good results that 2-FBz showed in previous works, this ligand will be used. Moreover, if 2-FBz containing only one fluorinated *ortho* position, increased the emission quantum yields, we hypothesized that 2,6-difluorobenzoate ligand also should present outstanding luminescence properties, as well as potential new structural features due to the extra fluorine atom. It should be noted that, as far as we know, only four lanthanide(III) coordination compounds with 2,6-difluorobenzoate ligand have been published.[13c-e] The second strategy will be to reduce or even eliminate coordinating water molecules to minimize the presence of O-H oscillators that effectively quench the lanthanide luminescence.

We have considered to prepare the 2-fluorobenzoate monohydrate compound of formula $[Ln_2(\mu\text{-}2\text{-}FBz)_4(2\text{-}FBz)_2(2\text{-}HFBz)_2(H_2O)_2]$ (2-HFBz is 2-fluorobenzoic acid) with the aim to increase the emission quantum yield considering that the number of quenching water molecules in the presented compound is a half with respect to the previously published compounds $[Eu_2(\mu\text{-}2\text{-}FBz)_4(2\text{-}FBz)_2(H_2O)_4]$ and $[Tb_2(\mu\text{-}2\text{-}FBz)_4(2\text{-}FBz)_2(H_2O)_4]$.[13a] This family of lanthanide fluorobenzoates is presented in *Section 3.1.1*. However, still remains one coordinating H_2O molecule per lanthanide central atom.

To further minimize the presence of coordinating water molecules of the above compounds with formula [Ln_2(μ-2-FBz)$_4$(2-FBz)$_2$(2-HFBz)$_2$(H_2O)$_2$], alternative species were introduced into the synthesis to serve as counter ions in the final structure as well as an excess of basic agent to obtain an anhydrous compound with hypothetical structure that should resemble to $[Ln_2(\mu\text{-2-FBz})_4(\text{2-FBz})_4]^{2-}$. The aim is that in structures presenting the [Ln_2(μ-2-FBz)$_4$(2-FBz)$_2$(2-HFBz)$_2$(H_2O)$_2$] formula, the 2-fluorobenzoic acid coordinated to the lanthanide ion can be deprotonated and further coordinated as chelating ligand removing in this way the H_2O molecules. Since the formal charge of the dinuclear compound will be -II, a counterion will be needed to neutralize the final structure. To do so, we tried tetraethylammonium chloride, tetramethylammonium hydroxide and tetraphenylphosphonium chloride. When using the first two ammonium salts, we obtained the same dinuclear complexes presented in *Section 3.1.1*. However, when using tetraphenylphosphonium chloride (PPh_4Cl) a new structural motif of formula (PPh_4)$_2$[Eu_2(μ-2-FBz)$_2$(2-FBz)$_6$(H_2O)$_2$] was obtained resulting in the family of lanthanide compounds presented in *Section 3.1.2*. Unfortunately, in the new dinuclear structure a H_2O molecule coordinated to each lanthanide ion is still present. For the new 2-fluorobenzoate lanthanide series, the syntheses, structure characterization by Single Crystal X-Ray Diffraction, luminescence properties as well as magnetic properties are presented.

3.1. Compounds derived from 2-fluorobenzoic acid (2-HFBz):

3.1.1 [Ce_2(μ-2FBz)$_4$(2FBz)$_2$(H_2O)$_4$]$_n$ and a series of compounds with formula [Ln_2(μ-2-FBz)$_4$(2-FBz)$_2$(2-HFBz)$_2$(H_2O)$_2$]

With the aim of reducing the number of H_2O molecules coordinated to the Ln^{3+} ion and therefore increase the emission quantum yield, eight lanthanide compounds derived from the 2-fluorobenzoic acid (2-HFBz) are presented in this section. The lanthanide ions used are Ce^{3+}(**8-Ce**), Sm^{3+}(**9-Sm**), Eu^{3+}(**10-Eu**), Gd^{3+}(**11-Gd**), Tb^{3+}(**12-Tb**), Dy^{3+}(**13-Dy**), Er^{3+}(**14-Er**) and Yb^{3+}(**15-Yb**). Compounds **9-Sm** to **15-Yb** presented the formula [Ln_2(μ-2-FBz)$_4$(2-FBz)$_2$(2-HFBz)$_2$(H_2O)$_2$] and they are isostructural to the previously reported Terbium(III) and Neodymium(III) analogues.[14] For the previously published [Tb_2(μ-2-FBz)$_4$(2-FBz)$_2$(2-

HFBz)$_2$(H$_2$O)$_2$] compound, luminescence emission spectrum was obtained though no study of the emission quantum yield nor luminescence lifetime was performed while for the Neodymium analogue only the crystal structure was published. Meanwhile, compound **8-Ce** crystallized in a new layer-like structure with formula $[Ce_2(\mu\text{-}2FBz)_4(2FBz)_2(H_2O)_4]_n$. Next, the structural description of compounds **8-Ce** and **10-Eu** are presented, followed by the characterization and description of luminescence and magnetic properties of all compounds.

3.1.1.1 Experimental procedure

To obtain compounds **8-Ce** to **15-Yb**, the same synthesis was carried out. Addition of an excess of 2-fluorobenzoic acid (2-HFBz) to the respective lanthanide(III) nitrate salt in basic medium led to dinuclear 2-fluorobenzoate compounds of formula $[Ce_2(\mu\text{-}2FBz)_4(2FBz)_2(H_2O)_4]_n$ for **8-Ce** and of formula $[Ln_2(\mu\text{-}2\text{-}FBz)_4(2\text{-}FBz)_2(2\text{-}HFBz)_2(H_2O)_2]$ for **9-Sm** to **15-Yb**. The synthesis procedure was conducted as follows: 2-fluorobenzoic acid (140.1 mg, 1 mmol) and pyridine* (79.1 mg, 1 mmol) were dissolved to an ethanol/H_2O (1:1) solution (20 mL). After the complete dissolution, a 10 mL ethanol solution containing the respective lanthanide salt, $Ln(NO_3)_3{\cdot}nH_2O$ (0.22 mmol) was added dropwise. The solution was magnetically stirred for 30 minutes and then left to crystallize at room temperature. After 2 weeks (1 day for **8-Ce**), white crystals suitable for monocrystal X-Ray diffraction appeared. The crystals were obtained by filtration and washed with a small amount of cold ethanol. All compounds were obtained in high yields, above 80%.

*Same compounds were obtained when using triethylamine (101.19 mg, 1 mmol) instead of pyridine as the basic agent.

It is interesting to highlight that the presented compounds with formula $[Ln_2(\mu\text{-}2\text{-}FBz)_4(2\text{-}FBz)_2(2\text{-}HFBz)_2(H_2O)_2]$ have been obtained in a simpler, room temperature straightforward synthesis avoiding this way the need of reflux or solvothermal techniques as were used in the syntheses of the already published Tb^{3+} and Nd^{3+} analogues.[14]

Further characterization of these compounds was realized by carrying out elemental analysis, Table 3. 1 and ATR-Infrared spectroscopy, Table 3. 2.

Table 3. 1 Elemental analysis of compounds **8-Ce** to **15-Yb**

	Calculated		Found	
Compound	**%C**	**%H**	**%C**	**%H**
8-Ce **$C_{42}H_{32}Ce_2F_6O_{16}$, 1186.9 g/mol**	42.5	2.7	42.0	2.6
9-Sm **$C_{56}H_{38}F_8O_{18}Sm_2$, 1451.6 g/mol**	46.3	2.6	46.0	2.4
10-Eu **$C_{56}H_{38}Eu_2F_8O_{18}$, 1454.8 g/mol**	46.2	2.6	46.0	2.4
11-Gd **$C_{56}H_{38}F_8O_{18}Gd_2$, 1465.4 g/mol**	45.8	2.6	45.2	2.5
12-Tb **$C_{56}H_{38}F_8Tb_2O_{18}$, 1468.7 g/mol**	45.9	2.6	45.7	2.6
13-Dy **$C_{56}H_{38}Dy_2F_8O_{18}$, 1475.9 g/mol**	45.6	2.6	45.4	2.6
14-Er **$C_{56}H_{38}Er_2F_8O_{18}$, 1485.4 g/mol**	45.3	2.6	45.2	2.6
15-Yb **$C_{56}H_{38}F_8O_{18}Yb_2$, 1496.9 g/mol**	44.9	2.6	45.2	2.5

Table 3. 2 Selected bands (cm^{-1}) for **8-Ce** to **15-Yb** (s=strong, m=medium and w=weak, br=broad) obtained in ATR-IR spectroscopy.

8-Ce	3256(br), 1612(m), 1589(s), 1526(s), 1486(m), 1449(m), 1399(s), 1210(m, split), 1094(m), 868(s), 795(w), 755(s), 648 (m)
9-Sm	3422(br), 1671(w), 1603(s, split), 1564(m), 1531(m), 1486(w), 1448(m), 1425(m), 1385(s), 1295(m), 1250(w), 1238(m), 1160(w), 1137(w), 1099(m), 1033(w), 953(w), 876(m), 857(m), 843(m), 809(m), 790(w), 751(s), 691(w), 650(m), 565(m)
10-Eu	3418(br), 1666(w), 1604(s, split), 1565(m), 1528(m), 1488(w), 1454(m), 1422(m), 1381(s), 1293(m), 1250(w), 1210(m), 1164(w), 873(m) 856(m), 841(m), 808(m), 789(w), 748(s), 693(w), 655(m), 569(m)
11-Gd	3419(br), 1667(w), 1605(s, split), 1567(m), 1529(m), 1489(w), 1455(m), 1423(m), 1381(s), 1295(m), 1252(w), 1215(m), 1166(w), 874(m) 857(m), 842(m), 809(m), 790(w), 749(s), 695(w), 656(m), 570(m)
12-Tb	3419(br), 1669(w), 1602(s, split), 1562(m), 1529(m), 1483(w),

	1446(m), 1423(m), 1383(s), 1293(m), 1247(w), 1234(m), 1157(w), 1131(w), 1097(m), 1031(w), 951(w), 875(m), 855(m), 842(m), 808(m), 789(w), 749(s), 689(w), 649(m), 563(m)
13-Dy	3420(br), 1669(w), 1602(s, split), 1563(m), 1530(m), 1485(w), 1447(m), 1424(m), 1384(s), 1294(m), 1249(w), 1235(m), 1158(w), 1135(w), 1098(m), 1033(w), 953(w), 876(m), 857(m), 843(m), 809(m), 790(w), 751(s), 691(w), 650(m), 565(m)
14-Er	3417(br), 1665(w), 1604(s, split), 1564(m), 1527(m), 1487(w), 1452(m), 1421(m), 1379(s), 1291(m), 1247(w), 1209(m), 1162(w), 872(m) 854(m), 839(m), 802(m), 788(w), 745(s), 691(w), 654(m), 564(m)
15-Yb	3420(br), 1669(w), 1602(s, split), 1563(m), 1530(m), 1485(w), 1447(m), 1424(m), 1384(s), 1294(m), 1249(w), 1235(m), 1158(w), 1135(w), 1098(m), 1033(w), 953(w), 876(m), 857(m), 843(m), 809(m), 790(w), 751(s), 691(w), 650(m), 565(m)

3.1.1.2 Structural characterization

The following lanthanide 2-fluorobenzoate coordination compounds were obtained performing the same reaction pathway that uses an excess of the 2-fluorobenzoic acid in a 1:4.5 metal: ligand ratio. The reaction in a water/ethanol (1:1) solution provided with basic medium led to single crystals with molecular formula $[Ln_2(\mu\text{-}2FBz)_4(2FBz)_2(2\text{-}HFBz)_2(H_2O)_2]$ for **9-Sm** to **15-Yb**. Molecules gathered in crystals containing the Ce^{3+} cation (**8-Ce**), showed a different and new arrangement in space compared to the other lanthanides with a molecular formula: $[Ce_2(\mu\text{-}FBz)_4(2\text{-}FBz)_2(H_2O)_4]_n$. Single crystal X-Ray diffraction measurements have been carried out for compounds **8-Ce**, **10-Eu**, **14-Er** and **15-Yb**. Compounds **10-Eu**, **14-Er** and **15-Yb** are isostructural therefore only the **10-Eu** structure will be described herein, in addition to **8-Ce**. Selected bond distances and crystallographic details are compiled in Table 3. 3, Table 3. 4 and Table APX.V.1

Table 3. 3 Selected bond lengths (Å) of compound **8-Ce**. The symmetry transformation used to generate equivalent atoms is b: 1+x,y,z; _c: -x,1-y,1-z; _d: 1-x,1-y,-z.

Ce1-O2	2.4851(16)	**Ce2-O4**	2.511(2)
Ce1-O5	2.3885(18)	**Ce2-O14**	2.4452(18)
Ce1-O7	2.4991(19)	**Ce2-O15**	2.4772(19)
Ce1-O9	2.5796(17)	**Ce2-O16**	2.5582(17)
Ce1-O11	2.6891(17)	**Ce2-O17**	2.5764(18)
Ce1-O12	2.5661(18)	**Ce2-O8_c**	2.6036(18)
Ce1-O13	2.6206(18)	**Ce2-O16_c**	2.6966(17)
Ce1-O6_b	2.4546(18)	**Ce1---Ce1_d**	4.464
Ce1-O11_d	2.5732(17)	**Ce2---C2_c**	4.461
Ce2-O1	2.6260(18)	**Ce1---Ce2**	5.948
Ce2-O3	2.4033(18)		

Table 3. 4 Selected bond lengths (Å) of compounds **10-Eu**, **14-Er** and **15-Yb**.

	10-Eu	**14-Er**	**15-Yb**
Ln-O1	2.586(13)	2.549(14)	2.541(10)
Ln-O2	2.430(13)	2.365(14)	2.343(10)
Ln-O3	2.354(13)	2.273(13)	2.267(10)
Ln-O4	2.356(13)	2.296(14)	2.241(9)
Ln-O5	2.638(13)	2.443(15)	2.439(11)
Ln-O5_a	2.638(13)	2.630(14)	2.326(10)
Ln-O6_a	2.463(14)	2.391(14)	2.273(11)
Ln-O7	2.481(13)	2.297(15)	2.661(10)
Ln-O9	2.427(13)	2.356(14)	2.373(10)
Ln---Ln	3.964	3.903	3.897

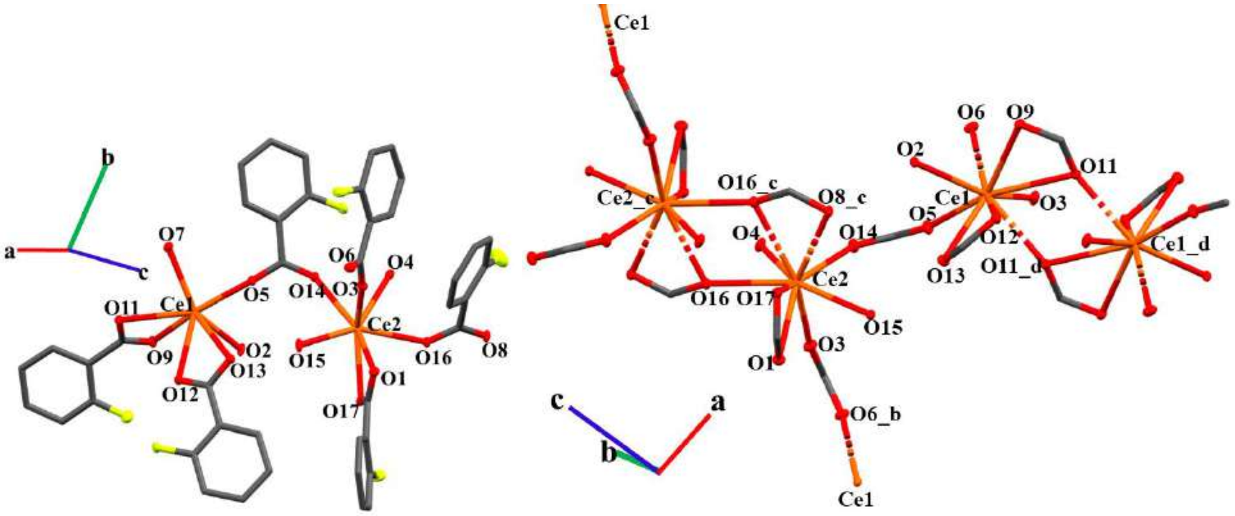

Figure 3. 1 Left, asymmetric unit of single crystal structure of **8-Ce**. Hydrogen atoms have been omitted for clarity. Right, molecular arrangement of **8-Ce** along the plane (0 1 0), hydrogen atoms and phenyl groups have been omitted for better clarification. Color code: Ce=orange, O=red, C=grey, F= green

Compound **8-Ce** crystallizes in a triclinic crystal system in a P-1 space group. Each asymmetric unit holds two crystallographically independent Ce^{3+} centers (Ce1 and Ce2), each one with a coordination number of 9, Figure 3. 1. The O atoms in each CeO_9 moiety are displayed around the Ce atoms with a coordination geometry that exhibits a distorted polyhedron between the Spherical capped square antiprism (CSAPAR-9, C_{4v}) and Muffin (MFF-9, Cs) geometries, Figure 3. 2. The calculated Continuous Shape Measurements (CShM) values with the SHAPE program[15] are compiled in Table 3. 5.

Table 3. 5 Calculated continuous Shape measurements of coordination polyhedra presented for Ce^{3+} atoms in structure of **7-Ce.**

	Ce1	**Ce2**
CSAPR-9 (C_{4v})	1.803	1.870
MFF-9 (C_s)	1.908	1.982

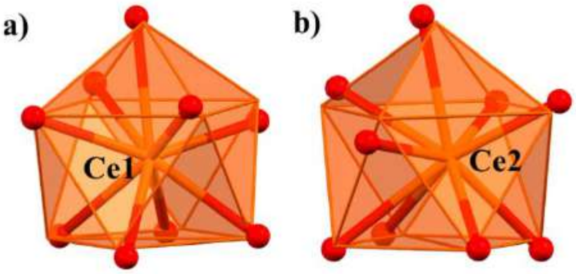

Figure 3. 2 Coordination polyhedra of Ce1 and Ce2 of **8-Ce** superimposed to an ideal Spherical Capped Square Antiprism (CSAPR) polyhedron geometry.

In **8-Ce**, each Ce^{3+} ion is coordinated to two O atoms (O12, O13 and O1, O17 for Ce1 and Ce2 respectively) from one 2-FBz ligand in the chelating coordination mode Scheme 3.2 a) with Ce-O bond distances in the 2.566-2.626 Å range and to two O atom from two H_2O molecules with Ce-O bond distances in the 2.477-2.511 range.

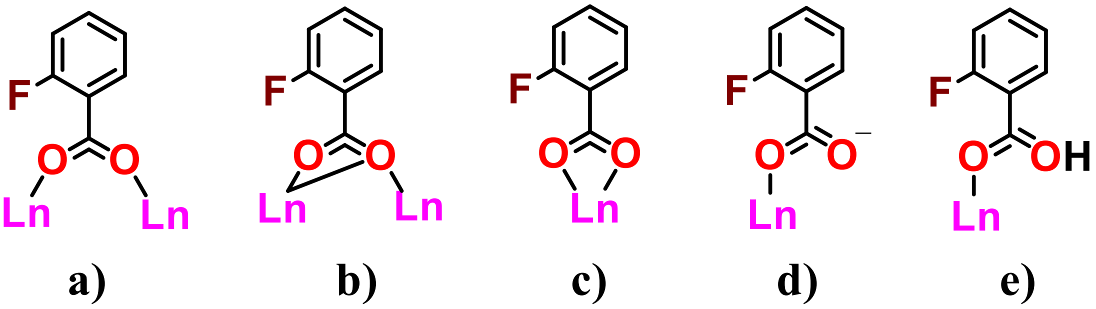

Scheme 3.2 Coordination modes of 2-FBz found in compounds of *Chapter 3*: a) symmetrical *syn-syn* bidentate bridging, b) chelating-bridging c) chelating d) monodentate coordination mode and e) monodentate 2-fluorobenzoic acid.

Furthermore, the cerium atoms are connected along the crystal lattice through 2-FBz ligands in both, the symmetrical *syn-syn* bidentate bridging (η_1:η_1:μ *or 2.11* using Harris notation[16]) and chelating-bridging (η_1:η_2:μ or 2.21 using Harris notation) coordination mode, Scheme 3.1 b) and c) and Figure 3. 1 *right*. On one hand, Ce1 and Ce1_d from the adjacent asymmetric unit are bridged through two 2-FBz ligands in the chelating-bridging coordination mode by O9, O11 and O11_d with Ce-O bond distances in the 2.573-2.580 Å range. On the other hand, Ce2 and Ce2_c from the next asymmetric unit are also connected through two 2-FBz molecules in the bridging chelating coordination mode (O16, O16_c and O8_c) with Ce-O distances in the 2.558-2.697 Å range. Moreover, Ce1 and Ce2 from each asymmetric unit are linked by one 2-FBz ligand in the symmetrical *syn-syn* bidentate bridging mode. Linkage of Ce1 and Ce2 occurs in two directions along the crystal lattice vectors [1 0 0] and [0 0 1], through O5, O14 and O6_b, O3 from two different 2-FBz ligands with Ce-O bond distances ranging from 2.389 to 2.455 Å. Bridging of Ce1 and Ce2 results in the growth of the molecular arrangement in layers along the (0 1 0) plane. The shortest Ce---Ce distances are 4.464, 4.461, 5.948 Å for Ce1---Ce1_d, Ce2---Ce2_c and Ce1---Ce2, Figure 3. 3 *left*. The layers overlap along the *b* crystallographic axis by means of weak Van der Walls intermolecular interactions, Figure 3. 3 *right*. The symmetry transformation used to generate equivalent atoms is _a: -1+x,y,z; _b: 1+x,y,z; _c: -x,1-y,1-z; _d: 1-x,1-y,-z.

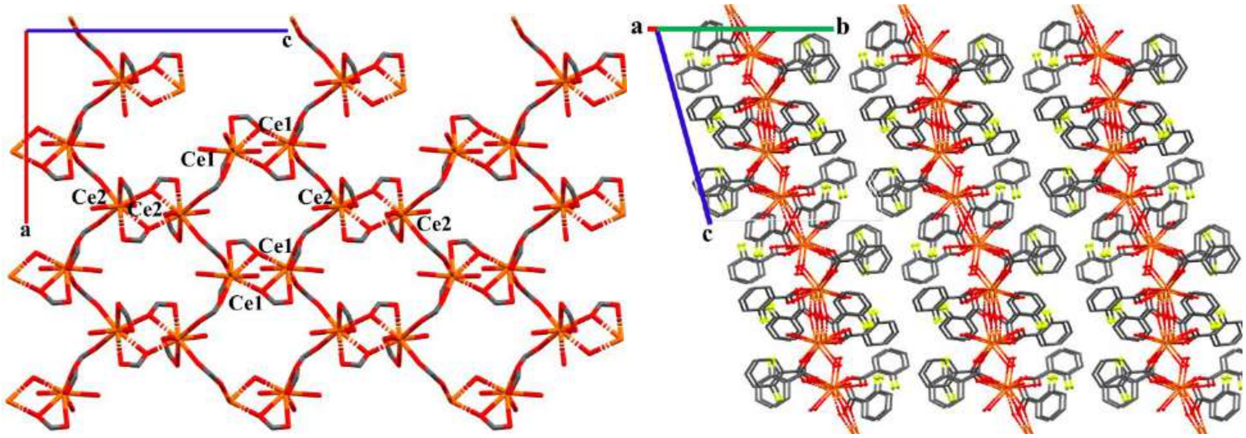

Figure 3. 3 Left, molecular arrangement of compound **8-Ce** along the (0 1 0) crystallographic plane. Hydrogen atoms and phenyl groups have been omitted for better clarification. Right, depiction of the layered crystal structure of **8-Ce**.

On the other hand, compound **10-Eu** crystallizes in a triclinic crystal system and a P-1 space group. The molecules in the crystal structure are arranged forming dinuclear entities, however the asymmetric unit is formed by half of the dinuclear structure therefore there is only one crystallographically independent Ln^{3+} ion. The coordination number of each Eu^{3+} center is 9. The oxygen atoms coordinated to each EuO_9 are set up forming a distorted polyhedron that is close to an ideal Muffin-like geometrical shape (MFF-9, Cs) with a CShM value of 2.000. The CShM values from the LnO_9 coordination sphere of **14-Er** and **15-Yb**, which crystal structures were also measured, are 1.839 and 1.807 respectively, Figure 3. 4.

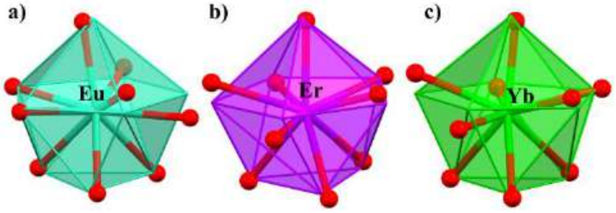

Figure 3. 4 Coordination geometry of compounds a) **10-Eu**, b) **14-Er** and c) **15-Yb** superimposed to the ideal Muffin-like polyhedron.

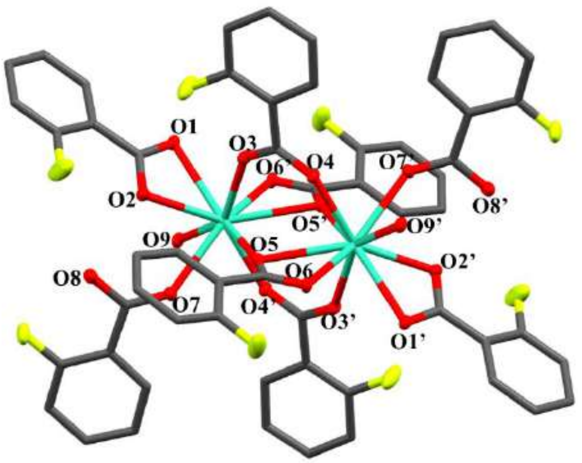

Figure 3. 5 Partially labelled structure of compound **10-Eu**. Hydrogen atoms have been omitted for better clarity. Color code Eu=blue, O=red, C=grey, F=green.

The coordination sphere of each Eu^{3+} in [Eu$_2$(μ-2-FBz)$_4$(2-FBz)$_2$(2-HFBz)$_2$(H$_2$O)$_2$] **10-Eu** is formed by O1 and O2 from a 2-FBz ligand in the bidentate chelating coordination mode and O7 from an 2-HFBz, Figure 3. 5. There are two 2-FBz ligands in the bidentate bridging coordination mode (Scheme 3.2 a) that are bonded to the Eu^{3+} atoms through O3 and O4_a and two 2-FBz ligands that are in the bidentate chelating-bridging coordination mode (Scheme 3.2 b) bonded to the lanthanide atom through the O5, O6_a and O5_a atoms. The latest O5_a atoms are doubly bridging both Eu^{3+} centers of the dinuclear structure. Finally, the coordination sphere is completed by O9 from a H$_2$O molecule. Eu-O bond lengths are in the 2.348(2)-2.638(2) Å range. The Eu---Eu_a intramolecular distance is 3.964(3) Å. The symmetry transformation used to generate equivalent atoms is _a: -x+1,-y+1,-z+2.

Intermolecular interactions to consider are the O-H---O H-bond from the H$_2$O molecule and O1 and O6 of two carboxylate groups in the bidentate chelating and bidentate bridging-chelating coordination mode respectively. The H9OA/H9OB---O1/O6 distance is 2.020 Å and the O9-H9OA---O1 and O9-H9OB---O6. This arrangement propagates along the [1 0 0] direction of the crystal lattice, thus the final supramolecular structure consists of a 1D chain Figure 3. 6.

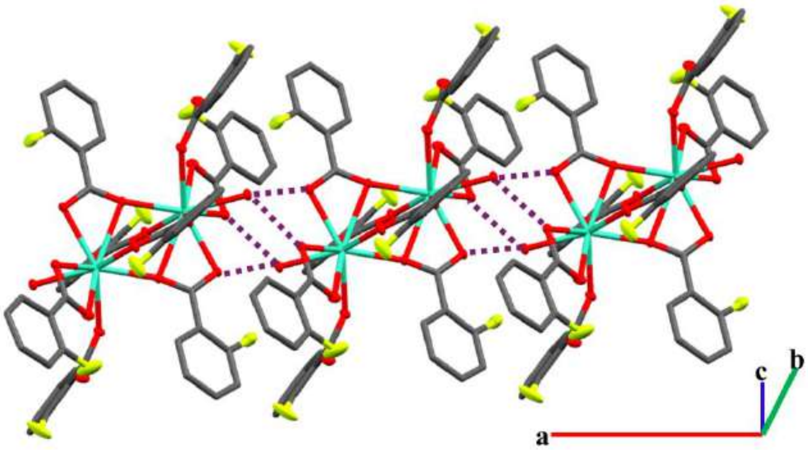

Figure 3. 6 Supramolecular arrangement representation of compound **10-Eu** in the [100] direction. Purple dotted lines indicate H-O---H intermolecular hydrogen bonds.

Moreover, Powder X-Ray Diffraction (PXRD) was performed to compounds **8-Ce**, **10-Eu**, **14-Er** and **15-Yb** to ensure phase purity along all the obtained polycrystalline powder. The comparison of the measured diffractograms with the Powder Patterns calculated from the crystal structures, corroborate phase purity, Figure 3. 7.

Besides, PXRD was measured to **9-Sm, 11-Gd, 12-Tb**, **13-Dy** to check if these compounds are isostructural to **10-Eu**, **14-Er** and **15-Yb** compounds. Also, comparison of the respective powder diffractograms indicate that **9-Sm**, **11-Gd**, **12-Tb**, **13-Dy** are isostructural to **10-Eu**, **14-Er** and **15-Yb.**

8-Ce crystallizes in a different structural motif than the rest of the lanthanide family. This may be due to the difference in the ionic radius though coordination number of Ce^{3+} in **8-Ce** doesn’t increase compared to the other lanthanide structures. In fact, it remains 9 as in compounds **9-Sm** to **15-Yb**.

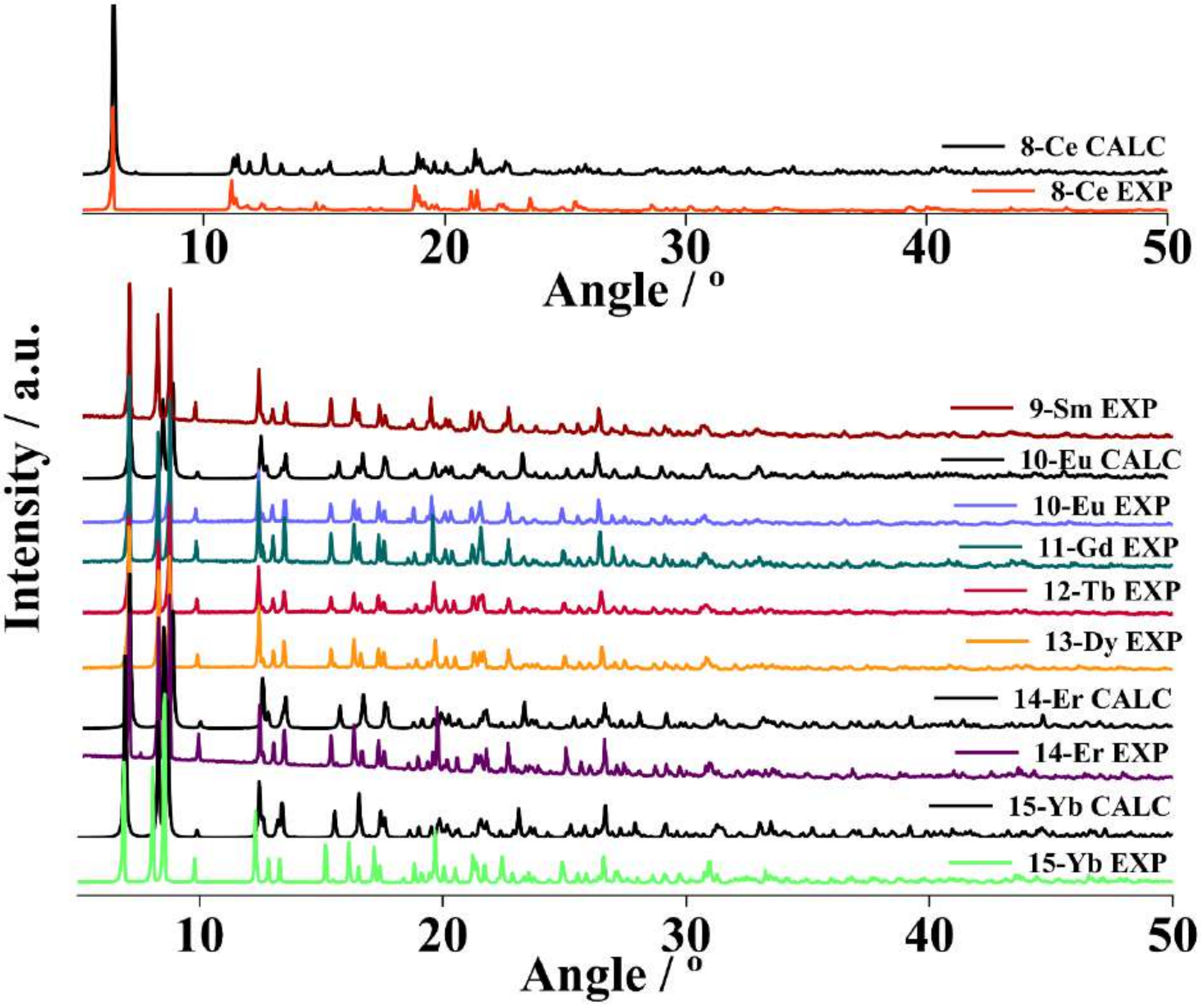

Figure 3. 7 PDRX diffractograms of compounds **8-Ce** to **15-Yb**. Black patterns correspond to the diffractograms calculated from the crystal structure.

3.1.1.3 Luminescence properties

Luminescence properties have been studied in solid state at room temperature for compounds **9-Sm**, **10-Eu**, **12-Tb**, **13-Dy**, **14-Er**, **15-Yb**. Excitation spectra collected at the maximum emission wavelength (λ_{em}) of 597 nm ($^4G_{5/2}\rightarrow^6H_{7/2}$) for **9-Sm**, 617 nm ($^5D_0\rightarrow^7F_2$) for **10-Eu**, 544 nm ($^5D_4\rightarrow^7F_5$) for **12-Tb**, 574 nm ($^4F_{9/2}\rightarrow^6H_{13/2}$) for **13-Dy** and 1070 nm ($^2F_{5/2}\rightarrow^2F_{7/2}$) for **15-Yb** are illustrated in Figure 3. 8.

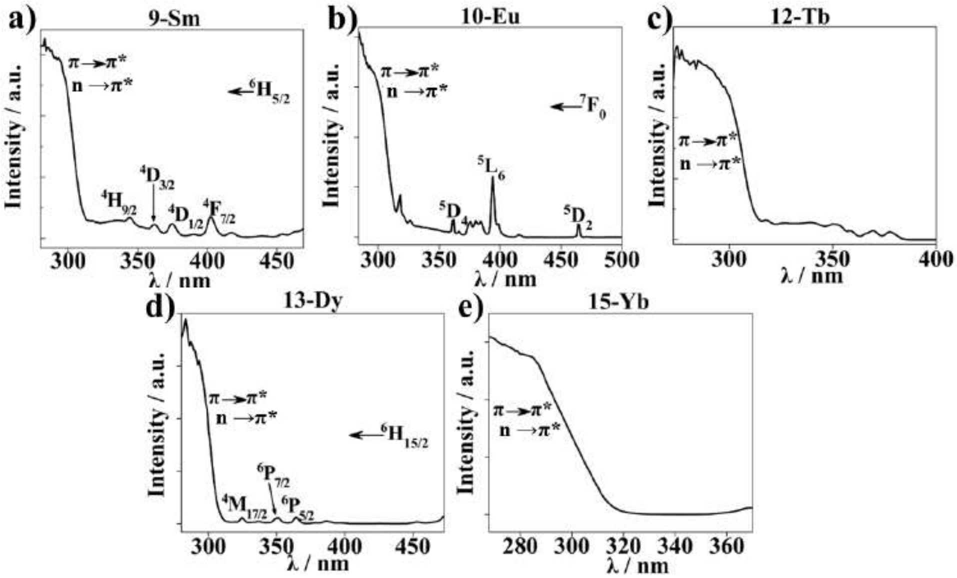

Figure 3. 8 Excitation spectra for compounds **9-Sm** to **15-Yb** measured at room temperature.

All compounds showed and intense and broad band at around 270-310 nm assigned to the 2-FBz ligand centered π→π* and n→π* excitation transitions. Moreover, weaker bands corresponding to the direct *f-f* excitation transitions from the respective lanthanide ion can be discerned. For **9-Sm** the bands appearing at 347, 363, 374 and 402 nm are assigned to transitions from the $^6H_{5/2}$ ground state to $^4H_{9/2}$, $^4D_{3/2}$, $^4D_{1/2}$, $^4F_{7/2}$ excited states respectively[17], Figure 3. 8a, while for **10-Eu**, the bands appearing at 362, 394 and 465 nm correspond to excitation transitions from the $^7F_0$ ground state to $^5D_4$, $^5L_6$ and $^5D_2$ europium's excited states, respectively[18a], Figure 3. 8b. On the other hand, transitions originating from the lanthanide in **12-Tb** and **13-Dy** are very weak. Excitation spectrum of **13-Dy** shows three small peaks at 325, 351 and 364 nm which are allocated to $^6H_{15/2}\rightarrow{}^4M_{17/2}$, $^6P_{7/2}$ and $^6P_{5/2}$ respectively[19], Figure 3. 8d, while the relief appearing in the 350-400 nm range of **12-Tb** spectrum could be due to $^7F_6\rightarrow{}^5D_1$, $^5D_0$, $^5D_2$, $^5L_{10}$ and $^5D_3$, from more to less energetic,[20] Figure 3. 8c. Finally, the excitation spectrum of **15-Yb** do not exhibit any lanthanide(III) intrinsic excitation transitions within the visible range. This is attributed to the $4f^{13}$ electronic configuration of Yb^{3+}, which results in only two electronic states $^2F_{7/2}$ (ground state) and $^2F_{5/2}$ (excited state) with a small energy gap between them. Thus, the absorption and emission occur at lower energy range, specifically in the nIR. Excitation corresponding to $^2F_{7/2}\rightarrow{}^2F_{5/2}$ appears at around 910-930 nm, but for **15-Yb** it was not observed, mainly due to the low luminescence intensity that this compound showed.[21a] The luminescence of compound **14-Er** was totally quenched.

Excitation spectra of luminescent coordination compounds that are essentially dominated by the ligand absorption transitions may indicate efficient sensitization effect. Therefore, the antenna effect is clearly effective for **12-Tb** which intrinsic *f-f* excitation transitions are barely discerned. However, the excitation of all lanthanide fluorobenzoate samples at ligand wavelength induced the characteristic lanthanide emission transitions, Figure 3. 9. Excitation wavelengths were monitored at 280, 274, 290, 283 and 275 nm for **9-Sm**, **10-Eu**, **12-Tb**, **13-Dy** and **15-Yb**, respectively.

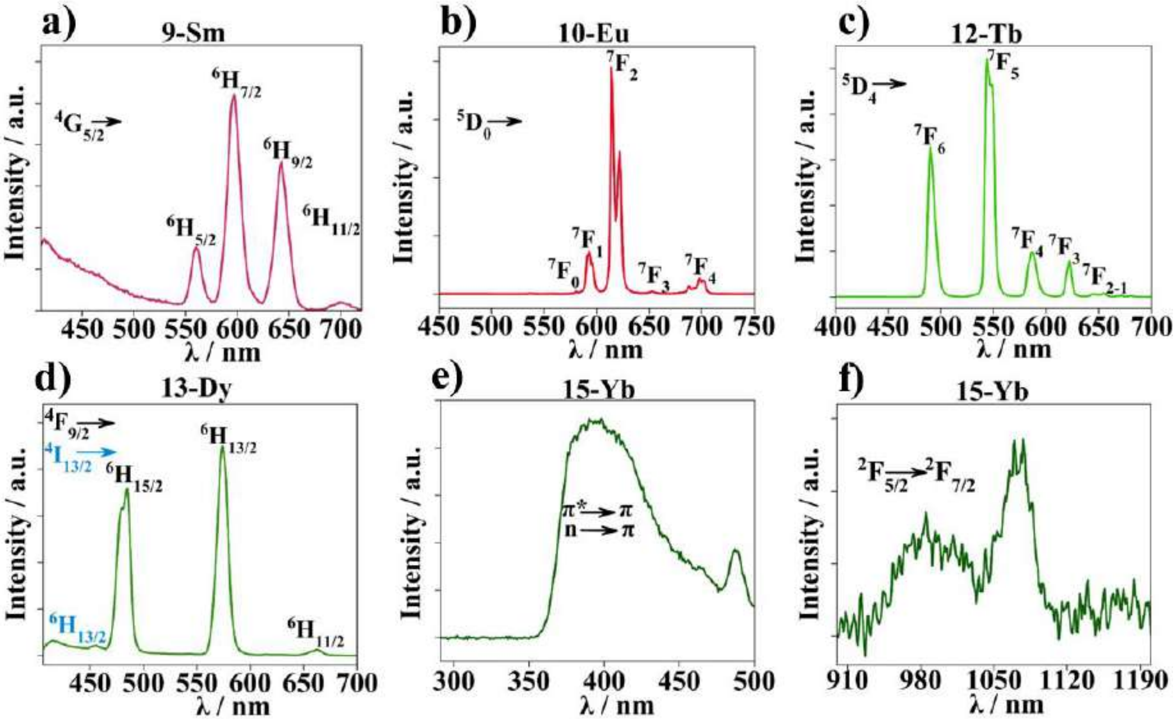

Figure 3. 9 Emission spectra of polycrystalline compounds **9-Sm** to **15-Yb** measured at room temperature.

Emission bands arising at 560, 597, 643 and 699 nm in **9-Sm** spectrum are assigned to emission from the $^4G_{5/2}$ emitting state to $^6H_{J=5/2-11/2}$ ground state, respectively. Despite ligand residual emission is observed at 400-500 nm, the pink color from Sm^{3+} luminescence could be seen by the naked eye, Figure 3. 10.

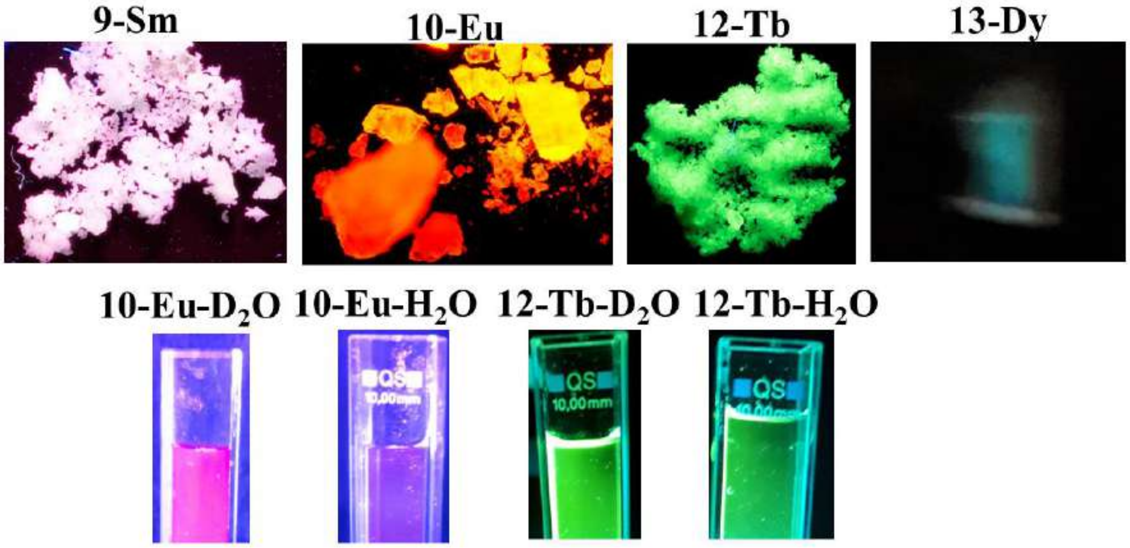

Figure 3. 10 Emission color of compounds **9-Sm** to **13-Dy** polycrystalline samples and compounds **10-Eu** and **12-Tb** dissolved in H_2O (**10-Eu-H$_2$O** and **12-Tb-H$_2$O**) and D_2O (**10-Eu-D$_2$O** and **12-Tb-D$_2$O**), under 365 nm irradiation from a UV lamp.

Emission spectrum of **10-Eu** shows different bands originating from Eu^{3+} expected transitions at 580, 593, 614, 653 and 698 nm that can be assigned to $^5D_0 \rightarrow ^7F_{J=0-4}$, besides the characteristic red color of Eu^{3+} could be seen by the naked eye, Figure 3. 10. In the emission spectrum of **12-Tb** the first band at 490 nm is assigned to $^5D_4 \rightarrow ^7F_6$ whereas the most intense band centered at 544 nm corresponds to the $^5D_4 \rightarrow ^7F_5$ transition, responsible for the green emission color that can be seen in the naked eye under UV light excitation, Figure 3. 10. Furthermore, the weaker intense bands at 586 and 622 nm were assigned to $^5D_4 \rightarrow ^7F_4$ and $^5D_4 \rightarrow ^7F_3$ transitions, respectively. The emission spectrum of dysprosium analogue, **13-Dy**, shows three well discerned bands at 485, 574 and 663 nm matching transitions from $^4F_{9/2}$ emitting state to $^6H_{15/2}$, $^6H_{13/2}$ and $^6H_{11/2}$ ground state respectively. In addition, the very low intense signal observed at 455 nm is assigned to the forbidden magnetic dipole transition ($\Delta J=0$) $^4I_{13/2} \rightarrow ^6H_{13/2}$. Its forbidden character makes it very weak in intensity.[22] Emission from the 2-FBz ligand was observed for **13-Dy** within the 350-400 nm range (spectrum not shown). This emission predominated over the Dy^{3+} luminescence, as evidenced by the blue color observed by the naked eye under UV light, Figure 3. 10. Finally, in the case of the nIR emitter compound **15-Yb,** the band observed at 980 nm is attributed to the distinctive $^2F_{5/2} \rightarrow ^2F_{7/2}$ Ytterbium transition. Emission spectrum of **15-Yb** is obtained with low signal-to-noise ratio. In addition, the emission spectrum of **15-Yb** in the Visible range was recorded to verify if the low signal in the nIR was due to inefficient energy transfer of the ligand to ytterbium's $^{2}F_{5/2}$ emitting state. If this was the case, then in the Visible range, a broad and intense band corresponding to ligand emission should be seen. Effectively, a broad band at 350 to 500 nm range appeared, Figure 3. 9, thus indicating low ligand to Yb^{3+} ion sensitization and poor luminescence.[21]

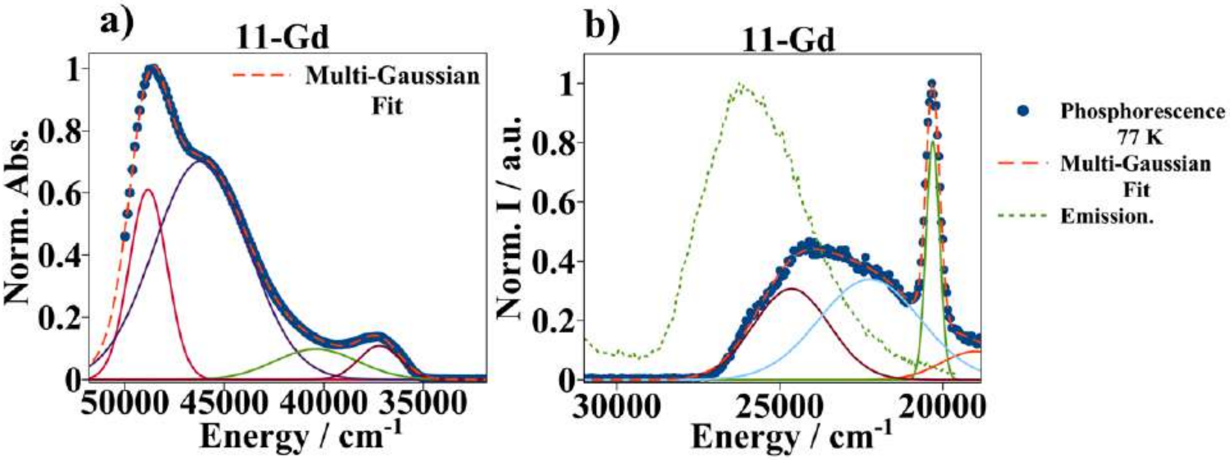

Figure 3. 11 a) Absorption spectrum of compound **11-Gd** dispersed in a KBr matrix. The lowest S_1 state is extracted from the edge of the less energetic absorption band. b) Blue dotted line: phosphorescence spectrum measured at 77 K. The T_1 state is extracted from the barycenter of the 0-phonon band. Green dotted line: emission spectrum of **11-Gd**. Both, phosphorescence and emission spectra were monitored at a λ_{exc}=280 nm.

To determine the energy of singlet and triplet states of the fluorobenzoate ligand in these coordination complexes, absorption spectrum and phosphorescence at 77 K measurements were conducted for the gadolinium analogue, **11-Gd**, Figure 3. 11. The lowest energy singlet excited state (S_1) was 35,149 cm^{-1} (284 nm) and the lowest triplet state (T_1) assessed from the 0-phonon phosphorescence spectrum resulted of 24,640 cm^{-1} (405 nm). Singlet and Triplet states of 2-FBz ligand are of high energy, compared to other chromophore ligands such as the β-diketone ligand (T_1=21,229 cm^{-1}) presented in *Chapter 2*. This indicates that 2-FBz might be a good sensitizer for visible emitters such as the Tb^{3+} and Eu^{3+} ions, which emitting states are closer in energy to the ligand triplet state ($^{5}D_4$ at 20,400 cm^{-1} for a Tb^{3+} ion and $^{5}D_0$ at 17,267 cm^{-1} for Eu^{3+} ion). However, the energy difference between 2-FBz triplet and Ytterbium's $^{2}F_{5/2}$ emitting states might be too large hindering lanthanide sensitization and allowing ligand's emission instead. The inefficient antenna effect of 2-FBz ligand to Yb^{3+} and the presence of high energy oscillating bonds from the coordinating H_2O molecules, hold back ytterbium luminescence in **15-Yb**. Nonetheless, compounds **10-Eu** and **12-Tb** didn't show ligand emission in the 350-400 nm range and both compounds presented high luminescence intensities, proposing an effective antenna effect.

As stated before, highly luminescent lanthanide(III) coordination compounds can be potentially used as bio-probes. For that, it is important to study the solubility in aqueous solution. For compounds **10-Eu** and **12-Tb** (which were the compounds showing best luminescence properties) the solubility values in deionized water were 8.0 and 6.2 mmol/L respectively. Furthermore, photophysical measurements were performed in H_2O and in D_2O solutions at their respective solubility concentrations, in order to study the possible structural changes and the optical properties of **10-Eu** and **12-Tb** in this media.

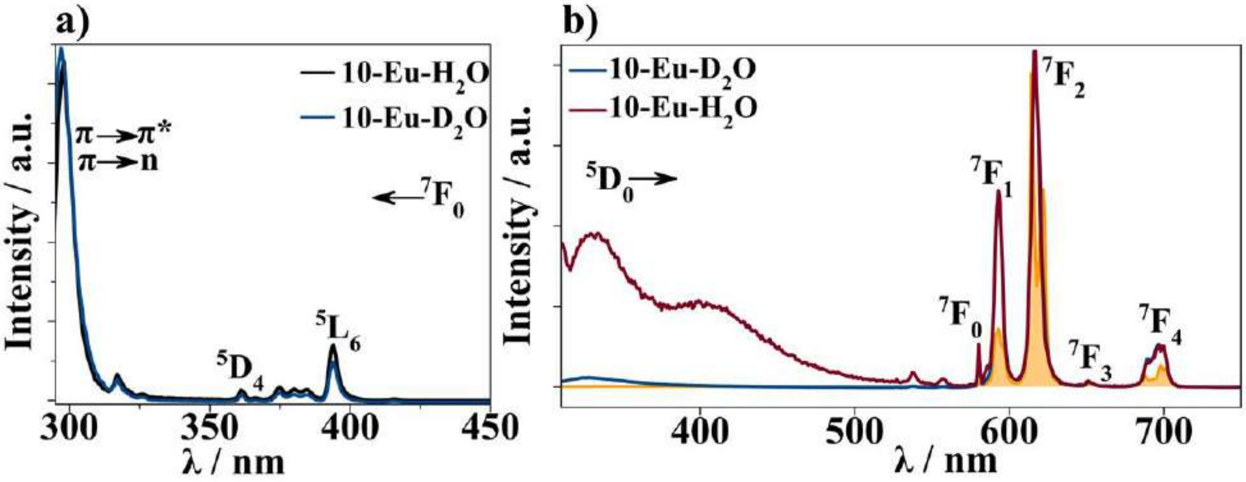

Figure 3. 12 a) Excitation spectra measured at a λ_{em} of 617 nm of **10-Eu** in H_2O and D_2O solutions. b) Emission spectra measured at a λ_{exc} of 298 nm of **10-Eu** in H_2O and D_2O solutions superimposed to the polycrystalline **10-Eu** sample (yellow spectrum). The spectra have been normalized for sake of comparison.

Emission spectra of **10-Eu** in H_2O and D_2O solution (**10-Eu-H$_2$O** and **10-Eu-D$_2$O**) were monitored at a λ_{exc} of 298 nm, corresponding to ligand absorption, as found in their respective excitation spectra, Figure 3. 12a. Excitation at ligand π→π* transitions induced the expected europium $^5D_0\rightarrow{}^7F_{0-4}$ bands. However, residual emission of the ligand could be seen at 300-500 nm. For **10-Eu-D_2O,** emission from the lanthanide ion was clearly more intense. The Eu^{3+} emission bands were found at the same wavelength in both, solid and solution samples, Figure 3. 12b. Furthermore, $^5D_0 \rightarrow ^7F_0$ transition appears as a single band for the three samples. Thus, we could assume that the lanthanide ion presents only one type of coordination sphere though high-resolution emission spectra at low temperature measurements are required to confirm this statement. Since the splitting caused by the ligand field effect in the $^7F_0$ ground state ($2J+1$) is one for a Eu^{3+} ion, any splitting observed in the 0 → 0 transition will be due to presence of compounds with different coordination environment.[18a] However, several changes in intensity and shape of emission bands, that are related to a change in the coordination environment of Eu^{3+} ion, were observed when dissolving the compounds into aqueous solutions. The $^5D_0 \rightarrow ^7F_2$ hypersensitive band is the responsible for the red emission of europium and it is sensible to Eu^{3+} surroundings. The red emission color can be seen with the naked eye, also, for **10-Eu-H_2O** and **10-Eu-D_2O** samples, Figure 3. 10. For polycrystalline **10-Eu**, this band is split, meaning that the lanthanide cation is not placed in a position with inversion symmetry inside the structure, but no splitting is seen for **10-Eu-H_2O** nor **10-Eu-D_2O**. In addition, the intensity ratio of the $^5D_0 \rightarrow ^7F_1$ and $^5D_0 \rightarrow ^7F_2$ transitions ($0 \rightarrow 1/0 \rightarrow 2$ ratio) gives us information about the symmetry of the coordination environment. Hence a decrease of this ratio is attributed to an increase of asymmetry around Eu^{3+} surroundings.[23] For **10-Eu**, the $0 \rightarrow 1/0 \rightarrow 2$ ratio is 0.2 in the solid state and 0.5 in water and deuterated oxide solutions respectively, indicating higher symmetry around the Eu^{3+} ions in the solution samples. This fact indicates a significant change in the coordination environment of the lanthanide anion and therefore a structural change of the $[Eu_2(\mu\text{-}2\text{-}FBz)_4(2\text{-}FBz)_2(2\text{-}HFBz)_2(H_2O)_2]$ arrangement when the microcrystalline sample is dissolved in water solution.

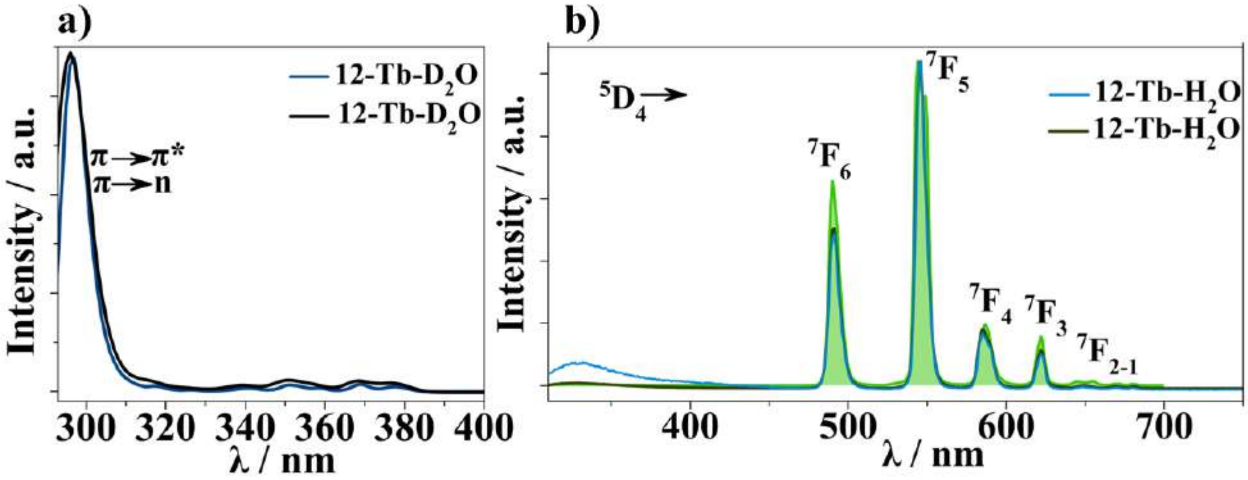

Figure 3. 13 a) Excitation spectra measured at a λ_{em} of 546 nm of **12-Tb** in H_2O and D_2O solutions. b) Emission spectra measured at a λ_{exc} of 297 nm of **12-Tb** in H_2O and D_2O solutions superimposed to the polycrystalline **12-Tb** sample (light green spectrum). The spectra have been normalized for sake of comparison.

Moreover, emission spectra under the respective ligand excitation wavelength, λ_{ex} of 297 nm for **12-Tb-H$_2$O** and **12-Tb-D$_2$O** samples, gave rise to the characteristic bands from the *f*-*f* transitions of the Tb^{3+} ion, $^5D_4 \rightarrow ^7F_{6-1}$ as observed in Figure 3. 13. Therefore, terbium characteristic green luminescence color is still evident when dissolving compound **12-Tb** in aqueous media, Figure 3. 10. Besides, weak residual emission from the ligand moieties is observed in **12-Tb-H$_2$O** but it is not as intense as the ligand emission observed in the europium's analogue compound. Nevertheless, there is a slight change in the emission spectra when comparing **12-Tb** in solid and aqueous samples. As can be seen in Figure 3. 13, the intensity ratio of the first and second emission band changes from polycrystalline to H_2O samples accounting to a structural change due to solvation effects.

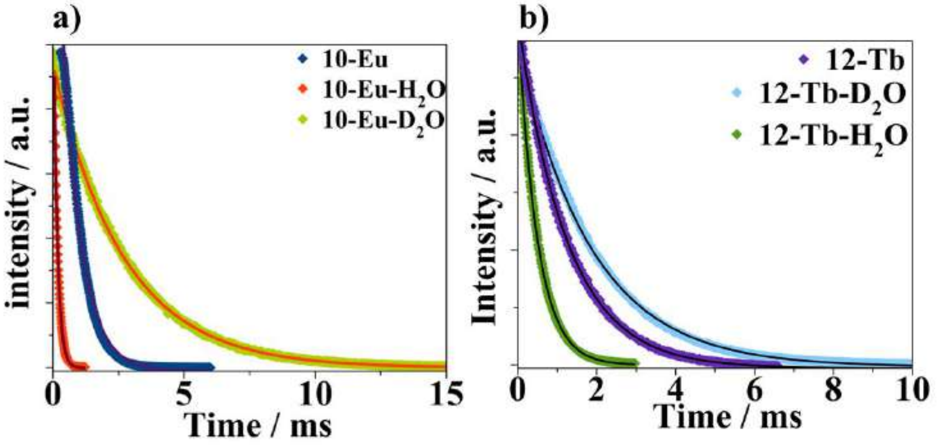

Figure 3. 14 Luminescence lifetimes of a) **10-Eu**, **10-Eu-H_2O** and **10-Eu-D_2O** samples and b**) 12-Tb**, **12-Tb-D_2O** and **12-Tb-H_2O**. Continuous lines correspond to the fit with the monoexponential equation.

To know the number of H_2O molecules coordinated to Eu^{3+} and Tb^{3+} centers once **10-Eu** and **12-Tb** are dissolved in aqueous media, photoluminescence lifetimes (τ_{obs}) in H_2O and D_2O solutions were performed as well as for polycrystalline samples. The emission decays, monitored at their respective excitation and emission wavelengths, can be fitted monoexponentially following $I(t) = I_0 \exp(-t/\tau_{obs})$, Figure 3. 14. The τ_{obs} values obtained from the best fit are compiled in Table 3. 6. Compound **12-Tb** showed longer τ_{obs} than **10-Eu**, both in solid and in solution.

Table 3. 6 Measured lifetimes (τ_{obs}) and overall quantum yields (ϕ_{Ln}^{L}) of **10-Eu** and **12-Tb** compounds in solid state and in H_2O and D_2O solutions. Calculated photoluminescence parameters for the Europium analogues: radiative lifetimes (τ_{rad}), intrinsic quantum yield (ϕ_{Ln}^{Ln}) and sensitization efficiency (η_{sens}).

	τ_{obs} (ms)	ϕ_{Ln}^{L}	τ_{rad} (ms)	ϕ_{Ln}^{Ln}	η_{sens}
10-Eu	0.72	0.27	2.58	0.28	0.96
10-Eu-H_2O 8.0 mmol L^{-1}	0.14	0.01	7.48	0.02	0.30
10-Eu-D_2O 8.0 mmol L^{-1}	2.68	0.30	7.86	0.34	0.88
12-Tb	1.43	0.76			
12-Tb-H_2O 6.2 mmol L^{-1}	0.50	0.04			
12-Tb-D_2O 6.2 mmol L^{-1}	1.86	0.26			

The number of the H_2O (q) molecules in the first coordination sphere was calculated using the equation presented by Horrocks and Sudnick, Equation 3.1:[24a]

$$q = A\left(\frac{1}{\tau_{obs(H2O)}} - \frac{1}{\tau_{obs(D2O)}}\right) \qquad \textbf{Equation 3.1}$$

Where $\tau_{obs(H2O)}$ and $\tau_{obs(D2O)}$ are the measured lifetimes in ms of **10-Eu** and **12-Tb** dissolved in H_2O and D_2O respectively. A values are 1.05 and 4.2 water molecules·ms for a Eu^{3+} and Tb^{3+} ions respectively.[24a] From this equation, q values were 7.1 for **10-Eu-H$_2$O** and 6.1 for **12-Tb-H$_2$O**.

About twenty-three years later, Supkowski and Horrocks presented a revised equation,[24b] which also considers the H_2O m

$$q = A\left(\frac{1}{\tau_{obs(H2O)}} - \frac{1}{\tau_{obs(D2O)}} - B\right) \qquad \textbf{Equation 3. 1}$$

Where A is 1.11 for Eu^{3+} and 5 for Tb^{3+} ions. The B parameter accounts for the number and contribution of the XH oscillators and it is 0.31 for Eu^{3+} and 0.06 for Tb^{3+}. The outcome number of coordination water molecules was also 7.1 for **10-Eu-H$_2$O** while for **12-Tb-H$_2$O** yielded 7.

Thus, when compounds **10-Eu** and **12-Tb** are dissolved in water they coordinate to five additional H_2O molecules. This collapses the dinuclear systems and initiates a fluxional equilibrium between different species where H_2O molecules but also 2-FBz ligands are coordinated to the Ln^{3+} ions. Coordination of the ligands to the metal is confirmed since, even in water solutions, the expected red and green luminescence arising from Tb^{3+} and Eu^{3+} is seen on exciting the samples at the ligand absorption wavelength.

Following with the study of the luminescence and sensitization efficiency of **10-Eu** and **12-Tb** in solid and solution samples, overall quantum yields (ϕ_{Ln}^{L}) were measured. Polycrystalline **10-Eu** compound yielded a ϕ_{Ln}^{L} of 0.27 upon excitation at 274 nm. Moreover, ϕ_{Ln}^{L} was 0.3 for **10-Eu-D$_2$O** and it decreased dramatically to 0.01 for **10-Eu-H$_2$O**. Luminescence quantum yield of polycrystalline **12-Tb** was 0.76, higher than the Europium analogue. Deuterated **12-Tb-D$_2$O** solution presented a ϕ_{Ln}^{L} of 0.26 while in water solution, **12-Tb-H$_2$O**, quantum yield decreased down to 0.04.

The measured ϕ_{Ln}^{L} of **10-Eu** and **12-Tb** polycrystalline samples were significantly larger than the previous values published for the [Ln_2(μ-2-FBz)$_4$(2-FBz)$_2$(H_2O)$_4$] compounds which resulted of 0.15 and of 0.5 for Eu^{3+} and Tb^{3+} analogues, respectively[13a] thus verifying that lowering the number of coordinating H_2O molecules in these lanthanide fluorobenzoates is a good strategy to increase the luminescence quantum yield. The lower quantum yield in **10-Eu-H$_2$O** and **12-Tb-H$_2$O** samples evidence the prevalence of non-radiative pathways, likely due to the presence of high energy bond vibrations within the lanthanide ion environment. This is attributed to the inner-sphere H_2O molecules present in the aqueous medium. However, deuterated solutions showed greater ϕ_{Ln}^{L} because O-D bonds oscillate at lower frequencies than O-H bonds, preventing quenching of the excited lanthanide.

Finally, additional parameters regarding the sensitization phenomena of **10-Eu** system can be calculated. The radiative lifetime (τ_{rad}) from europium's $^5D_0$ emissive level can be calculated from the corrected emission spectrum of **10-Eu**, **10-Eu-D$_2$O** and **10-Eu-H$_2$O** by means of Equation 1.8[25] (see *Section 1.2.4* of *Chapter 1*). τ_{rad} was 2.58 for the polycrystalline sample and 7.48 and 7.86 ms for deuterated and water solutions respectively. The intrinsic quantum yield (ϕ_{Ln}^{Ln}) was 0.28, 0.02 and 0.34 for **10-Eu**, **10-Eu-D$_2$O** and **10-Eu-H$_2$O** samples respectively. Following to that, sensitization efficiency (η_{sens}) is known as the amount of energy absorbed by the chromophore ligand that is transferred to the excited state of the lanthanide ion and is a pivotal factor of the overall quantum yield definition: $\phi_{Ln}^{L} = \eta_{sens} \cdot \phi_{Ln}^{Ln}$. Thus, the calculated η_{sens} values for **10-Eu**, **10-Eu-D$_2$O** and **10-Eu-H$_2$O** samples were 0.96, 0.30 and 0.88 showing a sensitization efficiency close to the unit for **10-Eu** system in solid state, indicating great sensitization efficiency of the europium compound. According to Latva's empirical rule, the optimal energy difference between the lowest lying triplet state and Eu^{3+} emitting level ($^5D_0$: 17,267 cm^{-1}) for an efficient $S_1 \rightarrow T_1 \rightarrow {}^5D_0$ energy transfer should be in the range of 2,500-5,500 cm^{-1}. While for a Tb^{3+} compound the energy difference between T_1 and $^5D_4$ (20,400 cm^{-1}) should be at least 1,850 cm^{-1} to avoid back energy transfer.[11] Compound **12-Tb** accomplish this requirement: the energy difference between T_1 of 2-FBz ligand (assessed from the Gd^{3+} analogue phosphorescence spectrum) and $^5D_4$ is 4,240 cm^{-1} whereas this energy difference is slightly larger than the optimal one stated for Latva's rule, 7,376 cm^{-1}, for the europium analogue, leading to less efficient sensitization effect. This may explain the lower quantum yield obtained for **10-Eu** with respect to **12-Tb**. Nevertheless, the slight deviation of T_1-$^5D_0$ energy difference in **10-Eu** from the optimal energy range isn't a major concern, as it still yields a good value of η_{sens}.

All in all, the emission and sensitization efficiency decreased considerably when compounds **10-Eu** and **12-Tb** were dissolved in water because of luminescence quenching produced by the high O-H oscillators from the water molecules that promote energy loss by non-radiative processes.[21,26] However, the luminescence properties were still present in H_2O solution taking into account that **10-Eu** and **12-Tb** luminescence can be seen in the naked eye, making them a choice for candidates for bioanalytical applications.

3.1.1.4 Magnetic properties

Direct current (dc) measurements

Direct current magnetic susceptibility (χ_M) and magnetization (M) experiments were carried out on **8-Ce**, **9-Sm**, **10-Eu**, **11-Gd**, **12-Tb**, **13-Dy**, **14-Er** and **15-Yb** polycrystalline samples. The χ_M measurements were carried out under an external direct current (dc) magnetic field of 0.3 T in the 2-300 K temperature range. The $\chi_M T$ dependence with T plots are presented in Figure 3. 15. At room temperature (300 K) the $\chi_M T$ values are 1.52, 2.18, 2.78, 15.6, 23.70, 27.70, 22.96 and 4.90 $cm^3mol^{-1}K$ for **8-Ce**, **9-Sm**, **10-Eu**, **11-Gd**, **12-Tb**, **13-Dy**, **14-Er** and **15-Yb** respectively. For two isolated Ln^{3+} cations, the calculated $\chi_M T$ values are: 1.6 $cm^3mol^{-1}K$ for Ce^{3+} ground state $^2F_{5/2}$ and g_J=6/7; 0.18 $cm^3mol^{-1}K$ for Sm^{3+} ground state $^6H_{5/2}$ and g_J=2/7; 0 $cm^3mol^{-1}K$ for Eu^{3+} ground state $^7F_0$; 15.75 $cm^3mol^{-1}K$ for Gd^{3+} ground state $^8S_{7/2}$ and g=2; 23.64 $cm^3mol^{-1}K$ for Tb^{3+} ground state $^7F_6$ and g_J=3/2; 28.34 $cm^3mol^{-1}K$ for Dy^{3+} ground state $^6H_{15/2}$ and g_J=4/3; 22.96 $cm^3mol^{-1}K$ for Er^{3+} ground state $^2F_{7/2}$ and g_J=6/5 and 5.14 $cm^3mol^{-1}K$ for Yb^{3+} ground state $^2F_{7/2}$ and g_J=8.7.[21a]

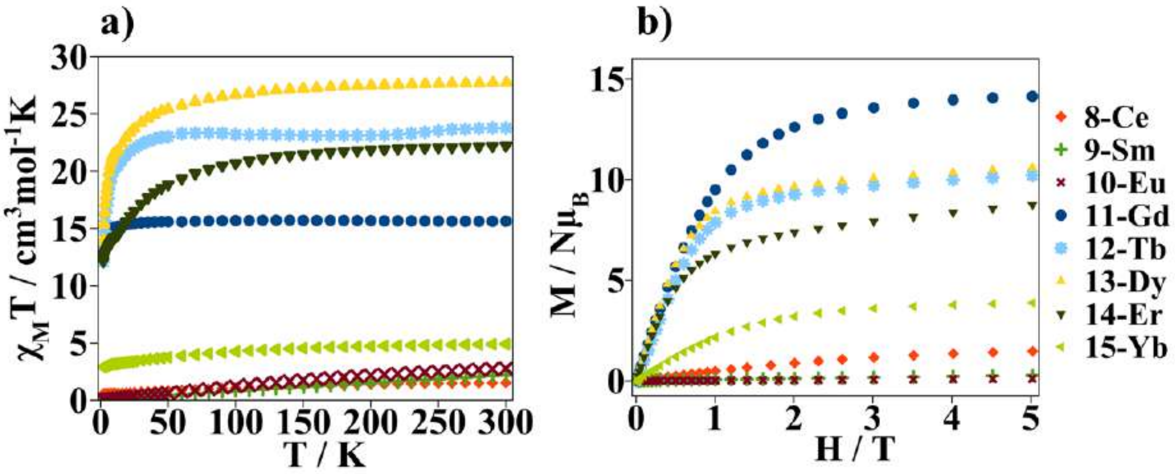

Figure 3. 15 a) $\chi_M T$ *vs* T plots, measured under an external magnetic dc field of 0.3 T and b) Magnetization with external magnetic field dependence measured at 2 K of compounds **8-Ce** to **15-Yb**.

The experimental $\chi_M T$ values measured at room temperature of samples **9-Sm** and **10-Eu** are notably larger than the calculated values. In this lanthanide coordination compounds, the electronic ground state of a Sm^{3+} ion (^6H) and a Eu^{3+} ion (^7F) split due to spin-orbit coupling into the respective *J* states ($^6H_{J=5/2-15/2}$ and $^7F_{J=0-6}$). The parameter defining the spin-orbit coupling energy gap (λ) between the ground and excited *J* states are relatively small, around 200 cm^{-1} for Sm^{3+} and of 300 cm^{-1} for Eu^{3+} ions. Due to this smaller λ values, the excited *J* states are closer in energy and are thermally populated at room temperature. Consequently, the $\chi_M T$ component at 300 K exceeds the calculated value for isolated Sm^{3+} or Eu^{3+} ions, which only considers the population of the $^6H_{5/2}$ and $^7F_0$ ground states, respectively. The decrease of $\chi_M T$ *vs* T curves upon cooling the samples is attributed to thermal depopulation of the excited *J* states of these ions. At 2 K, the $\chi_M T$ value of **10-Eu** is 0.03 $cm^3mol^{-1}K$, confirming that at low temperatures, the non-magnetic ground state ($J = 0$) is stabilized.[27]

The room temperature $\chi_M T$ values agree well with the calculated ones for the rest of the compounds.

For compound **11-Gd,** $\chi_M T$ *vs* T curve stays constant at 15.6 $cm^3mol^{-1}K$ until 15 K where $\chi_M T$ slightly decreases to 12.85 $cm^3mol^{-1}K$ at 2 K. Gadolinium(III) is an isotropic ion, $^8S_{7/2}$ with S=7/2 and L=0 quantum numbers, thus its ground state doesn't have spin-orbit coupling. It follows the Curie law, hence the small decrease of $\chi_M T$ values at low temperatures can be attributed to weak antiferromagnetic coupling between the two Gd^{3+} centers forming the dinuclear $[Ln_2(\mu\text{-}2\text{-}FBz)_4(2\text{-}FBz)_2(2\text{-}HFBz)_2(H_2O)_2]$ unit.[28, 29]

The $\chi_M T$ *vs* T curves of compounds **8-Ce** and **15-Yb** decrease gradually on cooling the samples. At the limit temperature of 2 K the $\chi_M T$ values are 0.56 and 2.89 $cm^3mol^{-1}K$, for **8-Ce** and **15-Yb** respectively. Regarding the polycrystalline samples **12-Tb, 13-Dy** and **14-Er**, the $\chi_M T$ *vs* T curves present similar behavior. The $\chi_M T$ magnetic susceptibility values stay practically constant on lowering the temperature down to ~50 K. Below this temperature, $\chi_M T$ drop suddenly to 12.07, 13.90 and 12.16 $cm^3mol^{-1}K$ for **12-Tb, 13-Dy** and **14-Er** respectively at 2 K. The decrease observed in the $\chi_M T$ *vs* T curves can be attributed to one or a combination of different phenomena: first, to the thermal depopulation of the excited m_j doublets (of the ground J state) generated by the crystal field perturbation. Second, to dipolar interactions between the molecules of the crystal lattice. Third, to weak antiferromagnetic coupling between the Ln^{3+} centers, as can be seen for the isotropic Gd^{3+} analogue. The contracted nature of 4*f* electrons in lanthanide(III) ions make magnetic exchange coupling interactions rather weak. However, the intramolecular distance between Ln---Ln of the same dinuclear unit is fairly short of 3.964 Å for **10-Eu**, 3.903 Å for **14-Er** and 3.897 Å for **15-Yb** crystal structures for the weak magnetic exchange to occur.[21a,30]

Magnetization dependence with applied magnetic field curves measured at 2 K for the former compounds are depicted in Figure 3. 15. Magnetization increases suddenly on applying an external magnetic field from 0 to ~1 T for all compounds. Then, for all compounds but **11-Gd** the *M vs* H curves increase gradually without reaching saturation of the magnetization $g_J \cdot J$. The *M vs* H curve of compound **11-Gd**, arrives to a plateau with saturation of the magnetization ($g \cdot S$). Finally, magnetization of **10-Eu** at 2 K is maintained at 0 $N\mu_B$, as expected.

Alternating current (ac) measurements

Alternating current (ac) magnetic susceptibility measurements were performed for all lanthanide samples except for **10-Eu**. To investigate spin dynamics in case of slow relaxation of the magnetization, the magnetic measurements were monitored at an ac magnetic field of $4\cdot10^{-4}$ T, oscillating between a frequency range of 1-1488 Hz for **8-Ce**, **11-Gd** and **13-Dy** and of 9-1488 Hz for **14-Er** and **15-Yb**.

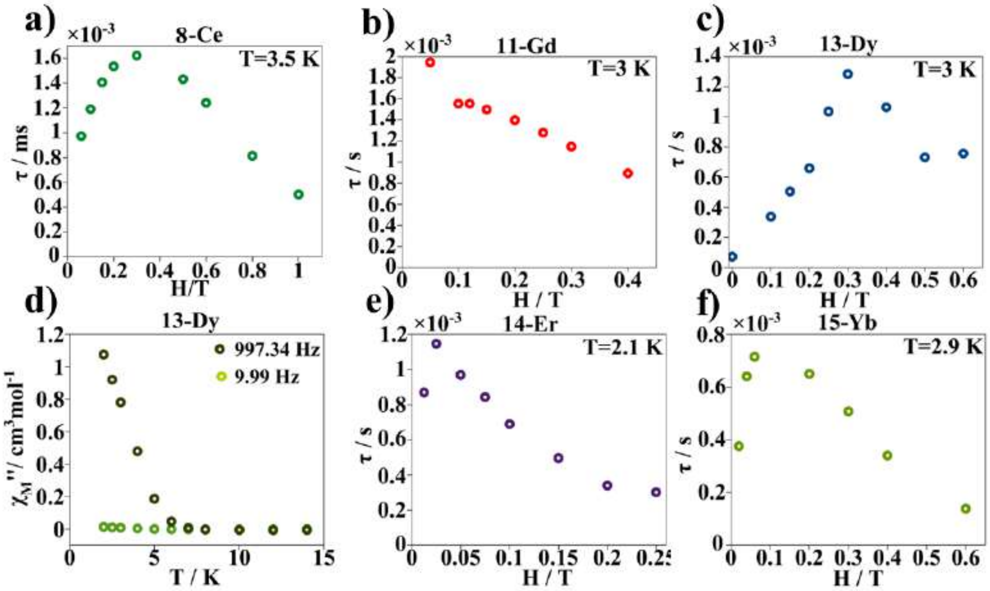

Figure 3. 16 a), b), c), e) and f) show the relaxation times in front of static magnetic fields measured at the constant temperature of 3.5 K for **8-Ce**, of 3 K for **11-Gd** and **13-Dy**, 2.1 K for **14-Er** and 2.9 K for **15-Yb**. The measurements are set under an ac magnetic field of $4\cdot10^{-4}$ T oscillating between 1 and 1488 Hz and d) χ_M'' *vs* T curve measured at a $H_{dc} = 0$ G at two oscillating frequencies of 9997.3 and 9.9 Hz for **13-Dy**.

Under no direct current magnetic field ($H_{dc} = 0$ T), only **13-Dy** showed out-of-phase magnetic susceptibility component dependence with temperature. The χ_M'' *vs* T curve increases on cooling the temperature until 2 K without reaching a maximum, Figure 3. 16d), probably due to fast Quantum Tunnelling of the Magnetization (QTM) relaxation process which is taking place at such low temperatures.[31] This issue can be addressed by applying an external direct (dc) current magnetic field (H_{dc}).

Compounds **8-Ce**, **11-Gd**, **14-Er** and **15-Yb**, didn't show χ_M'' dependence with temperature or oscillating frequency at $H_{dc} = 0$ T. However, they showed slow relaxation of the magnetization when an actual dc magnetic field was applied. Compounds **9-Sm** and **12-Tb** didn't show χ_{AC} response neither, under 0 T nor under an applied direct current magnetic field.

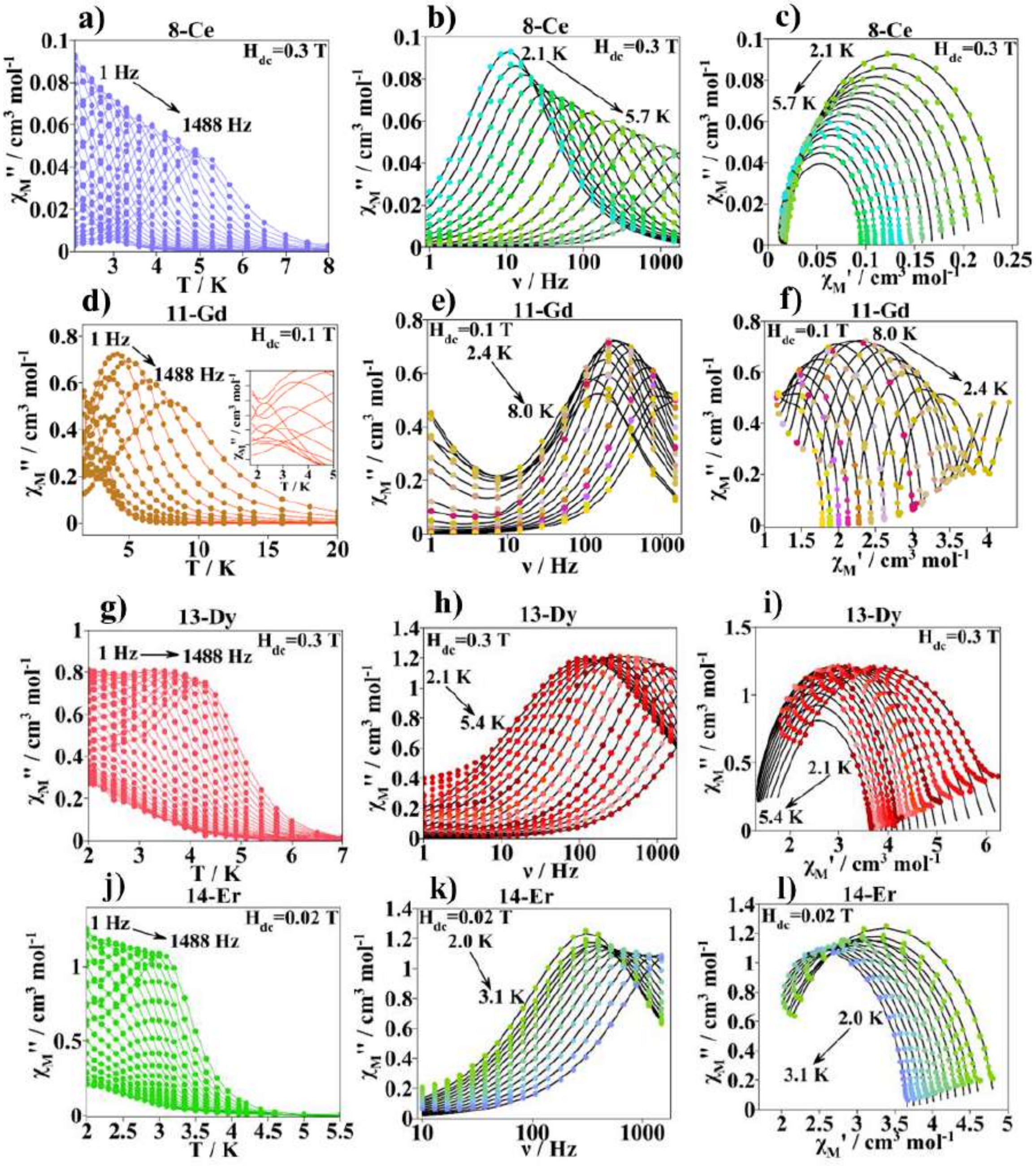
a)
8-Ce
H_dc=0.3 T
1 Hz
1488 Hz
χ_M'' / cm³ mol⁻¹
T / K
b)
8-Ce
H_dc=0.3 T
2.1 K
5.7 K
χ_M'' / cm³ mol⁻¹
ν / Hz
c)
8-Ce
H_dc=0.3 T
2.1 K
5.7 K
χ_M'' / cm³ mol⁻¹
χ_M' / cm³ mol⁻¹
d)
11-Gd
H_dc=0.1 T
1 Hz
1488 Hz
χ_M'' / cm³ mol⁻¹
T / K
e)
11-Gd
H_dc=0.1 T
2.4 K
8.0 K
χ_M'' / cm³ mol⁻¹
ν / Hz
f)
11-Gd
H_dc=0.1 T
8.0 K
2.4 K
χ_M'' / cm³ mol⁻¹
χ_M' / cm³ mol⁻¹
g)
13-Dy
H_dc=0.3 T
1 Hz
1488 Hz
χ_M'' / cm³ mol⁻¹
T / K
h)
13-Dy
H_dc=0.3 T
2.1 K
5.4 K
χ_M'' / cm³ mol⁻¹
ν / Hz
i)
13-Dy
H_dc=0.3 T
2.1 K
5.4 K
χ_M'' / cm³ mol⁻¹
χ_M' / cm³ mol⁻¹
j)
14-Er
H_dc=0.02 T
1 Hz
1488 Hz
χ_M'' / cm³ mol⁻¹
T / K
k)
14-Er
H_dc=0.02 T
2.0 K
3.1 K
χ_M'' / cm³ mol⁻¹
ν / Hz
l)
14-Er
H_dc=0.02 T
2.0 K
3.1 K
χ_M'' / cm³ mol⁻¹
χ_M' / cm³ mol⁻¹

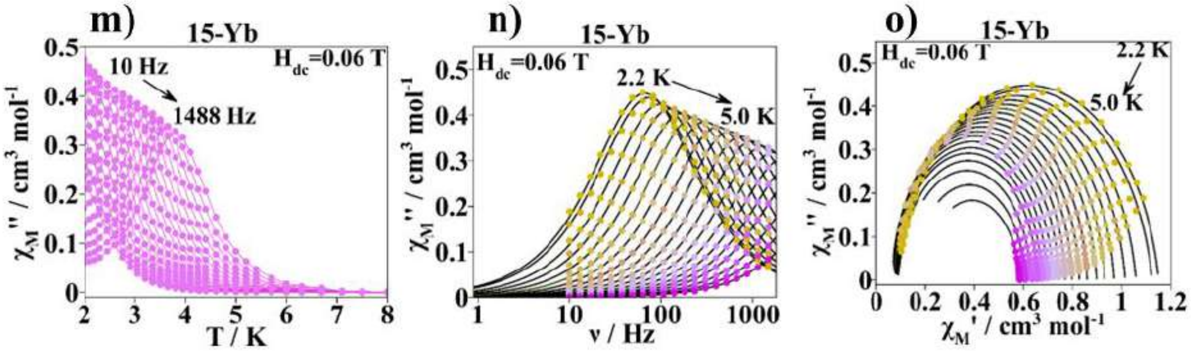

Figure 3. 17 a), d), g), j) and m) χ_M'' *vs* T plots for **8-Ce** to **15-Yb**. The continuous line is a guide to the eye b), e), h) k) and n) are the χ_M'' vs ν plots for **8-Ce** to **15-Yb.** The continuous black line is the fitting to the Generalized Debye model. c), f), i), l) and o) are the Cole-Cole plots for **8-Ce** to **15-Yb**. Continuous black line represents the fitting to the Generalized Debye model.

Then χ_{AC} measurements were first collected at different magnetic fields and at the constant temperature of 3.5 K for **8-Ce**, of 3 K for **11-Gd** and **13-Dy**, 2.1 K for **14-Er** and 2.9 K for **15-Yb** to determine the H_{dc} optimal field, Figure 3. 16. Thus, dynamic magnetic responses of **8-Ce**, **11-Gd**, **13-Dy**, **14-Er** and **15-Yb** were measured under the optimal H_{dc} of 0.3, 0.1, 0.3, 0.02 and 0.06 T, respectively. The plots of the out-of-phase magnetic susceptibility component varying with temperature and frequency of these complexes are illustrated in Figure 3. 17.

Compounds **8-Ce**, **13-Dy**, **14-Er** and **15-Yb**, show χ_M'' maxima upon cooling the samples down to the temperature range of 2-5.5 K for **8-Ce**, 2-4.5 K for **13-Dy** and **15-Yb** and to a smaller temperature range of 2-3.3 K for **14-Er,** Figure 3. 17a), g), j), m)**.** As for the χ_M'' tendency with the oscillating frequency, compound **8-Ce** starts showing χ_M'' maxima at shorter frequencies whereas **14-Er** χ_M'' *vs* ν curves show peaks at higher ones. For all compounds, the χ_M''*vs* ν maxima move progressively to higher frequencies on increasing temperature, Figure 3. 17b), h), k), n). Representation of the ac magnetic data in the Cole-Cole plots shows asymmetric semicircles for **8-Ce**, **13-Dy** and **15-Yb**, while the semicircles of **14-Er** are asymmetric and uncompleted. Nevertheless, the magnetic data of **8-Ce**, **13-Dy**, **14-Er** and **15-Yb** could be successfully fitted with the one component Debye model function with Equation 1.32, as shown in Figure 3. 17c), i), l), o). The α values obtained from such fittings were in the range of 0.1(2.1 K)-0.02(5.7 K) for **8-Ce**, 0.4(2.1 K)-0.2(5.4 K) for **13-Dy**, 0.1(2 K)-0.08(3.1 K) for **14-Er** and 0.1(2.2 K)-0.02(5 K) for **15-Yb**. For all compounds α decreases on increasing temperature indicating a narrower distribution of the relaxation times at higher temperatures. Moreover, relaxation of the magnetization times with temperature in ln(τ) *vs* T^{-1} plots are depicted in Figure 3. 18. The parameters obtained from the best fit of the ln(τ) *vs* T^{-1} curves for **8-Ce** to **15-Yb** are compiled in Table 3. 7.

$$\tau^{-1} = \tau_0^{-1} \exp\left(\frac{-\Delta E}{k_B T}\right) \qquad \textbf{Equation 3. 2}$$

$$\tau^{-1} = CT^n + AT \qquad \textbf{Equation 3. 3}$$

$$\tau^{-1} = \tau_0^{-1} \exp\left(\frac{-\Delta E}{k_B T}\right) + AT \quad \textbf{Equation 3. 4}$$

Regarding compound **8-Ce**, the beginning of a linear trend can be distinguished in four experimental points. The fit of the magnetic data with the Arrhenius law that considers the Orbach relaxation of the magnetization (τ−1=$\tau_0^{-1} \exp\left(\frac{-\Delta E}{k_B T}\right)$ **Equation 3. 2**) yielded ΔE and τ_0 values of 26.0 cm^{-1} and $7.41 \cdot 10^{-8}$ s respectively. Conversely, the best fit obtained for compound **8-Ce** was when the equation describing Raman and Direct relaxation of the magnetization mechanism (τ−1=$CT^n + AT$ **Equation 3. 3**), was considered. The values of the parameters obtained from such fitting were A = 26.10 $s^{-1}K^{-1}$ for Direct and C = 0.05 $s^{-1}K^{-n}$ and n = 7.38 for Raman. For **8-Ce** the Orbach mechanism was disregarded for two reasons: *i*) a clear linear trend is not followed along representative magnetic data in the ln(τ) *vs* T^{-1} curve showed by **8-Ce** *ii*) as it was explained in *Chapter 2.2,* Ce^{3+} compounds are not prone to relax by the Orbach mechanism. For the previous Ce^{3+} compounds found in the literature as well as the Ce^{3+} compounds **1-H₂O** to **5-bathophen** presented in *Chapter 2.2*, the effective energy barrier values obtained in the experimental magnetic data are notably lower than the energy difference between the ground ±m_j and the excited ±m_j doublets obtained by ab initio calculations. With these precedents other temperature dependent mechanisms such as Raman or the Local mode should be considered.[32]

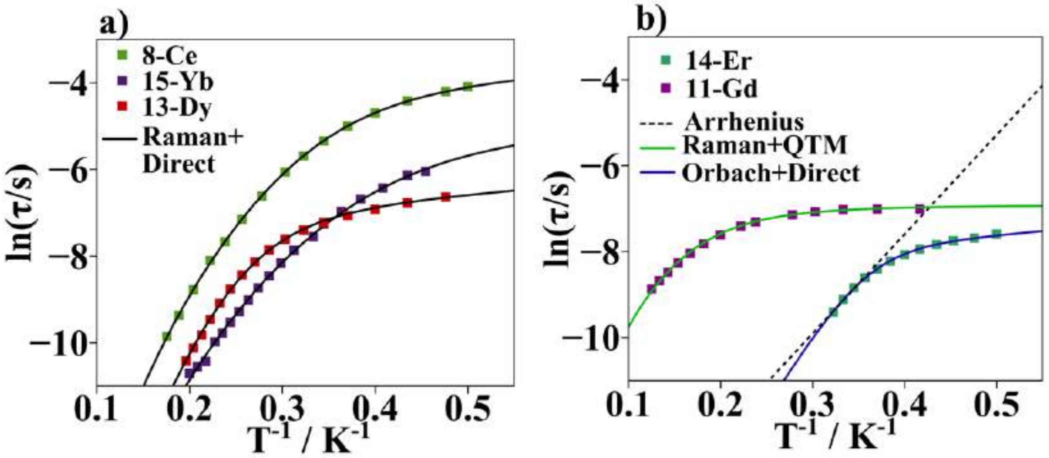

Figure 3. 18 a) ln(τ) *vs* T^{-1} plot for a) **8-Ce**, **13-Dy** and **15-Yb** and b) **11-Gd** and **14-Er** from the magnetic data measured at the H_{dc} of 0.3, 0.1 0.30.06 and 0.02 T respectively. In both figures, continuous lines represent the best fit using the stated equations of the relaxation of magnetization mechanisms. The black dotted line in b) represents the fit of the high temperature range following the Arrhenius law.

Moreover, compounds **13-Dy** and **15-Yb** show similar behavior as **8-Ce**. Both compounds showed a linear trend at higher temperatures that can be fitted with the Arrhenius law. The obtained parameters were ΔE = 25.5 cm^{-1} and $\tau_0 = 2.3 \cdot 10^{-8}$ s for **13-Dy** and ΔE = 18.7 cm^{-1} and $\tau_0 = 9.8 \cdot 10^{-8}$ s for **15-Yb**, Figure APX.V.1. The effective energy values are quite low, especially for **13-Dy**, where the energy of the first excited m_j state is normally found at higher energy levels in Dy^{3+} compounds with SMM behavior. This fact suggest that relaxation of **13-Dy** occurs through an underbarrier mechanism.[4,33] Besides, the best fit of ln(τ) *vs* T^{-1} curves were obtained when the equation describing Raman and Direct mechanism was used, $\tau{-}1=CT^{n}+AT$ **Equation 3. 3**.

For the **14-Er** compound, the Arrhenius law that describes the over barrier Orbach relaxation mechanism was used to fit the linear segment in the higher temperature range. The obtained effective energy barrier was 16.1 cm^{-1} and the pre-exponential factor was $4.9 \cdot 10^{-8}$ s. The linear trend is not followed along all the curve, therefore a function with the equation including Orbach and Direct relaxation mechanisms, $\tau{-}1=\tau_0^{-1}\exp\left(\frac{-\Delta E}{k_BT}\right)+AT$ **Equation 3. 4**, gave the best fit, Figure 3. 18b). The obtained parameters were ΔE = 23.90 cm^{-1}, $\tau_0 = 1.72 \cdot 10^{-9}$ s, A = 1015.56 $s^{-1}K^{-1}$.

Table 3. 7 Compilation of the fitted parameters from the relaxation of the magnetization mechanisms of compounds **8-Ce** to **15-Yb**.

	H_{dc} (T)	Orbach		QTM	Raman		Direct
		ΔE (cm^{-1})	τ_0 (s)	τ_{QTM} (s)	C (s^{-1}K^{-n})	n	A (s^{-1}K^{-1})
8-Ce	0.3				0.05	7.38	26.10
11-Gd	0.1				1.28	4.10	
13-Dy	0.3				0.04	8.35	357.95
14-Er	0.02	23.91	$1.72 \cdot 10^{-9}$				1015.56
15-Yb	0.06				0.75	6.91	101.60

Finally, the compound containing the isotropic lanthanide **11-Gd** (ground state $^8S_{7/2}$) showed a slightly different magnetic behavior compared to the other analogues, Figure 3. 17d), e), f). Compound **11-Gd** show χ_M" maxima in 2-10 K temperature range under a direct current magnetic field of 0.1 T. From the χ_M" *vs* T plot, two maxima can be discerned. One appearing at higher temperatures whereas the second one arise nearly at 2 K, Figure 3. 17d). This is also seen in the χ_M'' *vs* ν plot where two different behaviors are well discerned, one occurring at high frequencies and the other at low frequencies. From the high frequencies set, clear maxima dependent on frequency and temperature are differentiated. On the other hand, in the low frequency set, χ_M'' increases on lowering the oscillating frequency, however, the signals exhibit poor dependency on frequency and no maxima are observed. The distinct contributions of χ_M'' at high and low frequencies are also reflected in the representation of χ_M' *vs* χ_M'' magnetic data. The Cole-Cole plots display well defined semicircles for the curves corresponding to the high temperature and high frequency magnetic data. As the temperature decreases, a second peak begins to appear at the edge of these semicircles. This corresponds to the tails observed at lower frequencies and lower temperatures in the χ_M'' *vs* T and χ_M'' *vs* ν plots. We could successfully fit the Cole-Cole plots of **11-Gd** with the extended Generalized Debye model (Equation 1.37) from which we obtained τ and α values for both relaxation processes, Figure 3. 17f). The α values for the process occurring at higher frequencies and temperatures range from 0.1(2.4 K) to 0.02(8 K). For the process occurring at lower frequencies and temperatures, the τ values didn't seem to follow a concrete trend with temperature therefore we couldn't proceed with a proper fit, FigureAPX.V.2. However, the extracted τ values from the process happening at higher frequencies were dependent on temperature, Figure 3. 18b). As a first approximation, the ln(τ) *vs* T^{-1} values could only be fitted with a combination of equations describing Raman and Quantum Tunneling of the Magnetization ($\tau^{-1} = CT^{n} + \tau_{QTM}$) with values of C = 1.28 and n = 4.1 for Raman and τ_{QTM} = 1016.9 s.

However, for an isotropic metal with a spherical quadrupole moment such as Gd^{3+}, talking about the conventional QTM as well as the Orbach spin relaxation mechanism is not accurate. An asymmetry around the Gd^{3+} ion produced by the crystal field may induce small values of axial zero field splitting (previously reported values calculated by EPR spectroscopy are found to be around 0.1 cm^{-1}). The induced anisotropy would break the degeneration of the 7/2 spin level of the Kramer doublets. Then, exposure of moderate magnetic fields may produce multiple crossing of the 7/2, 5/2, 3/2 and 1/2 levels allowing different ΔS transitions of the adequate energy to interact with low-energy phonons that promote a relaxation of the magnetization, as suggested by S. Gao and M. Yamashita.[28] Therefore, in the absence of an energy gap between ground and excited states generated by spin-orbit coupling, as is the case of isotropic Gd^{3+}, the slow relaxation of the magnetization response under moderate dc magnetic fields, is not a result of suppressing Quantum Tunneling or an over-barrier process. This behavior contrasts with what is typically observed in conventional anisotropic systems, where Orbach as well as QTM become more relevant. EPR spectroscopic measurements as well as magnetic dilution could be performed to better understand relaxation of the magnetization taking place for **11-Gd**, however spin dynamics of coordination compounds containing isotropic (or quasi-isotropic) cations are out of the scope of this *Thesis* work.[34]

3.1.2 Lanthanide (III) 2-Fluorobenzoate compounds with formula $(PPh_4)_2[Ce_2(\mu\text{-}2\text{-}FBz)_2(2\text{-}FBz)_6(H_2O)_2]\cdot 2H_2O$ and $(PPh_4)_2[Ln_2(\mu\text{-}2\text{-}FBz)_2(2\text{-}FBz)_6(H_2O)_2]$

3.1.2.1 Experimental procedure

In this section of *Chapter 3*, six new lanthanide coordination compounds derived from the 2-fluorobenzoic acid (2-HFBz) were synthetized. The complexes show the molecular formula $(PPh_4)_2[Ce_2(\mu\text{-}2\text{-}FBz)_2(2\text{-}FBz)_6(H_2O)_2]\cdot 2H_2O$ where Ln is Ce^{3+} for **16-Ce** and $(PPh_4)_2[Ln_2(\mu\text{-}2\text{-}FBz)_2(2\text{-}FBz)_6(H_2O)_2]$ where Ln is Eu^{3+} for **17-Eu**, Tb^{3+} for **18-Tb**, Dy^{3+} for **19-Dy**, Er^{3+} for **20-Er** and Yb^{3+} for **21-Yb**. The synthesis procedure consists as follows: 2-fluorobenzoic acid (140.1 mg, 1 mmol) and potassium hydroxide (61.7 mg, 1.1 mmol) were dissolved in 20 mL of ethanol/water (1:1). The mixture was magnetically stirred till dissolution of the reactants. Then, the tetraphenylphosphonium chloride (PPh_4Cl) was slowly added to the mixture containing the deprotonated 2-fluorobenzoate anion (2-FBz). The reaction mixture was stirred for about 30 minutes always verifying the complete dissolution of PPh_4Cl. After, an ethanolic solution (10 mL) containing the respective $Ln(NO_3)_3\cdot nH_2O$ salt (0.25 mmol) was added to the pot reaction and the mixture was stirred for one hour. The clear solutions were allowed to crystallize at room temperature by slow evaporation. After 10-15 days square-shaped crystals suitable for monocrystal X-Ray diffraction appeared. The crystals were obtained by filtration with high yields above 75%. Despite our attempts, we were unable to obtain the samarium compound. The obtained powder concerning this lanthanide ion doesn’t match to the powder patterns as will be showed in the following Section.

Further characterization of these compounds was realized by carrying out elemental analysis, Table 3. 8 Elemental analysis of compounds **16-Ce** to **20-Yb** and Infra-red Spectroscopy Table 3. 9.

Table 3. 8 Elemental analysis of compounds **16-Ce** to **20-Yb**

	Calculated		Found	
Compound	**%C**	**%H**	**%C**	**%H**
16-Ce **$C_{56}H_{36}Ce_2F_8$ O_{18},2($C_{24}H_{20}P$),2(H_2O), 2157.9 g/mol**	57.88	3.73	58.01	3.80
17-Eu **$C_{56}H_{36}F_8O_{18}Eu_2$, 2($C_{24}H_{20}P$), 2131.6 g/mol**	58.60	3.59	59.00	3.20
18-Tb **$C_{56}H_{36}F_8O_{18}Tb_2$, 2($C_{24}H_{20}P$), 2145.4 g/mol**	58.22	3.50	58.80	3.10
19-Dy **$C_{56}H_{36}F_8O_{18}Dy_2$, 2($C_{24}H_{20}P$), 2152.6 g/mol**	58.02	3.55	58.00	3.70
20-Er **$C_{56}H_{36}F_8O_{18}Er_2$, 2($C_{24}H_{20}P$), 2162.2 g/mol**	57.77	3.54	57.5	3.80
21-Yb **$C_{56}H_{36}F_8O_{18}Yb_2$, 2($C_{24}H_{20}P$), 2173.7 g/mol**	57.46	3.52	57.91	3.21

Table 3. 9 Selected bands (cm^{-1}) for **15-Ce** to **20-Yb** (s=strong, m=medium and w=weak, br=broad) obtained in ATR-IR spectroscopy.

15-Ce	3313(br), 1592(s), 1539(s), 1483(m), 1439(m), 1389(s, split), 1214(s), 1104(m, split), 862(s), 759(m), 719(m),682(m), 659(m), 519(s)
16-Eu	3313(br), 1592(s), 1539(s), 1483(m), 1439(m), 1389(s, split), 1214(s), 1104(m, split), 862(s), 759(m), 719(m),682(m), 660(m), 519(s)
17-Tb	3313(br), 1592(s), 1539(s), 1483(m), 1439(m), 1389(s, split), 1214(s), 1104(m, split), 862(s), 759(m), 719(m),682(m), 660(m), 519(s)
18-Dy	3355(br), 1592(s), 1539(s), 1482(m), 1440(m), 1390(s, split), 1215(s), 1105(m, split), 863(s), 759(m), 719(m),682(m), 659(m), 519(s)
19-Er	3357(br), 1593(s), 1539(s), 1483(m), 1440(m), 1391(s, split), 1215(s), 1106(m, split), 864(s), 759(m), 722(m),682(m), 659(m),

	520(s)
20-Yb	3100(br), 1592(s), 1539(s), 1483(m), 1440(m), 1402(s, split), 1215(s), 1110(m, split), 864(s), 755(m), 723(m),682(m), 659(m), 520(s)

3.1.2.2 Structural characterization

Single Crystal X-Ray diffraction was measured on crystals of **16-Ce**, **18-Tb** and **21-Yb**. Compounds **18-Tb** and **21-Yb** showed the same structural motif while in the structure of **16-Ce** there is a slight difference in the coordination mode of the bridging ligands. Thus, crystal structure of both, **16-Ce** and **21-Yb** will be illustrated hereafter. Selected bond distances and crystallographic details are compiled in Table 3. 10 and Table APX.VI.1.

Table 3. 10 Selected bond lengths (Å) of compounds **16-Ce**, **18-Tb** and **21-Yb**. The symmetry transformation used to generate equivalent atoms is _a: 1-x,1-y,1-z.

	16-Ce		**18-Tb**	**21-Yb**
Ce1-O1	2.556(2)	**Ln-O1**	2.493(2)	2.444(13)
Ce1-O2	2.515(2)	**Ln-O2**	2.425(2)	2.362(13)
Ce1-O3	2.611(2)	**Ln-O3**	2.417(2)	2.387(13)
Ce1-O4	2.547(2)	**Ln-O4**	2.434(2)	2.378(13)
Ce1-O5	2.483(2)	**Ln-O5**	2.291(2)	2.233(13)
Ce1-O5_a	2.814(2)	**Ln-O6_a**	2.335(2)	2.265(14)
Ce1-O6_a	2.509(2)	**Ln-O7**	2.312(2)	2.254(12)
Ce1-O7	2.403(2)	**Ln-O8**	2.447(2)	2.396(14)
Ce1-O8	2.524(2)	**Ln---Ln_a**	4.838	4.810
Ce1---Ce1_a	4.388			

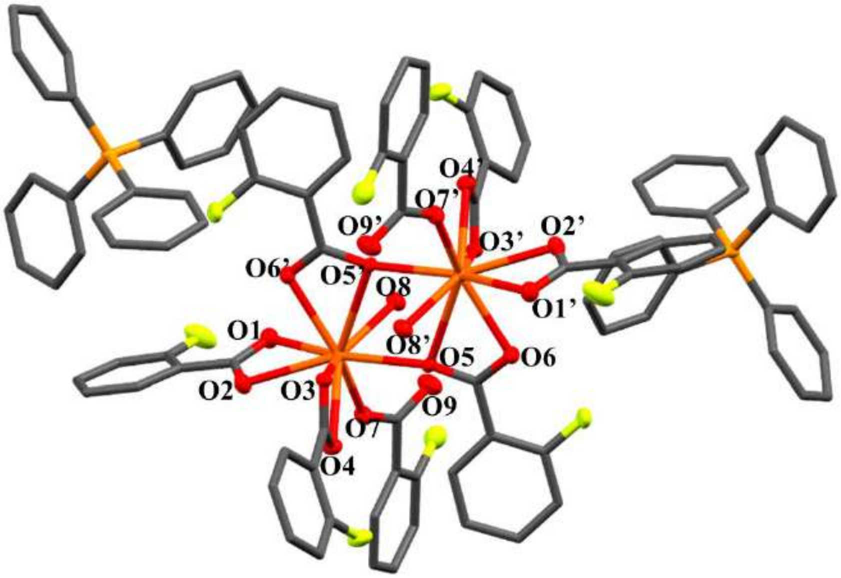

Figure 3. 19 Partially labelled representation of **16-Ce** crystal structure. Hydrogen atoms have been omitted for clarity. Color code: Ce=dark orange, O=red, C=grey, F=green, P=light orange. The symmetry transformation used to generate equivalent atoms is ‘: 1-x,1-y,1-z

Figure 3. 20 Coordination geometry of compound **16-Ce** superimposed to the ideal muffin-like polyhedron.

Compound **16-Ce** crystallizes in a monoclinic crystal system in a P 21/c space group. It consists of a dinuclear entity where each Ce^{3+} ion has a coordination number of 9, Figure 3. 19. The CeO_9 coordination sphere is set up forming a geometry that is close to an ideal Muffin-like (MFF-9, C_s) polyhedron with a CShM value of 2.511, Figure 3. 20. There are two 2-FBz ligands in the chelating coordination mode (O1, O2, O3 and O4), with Ce-O bond distances ranging 2.515-2.611 Å, and one 2-FBz molecule that coordinates only by one oxygen atom of the carboxylate group (O7) in a monodentate coordination mode, Scheme 3.2d), with Ce-O bond length of 2.403 Å. The Ce^{3+} centers, in the dinuclear structure, are linked through two 2-FBz ligands by three O atoms (O5, O5_a and O_6) in the chelating-bridging coordination mode, Scheme 3.2 b), with Ce-O distances in the range of 2.483-2.814 Å. Finally, coordination sphere of Ce^{3+} is completed by an O atom (O8) from a H_2O molecule with Ce-O bond distance of 2.523 Å. The intramolecular Ce1---Ce1_a distance is 4.388 Å. Two PPh_4^+ cations counteract the -II negative charge of the coordination compound. In addition, two water molecules crystallize within the crystal lattice. The symmetry transformation used to generate equivalent atoms is _a: 1-x,1-y,1-z.

On the other hand, the crystal structures of **18-Tb** and **21-Yb** are slightly different from **16-Ce**. Compounds **18-Tb** and **21-Yb** are isostructural therefore only structure of **18-Tb** will be described.

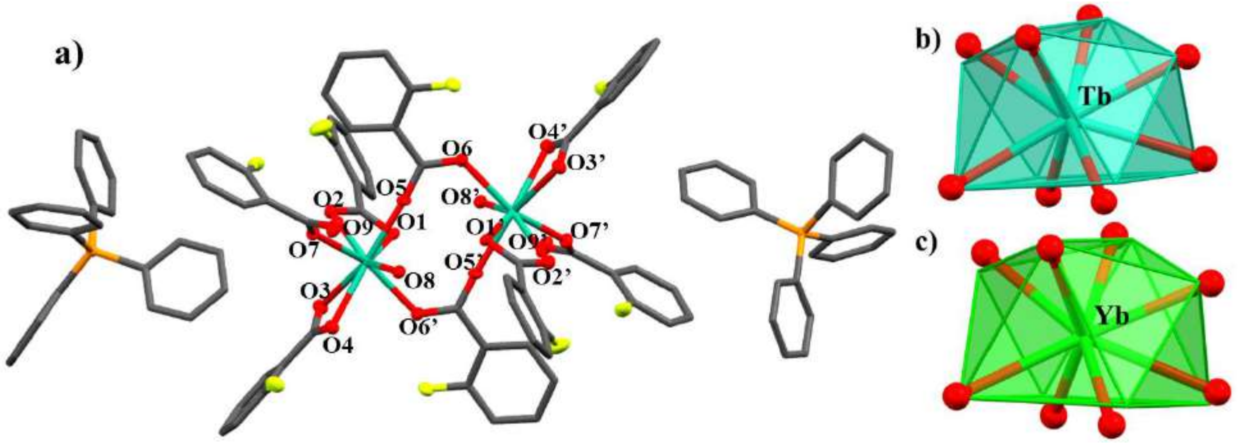

Figure 3. 21 a) Partially labelled plot of structure **18-Tb**. Hydrogen atoms are omitted for better clarification. Color code: Tb=blue, O=red, C=grey, F=green and P=light orange. The symmetry transformation used to generate equivalent atoms is ‘: 1-x,1-y,1-z b) and c) Coordination geometry of compounds **18-Tb** and **21-Yb** respectively**,** superimposed to the ideal Biaugmented Trigonal Prism polyhedron.

18-Tb consists of a dinuclear molecule that crystallizes in a monoclinic crystal system in a P21/n space group, Figure 3. 21 a). Each Tb^{3+} center is found octacoordinated with a coordination TbO$_8$ geometry that resembles to a distorted Biaugmented trigonal prism (BTPR-8, C$_{2v}$) with a CShM value of 2.444. The CShM value calculated for **21-Yb** structure was 2.475, Figure 3. 21 b) and c). Furthermore, Terbium’s coordination sphere consists of two 2-FBz ligands coordinating in the bidentate chelating mode with Tb-O (O1, O2, O3 and O4) bond lengths ranging from 2.417 to 2.493 Å and the O7 atom from a 2-FBz coordinating in the monodentate coordination mode with a Tb-O bond distance of 2.312 Å. Moreover, a H$_2$O molecule is also coordinated to the Tb^{3+} ion by O8 with a Tb-O distance of 2.447 Å. Finally, two PPh$_4^+$ cations counteract the -II negative charge of the coordination compound. The main difference between structures **18-Tb** and **16-Ce** is that in the Terbium’s motif, the lanthanide centers are bridged through two 2-FBz ligands in the symmetrical *syn-syn* bidentate bridging coordination mode, Scheme 3.2a), by O5 and O6_a (2.291 and 2.335 Å) instead of the bridging-chelating mode found in **16-Ce**. Variation in the coordination arrangement of the bridging ligands causes the Tb^{3+} ion coordination number to decrease from 9 to 8. Furthermore, the two H_2O molecules that co-crystallize in the crystal lattice of compound **16-Ce** are absent in structures of **18-Tb** and **21-Yb**.

The observed structural change in both 2-FBz families (**8-Ce** to **15-Yb** and **16-Ce** to **21-Yb**), where the Ce^{3+} complexes exhibit a distinct molecular arrangement compared to other lanthanides, may be attributed to the phenomenon known as lanthanide contraction.[21] This effect refers to the gradual decrease in the ionic radius of lanthanide(III) ions as the atomic number increases. Ce^{3+} has a greater ionic radius than the rest of Ln^{3+} used in this work. Due to larger size, it tends to coordinate to more donor atoms, thus increasing the coordination number. In this case, this produces a structural change in the Cerium compounds respect to the rest of the lanthanide ions. This effect is also seen in the overall Ln-O distances which are larger for the **16-Ce** compounds, and they become shorter on diminishing the ionic radius **18-Tb** >**21-Yb**. However, the Ln---Ln intermolecular distance, is larger for **18-Tb** (4.838 Å) and **21-Yb** (4.810 Å**)** in comparation to the **16-Ce** (4.388 Å). This is due to the bridging ligand coordination mode. The bridging-chelating mode offer an extra coordination ligand generating the Ln-O-Ln angle of 111.73º, shortening in this way the Ce1---Ce1_a intramolecular distance.

The dinuclear molecules together with the PPh_4^+ counterions set in the crystal lattice by means of H---π stacking interactions and other weak Van der Waals interactions, Figure 3. 22. In both structures, **16-Ce** and **18-Tb**, the H---π interactions take place between *i)* a ring from a PPh_4^+ entity and a H atom from an sp^2 C of a 2-FBz bridging ligand, *ii)* the centroid of a 2-FBz ligand in the chelating coordination mode and a H from an sp^2 C atom from an aromatic ring of a PPh_4^+ counterion and *iii)* the centroid of an aromatic ring of a 2-FBz bridging ligand and the H atom of a sp^2 C from another PPh_4^+ unit. The Centroid---H intermolecular distances range from 2.620 to 2.890 Å in **16-Ce**, from 2.810 to 2.920 Å in **18-Tb** and from 2.800 to 2.940 Å in **21-Yb**. Moreover, it is worth considering a π---π stacking interaction that appears in structures **18-Tb** and **21-Yb**, which is not present in **16-Ce** because the centroids in the latter are too far apart. The π---π stacking interaction occurs between the centroids of the aromatic ring from a 2-FBz in the chelating coordination mode and a ring of a PPh_4^+. The considered intermolecular distances are found between the molecules that constitute each $(PPh_4)_2[Ln_2(\mu\text{-}2\text{-}FBz)_2(2\text{-}FBz)_6(H_2O)_2]$

structural unit. Then each structural unit expands in the crystal lattice by means of weak Van der Waals interactions.

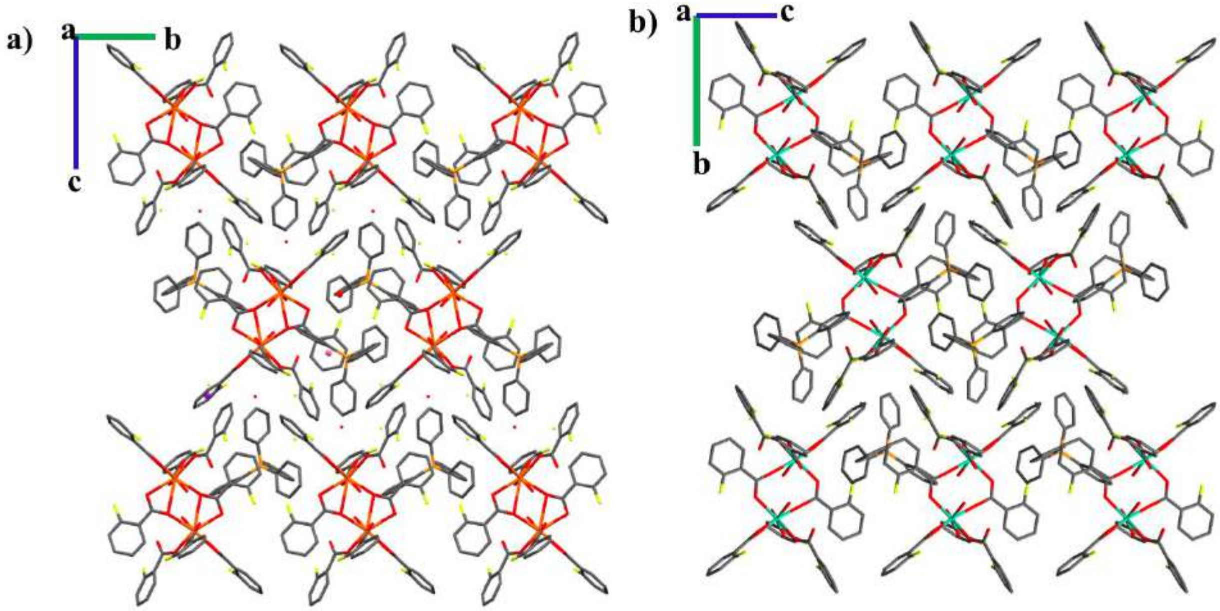

Figure 3. 22 Crystal packing of compounds a) **16-Ce** and b) **18-Tb.**

To ensure phase purity along all the polycrystalline powder compounds, PXRD measurements were carried out for **16-Ce**, **18-Tb** and **21-Yb** and compared to the PXRD patterns calculated from the crystal structures. For the three of them, the powder measurement agrees with the calculated one. Owing to the structural differences between **16-Ce** compared to **18-Tb** and **21-Yb**, their powder patterns are different. Furthermore, PXRD were measured to polycrystalline samples containing Eu^{3+}, Dy^{3+} and Er^{3+} lanthanides (compounds **17-Eu**, **19-Dy** and **20-Er** respectively). The obtained diffractograms matched the calculated patterns of structures **18-Tb** and **21-Yb**, confirming their isostructural nature as well as phase purity in all the powder samples, Figure 3. 23. Finally, synthesis with Samarium was also carried out, nevertheless the obtained powder diffractogram was significantly different from the powder patterns of **16-Ce**, **18-Tb** and **21-Yb**.

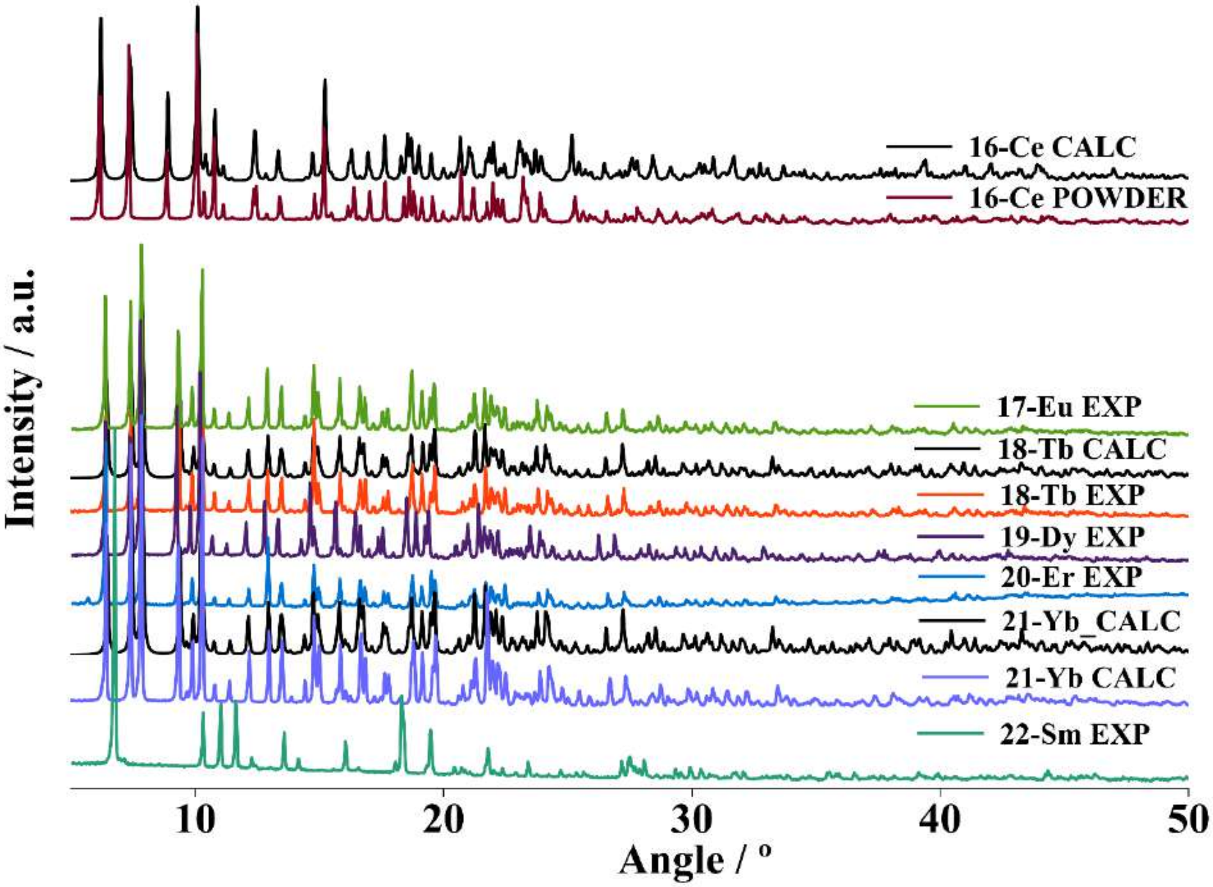

Figure 3. 23 Powder X-Ray Diffraction of compounds **16-Ce** to **22-Sm**. CALC stands for the calculated Powder patterns obtained from the crystal structure and EXP for the measured diffractograms of those samples.

3.1.2.3 Luminescence studies

Photoluminescent properties of compounds **17-Eu**, **18-Tb** and **19-Dy** have been studied in solid state at room temperature. Unfortunately, Erbium and Ytterbium analogues (**20-Er** and **21-Yb**) showed very weak luminescence response, therefore meaningful excitation and emission spectra couldn't be obtained.

Excitation spectra collected at the maximum emission wavelength (λ_{em}) of 614 nm ($^5D_0 \rightarrow {}^7F_2$) for **17-Eu**, of 545 nm ($^5D_4 \rightarrow {}^7F_5$) for **18-Tb** and of 574 nm ($^4F_{9/2} \rightarrow {}^6H_{13/2}$) for **19-Dy** are showed in Figure 3. 24a), b) and c). The excitation spectra show a broad and intense band above 300 nm for **18-Tb** and **19-Dy** while for **17-Eu** the band is even broader and the signal starts appearing at wavelengths above 400 nm. It is assigned to 2-FBz ligand centered $\pi \rightarrow \pi^*$ and $n \rightarrow \pi^*$ excitation transitions. Moreover, in excitation spectrum of **19-Dy** some bands, way weaker than ligand excitation, appear at 325, 351 and 364 nm which correspond to Dy^{3+} excitation transitions from its own electronic states, and they are assigned to $^6H_{15}\rightarrow{}^4M_{17/2}$ at 325 nm, $^6H_{15}\rightarrow{}^6P_{7/2}$ at 351 nm and $^6H_{15}\rightarrow{}^6P_{5/2}$ at 364 nm respectively.[19] In the three excitation spectra the band corresponding to ligand absorption clearly prevail, anticipating a rather good sensitization effect.

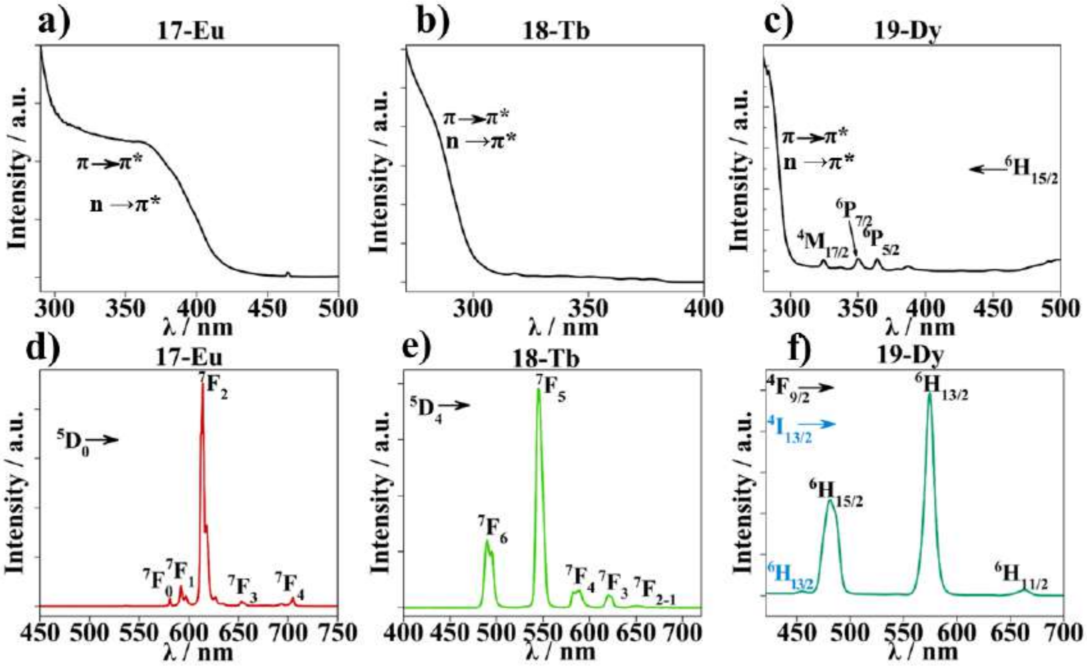

Figure 3. 24 a), b) and c) show excitation spectra of **17-Eu**, **18-Tb** and **19-Dy,** respectively, and d), e) and f) show emission spectra of **17-Eu**, **18-Tb** and **19-Dy**. Excitation spectra were monitored at the λ_{em} of 614 nm for **17-Eu**, at 545 nm for **18-Tb** and at 574 nm for **19-Dy**. Emission spectra were monitored at the λ_{exc} of 281 nm for **17-Eu**, at 280 nm for **18-Tb** and at 300 nm for **19-Dy**.

Exposure of **17-Eu**, **18-Tb** and **19-Dy** polycrystalline samples at the excitation wavelength (λ_{exc}) of 281, 280 and 300 nm led to the characteristic lanthanide *f-f* emission transitions, Figure 3. 24d), e) and f). The distinctive red and green luminescence could be seen with the naked eye from **17-Eu** and **18-Tb** samples, Figure 3. 25.

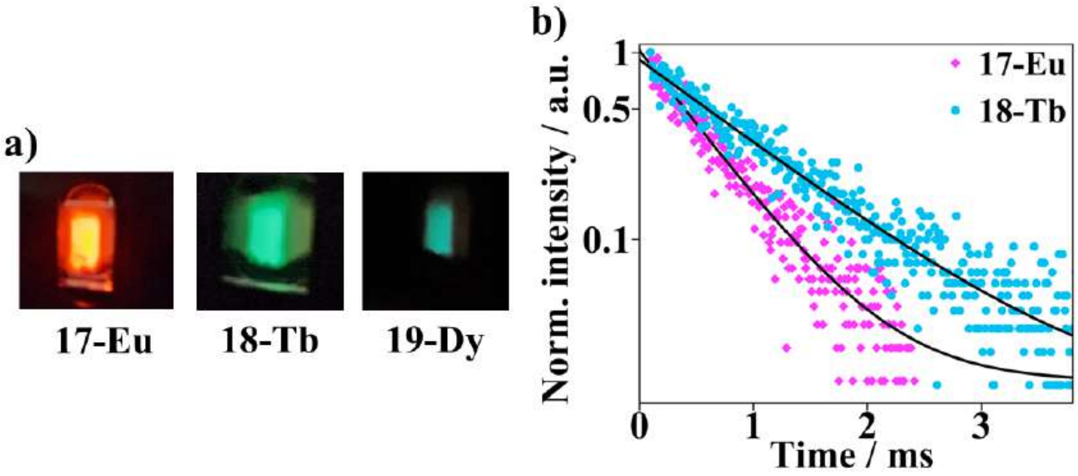

Figure 3. 25 a) Emission colors of compounds **17-Eu**, **18-Tb** and **19-Dy** under irradiation of a UV lamp and b) Luminescence lifetimes of componds **17-Eu** and **18-Tb** monitored at a λ_{exc}=300 nm and λ_{em}=614 nm for **17-Eu** and at λ_{exc}=280 nm and λ_{em} =545 nm for **18-Tb**. Continuous black line corresponds to the monoexponential fitting with: $I(t) = I_0 e^{-\frac{t}{\tau_{obs}}} + C$

The emission spectrum of **17-Eu** reveals multiple bands at 581, 592 and 614 nm, the latter being the most intense one. These bands correspond to the $^5D_0 \rightarrow {}^7F_0$ (ΔJ=0), $^5D_0 \rightarrow {}^7F_1$ (which is split into two components due to crystal field) and $^5D_0 \rightarrow {}^7F_2$ transitions, respectively. The band at 591 nm is a pure magnetic dipole transition which intensity is practically unaffected by the Eu^{3+} environment. On the other hand, the 614 nm band is an hypersensitive band since it is an electric dipole transition. At least three components of this band can be discerned which may indicate that the Eu^{3+} emitting center is not occupying an inversion symmetry site inside the structure. This is consistent with the coordination geometry derived from the SHAPE calculation which revealed a distorted Biaugmented trigonal prism polyhedron with a C_{2v} symmetry. In addition, the less intense bands found at 653 and 705 nm are assigned to $^5D_0 \rightarrow {}^7F_3$ and $^5D_0 \rightarrow {}^7F_4$ transitions respectively.[18a,21] For compound **18-Tb**, the bands found at 490, 545, 586 and 621 nm are assigned to the transitions from terbium's $^5D_4$ emissive state to the ground $^7F_6$, $^7F_5$, $^7F_4$ and $^7F_3$ states, respectively. Residual emission from the ligand molecules was not observed, neither in **17-Eu** nor in **18-Tb** spectra, indicating a good sensitization effect from the 2-FBz to the lanthanide emitting states.

Three emission bands originating from Dy^{3+} $^4F_{9/2}$ emissive energy level are differentiated in the **19-Dy** spectrum, at 481, 575 nm and a weaker one at 664 nm. The bands are assigned to $^7F_{9/2}\rightarrow{}^6H_{15/2}$, $^7F_{9/2}\rightarrow{}^6H_{13/2}$ and $^7F_{9/2}\rightarrow{}^6H_{11/2}$ transitions, respectively. A very weak signal at 454 nm is observed. This band is assigned to the forbidden magnetic dipole transition ($\Delta J=0$) $^4I_{13/2}\rightarrow{}^6H_{13/2}$, such as in the case of $^5D_0\rightarrow{}^7F_0$ of the Eu^{3+} ion.[22] However, 2-FBz ligand emission was observed for **19-Dy** within the 350-400 nm range (spectrum not shown) just as the Dy^{3+} analogue of the previous *Section*, compound **13-Dy**. This emission predominated over dysprosium's luminescence, as evidenced by the blue color observed by the naked eye under UV light, Figure 3. 25.

Moreover, overall photoluminescence quantum yields (ϕ_{Ln}^{L}) and luminescence lifetimes (τ_{obs}) were measured for the brightest polycrystalline samples, **17-Eu** and **18-Tb**, at the excitation wavelength of 300 and 280 nm respectively. Terbium compound yielded higher ϕ_{Ln}^{L} and τ_{obs} compared to Europium analogue. The ϕ_{Ln}^{L} resulted of 0.20 for **17-Eu** while it increased to 0.34 for **18-Tb**. Luminescence lifetimes were monitored at the emission wavelength of 614 nm ($^5D_0\rightarrow{}^7F_2$) for **17-Eu** and of 545 nm ($^5D_4\rightarrow{}^7F_5$) for **18-Tb**. Both decay curves followed a monoexponential law and the resulting τ_{obs} values were 0.61 and 1.02 ms for **17-Eu** and **18-Tb** respectively. The presence of a single decay time component suggests a single radiative deactivation process.[18a, 21]

In addition, the radiative lifetime (τ_{rad}) from the $^5D_0$ emissive level of **17-Eu** was calculated from the corrected emission spectrum, with Equation 1.8,[25] and it resulted of 1.50 ms. Then the intrinsic quantum yield (ϕ_{Ln}^{Ln}) was calculated from $\phi_{Ln}^{Ln} = \frac{k_r}{k_r+k_{nr}} = \frac{\tau_{obs}}{\tau_{rad}}$, and it was 0.41 for **17-Eu**. The sensitization efficiency (η_{sens}) calculated with Equation 1.2 resulted of 0.50. As stated before, this parameter gives us information about the efficiency of transferred energy from the ligand moieties to the resonant emissive state of the lanthanide ion. Sensitization efficiency of **17-Eu** has turned out to be almost half that the value obtained for compound $[Eu_2(\mu\text{-}2\text{-}FBz)_4(2\text{-}FBz)_2(H2\text{-}FBz)_2(H_2O)_2]$ (**10-Eu**). Also, the overall quantum yields of Tb and Eu are reduced respect to the obtained for compounds **10-Eu** and **12-Tb,** *see section 3.1.1.3*. This may be due to the presence of monodentate 2-FBz ligand which may act as an electron-withdrawing group retaining electron density, thus slightly quenching sensitization efficiency of **17-Eu** and **18-Tb**.

Besides, compounds **17-Eu** and **18-Tb** with formula $(PPh_4)_2[Ln_2(\mu\text{-}2\text{-}FBz)_2(2\text{-}FBz)_6(H_2O)_2]$, hold a slight distorted Biaugmented Trigonal prism (C_{2v} point group) octacoordinated geometry whereas compounds **10-Eu** and **12-Tb** showed a Muffin-like (Cs point group) nonacoordinate polyhedron geometry**.** The symmetry around the coordination environment of the lanthanides centers is higher in the presented **17-Eu** and **18-Tb** compounds. As previously mentioned, to enhance lanthanide *f-f* emission transitions (as well as excitation transitions), the greater the asymmetry around the Ln^{3+} center, the better. Since larger asymmetry may produce *f*-mixing, making in this way the intraconfigurational transitions less prohibited. The asymmetry around **10-Eu** and **12-Tb** (*section 3.1.1.3.*) provided by the O atoms from the ligands, may enhance *f-f* transitions leading to higher luminescence intensity compared to **17-Eu** and **18-Tb.**

3.1.2.4 Magnetic studies

Direct current (dc) measurements

Direct current magnetic susceptibility (χ_M) and magnetization (M) experiments were measured on **16-Ce**, **17-Eu**, **18-Tb**, **19-Dy**, **20-Er** and **21-Yb** polycrystalline samples. The χ_M measurements were carried out under an external direct current (dc) magnetic field of 0.3 T in the 2-300 K temperature range. The $\chi_M T$ dependence with T plots are presented in Figure 3. 26. At room temperature (300 K) the $\chi_M T$ values are 0.98, 2.78, 25.00, 28.33, 22.21, 4.87 $cm^3mol^{-1}K$ for **16-Ce**, **17-Eu**, **18-Tb**, **19-Dy**, **20-Er** and **21-Yb** respectively. For two isolated Ln^{3+} cations, the calculated $\chi_M T$ values are: 1.6 $cm^3mol^{-1}K$ for Ce^{3+} ground state $^2F_{5/2}$ and g_J=6/7; 0 $cm^3mol^{-1}K$ for Eu^{3+} ground state $^7F_0$; 23.64 $cm^3mol^{-1}K$ for Tb^{3+} ground state $^7F_6$ and g_J=3/2; 28.34 $cm^3mol^{-1}K$ for Dy^{3+} ground state $^6H_{15/2}$ and g_J=4/3; 22.96 $cm^3mol^{-1}K$ for Er^{3+} ground state $^2F_{7/2}$ and g_J=6/5 and 5.14 $cm^3mol^{-1}K$ for Yb^{3+} ground state $^2F_{7/2}$ and g_J=8.7.[21a]

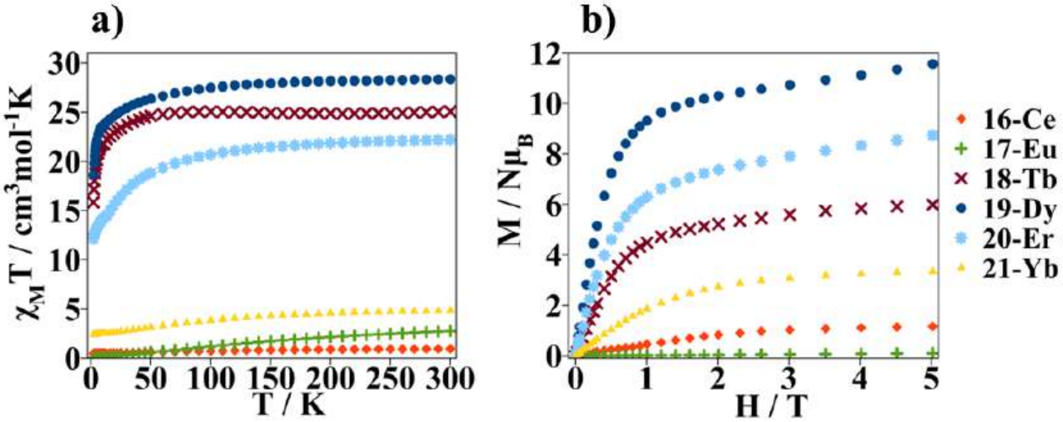

Figure 3. 26 a) χ_MT *vs* T plot, measured under an external magnetic dc field of 0.3 T and b) Magnetization with external magnetic field dependence measured at 2K of compounds **16-Ce** to **21-Yb.**

The experimental $\chi_M T$ value measured at room temperature of sample **17-Eu** is larger than the calculated value. The electronic ground state of an Eu^{3+} ion (^{7}F) splits due to spin-orbit coupling into the respective *J* states which are $^7F_{J=0-6}$. For the Eu^{3+} ion, the spin-orbit coupling energy gap (λ) between the excited *J* states and the ground state is defined by the small value of 300 cm^{-1}. Thus, excited *J* states, particularly the $^7F_1$, are closer in energy to the ground state so they become thermally populated at room temperature as a result of the small λ value. Consequently, the $\chi_M T$ parameter at 300 K exceeds the calculated value for an isolated Eu^{3+} ion, which only considers the population of the $^7F_0$ ground state. The decrease of $\chi_M T$ *vs* T upon cooling the sample is attributed to thermal depopulation of the higher in energy ^7F_J states. At 2 K, the $\chi_M T$ value of **17-Eu** is 0.03 cm^{3}mol^{-1}K, confirming that at low temperatures, the non-magnetic ground state (*J* = 0) is stabilized.[27] For the rest of compounds, experimental room temperature $\chi_M T$ values closely match the calculated ones.

In compounds **16-Ce** and **21-Yb,** the $\chi_M T$ *vs* T curves gradually decrease on cooling the samples. At the limit temperature of 2 K the $\chi_M T$ values are 0.50 and 2.35 cm^{3}mol^{-1}K, for **16-Ce** and **21-Yb** respectively. For **18-Tb, 19-Dy** and **20-Er** polycrystalline samples, the $\chi_M T$ *vs* T curves show similar behavior. The $\chi_M T$ magnetic susceptibility values stay practically constant on lowering the temperature down to ~50 K. Below this temperature, $\chi_M T$ values drop suddenly to 15.84 and 18.63 cm^{3}mol^{-1}K at 2 K for **18-Tb** and **19-Dy** while the decrease of $\chi_M T$ to 12.16 cm^{3}mol^{-1}K at 2

K is more progressive for **20-Er**. The diminution of $\chi_M T$ on cooling the samples, can be attributed to one or a combination of different phenomena: *i)* due to thermal depopulation of the excited m_j doublets (of the ground J state) generated by the crystal field perturbation, *ii)* due to dipolar interactions between the molecules of the crystal lattice and *iii)* due to weak antiferromagnetic coupling between the Ln^{3+} centers constituting each dinuclear unit. The contracted nature of the 4*f* electrons in lanthanide(IIII) ions make magnetic exchange coupling interactions rather weak. The intramolecular distance between Ln---Ln of the same dinuclear unit is of 4.388 Å for **16-Ce**, 4.838 Å for **18-Tb** and 4.810 Å for **21-Yb** crystal structures. In structures **16-Ce** to **21-Yb**, the Ln^{3+} cations are connected through two 2-FBz molecules in the bridging-chelating (**16-Ce**) and bridging (**17-Eu** to **21-Yb**) coordination mode. The two extra 2-FBz bridging-chelating ligands found in structures **8-Ce** to **15-Yb** (See *Section 3.1.1.1* of this *Chapter*) are not present for the former dinuclear units, enlarging this way the Ln---Ln intramolecular distance leading to a precluded magnetic superexchange between lanthanide centers.[21a,30,29]

Magnetization dependence with applied magnetic field curves measured at 2 K for the former compounds are depicted in Figure 3. 26b). Magnetization increases suddenly on applying an external magnetic field from 0 to ~1 T for all compounds. Then, for all compounds the *M vs* H curves increase gradually without reaching saturation of the magnetization $g_J \cdot J$. Finally, the magnetization values of **17-Eu** at 2 K are maintained at 0 $N\mu_B$, as expected.

Alternating current (ac) measurements

Alternating current (ac) measurements were performed for compounds **16-Ce** to **21-Yb** (except for **17-Eu**) to investigate spin dynamics in case of slow relaxation of the magnetization. At H_{dc} = 0 T, the magnetic moment of all the above compounds followed the oscillating field consistently, leading to no dependence of the χ_M'' component with temperature and frequency. Nonetheless, under exposure of a direct current (dc) magnetic field, compounds **16-Ce** and **21-Yb** showed slow relaxation of the magnetization. Measurement of χ_M' and χ_M'' at different dc magnetic fields at the constant temperature of 2 K and 2.5 K for **16-Ce** and **21-Yb** respectively, revealed that the H_{dc} optimal field was 0.3 T for **16-Ce** and 0.2 T for **21-Yb**, Figure 3. 27.

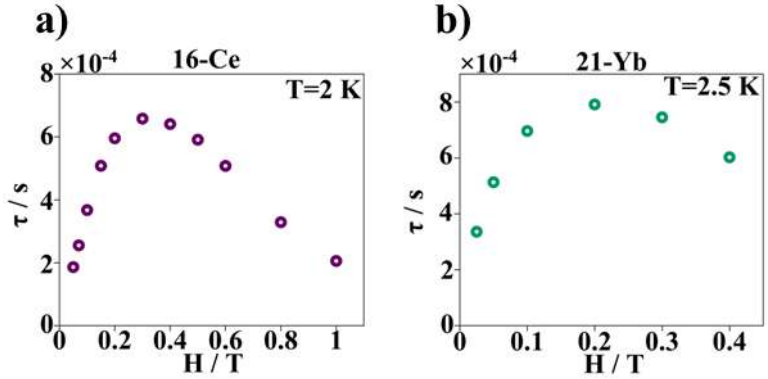

Figure 3. 27 Relaxation times in front of static magnetic field measured at the constant temperature of 2 K for a) **16-Ce** and of 2.5 K for b) **21-Yb**.

Regarding compound **19-Dy**, measurements of χ_M'' were tried under different H_{dc} fields and at different oscillating frequencies. Out-of-phase magnetic susceptibility showed somehow dependence with oscillating frequency and temperature; however, this dependence was spotted as tails at 2 K and not as maxima data points, Figure APX.VI.1. This suggests a strong QTM that cannot be eliminated even with the application of an external magnetic field, due to the lack of axial symmetry which promotes rhombic contribution in dysprosium's m_j ground state.

Under the optimal H_{dc} of 0.3 T, compound **16-Ce**, showed χ_M'' maxima in both, the χ_M'' *vs* T and χ_M'' *vs* oscillating frequency plots, indicating slow relaxation of the magnetization. The χ_M'' maxima appeared on cooling the polycrystalline sample at about 4 K down to 2 K, Figure 3. 28a). Moreover, χ_M'' maxima are dependent on temperature and move progressively to higher frequencies on increasing temperature indicating that magnetization relaxes via a temperature dependent mechanism, Figure 3. 28b).

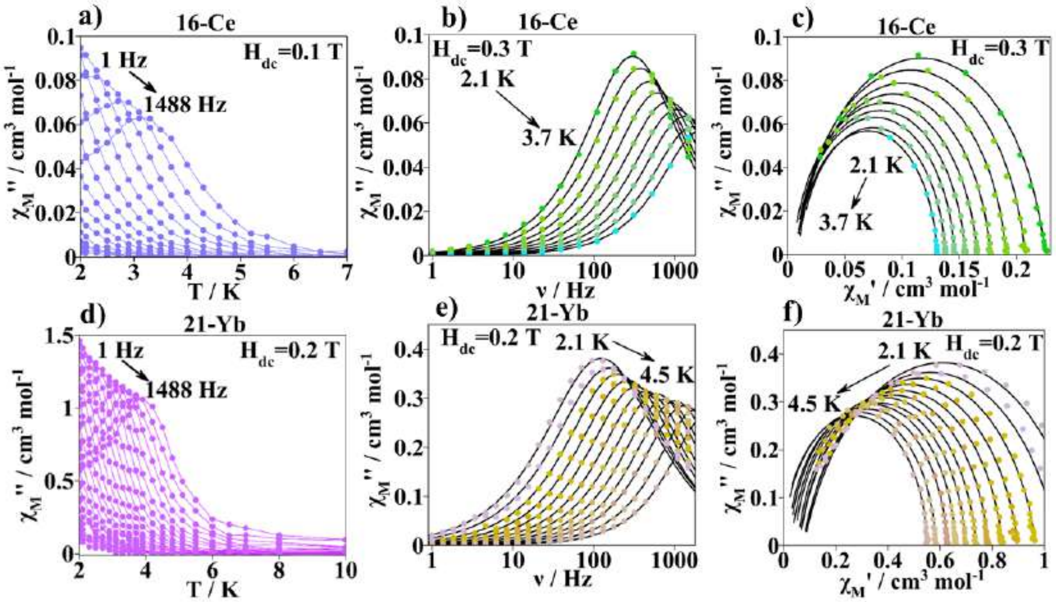

Figure 3. 28 a) and d) χ_M'' *vs* T plots of **16-Ce** and **21-Yb**. The continuous line is a guide to the eye b) and e) are the χ_M'' *vs* ν plots of **16-Ce** and **21-Yb**. The continuous black line corresponds to the fitting to the Generalized Debye model and c) and f) are the Cole-Cole plots for **16-Ce** and **21-Yb**. Continuous black line represents the fitting to the Generalized Debye model.

Representation of **16-Ce** magnetic data in the so-called Cole-Cole plots leads to unsymmetrical semicircles that can be successfully fitted to the Generalized Debye model with Equation 1.32 of *Chapter 1*, in the 2.1 to 3.7 K temperature range, Figure 3. 28c). The α values obtained from such fitting are in the range of 0.1(2.1 K) to 0.04(3.7 K). Regarding compound **21-Yb**, it showed χ_M'' maxima with temperature in the 2 to 4.5 K temperature range whereas χ_M'' *vs* ν peaks move progressively to higher oscillating frequencies on increasing temperature from 2 to 4.5 K, Figure 3. 28d) and e). Representation of χ_M' and χ_M'' components in the Cole-Cole plots shows semicircles that become incomplete on increasing temperature. Even so, **21-Yb** magnetic data could be fitted with the generalized Debye model for the semicircles in the 2.1-4.5 K temperature range and the obtained α values range from 0.2(2.1 K) to 0.009(4.5 K). The α values decrease on increasing temperature till a value of almost 0 at 4.5 K. This indicates that at high temperature only one mechanism dominates respect to the others, since distribution of relaxation times is practically zero.

$$\tau^{-1} = \tau_0^{-1} \exp\left(\frac{-\Delta E}{k_B T}\right)$$ **Equation 3.3**

$$\tau^{-1} = CT^n + AT$$ **Equation 3. 4**

Thereafter, relaxation of magnetization times with temperature in the ln(τ) *vs* T^{-1} plots of compounds **16-Ce** and **21-Yb**, Figure 3. 29, show a rather inexistent linear trend in the higher temperature range. Nevertheless, as a first approximation, the curves were fitted with the Arrhenius law that describes the Orbach relaxation mechanism, Equation 3.3, and the obtained values were ΔE =10.13 cm^{-1} and τ_0 = $1.44 \cdot 10^{-6}$ for **16-Ce** and ΔE = 13.52 cm^{-1} and τ_0 = $9.14 \cdot 10^{-7}$ for **21-Yb,** FigureAPX.VI.2. The values of the effective energy barrier are very low indicating that relaxation of the magnetization may proceed by an under-barrier mechanism. The best fit of the ln(τ) vs T^{-1} curves was obtained when a combination of Raman and Direct mechanisms were considered, τ−1=$CT^n + AT$ **Equation 3.** . The fitted parameters yielded C = 25.89 $s^{-1}K^{-n}$ and n = 4.68 for Raman and A = 459.33 $s^{-1}K^{-1}$ for Direct mechanism for **16-Ce** and C = 3.67 $s^{-1}K^{-n}$ and n = 5.57 for Raman and A = 260 $s^{-1}K^{-1}$ for Direct mechanism for **21-Yb.**

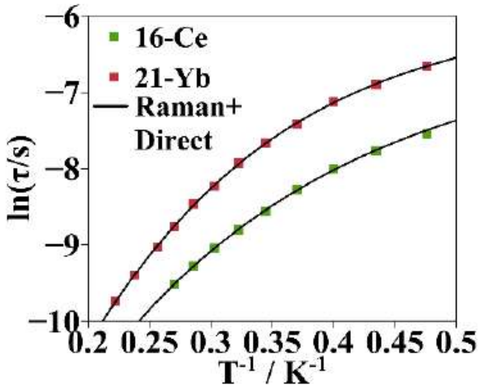

Figure 3. 29 ln(τ) *vs* T^{-1} plots for compounds **16-Ce** and **21-Yb** of ac magnetic data measured under an external direct current magnetic field of 0.3 T and of 0.2 T for **16-Ce** and **21-Yb**, respectively. Continuous black lines correspond to the fit considering equation for Raman and Direct relaxation mechanisms.

3.2 Compounds derived from 2,6-Difluorobenzoic acid (2,6-HF2Bz):

As already stated, presence of H_2O molecules coordinated to the lanthanide ion is a drawback in terms of luminescence efficiency due to presence of high oscillator bonds such as O-H.

Several trials were made to obtain a coordination sphere where the lanthanide is totally coordinated by deprotonated 2-FBz ligands with a predicted formula of $[Ln_2(2\text{-FBz})_8]^{2-}$. However, by using 2-Fluorobenzoic acid we couldn't obtain any kind of anhydrous fluorobenzoate lanthanide coordination compound.

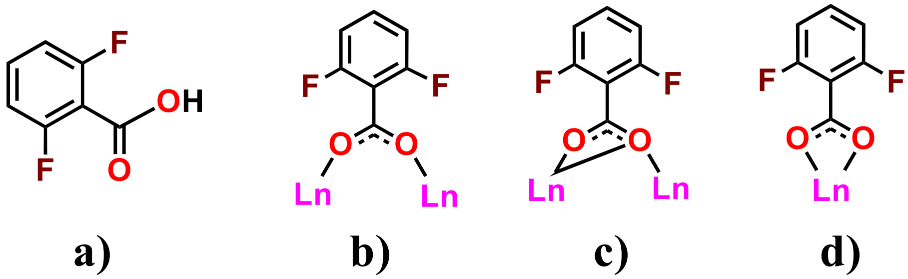

Scheme 3.3. a) 2,6-Difluorobenzoic acid (2,6-HF2Bz). Coordination modes of 2,6-F2Bz found in compounds of *Chapter 3*: b) symmetrical *syn-syn* bidentate bridging, c) chelating-bridging and d) chelating.

Following this research line, we have used other fluorinated ligand: the 2,6-difluorobenzoate, 2,6-F2Bz (Scheme 3.3a) which was not studied before in multi-property lanthanide coordination compounds.[13c-e] With this ligand, both C-H ortho positions (the ones closer to the emitting lanthanide) are fluorinated. Moreover, the addition of a second fluorine atom should provide more steric hindrance, thereby making it more difficult for H_2O molecules to enter in the coordination sphere. With the hypothesis of increasing the luminescence overall quantum yield by *i)* adding a second C-F bond in the benzene *orto* position and *ii)* totally removing the H_2O molecules coordinated to the Ln^{3+}, the 2,6-F2Bz ligand was used in two different straightforward synthetic ways from which two families of lanthanide compounds with anhydrous structural motifs were obtained. The first showed a general formula of $(HPy)_2[Ln_2(\mu\text{-}2,6\text{-F2Bz})_4(NO_3)_4]$ (**23-Eu**, **24-Tb**, **25-Dy**, **26-Nd** and **27-Yb**) while the second presented the $(HPy)_2[Ln_2(\mu$-2,6-

F2Bz)$_4$(2,6-F2Bz)$_4$] formula (**28-Eu**, **29-Tb**, **30-Dy**, **31-Nd** and **32-Gd**), HPy^+ is the pyridinium cation. Interestingly, only a slight change in the solvent used during the reaction made possible the isolation of two different series of compounds. Finally, neither of the two obtained structural series has water molecules in their coordination sphere.

Obtention of **23-Eu** to **27-Yb** and of **28-Eu** to **32-Gd** took place in a basic medium with a clear excess of the carboxylate molecule to ensure its coordination. Pyridine was used to grant the basic media and to provide a counter ion in the final structure. Two different structural motifs were obtained when the same synthesis was carried out at different proportions of H_2O/EtOH solvents (Scheme 3.4). When a mix of EtOH/H_2O (1:1) is used as solvent reaction, the final compounds consist of a dinuclear entity with eight 2,6-F2Bz ligands coordinated to the lanthanide centers (**28-Eu** to **32-Gd**). On the other hand, when the solvent is EtOH 99%, the final compound encompasses a dinuclear structure where the two Ln^{3+} atoms are linked by four 2,6-F2Bz bridging ligands and four NO_3^- anions acting as chelating ligands resulting in a never published $[Ln_2(\mu\text{-}2,6\text{-F2Bz})_4(NO_3)_4]^{2-}$ structural motif (**23-Eu** to **27-Yb)**. In the following sections of *Chapter 3*, *Section 3.2.1* and *Section 3.2.2*, the structural description, luminescence and magnetic properties will be developed for all of the above compounds.

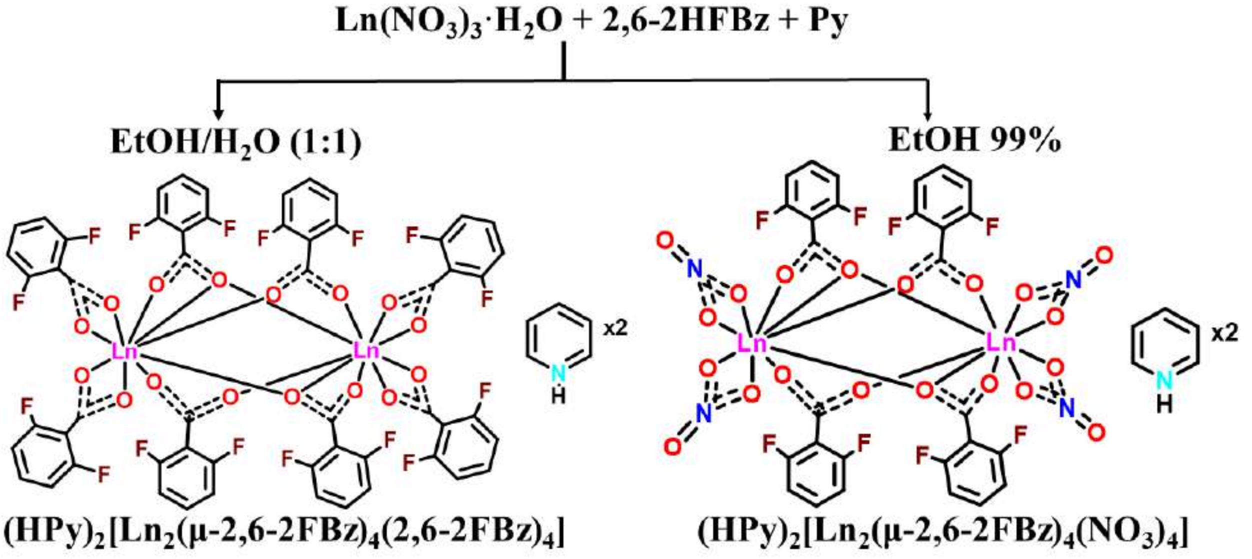

Scheme 3.4. Figure of $(HPy)_2[Ln_2(\mu\text{-}2,6\text{-F2Bz})_4(2,6\text{-F2Bz})_4]$ (right) and $(HPy)_2[Ln_2(\mu\text{-}2,6\text{-F2Bz})_4(NO_3)_4]$ (left).

3.2.1 Compounds with formula $(HPy)_2[Ln_2(2,6\text{-}F2Bz)_4(NO_3)_2]$

3.2.1.1 Experimental procedure

Synthesis to obtain compounds **23-Eu**, **24-Tb**, **25-Dy**, **26-Nd** and **27-Yb** was carried out as follows: an ethanol 99% solution (20ml) containing $Ln(NO_3)_3{\cdot}nH_2O$ (0.9 mmol) was added to another ethanol 99% solution (20 ml) containing 2,6-difluorobenzoic acid (632.4 mg, 4.0 mmol) and pyridine (316.4 mg, 4 mmol). The solution was stirred for 30 minutes and then left to stand at room temperature. Single crystals with a rhombic shape suitable for X-Ray diffraction were obtained within one month. The crystals were separated by filtration and washed with the lowest amount of cold ethanol. The compounds were obtained with yields ranging from 40 to 65 %.

Through this straightforward room temperature synthetic procedure, lanthanide(III) dinuclear compounds showing the molecular formula $(HPy)_2[Ln_2(\mu\text{-}2,6\text{-}F2Bz)_4(NO_3)_2]$ were successfully isolated. This series of compounds show anew structural motif. The Ln^{3+}, 2,6-difluorobenzoic acid and pyridine ratio used in the syntheses was 1: 4.4: 4.4. Even though an excess of fluorinated ligand with respect to the lanthanide ion was used, nitrate molecules in the chelating coordination mode from the reactant lanthanide(III) salt were left in the final structure.

Further characterization of these compounds was performed by carrying out elemental analysis, Table 3. 11 and ATR-Infrared Spectroscopy, Table 3. 12.

Table 3. 11 Elemental analysis of compounds **23-Eu** to **27-Yb**

	Calculated			**Found**		
Compound	**%C**	**%N**	**%H**	**%C**	**%N**	**%H**
23-Eu $C_{28}H_{12}Eu_2F_8N_4O_{20}, 2(C_5H_6N)$ **1340.5 g/mol**	34.04	6.27	1.80	34.56	6.00	1.67
24-Tb $C_{28}H_{12}Tb_2F_8N_4O_{20}, 2(C_5H_6N)$ **1354.5 g/mol**	33.69	6.20	1.78	34.01	6.01	1.62
25-Dy $C_{28}H_{12}Dy_2F_8N_4O_{20}, 2(C_5H_6N)$ **1361.6 g/mol**	33.51	6.17	1.77	34.8	5.90	1.30
26-Nd $C_{28}H_{12}F_8N_4Nd_2O_{20},2(C_5H_6N)$ **1325 g/mol**	34.44	6.34	1.82	35.03	6.02	1.72
27-Yb $C_{28}H_{12}Nd_2F_8N_4O_{20}Yb_2,2(C_5H_6N)$ **1382.7 g/mol**	33.00	6.08	1.74	33.9	5.89	1.52

Table 3. 12 Selected bands (cm^{-1}) of **23-Eu** to **27-Yb** (s=strong, m=medium and w=weak, br=broad) obtained in ATR-IR spectroscopy.

23-Eu	3256-2891 (w), 1602(s, split), 1539(w),1506(w), 1493(w), 1459(s), 1406(s), 1317(m), 1270(w), 1230(m), 1001(s), 865(m),795(m), 735(m), 996(m), 579(s), 516(m)
24-Tb	3256-2891 (w), 1599(s, split), 1540(w),1506(w), 1494(w), 1460(s), 1406(s), 1317(m), 1270(w), 1230(m), 1001(s), 865(m),795(m), 735(m), 996(m), 579(s), 516(m)
25-Dy	3252-2897 (w), 1599(s, split), 1543(w),1506(w), 1494(w), 1462(s), 1407(s), 1317(m), 1270(w), 1231(m), 1001(s), 865(m),795(m), 735(m), 996(m), 579(s), 516(m)
26-Nd	3252-2897 (w), 1618(s, split), 1544(w),1506(w), 1496(w), 1463(s), 1407(s), 1318(m), 1270(w), 1232(m), 1003(s), 865(m),796(m), 736(m), 996(m), 583(s), 516(m)
27-Yb	3252-2897 (w), 1619(s, split), 1545(w),1506(w), 1497(w), 1464(s), 1407(s), 1319(m), 1270(w), 1233(m), 1004(s), 866(m),797(m), 737(m), 997(m), 584(s), 516(m)

3.2.1.2 Structural characterization

Single crystal X-Ray diffraction was performed for europium (**23-Eu**) and terbium (**24-Tb**) analogues. Selected bond distances and crystallographic information are listed in Table 3. 13 and Table APX.VII.1. Since both compounds yielded the same structural motif, only the structure of compound **23-Eu** is discussed below. A partially labelled plot of **23-Eu** structure is depicted in Figure 3. 30a. Compound **23-Eu** crystallized in a monoclinic crystal system in a P21/n space group. Each asymmetric unit is constituted of one Eu^{3+} ion, two chelating nitrate molecules and two 2,6-difluorobenzoate (2,6-F2Bz) ligands in the bridging coordination mode. To neutralize the negative charge, a protonated pyridine molecule (HPy) acts as the counterion. After application of symmetry operations provided by P21/n space group the asymmetric unit expands in space forming the dinuclear entities. In each dinuclear unit, both Eu^{3+} atoms are connected through four 2,6-F2Bz ligands acting as bridging ligands. The ligands are found in two different coordination modes, two of them are in the symmetrical *syn-syn* bidentate bridging coordination mode (η_1:η_1:μ_2) (Scheme 3.3b) with Eu-O bond lengths of 2.348 and 2.345 Å. The other two 2,6-F2Bz molecules are best described as chelating-bridging (η_1:η_2:μ_2) (Scheme 3.3c) and the Eu-O bond distances range from 2.353 to 2.554 Å. The Eu---Eu_a intramolecular distance is 3.886 Å. Moreover, there are two NO_3^- molecules coordinated to each Eu^{3+} center in the chelating coordination mode, with Eu-O bond distances in the range of 2.451-2.539 Å. Each Eu^{3+} ion exhibits a coordination number of nine. The degree of distortion with respect to the ideal polyhedron is quantified as Continuous Shape Measurements (CShM) values with the SHAPE program.[15] For compound **23-Eu**, the polyhedron defining europium's coordination sphere is close to a Muffin geometry (MFF-9, C_s) with a CShM value of 2.105, Figure 3. 30b. For compound **24-Tb**, the TbO_9 coordination was close to the same polyhedral geometry as **23-Eu** with a CShM value of 2.016 for the MFF-9.

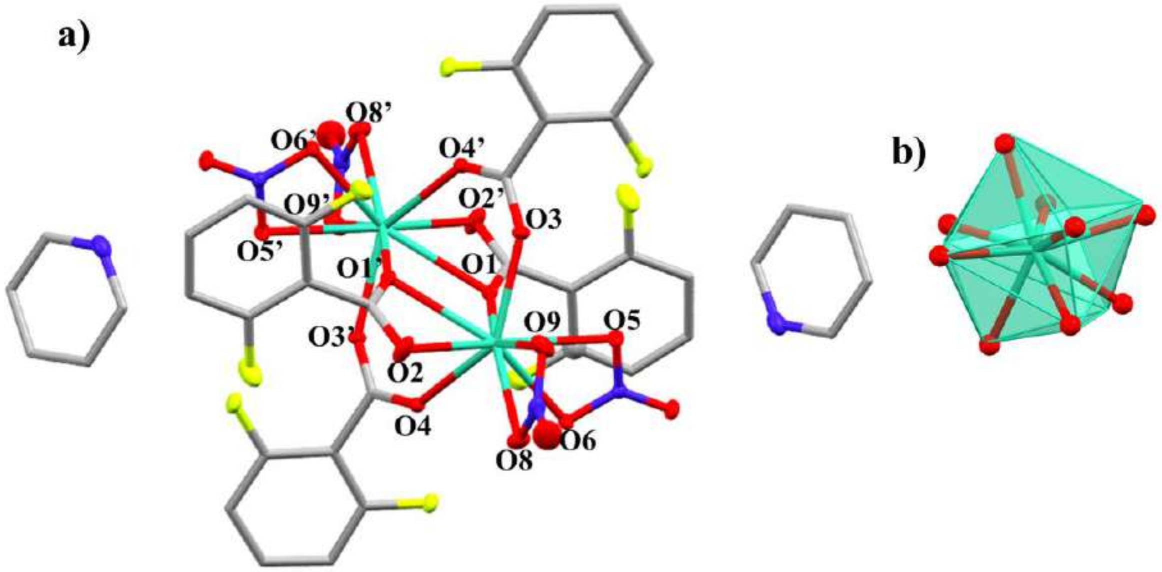

Figure 3. 30 a) Partially labelled plot of compound **23-Eu**. Hydrogen atoms have been omitted for clarity. The symmetry transformation used to generate equivalent atoms is ': 1-x, 1-y, 1-z. Color code: grey = C, red = O, green = F, light blue = N and turquoise = Eu, b) Muffin polyhedron (MFF-9, C_s) compared with the real positions of **23-Eu** coordinating atoms.

The Eu^{3+} dinuclear molecules are packed through π---π and H---π stacking intermolecular interactions along the crystal lattice. The pyridinium cation (Cg1) and one aromatic ring from one of the 2,6-F2Bz ligands in the bridging coordination mode (Cg2) interact through a π---π stacking interaction with a Cg1---Cg2 distance of 3.571 Å. Moreover, the H---π stacking interaction is established by Cg2 and one H-atom (H5) from the aromatic ring of the 2,6-F2Bz ligand in the chelating bridging coordination mode, Figure 3. 31, with a H5---Cg2 intermolecular distance of 2.840 Å.[35] In the crystal structure of compound **24-Tb**, these intermolecular distances are 3.570 Å for the π---π stacking and 2.850 Å for the H----π stacking interactions.

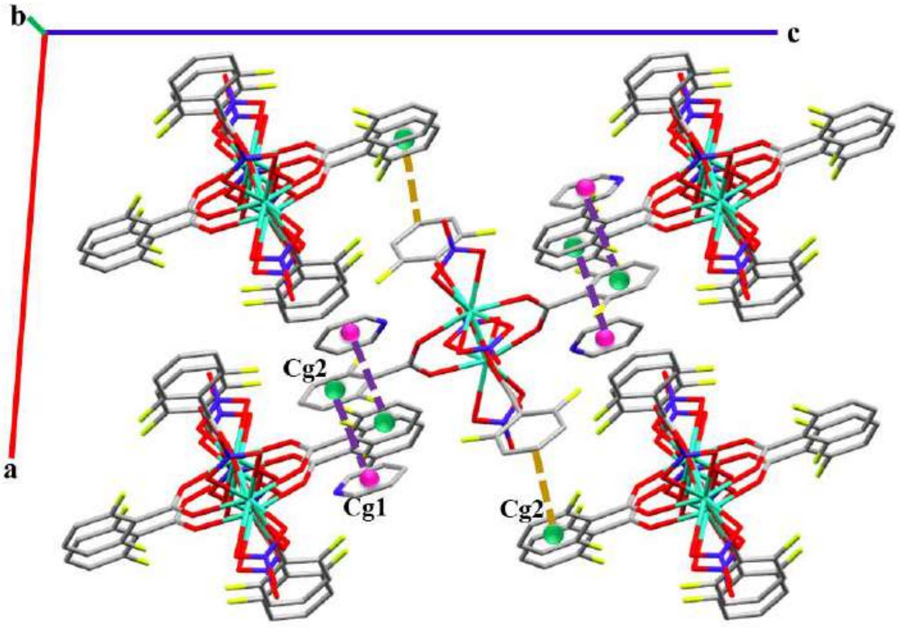

Figure 3. 31 Crystal packing of dinuclear molecules of **23-Eu**. Discontinuous purple lines represent π-π interactions and discontinuous yellow lines represent H-π interactions.

Table 3. 13 Selected bond distances (Å) of **23-Eu** and **24-Tb**. Translation of symmetry to generate equivalent atoms code is _a: 1-x,1-y,1-z

23-Eu		**24-Tb**	
Eu1-O1	2.353(8)	**Tb1-O1**	2.445(13)
Eu1-O3	2.345(9)	**Tb1-O2**	2.426(12)
Eu1-O5	2.491(9)	**Tb1-O4**	2.461(11)
Eu1-O6	2.539(9)	**Tb1-O5**	2.520(11)
Eu1-O8	2.451(11)	**Tb1-O7**	2.488(13)
Eu1-O9	2.470(11)	**Tb1-O8**	2.534(11)
Eu1-O1_a	2.554(8)	**Tb1-O9**	2.320(11)
Eu1-O2_a	2.509(11)	**Tb1-O8_a**	2.325(10)
Eu1-O4_a	2.348(9)	**Tb1-O11_a**	2.320(11)
Eu---Eu_a	3.886(9)	**Tb---Tb'**	3.849(11)

To ensure phase purity along all the polycrystalline powders, Powder X-Ray Diffraction (PXRD) of **23-Eu** and **24-Tb** were carried out. The measured diffractograms and the calculated patterns from the single crystal structure matched, verifying phase purity. Moreover, to validate the isostructural nature of the synthetized **25-Dy**, **26-Nd** and **27-Yb** complexes, PXRD was measured also to those polycrystalline samples. Once more, the obtained diffractograms match the calculated ones from structures **23-Eu** and **24-Tb** therefore confirming that **23-Eu** to **27-Yb** are isostructural and only one type of structure is present in the polycrystalline powder, Figure 3. 32.

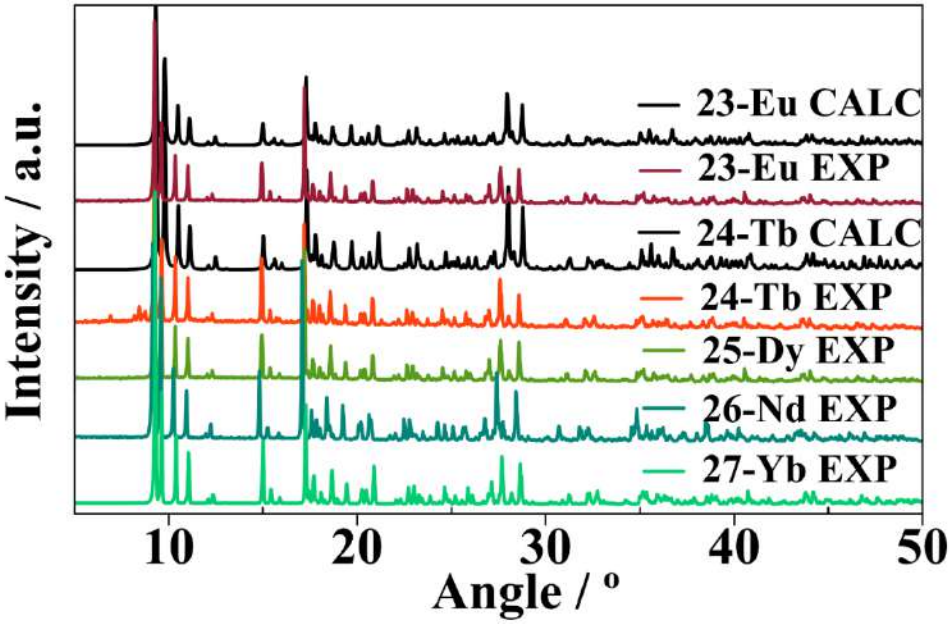

Figure 3. 32 Powder X-Ray Diffraction of compounds **23-Eu** to **27-Yb**. CALC stands for the calculated patterns form the Single Crystal structure and EXP for the diffractograms obtained from the PDRX measurement.

3.2.1.3 Luminescence properties

Luminescence studies were carried out for all the compounds in the solid state at room temperature. Excitation spectra were monitored at the emission wavelength (λ_{em}) of 616 nm ($^5D_0 \rightarrow ^7F_2$) for **23-Eu**, of 546 nm ($^5D_4 \rightarrow ^7F_5$) for **24-Tb**, of 574 nm ($^4F_{9/2} \rightarrow ^6H_{13/2}$) for **25-Dy**, of 1061nm ($^4F_{3/2} \rightarrow ^4I_{11/2}$) for **26-Nd** and of 988 nm ($^2F_{5/2} \rightarrow ^2F_{7/2}$) for **27-Yb**. All spectra show an increase of signal intensity above 300 nm, Figure 3. 33. It is assigned to $\pi \rightarrow \pi^*$ and $n \rightarrow \pi^*$ excitation transitions of the 2,6-F2Bz ligand. This band couldn't be fully recorded due to the instrument limitation measurement below 70 nm. Furthermore, bands due to lanthanide(III) intrinsic *f-f* excitation transitions are also discerned for **23-Eu** to **27-Yb**. The bands are assigned in each spectrum and a compilation of each band to the excitation transitions is found in Table 3. 14.

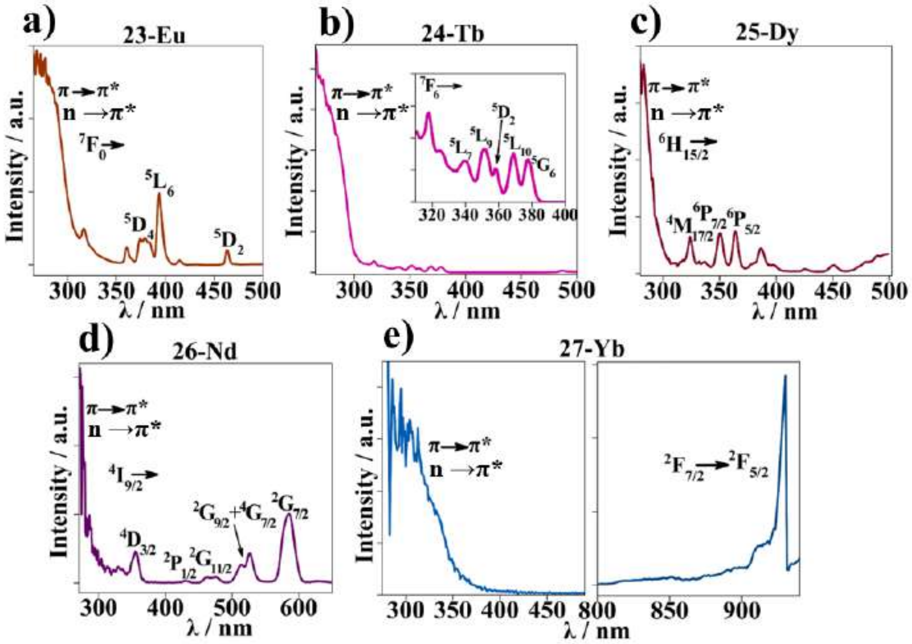

Figure 3. 33 Excitation spectra of **23-Eu** to **27-Yb** polycrystalline samples measured at room temperature.

Table 3. 14 Compilation of assignation of the bands to the excitation transitions of compounds **23-Eu** to **27-Yb**, left column, and to the emission transitions of **23-Eu** to **27-Yb**, right column.

23-Eu	**23-Eu**
$^{7}F_{0}\rightarrow{}^{5}D_{4}$ at 375 nm, $^{7}F_{0}\rightarrow{}^{5}L_{6}$ at 394 nm and $^{7}F_{0}\rightarrow{}^{5}D_{2}$ at 464 nm	$^{5}D_{0}\rightarrow{}^{7}F_{0}$ at 581 nm, $^{5}D_{0}\rightarrow{}^{7}F_{1}$ at 594 nm, $^{5}D_{0}\rightarrow{}^{7}F_{2}$ at 616 nm, $^{5}D_{0}\rightarrow{}^{7}F_{3}$ not seen, $^{5}D_{0}\rightarrow{}^{7}F_{4}$ at 697 nm
24-Tb	**24-Tb**
$^{7}F_{6}\rightarrow{}^{5}L_{7}$ at 340 nm, $^{7}F_{6}\rightarrow{}^{5}L_{9}$ at 352 nm, $^{7}F_{6}\rightarrow{}^{5}D_{2}$ at 359 nm, $^{7}F_{6}\rightarrow{}^{5}L_{10}$ at 369 nm and $^{7}F_{6}\rightarrow{}^{5}G_{6}$ at 378 nm	$^{5}D_{4}\rightarrow{}^{7}F_{6}$ at 491 nm, $^{5}D_{4}\rightarrow{}^{7}F_{5}$ at 546 nm, $^{5}D_{4}\rightarrow{}^{7}F_{4}$ at 587 nm, $^{5}D_{4}\rightarrow{}^{7}F_{3}$ at621 nm and $^{5}D_{4}\rightarrow{}^{7}F_{2-0}$ at 642-676 nm
25-Dy	**25-Dy**
$^{6}H_{15/2}\rightarrow{}^{4}M_{17/2}$ at 324 nm, $^{6}H_{15/2}\rightarrow{}^{6}P_{7/2}$ at 350 nm and $^{6}H_{15/2}\rightarrow{}^{6}P_{5/2}$ at 364 nm	$^{4}F_{9/2}\rightarrow{}^{6}H_{15/2}$ at 483 nm, $^{4}F_{9/2}\rightarrow{}^{6}H_{13/2}$ at 577 nm and $^{4}F_{9/2}\rightarrow{}^{6}H_{11/2}$ at 660 nm
26-Nd	**26-Nd**
$^{4}I_{9/2}\rightarrow{}^{4}D_{3/2}$ at 355 nm, $^{4}I_{9/2}\rightarrow{}^{2}P_{1/2}$ at 430 nm, $^{4}I_{9/2}\rightarrow{}^{2}G_{11/2}$ at 469 nm, $^{4}I_{9/2}\rightarrow{}^{2}G_{9/2}+{}^{4}G_{7/2}$ at 515-526 nm and $^{4}I_{9/2}\rightarrow{}^{2}G_{7/2}+{}^{2}G_{5/2}$ at 586 nm	$^{4}F_{3/2}\rightarrow{}^{4}I_{9/2}$ at 889 nm, $^{4}F_{3/2}\rightarrow{}^{4}I_{11/2}$ at 1061 nm, $^{4}F_{3/2}\rightarrow{}^{4}I_{13/2}$ at 1338 nm
27-Yb	**27-Yb**
$^{2}F_{7/2}\rightarrow{}^{2}F_{5/2}$ at 930 nm	$^{2}F_{5/2}\rightarrow{}^{2}F_{7/2}$ at 1008 nm

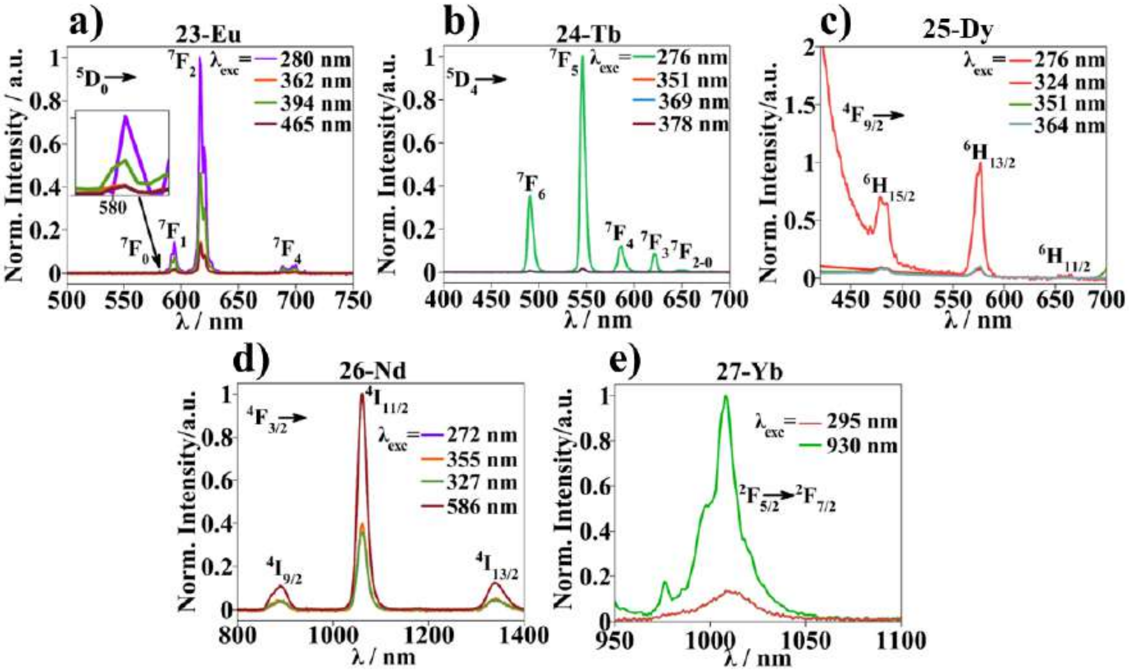

Figure 3. 34 Emission spectra of **23-Eu** to **27-Yb** polycrystalline samples measured at room temperature.

Emission spectra of all compounds were measured exciting the samples at the ligand centered absorption wavelength and at the *f-f* intrinsic lanthanide transitions. Excitation at the different λ_{exc} of all compounds induced the expected Ln^{3+} emission transitions, Figure 3. 34. For the sake of comparison of emission intensities, the same sample was excited at the different wavelengths at the same measurement conditions. Then emission spectra have been normalized to the higher in intensity band of the more intense spectrum for each lanthanide sample to compare the relative intensities on changing the excitation wavelength. Moreover, assignation of each emission band to the corresponding lanthanide(III) transition of **23-Eu** to **27-Yb** is found in Table 3. 14.

For the visible emitters **23-Eu**, **24-Tb** and **25-Dy**, stronger emission spectra are obtained when the polycrystalline samples are exposed at the λ_{exc} corresponding to 2,6-F2Bz ligand absorption wavelength, leading to luminescence that could be seen by the naked eye for the Eu^{3+} (red) and Tb^{3+} (green) analogues, Figure 3. 34 a) and b) and Figure 3. 35 b and c. Regarding **23-Eu** emission spectrum, $^5D_0\rightarrow{}^7F_0$ accounts to a forbidden transition by the ΔJ rule ($\Delta J=0, \pm1$, $J=0\nleftrightarrow0$), though for coordination geometries with C_{nv}, C_n or C_s symmetry, the electric dipole transition takes place due to mixing of higher configurations in the 4*f* wavefunctions due to crystal field perturbation (*J*-mixing). Nevertheless, $^5D_0\rightarrow{}^7F_0$ is still very weak compared to the other Eu^{3+} $^5D_0 \rightarrow ^7F_J$ emission transitions, Figure 3. 34 inset. In addition, the band at 594 nm which is assigned to $^5D_0 \rightarrow ^7F_1$ is practically independent of europium's environment due to its pure magnetic dipole character. The stronger band at 616 nm assigned to $^5D_0 \rightarrow ^7F_2$ is a hypersensitive band since it accounts for an electric dipole transition ($\Delta J = 2$). It appears split due to crystal field, indicating that europium ions are not occupying an inversion symmetry site inside the dinuclear structure which agrees with the coordination geometry obtained from the SHAPE calculations which resulted in a polyhedron with coordination geometry close to the ideal Muffin (C_s symmetry) and Spherical capped square antiprism (C_{4v} symmetry).[18a]

Nevertheless, though the characteristic emission bands of Dy^{3+} were observed in **25-Dy**, ligand emission fluorescence is perceived below 450 nm indicating a rather inefficient sensitization effect, Figure 3. 34 c). On the other hand, the nIR emitters, **26-Nd** and **27-Yb**, showed intense luminescence when the samples were excited at the wavelengths corresponding to the intrinsic *f-f* excitation transitions, at 586 nm ($^4I_{9/2} \rightarrow ^2G_{7/2} + ^2G_{5/2}$) for **26-Nd** and at 930 nm ($^2F_{7/2} \rightarrow ^2F_{5/2}$) for **27-Yb**, Figure 3. 34 d) and e). For **27-Yb**, splitting of the $^2F_{5/2} \rightarrow ^2F_{7/2}$ emission band due to crystal field is seen when exciting at the Yb^{3+} intrinsic *f-f* transition.[18]

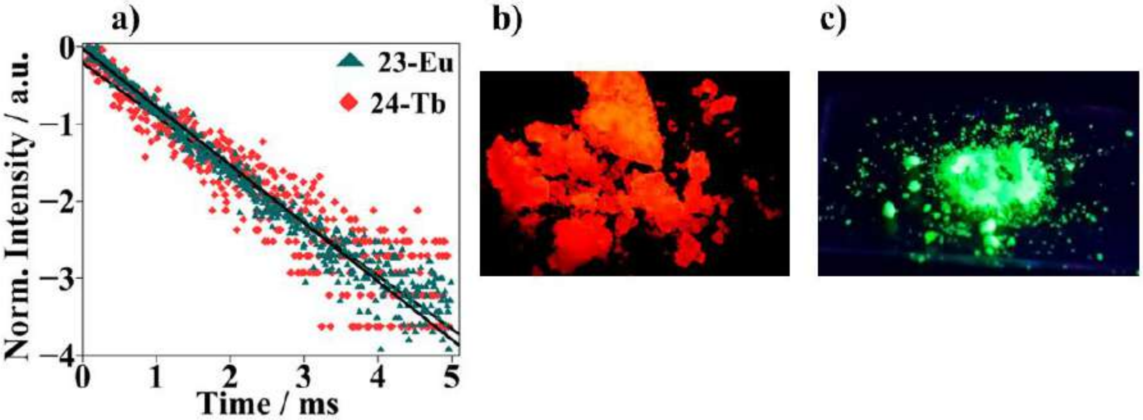

Figure 3. 35 a) Luminescence lifetime curves of compounds **23-Eu** and **24-Tb** presented in a semi-logarithmic plot. Solid black lines refer to the mono-exponential fit with $I(t) = I_0 e^{-\frac{t}{\tau_{obs}}} + C$. b) and c) emission color observed with the naked eye of **23-Eu** and **24-Tb** polycrystalline samples, respectively, under the radiation of the laboratory UV lamp.

Overall photoluminescence quantum yields (ϕ_{Ln}^{L}) and luminescence lifetimes (τ_{obs}) were measured for the brightest polycrystalline samples, **23-Eu** and **24-Tb**, at the excitation wavelength of 280 and 276 nm respectively. Both, ϕ_{Ln}^{L} and τ_{obs} yielded similar values for Eu^{3+} and Tb^{3+} complexes. The ϕ_{Ln}^{L} resulted of 0.07 for **23-Eu** and of 0.08 for **24-Tb**. Luminescence lifetimes were monitored at the emission wavelength of 616 nm ($^5D_0 \rightarrow {}^7F_2$) for **23-Eu** and of 546 nm ($^5D_4 \rightarrow {}^7F_5$) for **24-Tb**. Both decay curves followed a monoexponential law with τ_{obs} of 1.42 and of 1.48 ms for **23-Eu** and **24-Tb** respectively. The presence of a single decay time component is suggestive of a single radiative deactivation process.[18a,21]

In addition, the radiative lifetime (τ_{rad}) from the $^5D_0$ emissive level of **23-Eu** was calculated from the corrected emission spectrum, with Equation 1.8,[25] giving 1.60 ms. Then the intrinsic quantum yield (ϕ_{Ln}^{Ln}) can be calculated from $\phi_{Ln}^{Ln} = \frac{k_r}{k_r + k_{nr}} = \frac{\tau_{obs}}{\tau_{rad}}$ and it was 0.89. Following to that, the sensitization efficiency (η_{sens}) calculated with Equation.1.2 resulted of 0.08. As stated before, this parameter gives us information about the transferred energy from the ligands to the emissive excited state of the lanthanide ions. For **23-Eu**, η_{sens} resulted quite low indicating a rather poor sensitization efficiency of the ligand moieties to the Eu^{3+} ion [18a,36] Considering that in **23-Eu** and **24-Tb** crystal structures the coordinating H_2O molecules where erased, they showed rather low quantum yields and sensitization efficiency. This may account to the fact that four coordination positions of the each Ln^{3+} ion are occupied by two NO_3^- ions instead of the chromophore 2,6-F2Bz ligand, thus reducing the photons absorbed by the ligand transferred to the emitting lanthanide. However, the ϕ_{Ln}^{Ln} of **23-Eu** (0.89) is high compared to the Eu^{3+} complexes with 2-FBz previously presented in *Sections 3.1.1.3* and *3.1.2.3*, compounds **10-Eu** and **17-Eu** respectively. For **10-Eu** the ϕ_{Ln}^{Ln} was 0.28 whereas for **17-Eu** it yielded 0.41. This is on account of the absence of coordinating H_2O. The drawback in the $(HPy)_2[Ln_2(\mu\text{-}2,6\text{-}F2Bz)_4(NO_3)_4]$ systems is that they may present low extinction coefficient, because the number of 2,6-F2Bz antenna ligands has been reduced by half, leading poorer sensitization effect. Moreover, 2,6-F2Bz is a symmetric ligand, compared to 2-FBz. This increased symmetry around the Ln^{3+} could result in less *f*-orbital mixing, making the *f-f* transitions more forbidden by Laporte's rule compared to those in the 2-FBz family.

3.2.1.4 Magnetic properties

Direct current measurements

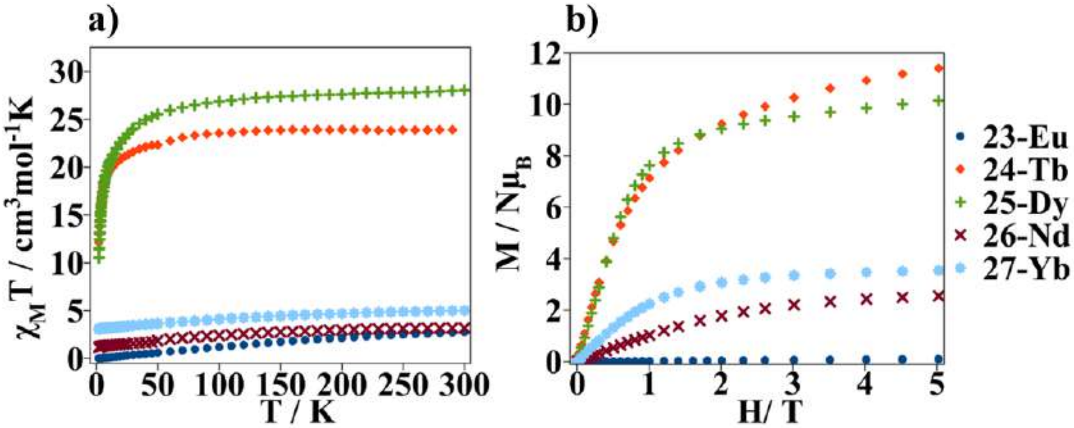

Figure 3. 36 a) Temperature dependence of $\chi_M T$ measured at an external static field of 0.3 T, for compounds **23-Eu** to **27-Yb** and b) Magnetization dependence with an external magnetic field measured at 2 K for compounds **23-Eu** to **27-Yb**.

Direct current (dc) magnetic susceptibility (χ_M) and magnetization (M) data were measured on **23-Eu** to **27-Yb** polycrystalline samples under a dc magnetic field of 0.3 T in the 2-300 K temperature range. Temperature dependence of $\chi_M T$ plot is shown in Figure 3. 36. After diamagnetic correction, $\chi_M T$ values at room temperature (300 K) are 2.78, 23.90, 28.03, 3.20 and 5.03 cm^3 mol^{-1} K for **23-Eu**, **24-Tb**, **25-Dy**, **26-Nd** and **27-Yb** respectively. For two isolated Ln^{3+} cations, the calculated $\chi_M T$ values are: 0 cm^3 mol^{-1} K for Eu^{3+} ground state $^7F_0$; 23.64 cm^3 mol^{-1} K for Tb^{3+} ground state $^7F_6$ and g_j=3/2, 28.34 cm^3 mol^{-1} K for Dy^{3+} ground state $^6H_{15/2}$ and g_j=4/3, 3.28 cm^3 mol^{-1} K for Nd^{3+} ground state $^4I_{9/2}$ and g_j=8/11 and 5.14 cm^3 mol^{-1} K for Yb^{3+} ground state $^2F_{7/2}$ and g_j=8.7.[21a] Experimental room temperature $\chi_M T$ values agree with the calculated ones for all compounds but **23-Eu** which value is higher than the expected 0 cm^3 mol^{-1} K. At room temperature, higher energy ^7F_J states, closer to the ground state ($^7F_0$), are thermally populated (mainly the $^7F_1$ state) due to the rather small spin-orbit coupling parameter (λ) between the $^7F_{(0\text{-}1)}$ electronic states. Then, on cooling the sample, the $\chi_M T$ *vs* T curve decreases gradually due to thermal depopulation of the excited ^7F_J states. At 2 K, $\chi_M T$ achieves the value of 0.03 cm^{3}mol^{-1}K confirming that at low temperature the non-magnetic ground state (J=0) is stabilized.[27]

For **24-Tb** and **25-Dy** polycrystalline samples the $\chi_M T$ *vs* T curves show similar behavior. On lowering the temperature, magnetic susceptibility values stay practically constant till 50 K are reached. Below this temperature, $\chi_M T$ values drop suddenly to 12.11 and 10.52 $cm^3mol^{-1}K$ for **24-Tb** and **25-Dy,** respectively, at 2 K. Regarding compounds **26-Nd** and **27-Yb**, the $\chi_M T$ *vs* T curves decrease gradually on cooling the samples along all the temperature range. The $\chi_M T$ values found at the limit temperature of 2 K are 1.19 and 3.06 $cm^3mol^{-1}K$ for **26-Nd** and **27-Yb** respectively. For the presented dinuclear compounds, Ln---Ln intramolecular distance are relatively short (3.886 Å for **23-Eu** and 3.849 Å for **24-Tb**). The decrease of $\chi_M T$ *vs* T curves on cooling the samples could be attributed to one a combination of different phenomena. Due to thermal depopulation of the excited m_j doublets (of the ground *J* state) generated by the crystal field perturbation or due to weak antiferromagnetic coupling between the Ln^{3+} centers though the contracted nature of 4*f* electrons in lanthanide(III) ions make magnetic exchange coupling interactions rather weak.[21a,30]

Magnetization (*M*) dependence with an applied magnetic field, monitored at 2 K of the presented compounds is depicted in Figure 3. 36. Magnetization was collected in an applied magnetic field ranging from 0 to 5 T for all compounds. M *vs* H curves increase suddenly from 0 to 1 T, approximately. Magnetization of **23-Eu** is maintained at 0 $N\mu_B$, as expected, while compounds **24-Tb**, **25-Dy**, **26-Nd** and **27-Yb** don’t show saturation of the magnetization ($g_J \cdot J$). Absence of saturation of the magnetization can be attributed to the crystal-field induced perturbation of the m_j levels as well as magnetic anisotropy.[37]

Alternating current measurements

Alternating current (ac) measurements were performed for compounds **24-Tb** to **27-Yb** to investigate spin dynamics in case of slow relaxation of the magnetization. Under an ac magnetic field of $4\cdot10^{-4}$ T oscillating between a 1-1488 Hz frequency range, compound **25-Dy** showed Single Molecule Magnet (SMM) behavior in the 1.9 to 3.7 K temperature range. Moreover, under an external direct current magnetic field (H_{dc}) of 0.3 and 0.15 T, compounds **26-Nd** and **27-Yb** respectively, showed slow relaxation of the magnetization. Compound **24-Tb** didn’t show out-of-phase magnetic susceptibility response neither at 0 dc magnetic field nor by applying external direct current magnetic fields (H_{dc}).

As mentioned, **25-Dy** is a SMM since it shows dependence of the out-of-phase magnetic susceptibility component (χ_M'') with temperature and the oscillating frequency under a 0 T H_{dc} field. For **25-Dy**, χ_M'' maxima appear in a rather narrow temperature range (2.1-3.5 K). Then on further cooling, χ_M'' *vs* T curves increase again without reaching a maximum, probably due to the Quantum Tunnelling of the Magnetization relaxation process that is taking place at such low temperatures, Figure 3. 37a).[31] As for the dependence of χ_M'' component with the oscillating frequency plot, at 1.9 K maxima are perceived at about 600 Hz. These maxima stay constant on increasing the temperature for a few more temperature measurements. χ_M'' peaks move progressively to higher frequencies suggesting that at low temperatures relaxation of the magnetization takes place through a temperature independent mechanism. Then, on increasing T, relaxation is governed by thermally activated processes such as Orbach or Raman mechanisms, Figure 3. 37b).[38] Representation of in-phase and out-of-phase magnetic susceptibility components (χ_M'' *vs* χ_M') in the Cole-Cole plot[39] lead to uncompleted and asymmetrical semicircles, Figure 3. 37c). Nevertheless, the curves can be successfully fitted to the Generalized Debye model described by the Casimir-Du Pré function (Equation 1.32)[40] using the CCFit software.[41] The obtained α parameters are in the range of 0.34 (at 1.9 K) to 0.05 (at 3.7 K) indicating that distribution of the time constants around magnetization relaxation times (τ) decrease on increasing temperature.

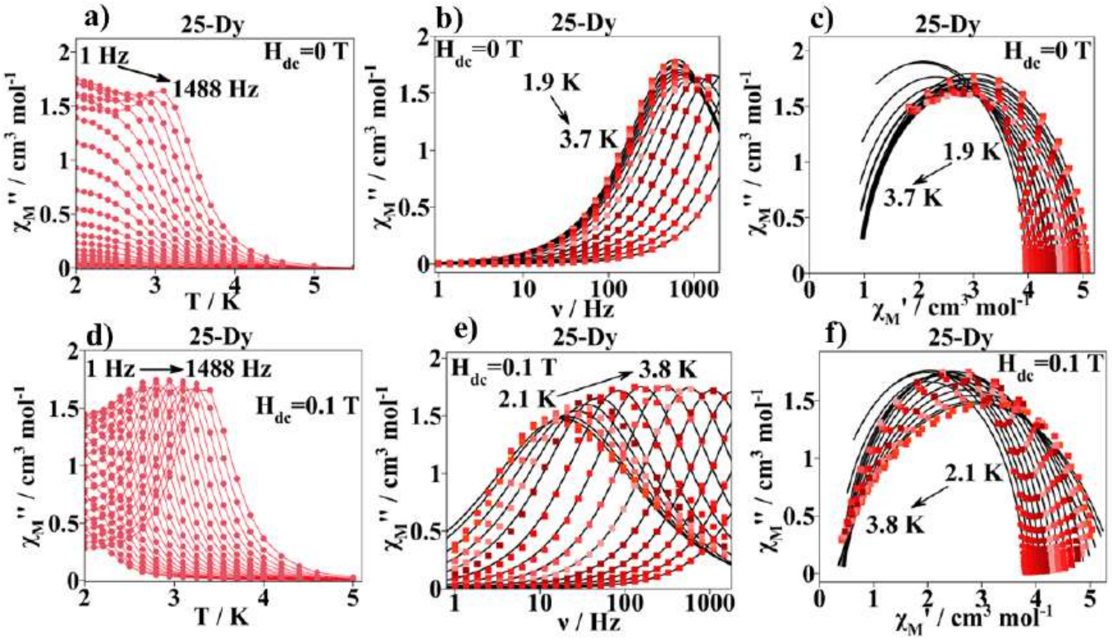

Figure 3. 37 a) and d) χ_M'' *vs* T plots of **25-Dy** measured at $H_{dc} = 0$ and $H_{dc} = 0.1$ T. The continuous line is a guide to the eye; b) and e) are the χ_M'' *vs* ν plots of **25-Dy** measured at $H_{dc} = 0$ and $H_{dc} = 0.1$ T. The continuous black line corresponds to the fitting to the Generalized Debye model and c) and f) are the Cole-Cole plots of **25-Dy** measured at $H_{dc} = 0$ and $H_{dc} = 0.1$ T. The continuous black line corresponds to the fitting to the Generalized Debye model.

The plot of τ *vs* T^{-1} represented in a semi-log scale is found in Figure 3. 38. A linear trend is observed in the higher temperature region, then on cooling the sample, ln(τ) values reach a plateau region indicating that the spin returns to the equilibrium phase via the faster QTM process. First, the lineal segment was fitted considering an Arrhenius type law (Equation 3.3) that describes the thermally assisted Orbach relaxation process that takes place between the ±m_j ground state doublet through an excited m_j state of higher energy.

$$\tau^{-1} = \tau_0^{-1} \exp\left(\frac{-\Delta E}{k_B T}\right) \qquad \textbf{Equation 3.3}$$

$$\tau^{-1} = CT^n + \tau_0^{-1} \exp\left(\frac{-\Delta E}{k_B T}\right) + \tau_{QMT}^{-1} \qquad \textbf{Equation 3.5}$$

By fitting the magnetic data in the 3.1-3.7 K temperature range with Equation 3.3 the effective energy barrier (*ΔE*) yielded 24.07 cm^{-1} (34.62 K) and the pre-exponential factor (τ_0) was $1.39\cdot10^{-9}$ s. However, the linear trend fades away on cooling the sample to enter to the temperature independent regime. Therefore, the whole curve was fitted considering other relaxation of the magnetization mechanisms. The best fit of ln(τ) *vs* T^{-1} curve was obtained when considering Orbach, taking place at higher temperatures, Raman and finally QTM dominating relaxation at the lower temperatures with Equation 3.5. The parameters obtained from the fitting were: ΔE =31.40 cm^{-1} and τ_0 = 3734.70 s for Orbach, C=4.20 s^{-1} K^{-n} and n = 5.24 for Raman and τ_{QTM} = $2.70 \cdot 10^{-4}$ s.

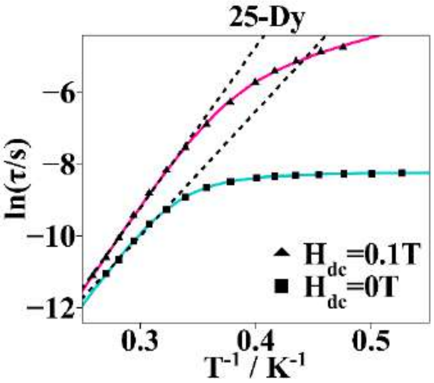

Figure 3. 38 ln(τ) *vs* T^{-1} plots of compound **25-Dy** measured at a H_{dc} of 0 and 0.1 T. Continuous blue line represents the fitting with Orbach, Raman and QTM (equation 3.5). Continuous pink line corresponds to the fitting considering Orbach and Raman mechanisms while black dotted lines are the fit with the Arrhenius law.

Application of an external magnetic field (H_{dc}) breaks the degeneracy between the $\pm m_j$ states of Dy^{3+} ground state, reducing or even eliminating the QTM. Thus, to establish the optimal H_{dc} field for **25-Dy**, ac measurements were carried out at a constant temperature (2.5 K) and by applying different external magnetic fields in the 0 to 0.2 T range. A simple representation of τ with respect to H_{dc} shows an increase of relaxation times on applying the external magnetic field, probably due to quenching of QTM, till 0.1 T where the optimal magnetic field is reached. After this point, τ starts diminishing again due to enhancement of the Direct mechanism which has a strong dependence with the applied magnetic field ($\tau^{-1} = AH^4$), Figure 3. 39a).[31]

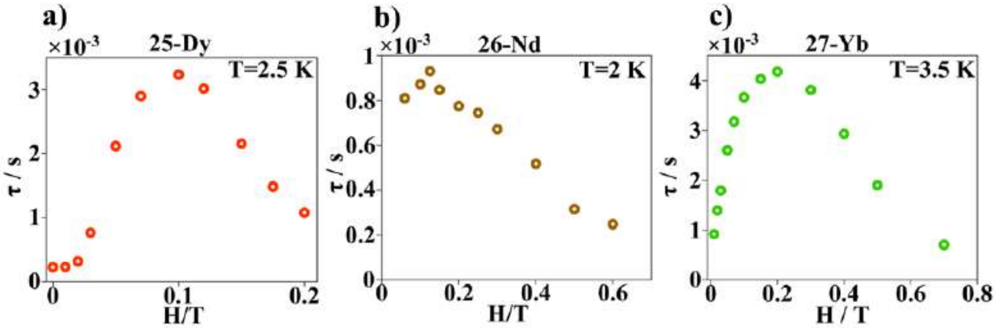

Figure 3. 39 Relaxation times in front of static magnetic field measured at the constant temperature of 2.5 K for a) **25-Dy**, of 2.0 K for b) **26-Nd** and of 3.5 K for c) **27-Yb.**

Ac measurements were performed for **25-Dy** under the H_{dc} of 0.1 T to see if there was an improvement of magnetic behavior. Now in the χ_M'' *vs* T plot Figure 3. 37d), maxima appear at similar temperature range (2.1-3.8 K) though the tails observed at the lowest temperature region due to QTM in the H_{dc} = 0 T measurement are reduced instead, χ_M'' maxima are enhanced. Moreover, χ_M'' *vs* ν plot, Figure 3. 37 e), shows that maxima start appearing at lower oscillating frequencies and they move progressively to higher frequencies on increasing the temperature indicating that thermally assisted relaxation of the magnetization mechanism are present along practically all the temperature range compared to the H_{dc} = 0 T measurement where part of ac signal was temperature independent. Cole-Cole plots of the H_{dc}=0.1 T experiment shows asymmetrical and completed semicircles that were fitted to the one component Generalized Debye model and the obtained α values are in the 0.34-0.05 range, Figure 3. 37f). Moreover, ln(τ) versus T^{-1} plot for H_{dc} = 0.1 T measurement is shown in Figure 3. 38. Relaxation of the magnetization times follow a liner trend in the higher temperature range assigned to the Orbach relaxation mechanism. The linear segment was fitted to the Arrhenius law equation (Equation 3.3) and the resulting effective energy barrier was ΔE =31.08 cm^{-1} (44.73 K) and the pre-exponential factor was τ_0 =$1.46 \cdot 10^{-10}$ s. The dependence of τ with temperature changes on cooling the sample. The linear trend is lost at lower temperatures indicating that other relaxation mechanisms different than Orbach are taking place. In any case, no plateau is observed in the ln(τ) *vs* T^{-1} curve thus validating the removal of QTM on applying an H_{dc}. Then, fit of ln(τ) vs. T^{-1} curve was achieved taking out the τ_{QMT}^{-1} factor of Equation 3.5. The best fit was obtained with ΔE = 33.29 cm^{-1} and τ_0 = $6.30 \cdot 10^{-11}$ s for Orbach and C = 4.39 s^{-1} K^{-n} and n = 4.33 for Raman processes. Apparently, no improvement of magnetic behavior is discerned on applying an external magnetic field since effective energy barrier remains comparable on applying H_{dc} and the ac signal persists in a narrow range of low temperatures. Nevertheless, the absence of τ dependence with T, attributed to the QTM, is removed in the second measurement where the magnetic field of 0.1 T is applied. The effective energy barrier obtained from the magnetic data of **25-Dy** is rather low (24.1 cm^{-1} at $H_{dc} = 0$). Though **25-Dy** shows SMM behavior, the effect of rhombic contribution might significantly lower the effective energy barrier due to an enhances QTM mechanism.

For compounds **26-Nd** and **27-Yb**, slow relaxation of the magnetization was detected just under an external direct current magnetic field due to the strong efficiency of QTM at 0 T dc field. Ac measurements of **26-Nd** and **27-Yb** were carried out under the optimal dc fields of 0.3 and 0.15 T respectively, Figure 3. 39b) and c). Plots depicting the out-of-phase magnetic susceptibility components in relation to temperature and frequency are displayed in Figure 3. 40.

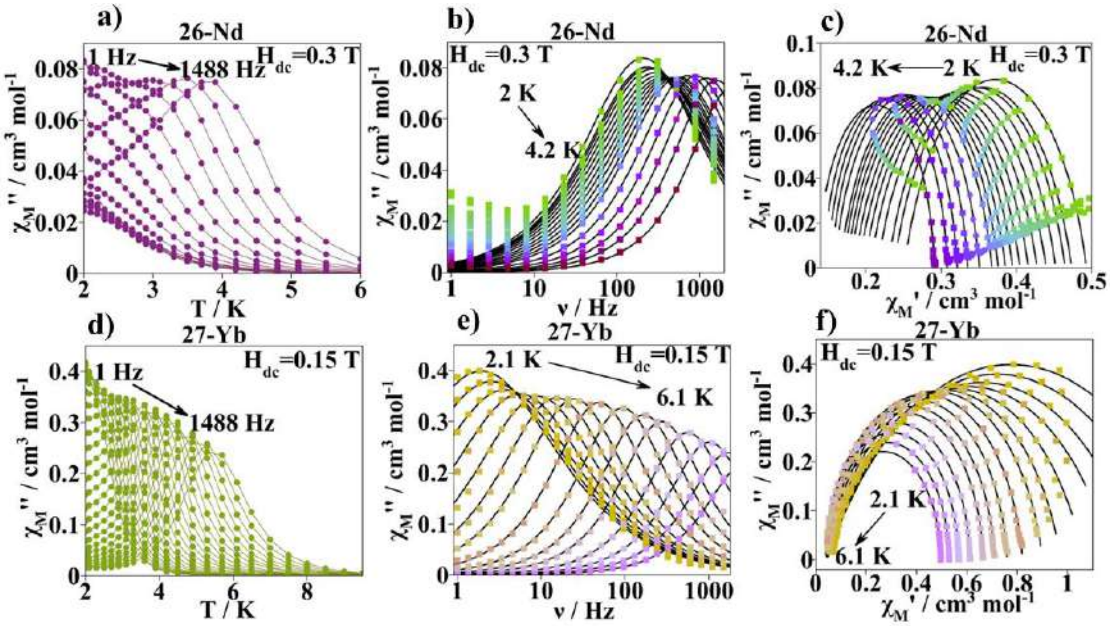

Figure 3. 40 a) and d) χ_M'' *vs* T plots of **26-Nd** and **27-Yb,** respectively. The continuous line is a guide to the eye b) and e) are the χ_M'' *vs* ν plots of **26-Nd** and **27-Yb**, respectively. The continuous black line corresponds to the fitting to the Generalized Debye model and c) and f) are the Cole-Cole plots of **26-Nd** and **27-Yb**, respectively**.** The continuous black line corresponds to the fitting to the Generalized Debye model.

χ_M*'' vs* T plot of **26-Nd** shows maxima in the 2.5 to 4.2 K temperature range, and a second set of less intense peaks appear at nearly liquid helium temperature, 2 K, Figure 3. 40a). This effect is translated in the χ_M*'' vs* ν plot with two maxima appearing at different ranges of oscillating frequencies. More intense and well-defined peaks are differentiated at higher frequencies and non-zero going signals seen as tails appear at low frequencies indicating two distinct relaxation processes taking place at the higher and lower frequency regions, Figure 3. 40b). These tails are also seen in the Cole-Cole representation of **26-Nd**, though in any case a second semicircle is discerned, Figure 3. 40c). Due to the few experimental data concerning these second relaxation process appearing at lower temperatures and frequencies, the fitting with the extended Debye model wasn't successful. Nevertheless, for the other process appearing at higher temperatures and frequencies, χ_M*' vs* χ_M*''* representation shows well defined semicircles. It can, certainly, be fitted with the one component Generalized Debye model leading to α values in the 0.23-0.04 range on increasing temperature from 2 K to 4.2 K. On the other hand, compound **27-Yb** show maxima of the χ_M*''* component in the 2.1 to 6.1 K temperature range at the optimal external magnetic field of 0.15 T, Figure 3. 40 d). Peaks of the χ_M*''* start appearing at 1.8 Hz, then they move progressively to higher frequencies on increasing temperature, Figure 3. 40e). Cole-Cole representation of **27-Yb** is shown in Figure 3. 40f). The lower temperature curves appear as wide and uncompleted semicircles while they come narrower on increasing temperature. After fitting the Cole-Cole curves to the Debye model, the obtained α values go from 0.36 at 2.1 K to 0.02 at 6.1 K.

$$\tau^{-1} = CT^n + AT \qquad \textbf{Equation 3.4}$$

The relaxation of magnetization times with temperature characteristics of **26-Nd** and **27-Yb** are plotted in Figure 3. 41. The ln(τ) *vs*. T^{-1} curves show a short linear trend in the higher temperature range. Nevertheless, as a first approximation, the curves were fitted with the Arrhenius law that describes the Orbach relaxation mechanism with Equation 3.3, and the obtained values were ΔE =15.07 cm^{-1} and τ_0 = 3.77·10^{-7} for **26-Nd** and ΔE =40.00 cm^{-1} and τ_0 = 8.17·10^{-8} s for **27-Yb**, FigureAPX.VII.1. However, the best fit of the ln(τ) *vs*. T^{-1} curves of **26-Nd** and **27-Yb** is acquired when the equation describing the Raman and Direct relaxation of the magnetization processes are considered, Equation 3.4. The obtained parameters are C = 0.47 s^{-}

^{1}K^{-n}, $n = 7.01$ and $A = 675.73$ s^{-1}K^{-1} for **26-Nd** and $C = 0.01$ s^{-1}K^{-n}, $n = 8.07$ and $A = 3.34$ s^{-1}K^{-1} for **27-Yb**. Relaxation of the magnetization mainly governed by Raman and Direct mechanisms instead of the Orbach process, points out to a largely rhombic contribution in the ground and excited ±m_j doublets. Other Nd^{3+} and Yb^{3+} coordination compounds where slow relaxation of the magnetization process is mainly dominated by Raman and Direct mechanisms rather than Orbach, are found in the literature.[42,43] A compilation of the fitted parameters for all compounds is found in Table 3. 15.

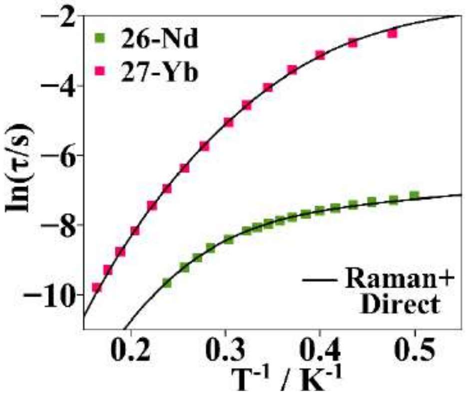

Figure 3. 41 ln(τ) *vs* T^{-1} plots of compounds **26-Nd** and **27-Yb** from the magnetic data measured at the H$_{dc}$ of 0.3 T and 0.15 T, respectively. Continuous black lines correspond to the fitting with Raman and Direct relaxation of the magnetization mechanisms.

Table 3. 15 Compilation of the best fitting parameters from the relaxation of the magnetization mechanisms of compounds **25-Dy**, **26-Nd** and **27-Yb**.

	H$_{dc}$	**Orbach**		**QTM**	**Raman**		**Direct**
	(T)	ΔE	τ_0	τ_{QTM}	C	n	A
		(cm^{-1})/(K)	(s)	(s)	s^{-1}K^{-n}		s^{-1}K^{-1}
25-Dy	0	31.39 /45.16	8.73·10^{-11}	3734.70	4.20	5.24	
	0.1	33.29 /47.90	6.30·10^{-11}		4.39	4.33	
26-Nd	0.3				0.47	7.10	675.73
27-Yb	0.15				0.01	8.07	3.34

3.2.2 Compounds with formula $(HPy)_2[Ln_2(\mu\text{-}2,6\text{-}F2Bz)_4(2,6\text{-}F2Bz)_4]$

3.2.2.1 Experimental procedure

The general synthetic procedure to obtain compounds **28-Eu**, **29-Tb**, **30-Dy**, **31-Nd** and **32-Gd** was carried out as follows: an ethanol/H_2O (1:1) solution (10 ml) containing $Ln(NO_3)_3{\cdot}nH_2O$ (0.9 mmol) was added to another ethanol/H_2O solution (20 ml) containing 2,6-difluorobenzoic acid (632.4 mg, 4.0 mmol) and pyridine (316.4 mg, 4 mmol). The resulting solution was stirred for 30 minutes and then left to stand at room temperature. Prism-like single crystals, suitable for X-Ray diffraction, were obtained within one month. The crystals were obtained by filtration and washed with the lowest amount of cold ethanol possible. The compounds were obtained with yields ranging from 30 to 40 %.

The synthetic procedure carried out to obtain **28-Eu** to **32-Gd** was mainly the same used for obtaining compounds **23-Eu** to **27-Yb**. Just by using an ethanol/H_2O (1:1) mixture instead of only ethanol as solvent, the obtained structures changed. By increasing the amount of H_2O in the solvent of the reaction, the two chelating nitrate molecules found in the dinuclear **23-Eu** to **27-Yb** complexes were substituted by two chelating 2,6-F2Bz ligands, leaving to a molecular formula of $(HPy)_2[Ln_2(\mu\text{-}2,6\text{-}F2Bz)_4(2,6\text{-}F2Bz)_4]$ for **28-Eu**, **29-Tb** and **32-Gd** and of $(HPy)_2[Ln_2(\mu\text{-}2,6\text{-}F2Bz)_4(2,6\text{-}F2Bz)_4]{\cdot}H_2O$ for **30-Dy**.

Further characterization of these compounds was realized by carrying out elemental analysis, Table 3. 16 and ATR-Infrared Spectroscopy, Table 3. 17.

Table 3. 16 Elemental analysis of compounds **28-Eu** to **32-Gd.**

	Calculated			Found		
Compound	**%C**	**%N**	**%H**	**%C**	**%N**	**%H**
28-Eu **$C_{56}H_{24}F_{16}O_{16}Eu_2$, 2($C_5H_6N$),** **1720.89 g/mol**	46.06	1.62	2.11	46.20	1.58	2.05
29-Tb **$C_{56}H_{24}F_{16}O_{16}Tb_2$, 2($C_5H_6N$),** **1778.00 g/mol**	45.69	1.61	2.09	45.32	1.50	1.96
30-Dy **$C_{56}H_{24}F_{16}O_{16}Dy_2$,** **2($C_5H_6N$),2($H_2O$)** **1778.00 g/mol**	44.58	1.57	2.26	44.21	1.50	2.12
32-Gd **$C_{56}H_{24}F_{16}O_{16}Gd_2$, 2($C_5H_6N$),** **1731.5 g/mol**	45.78	1.62	2.09	46.01	1.53	2.00

Table 3. 17 Selected bands (cm^{-1}) of **28-Eu** to **32-Gd** (s=strong, m=medium and w=weak, br=broad) obtained in ATR-IR spectroscopy

28-Eu	3263-2894(w), 1606(s, split), 1536(w),1502(m), 1459(s), 1406(s), 1313(s), 1270(m), 1234(m),1007(s), 791(m), 735(m), 669(m), 579(m), 512(m)
29-Tb	3080-2778(w), 1598(s, split), 1536(w),1502(m), 1460(s), 1407(s), 1314(s), 1271(m), 1235(m), 1008(s), 793(m), 737(m), 670(m), 579(m), 513(m)
30-Dy	3080-2778(w), 1599(s, split), 1536(w),1502(m), 1460(s), 1407(s), 1314(s), 1271(m), 1235(m), 1008(s), 793(m), 737(m), 670(m), 579(m), 513(m)
32-Gd	3080-2778(w), 1612(s, split), 1537(w), 1502(m), 1461(s), 1383(s), 1315(s), 1272(m), 1235(m), 845(s), 793(m), 738(m), 671(m), 579(m), 514(m)

3.2.2.2 Structural characterization

Single crystal X-Ray Diffraction was performed for compounds **29-Tb** and **30-Dy**. Selected bond distances are compiled in Table 3. 18 and Table 3. 19. Crystallographic information is found in Table APX.VIII.1. The molecules forming the dinuclear unit arrange in the same manner for compounds **29-Tb** and **30-Dy**. However, in the dysprosium structure there are two water molecules crystallizing within the crystal lattice while they are absent in **29-Tb**. Additionally, the dinuclear entities are disposed differently along the crystal lattice. These differences cause that the two compounds show different crystal systems as well as space groups.

Table 3. 18 Selected bond distances (Å) of compound **29-Tb**.

29-Tb			
Tb1-O1	2.413(19)	**Tb2-O6**	2.340(17)
Tb1-O2	2.538(18)	**Tb2-O8**	2.315(17)
Tb1-O3	2.462(2)	**Tb2-O10**	2.367(17)
Tb1-O4	2.422(16)	**Tb2-O11**	2.516(18)
Tb1-O5	2.376(19)	**Tb2-O12**	2.508(16)
Tb1-O6	2.747(19)	**Tb2-O13**	2.481(16)
Tb1-O7	2.358(17)	**Tb2-O14**	2.519(17)
Tb1-O9	2.351(17)	**Tb2-O15**	2.496(17)
Tb1-O12	2.330(16)	**Tb2-O16**	2.373(17)
		Tb1---Tb2	3.911

Table 3. 19 Selected bond distances (A) of compound **30-Dy**. The symmetry transformation used to generate equivalent atoms is _a: 1-x, 1-y, 1-z and _b: 2-x, 2-y, 2-z.

30-Dy			
Dy1-O1	2.397(2)	**Dy2-O9**	2.435(2)
Dy1-O2	2.474(19)	**Dy2-O10**	2.455(2)
Dy1-O3	2.459(19)	**Dy2-O11**	2.470(2)
Dy1-O4	2.525(2)	**Dy2-O12**	2.466(2)
Dy1-O5	2.313(18)	**Dy2-O13**	2.317(19)
Dy1-O7	2.301(19)	**Dy2-O15**	2.354(19)
Dy1-O6_a	2.477(19)	**Dy2-O13_b**	2.568(19)
Dy1-O8_a	2.332(19)	**Dy2-O14_b**	2.442(2)

Dy1-O5_a	2.586(18)	**Dy2-O16_b**	2.372(19)
Dy1---Dy1_a	3.854	**Dy2---Dy2_b**	3.934

Compound **29-Tb** crystallizes in a monoclinic crystal system in a P21/n space group, Figure 3. 42a. In contrast to the lanthanide fluorobenzoate dinuclear complexes previously presented in this *Thesis* work, the asymmetric unit of **29-Tb** is made up by the whole dinuclear unit, therefore there are two Tb^{3+} ions that are crystallographically independent. Each Terbium ion is nonacoordinated. The TbO_9 coordination sphere encompasses four O atoms from two 2,6-F2Bz ligands in the chelating coordination mode, Scheme 3.3d, with Tb-O bond lengths in the 2.373-2.538 Å range. Two O atoms from two 2,6-F2Bz molecules in the symmetrical *syn-syn* bidentate bridging coordination mode, Scheme 3.3b with Tb-O distances in the 2.315-2.367 Å range and three O atoms from two 2,6-F2Bz ligands in the chelating-bridging coordination mode with Tb-O bond lengths in the 2.330-2.516 Å range. To neutralize the negative charge of the dinuclear coordination compound, two pyridinium counterions are found for each dinuclear entity. The nine O atoms are placed around each Tb^{3+} ion (Tb1 and Tb2) in a coordination geometry that is close to an ideal Muffin-like (MFF-9, C_s symmetry) polyhedron with CShM values of 2.050 for Tb1 and of 2.014 for Tb2, Figure 3. 42b. The Tb1---Tb2 intramolecular distance is 3.911Å.

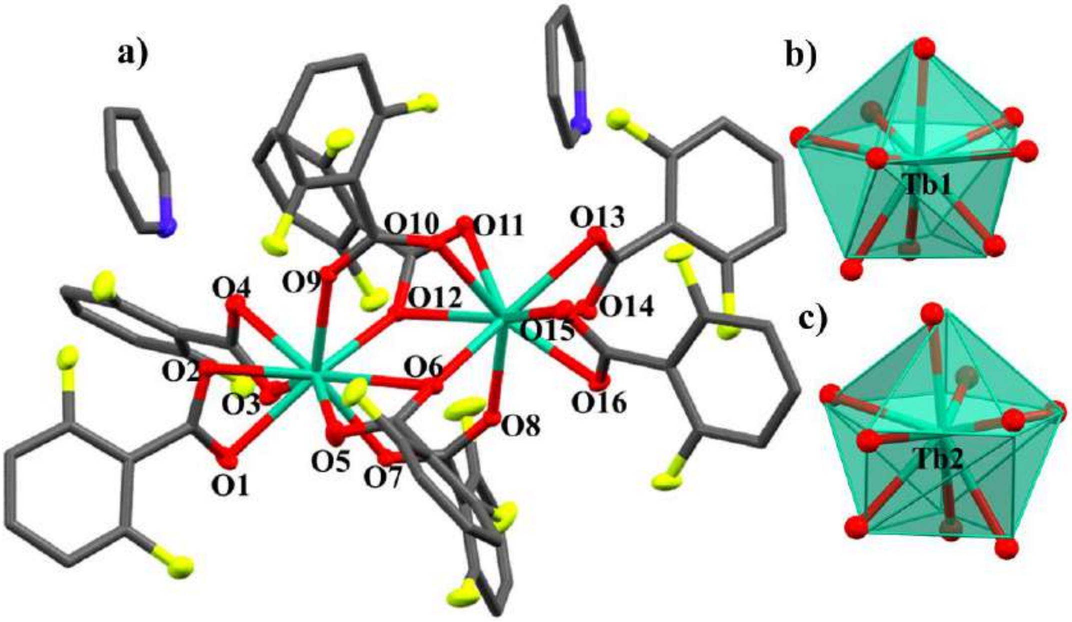

Figure 3. 42 a) Partially labelled plot of structure **29-Tb**. Color code O=red, Tb=turquoise, C=grey, F=green and N=blue. Muffin polyhedra (MFF-9, C_s) compared to the real positions of coordinating Oxygen atoms of b) Tb1 and c) Tb2 of structure **29-Tb**.

The dinuclear $(HPy)_2[Ln_2(\mu\text{-}2,6\text{-}F2Bz)_4(2,6\text{-}F2Bz)_2]$ molecules of **29-Tb** are organized in the crystal lattice through Van der Walls interactions. Two interactions worth to consider are π---π and H---π stacking intermolecular interactions that occur along the **29-Tb** crystal lattice. On one hand, the centroid (Cg1) from one of the chelating 2,6-F2Bz ligand coordinated to Tb1 and the centroid (Cg2) from one chelating-bridging 2,6-F2Bz ligand interact through π---π stacking along the [0 1 0] base vector. On the other hand, the centroid (Cg3) from the aromatic ring of a chelating 2,6-F2Bz molecule coordinated to Tb2 and the H atom from a sp^2 carbon of another chelating 2,6-F2Bz coordinated to Tb1, interact by means of H---π stacking interaction throughout the [1 0 0] base vector, Figure 3. 43.

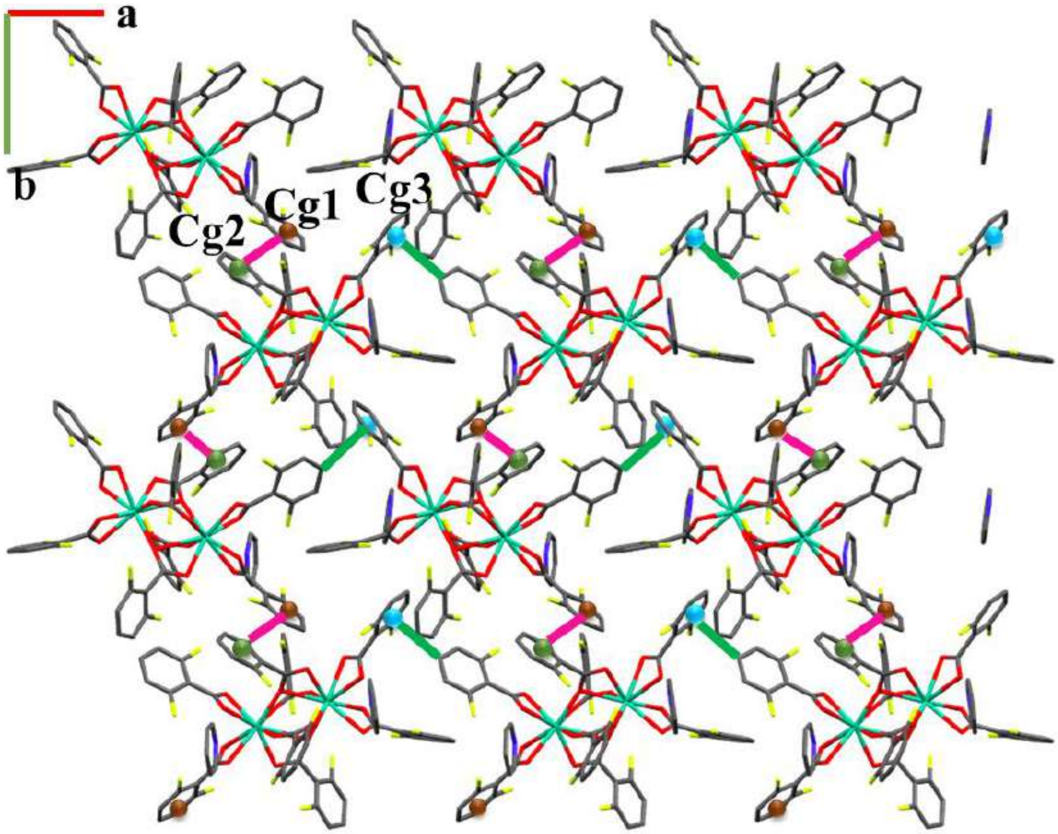

Figure 3. 43 Crystal packing along the (0 0 1) plane of compound **29-Tb**. Continuous pink lines indicate the π---π stacking interaction between Cg1 and Cg2 while continuous green lines illustrate the H---π interactions between Cg3 and H12.

As previously mentioned, the dinuclear structure observed in **30-Dy** exhibits a molecular arrangement that is fundamentally similar to that of **29-Tb**. However, **30-Dy** crystallizes in a triclinic crystal system and a P-1 space group, different than the monoclinic crystal system and P21/n space group found in **29-Tb**. The asymmetric unit is formed by two halves of two dinuclear units. After application of symmetry operations provided by P-1 space group the asymmetric unit expands in space forming the dinuclear entities. **30-Dy** is constituted by two Dy^{3+} ions bridged through four 2,6-F2Bz ligands. Two of them found in the symmetrical *syn*-*syn* coordination mode and the other two in the bridging-chelating mode. The coordination sphere of each Dy^{3+} ion is completed by two chelating 2,6-F2Bz ligands, Table 3. 19a. The arrangement of the O atoms coordinating the Dy^{3+} ion in **30-Dy** structure also form a distorted Muffin-like polyhedron with CShM values of 1.954 for Dy1 and 1.848 for Dy2, Table 3. 19b and c. Two protonated pyridine molecules neutralize the II- formal charge of the dinuclear coordination compound. Moreover, there are two H_2O molecules crystallizing within the crystal lattice.

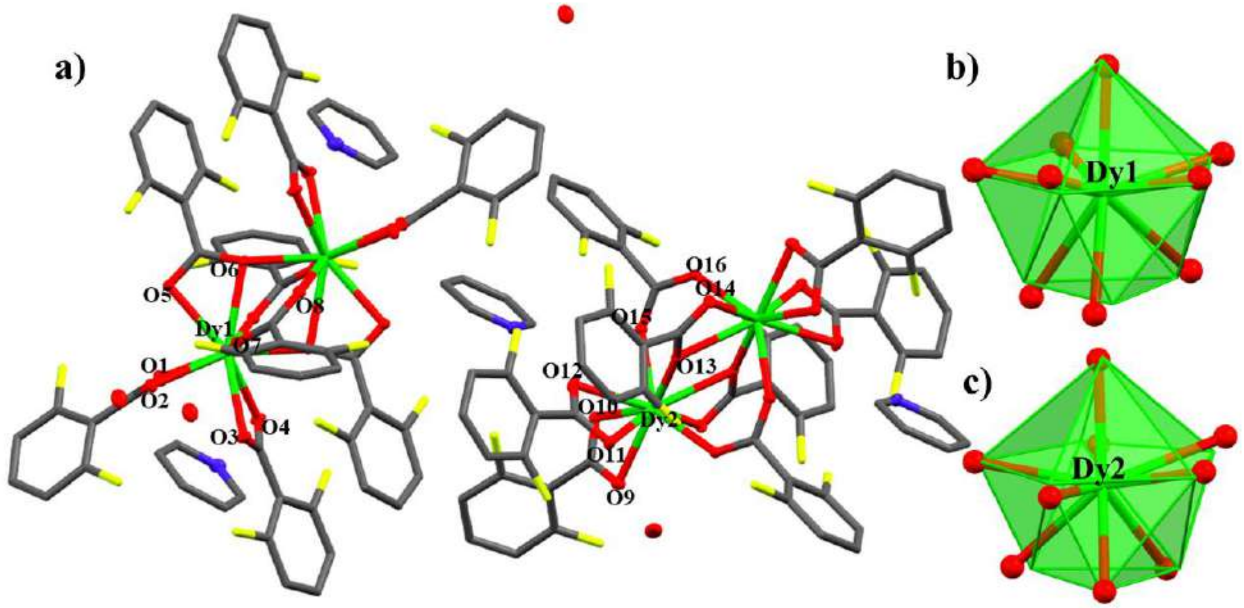

Figure 3. 44 a) Partially labeled plot of crystal structure of **30-Dy**. Color code: Dy=green, O=red, C=grey, F=light green and N=blue. Coordination sphere of b) Dy1 and c) Dy2 superimposed to an ideal Muffin-like (Cs) polyhedron.

Due to the large presence of aromatic rings, π---π stacking interactions build the 3D supramolecular structure that defines **30-Dy**. The π---π stacking interactions worth to consider are: *i)* the interaction between the aromatic rings of a chelating 2,6-F2Bz ligand coordinated to Dy2 (Cg1) with Cg1---Cg1' intermolecular distance of 3.734 Å, *ii)* interaction between the aromatic rings from a 2,6-F2Bz ligand in the chelating bridging mode coordinated to Dy2 (Cg2) and a another chelating 2,6-F2Bz molecule, also, coordinated to Dy2 (Cg3) with Cg2---Cg3 intermolecular distance of 3.677 Å and *iii)* the aromatic rings interaction from a 2,6-F2Bz chelating bridging ligand coordinated to Dy2, (Cg4) Figure 3. 45.

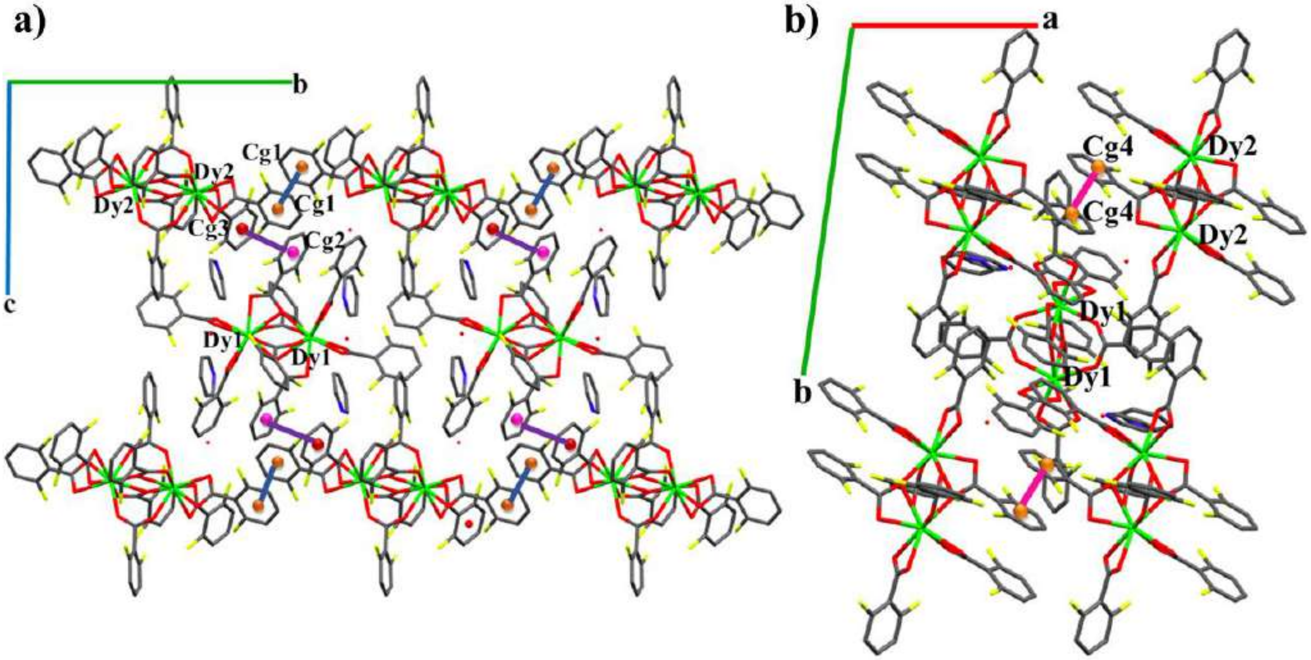

Figure 3. 45 Crystal packing of **30-Dy** a) along the (1 0 0) plane and b) the (0 0 1) plane. Continuous blue, purple and pink lines illustrate π---π stacking between Cg1 and Cg1, Cg2 and Cg3, Cg4 and Cg4 respectively.

Finally, to check phase purity in all the synthesized powder samples, PXRD of **29-Tb** and **30-Dy** were carried out. The measured powder diffractograms were compared to the calculated pattern from each crystal structure. We can assert that all the polycrystalline sample of **29-Tb** and **30-Dy** have the same crystal structure that the one found in the monocrystal XRD. Even though the ligand arrangement in each dinuclear unit of **29-Tb** and **30-Dy** is rather the same, the difference in the crystal packing and presence of H_2O molecules in the crystal lattice of **30-Dy** conduct to different X-ray Powder diffractograms. Furthermore, PXRD analyses were conducted on polycrystalline samples of **28-Eu**, **31-Nd** and **32-Gd** to confirm their isostructural similarity with either **29-Tb** or **30-Dy**. **28-Eu** and **32-Gd** were isostructural to **29-Tb**, nevertheless, the powder diffractogram of **31-Nd** doesn’t match neither **29-Tb** nor **30-Dy** patterns, Figure 3. 46.

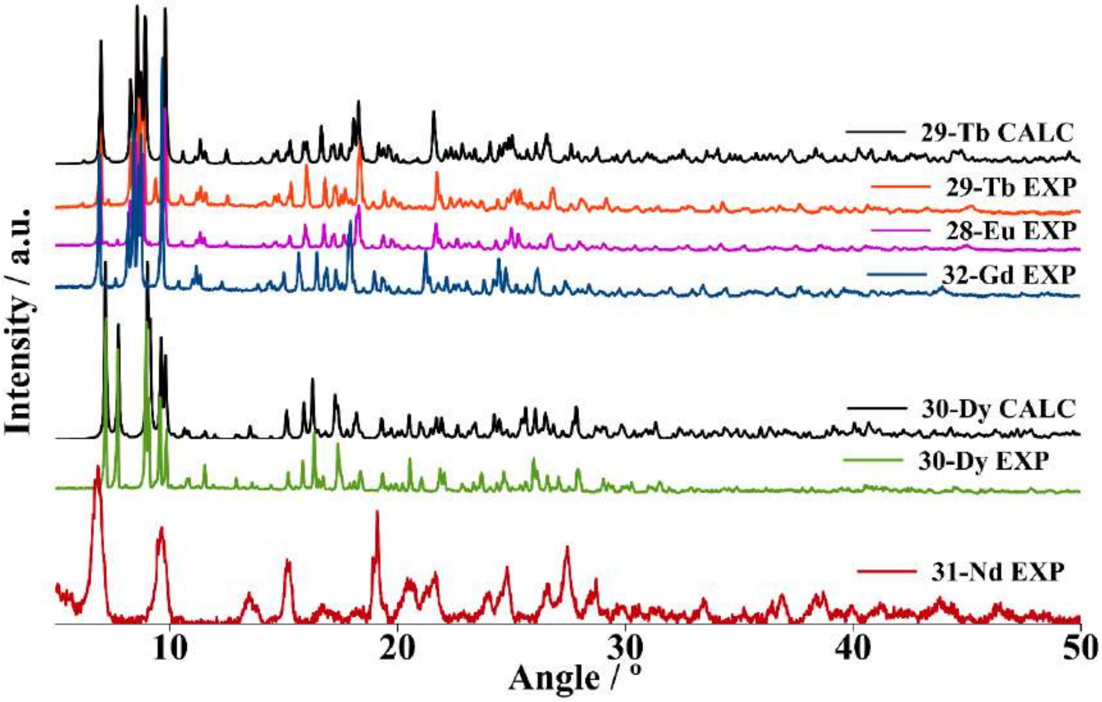

Figure 3. 46 Powder X-Ray Diffraction of compounds **28-Eu** to **32-Gd**. CALC stands for the calculated Powder patterns obtained from the crystal structure and EXP for the measured diffractograms of those samples.

3.2.2.3 Luminescence properties

Photoluminescent properties of compounds **28-Eu**, **29-Tb** and **30-Dy** have been studied in solid state at room temperature. Additionally, absorption and phosphorescence spectra were measured, the latter spectrum at 77K. Then the lowest excited singlet (S_1) and lowest lying triplet (T_1) states of 2,6-F2Bz ligand were obtained. For **32-Gd**, S_1 was 36,036 cm^{-1} (277.5 nm) while T_1 was found at 22,170 cm^{-1} (451 nm), Figure 3. 47. The Intersystem Crossing (ISC) energy for the $(HPy)_2[Gd_2(\mu\text{-}2,6\text{-}F2Bz)_4(2,6\text{-}F2Bz)_2]$ system resulted of 13,866 cm^{-1}. A difference in energy of less than 7,000 cm^{-1} between the excited states S_1 and T_1 promotes the transition to the triplet state through ISC, rather than returning to the ground state (S_0) through other competitive relaxation mechanism. Thus, the ISC energy of 2,6-F2Bz in this dinuclear compounds may be too large favoring other deactivation pathways and reducing subsequent $S_1 \rightarrow T_1 \rightarrow Ln^{3+*}$ energy transfer.[44]

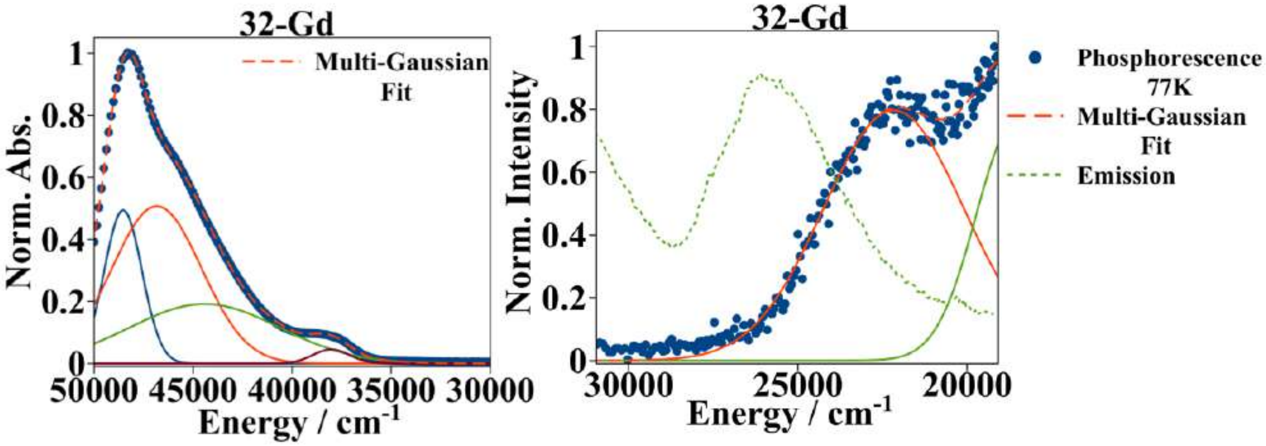

Figure 3. 47 Absorption spectrum of compound **32-Gd** dispersed in a KBr matrix. The lowest S_1 state is extracted from the edge of the less energetic band. b) Blue dotted line: phosphorescence spectrum of **32-Gd** measured at 77K. The T_1 state is extracted from the barycenter of the 0-phonon band. Green dotted line: emission spectrum of **32-Gd**. Both, phosphorescence and emission spectra were monitored at a λ_{exc}=274 nm.

Excitation spectra collected at the maximum emission wavelength (λ_{em}) of 616 nm ($^5D_0 \rightarrow {}^7F_2$) for **28-Eu**, of 545 nm ($^5D_4 \rightarrow {}^7F_5$) for **29-Tb** and of 575 nm ($^4F_{9/2} \rightarrow {}^6H_{13/2}$) for **30-Dy** are illustrated in Figure 3. 48a)n b) and c) respectively. The broad and intense band above 300 nm is assigned to 2,6-F2Bz ligand centered $\pi \rightarrow \pi^*$ and $n \rightarrow \pi^*$ excitation transitions. Furthermore, bands due to lanthanide(III) intrinsic excitation transitions from the shielded *f* orbitals are discerned for **28-Eu**, **29-Tb** and **30-Dy**. The bands are assigned in each spectrum and a compilation of assignation to the excitation transitions is found in Table 3. 20.

Table 3. 20 Compilation of assignation of the bands to the excitation transitions of compounds **28-Eu** to **30-Dy**, *left column*, and to the emission transitions of **28-Eu** to **30-Dy**, *right column.*

28-Eu	**28-Eu**
$^7F_0 \rightarrow {}^5D_4$ at 377 nm, $^7F_0 \rightarrow {}^5L_6$ at 393 nm and $^7F_0 \rightarrow {}^5D_2$ at 462 nm	$^5D_1 \rightarrow {}^7F_2$ at 565 nm, $^5D_0 \rightarrow {}^7F_0$ at 581 nm, $^5D_0 \rightarrow {}^7F_1$ at 594 nm, $^5D_0 \rightarrow {}^7F_2$ at 616 nm, $^5D_0 \rightarrow {}^7F_3$ 652, $^5D_0 \rightarrow {}^7F_4$ at 690 nm
29-Tb	**29-Tb**
$^7F_6 \rightarrow {}^5L_7$ at 340 nm, $^7F_6 \rightarrow {}^5L_9$ at 352 nm, $^7F_6 \rightarrow {}^5D_2$ at 359 nm, $^7F_6 \rightarrow {}^5L_{10}$ at 369 nm and $^7F_6 \rightarrow {}^5G_6$ at 377 nm	$^5D_4 \rightarrow {}^7F_6$ at 490 nm, $^5D_4 \rightarrow {}^7F_5$ at 545 nm, $^5D_4 \rightarrow {}^7F_4$ at 586 nm and $^5D_4 \rightarrow {}^7F_3$ at 622 nm
30-Dy	**30-Dy**
$^6H_{15/2} \rightarrow {}^4M_{17/2}$ at 324 nm, $^6H_{15/2} \rightarrow {}^6P_{7/2}$ at 350 nm and $^6H_{15/2} \rightarrow {}^6P_{5/2}$ at 364 nm	$^4F_{9/2} \rightarrow {}^6H_{15/2}$ at 480 nm, $^4F_{9/2} \rightarrow {}^6H_{13/2}$ at 575 nm and $^4F_{9/2} \rightarrow {}^6H_{11/2}$ at 663 nm

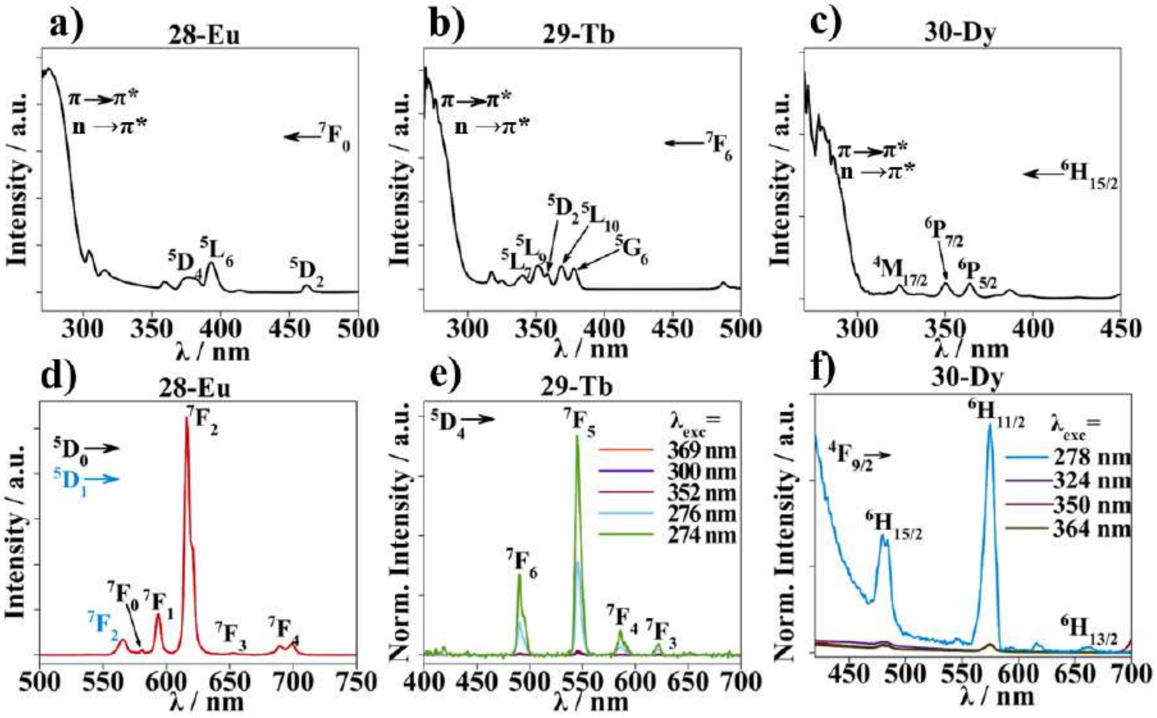

Figure 3. 48 Emission spectra of **28-Eu** to **30-Dy** (a, b and c) and emission spectra of **28-Eu** to **30-Dy** (d, e and f) polycrystalline samples measured at room temperature.

The emission spectra of all compounds were measured exciting the samples at the corresponding ligand centered absorption wavelength which was 276 nm for **28-Eu**, 274 nm for **29-Tb** and 278 nm for **30-Dy**. Excitation at the referred λ_{exc} induced the expected Ln^{3+} emission transitions. Additionally, for the three compounds, emission spectra were recorded at the wavelengths corresponding to the intrinsic lanthanide excitation transitions. For **28-Eu**, the emission spectra obtained when exciting the polycrystalline sample at 377, 393 and 462 nm (corresponding to $^7F_0 \rightarrow {}^5D_4$, $^5L_6$ and $^5D_2$ respectively) are not shown since the intensity of the spectra obtained at 274 nm (corresponding to ligand absorption) was by far more intense. Assignation of bands found in the emission spectra to the corresponding lanthanide(III) transition of **28-Eu, 29-Tb** and **30-Dy** is presented in Table 3. 20.

For the visible emitters **28-Eu**, **29-Tb** and **30-Dy**, stronger emission spectra are obtained when exciting the polycrystalline samples at the λ_{exc} corresponding to the 2,6-F2Bz ligand absorption wavelength, Figure 3. 48 d), e) and f) respectively. For Eu^{3+} and Tb^{3+} analogues, emission from the ligand at 300-500 nm wasn't noticed even their indistinguishable red and green luminescence color could be seen with the naked eye, Figure 3. 49a.

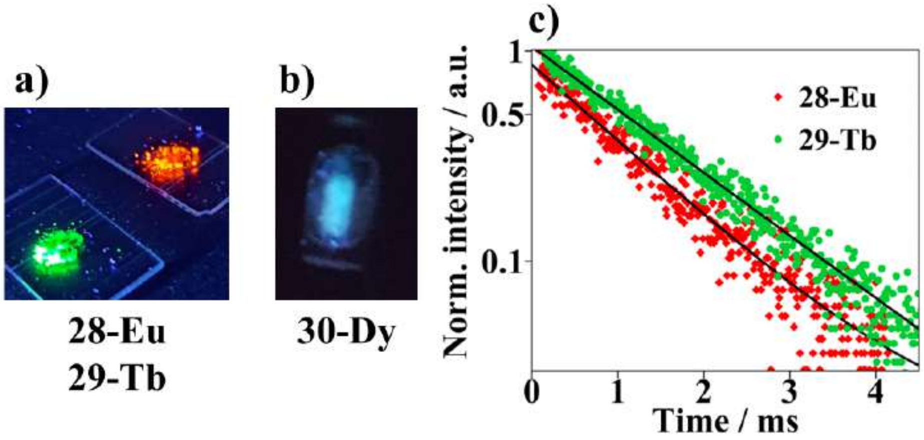

Figure 3. 49 a) and b) emission color observed with the naked eye of **28-Eu**, **29-Tb** and **30-Dy** polycrystalline samples under exposure of UV radiation from a laboratory lamp. c) Luminescence lifetime curves of compounds **28-Eu** and **29-Tb** presented in a semi-log plot. Solid black lines refer to the mono-exponential fit with $I(t) = I_0 e^{-\frac{t}{\tau_{obs}}} + C$.

As for **28-Eu**, the weaker band at 581 nm accounts to $^5D_0 \rightarrow ^7F_0$ which is a forbidden transition by the ΔJ rule (ΔJ=0, ±1, J=0↮0). However, due to crystal field perturbation the electric dipole transition can occur due to mixing of higher configurations in the 4f wavefunctions. This can happen if the Eu^{3+} ion is found in a coordination geometry with C_{nv}, C_n or C_s symmetries as it is the case of **28-Eu**. Furthermore, the electric dipole transition at 616 nm ($^5D_0 \rightarrow ^7F_2$) is not clearly split but a shoulder can be differentiated in the band suggesting two components. Further to this, an additional band appears at 565 nm. It is consistent with a transition from an excited state higher in energy than the $^5D_0$, specifically from the $^5D_1$ excited state to the lower energy $^7F_2$ state. Emission from the $^5D_1$, $^5D_2$ or even $^5D_3$ europium excited states are unusual in molecular compounds since these emitting states have weaker radiation and shorter decay times compared to $^5D_0$ excited state, thus being prone to fast deactivation.[18] Excitation at the ligand absorption wavelength of **29-Tb** resulted in the expected $^5D_4 \rightarrow ^7F_{J=6-3}$ transitions at 490, 545, 586 and 622 nm, respectively.

Moreover, even though emission intensity was greater when **30-Dy** was excited at 278 nm corresponding to the ligand excitation transition, emission form the 2,6-F2Bz ligands appeared overlapping dysprosium's $^4F_{9/2} \rightarrow {}^6H_{15/2}$ transition. Emission of **30-Dy** compound is mainly governed by the ligand radiative deactivation as also suggests the blue color of **30-Dy** seen with the naked eye, Figure 3. 49b.

Overall photoluminescence quantum yields (ϕ_{Ln}^{L}) and luminescence lifetimes (τ_{obs}) were measured for **28-Eu** and **29-Tb**, at the excitation wavelength of 276 and 274 nm respectively. For this family of compounds, the followed trend was the same as found in all the previous lanthanide fluorobenzoate complexes synthetized in this *Thesis* work where the Terbium analogue yielded a higher ϕ_{Ln}^{L} and τ_{obs} compared to the Europium analogue. The ϕ_{Ln}^{L} resulted of 0.26 for **28-Eu** while it increased to 0.29 for **29-Tb**. Moreover, luminescence lifetimes were monitored at the emission wavelength of 616 nm ($^5D_0 \rightarrow {}^7F_2$) for **28-Eu** and of 545 nm ($^5D_4 \rightarrow {}^7F_5$) for **29-Tb**. Both decay curves followed a monoexponential law which could be fitted following $I(t) = I_0 e^{-\frac{t}{\tau_{obs}}} + C$, Figure 3. 49c. The resulting τ_{obs} values were 1.31 and 1.6 ms for **28-Eu** and **29-Tb** respectively. The presence of a single decay time component suggests a single radiative deactivation process.[18a,21]

In addition, the radiative lifetime (τ_{rad}) from the $^5D_0$ emissive state of the europium analogue was calculated from the corrected emission spectrum following Equation 1.8.[25] Careful attention must be paid in case of **28-Eu** since in the emission spectra, the band corresponding to $^5D_1 \rightarrow {}^7F_2$ at 565 nm is also appearing. Since we are calculating τ_{rad} from the $^5D_0$ excited state, integration of emission bands from any excited state different than $^5D_0$ would be a wrong approach. For **28-Eu**, τ_{rad} was 2.20 ms. The intrinsic quantum yield (ϕ_{Ln}^{Ln}) can be calculated from $\phi_{Ln}^{Ln} = \frac{k_r}{k_r + k_{nr}} = \frac{\tau_{obs}}{\tau_{rad}}$ and for **28-Eu** it was 0.28. The sensitization efficiency (η_{sens}) calculated with Equation 1.2 resulted of 0.92. Sensitization efficiency of 2,6-F2Bz ligand to the $^5D_0$ state in compound **28-Eu** is rather good. It increased with respect to $(HPy)_2[Eu_2(\mu\text{-}2,6\text{-}F2Bz)_4(NO_3)_2]$ (**23-Eu**) which η_{sens} was only of 0.08. On substituting the chelating NO_3^- ions for 2,6-F2Bz ligands, sensitization as well as luminescence properties of both, **28-Eu** and **29-Tb,** are greatly enhanced.

Despite ISC may not be entirely efficient as we previously referred, the energy transfer to $^5D_0$ europium emitting center is rather good as the ϕ_{Ln}^{L} and η_{sens} indicate. For **28-Eu** the energy difference between the T_1 and $^5D_0$ states is 4,903 cm^{-1}. In this case, this energy difference is found in the energy gap between 2,500-5,500 cm^{-1} in which energy transfer to $^5D_0$ state is optimal.[11]

3.2.2.4 Magnetic properties

Direct current measurements

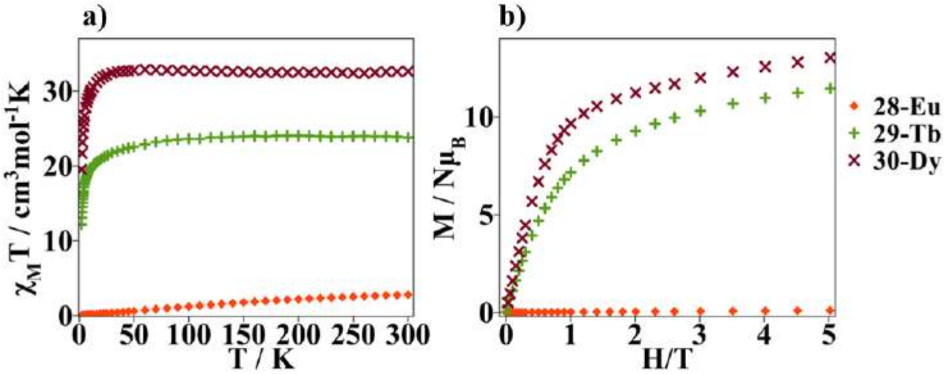

Figure 3. 50 a) Temperature dependence of χ_MT measured at an external static field of 0.3 T, for compounds **28-Eu** to **30-Dy** and b) Magnetization dependence with an external magnetic field measured at 2 K for compounds **28-Eu** to **30-Dy**.

Direct current (dc) magnetic susceptibility (χ_M) and magnetization (M) data were measured on **28-Eu**, **29-Tb** and **30-Dy** polycrystalline samples under a dc magnetic field of 0.3 T in the 2-300 K temperature range. Temperature dependence of $\chi_M T$ plot is shown in Figure 3. 50a). The $\chi_M T$ values at room temperature (300K) are 23.79, 2.70 and 32.62 cm^3 mol^{-1} K for **28-Eu**, **29-Tb** and **30-Dy**, respectively. For two isolated Ln^{3+} cations, the calculated $\chi_M T$ values are: 0 cm^3 mol^{-1} K for Eu^{3+} ground state $^7F_0$; 23.64 cm^3 mol^{-1} K for Tb^{3+} ground state $^7F_6$ and g_j=3/2, 28.34 cm^3 mol^{-1} K for Dy^{3+} ground state $^6H_{15/2}$.[21a] Experimental room temperature $\chi_M T$ values quite agree with the calculated ones for all compounds except for **28-Eu** which value is higher than the calculated 0 cm^3 mol^{-1} K. At room temperature, higher energy ^7F_J states, closer to the ground state ($^7F_0$), are thermally populated (mainly the $^7F_1$ state) due to the rather small spin-orbit coupling parameter (λ) between the $^7F_{(0\text{-}1)}$ electronic states. Then, on cooling the sample, the $\chi_M T$ *vs* T curve decreases gradually due to thermal depopulation of the excited ^7F_J states. At 2 K, $\chi_M T$ achieves the value of 0.03 $cm^3mol^{-1}K$ confirming that at low temperature the non-magnetic ground state (J=0) is stabilized.[27]

As for the rest of polycrystalline samples, **29-Tb** and **30-Dy**, the $\chi_M T$ *vs* T curves show similar behavior. On lowering the temperature, magnetic susceptibility values stay practically constant till 50 K are reach. Below this temperature, $\chi_M T$ curves drop down to 12.1 and 19.51 $cm^3mol^{-1}K$ for **29-Tb** and **30-Dy,** respectively, at 2 K. For the presented dinuclear compounds, Ln---Ln intramolecular distance is relatively short (of 3.934 Å for **29-Tb** and of 3.911 Å for **30-Dy**). The decrease in the $\chi_M T$ *vs* T curves as the sample is cooled, could be attributed to one or a combination of different phenomena. This might be due to thermal depopulation of excited m_j doublets (of the ground J state) generated by the crystal field perturbation. Or due to weak antiferromagnetic coupling between the Ln^{3+} centers though the contracted nature of 4*f* electrons in lanthanide(III) ions make magnetic exchange coupling interactions rather weak.[21a,30]

Magnetization (*M*) dependence with an applied magnetic field, monitored at 2 K, of the presented compounds is depicted in Figure 3. 50b). Magnetization was collected in an applied magnetic fields ranging from 0 to 5 T for all compounds. *M vs* H curves increase suddenly from 0 to 1 T, approximately. Magnetization of **28-Eu** is maintained at 0 $N\mu_B$, as expected, while compounds **29-Tb** and **30-Dy** don't show saturation of the magnetization ($g_J \cdot J$) at 5 T. Crystal-field induced perturbation of the m_j level as well as magnetic anisotropy may be responsible for the absence of saturation of magnetization.[37]

Alternating current measurements

Altern current (ac) measurements were performed for compounds **29-Tb** and **30-Dy** to investigate spin dynamics in case of slow relaxation of the magnetization. Under an ac magnetic field of $4 \cdot 10^{-4}$ T oscillating between a 1-1488 Hz frequency range, only compound **29-Dy** showed Single Molecule Magnet (SMM) behavior in the 1.9 to 3.5 K temperature range. However, compound **29-Tb** didn't show out-of-phase magnetic susceptibility response neither at 0 dc magnetic field (H_{dc}) nor by applying a H_{dc}.

30-Dy is an SMM since it shows dependence of the out-of-phase magnetic susceptibility component (χ_M'') with temperature and the oscillating frequency, under a 0 T H_{dc}. **25-Dy** presented in *Section 3.2.1.4* showed a similar behavior. For **30-Dy**, χ_M'' maxima also appear in a narrow temperature range (1.9-3.5 K). On further cooling, χ_M'' *vs* T curves increase again without reaching a maximum, due to the Quantum Tunnelling of the Magnetization (QTM) relaxation process that is taking place at such low temperatures, Figure 3. 51a).[31] For the dependence of χ_M'' component with the oscillating frequency plot, maximum starts at about 500 Hz. Then the χ_M'' maxima stay constant on increasing the temperature. Subsequently, the χ_M'' peaks gradually shift towards higher frequencies indicating that a temperature independent process promotes the magnetization's relaxation at lower temperatures. Then, when temperature increase, thermally processes including Orbach or Raman mechanisms may drive the relaxation, Figure 3. 51b).[38] Representation of in-phase and out-of-phase magnetic susceptibility components (χ_M'' *vs* χ_M') in the Cole-Cole plot[39] lead to uncompleted and distorted semicircles, Figure 3. 51c). Nevertheless, the curves can be successfully fitted to the Generalized Debye model described with the Casimir-Du Pré function.[40] The obtained α parameters are in the range of 0.09 (at 1.9K) to 0.02 (at 3.5K) indicating a rather constant, and close to zero, distribution of the time constants around magnetization relaxation times (τ). Depiction of ln(τ) with temperature (T^{-1}) represented in a semi-log scale is found in Figure 3. 51e). At the higher temperature range, a linear trend can be discerned, however it is constituted by a few experimental data points. Then, ln(τ) values reach a plateau region indicating that the spin returns to the equilibrium phase via the faster QTM process. First, the lineal segment was fitted with the Arrhenius equation (Equation 3.3) that describes the thermally assisted Orbach relaxation process taking place between the $\pm m_j$ ground state doublet through an excited m_j state of higher energy.

$$\tau^{-1} = \tau_0^{-1} \exp\left(\frac{-\Delta E}{k_B T}\right) \qquad \textbf{Equation 3.3}$$

$$\tau^{-1} = CT^n + \tau_0^{-1} \exp\left(\frac{-\Delta E}{k_B T}\right) + \tau_{QMT}^{-1} \qquad \textbf{Equation 3.5}$$

By fitting the magnetic data in the 3.1-3.5 K temperature range with Equation 3.3, the effective energy barrier (*ΔE*) yielded 18.21 cm^{-1} (26.2 K) and the pre-exponential factor (τ_0) was $1.81 \cdot 10^{-8}$ s. As the sample cools down, the linear trend disappears, causing τ to become temperature independent. Therefore, the whole curve was fitted considering other relaxation of the magnetization mechanisms. The best fit of ln(τ) vs. T^{-1} was obtained when Orbach, Raman and QTM were considered, the latter dominating relaxation at the lower temperatures. The parameters obtained from the fitting were: $\Delta E = 32.01\ \mathrm{cm}^{-1}$ and $\tau_0 = 4.67 \cdot 10^{-4}$ s for Orbach, $C = 0.27\ \mathrm{s}^{-1}\ \mathrm{K}^{-n}$ and $n = 5.50$ for Raman and $\tau_{QTM} = 3598.10$ s. These results are similar to **25-Dy** with formula $(HPy)_2[Dy_2(\mu\text{-}2,6\text{-}F2Bz)_4(NO_3)_4]$.

Furthermore, application of an external magnetic field (H_{dc}) breaks the degeneracy between the $\pm m_j$ states reducing or even eliminating the QTM. To establish the optimal H_{dc} field for **30-Dy**, ac measurements were carried out at a constant temperature of 2 K and by applying different external magnetic fields in the 0 to 0.2 T range, Figure 3. 1d). The representation of τ with the applied H_{dc} shows an increase of relaxation times on increasing the external magnetic field, probably due to quenching from QTM, till 0.12 T where the optimal magnetic field is reached. After this point, τ starts diminishing again due to enhancement of the Direct mechanism which has a strong dependence with the applied magnetic field.[31,33]

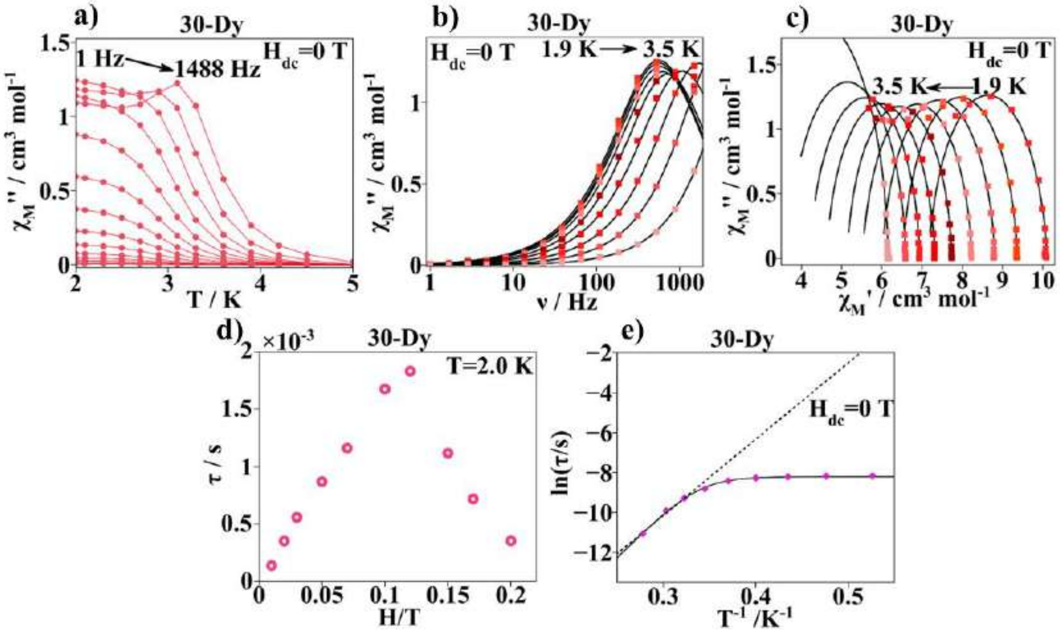

Figure 3. 51 a) χ_M'' *vs* T plot of **30-Dy** measured at H_{dc}=0 T. The continuous black line is a guide to the eye, b) χ_M'' *vs* ν plot of **30-Dy** measured at H_{dc}=0 T. The continuous black line corresponds to the fitting to the Generalized Debye model, c) Cole-Cole plot of **30-Dy** measured at H_{dc} = 0 T. The continuous black line is a guide to the eye d) Relaxation times in front of static magnetic field measured at the constant temperature of 2 K for **30-Dy** and e) ln(τ) *vs* T^{-1} plot of **30-Dy**, measured at H_{dc} = 0 T. The continuous black line corresponds to the fit with Orbach and QTM mechanisms and the dotted black line corresponds to the fit with the Arrhenius law that describes the Orbach relaxation of the magnetization mechanism.

Ac measurements were performed for **30-Dy** under the H_{dc} of 0.12 T to see how the exposure of the external magnetic field affects relaxation of magnetization of the dysprosium compound and to reduce the QTM. Now in the χ_M'' *vs* T plot Figure 3. 52a), maxima appear at similar temperature range (2.1-3.5 K) though the tails observed at the lowest temperature region due to QTM in the H_{dc} = 0 T measurement are not seen, instead a second set of χ_M'' maxima appear. This suggests that at H_{dc} = 0 T, the fast QTM was covering this second relaxation process, but when a H_{dc} is applied, QTM is reduced opening a way to the slower relaxation process. In the χ_M'' *vs* ν the two different kinds of χ_M'' maxima are observed, Figure 3. 52b). One, less intense, that appears in a wider range of oscillating frequencies and the other, more intense, that emerges at higher frequencies. At lower temperatures, both processes are taking place while on increasing temperature the less intense process appearing in a wider range oscillating frequency, remains.

This is also well portrayed in the Cole-Cole plots, were for the lower temperature curves two merged semicircles can be differentiated while on increasing temperature only one semicircle remains, Figure 3. 52c). A successful fit could be obtained with the extended Debye model, Equation 1.32. From the fit two different relaxation of the magnetization times and the corresponding α values were obtained from each process. From the relaxation process appearing at higher frequencies and lower temperatures (τ_1), the α values were in the range of 0.1(1.8 K) to 0.4(2.7 K) while for the process appearing at higher temperatures and in a wider frequency range (τ_2) the obtained α values were practically zero. A representation of relaxation of the magnetization times τ_1 and τ_2 in the ln(τ) *vs* T^{-1} plots is shown in Figure 3. 52d). The calculated ΔE and τ_0 values were 20.81 cm^{-1} and $5.29 \cdot 10^{-10}$ s for the τ_1 process and 29.73 cm^{-1} and $2.45 \cdot 10^{-10}$ s for the τ_2 process. Nevertheless, the entire ln(τ) *vs* T^{-1} curves don't follow a linear trend in all the temperature range, therefore, they were fitted considering other relaxation of the magnetization processes. For τ_1 process, a plateau emerges at lower temperatures thus, the best fit of ln(τ_1) *vs* T^{-1} curve was obtained when Orbach and QTM equation were considered with values of ΔE =22.71 cm^{-1} and $\tau_0 = 2.11 \cdot 10^{-10}$ s and $\tau_{QTM} = 0.001$ s. On the other hand, τ_2 changes its dependence on cooling the sample from a linear trend to a T^3 power law. Hence the best fit of ln(τ_2) *vs* T^{-1} curve was obtained when equations describing both, Orbach and Raman mechanisms, were considered and the fitted parameters yielded ΔE =30.7 cm^{-1}, $\tau_0 = 1.53 \cdot 10^{-10}$ s, $C = 3.52$ and $n = 3.39$.[45]

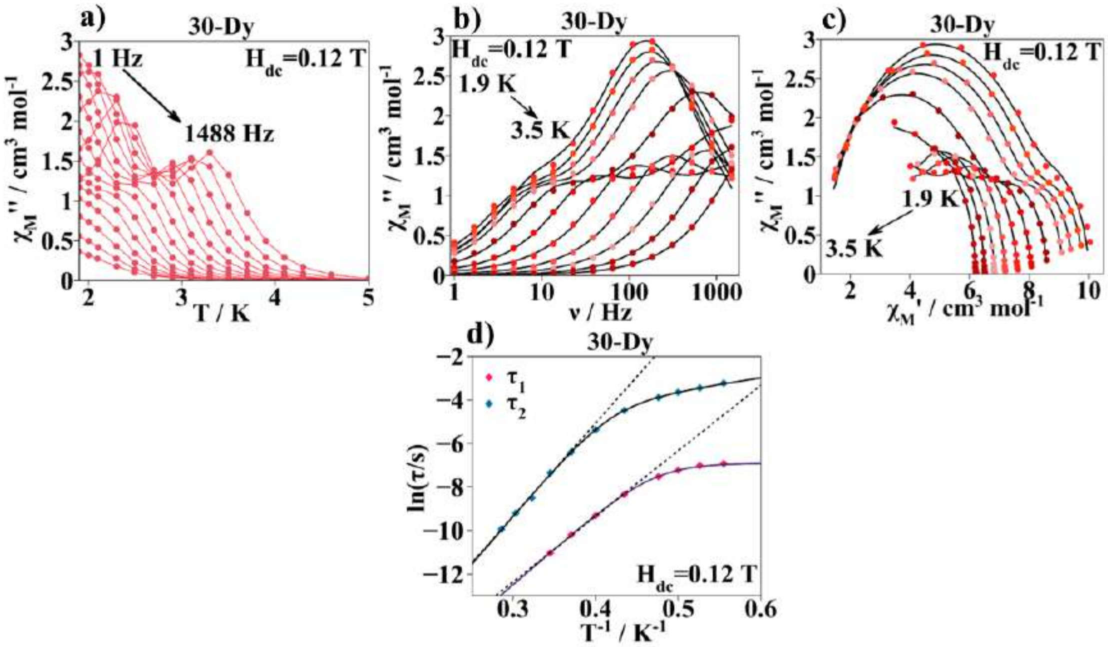

Figure 3. 52 a) χ_M'' *vs* T plot of **30-Dy** measured at H_{dc} = 0.12 T. The continuous black line is a guide to the eye, b) χ_M'' *vs* ν plot of **30-Dy** measured at H_{dc} = 0.12 T. The continuous black line corresponds to the fitting to the two component Debye model, c) Cole-Cole plot of **30-Dy** measured at H_{dc} = 0.12 T. The continuous black line represents the fit with the extended Debye model and d) ln(τ) *vs* T^{-1} plot of the two magnetic processes taking place in the spin relaxation of compound **30-Dy** under exposure of a H_{dc} = 0.12 T.

3.3 Conclusions

The lanthanide fluorobenzoates coordination compounds (**8-Ce** to **32-Gd**) are synthetized in *Chapter 3*. Lanthanide compounds derived from the 2-fluorobenzoate (2-FBz) and 2,6-difluorobenzoate (2,6-F2Bz) ligands are obtained herein with the aim of obtaining complexes presenting both, luminescence and magnetic properties, specially focusing on the emissive characteristics. To improve luminescence of the synthetized compounds, the syntheses were conducted to decrease or even remove the coordinating H_2O molecules. The variety of coordination modes that characterize the carboxylate ligands (Scheme 3.1, 3.2 and 3.3) are also manifested in compounds **8-Ce** to **32-Gd.** All of them were obtained under “soft” synthetic conditions since the reactions were performed at room temperature with achievable solvents, where H_2O is protagonist. Moreover, the amount of time needed for each reaction was actually short (30 min) and all of them crystallized relatively fast, within a maximum time of two weeks. A compilation of compounds presented in this Chapter is found in Table 3. 21.

The first family of 2-FBz lanthanide derivatives present a compound with layer-like structure and formula $[Ce_2(\mu\text{-}2\text{-}FBz)_4(2\text{-}FBz)_2(H_2O)_4]_n$ (**8-Ce**) and seven compounds with dinuclear structures and formula $[Ln_2(\mu\text{-}2\text{-}FBz)_4(2\text{-}FBz)_2(2\text{-}HFBz)_2(H_2O)_2]$ (**9-Sm** to **15-Yb**). The latter molecular structure was already published for the Terbium and Neodymium analogues with different synthetic pathways.[14] However, studies on photoluminescence efficiency weren’t performed for the compounds found in the literature. On introducing tetraphenylphosphonium chloride (PPh_4Cl) to the reaction, the obtained lanthanide 2-fluorobenzoate compounds present an anionic coordination structure of formula $(PPh_4)_2[Ce_2(\mu\text{-}2\text{-}FBz)_2(2\text{-}FBz)_6(H_2O)_2]\cdot 2H_2O$ for **16-Ce** and $(PPh_4)_2[Ln_2(\mu\text{-}2\text{-}FBz)_2(2\text{-}FBz)_6(H_2O)_2]$ for **17-Eu** to **21-Yb**. The difference between **16-Ce** and **17-Eu** is mainly due to the coordination mode of the two 2-FBz bridging ligands. For **16-Ce** these are found in the bridging-chelating mode whereas in **17-Eu** to **21-Yb**, they are in the bidentate *syn*-*syn* bridging mode. The change on the coordination mode of the bridging ligand makes a change in the coordination number which decreases from 9 (**16-Ce**) to 8 (**17-Eu** to **21-Yb**) and also affects the coordination geometry which changes from a distorted Muffin-like polyhedron in **16-Ce** to a Biaugmented trigonal prism in **17-Eu** to **21-Yb.**

Table 3. 21 Compilation of molecular formula, coordination number and coordination polyhedron and Identification code of compounds **8-Ce** to **32-Gd**.

Formula	**Coordination number and coordination polyhedron**	**Identification code**
$[Ce_2(\mu\text{-}2FBz)_4(2FBz)_2(H_2O)_4]_n$	9 MFF-9(C_s) and CSAPR-9 (C_{4v})	**8-Ce**
$[Ln_2(\mu\text{-}2\text{-}FBz)_4(2\text{-}FBz)_2(2\text{-}HFBz)_2(H_2O)_2]$	9 MFF-9(C_s)	**9-Sm**, **10-Eu**, **11-Gd**, **12-Tb**, **13-Dy**, **14-Er**, **15-Yb**
$(PPh_4)_2[Ce_2(2\text{-}FBz)_2(2\text{-}FBz)_6(H_2O)_2]\cdot 2H_2O$	9 MFF-9(C_s)	**16-Ce**
$(PPh_4)_2[Ln_2(2\text{-}FBz)_2(2\text{-}FBz)_6(H_2O)_2]$	8 BTPR-8(C_{2v})	**17-Eu**, **18-Tb**, **19-Dy**, **20-Er, 21-Yb**
$(HPy)_2[Ln_2(\mu\text{-}2,6\text{-}F2Bz)_4(NO_3)_4]$	9 MFF-9(C_s)	**23-Eu**, **24-Tb**, **25-Dy**, **27-Yb**
$(HPy)_2[Ln_2(\mu\text{-}2,6\text{-}F2Bz)_4(2,6\text{-}F2Bz)_4]$	9 MFF-9(C_s)	**28-Eu**, **29-Tb**, **32-Gd**
$(HPy)_2[Ln_2(\mu\text{-}2,6\text{-}F2Bz)_4(2,6\text{-}F2Bz)_4]\cdot 2H_2O$	9 MFF-9(C_s)	**30-Dy**

Lanthanide contraction effect may be the cause of the structural changes seen in both 2-FBz families (**8-Ce** to **15-Yb** and **16-Ce** to **21-Yb**), where the Ce^{3+} complexes show different molecular configuration compared to the other lanthanide structures. This effect is also observed in the overall Ln-O distances which are larger for the **8-Ce** and **16-Ce** compounds, and they become shorter on diminishing the ionic radius.

Furthermore, two different families of lanthanide coordination compounds derived from the 2,6-F2Bz ligand were obtained in *Chapter 3*. The first family showed the general formula $(HPy)_2[Ln_2(\mu\text{-}2,6\text{-}F2Bz)_4(NO_3)_4]$ (**23-Eu**, **24-Tb**, **25-Dy**, **26-Nd** and **27-Yb**) whereas the second presented the $(HPy)_2[Ln_2(\mu\text{-}2,6\text{-}F2Bz)_4(2,6\text{-}F2Bz)_4]$ formula (**28-Eu**, **29-Tb**, **30-Dy**, **31-Nd** and **32-Gd**). In both families, the Ln^{3+} centers are linked through four 2,6-F2Bz ligands in both, bridging-chelating and bidentate *syn-syn* coordination modes. Interestingly, to obtain the two different families only a slight change in the solvent used during the reaction made possible their isolation. Focusing on the $(HPy)_2[Ln_2(\mu\text{-}2,6\text{-}F2Bz)_4(2,6\text{-}F2Bz)_4]$ family, in the dysprosium structure (**30-Dy**), there are two water molecules crystallizing within the crystal lattice while they are absent in **28-Eu**, **29-Tb** and **32-Gd**. The presence of this two H_2O molecules in **30-Dy**, make the dinuclear entities dispose differently along the crystal lattice. This difference causes **30-Dy** to crystallize in a different crystal system as well as space group compared to **28-Eu**, **29-Tb** and **32-Gd** structures**.** Moreover, single crystals of **31-Nd** couldn't be isolated and Powder X-Ray Diffraction revealed that it does not consists of the structure presented by **29-Tb** with $(HPy)_2[Ln_2(\mu\text{-}2,6\text{-}F2Bz)_4(2,6\text{-}F2Bz)_4]$ formula.

Following with luminescent properties, the lowest energy singlet excited state (S_1) and the lowest triplet state (T_1) of 2-FBz and 2,6-F2Bz were measured from the Gadolinium analogues (**11-Gd** and **32-Gd**). For 2-FBz the S_1 was 35,149 cm^{-1} (284 nm) and the T_1 was 24,640 cm^{-1} (405 nm) whereas for 2,6-F2Bz, the measured S_1 was 36,036 cm^{-1} (277.5 nm) and T_1 was 22,170 cm^{-1} (451 nm).

Both fluorobenzoate ligands 2-FBz and 2,6-F2Bz showed rather good sensitization effect for the visible Ln^{3+} emitters (**9-Sm**, **10-Eu**, **12-Tb**, **17-Eu**, **18-Tb**, **23-Eu**, **24-Tb**, **28-Eu** and **29-Tb**) since stronger emission spectra is obtained when exciting the sample at the ligand excitation wavelength than at the intrinsic *f-f* transitions of the Ln^{3+} ion. However, for the dysprosium complexes **13-Dy** and **19-Dy**, radiative emission from the ligand was also observed. For the nIR emitters, both 2-FBz and 2,6-F2Bz ligands showed poor sensitization, added to the presence of coordinating H_2O molecules in compounds **14-Er**, **15-Yb**, **20-Er** and **21-Yb** that led to nearly or even totally quenched luminescence within the nIR range. However, when polycrystalline **26-Nd** and **27-Yb** samples are excited at their characteristic intraconfigurational excitation transitions, enhanced nIR luminescence is observed, as these compounds do not contain coordinating H_2O molecules.

Luminescence quantum yields and lifetimes of all europium and terbium compounds presented in *Chapter 3* are compiled in Table 3. 22.

Table 3. 22 Photoluminescent parameters compilation of all Eu and Tb analogues of lanthanide fluorobenzoates presented in *Chapter 3*.

	τ obs / ms	ϕ_{Ln}^{L}	τ rad / ms	ϕ_{Ln}^{Ln}	η_{sens}
10-Eu	0.72	0.27	2.58	0.28	0.96
10-Eu-H2O	0.14	0.01	7.48	0.02	0.30
10-Eu-D2O	2.68	0.30	7.86	0.34	0.88
12-Tb	1.43	0.76			
12-Tb-H2O	0.50	0.04			
12-Tb-D2O	1.86	0.26			
17-Eu	0.61	0.20	1.20	0.41	0.50
18-Tb	1.02	0.34			
23-Eu	1.42	0.07	1.60	0.89	0.08
24-Tb	1.48	0.08			
28-Eu	1.31	0.26	2.20	0.28	0.92
29-Tb	1.6	0.29			

Relative to the previously published $[Ln_2(\mu\text{-}2\text{-}FBz)_4(2\text{-}FBz)_2(H_2O)_4]$ compounds,[13a] the measured ϕ_{Ln}^{L} of **10-Eu** and **12-Tb** polycrystalline samples with general formula $[Ln_2(\mu\text{-}2\text{-}FBz)_4(2\text{-}FBz)_2(2\text{-}HFBz)_2(H_2O)_2]$ (two less water molecules) resulted significantly larger. For the previous Eu and Tb compounds the quantum yields were of 0.15 and 0.50, respectively, whereas for **10-Eu** and **12-Tb** 2-Fluorobenzoates, presented herein, the quantum yield increases up to 0.27 and 0.76, respectively. This confirms that reducing the coordinating H_2O molecules of these lanthanide fluorobenzoates is an effective method to increase the luminescence quantum yield.

Moreover, compounds **17-Eu** and **18-Tb** with general fomula $(PPh_4)_2[Ln_2(\mu\text{-}2\text{-}FBz)_2(2\text{-}FBz)_6(H_2O)_2]$ show poorer luminescence and sensitization efficiency compared to $[Ln_2(\mu\text{-}2\text{-}FBz)_4(2\text{-}FBz)_2(H2\text{-}FBz)_2(H_2O)_2]$ compounds (**10-Eu** and **12-Tb**). This may be due to two reasons: *i)* the presence of monodentate 2-FBz ligands which may act as an electron-withdrawing group retaining electron density, thus slightly quenching sensitization efficiency or *ii)* the higher symmetry presented in coordination environment of **17-Eu** and **18-Tb** (C_{2v}) compared to **10-Eu** and **12-Tb** (C_s).

Though H_2O molecules coordinated to the lanthanide ion could be removed completely from structures containing the 2,6-F2Bz, overall quantum yields of **23-Eu**, **24-Tb**, **28-Eu** and **29-Tb** were significantly lower than the ones observed for the lanthanide dinuclear complexes with 2-FBz (**10-Eu**, **12-Tb**, **17-Eu** and **18-Tb**). In this work, it has been demonstrated that sensitization of 2,6-F2Bz ligand to Eu^{3+} and Tb^{3+} lanthanides is less effective than 2-FBz ligand. One of the possible explanations could be because of less efficient intersystem crossing between S_1 and T_1 states in the 2,6-F2Bz ligand. A difference in energy of less than 7,000 cm^{-1} between the excited states S_1 and T_1 promotes the transition to the triplet state through ISC, rather than returning to the ground state (S_0) through other competitive relaxation mechanisms. Thus, the ISC energy for 2,6-F2Bz in this dinuclear compounds may be too large favoring other deactivation pathways and reducing subsequent $S_1 \rightarrow T_1 \rightarrow Ln^{3+*}$ energy transfer. Additionally, 2,6-F2Bz is a symmetric ligand compared to 2-FBz, which is not, thus the first provides enhanced symmetry around the Ln^{3+} coordination environment. This greater symmetry around the Ln^{3+} ion may lead to reduced *f*-orbital mixing, causing the *f-f* transitions to be more restricted by Laporte's rule compared to those in the 2-FBz family.

According to the luminescence efficiency between **23-Eu** and **24-Tb** with **28-Eu** and **29-Tb**, the compounds with $(HPy)_2[Ln_2(\mu\text{-}2,6\text{-}F2Bz)_4(NO_3)_4]$ formula show lower quantum yields. This may account to the fact that four coordination positions of the Ln^{3+} ion are occupied by two NO_3^- ions (in **23-Eu** and **24-Tb**) instead of the chromophore 2,6-F2Bz ligand (in **28-Eu** and **29-Tb**), thus reducing the photons absorbed by the ligand transferred to the emitting lanthanide. The drawback in the $(HPy)_2[Ln_2(\mu\text{-}2,6\text{-}F2Bz)_4(NO_3)_2]$ systems is that they may present low extinction coefficient, because the 2,6-F2Bz has been reduced by a half, leading poorer sensitization effect. However, luminescence lifetimes and ϕ_{Ln}^{Ln} increase in 2,6-F2Bz compounds compared to 2-FBz derived compounds. The absence of coordinating H_2O molecules enhances the emission transitions once the Ln^{3+} emitting state is populated.

Finally, for the compounds presenting the best luminescence properties (**10-Eu** and **12-Tb**), their emission characteristics were also studied in aqueous solution. When both compounds, **10-Eu** and **12-Tb**, are dissolved in water solution they coordinate to five additional H_2O molecules. This collapses the dinuclear systems and initiates a fluxional equilibrium between different species where H_2O molecules but also, 2-FBz ligand are coordinated to the Ln^{3+} ions. Coordination of the ligand to the metal is confirmed since even in water solutions, the expected red and green luminescence arising from Tb^{3+} and Eu^{3+} is seen on exciting the samples at the ligand absorption wavelength.

Regarding the magnetic properties, compounds **8-Ce**, **13-Dy**, **14-Er** and **15-Yb** showed slow relaxation of the magnetization under the optimal 0.3, 0.1, 0.3, 0.02 and 0.06 T static magnetic fields, respectively. Further analysis of the measured magnetic data revealed that the relaxation of the magnetization is not taking place through a purely Orbach mechanism for these compounds. Instead, relaxation is better described by the other underbarrier mechanisms. This may be due to the strong rhombic contribution in the $\pm m_j$ ground state generated due to a lack of the adequate symmetry around the lanthanide cation. Moreover, relaxation of the magnetization was also observed for the isotropic **11-Gd** compound.

Compounds **16-Ce** and **21-Yb** showed slow relaxation of the magnetization under the optimal external magnetic field of 0.3 and 0.2 T, respectively. Spin relaxation of these compounds was best described by Raman and Direct mechanisms.

Compound **25-Dy** showed Single Molecule Magnet behavior in the 1.9 to 3.7 K temperature range. Moreover, under an external direct current magnetic field of 0.3 and 0.15 T, compounds **26-Nd** and **27-Yb**, showed slow relaxation of the magnetization. Relaxation of the magnetization of **25-Dy** was mainly governed by Orbach, Raman and QTM in the lower temperature range. The QTM effect of **25-Dy** could be removed by applying a static magnetic field. The effective energy barrier obtained from the magnetic data of **25-Dy** is rather low (24.1 cm^{-1} at $H_{dc} = 0$ T). Though **25-Dy** shows SMM behavior, the effect of rhombic contribution significantly lowers the effective energy barrier. Additionally, **26-Nd** and **27-Yb** spin relaxation was best described with Raman and Direct mechanisms.

Finally, compound **30-Dy**, also showed SMM behavior under the narrow temperature range of 1.9-3.5 K and at $H_{dc} = 0$ T, relaxation of the magnetization was dominated by Orbach, Raman and QTM. Interestingly, on applying a static dc magnetic field, the QTM was partially removed and a second process taking place at lower temperatures (close to 2 K) appeared. The presence of two different relaxation of the magnetization processes can be explained due to the presence of two crystallographycally independent Dy^{3+} ions in structure **30-Dy**. However sometimes the presence of two processes is unclear. It can also be assigned due to direct processes originating from intermolecular interactions or from the multi-level system, caused because an external direct current magnetic field is applied to the dysprosium sample.[46]

3.4 References

[1] A. Ouchi, Y. Suzuki, Y. Ohki, Y. Koizumi, Structure of rare earth carboxylates in dimeric and polymeric forms, *Coord. Chem. Rev*. 1988, **92**, 29-43.

[2] R. J. Batrice, J. A. Ridenour, R. L. AyscueIII, J. A. Bertke, K. E. Knope, Synthesis, structure and photoluminescent behavior of molecular lanthanide-2-thiophenecarboxylate-2,2':6',2''-terpyridine materials, *CrystEngComm*, 2017, **19**, 5300-5312.

[3] R.J. Batrice, A.K. Adcock, P.M. Cantos, J.A. Bertke, K.E. Knope, Synthesis and characterization of an isomorphous lanthanide-thiophenemonocarboxylate series (Ln=La-Lu, except Pm) amenable to color tuning, *Cryst. Growth Des*. 2017, **17**, 4603-4612.

[4] W.H. Zhu, X. Xiong, C. Gao, S. Li, Y. Zhang, J. Wang, C. Zhang, A.K. Powell, S. Gao, A family of one-dimensional lanthanide complexes bridged by two distinct carboxylate ligands with the Dy analogue displaying magnetic relaxation behaviour, *Dalton Trans*. 2017, **46**, 14114-14121.

[5] M. Hu, H. Zhao, E.C. Sañudo, M. Chen, Four lanthanide-carboxylate coordination polymers with mixed 2, 3-naphthalenedicarboxylate and phen ligands: syntheses, structures, luminescent and magnetic properties, *Polyhedron*, 2015, **101**, 270-275

[6]. V. V. Utochnikova, A. S. Kalyakina, N. N. Solodukhin, A. N. Aslandukov, On the Structural Features of Substituted Lanthanide Benzoates, *Eur. J. Inorg. Chem*. 2019, 2320-2332.

[7] J.-C. G. Bünzli, Lanthanide luminescent bioprobes, *Chem. Lett*. 2009, **38**, 104-109

[8] J. Perles, M. Iglesias, C. Ruiz-Valero, N. Snejko, Rare-earth as catalytic centers in organo-inorganic polymeric frameworks, *J. Mater. Chem*. 2004, **14**, 2683-2689.

[9] W. Gao, F. Liu, B.Y. Zhang, X.M. Zhang, J.P. Liu, E.Q. Gao, Q.Y. Gao, 2D carboxylate-bridged LnIII coordination polymers: displaying slow magnetic relaxation and luminescence properties in the detection of Fe^{3+}, $Cr_2O_7^{2-}$ and nitrobenzene, *Dalton Trans.*, 2017, **46**, 13878-13887.

[10] D. Peng, L. Yin, P. Hu, B. Li, Z.W. Ouyang, G.L. Zhuang, Z. Wang, Series of highly stable lanthanide-organic frameworks constructed by a bifunctional linker: synthesis, crystal structures, and magnetic and luminescence properties, *Inorg. Chem,* 2018, **57**, 2577-2583.

[11] M. Latva, H. Takalo, V.M. Mukkala, C. Matachescu, J.C. Rodríguez-Ubis, J. Kankare, Correlation between the lowest triplet state energy level of the ligand and lanthanide(III) luminescence quantum yield. *Journal of Luminescence,* 1997, **75**, 149-169.

[12] a) L. Sevéus, M. Väisälä, I. Hemmilä, H. Kojola, G.M. Roomans, E. Soini, Use of fluorescent europium chelates as labels in microscopy allows glutaraldehyde fixation and permanent mounting and leads to reduced autofluorescence and good long-term stability, *Microsc. Res. Tech*. 1994, **28**, 149-154 b) G.Z. Bosshard, G.A. Brito, J.H.S.K. Monteiro, A. de Bettencourt-Dias, I.O. Mazali, F.A. Sigoli, Photophysical properties of asymmetric and water-soluble dinuclear lanthanide complexes of polyglycol chain flunctionalized-benzoic acid derivative: experimental and theoretical approaches, *RSC Adv.*, 2016, **6**, 101133-101141

[13] a) A. S. Kalyakina, V. V. Utochnikova, I. S. Bushmarinov, I. M. Le-Deygen, D. Volz, P. Weis, U. Schepers, N. P. Kuzmina and S. Bräse, Lanthanide Fluroobenzoates as Bio-Probes: a Quest for the Optimal Ligand Fluorination Degree, *Chem. Eur. J.* 2017, **23**, 14944-14953. b) A. S. Kalyakina, V. V. Utochnikova, I. S. Bushmarinov, I. V. Ananyev, I. L. Eremenko, D. Volz, F. Rönicke, U. Schepers, R. Van Deun, A. L. Trigub, Y. V. Zubavichus, N. P. Kuzmina, S. Bräse, *Chem. Eur. J.* 2015, **21**, 17921-17932 c) X.-X. Peng, W.-M. Wang, Y.-F. Zhong, W. Xiao, G.-M. Bao and H.-Q. Yuan, Synthesis, Crystal Structures of Two Lanthanides Complexes with 2,6-Difluorobenzoic Acid, *Chin. J. Inorg. Chem*. 2020, **36**, 921-926 d) A.G. Karipides, J. Jai-Nhuknan and J. S. Cantrell, Aquatris(2,6-difluorobenzoato)praseodymium(III) *Acta Cryst. Sect. C. Crystal Structure Communications*, 1996, **52**, 2740-2742 e) Z. Yu-Fei , W. Wen-Min , P. Xiong-Xin , B. Guang-Ming , H. Chun-Yan and Y. Hou-Qun, The crystal structure of [(tetra-μ_2-2,6-difluorobenzoato-$\kappa^2 O:O'$)-bis-(2,6-difluorobenzoato-$\kappa^2 O:O'$)-bis-(1,10-phenanthroline-$\kappa^2 N:N'$)]dierbium(III) $C_{66}H_{34}N_4O_{12}F_{12}Er_2$, *Zeitschrift für Kristallographie - New Crystal Structures*, 2020, **235**, 473-475.

[14] a) X. Li, Z.-Y. Zhang, Y.-Q. Zou, Synthesis, Structure and Luminescence Properties of Four Novel Terbium 2-Fluorbenzoate Complexes. *Eur. J. Inorg. Chem*. 2005, 2909-2918 b) X. Li, Y.-

Q. Zou, H.-B. Song, Synthesis and Crystal Structure of Complex [Nd(2-$FC_6H_4COO)_3$·(2-$FC_6H_4COOH)$·$H_2O]_2$, *J. Chem. Cryst*. 2007, **37**, 555-559.

[15] (a) M. Llunell, D. Casanova, J. Cirera, P. Alemany, S. Alvarez, Shape Program., version 2, Universitat de Barcelona, Barcelona, Spain, 2010; (b) P. Alemany, D. Casanova, S. Alvarez, C. Dryzum, D. Avnir, Continuous Symmetry Measures: A New Tool in Quantum Chemistry, *Rev. Comput. Chem.*, 2017, **30**, 289-352.

[16] R. A. Coxall, S. G. Harris, D. K. Henderson, S. Parsons, P. A. Tasker, R. E. P. Winpenny, Inter-ligand reactions: in situ formation of new polydentate ligands, *J. Chem. Soc.*, *Dalton Trans.* 2000, 2349-2356.

[17] a) C. K. Jayasankar, E. Rukmini, Optical properties of Sm^{3+} ion in zinc and alkali zinc borosulphate glasses, *Optical Materials,* 1997, **8,** 193-205 b) R. Yu, N. Xue, T. Wang, Z. Zhao, J. Wang, Z. Hei, M. Li, H. Mi Noh, J. H. Jeong, Photoluminescence characteristics of high thermal stable fluorosilicate apatite $Ba_2Y_3(SiO_4)_3F:Sm^{3+}$ orange-red emitting phosphor, *Ceramics international*, 2015, **41**, 6030-6036.

[18] a) Binnemans, K., Interpretation of europium (III) spectra, *Coordination Chemistry Reviews*, 2015, **295**, 1-45, b) Carnall, W. T., Fields, P. R., & Rajnak, K., *The Journal of chemical physics*, Electronic Energy Levels of the Trivalent lanthanide Aquo Ions. III. Tb^{3+}, 1968**, 49**, 10, 4447-4449, c) A. M. Kaczmarek, K. Van Hecke and R. Van Hecke, Enhanced Luminescence in Ln^{3+}-Doped Y_2WO_6 (Sm, Eu, Dy) 3D Microstructures through Gd^{3+} Codoping *Inorg. Chem*., 2014, **53**, 9498-9508, d) S. Chemingui, M. Ferhi, K. Horchani-Naifer, M. Férid, Synthesis and luminescence characteristics of Dy^{3+} doped KLa $(PO_3)_4$, *Journal of Luminescence*, 2015, **166**, 82-87, e) M. J. Weber, T.E. Varitimos, Optical Spectra and Intensities of Nd^{3+} in $YAlO_3$ *J. Appl. Phys*., 1971, **42**, 4996-5005, f) Y. Hasegawa, K. Murakoshi, Y. Wada, S. Yanagida, J.H. Kim, N. Nakashima and T. Yamanaka, Enhancement of luminescence of Nd^{3+} complexes with deuterated hexafluoroacetylacetonato ligands in organic solvent, *Chemical physics letters,* 1996, **248**, 8-12 g) Y. Hasegawa, Y. Kimura, K. Murakoshi, Y. Wada, J. H. Kim, N. Nakashima, T. Yamanaka and S. Yanagida, Enhanced Emission of Deuterated Tris(hexafluoroacetylacetonato) neodymium(III) Complex in Solution by Suppression of Radiationless Transition via Vibrational Excitation, *J. Phys. Chem.* 1996, **100**, *24*, 10201-10205, h) R. Vicente, À. Tubau, S. Speed, F. A.

Mautner, F. Bierbaumer, R. C. Fisher and S.S. Massoud, Slow magnetic relaxation and luminescence properties in neodymium (III)-4, 4, 4-trifluoro-1-(2-naphthyl) butane-1, 3-dionato complexes incorporating bipyridyl ligands *New J. Chem.*, 2021, **45**,14713-14723, i) C. Strohhöfer, A. Polman, Absorption and emission spectroscopy in Er^{3+}–Yb^{3+} doped aluminum oxide waveguides, *Optical Materials*, 2003, **21**, 705-712 j) W. G. Perkins, G. A. Crosby, Crystal-Field Splitting in Yb^{3+} Chelates, *J. Chem. Phys.*, 1965, **42**, 407-414.

[19] V. Thomas , A. Elizebeth, H. Thomas, G. Jose, N. V. Unnikrishnan, C. Joseph, M. A. Ittyachen, Studies on the growth and optical characterization of dysprosium praseodymium oxalate single crystals. *J Optoelectron Adv Mater*, 2005, **7,** 2687.

[20] Y.C. Li, Y.H. Chang, Y.S. Chang, Y.J. Lin, C.H. Laing, Luminescence and Energy Transfer Properties of Gd^{3+} and Tb^{3+} in $LaAlGe_2O_7$*, J. Phys. Chem. C* 2007, **111**, 10682-10688.

[21] a) *The Rare Earth Elements: Fundamentals and Applications*, ed. D. A. Atwood, John Wiley & Sons Ltd, 2012; (b) *Luminescence of Lanthanide Ions in Coordination Compounds and Nanomaterials*, ed. A. de Bettencourt-Dias, John Wiley & Sons Ltd, 2014.

[22] C. M. Reddy, B. D. P. Raju, N. J. Sushma, N. S. Dhoble, S.J. Dhoble, A review on optical and photoluminescence of RE^{3+} (RE= Sm, Dy, Eu, Tb and Nd) ions doped LCZSFB glasses. *Renewable and Sustainable Energy Reviews*, 2015, **5**, 566-584.

[23] J. W. de Oliveira Maciel, M. A. Lemes, A. K. Valdo, R. Rabelo, F. Terra Martins, L. J. Queiroz Maia, R. Costa de Santana, F. Lloret, M. Julve and D. Cangussu. Europium(III), Terbium(III) and Gadolinium(III) Oxamato-Based Coordination Polymers: Visible Luminescence and Slow Magnetic Relaxation. *Inorg. Chem.,* 2021, **60**, 6176−6190.

[24] a) W. De W. H. Jr. and D. R. Sudnick, Lanthanide ion probes of structure in biology. Laser-induced luminescence decay constants provide a direct measure of the number of metal-coordinated water molecules, *J. Am. Chem. Soc.* 1979, **101**, 334–340 b) Supkowski, R. M.; Horrocks, W. D. W., Jr. On the determination of the number of water molecules, q, coordinated to europium (III) ions in solution from luminescence decay lifetimes *Inorg. Chim. Acta,* 2002, **340**, 44−48.

[25] M. H. V. Werts, R. T. F. Jukes, J. W. Verhoeven, The emission spectrum and the radiative lifetime of Eu^{3+} in luminescent lanthanide complexes. *Phys. Chem. Chem. Phys.*, 2002, **4**, 1542-1548.

[26] J.-C. G. Bünzli, On the design of highly luminescent lanthanide complexes, *Coord. Chem. Rev.*, 2015, **19**, 293–294

[27] a) M. Andruh, E. Bakalbassis, O. Kahn, J. C. Trombe and P. Porcher, Structure, spectroscopic and magnetic properties of rare earth metal (III) derivatives with the 2-formyl-4-methyl-6-(N-(2-pyridylethyl)formimidoyl)phenol ligand. *Inorg. Chem.* 1993, **32**, 1616-1622. b) O. Kahn, *Molecular Magnetism*, VHC Publishers, Inc., USA, 1993.

[28] a) M. Orendáč, L. Sedláková, E. Čižmár, A. Orendáčová, A. Feher, S. A. Zvyagin, J. Wosnitza, W. H. Zhu, Z. M. Wang, and S. Gao, Spin relaxation and resonant phonon trapping in $[Gd_2(fum)_3(H_2O)_4]\cdot 3H_2O$, *Phys. Rev. B: Condens. Matter Mater, Phys*., 2010, **81**, 214410 b) Y. Horii, K. Katoh, Y. Miyazaki, M. Damjanović, T. Sato, L. Ungur, L.F. Chibotaru, B.K. Breedlove, Prof. Dr. M. Nakano, W. Wernsdorfer, M. Yamashita, Coexistence of Spin-Lattice Relaxation and Phonon-Bottleneck Process in Gd^{III}-Phthlocyaninato Triple-Decker Complexes under Highly Diluted Conditions, *Chem. Eur. J*- 2020, **26**, 8076-8082

[29] L. E. Roy, T. Hughbanks, Magnetic Coupling in Dinuclear Gd Complexes, *J. Am. Chem. Soc.*, 2006, **128**, 568-575.

[30] a) J. Tang, I. Hewitt, N.T. Madhu, G. Chastanet, W. Wernsdorfer, C. E. Anson, C. Benelli, R. Sessoli and A. K. Powell, Dysprosium Triangles Showing Single-Molecule Magnet Behavior of Thermally Excited Spin States, Angew. Chem. Int. Ed. 2006, **45**, 1729-1733. b) P.-H. Lin, W.-B. Sun, M.-F. Yu, G.-M. Li, P.-F. Yan and M. Murugesu, An unsymmetrical coordination environment leading to relaxation in a Dy_2 single-molecule magnet, Chem. Commun., 2011, **47**, 10993-10995.

[31] A. Zabala-Lekuona, J. M. Seco, E. Colacio, Single-Molecule Magnets: From Mn_{12}-ac to dysprosium metallocenes, a travel in time. *Coord. Chem. Rev.*, 2021, **441**, 213984.

[32] F. A. Mautner, F. Bierbaumer, R. C. Fischer, À. Tubau, S. Speed, E. Ruiz, S. S. Massoud, R, Vicente, S. Gómez-Coca. Insights into the Spin Dynamics of Mononuclear Cerium(III) Single-Molecule Magnets. *Inorg. Chem.,* 2022, **61**, 11124-11136

[33] S. T. Liddle, J. van Slageren, Improving f-element single molecule magnets, *Chem. Soc. Rev*., 2015, **44**, 6655.

[34] a) J. Mayans, A. Escuer, Correlating the axial Zero Field Splitting with the slow magnetic relaxation in Gd^{III} SIMs, *Chem. Commun.,* 2021, **57**, 721 b) E. Pilichos, M. Font-Bardia, A. Escuer, J Mayans, Structural and magnetic studies of mononuclear lanthanide complexes derived from N-rich chiral Schiff bases, *Dalton Trans*., 2021, **50**, 1746-1753 c) A. Vráblová, M. Tomás, L. R. Falvello, L. Dlhán, J. Titis, J. Cernák and R. Boca, Slow magnetic relaxation in Ni-Ln (Ln=Ce, Gd, Dy dinuclear complexes), *Dalton Trans.*, 2019, **48**, 13943-13952 d) TK Ghosh, S Maity, J Mayans, A Ghosh, Family of Isomeric Cu^{II}-Ln^{III} (Ln=Gd, Tb and Dy) Complexes Presenting Field-Induced Slow Relaxation of Magnetization Only for the Members Containing Gd^{III}, *Inorg. Chem.*, 2021, **60**, 438-448.

[35] a) C. Janiak, A critical account on π–π stacking in metal complexes with aromatic nitrogen-containing ligands, *J. Chem. Soc., Dalton Trans*., 2000, **21**, 3885-3896 b) S. Alvarez, A cartography of the van der Waals territories, *Dalton Trans*., 2013, **42**, 8617-8636.

[36] A. Aebischer, F. Gumy, J.-C. G. Bünzli, Intrinsic quantum yields and radiative lifetimes of lanthanide tris(dipicolinates). *Phys. Chem. Chem. Phys*., 2009, **11**, 1346-1353.

[37] W.-M. Wang, W.-Z. Qiao, H.-X. Zhang, S.-Y. Wang, Y.-Y. Nie, H.-M. Chen, Z. Liu, H.-L. Gao, J.-Z- Cui and B. Zhao, Structures and magnetic properties of several phenoxo-O bridged dinuclear lanthanide complexes: Dy derivatives displaying substituent dependent magnetic relaxation behavior *Dalton Trans*., 2016, **45**, 8182-8191.

[38] a) K. N. Shrivastava, Theory of Spin–Lattice Relaxation, *Physica status solidi (b),* 1983, **117**, 437-458. b) R. Orbach, On the theory of spin-lattice relaxation in paramagnetic salts. *Proc. Phys. Soc.* 1961, **77**, 821-826. c) H. B. G. Casimir, F. K. Du Pré, Note on the thermodynamic interpretation of paramagnetic relaxation phenomena, *Physica.* 1938, **5**, 507-511.

[39] Y.-N. Guo, G.-F. Xu, Y. Guo and J. Tang, Relaxation dynamics of dysprosium(III) single molecule magnets, *Dalton Trans*., 2011**, 40**, 9953-9963.

[40] H.B.G. Casimir, D. Bijl, F.K. Du Pré, Measurements on Paramagnetic relaxation in chromium potassium alum. *Physica*, 1941, **8**, 449-460.

[41] N. F. Chilton, CC-FIT, program/ https://www.nfchilton.com/ software.html, 2014.

[42] a) F. Guégan, J. Jung, B. L. Guennic, F. Riobé, O. Maury, B. Gillon, J. F. Jacquot, Y. Guyot, C. Morell, D. Luneau, Evidencing under-barrier phenomena in a Yb(iii) SMM: a joint luminescence/neutron diffraction/SQUID study. *Inorg. Chem. Front.*, 2019, **6**, 3152-3157. b) K. S. Pedersen, J. Dreiser, H. Weihe, R. Sibille, H. V. Johannesen, M. A. Sørensen, B. E. Nielsen, M. Sigrist, H. Mutka, S. Rols, J. Bendix, S. Piligkos, Design of Single-Molecule Magnets: Insufficiency of the Anisotropy Barrier as the Sole Criterion *Inorg. Chem*., 2015, **54**, 7600-7606. c) D. Q. Wu, D. Shao, X. Q. Wei, F. X. Shen, L. Shi, Y. Q. Zhang, X. Y. Wang, Single-ion magnetism in seven-coordinate YbIII complexes with distorted D_{5h} coordination geometry. *Dalton Trans.*, 2017, **46**, 12884-12892. d) W. Zhao, H. Cui, X.-Y. Chen, G. Yi, L. Chen, A. Yuan, C. L. Luo, An eight-coordinate ytterbium complex with a hexagonal bipyramid geometry exhibiting fieldinduced single-ion magnet behaviour. *Dalton Trans*., 2019, **48**, 5621-5626.

[43] a) J. Mayans, L. Tesi, M. Briganti, M. E. Boulon, M. Font-Bardía, A. Escuer, L. Sorace, Single-Ion Anisotropy and Intramolecular Interactions in Ce^{III} and Nd^{III} Dimers, *Inorg. Chem*. 2021, **60**, 8692-8703 b) E. Lucaccini, J. J. Baldoví, L. Chelazzi, A.-L. Barra, F. Grepioni, J.-P- Costes, and L. Sorace, Electronic Structure and Magnetic Anisotropy in Lanthanoid Single-Ion Magnets with C3 Symmetry: The Ln(trenovan) Series, *Inorg. Chem*. 2017, **56**, 4728-4738. c) E. Rousset, M. Piccardo, M.-E. Boulon, R. W. Gable, A. Soncini, L. Sorace and C. Boskovic, Slow magnetic relaxation in lanthanoid crown ether complexes: interplay of Raman and anomalous phonon bottleneck processes, *Chem. Eur. J*. 2018, **24,** 14768-14785. d) S. K. Gupta, T. Rajeshkumar, G. Rajaraman and R. Murugavel, An unprecedented zero field neodymium (III) single-ion magnet based on a phosphonic diamide, *Chem. Commun*., 2016, **52**, 7168. e) Y.-C. Chen, X.-S. Huang, J.-L- Liu and M.-L. Tong, Magnetic Dynamics of a Neodymium (III) Single-Ion Magnet *Inorg. Chem.* 2018, **57**, 11782-11787.

[44] M.C. Heffern, L.M. Matosziuk, T.J. Meade, Lanthanide probes for bioresponsive imaging, *Chem. Rev*. 2014, **8**, 4496-4539.

[45] Y.-N. Guo, G.-F. Xu, Y. Guo and J. Tang, Relaxation dynamics of dysprosium(III) single molecule magnets, *Dalton Trans*. 2011, **40**, 9953-9963.

[46] a) Y.N. Guo, G.F. Xu, P. Gamez, L. Zhao, S.Y. Lin, R. Deng, J. Tang, H.J. Zhang, Two-step relaxation in a linear tetranuclear dysprosium(III) aggregate showing single-molecule magnet behavior. *J. Am. Chem. Soc.*, 2010, **132**, 8538–8539 b) J. Ruiz, A.J. Mota, A. Rodríguez-Diéguez, S. Titos, J.M. Herrera, E. Ruiz, E. Cremades, J.P. Costes, E. Colacio, Field and dilution effects on the slow relaxation of a luminescent DyO_9 low-symmetry single-ion magnet, *Chem. Commun*., 2012, **48**, 7916-7918 c) A. Arauzo, A. Lazarescu, S. Shova, E. Bartolomé, R. Cases, J. Luzón, J. Bartolomé, C. Turta, Structural and magnetic properties of some lanthanide (Ln=Eu(III), Gd(III) and Nd(III)) cyanoacetate polymers: field-induced slow magnetic relaxation in the Gd and Nd substitutions, *Dalton Trans*., 2014, **43**, 12342–12356

4. Lanthanide coordination compounds derived from chiral carboxylates

4. Lanthanide coordination compounds derived from chiral carboxylates

In *Chapter 3* we have studied multiproperty lanthanide complexes derived from fluorocarboxylate ligands, which until now, includes luminescence and magnetic properties. In *Chapter 4*, continuing with the study of multiproperty lanthanide compounds, the study of the chiroptical characteristics is also developed. In this *Thesis*, the chiroptical properties of the final compounds are characterized by means of Circular Dichroism (CD) and Circular Polarized Luminescence (CPL). As stated in the introduction, chiral ligands may induce chirality to the final coordination compound conferring polarized luminescence in case of the compounds showing luminescence properties. The chiral ligands in charge to induce chirality to the new lanthanide(III) synthetized compounds which will be described in this *Chapter* are the pure enantiomeric *R*- or *S*-(+ or -)-α-methoxyphenylacetic acid (*R*- and *S*-HMPA), Scheme 4.1a) and *R* or *S*-(- or +)-2-Phenylbutiric acid (R/S-2-HPhBut), Scheme 4.2c). Moreover, because of the weak *f-f* absorption transitions of the trivalent ions, suitable chromophore organic ligands able to effectively transfer the absorbed energy to the emitting states of the lanthanide ions, are employed in the design of the presented compounds. In *Chapter 4*, 1,10-phenantholine (phen) and 4,7-Diphenyl-1,10-phenanthroline (bathophen) molecules, Scheme 4.1b) and d), are chosen to play the role of the sensitizer.

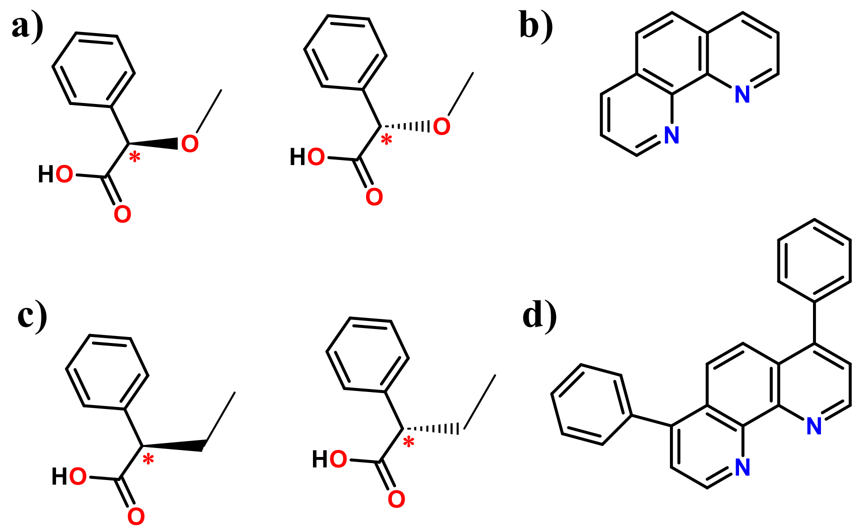

Scheme 4.1 a) *R*- and *S*-α-methoxyphenylacetic acid (*R*- and *S*-HMPA) b) 1.10-phenantroline (phen) c) *R* and *S*-2-phenylbutanoic acid (*R* and *S*-2-HPhBut) and d) 4,7-Diphenyl-1,10-phenanthroline (bathophen).

The reaction with *R*- and *S*-HMPA with Ln^{3+} salts, with the addition to the 1.10-phenantroline (phen) auxiliary ligand, led to new 1D complexes showing general formula [Ln(μ-*R*-MPA)(*R*-MPA)$_2$(phen)]$_n$ or [Ln(μ-*S*-MPA)(*S*-MPA)$_2$(phen)]$_n$ (*Section 4.1)*. The enantiomeric pairs obtained in the first chiral family are ***R*-33-Ce** and ***S*-34-Ce**, ***R*-35-Nd** and ***S*-36-Nd**, ***R*-37-Eu** and ***S*-38-Eu**, ***R*-39-Tb** and ***S*-40-Tb**, ***R*-41-Dy** and ***S*-42-Dy**, ***R*-43-Sm** and ***S*-44-Sm** and ***R*-45-Er** and ***S*-46-Er**. The presence of the methoxy group in the α-methoxyphenylacetate ligand induces the formation of a 1D polymeric chain. In the literature, solved crystal structures of compounds derived from the *R/S*-MPA ligand are only found in transition metal coordination complexes (Co, Cu and Ni), where their magnetic properties were studied. However, lanthanide coordination compounds derived from the *R/S*-MPA ligand, focusing on their chiroptical properties, were still not reported.[1]

Moreover, a second group of lanthanide chiral compounds is presented herein (*Section 4.2*), with the enantiopure *R* or *S*-(- or +)-2-Phenylbutirate ligand (*R/S*-2-PhBut) as the chiral ligand and the 4,7-Diphenyl-1,10-phenanthroline (bathophen) molecule as the chromophore moiety. From these ligands, a new family of dinuclear lanthanide compounds of formula [Ln$_2$(μ-*R/S*-2-PhBut)$_4$(*R/S*-2PhBut)$_2$(bathophen)$_2$] was obtained. Interestingly this family of chiral complexes undergo through a structural change along the lanthanide 6th period, showing two different structural motifs *a* and *b* with coordination numbers of 9 and 8 respectively where Ln = Nd^{3+} (***R*-47-Nd-a** and ***S*-48-Nd-a**), Sm^{3+} (***R*-49-Sm-a** and ***S*-50-Sm-a**), Eu^{3+} (***R*-51-Eu-a** and ***S*-52-Eu-a**), Tb^{3+} (***R*-53-Tb-a** and ***S*-54-Tb-a**, ***R*-55-Tb-b** and ***S*-56-Tb-b**), Dy^{3+} (***R*-57-Dy-a** and ***S*-58-Dy-a**, ***R*-59-Dy-b** and ***S*-60-Dy-b**), Tm^{3+} (***R*-61-Tm-b** and ***S*-62-Tm-b**) and Yb^{3+} (***R*-63-Yb-b** and ***S*-64-Yb-a**) for *R*- or *S*-2-PhBut respectively. The structural motif *a* with coordination number 9 is found in lighter lanthanides whereas the structural motif *b* with coordination number 8 is found in heavier lanthanides.

H.-R. Wen *et al.*[2] published a family of dinuclear lanthanide compounds containing the *R*- or *S*-2-PhBut and phen ligands with formula $[Ln_2(\mu\text{-}R/S\text{-2-PhBut})_4(R/S\text{-2PhBut})_2(phen)_2]$. From those compounds only the circular dichroism measurements were conducted in solution, but no CPL studies were achieved. In the published report the europium and terbium analogues presented good luminescence properties. By replacing the phen ligand with a chromophore molecule that has higher electron delocalization such as bathophen, we expect to increase the luminescence efficiency of our compounds. Moreover, another study was realized by S. Kaizaki *et al.*[3] where chiroptical properties via near Infrared CD were studied for a series of nIR emitters (Ho^{3+}, Dy^{3+}, Nd^{3+} and Yb^{3+}) coordination compounds derived from the *R/S*-2-PhBut chiral ligand and a hydrotris(pyrazol-1-yl)borate molecule.

Further lanthanide compounds derived from the *R/S*-2-PhBut ligand are found in the literature. For instance, a mononuclear Lanthanum compound with formula $[La(R/S\text{-2-PhBut})_2(phen)_2(NO_3)]$ which showed cleaving efficiency to the DNA or a dinuclear Nd-based compound of formula $[Nd_2(\mu\text{-}R/S\text{-2-PhBut})_4(R/S\text{-2-PhBut})_2(R/S\text{-2-HPhBut})_4]$ which could act as a neodymium carboxylate precursor for diene polymerization catalysis.[4,5]

Returning to the new chiral compounds presented in this *Chapter* with formula $[Ln_2(\mu\text{-}R/S\text{-2-PhBut})_4(R/S\text{-2PhBut})_2(bathophen)_2]$, the structural analyses were performed with single crystal X-Ray diffraction. Moreover, the luminescence as well as their chiroptical characteristics were analysed by means of Circular Dichroism and Circularly Polarized Luminescence. Magnetic studies are further studied herein as most of the compounds show both, luminescence and magnetic properties.

4.1 Compounds derived from (*S*)-(-)- or (*R*)-(+)-α-Methoxyphenylacetic acid (R/S-HMPA)

4.1.1 Experimental procedure

Compounds ***R*-** and ***S*- 33-46** were obtained through the following experimental procedure: into 20 mL of an ethanol/water solution in the 1:1 ratio, the respective *R/S*-α-methoxyphenilacetic acid (*R/S*-HMPA) (1.5 mmol, 249 mg) and KOH (1.5 mmol, 84.2 mg) were dissolved. Then, 1,10-phenantroline (0.3 mmol, 54 mg) dissolved in 5 mL of ethanol/water (1:1) was added. Afterward, a solution (5mL) in the same ethanol/water ratio with the $Ln(NO_3)_3\cdot nH_2O$ salt (0.22 mmol) was added dropwise into the reaction mixture. The colorless solution was magnetically stirred for 1h and then left to stand at room temperature. After 1 week, needle shaped white single crystals suitable for monocrystal X-Ray diffraction appeared in fairly high yields between 70-80 %.

Through this synthetic procedure, enantiomerically pure compounds of formula [Ln(μ-*R*-MPA)(*R*-MPA)$_2$(phen)]$_n$ or [Ln(μ-*S*-MPA)(*S*-MPA)$_2$(phen)]$_n$ were obtained. The lanthanide used to obtain ***R*-** or ***S*- 33-46** complexes were Ce^{3+} for ***R*-33-Ce** and ***S*-34-Ce**, Nd^{3+} for ***R*-35-Nd** and ***S*-36-Nd**, Eu^{3+} for ***R*-37-Eu** and ***S*-38-Eu**, Tb^{3+} for ***R*-39-Tb** and ***S*-40-Tb**, Dy^{3+} for ***R*-41-Dy** and ***S*-42-Dy**, Sm^{3+} for ***R*-43-Sm** and ***S*-44-Sm** and Er^{3+} for ***R*-45-Er** and ***S*-46-Er**.

Further characterization of these compounds was realized by carrying out elemental analysis Table 4. 1 and ATR Infra-Red spectroscopy, Table APX.IX.1.

Table 4. 1 Elemental analysis of compounds **R-** or **S- 33-46**.

	Calculated			**Found**				**Calculated**			**Found**		
Compound	**%C**	**%H**	**%N**	**%C**	**%H**	**%N**	**Compound**	**%C**	**%H**	**%N**	**%C**	**%H**	**%N**
***R*-33-Ce**	57.4	4.3	3.4	57.1	4.4	3.4	***S*-34-Ce**	57.4	4.3	3.4	57.2	4.1	3.5
***R*-35-Nd**	57.1	4.3	3.4	56.8	4.5	3.6	***S*-36-Nd**	57.1	4.3	3.4	57.1	4.3	3.5
***R*-37-Eu**	56.6	4.3	3.4	57.0	4.4	3.4	***S*-38-Eu**	56.6	4.3	3.4	56.6	4.6	3.4
***R*-39-Tb**	56.1	4.2	3.4	56.5	4.4	3.4	***S*-40-Tb**	56.1	4.2	3.4	56.2	4.3	3.4
***R*-41-Dy**	55.9	4.2	3.3	56.2	4.2	3.3	***S*-42-Dy**	55.9	4.2	3.3	56.2	4.2	3.3
***R*-43-Sm**	56.7	4.3	3.4	57.0	4.3	3.4	***S*-44-Sm**	56.7	4.3	3.4	56.5	4.4	3.4
***R*-45-Er**	55.6	4.2	3.3	55.8	4.2	3.1	***S*-46-Er**	55.6	4.2	3.3	55.6	4.3	3.4

4.1.2 Structural characterization

Single Crystal X-Ray diffraction measurements were performed for compounds ***R*-37-Eu** and ***S*-38-Eu, *R*-39-Tb** and ***S*-40-Tb**, ***S*-42-Dy** and ***S*-44-Sm.** All compounds crystallize in the monoclinic $P2_1$ space group. Their asymmetric unit consists of a unit formed by one Ln^{3+} ion, two chelating *R/S*-α-methoxyphenylacetate (*R/S*-MPA) ligands, one *R/S*-MPA bridging ligand and one phen molecule. The asymmetric unit is expanded in space forming a 1D polymeric chain along the crystallographic *a* axis. All lanthanide compounds presented the same structural motif therefore only structure of compound ***R*-37-Eu** is described below.

A partially labelled plot of ***R*-37-Eu** is shown in Figure 4. 1 and the mirror image of ***R*-37-Eu** and ***S*-38-Eu** compounds is depicted in Figure 4. 2. Selected bond distances of compounds ***R*-37-Eu** and ***S*-38-Eu, *R*-39-Tb** and ***S*-40-Tb**, ***S*-42-Dy** and ***S*-44-Sm** and crystallographic information are listed in Table 4. 3 and Table APX.IX.2 respectively.

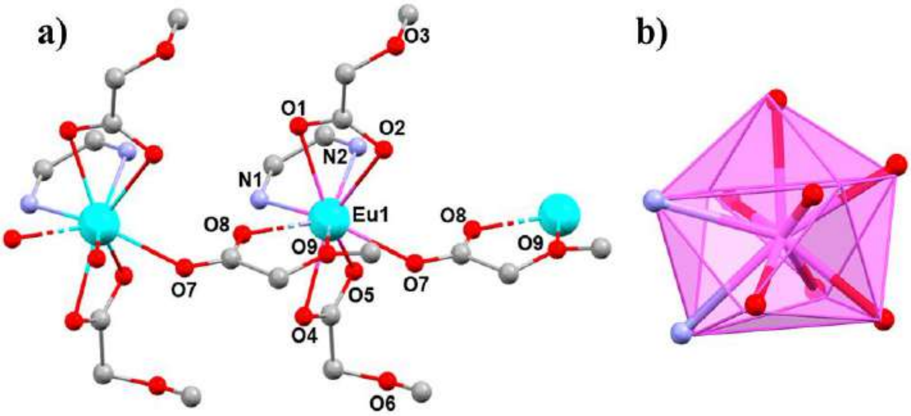

Figure 4. 1 a) partially labelled plot of compound ***R*-37-Eu**. Phenyl groups and H atoms have been omitted for a better view of the 1D structure and b) idealized coordination polyhedron (Spherical tricapped trigonal prism) compared with the real positions of the coordinating atoms in ***R*-37-Eu.**

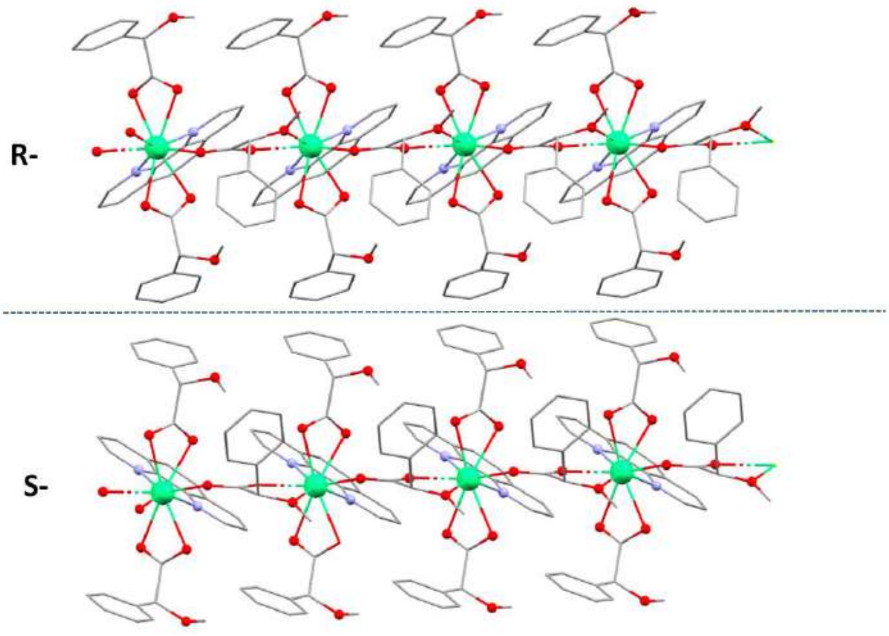

Figure 4. 2 Compounds ***R*-37-Eu** and ***S*-38-Eu** presented as the mirror image of each other.

Structure ***R*-37-Eu** consists of a 1D polymeric chain of formula [Eu(μ-*R*-MPA)(*R*-MPA)$_2$(phen)]$_n$ where each Eu^{3+} is nonacoordinated. The polymeric chain extends along the [1 0 0] direction. The EuO$_7$N$_2$ coordination sphere encompasses two *R*-MPA ligands that are coordinated in the bidentate carboxylate chelating coordination mode (Scheme 4.2a) to Eu1 by O1, O2 and O4, O5 atoms, with Eu-O bond distances in the range of 2.450-2.500 Å. Another *R*-MPA ligand is bridging two Eu^{3+} cations through the O7 and O8 atoms from the carboxylate group in the *syn-anti* conformation mode (Scheme 4.2b). The O9 oxygen atom from the methoxy group of this *R*-MPA ligand coordinates also to the neighbouring europium atom, Figure 4. 1a). The Eu-O7, Eu-O8 and Eu-O9 bond distances are 2.396, 2.388 and 2.539 Å respectively. Finally, the coordination sphere of the lanthanide ion is completed by two N atoms (N1 and N2) from the 1,10-phenantroline molecule in the chelating coordination mode with Eu-N distances of 2.569 and 2.558 Å for Eu-N1 and Eu-N2 respectively. The Eu1---Eu1_a intrachain distance is 6.048 Å and the shortest Eu---Eu interchain distance is 12.298 Å. The crystal structure of ***S*-38-Eu** is very similar to ***R*-37-Eu** but its configuration is mirror symmetrical with ***R*-37-Eu.** Symmetry operators for generating equivalent positions are: _a) -1+x, y, z. The 1D chains along the [1 0 0] base vector stands through weak Van der Waals interactions forming the chiral crystal.

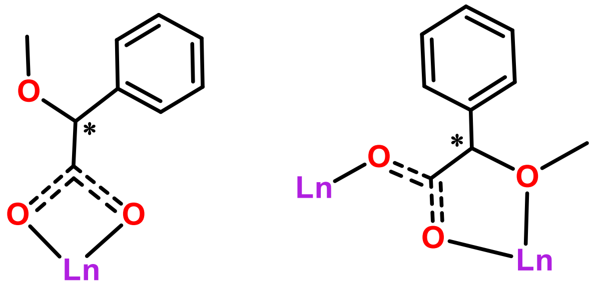

a) Chelating

b) syn-anti, bridging and chelating

Scheme 4.2. Coordination modes of *R/S*-α-methoxyphenylacetate (R/S-MPA) found in compound ***R*-37-Eu.**

The SHAPE software,[6] was used to determine the degree of distortion of the coordination polyhedron in compound ***R*-37-Eu**. The O and N atoms around the Eu^{3+} cation are set in a distorted polyhedron close to a Spherical tricapped trigonal prism (TCTPR-9, D_{3h}), with a Continuous Shape Measurement (CShM) value of 1.821, Figure 4. 1b). Moreover, coordination geometry found for compounds ***S*-38-Eu, *R*-39-Tb** and ***S*-40-Tb**, ***S*-42-Dy** and ***S*-44-Sm** also consisted of a distorted Spherical tricapped trigonal prism (TCTPR-9, D_{3h}). The CShM values are compiled in Figure 4. 2.

Table 4. 2 Continuous Shape measurements (CShM) obtained for the coordination geometry of compounds ***R*-37-Eu, *S*-38-Eu, *R*-39-Tb** and ***S*-40-Tb**, ***S*-42-Dy** and ***S*-44-Sm**.

Compound	**TCTPR-9 (D$_{3}$h)**
***R*-37-Eu**	1.821
***S*-38-Eu**	1.928
***R*-39-Tb**	1.821
***S*-40-Tb**	1.832
***S*-42-Dy**	1.775
***S*-44-Sm**	1.992

The Ln-O and Ln-N bond lengths diminish following $Sm^{3+}>Eu^{3+}>Tb^{3+}>Dy^{3+}$, confirming the lanthanide(III) contraction tendency along the 6th period.[7]

Table 4. 3 Selected bond distances (Å) of compounds **R-37-Eu**, **S-38-Eu**, **R-39-Tb**, **S-40-Tb**, **S-42-Dy** and **S-44-Sm**.

Bond distance (Å)	***R*-37-Eu**	***S*-38-Eu**	***R*-39-Tb**	***S*-40-Tb**	***S*-42-Dy**	***S*-44-Sm**
Ln-O1	2.500(5)	2.478(3)	2.417(2)	2.461(3)	2.456(6)	2.461(2)
LnO2	2.489(5)	2.445(4)	2.4601(18)	2.416(3)	2.464(5)	2.4891(19)
Ln-O4	2.450(6)	2.489(3)	2.4740(18)	2.470(3)	2.395(6)	2.510(2)
Ln-O5	2.476(5)	2.498(3)	2.4674(19)	2.475(3)	2.453(5)	2.4988(18)
Ln-O7	2.396(5)	2.394(3)	2.3688(18)	2.371(2)	2.364(4)	2.4050(19)
Ln-O8	2.388(4)	2.395(2)	2.3639(13)	2.365(2)	2.356(5)	2.4039(19)
Ln-O9	2.539(5)	2.540(3)	2.525(19)	2.521(3)	2.513(5)	2.557(2)
Ln-N1	2.569(5)	2.564(4)	2.545(2)	2.537(3)	2.527(7)	2.583(2)
Ln-N2	2.558(6)	2.567(4)	2.538(2)	2.545(4)	2.523(6)	2.582(2)
Ln---Ln (intrachain)	6.048(5)	6.047(4)	6.054(8)	6.036(4)	6.025(4)	6.052(3)
Ln---Ln Shortest interchain distance	12.298	12.310	12.312	12.326	12.353	12.297

Powder X-Ray Diffraction (PXRD) measurements were performed on ***S*-38-Eu, *R*-39-Tb** and ***S*-40-Tb**, ***S*-42-Dy** and ***S*-44-Sm** powder samples to confirm phase purity along all the polycrystalline sample. The measured diffractograms were compared to the calculated patterns from the crystal structures, Figure 4. 3. Moreover, the calculated patterns were compared to the measured diffractograms of ***R*-33-Ce**, ***S*-34-Ce**, ***R*-35-Nd**, ***S*-36-Nd**, ***R*-41-Dy**, ***R*-43-Sm**, ***R*-45-Er** and ***S*-46-Er** polycrystalline samples. All PXRD measurements matched to the calculated patterns from crystal structures confirming that the obtained powders are phase pure and isostructural, Figure 4. 4.

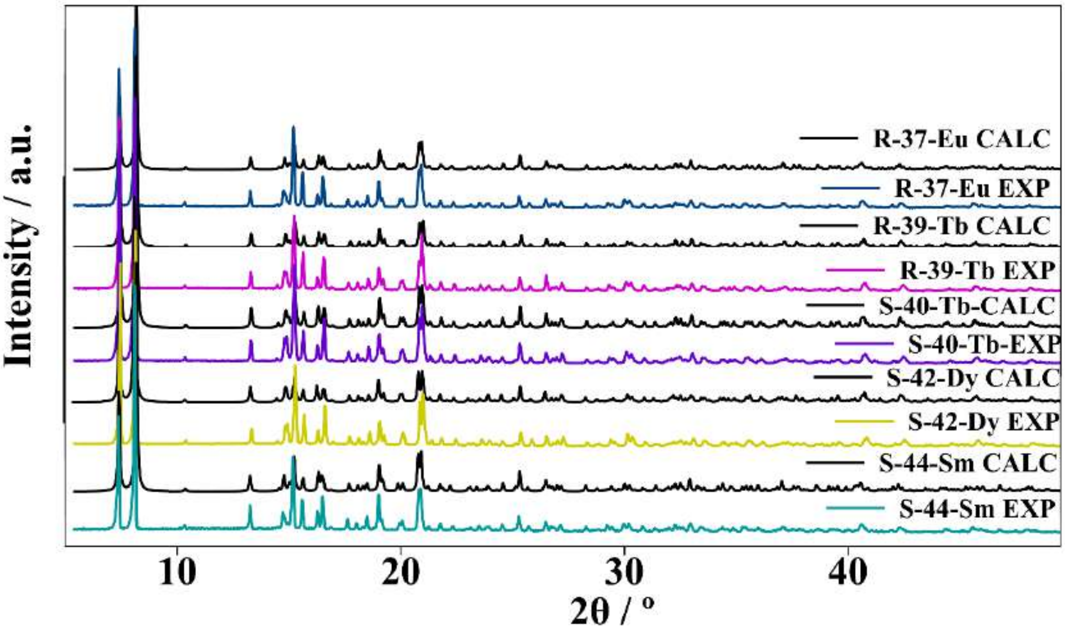

Figure 4. 3 Powder X-Ray Diffraction of compounds ***S*-38-Eu, *R*-39-Tb** and ***S*-40-Tb**, ***S*-42-Dy** and ***S*-44-Sm.** CALC stands for the patterns calculated from the crystal structure and EXP stands for the calculated diffractograms.

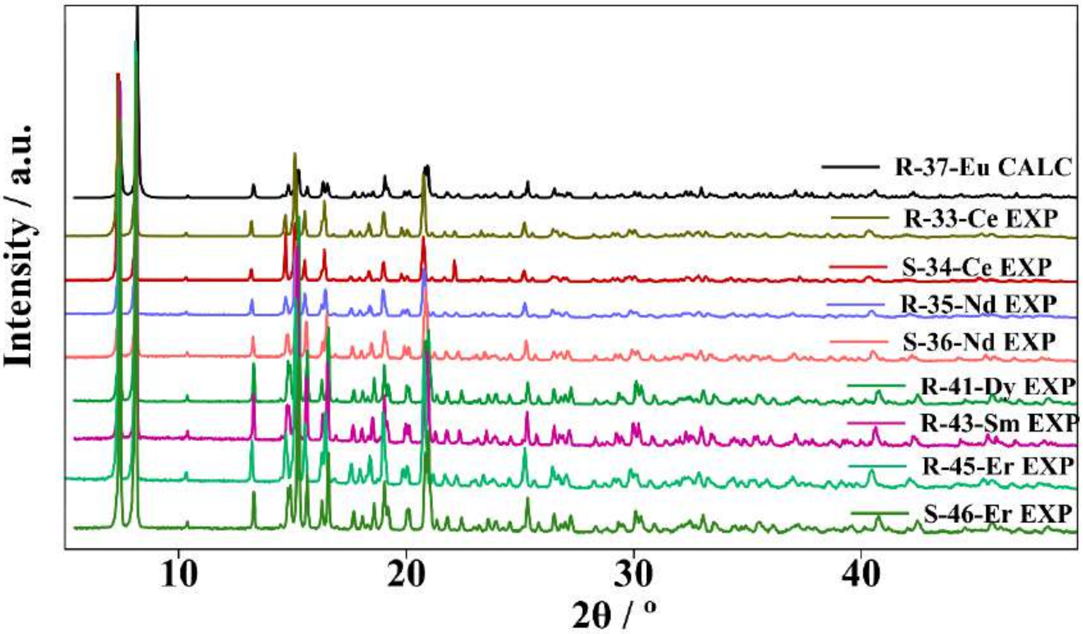

Figure 4. 4 Powder X- Ray Diffraction of compounds ***R*-33-Ce**, ***S*-34-Ce**, ***R*-35-Nd**, ***S*-36-Nd**, ***R*-41-Dy**, ***R*-43-Sm**, ***R*-45-Er** and ***S*-46-Er** compared to the calculated pattern of **R-33-Eu**. CALC stands for the patterns calculated from the crystal structure and EXP stands for the calculated diffractograms.

4.1.3 Luminescence properties

Luminescence properties of all compounds were studied and measured in the solid state at room temperature. Since each enantiomer pair shows the same excitation and emission spectra, only the ***R***- enantiomer of each lanthanide compound is discussed in this section.

Excitation spectra were recorded at the emission wavelength (λ_{em}) of 1064 nm ($^4F_{3/2}\rightarrow^4I_{11/2}$) for ***R*-35-Nd-a**, at 614 nm ($^5D_0\rightarrow^7F_2$) for ***R*-37-Eu**, at 546 nm ($^5D_4\rightarrow^7F_5$) for ***R*-39-Tb**, at 572 nm ($^4F_{9/2}\rightarrow^6H_{13/2}$) for ***R*-41-Dy**, at 644 nm ($^4G_{5/2}\rightarrow^6H_{9/2}$) for ***R*-42-Sm** and at 1515 nm for ($^4I_{13/2}\rightarrow^4I_{15/2}$) ***R*-42-Er**. The six spectra show an intense and broad band around 300 to 360 nm corresponding to the $\pi\rightarrow\pi^*$ and $n\rightarrow\pi^*$ ligand centred excitation transitions from the *R*-MPA and phen ligands, Figure 4. 5.

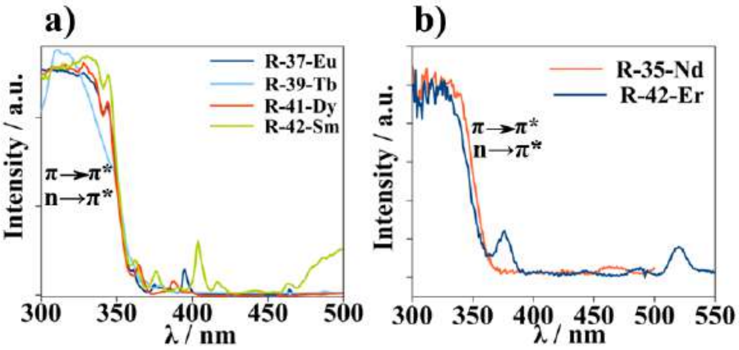

Figure 4. 5 Excitation spectra of polycrystalline samples ***R*-35-Nd** to ***R*-42-Er**. Measurements were monitored at the λ_{em} of 1064 nm ($^4F_{3/2}\rightarrow^4I_{11/2}$) for ***R*-35-Nd-a**, at 614 nm ($^5D_0\rightarrow^7F_2$) for ***R*-37-Eu**, at 546 nm ($^5D_4\rightarrow^7F_5$) for ***R*-39-Tb**, at 572 nm ($^4F_{9/2}\rightarrow^6H_{13/2}$) for ***R*-41-Dy**, at 644 nm ($^4G_{5/2}\rightarrow^6H_{9/2}$) for ***R*-42-Sm** and at 1515 nm for ($^4I_{13/2}\rightarrow^4I_{15/2}$) ***R*-42-Er**.

Room temperature emission spectra of ***R*-35-Nd** to ***R*-42-Er** were obtained exposing the samples at an excitation wavelength (λ_{exc}) of 330 nm.

In the emission spectra of ***R*-37-Eu**, different bands can be observed at 580, 595, 614, 650 and 691 nm corresponding to the $^5D_0\rightarrow^7F_{J=0-4}$ transitions, Figure 4. 6b. $^5D_0\rightarrow^7F_0$ corresponds to a forbidden transition (ΔJ=0), therefore its intensity is very weak and, in this case, it is almost imperceptible. The magnetically allowed $^5D_0\rightarrow^7F_1$ transition, with intensity independent of the environment, is split due to the crystal field. For the presented Eu^{3+} compound, all the three components (2*J*+1) can be discerned in the emission spectra. Furthermore, $^5D_0\rightarrow^7F_2$ is the most intense band located in the red range and responsible for the red-orange emission colour that could be seen by the naked eye for ***R*-37-Eu**, Figure 4. 6a. This band is a hypersensitive transition, and in the case of ***R*-37-Eu**, its splitting indicates that the lanthanide ion is not located at a site with inversion symmetry within the structure.[7,8]

The ***R*-39-Tb** compound shows green emission that could be seen by the naked eye, Figure 4. 6a. Moreover, the bands arising from the *f-f* Tb^{3+} transitions can be differentiated at 491, 546, 585 and 623 nm corresponding to the $^5D_4 \rightarrow ^7F_{J=6-3}$ transitions, Figure 4. 6c.

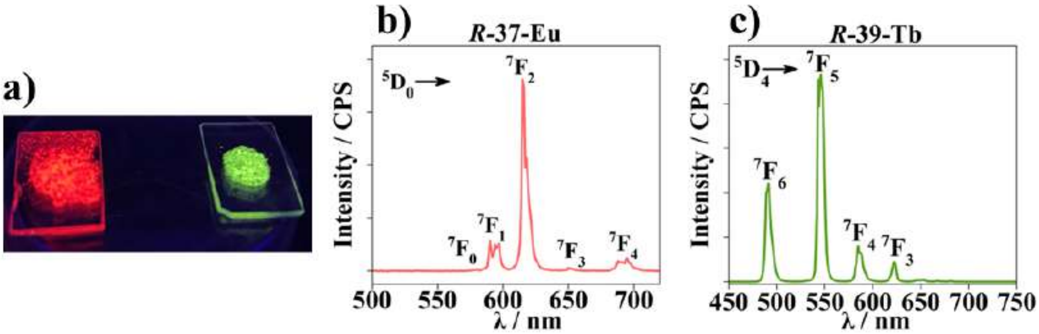

Figure 4. 6 a) emission of compounds ***R*-37-Eu** and ***R*-39-Tb** under exposure of a UV lamp. Emission spectra of b) ***R*-37-Eu** and c) ***R*-39-Tb** polycrystalline samples monitored at the λ_{exc} of 330 nm.

In the visible range, the bands arising from the ***R*-41-Dy** compound can be observed at 481 nm corresponding to the magnetically allowed $^4F_{9/2} \rightarrow ^6H_{15/2}$ transition, at 572 nm corresponding to the $^4F_{9/2} \rightarrow ^6H_{13/2}$ transition and at 659 nm (weak band) corresponding to the $^4F_{9/2} \rightarrow ^6H_{11/2}$ transition. Furthermore, in the near infrared range, two bands can be observed at 996 and 1144 nm, which are assigned to the transitions from the $^4F_{9/2}$ energy level to $^6F_{7/2}$ and $^6F_{5/2}$ respectively, Figure 4. 7a) and b).

For the ***R*-42-Sm** compound, four bands are identified at 563, 600, 644 and 705 nm in the visible range and assigned to the $^4G_{5/2} \rightarrow ^6H_{5/2-11/2}$ transitions. Furthermore, in the nIR range, the $^4G_{5/2} \rightarrow ^6H_{15/2}$ transition can be seen as a shoulder at 896 nm. The *f-f* emission transitions arising from the $^4G_{5/2}$ emitting level to the $^6F_{5/2-9/2}$ energy states are found at 940, 1016 and 1166 nm respectively, Figure 4. 7c) and d).[7]

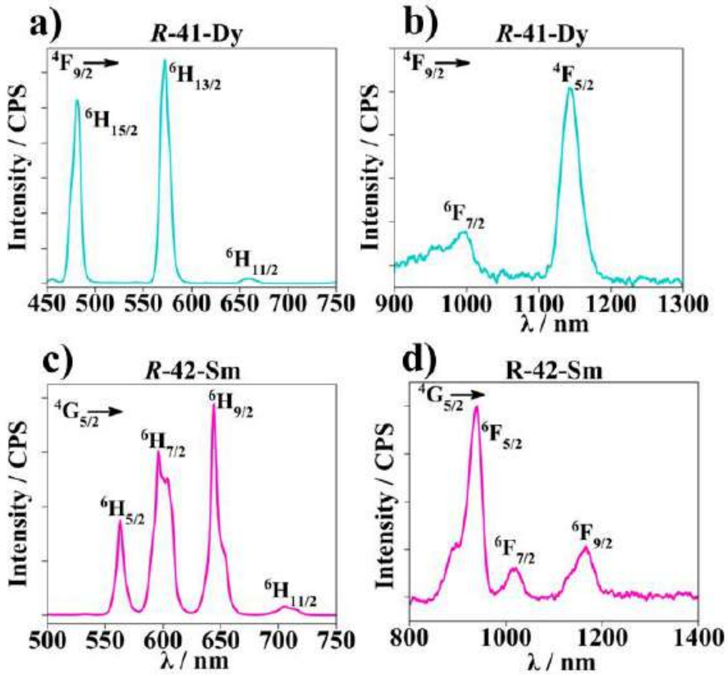

Figure 4. 7 Emission spectra of compounds a) and b) ***R*-42-Sm** and c) and d) ***R*-41-Dy** in the visible and nIR range. All measurements were monitored at the λ_{exc} of 330 nm.

As for the nIR emitters, ***R*-35-Nd** and ***R*-42-Er**, excitation at the ligand absorption wavelength induced the characteristic Nd^{3+} and Er^{3+} emission. The three emission bands observed in ***R*-35-Nd** spectrum are assigned to $^4F_{3/2}\rightarrow{}^4I_{9/2}$ at 902 nm, to $^4F_{3/2}\rightarrow{}^4I_{11/2}$ at 1064 nm and to $^4F_{3/2}\rightarrow{}^4I_{13/2}$ at 1336 nm. Whereas the solely band found at 1515 nm in ***R*-42-Er** emission spectrum is assigned to the $^4I_{13/2}\rightarrow{}^4I_{15/2}$ transition, Figure 4. 8a) and b).[7] The Er^{3+} emission was quite weak.

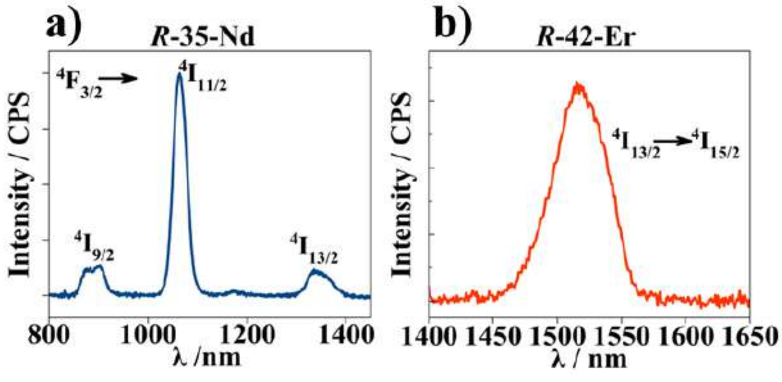

Figure 4. 8 Emission spectra of a) ***R*-42-Er** and b) ***R*-35-Nd** polycrystalline samples. Both measurements were monitored at a λ_{exc} of 330 nm.

Excitation at the ligand absorption wavelengths for all compounds induced the expected emission bands corresponding to the characteristic *f-f* transitions from each lanthanide ion. Also, below 450 nm, no emission from the ligands is detected (except for ***R*-42-Er**) indicating that energy transfer from the excited states of the organic moieties to the emitting energy level of the respective lanthanide (the antenna effect) takes place for these compounds. For the Erbium analogue, emission of the ligand was observed in the visible range (spectra not shown) indicating a rather poor sensitization effect of *R*-MPA and phen ligands to the Er^{3+} excited state.

Nonetheless, the overall quantum yield (ϕ_{Ln}^{L}), that is the ratio of the photons emitted by the lanthanide to the photons absorbed by the ligand, was measured with an integrating sphere with the intention to better characterize luminescent efficiency of the presented compounds. For ***R*-37-Eu**, the absolute quantum yield resulted to be 0.14. The photoluminescence time decay was recorded at the λ_{ex} of 330 nm by collecting the measurement at the λ_{em} of 614 nm, corresponding to the $^5D_0 \rightarrow {}^7F_2$ transition. The curve of the intensity against time (ms), showed in Figure 4. 9, was fitted using a mono-exponential equation. From the fit, the decay time (τ_{obs}) yielded 1.77 ms for ***R*-37-Eu** compound, confirming that the red emission of ***R*-37-Eu** comes from a single emitting centre and a single radiative deactivation process. In addition, more information about the sensitization mechanism that takes place for this system can be determined for the Eu^{3+} compound. The sensitization efficiency (η_{sens}) accounts to the percentage of energy absorbed by the chromophore ligands transferred to the excited state of the lanthanide ion and it is an important factor in the overall quantum yield, defined as: $\phi_{Ln}^{L} = \eta_{sens} \cdot \phi_{Ln}^{Ln}$. The other step that elucidates ϕ_{Ln}^{L} is the intrinsic quantum yield (ϕ_{Ln}^{Ln}) that refers to the quantum yield once the emitting level of the Ln^{3+} ion is populated. The intrinsic quantum yield is described as the ratio between the measured time decay and the radiative lifetime $\phi_{Ln}^{Ln} = \frac{k_{rad}}{k_{rad}+k_{non-rad}} = \frac{\tau_{obs}}{\tau_{rad}}$. Due to the pure magnetic dipole character of the $^5D_0 \rightarrow {}^7F_1$ transition, a simplified equation can be used to calculate the τ_{rad} from Eu^{3+}, $^5D_0$ excited state, corresponding to the lifetime in absence of non-radiative deactivations, Equation1.8.[8] For ***R*-37-Eu**, τ_{rad} is 3.05 ms. Thus, the ϕ_{Ln}^{Ln} resulted of 0.58. As expected, it is higher than the measured ϕ_{Ln}^{L}, because the intrinsic quantum yield do not depend on the efficiency of the ligand to Ln energy transfer, however, it takes into account deactivation mechanisms such as back-transfer energy or other quenching effects. Finally, the calculated η_{sens} results of 0.24 evidencing a sensitization effect that is rather low, nevertheless it is enough for ***R*-37-Eu** to present the desired optical properties.[8,9]

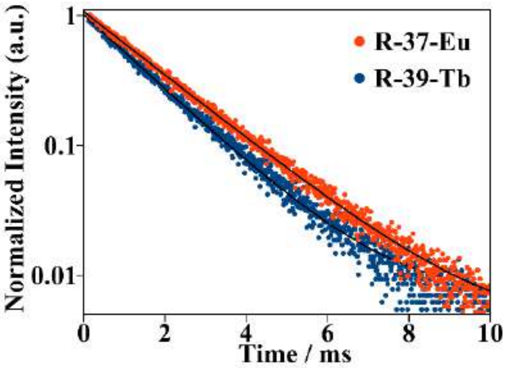

Figure 4. 9 Luminescence lifetime presented in semi-log plots for complexes ***R*-37-Eu** and ***R*-39-Tb**. Both measurements were monitored at the λ_{exc} of 330 nm. The solid black lines represent the mono-exponential fit with

$$I(t) = I_0 e^{-\frac{t}{\tau_{obs}}} + C$$

On the other hand, the measured ϕ_{Ln}^{L} for ***R*-39-Tb** sample was higher than the Eu^{3+} analogue, yielding 0.33. Moreover, the luminescence lifetime was measured by monitoring the emission decay at a λ_{em} of 546 nm, corresponding to the more intense emission band $^5D_4 \rightarrow {}^7F_5$, Figure 4. 9. The τ_{obs} calculated from the monoexponential fitting is 1.50 ms, also confirming the presence of one type of emitting specie and emission mechanism.

For ***R*-41-Dy** and ***R*-42-Sm**, ϕ_{Ln}^{L} and luminescent time decay couldn't be measured due to the low emission intensity that the compounds present.

4.1.4 Circular dichroism (CD) and Circular Polarized Luminescence measurements (CPL)

The Circular Dichroism measurements were carried out at solid state for samples ***R*-37-Eu**, ***S*-38-Eu**, ***R*-39-Tb**, ***S*-40-Tb**, ***R*-41-Dy**, ***S*-42-Dy**, ***R*-43-Sm** and ***R*-44-Sm**. The polycrystalline samples were dispersed in a KBr matrix and mounted on pellets. The complexes show rather weak Cotton effects. The bands around 200-460 nm are assigned mainly to the absorption of the phen ligand, with contributions from the π→π* and n→π* transition of *R/S*-MPA. For these 1D lanthanide chains the ligand arrangement formed by the chiral *R/S*-MPA and phen ligands are organized in space, around the metal ion, conferring low dissymmetry to the complex and leading to the weak CD associated to the ligand-centered electronic transitions, Figure 4. 10.

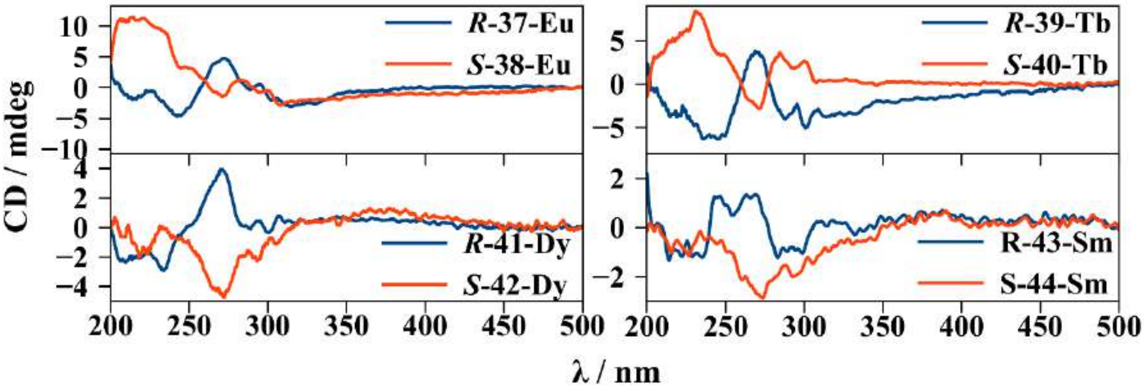

Figure 4. 10 Circular Dichroism spectra of compounds ***R*-37-Eu**, ***S*-38-Eu**, ***R*-39-Tb**, ***S*-40-Tb**, ***R*-41-Dy**, ***S*-42-Dy**, ***R*-43-Sm** and ***R*-44-Sm** measured in the solid state.

Circular Polarized Luminescence measurements were performed for ***R*-37-Eu**, ***S*-38-Eu**, ***R*-39-Tb** and ***S*-40-Tb** polycrystalline samples. The europium and terbium compounds were deposited in a quartz plate, from a suspension in n-pentane, which acts only as a dispersing agent, considering that the compounds are not soluble in this solvent. The emission spectra recorded simultaneously with CPL spectra were not significantly different from those measured on the polycrystalline samples. This suggests that n-pentane does not induce any change to the complexes, Figure APX.IX.1. The CPL spectra of compounds ***R*-37-Eu**, ***S*-38-Eu** recorded at the excitation wavelength of 254 nm are depicted in Figure 4. 11.

The Eu^{3+} enantiomeric pairs show low intensity CPL signal, nevertheless, the mirror image bands corresponding to $^5D_0 \rightarrow {}^7F_1$, $^7F_2$ and $^7F_4$ Eu^{3+} *f-f* transitions can be clearly discerned. The magnetic dipole transition, $^5D_0 \rightarrow {}^7F_1$, at 595 nm is the most intense one. Two well resolved components due to crystal field perturbation can be observed. The m_j component located in the higher energy region of the transition shows a splitting that appears as a bifid structure revealing the three crystal field splitting components. Next, at 614 nm the $^5D_0 \rightarrow {}^7F_2$ transition shows lower intensity and only one component is well differentiated. Finally, at 691 nm, the $^5D_0 \rightarrow {}^7F_4$ transition appears with very low intensity, though at least two m_j components can be differentiated.

$$g_{\text{lum}} = 2\frac{I_L - I_R}{I_L + I_R} = 2\frac{\Delta I}{I} \qquad \textbf{Equation 4.1}$$

The dissymmetry factor could be quantified with Equation 4.1 for the $^5D_0 \rightarrow {}^7F_1$ and $^5D_0 \rightarrow {}^7F_2$ transitions leading to a $g_{lum} = \Delta I/I$ values of ±0.013 (+ for ***S*-38-Eu**) for the

$^5D_0 \rightarrow {}^7F_1$ transition and ±0.003 (+ for the ***R*-37-Eu** enantiomer) for the hypersensitive transition, Table 4. 4. The presented g_{lum} values are similar to other reported Eu^{3+} coordination compounds with carboxylate ligands and to other Eu^{3+} polymeric chain complexes measured in the solid state.[10,11]

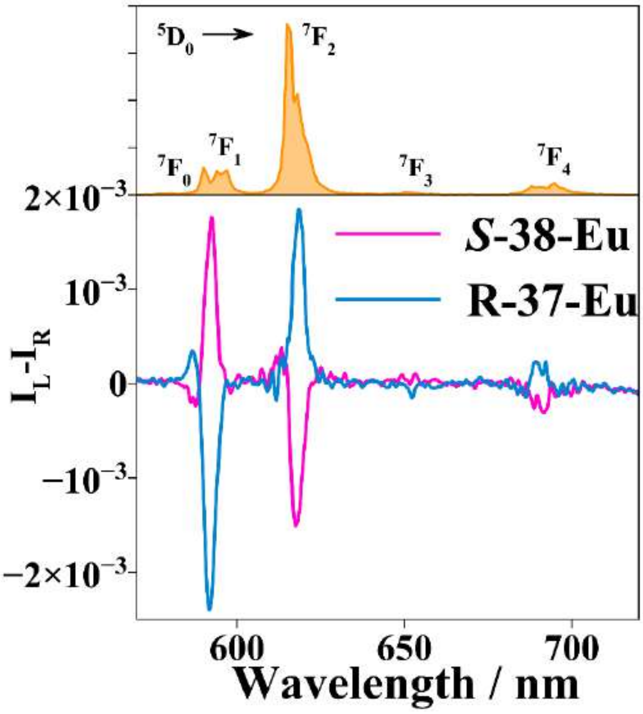

Figure 4. 11 CPL spectra of ***R*-37-Eu** and ***S*-38-Eu** enantiomers.

Table 4. 4 g_{lum} values of the ***R*-37-Eu** and ***S*-38-Eu** enantiomeric pair for the $^5D_0 \rightarrow {}^7F_1$ and the $^5D_0 \rightarrow {}^7F_2$ transitions.

***R*-37-Eu / *S*-38-Eu**	**$^5D_0 \rightarrow {}^7F_1$**	**$^5D_0 \rightarrow {}^7F_2$**
g_{lum}	±0.013 (+ for ***S*-38-Eu**)	±0.003 (+ for ***R*-37-Eu**)

Moreover, CPL measurements were performed for the ***R*-39-Tb** and ***S*-40-Tb** compounds as well, but the intensity of the obtained spectra is too low to extract meaningful information, FigureAPX.IX.2. CPL studies in polymeric lanthanide chains measured in the solid state remains rare.[12] Y. Hasegawa *et at.*[13] presented a polymeric chain complex with g_{lum} values for the magnetic dipole transition up to 0.17 measured in the solid state. Due to lower luminescence showed by ***R*-41-Dy**, ***S*-42-Dy**, ***R*-43-Sm** and ***S*-44-Sm**, CPL measurements could not be performed.

4.1.5 Magnetic properties

Direct current (dc) measurements

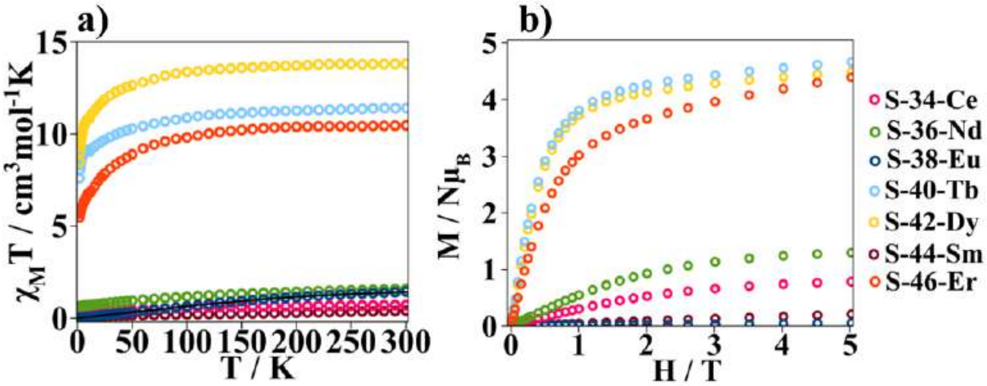

Figure 4. 12 a) $\chi_M T$ *vs* T plot, measured under an external magnetic dc field of 0.3 T of the *S*-enantiomers of compounds ***S*-34-Ce** to ***S*-46-Er.** Continuous black line corresponds to the fitting of the $\chi_M T$ *vs* T data of ***S*-38-Eu** using Equation 4.2 and b) Magnetization with external magnetic field dependence measured at 2 K of the *S*- enantiomers of compounds ***S*-34-Ce** to ***S*-46-Er**.

Since *S*- and *R*- enantiomers are expected to show the same magnetic properties, direct current (dc) magnetic susceptibility (χ_M) and magnetization (*M*) measurements were performed for the *S*-enantiomers on the polycrystalline samples. The χ_M measurements were carried out under a dc field of 0.3 T in the 2-300 K temperature range. The $\chi_M T$ dependence with T plots are presented in Figure 4. 12a. At room temperature (300 K) the $\chi_M T$ values are 0.70, 1.59, 1.43, 11.41, 13.82**,** 0.40 and 10.47 cm^{3}mol^{-1}K for ***S*-34-Ce**, ***S*-36-Nd**, ***S*-38-Eu**, ***S*-40-Tb**, ***S*-42-Dy**, ***S*-44-Sm** and ***S*-46-Er**, respectively. For one isolated Ln^{3+} cation, the calculated $\chi_M T$ values are: 0.80 cm^{3}mol^{-1}K for Ce^{3+} ground state $^2F_{5/2}$ and g_j=6/7; 1.64 cm^{3}mol^{-1}K for Nd^{3+} $^4I_{9/2}$ and g_j=1.64; 0 cm^{3}mol^{-1}K for Eu^{3+} ground state $^7F_0$; 11.82 cm^{3}mol^{-1}K for Tb^{3+} ground state $^7F_6$ and g_j=3/2; 14.17 cm^{3}mol^{-1}K for Dy^{3+} ground state $^6H_{15/2}$ and g_j=4/3; 0.09 cm^{3}mol^{-1}K for Sm^{3+} ground state $^6H_{5/2}$ and g_j=2/7 and 11.48 cm^{3}mol^{-1}K for Er^{3+} $^4I_{15/2}$ and g_j=6/5.[7a]

On cooling the samples, for ***S*-40-Tb**, ***S*-42-Dy** and ***S*-46-Er**, the $\chi_M T$ values remain almost constant until ~50 K (until ~100 K for ***S*-46-Er**) and below this temperature, the susceptibility values decrease up to 7.80 cm^{3}mol^{-1} K for ***S*-40-Tb** to 8.49 cm^{3}mol^{-1}K for ***S*-42-Dy** and to 5.46 cm^{3}mol^{-1}K for ***S*-46-Er**. Regarding ***S*-34-Ce** and ***S*-39-Nd** the $\chi_M T$ *vs* T curves decrease gradually on cooling the samples. At the limit temperature of 2 K the $\chi_M T$ values are 0.36 and 0.64 cm^{3}mol^{-1}K, for ***S*-34-Ce** and ***S*-39-Nd**, respectively. The decrease of $\chi_M T$ on cooling the polycrystalline samples is mainly due to thermal depopulation of the m_j states generated by crystal field perturbation. The possibility of magnetic coupling between the Ln^{3+} ions has not been considered for these compounds due to: *i)* the well shielded nature of electrons in the 4f^n orbitals *ii)* the Ln---Ln intra and inter-molecular shortest distances are too long (6.04±0.01 and 12.32±0.02 Å respectively).

Moreover, the experimental $\chi_M T$ value at room temperature of compound ***S*-38-Eu** is higher than the calculated 0 value. Due to the rather small spin-orbit coupling parameter (λ) between the ^{7}F$_{(0-1)}$ states, at room temperature the higher energy ^{7}F$_J$ states closer to the ground state are thermally populated (mainly the ^{7}F$_1$ state). Then the $\chi_M T$ values decrease gradually on cooling the sample due to the thermal depopulation of the ^{7}F$_J$ excited states. At 2 K, $\chi_M T$ is 0.017 cm^{3}mol^{-1}K confirming that at low temperature the non-magnetic ground state (*J*=0) is stabilized. If we consider the presented polymeric chain formed by non-magnetically coupled Eu^{3+} ions, the λ value can be calculated from the $\chi_M T$ *vs* T data considering Eu^{3+} as a free ion by using Equation 4.2[14,15]. A plot of the $\chi_M T$ *vs* T data only for ***S*-38-Eu** is shown in Figure APX.IX.3. Then from the best fit with Equation 4.2, the λ value is 335 cm^{-1}. Furthermore, the energy gap between the ^{7}F$_0$ and ^{7}F$_1$ should correspond to the λ parameter measured from the spectroscopic data. The λ value has been calculated from the emission spectra of ***S*-38-Eu** measured at 77 K, Figure APX.IX.4 and Table APX.IX.3. This value is 377 cm^{-1} for ***S*-38-Eu**. This result is similar to other Europium compounds.[16,17]

$$\chi_M T = ((N\beta^2/3kTx)[24 + (27x/2 - 3/2)e^{-x} + (135x/2 - 5/2)e^{-3x} + (189x - 7/2)e^{-6x} + (405x - 9/2)\,e^{-10x} + (1485x/2 - 11/2)e^{-15x} + (2457x/2 - 13/2)e^{-21x}]/[1 + 3e^{-x} + 5e^{-3x} + 7e^{-6x} + 9e^{-10x} + 11e^{-15x} + 13e^{-21x}])T \qquad \textbf{Equation 4.2}$$

With $x = \lambda/kT$

Finally, for ***S*-44-Sm** compound, the $\chi_M T$ value at room temperature is also higher than the one calculated for a free ion. For a Sm^{3+} ion, the ^{6}H ground state is split due to spin-orbit coupling by ^{6}H$_{J=5/2-15/2}$ with a λ parameter around 200 cm^{-1}. Therefore, at room temperature, the excited ^{6}H$_J$ states are thermally populated. The diminution of $\chi_M T$ on cooling the sample is due to the thermal depopulation of the *J* states.[14,15] ***S*-44-Sm** magnetic data could not be fitted successfully under the free ion approximation.

The plots of the magnetization dependence with an applied magnetic field at 2 K for all compounds are depicted in Figure 4. 12b). None of the presented compounds showed saturation of the magnetization.

Alternating current (ac) measurements

In order to study the dynamic magnetic properties of the *S*-[Ln(μ-MPA)(MPA)$_2$(phen)]$_n$ compounds, alternating current (ac) magnetic susceptibility measurements in a $4 \cdot 10^{-4}$ T oscillating field were recorded for ***S*-34-Ce**, ***S*-36-Nd**, ***S*-40-Tb**, ***S*-42-Dy**, ***S*-44-Sm** and ***S*-46-Er.**

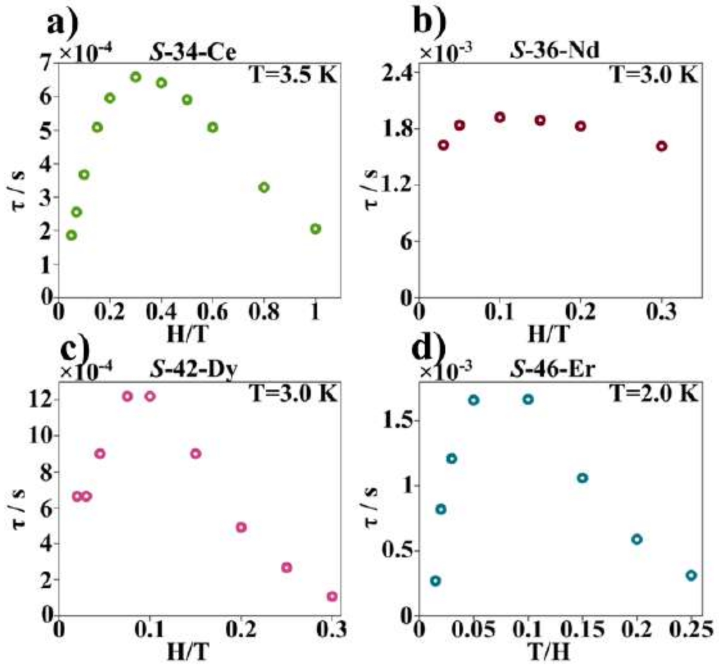

Figure 4. 13 Relaxation times in front of static magnetic fields measured at the constant temperature of 3.5 K for ***S*-34-Ce**, of 3 K for ***S*-36-Nd**, of 3 K for ***S*-42-Dy** and of 2 K for ***S*-46-Er**. The measurements were set under an ac magnetic field of $4 \cdot 10^{-4}$ T oscillating between 1 and 1488 Hz.

At a 0 Oe dc external magnetic field, the in-face (χ_M') and out-of-face (χ_M'') magnetic susceptibility components were measured under an ac magnetic field oscillating between 10 and 1000 Hz. None of the above compounds showed χ_M'' dependence with temperature or frequency. On applying an external magnetic dc field (H$_{dc}$), compounds ***S*-34-Ce**, ***S*-36-Nd**, ***S*-42-Dy** and ***S*-46-Er** showed maxima of the χ_M'' component below

7, 6, 8 and 4 K, respectively. This suggests that the relaxation of the magnetization goes through a shortcut path between the two bi-stable $\pm m_j$ states, the so-called quantum tunneling of the magnetization (QTM) when no H_{dc} is applied. To establish the optimum static magnetic field, measurements of the χ_M' and χ_M'' with frequency, at a constant temperature of 3.5 K for ***S*-34-Ce**, of 3 K for ***S*-36-Nd**, of 3 K for ***S*-42-Dy** and of 2 K for ***S*-46-Er** and applying different dc fields were performed. The plot of τ with H_{dc} showed that relaxation time is the greatest when the applied external magnetic field is 0.3 T for ***S*-34-Ce**, 0.15 T for ***S*-36-Nd**, 0.01 T for ***S*-42-Dy** and 0.05 T for ***S*-46-Er**, Figure 4. 13. Then those dc magnetic fields were chosen as the optimal ones to conduct the χ_M' and χ_M'' measurements with respect to temperature. The plots of the out-of-phase magnetic susceptibility components varying with temperature and frequency of these complexes are illustrated in Figure 4. 14.

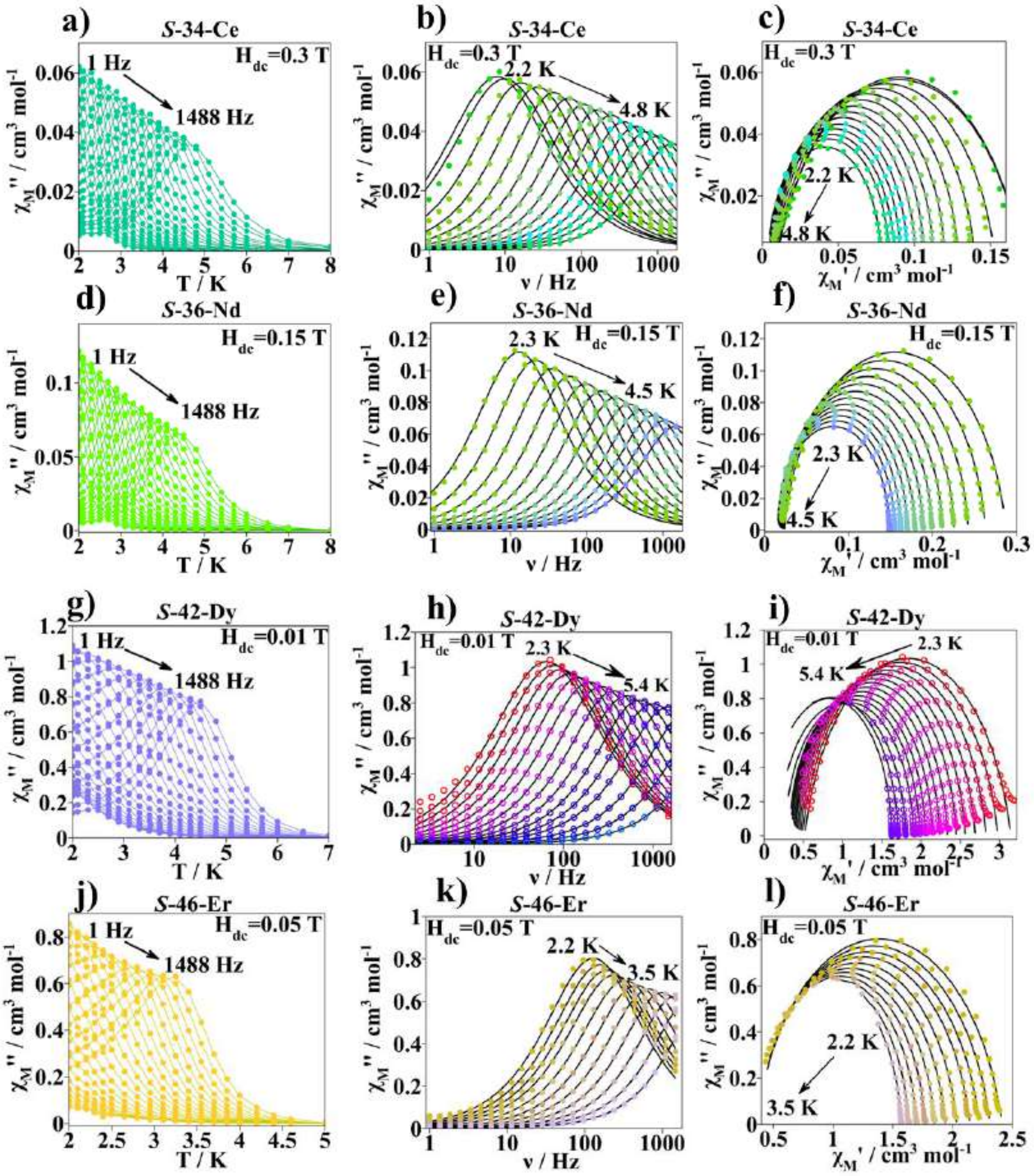

Figure 4. 14 a), d), g) and j) χ_M*''* *vs* T plots of ***S*-34-Ce** to ***S*-46-Er**. The continuous line is a guide to the eye b), e), h) and k) are the χ_M*''* *vs* ν plots of ***S*-34-Ce** to ***S*-46-Er**. Continuous black line is the fitting to the Generalized Debye model and c), f), i) and l) are the representation in the Cole-Cole plots of ***S*-34-Ce** to ***S*-46-Er**. Continuous black line is the fitting to the Generalized Debye model.

Compounds ***S*-34-Ce**, ***S*-36-Nd**, ***S*-42-Dy** and ***S*-46-Er**, showed χ_M*''* maxima upon cooling the samples down to the temperature range of 2.3-4.8 K for ***S*-34-Ce**, of 2.3-4.5 K for ***S*-36-Nd** and of 2.3-5.4 K for ***S*-42-Dy** and to a smaller temperature range of 2.2-3.5 for ***S*-46-Er**, Figure 4. 14a), d), g) and j)**.** Furthermore, at 2 K in the χ_M*''* *vs* T plot of ***S*-42-Dy**, a second maximum is perceived suggesting a faster relaxation process differentiated from the one occurring at higher temperatures. This faster mechanism probably accounts for the QTM, which is not totally removed on applying the external dc magnetic field.[18]

As for the χ_M'' tendency with the oscillating frequency, compounds ***S*-34-Ce**, ***S*-36-Nd** and ***S*-42-Dy** start showing χ_M'' maxima at smaller oscillating frequencies whereas ***S*-46-Er** χ_M'' *vs* ν curves show peaks at higher ones. For all compounds, the χ_M'' *vs* ν maxima move progressively to higher frequencies on increasing temperature, Figure 4. 14b), e), h), k). Representation of the ac magnetic data in the Cole-Cole plots shows asymmetric semicircles for ***S*-34-Ce**, ***S*-36-Nd** and ***S*-42-Dy** while the semicircles of ***S*-46-Er** are asymmetric and uncompleted. Moreover, in the Cole-Cole representation of ***S*-42-Dy,** a shoulder can be discerned corresponding to the χ_M' *vs* χ_M'' data points obtained at lower temperatures and lower frequencies accounting to the faster mechanism differentiated in the χ_M'' *vs* T plot.

Magnetic data of ***S*-34-Ce**, ***S*-36-Nd** and ***S*-46-Er** could be successfully fitted with the one component Debye model function as shown in Figure 4. 14 c), f), l). Additionally, the fit of ***S*-42-Dy** was not successful using the extended generalized Debye model because of the lack of enough experimental data points corresponding to the faster mechanism. Nevertheless, a good fit was obtained for the slower process using the one-component generalized Debye model, Figure 4. 14i).

Following to that, the α values obtained from such fittings were in the range of 0.01(2.3 K)-0.003(4.8 K) for ***S*-34-Ce**, 0.004(2.3 K)-0.003(4.5 K) for ***S*-36-Nd**, 0.150(2.3 K)-0.002(5.4 K) for ***S*-42-Dy** and 0.156(2.2 K)-0.05(3.5 K) for ***S*-46-Er**. For all compounds α values decrease on increasing temperature indicating a narrower distribution of the relaxation times at higher temperatures.

Representation of relaxation of the magnetization times with temperature in the ln(τ) *vs* T^{-1} plots are depicted in Figure 4. 15. The parameters obtained from the best fit of the ln(τ) *vs* T^{-1} curves, of the *S*- enantiomer ***S*-34-Ce** to ***S*-46-Er**, are compiled in Table 4. 5.

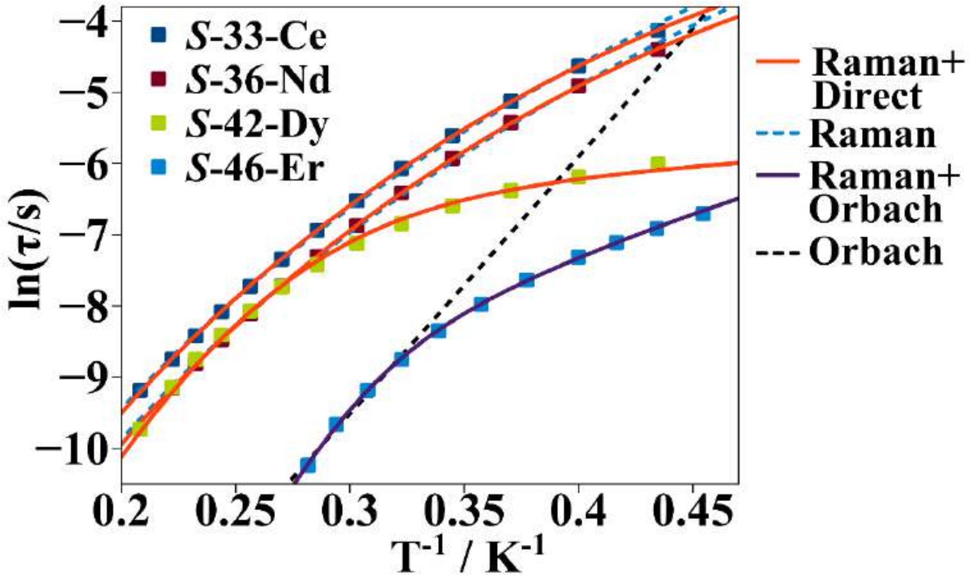

Figure 4. 15 a) ln(τ) *vs* T^{-1} plot of ***S*-34-Ce**, ***S*-36-Nd**, ***S*-42-Dy** and ***S*-46-Er** from the magnetic data measured at the H_{dc} of 0.3, 0.15, 0.01 and 0.05 T, respectively. Continuous orange lines correspond to the fit with Raman and Direct equations continuous purple line correspond to the fit with Raman and Orbach equation, dotted blue line correspond to the fit of ***S*-34-Ce** and ***S*-36-Nd** using only the Raman equation whereas dotted black line correspond to the fit with the Orbach mechanism.

Performance of relaxation of the magnetization times with temperature of compounds ***S*-34-Ce** and ***S*-36-Nd** was very similar. First, both curves were fitted considering the Arrhenius law that describes the Orbach relaxation of the magnetization with Equation 4.3, Figure APX.IX.5, and the obtained parameters were ΔE = 19.6 cm^{-1} and τ_0 = $3.07 \cdot 10^{-7}$ s for ***S*-34-Ce** and ΔE = 19.5 cm^{-1} and $\tau_0 = 2.16 \cdot 10^{-7}$ s for ***S*-36-Nd**. However, the best fit of τ along all the temperature range was obtained when equation describing Raman and Direct relaxation mechanisms was used, Equation 4.4. The parameters obtained from the fit were C = 0.113, n = 4.1 and A = 6.00 for ***S*-34-Ce** and C = 0.125, n = 7.47 and A = 7.44 for ***S*-36-Nd**. In addition, Cole-Cole plots of the Cerium and Neodymium compounds showed α values very close to 0 indicating a very narrow distribution of the relaxation times, suggesting that relaxation of the magnetization is mainly governed by one mechanism. The ln(τ) *vs* T^{-1} plots were tried to fit considering only the Raman mechanism (first part of Equation 4.4). A good fit was obtained from ***S*-34-Ce** and ***S*-36-Nd** ln(τ) *vs* T^{-1} curves especially in the higher temperature range. The obtained parameters were C = 0.17 and n = 6.98 for ***S*-34-Ce** and C = 0.19 and n = 7.17

for ***S*-36-Nd**. The last data points found in the lower temperature range don't follow exactly the Raman function indicating that relaxation of the magnetization of ***S*-34-Ce** and ***S*-36-Nd** is mainly governed by the Raman process along all the temperature range where these compounds show spin relaxation, though at lower temperatures the Direct mechanism starts to emerge.

$$\tau^{-1} = \tau_0^{-1} \exp\left(\frac{-\Delta E}{k_B T}\right)$$ **Equation 4.3**

$$\tau^{-1} = CT^n + AT$$ **Equation 4.4**

$$\tau^{-1} = \tau_0^{-1} \exp\left(\frac{-\Delta E}{k_B T}\right) + AT$$ **Equation 4.5**

The linear trend in the slope at higher temperature region of ***S*-42-Dy** ln(τ) *vs* T^{-1} plot was fitted by an Arrhenius law, Equation 4.3. This model describes the relaxation of the magnetization by the thermally assisted Orbach mechanism that occurs between the $\pm m_j$ degenerate states in the ground state via the highest energy excited m_j state of the Dy^{3+} ion. The calculated energy barrier (ΔE) was 31.6 cm^{-1} and the pre-exponential factor (τ_0) resulted of $4.9 \cdot 10^{-9}$ s, Figure APX.IX.5. But linearity is followed only for few points, suggesting that at lower temperatures more than one relaxation mechanism is active. Also, the distribution of the coefficient values, obtained in the fitting by using the generalized Debye model in the Cole-Cole plots, is in the 0.150-0.002 range, suggesting the presence of other relaxation mechanisms such as the QTM, Direct and Raman other than just the Orbach. Thus, the ln(τ) *vs* 1/T curve was adjusted considering all the above mechanisms. The best fit was obtained when the spin-lattice relaxation mechanisms Raman and Direct were considered, Equation 4.4. The obtained parameters were C = 0.011 $s^{-1}K^{-n}$, n = 9.07 and A = 183.29 $s^{-1}T^{-4}K^{-1}$. Other Dysprosium(III) coordination compounds found in the literature show similar behaviour as ***S*-42-Dy.**[18,19,20,21]

Finally, for ***S*-46-Er** compound, the Arrhenius law was used to fit the linear segment in the higher temperature range. The obtained effective energy barrier yielded 25.1 cm^{-1} and the pre-exponential factor was $1.44 \cdot 10^{-9}$ s. The linear trend is not followed along all the temperature range, therefore a function with the equation including the Orbach and Raman relaxation mechanisms, Equation 4.5, gave the best fit. The obtained parameters from the fit were ΔE = 40.61 cm^{-1}, τ_0 = $3.83 \cdot 10^{-12}$ s, C = 13.74 $s^{-1}K^{-n}$ and n = 5.12.

For a Kramer ion such as Ce^{3+}, Nd^{3+}, Dy^{3+} and Er^{3+} the dependence of τ with T should follow the power law $\tau \propto T^9$ when the relaxation of the magnetization goes through the two-phonon relaxation Raman process. Nevertheless, *n* values in the interval 1-6 has been claimed to be reasonable when the acoustic phonons, with less energy, are also considered in the spin-lattice relaxation of Raman. Important care must be taken when fitting the ac data with the different relaxation of the magnetization mechanisms due to over parametrization when using such equations.[22-25]

Table 4. 5 Compilation of the fitted parameters from the relaxation of the magnetization mechanisms of the *S*- enantiomers ***S*-34-Ce** to ***S*-46-Er**.

	H_{dc} (T)	**Orbach**		**QTM**	**Raman**		**Direct**
		ΔE (cm^{-1})	τ_0 (s)	τ_{QTM} (s)	C ($s^{-1}K^{-n}$)	n	A ($s^{-1}K^{-1}$)
***S*-34-Ce**	0.3				0.113	7.26	6.00
***S*-36-Nd**	0.15				0.13	7.47	7.44
***S*-42-Dy**	0.01				0.01	9.07	183.29
***S*-46-Er**	0.05	40.61	$3.83 \cdot 10^{-12}$		13.74		5.12

4.2 Compounds derived from (S)-(+) or (R)-(-)-2-Phenylbutyric acid (R/S-2-HPhBut)

4.2.1 Experimental procedure

Compounds ***R***- and ***S***- **47-64** were obtained as follows: into 20 mL of an ethanolic solution***** in the 1:1 ratio, the respective *R* or *S*-(- or +)-2-Phenylbutiric acid (1.5 mmol, 246.3 mg) and KOH (1.5 mmol, 84.2 mg) were dissolved. Separately, a DMF solution containing 4,7-Diphenyl-1,10-phenanthroline (bathophen) (0.5 mmol, 166 mg) was heated until dissolved (around 55 ºC). Then the bathophen solution was added to the previous ethanolic solution. The resulting solution was stirred for 10 min. Afterwards, a DMF solution containing the respective $Ln(NO_3)_3{\cdot}6H_2O$ salt (0.5 mmol) was added dropwise. The light pink transparent solution was magnetically stirred for 15 minutes at 55 ºC. Then the reaction solution was cooled down until room temperature and left to stand to crystallize through slow evaporation. White crystals appeared after two weeks. Crystals obtained in the synthesis were dissolved into 3 mL of DMF and the solutions were left to crystallize through slow vapor diffusion with acetonitrile to obtain suitable crystals for single crystal X-Ray Diffraction measurement of ***S*-52-Eu-a** and ***S*-62-Tm-b**. The compounds were obtained in yields ranging from 10 to 60 %.

*****To obtain *structure a* of the $[Tb_2(\mu\text{-}2\text{-}R/S\text{-}PhBut)_4(R/S\text{-}2\text{-}PhBut)_4(bathophen)_2]$ compound, the solvent used in this step should be methanol instead of ethanol.

Elemental analyses are depicted hereunder in Table 4. 6. Significant bands of Infrared spectroscopy are depicted only for the *R*- enantiomer in Table APX.X.1.

Table 4. 6 Elemental analysis of compounds ***R***- or ***S***- **47-64**

	Calculated			**Found**				**Calculated**			**Found**		
Compound	**%C**	**%H**	**%N**	**%C**	**%H**	**%N**	**Compound**	**%C**	**%H**	**%N**	**%C**	**%H**	**%N**
***R*-47-Nd-a**	67.1	5.2	2.9	67.0	5.2	2.9	***S*-48-Nd-a**	67.1	5.2	2.9	67.1	5.2	2.9
***R*-49-Sm-a**	66.7	5.1	2.9	66.6	5.2	2.9	***S*-50-Sm-a**	66.7	5.1	2.9	66.7	5.1	2.9
***R*-51-Eu-a**	66.7	5.1	2.9	66.6	5.2	2.9	***S*-52-Eu-a**	66.7	5.1	2.9	66.7	5.1	2.9
***R*-53-Tb-a**	66.1	5.0	2.8	65.9	5.1	2.8	***S*-54-Tb-a**	66.1	5.0	2.8	66.1	5.0	2.8
***R*-55-Tb-b**	66.1	5.0	2.8	66.0	5.0	2.8	***S*-56-Tb-b**	66.1	5.0	2.8	65.9	5.1	2.8
***R*-57-Dy-a**	65.9	5.0	2.8	65.5	5.1	2.8	***S*-58-Dy-a**	65.9	5.0	2.8	65.0	5.0	2.8
***R*-59-Dy-b**	65.9	5.0	2.8	66.0	2.8	5.2	***S*-60-Dy-b**	65.9	5.0	2.8	65.8	5.0	2.8
***R*-61-Tm-b**	65.5	5.0	2.8	65.4	4.9	2.8	***S*-62-Tm-b**	65.5	5.0	2.8	65.4	4.9	2.8
***R*-63-Yb-b**	65.2	5.0	2.8	65.2	5.0	2.8	***S*-64-Yb-b**	65.2	5.0	2.8	65.2	5.0	2.8

4.2.2 Structural characterization

Single crystal X-Ray diffraction measurements were performed for compounds ***S*-52-Eu-a** and ***S*-62-Tm-b**. Selected bond distances of ***S*-52-Eu-a** and ***S*-62-Tm-b** and crystallographic information are listed in Table 4. 7 and Table APX.X.2, respectively. Partially labelled plots of the crystal structure of ***S*-52-Eu-a** and ***S*-62-Tm-b** are shown in Figure 4. 16a) and b) respectively.

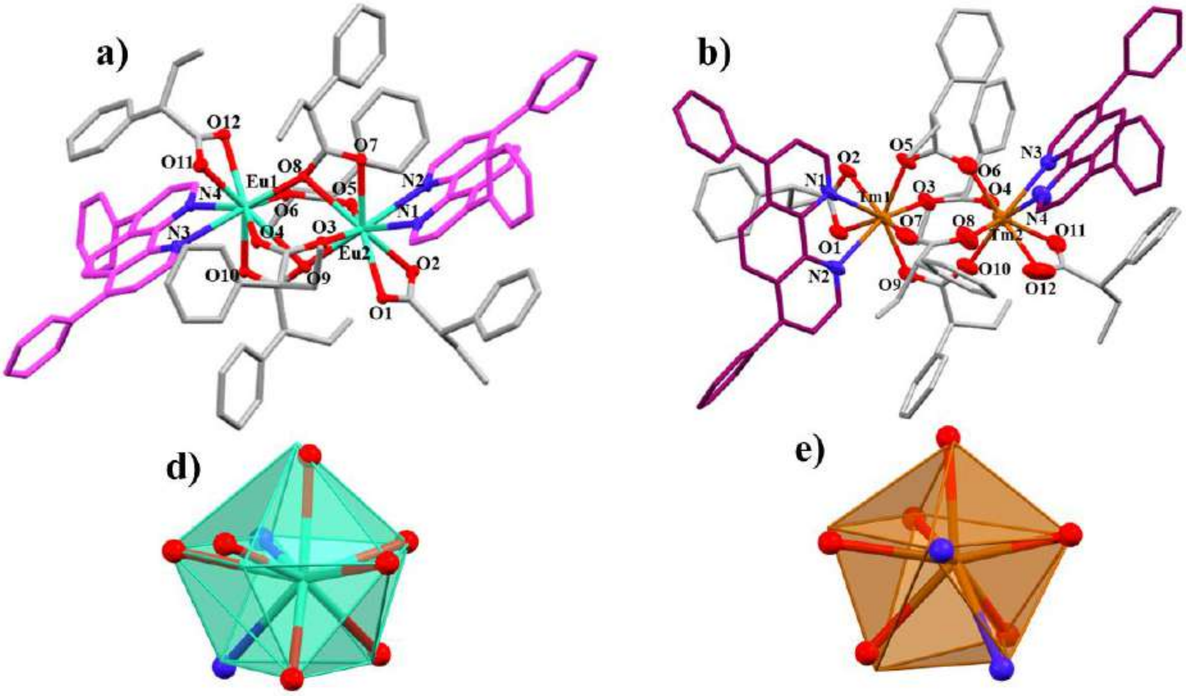

Figure 4. 16 Partially labelled plots of compound a) ***S*-52-Eu-a** and b) ***S*-62-Tm-b**. H atoms have been omitted for a better view of the structure. Idealized coordination polyhedron compared with the real positions of the coordinating atoms of d) ***S*-52-Eu-a** (blue) and e) ***S*-62-Tm-b** (orange).

Table 4. 7 Selected bond distances (Å) for ***S*-52-Eu-a** and ***S*-62-Tm-b.**

S-52-Eu-a				*S*-62-Tm-b			
Eu1-O1	2.481(4)	**Eu2-O4**	2.413(4)	**Tm1-O1**	2.356(8)	**Tm2-O4**	2.258(7)
Eu1-O2	2.434(5)	**Eu2-O6**	2.397(5)	**Tm1-O2**	2.382(8)	**Tm2-O6**	2.266(7)
Eu1-O3	2.356(5)	**Eu2-O8**	2.326(4)	**Tm1-O3**	2.268(9)	**Tm2-O8**	2.289(9)
Eu1-O5	2.366(4)	**Eu2-O9**	2.773(4)	**Tm1-O5**	2.290(9)	**Tm2-O10**	2.249(9)
Eu1-O7	2.518(5)	**Eu2-O10**	2.401(5)	**Tm1-O7**	2.234(9)	**Tm2-O11**	2.342(9)
Eu1-O8	2.594(4)	**Eu2-O11**	2.404(5)	**Tm1-O9**	2.291(7)	**Tm2-O12**	2.412(8)
Eu1-O9	2.439(4)	**Eu2-O12**	2.543(4)	**Tm1-N1**	2.516(10)	**Tm2-N3**	2.585(7)
Eu1-N1	2.583(4)	**Eu2-N3**	2.648(4)	**Tm1-N2**	2.579(7)	**Tm2-N4**	2.526(10)
Eu1-N2	2.649(4)	**Eu2-N4**	2.567(4)	**Tm1---Tm2**		4.287(7)	
Eu1---Eu2		4.000(5)					
Eu1-O8-Eu2		108.7					
Eu1-O9-Eu2		100.0					

All the synthetized compounds present the same molecular formula, but from the crystallographic data two different structural motifs can be found: structural type a (*structure a*) and structural type b (*structure b*).

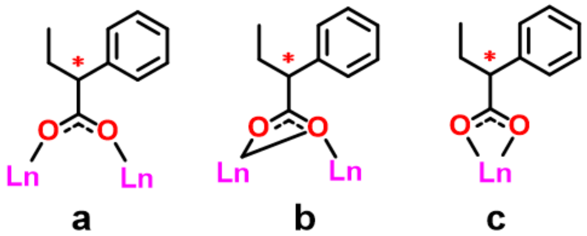

Scheme 4.3. Coordination modes of *S*/*R*-2-PhBut ligand a) symmetrical *syn-syn* bidentate bridging, b) chelating-bridging and c) chelating coordination mode.

S*tructure a* is found in ***S*-52-Eu-a** compound, which crystallizes in a triclinic crystal system in a P1 space group. Each asymmetric unit is constituted by a dinuclear entity in which each Eu^{3+} is nonacoordinated. In each dinuclear unit, the two Eu^{3+} atoms are bridged by four (*S*)-(+)-2-phenylbutirate ligands (*S*-2-PhBut) through two different coordination modes. Two of the bridging *S*-2-PhBut ligands are in the symmetrical *syn-syn* bidentate bridging coordination mode (η_1:η_1:μ_2 or 2.11 using Harris notation[26]) (Scheme 4.3a) with Eu-O bond lengths ranging 2.356(5)-2.413(4) Å. The other two *S*-2-PhBut bridging ligands are best described as chelating-bridging (η_1:η_2:μ_2 or 2.21) (Scheme 4.3b) in which O8 and O9 atoms connect the two Eu atoms with bond distances in the 2.326-2.773 Å range, meanwhile O7 and O10 are bonded only to a Eu atom with Eu-O bond lengths of 2.518 and 2.401 Å respectively. The Eu1···Eu2 intramolecular distance is 4.000 Å. Moreover, there are two *S*-2-PhBut ligands coordinated to each Eu^{3+} centre in the chelating coordination mode (Scheme 4.3c) with Eu-O bond distances in the 2.404-2.543 Å range. Finally, each EuN_2O_7 coordination sphere is completed by two N atoms of one bathophen ligand with Eu-N distances in the 2.567-2.649 Å range. To determine the distortion degree of each lanthanide ion coordination polyhedron, SHAPE software[6] was used, and it is quantified as Continuous Shape Measurements (CShM). For the former compound, the coordination polyhedron of the two Eu^{3+} atoms are close to a Muffin geometry (MFF-9, Cs) with a CShM value of 1.616 for both Eu^{3+} centres, Figure 4. 16c). The Europium ions of each dinuclear entity are crystallographically independent, but both show the same coordination environment. The molecules are arranged in space through π---H stacking from the bathophen ligands, Figure 4. 17. Centroid 1 (Cg1), formed by C97, C98, C99, C107, C108 and C109, interacts with H24 bonded to a sp^2 carbon (C24) from one aromatic ring of the bathophen ligand of the adjacent dinuclear unit, with a Cg1---H24 intermolecular distance of 2.540 Å. The π---H stacking interaction grows along the [0 0 1] space vector.

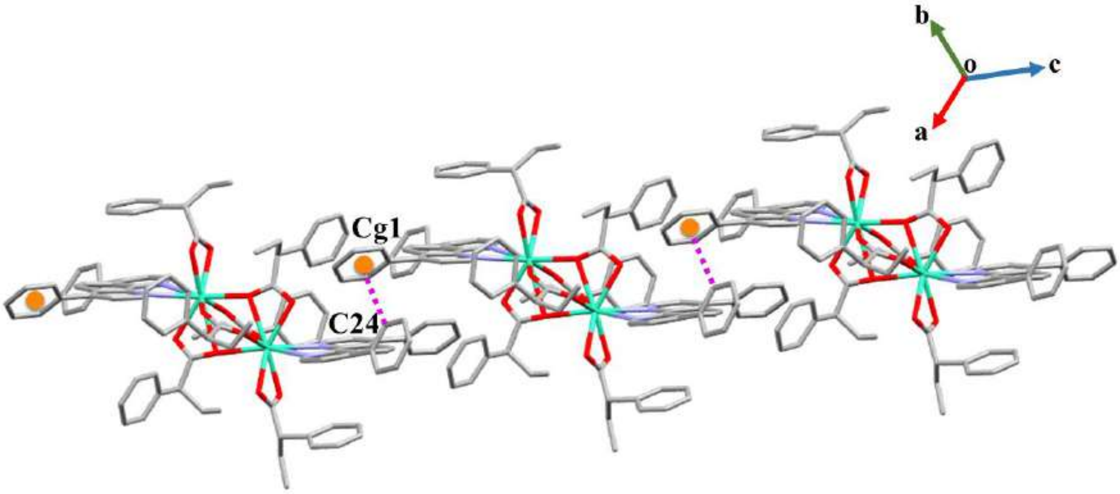

Figure 4. 17 π---H stacking intermolecular interactions along the ***S*-52-Eu-a** crystal lattice. The orange balls represent the calculated centroid of the bathophen aromatic rings. The π---H stacking interactions are represented by the pink dotted lines.

On the other hand, the structural type *b* is found in ***S*-62-Tm-b**. It crystallizes in the monoclinic crystal system and the C2 space group. The asymmetric unit of ***S*-62-Tm-b** is composed of a dinuclear system where each Tm^{3+} ion is octacoordinated. The Thulium centres are bridged through four carboxylate *S*-2-PhBut ligands in the symmetrical *syn*-*syn* bidentate bridging coordination mode with Tm-O distances ranging from 2.234 to 2.291 Å. The intramolecular distance between the two Tm metals is 4.287 Å. Also, there is one *S*-2-PhBut ligand coordinated to each lanthanide centre in the bidentate chelating coordination mode with Tm-O distances in the 2.312-2.412 Å range. Each TmN_2O_6 coordination sphere is fulfilled by two N atoms from one bathophen ligand with Tm-N distances in the 2.516-2.585 Å range. The coordinating N and O atoms are set around each Tm^{3+} ion in a geometry close to a triangular dodecahedron (TDD-8, D_2d) with a CShM value of 1.288. Each Tm centre of the same dinuclear unit is crystallographically independent but both are placed in the same environment inside the crystallographic lattice. In this case there are any *π*---H and *π*---*π* interaction with distances short enough to consider *π*-stacking between molecules therefore there are no intermolecular interaction promoting 2D or 3D supramolecular arrangement. The dinuclear molecules in ***S*-62-Tm-b** structure are set through weak Van der Walls interactions along the crystal lattice.

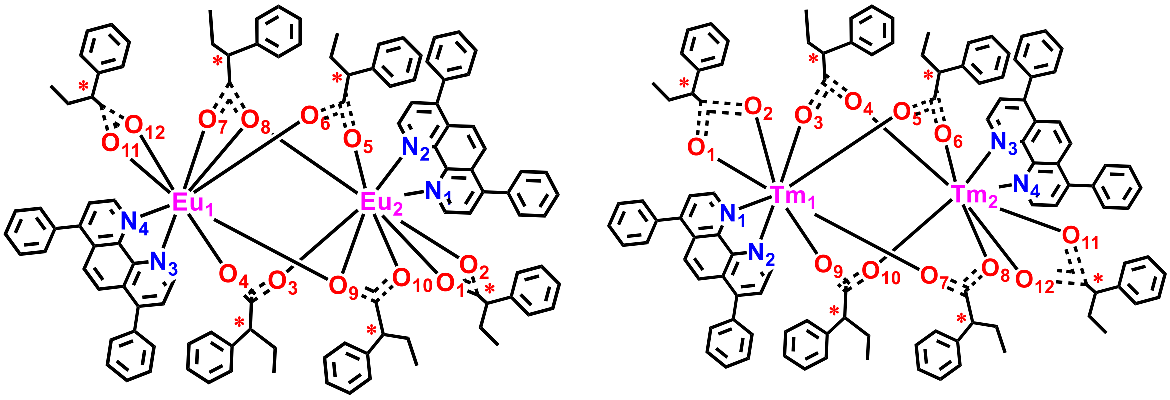

Scheme 4.4. Scheme of structural type a (left) and structural type b (right).

The main difference between *structure a* and *structure b* is the coordination mode of the bridging ligands, Scheme 4. 4. In *structure b*, the four bridging ligands are found in the same *syn-syn* bidentate bridging mode while in *structure a*, besides there are two carboxylate ligands in the *syn-syn* bidentate bridging mode, the other two are found in the chelating-bridging coordination mode. Consequently, the coordination number decreases from 9, in *structure a*, to 8, in *structure b*. The difference in the coordination number leads the chelating *S*-2-PhBut and bathophen ligands to rearrange differently in space also, changing the spatial group as well as the geometry of the coordination polyhedron from crystal motif *a* to *b*.

To verify the phase purity along the whole powder samples, powder X-Ray Diffraction (PXRD) measurements were performed for each of the presented new compounds.

PXRD diffractograms of ***S*-52-Eu-a** and ***S*-62-Tm-b** samples matched well with the calculated PXRD patterns obtained from the single crystal structure, confirming its phase purity, Figure 4. 18 and Figure 4. 19.

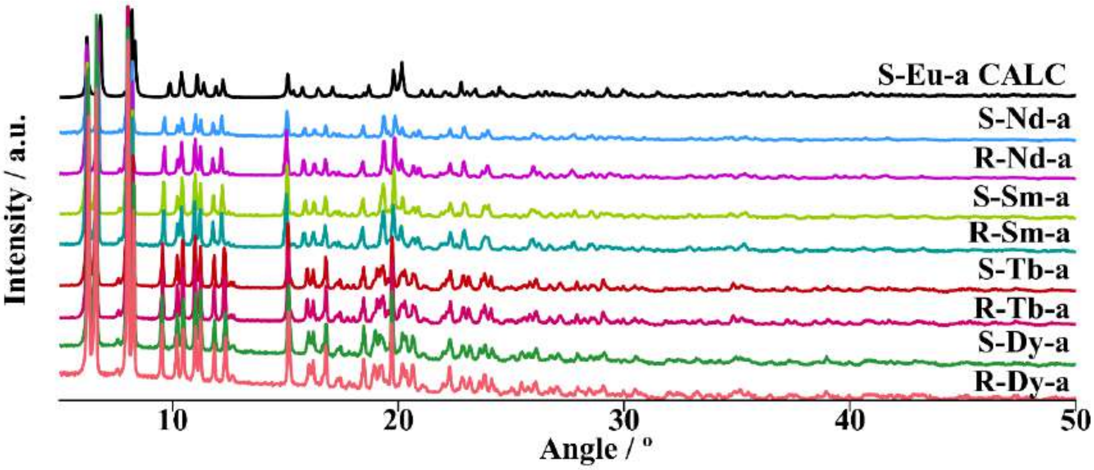

Figure 4. 18 Powder X-Ray Diffraction of all the enantiomeric pairs showing *structure a* type. First spectra, in black, corresponds to the calculated spectra from the single crystal structure of **S-52-Eu-a**.

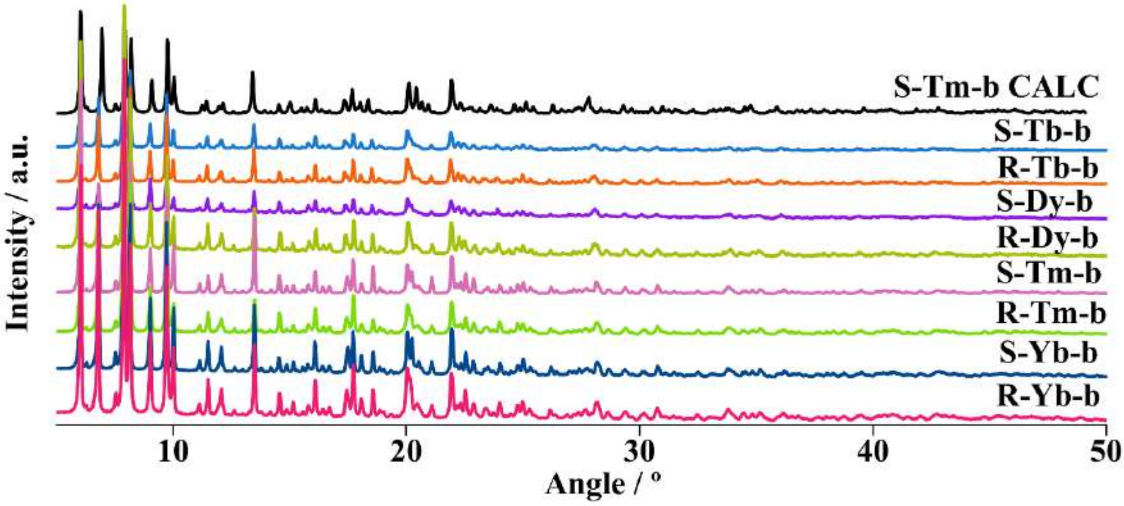

Figure 4. 19 Powder X-Ray Diffraction of all the enantiomeric pairs showing *structure b* type. First spectra, in black, corresponds to the calculated spectra from the single crystal structure of ***S*-62-Tm-a**.

Then enantiopure compounds ***R*-51-Eu-a** and ***R*-61-Tm-b** were synthetized, as well as both enantiomeric pairs using other lanthanide ions such as Nd^{3+}, Sm^{3+}, Tb^{3+}, Dy^{3+} and Yb^{3+}. PXRD were performed for all the analogues (Figure 4. 18 and Figure 4. 19). Different powder diffractions patterns were obtained corresponding to *structure a* and *structure b*, depending on the lanthanide ion. The trend goes as follows: (Scheme 4.5) *i)* for Nd^{3+}, Sm^{3+} and Eu^{3+} ions the final product crystallizes as *structure a* (***R*-47-Nd-a**, ***S*-48-Nd-a**, ***R*-49-Sm-a**, ***S*-50-Sm-b**, ***R*-51-Eu-a** and ***S*-52-Eu-b**) whereas *ii)* for Tm^{3+} and Yb^{3+}, the final product crystallizes as *structure b* (***R*-61-Tm-b**, ***S*-62-Tm-b**, ***R*-63-Yb-b** and ***S*-64-Yb-b**). *iii)* Meanwhile, for Tb^{3+} and Dy^{3+} ions, both structure types are obtained. For Tb^{3+} the final structure type depends on the solvent used during the synthetic procedure. If the reaction is carried out in a methanol/DMF solution, a Tb^{3+} compound with *structure a* (***R*-53-Tb-a** and ***S*-54-Tb-a**) type is obtained. However, when ethanol is used instead of methanol, the Tb^{3+} final compound shows the *structure b* (***R*-55-Tb-b** and ***S*-56-Tb-b**) type. For the Dy^{3+} analogue, a mix of both structures is obtained in each synthesis. However, since the crystals corresponding to *structure a* and *structure b* can be discerned by the naked eye, each structure type can be isolated for the ***S*** and ***R*-Dy** compounds (***R*-57-Dy-a, *S*-58-Dy-a, *R*-59-Dy-b, *S*-60-Dy-b**).

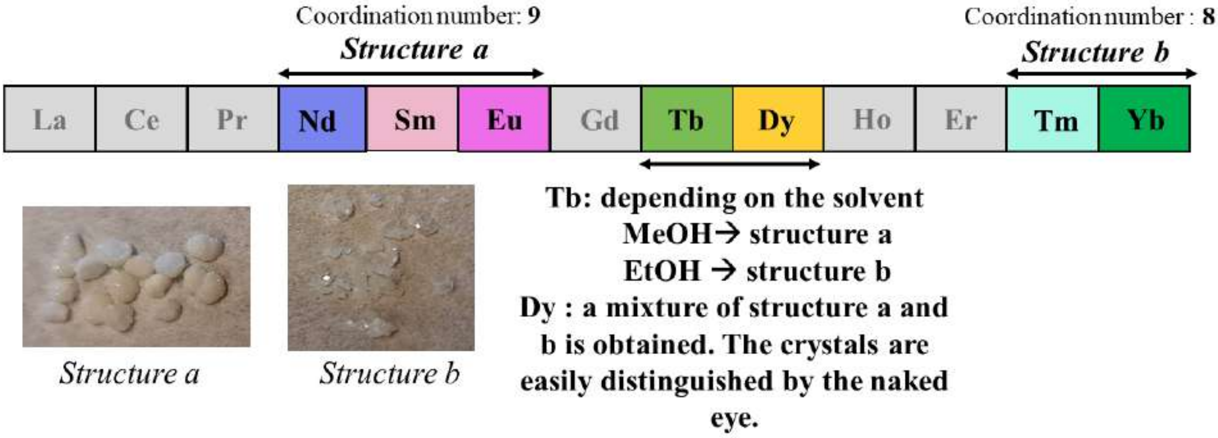

Scheme. 4.5 Structure trend along the lanthanide group summary.

This trend observed for the presented *R*/*S*-$[Ln_2(\mu\text{-}2\text{-}PhBut)_4(2\text{-}PhBu)_2(bathophen)_2]$ lanthanide family is mainly due to the gradual decrease in the lanthanide(III) ionic radius on increasing the atomic number which is a consequence of the so called lanthanide contraction.[7a,27] The reduction of the Ln^{3+} radii induces a decrease in the coordination number. For the former compounds, the decrease of the coordination number also implies a change in the structure due to stearic hindrance promoted by the ligand molecules. As the Ln^{3+} radius decreases, the coordination number diminishes from 9 (*structure a*), for the lighter lanthanides, to 8 (*structure b*) for the heaviest ones. The lanthanide elements located in the middle of the 6th period (Tb^{3+} and Dy^{3+}) can show both coordination numbers as *structure a* and *structure b*. For the Tb^{3+} analogue, obtaining one structural type or the other is discriminated by the solvent used in each synthesis.

In addition, the contraction along the lanthanide series can also be observed in the Ln-O and Ln-N bond distances in the ***S*-52-Eu-a** and ***S*-62-Tm-b** structures. The overall Eu-O and Eu-N bond lengths are larger than the Tm-O and Tm-N. The Ln---Ln intramolecular distance, though, is larger for ***S*-62-Tm-b** (4.287 Å) compared to the ***S*-52-Eu-a** (4.000 Å). This is because in ***S*-52-Eu-a** the Eu^{3+} ions are bridged, apart from the bridging ligand in the *syn-syn* coordination mode, through one oxygen atom from two chelating-bridging carboxylate ligands which generates two Ln-O-Ln angles of 108.7º and of 100.0º shortening in this way the Eu---Eu intramolecular distance.

4.2.3 Luminescence properties

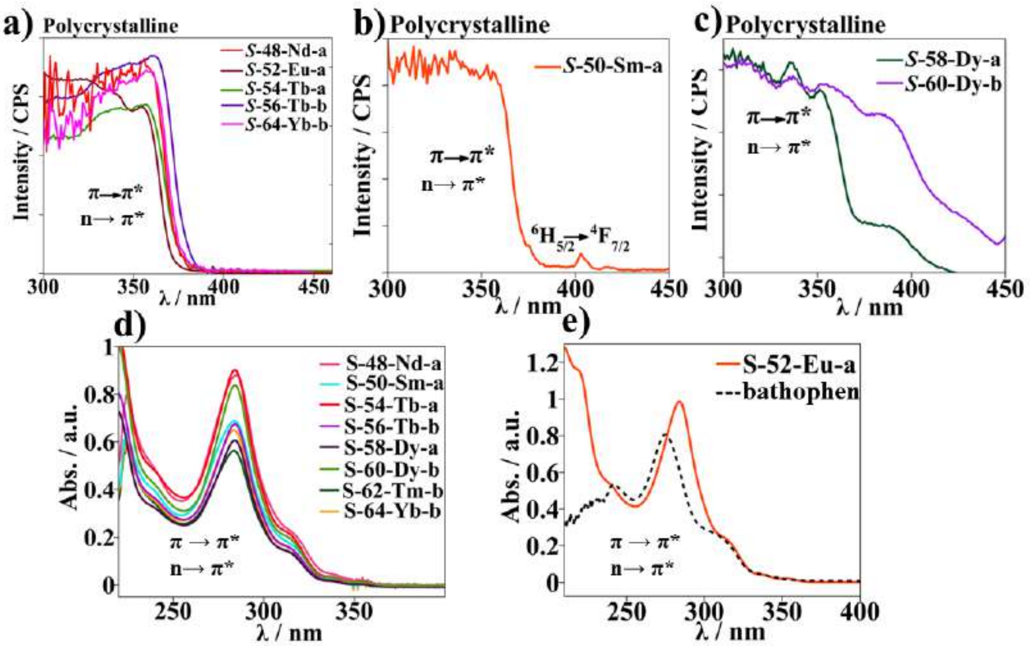

Figure 4. 20 a), b) and c) Excitation spectra of the polycrystalline samples monitored at λ_{em} of 1062 nm ($^4F_{3/2}\rightarrow{}^4I_{11/2}$) for ***S*-47-Nd-a**, 597 nm ($^4G_{5/2}\rightarrow{}^6H_{9/2}$) for ***S*-50-Sm-a**, 615 nm ($^5D_0\rightarrow{}^7F_2$) for ***S*-52-Eu-a**, at 546 nm ($^5D_4\rightarrow{}^7F_5$) for ***S*-54-Tb-a** and ***S*-56-Tb-b**, at 574 nm for ***S*-58-Dy-a** and 576 nm ($^4F_{9/2}\rightarrow{}^6H_{13/2}$) for ***S*-60-Dy-b** and at 975 nm ($^2F_{5/2}\rightarrow{}^2F_{7/2}$) for ***S*-64-Yb-b**. d) Absorption spectra of all compounds measured in 1mM DCM solution and e) Comparison of absorption spectrum of ***S*-52-Eu-a** and bathophen ligand in a 1 mM DCM solution.

Luminescence properties of all compounds were studied and measured in the solid state and in 1 mM dichloromethane (DCM) solution at room temperature. Since each enantiomer pair shows the same emission and excitation spectra, only the *S*- enantiomer of each lanthanide is discussed in this section. Excitation spectra of the polycrystalline enantiomers were recorded at the emission wavelength (λ_{em}) of 1062 nm ($^4F_{3/2}\rightarrow{}^4I_{11/2}$) for ***S*-47-Nd-a**, 597 nm ($^4G_{5/2}\rightarrow{}^6H_{9/2}$) for ***S*-50-Sm-a**, 615 nm ($^5D_0\rightarrow{}^7F_2$) for ***S*-52-Eu-a**, at 546 nm ($^5D_4\rightarrow{}^7F_5$) for ***S*-54-Tb-a** and ***S*-56-Tb-b**, at 574 nm for ***S*-58-Dy-a** and 576 nm ($^4F_{9/2}\rightarrow{}^6H_{13/2}$) for ***S*-60-Dy-b** and at 975 nm ($^2F_{5/2}\rightarrow{}^2F_{7/2}$) for ***S*-64-Yb-b**, Figure 4. 20a)-c). All the spectra show an intense and broad band around 300-400 nm that is assigned to the $\pi\rightarrow\pi^*$ and $n\rightarrow\pi^*$ ligand centred excitation transitions from the bathophen ligand. In addition, for compound ***S*-50-Sm-a**, a very weak band around 403 nm is differentiated and it is assigned to the $^6H_{5/2}\rightarrow{}^4F_{7/2}$ *f-f* transition arising from the Sm^{3+} ion. Moreover, the shoulder found in ***S*-58-Dy-a** and ***S*-60-Dy-b** spectra in the 375 to 400 nm range could be attributed to the $^6H_{15/2}\rightarrow{}^6P_{7/2}$ and $^6H_{15/2}\rightarrow{}^6P_{5/2}$ Dy^{3+} centred *f-f* excitation transitions.[28] Moreover, absorption spectra were recorded for all complexes and for the free bathophen ligand (c= 1 mM), Figure 4. 20d), e). All spectra show similar absorption patterns. The maxima appearing at 284 nm is assigned to the $\pi\rightarrow\pi^*$ and $n\rightarrow\pi^*$ from the bathophen ligand. In the superimposed spectra of the bathophen free ligand, the maximum is slightly blue shifted in comparison to the ***S*-52-Eu-a** spectrum indicating coordination to the metal.

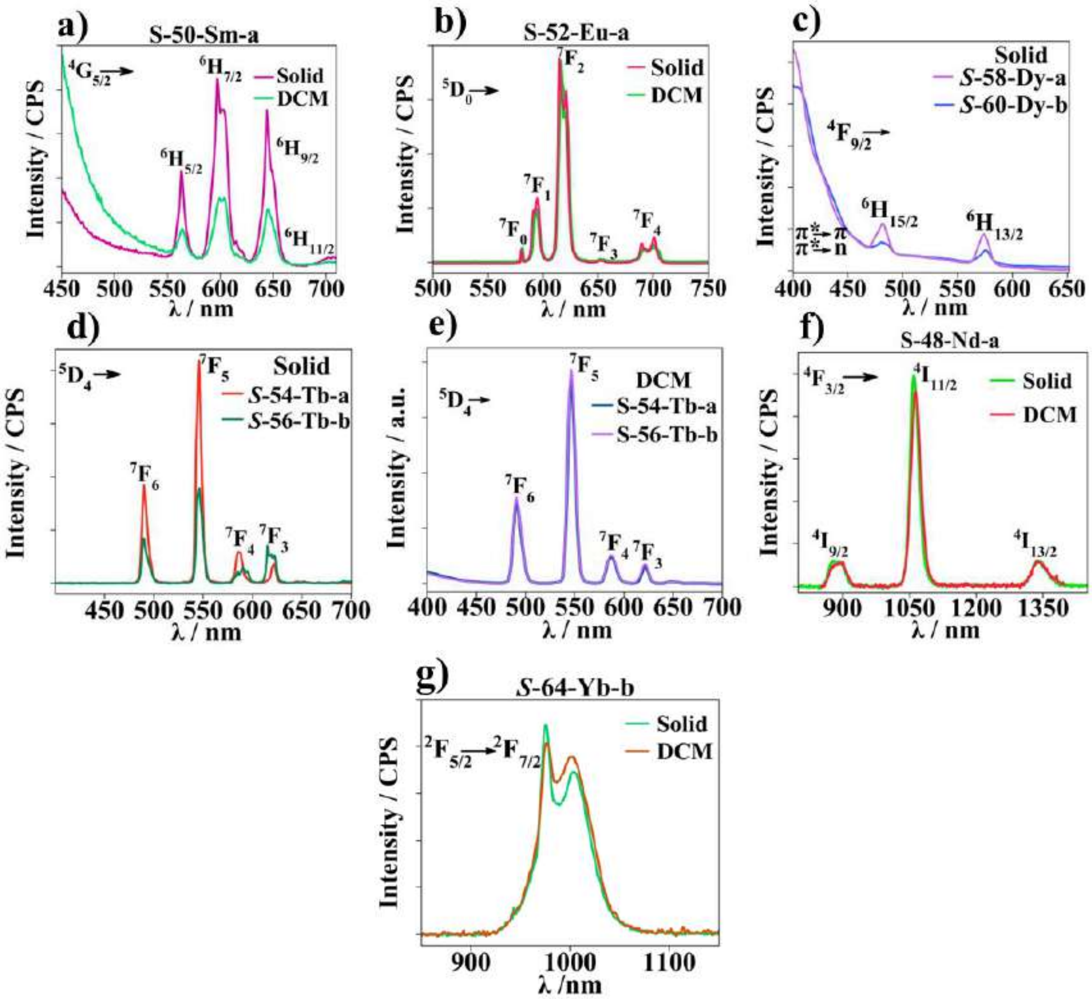

Figure 4. 21 Emission spectra of *S*- enantiomers of compounds ***S*-48-Nd-a** to ***S*-64-Yb-b**. The polycrystalline samples were excited at the λ_{exc} of 355, 354, 355, 355, 360, 360, 356 and 359 nm for ***S*-50-Sm-a**, ***S*-52-Eu-a**, ***S*-54-Tb-a**, ***S*-56-Tb-b**, ***S*-58-Dy-a**, ***S*-60-Dy-b**, ***S*-48-Nd-a** and ***S*-64-Yb-b** respectively whereas the 1mM DCM solutions were excited at a λ_{exc} of 284 nm.

To measure the emission spectra, solid state samples were excited at the excitation wavelength (λ_{exc}) of 355, 354, 355, 355, 360, 360, 356 and 359 nm for ***S*-50-Sm-a**, ***S*-52-Eu-a**, ***S*-54-Tb-a**, ***S*-56-Tb-b**, ***S*-58-Dy-a**, ***S*-60-Dy-b**, ***S*-48-Nd-a** and ***S*-64-Yb-b**, respectively. Emission spectra of the DCM solutions were monitored at λ_{exc} of 284 nm for all compounds. Excitation at the respective λ_{exc}, resulted in emission of the predicted lanthanide *f-f* transitions within the visible and nIR range. Besides, characteristic red and green luminescence colours of Eu and Tb-based systems respectively could be seen by the naked eye. For a more accurate comparison of their luminescence, emission spectra of the ***S*-54-Tb-a**/ ***S*-56-Tb-b** and ***S*-58-Dy-a**/***S*-60-Dy-b** pairs were monitored in the same exact conditions. The expected profiles were recorded in all cases, with some differences in the polycrystalline and solution samples, except for ***S*-58-Dy-a** and ***S*-60-

Dy-b, where no significant emission was observed in solution. Moreover, luminescence properties of ***S*-62-Tm-b** are not discussed as its emission spectra is entirely dominated by ligand emission. Emission bands exhibited by the former lanthanide complexes are given in Figure 4. 21.

Excitation of ***S*-50-Sm-a** led to emission bands at 563, 597, 644 and a very weak one at 705 nm, Figure 4. 21a). This bands correspond to the Sm^{3+} centred emission transitions from the $^4G_{5/2}$ emitting energy level to the ^6H_J ground state where J is 5/2, 7/2, 9/2 and 11/2 respectively. Residual emission from the ligand, which becomes more prominent in DCM solution, is detected at 450-500 nm indicating rather low sensitization efficiency for the ***S*-50-Sm-a**.

The expected Eu^{3+} bands corresponding to the $^5D_0 \rightarrow {}^7F_{J=0\text{-}4}$ are distinguished after excitation of ***S*-52-Eu-a**, Figure 4. 21b). The forbidden transition ($\Delta J=0$) appears as a sharp, low-intense band at 581 nm. For the J ground state $^7F_0$, the splitting due to crystal field perturbation is 1. Hence, any splitting of the emission band associated to the 0→0 transition suggests the presence of more than one Eu^{3+} emitting centre, each with different environment. In the crystal structure of the dinuclear ***S*-52-Eu-a** compound, there are two Eu^{3+} ions that are crystallographically independent, though each have the same chemical environment, and both present the same coordination geometry (CShM value is the same). Therefore, compound ***S*-52-Eu-a** shows one Eu^{3+} emitting centre with a single 0→0 emission band. The magnetically allowed $^5D_0 \rightarrow {}^7F_1$ transition, with intensity independent of the environment, arises at 594 nm and it is split into two components due to crystal field perturbation. Furthermore, the most intense band located in the red range at 615 nm is assigned to $^5D_0 \rightarrow {}^7F_2$ and it is mostly responsible for the red emission colour of ***S*-52-Eu-a**. The splitting of the hypersensitive band suggests that the lanthanide ion does not occupy an inversion symmetry site inside the structure found in solid and in solution samples. Finally, the broader band at 701 nm which also appears split due to crystal field perturbation, is assigned to $^5D_0 \rightarrow {}^7F_4$ transition.[8]

***S*-54-Tb-a** and ***S*-56-Tb-b** polycrystalline powders show the bands arising from the *f-f* Tb^{3+} transitions at 491, 546, 585 and 623 nm which are assigned to $^5D_4 \rightarrow {}^7F_{J=6\text{-}3}$ for both samples. As can be seen in the superimposed spectra (Figure 4. 21d) ***S*-54-Tb-a** and ***S*-56-Tb-b** luminescence present significant differences. The ***S*-54-Tb-a** signals are more intense than the corresponding to the ***S*-56-Tb-b** isomer, as it is also seen for the measured Quantum Yields (see below). Besides, for ***S*-Tb-b**, the bands corresponding to $^5D_4 \rightarrow ^7F_4$ and $^5D_4 \rightarrow ^7F_3$ transitions are split due to crystal field perturbation and the $^5D_4 \rightarrow ^7F_3$ band is higher in intensity than the $^5D_4 \rightarrow ^7F_4$ which it is not usually seen. Furthermore, spectra of both, ***S*-54-Tb-a** and ***S*-56-Tb-b**, show the same pattern when they are found in DCM solution (Figure 4. 21e) and at the same time the two spectra are different from the polycrystalline sample suggesting that the dinuclear unit is probably not maintained when ***S*-54-Tb-a** and ***S*-56-Tb-b** are dissolved in DCM.

As for the Dy-based systems, when exciting the polycrystalline ***S*-58-Dy-a** and ***S*-60-Dy-b** samples at the corresponding ligand excitation wavelengths, very weak emission corresponding to the Dy^{3+} luminescence could be measured, Figure 4. 21c. Weak bands at 481 and 574 nm can be discerned corresponding to the $^7F_{9/2} \rightarrow ^6H_{15/2}$ and $^7F_{9/2} \rightarrow ^6H_{13/2}$ transitions. Emission spectra are mainly governed by a more intense and broader band in the blue range (400-450 nm) corresponding to ligand emission. Superimposed spectra reveal that the emission of ***S*-58-Dy-a** is slightly more intense than ***S*-60-Dy-b**, following the same trend as the Tb^{3+} counterparts. For ***S*-58-Dy-a** and ***S*-60-Dy-b** in DCM solution the luminescence is totally quenched, and just emission from the ligand could be detected (spectra not shown).

Regarding the nIR emitters, after excitation of ***S*-48-Nd-a** powder to the ligand absorption wavelength, *f-f* transitions from the emission of the Nd^{3+} ion are clearly recognized, Figure 4. 21f). The more intense band arising at 1061 nm is assigned to $^4F_{3/2} \rightarrow ^4I_{11/2}$ whereas the two less intense bands at 886 and 1339 nm correspond to $^4F_{3/2} \rightarrow ^4I_{9/2}$ and $^4F_{3/2} \rightarrow ^4I_{13/2}$ transitions.

Finally, the expected luminescence band from the Yb^{3+} ion is induced after excitation of ***S*-64-Yb-b** at 359 nm. The band appearing at 976 nm concerns to the $^2F_{5/2} \rightarrow ^2F_{7/2}$ transition and it appears split due to crystal field perturbation.[7a]

In all compounds, the emission spectra in solution are slightly different compared to the polycrystalline spectra. This may indicate a change in the lanthanide coordination environment due to solvation effects therefore the stability of these compounds in solution should be considered.

For instance, regarding europium's pure magnetic dipole and electric dipole nature of the $^5D_0 \rightarrow ^7F_1$ and $^5D_0 \rightarrow ^7F_2$ transitions respectively, some structural information can be obtained from its luminescence spectra. The integrated areas of $^5D_0 \rightarrow ^7F_1$ band to the $^5D_0 \rightarrow ^7F_2$ band ratio (0→1/0→2) provides information about the symmetry around the Eu^{3+} environment and it is also often employed to compare the intensity of hypersensitive transitions among different Eu^{3+} compounds.[8] For the polycrystalline sample ***S*-52-Eu-a**, the ratio value is 0.3 while in solution it changes to 0.2 indicating that a slight change is produced around the Eu^{3+} site on dissolving the sample into DCM solution. Furthermore, spectra of ***S*-54-Tb-a** and ***S*-56-Tb-b** appear to be identical when they are found in DCM solution, as already mentioned, suggesting that the dinuclear unit is not maintained. Instead, a new compound, probably a mononuclear system, is found and perhaps equilibrium of different species is active in this medium. Because good luminescence properties remain in the solution samples, the solvated systems could correspond to a molecular system where the *S*-2-PhBut ligand is till coordinated to the Ln^{3+} cation to maintain the neutral charge and at least one chromophore bathophen molecule is also coordinated to the metal. Hence excitation at the ligand absorption wavelength induces the Ln^{3+} characteristic emission, also in DCM solution. In addition, residual ligand emission was observed in ***S*-54-Tb-a** and ***S*-56-Tb-b** spectra, pointing to back transfer energy from the Tb^{3+} emitting level to the triplet state of the ligand or a possible equilibrium between the free ligand and the lanthanide complex. There is no evidence trend on red or blue shifting of the emission bands in solid respect to the DCM solution ones. Moreover, ^1H-NMR spectra of ***S*-52-Eu-a** and ***S*-56-Tb-b** in deuterated DCM solutions were measured, Figure APX.X.1. The spectra are poorly resolved, and one can obtain only limited information. It is clear that the compounds go through a dynamic equilibrium between species of different geometries with possible exchange of bathophen ligand between a linked and a free form. On the contrary, the chiral carboxylate ligand appears mostly bonded to the Ln in both cases.

All things considered, excitation at the ligand absorption wavelengths resulted in the expected emission bands corresponding to the distinctive *f-f* transitions from each lanthanide ion for the Eu^{3+}, Tb^{3+}, Nd^{3+} and Yb^{3+} solid samples. Additionally, no emission from the ligands is sensed above 500 nm, showing that energy transfer from the excited states of the organic moieties towards the lanthanide(III) emitting energy level, the antenna effect, occurs for such Ln^{3+} coordination compounds.[7a] As for ***S*-50-**

Sm-a, the anticipated luminescence from the Sm^{3+} ion was recorded but also emission from the ligand was observed. The same is observed for the Tb-based compounds (***S*-54-Tb-a** and ***S*-56-Tb-b**) in 1 mM DCM solutions, indicating back transfer energy or equilibrium between the free ligand and the lanthanide complex. However, for the ***S*-58-Dy-a**, ***S*-60-Dy-b** and ***S*-62-Tm-b** analogues, the excited level of the ligand moieties is not in resonance with the Dy^{3+} and Tm^{3+} emitting energy level leading to ligand emission and weak luminescence from the Ln^{3+} symmetry forbidden *f-f* transitions. In addition, observed differences exist between the polycrystalline spectra and the DCM solution spectra, suggesting a structural change in solution that could involve the dissociation of the dinuclear entity.

In addition, the overall photoluminescence quantum yields (ϕ_{Ln}^{L}) and luminescence lifetimes (τ_{obs}) were measured for both, polycrystalline and solution samples at room temperature, of compounds showing higher emission intensity: ***S*-51-Eu-a**, ***S*-53-Tb-a** and ***S*-56-Tb-b** samples. The results are presented in Table 4. 8.

Table 4. 8 Overall quantum yields and luminescence lifetime of compounds ***S*-52-Eu-a**, ***S*-54-Tb-a** and ***S*-56-Tb-b** measured in polycrystalline samples (ϕ_{Ln}^{L} $_{\text{polycryst}}$ and $\tau_{\text{obs polycryst}}$) and DCM solutions ($\phi_{Ln}^{L}$ $_{\text{DCM}}$ and $\tau_{\text{obs DCM}}$). Samples were excited at the corresponding λ_{exc}. [a] Value not recorded due to too low τ_{obs}.

	ϕ_{Ln}^{L} **polycryst**	ϕ_{Ln}^{L} **solution**	τ_{obs} **polycryst (ms)**	τ_{obs} **solution (ms)**
***S*-51-Eu-a**	0.71	0.31	1.90	1.80
***S*-53-Tb-a**	0.10	0.015	0.40	[a]
***S*-56-Tb-b**	0.05	0.015	0.30	[a]

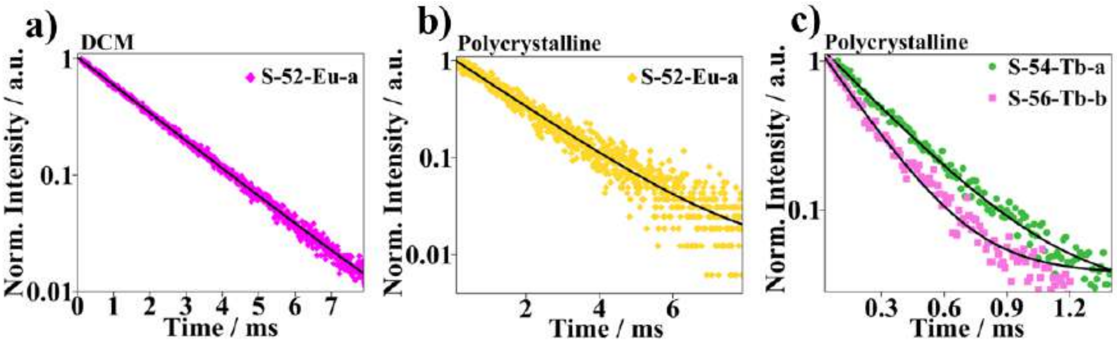

Figure 4. 22 Lifetime curves of compounds ***S*-51-Eu-a**, ***S*-53-Tb-a** and ***S*-56-Tb-b**. Solid lines represent the mono-exponential fit.

***S*-51-Eu-a** is the compound showing the highest ϕ_{Ln}^{L} which is about 2-fold in the polycrystalline sample compared to DCM solution. Also, ***S*-51-Eu-a** shows the longest luminescence lifetime (τ_{obs}) among the presented compounds. Comparing ***S*-54-Tb-a** and ***S*-56-Tb-b** complexes, ***S*-54-Tb-a** showed higher luminescence intensity when comparing the emission spectra of the polycrystalline samples. This trend is also corroborated with the measured ϕ_{Ln}^{L} , where ***S*-56-Tb-b** quantum yield was reduced to the half compared to ***S*-54-Tb-a**. While for the 1 mM DCM Tb^{3+} samples, the measured ϕ_{Ln}^{L} turned out to be the same for both, ***S*-54-Tb-a** and ***S*-56-Tb-b**, suggesting once more that the hinted Ln^{3+} compounds go through a structural change due to solvating effects and when the Tb polycrystalline complexes dissolve, whether it is *structure a* or *structure b*, the final arrangement found in solution is the same. In addition, $\tau_{obs\ \mathrm{polycryst}}$ of ***S*-54-Tb-a** is slightly greater than ***S*-56-Tb-b**.

All decay curves could be fitted by a monoexponential decay law following $I(t) = I_0 \exp\left(-\frac{t}{t_{obs}}\right)$, Figure 4. 22. The presence of a single decay time component, τ_{obs}, for the former compounds is suggestive of a single radiative deactivation process, both in the solid state and in solution. Interestingly, in the dinuclear compounds derived from the *R/S*-2-PhBut and phen ligands found in the literature, showing the [Ln_2(μ-*R/S*-2-PhBut)$_4$(*R/S*-2PhBut)$_2$(phen)$_2$] formula, the measured ϕ_{Ln}^{L} were 0.46 and 0.35 for the Eu^{3+} and Tb^{3+} polycrystalline samples, respectively.[2] Replacing the phen to bathophen (in this work), ϕ_{Ln}^{L} increases up to 0.71 for the Eu^{3+} derivative. However, for the Tb^{3+} derivatives the ϕ_{Ln}^{L} decreased notably for the compound with the bathophen ligand. This suggests that bathophen has lower sensitization efficiency for terbium cation compared to phen molecules.

In addition, more information concerning the sensitization mechanism of ***S*-51-Eu-a** can be extracted from the spectroscopic data. $\tau_{rad}^{\square}$ is consistent with the luminescence lifetime in absence of non-radiative deactivation and it is different from each compound, since it depends on the Eu^{3+} environment and on the refractive index of the medium in which the emitting sample is found. The radiative lifetime ($\tau_{rad}^{\square}$) from the $^5D_0$ emissive state can be calculated from the corrected emission spectrum of ***S*-51-Eu-a** compound by means of a simplified equation (Equation 1.8).[9,29] Just for the Eu^{3+} ion, we can avoid going through the tedious process of calculating spontaneous emission coefficients from Judd-Ofelt parameters given the pure magnetic dipole nature of $^5D_0 \rightarrow ^7F_1$ transition. For ***S*-51-Eu-a** in the polycrystalline sample, τ_{rad} is 2.29 ms and 3.40 ms in the DCM solution. Then the intrinsic quantum yield (ϕ_{Ln}^{Ln}) is 0.82 and 0.52 for the solid and solution samples respectively. Moreover, the sensitization efficiency (η_{sens}) is described as the amount of energy absorbed by the ligands that is transferred to the excited state of the lanthanide ion. It assumes a significant role in the overall quantum yield defined as $\phi_{Ln}^{L} = \eta_{sens} \cdot \phi_{Ln}^{Ln}$. Hence, the η_{sens} results of 0.86 in polycrystalline powder and of 0.60 in DCM solution determining a rather efficient sensitization effect from the ligand moieties to the Eu^{3+} emitting energy level specially when ***S*-51-Eu-a** is found as a polycrystalline sample. Moreover, if the dinuclear Eu^{3+} coordination compound ***S*-51-Eu-a** remained after dissolving it in the 1 mM DCM solution, the relation $\tau_{rad-DCM} = \frac{n_{polycryst.}^3}{n_{DCM}^3} \tau_{rad-polycryst.}$ ratio should be obeyed and $\tau_{rad-DCM}$ would yield 2.80 ms. However, the calculated $\tau_{rad-DCM}$ from the corrected emission spectra is 3.4 ms. The former fact suggests that the system found in solution differs from the one in the polycrystalline sample.[9]

4.2.4 Circular dichroism (CD) and Circular polarized Luminescence measurements (CPL).

Chiroptical studies were performed for the Eu^{3+}, Tb^{3+} and Dy^{3+} analogues. Circular Dichroism measurements were carried out in solid state in polycrystalline samples dispersed into a KBr matrix. CD spectra of powder samples turned out to be very weak and it was not possible to derive a significant interpretation. Mirror images could be discerned only for the ***S*-54-Tb-a** and ***S*-56-Tb-b** enantiomeric pair in the 210 to 400 nm range assigned to absorption of the ligand moieties, Figure 4. 23a).

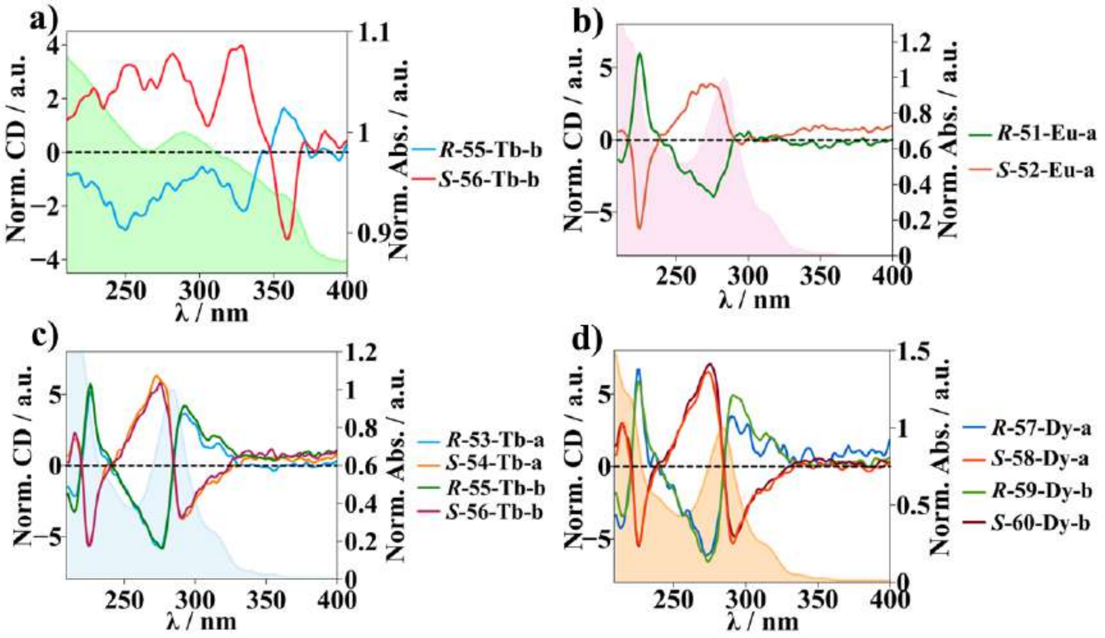

Figure 4. 23 Circular Dichroism spectra of compounds a) ***S*-54-Tb-a** and ***S*-56-Tb-b** measured in the solid state and of compounds b) ***R*-51-Eu-a** and ***S*-52-Eu-a** c) ***R*-53-Tb-a**, ***S*-54-Tb-a**, ***R*-55-Tb-b** and ***S*-56-Tb-b** and d) ***R*-57-Dy-a**, ***S*-58-Dy-b**, ***R*-59-Dy-b** and ***S*-60-Dy-b** compounds measured in 1 mM DCM solution.

Nevertheless, the spectrum shows rather weak Cotton effects. For the presented dinuclear complexes, bathophen ligands coordinating the lanthanide ion are quasi-coplanar in the crystal lattice, defining an overall low dissymmetry to the final compound, leading to the absence of significant exciton coupling. In addition, CD spectra were measured in 1 mM DCM solution for all the compounds. The dinuclear lanthanide entities undergo a structural change, as was already observed in the luminescence studies, probably forming a mononuclear arrangement with both, the enantiopure *R/S*-2-PhBut and bathophen ligands, coordinated to the lanthanide ion. The new species formed in DCM solution acquire higher dissymmetry, hence stronger CD spectra are obtained, Figure 4. 23b), c) d). Mirror image spectra are obtained for the enantiomer pairs of the complexes in the bathophen absorption wavelength, indicating that the chirality of *R/S*-2-PhBut ligand is transferred to the chromophore bathophen.

Circular Polarized Luminescence spectra were measured in solid state and 1 mM DCM solutions for compounds showing higher luminescence emission intensity: the ***R*-51-Eu-a** and **S-52-Eu-a, *R*-53-Tb-a** and ***S*-54-Tb-a**, ***R*-55-Tb-b** and ***S*-56-Tb-b** enantiomeric pairs at the excitation wavelength of 365 nm for solid and 254 nm for 1 mM DCM solution. The solid samples were dispersed in a quartz plate, from a suspension in n-pentane, considering that the compounds are not soluble in such solvent. Solid deposition of compounds ***R*-51-Eu-a** and **S-52-Eu-a** show rather weak but measurable mirror image signals for the $^5D_0 \rightarrow ^7F_1$ and $^5D_0 \rightarrow ^7F_2$ transitions, Figure 4. 24a. Due to the weak and noisy spectra obtained for the polycrystalline ***R*-51-Eu-a** and **S-52-Eu-a** pair, a reliably dissymmetry factor, g_{lum}, could not be extracted from CPL data. ***R*-55-Tb-b** and ***S*-56-Tb-b** were measured only for the most intense emission band corresponding to terbium(III)'s $^5D_4 \rightarrow ^7F_5$ transition. Three components with opposite sign (+, -, + for the *S*- enantiomer) can be distinguished Figure 4. 24b. The dissymmetry factor could be quantified and for the more intense component of Tb $^5D_4 \rightarrow ^7F_5$ transition $g_{lum} = \Delta I/I$ approximately equal to $\pm\ 2\cdot10^{-3}$ was found (+ for ***S*-*Tb-b***), Figure APX.X.2. Meaningful CPL spectra could not be measured for the ***R*-53-Tb-a** and ***S*-54-Tb-a** enantiomeric pair.

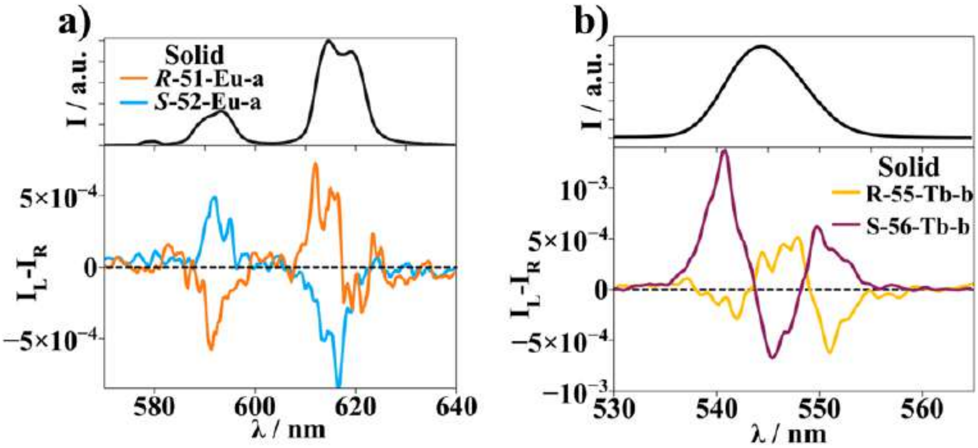

Figure 4. 24 a) Top, ***S*-52-Eu-a** emission of $^5D_0 \rightarrow ^7F_1$ and $^5D_0 \rightarrow ^7F_2$ transitions. Bottom, solid state CPL spectra for ***R*-51-Eu-a** and ***S*-52-Eu-a** complexes on a quartz plate deposition, b) Top, ***S*-56-Tb-b** emission of $^5D_4 \rightarrow ^7F_5$ transition. Bottom, solid state CPL spectra of ***R*-55-Tb-b** and ***S*-56-Tb-b** complexes on a quartz plate deposition.

CPL spectra of the 1 mM DCM solutions of Eu^{3+} and Tb^{3+} complexes were measured. Under such conditions, CPL spectra are significantly different form the ones measured in powder depositions. Following the same fashion as the CD spectra, CPL measurements of ***R*-51-Eu-a** and **S-52-Eu-a**, ***R*-53-Tb-a** and ***S*-54-Tb-a**, ***R*-55-Tb-b** and ***S*-56-Tb-b** DCM solutions were more intense and clearer. Well resolved mirror image spectra were obtained for the ***R*-51-Eu-a** and ***S*-52-Eu-a** enantiomeric pair, where all the bands can be distinguished, Figure 4. 25a). The most intense band, as usually happens in CPL spectra of luminescent Eu^{3+} compounds, was the pure magnetic dipole $^5D_0 \rightarrow ^7F_1$

transition. It is split into two components with opposite sign (+ and - for the *R*-enantiomer) corresponding to the m_j=±1 and 0 states generated by crystal field perturbation. The g_{lum} factors obtained for ***R*-51-Eu-a** and ***S*-52-Eu-a** pair range ±0.03 (+ for ***R*-51-Eu-a**) and ±0.02 (+ for ***S*-52-Eu-a**) for the most intense component of $^5D_0 \rightarrow ^7F_1$ and $^5D_0 \rightarrow ^7F_3$ transitions, respectively and $\pm 8 \cdot 10^{-4}$ (+ for ***R*-51-Eu-a**) for the electric dipole $^5D_0 \rightarrow ^7F_2$ transition, Figure APX.X.3. On the other hand, DCM solutions of Tb-based systems also presented well resolved CPL bands, Figure 4. 25b). ***R*-55-Tb-b** and ***S*-56-Tb-b** pair shows mirror image spectra where the band arising from $^5D_4 \rightarrow ^7F_5$ transition clearly stands out among the others. It presents three components, each with alternated different sign (-, + and - for the *S*- enantiomer). Interestingly, the sign of crystal field components of this band is the opposite for the CPL measurement in solid state of the ***R*-55-Tb-b** and ***S*-56-Tb-b** pair. The g_{lum} value for the most intense component of the $^5D_4 \rightarrow ^7F_5$ transition is ±0.03 (- for the *S*- enantiomer), Figure APX.X.4. DCM solutions of ***R*-53-Tb-a** and ***S*-54-Tb-a** showed the same CPL properties evidencing that the species obtained in solution were the same for both compounds regardless of the structure of the crystal phase (*structure a* or *structure b*), Figure 4. 25b) bottom). Similar CPL properties are found for other reported Eu^{3+} and Tb^{3+} polynuclear compounds measured in the solid state and in solution.[11,12,30,31]

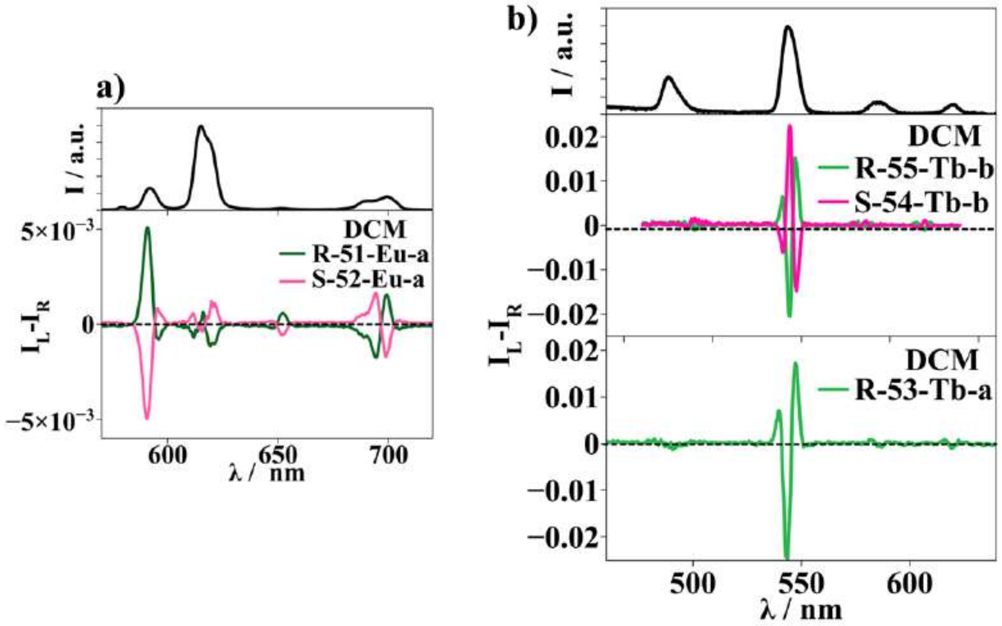

Figure 4. 25 CPL of 1 mM DCM solutions of compounds a) ***R*-51-Eu-a** and ***S*-52-Eu-a** and b) ***R*-55-Tb-b**, ***S*-54-Tb-b** and ***R*-53-Tb-a**. Black line in both figures shows the emission spectra of each luminescent compound.

4.2.5 Magnetic properties

Direct current (dc) magnetic susceptibility studies

Direct current magnetic susceptibility (χ_M) and magnetization (M) experiments were carried out primarily for the *R*- enantiomers on the polycrystalline samples, as *S*- and *R*-enantiomers are expected to exhibit identical magnetic properties. The χ_M measurements were carried out under an external direct current (dc) magnetic field of 0.3 T in the 2-300 K temperature range. The $\chi_M T$ dependence with T plots are presented in Figure 4. 26a) and b). At room temperature (300 K) the $\chi_M T$ values are 3.08, 2.18, 2.78, 23.17, 23.34, 28.48, 28.24, 14.45 and 4.78 cm^{3}mol^{-1}K for ***R*-47-Nd-a**, ***R*-49-Sm-a**, ***R*-51-Eu-a**, ***R*-53-Tb-a**, ***R*-55-Tb-b**, ***R*-57-Dy-a**, ***R*-59-Dy-b**, ***R*-61.Tm-b** and ***R*-63-Yb-b** respectively. For two isolated Ln^{3+} cations, the calculated $\chi_M T$ values are: 3.28 cm^{3}mol^{-1}K for Nd^{3+} ground state $^4I_{9/2}$ and g_j=8/11; 0.18 cm^{3}mol^{-1}K for Sm^{3+} ground state $^6H_{5/2}$ and g_j=2/7; 0 cm^{3}mol^{-1}K for Eu^{3+} ground state $^7F_0$; 23.64 cm^{3}mol^{-1}K for Tb^{3+} ground state $^7F_6$ and g_j=3/2; 28.34 cm^{3}mol^{-1}K for Dy^{3+} ground state $^6H_{15/2}$ and g_j=4/3, 7.15 cm^{3}mol^{-1}K for Tm^{3+} ground state $^3H_6$ and g_j=7/6 and 5.14 cm^{3}mol^{-1}K for Yb^{3+} ground state $^2F_{7/2}$ and g_j=8.7.[7a]

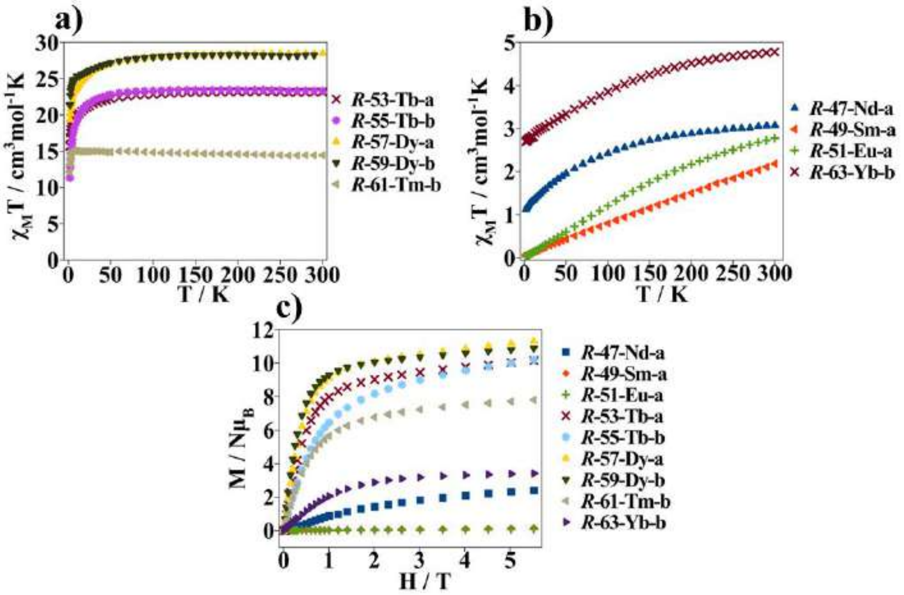

Figure 4. 26 a) $\chi_M T$ *vs* T plots, measured under an external magnetic dc field of 0.3 T, of compounds ***R*-53-Tb-a, *R*-55-Tb-b**, ***R*-57-Dy-a**, ***R*-59-Dy-b** and ***R*-61-Tm-b** and b) $\chi_M T$ vs T plots, measured under an external magnetic dc field of 0.3 T, of compounds ***R*-47-Nd-a**, ***R*-49-Sm-a**, ***R*-51-Eu-a** and ***R*-63-Yb-b** and c) *M vs* the magnetic field plots measured at 2K for all compounds.

The experimental $\chi_M T$ values at room temperature obtained for ***R*-47-Sm-a** and ***R*-51-Eu-a** compounds are noticeably larger than the calculated ones. The electronic ground state ^{6}H, of a Sm^{3+} ion and ^{7}F, of an Eu^{3+} ion, in a coordination compound, split due to spin-orbit coupling by $^6H_{J=5/2-15/2}$ and $^7F_{J=0-6}$, *J* states respectively. The parameter (λ) defining the spin orbit coupling energy gap between the ground and excited *J* states is rather small, around 200 cm^{-1} for Sm^{3+} and 300 cm^{-1} for Eu^{3+} ion. Because of these smaller λ values, excited *J* states are closer in energy, and these are found thermally populated at room temperature. Thus, the $\chi_M T$ value at 300 K is higher than the calculated one which only considers the population of the $^6H_{5/2}$ and $^7F_0$ ground states (for Sm^{3+} and Eu^{3+} respectively). The decrease of the $\chi_M T$ values on cooling the sample is due to thermal depopulation of the excited *J* states of these ions. At 2 K, $\chi_M T$ value of ***R*-51-Eu-a** is 0.01 cm^{3}mol^{-1}K confirming that at low temperature the non-magnetic ground state (*J*=0) is stabilized.[16,17]

The $\chi_M T$ *vs* T plots of compounds ***R*-47-Nd-a** and ***R*-63-Yb-b**, decrease gradually on cooling the samples. The continuous diminution is ascribed to a progressive thermal depopulation of the excited m_j doublets, generated by the crystal field perturbation. At the limit temperature of 2 K the $\chi_M T$ values are 1.12 and 2.69 cm^{3}mol^{-1}K, for ***R*-47-Nd-a** and ***R*-63-Yb-b** respectively, where apparently only the m_j ground state is populated.[16]

Regarding the polycrystalline samples ***R*-53-Tb-a**, ***R*-55-Tb-b**, ***R*-57-Dy-a**, ***R*-59-Dy-b** and ***R*-61-Tm-a**, the $\chi_M T$ *vs* T curves show similar behaviour. The $\chi_M T$ magnetic susceptibility values stay practically constant on lowering the temperature down to ~50 K. Below this temperature, $\chi_M T$ drop suddenly to 15.69, 11.34, 19.34, 21.39, 12.13 cm^{3}mol^{-1}K respectively at 2 K. The decrease of $\chi_M T$ is attributed to thermal depopulation of the excited $\pm m_j$ states of the ground *J* state. Different trends are observed when comparing structures *type a* and *b* of those lanthanides that present both structure types (Tb^{3+} and Dy^{3+}). At the lowest temperature limit, sample ***R*-55-Tb-b** drop to smaller $\chi_M T$ values compared to ***R*-53-Tb-a** while ***R*-57-Dy-a** decreases more compared to ***R*-59-Dy-b**. The difference of the decrease in $\chi_M T$ *vs* T curves between *structure a* and *b* could be attributed to one or a combination of different phenomena. First, due to thermal depopulation of the excited m_j doublets (of the ground *J* state) generated by the crystal field perturbation. Second, due to weak antiferromagnetic coupling between the Ln^{3+} centres though the contracted nature of 4*f* electrons in lanthanide (III) ions make magnetic exchange coupling interactions rather weak. Third due to dipolar interactions between the molecules of the crystal lattice. For the former compounds, the lanthanide ions in the dinuclear molecules are separated by 4.000 and 4.287 Å (for the ***S*-52-Eu-a** and ***S*-62-Tm-b** single crystal structures respectively).[7a,32]

Magnetization dependence with applied magnetic field curves monitored at 2 K for the former compounds are depicted in Figure 4. 26. Magnetization increases suddenly on applying an external magnetic field from 0 to ~1 T. The compounds do not show saturation of the magnetization while for ***S*-52-Eu-a**, the magnetization value at 2 K is maintained at 0 $N\mu_B$, as expected.

Alternating current (ac) magnetic susceptibility studies

Furthermore, alternating current (ac) magnetic susceptibility measurements, under an oscillating $4 \cdot 10^{-4}$ T magnetic field, were carried out for compounds ***R*-47-Nd-a**, ***R*-49-Sm-a**, ***R*-53-Tb-a**, ***R*-55-Tb-b**, ***R*-57-Dy-a**, ***R*-59-Dy-b**, ***R*-61-Tm-b** and ***R*-63-Yb-b**. The samples containing Dy^{3+}, Nd^{3+} and Yb^{3+} showed slow relaxation of the magnetization.

Concerning Dy-based compounds, magnetic behaviour is quite different when varying from *structure a* (***R*-57-Dy-a**) to *structure b* (***R*-59-Dy-b**). At a 0 T direct current (H_{dc}) magnetic field, ac response of ***R*-57-Dy-a** was absent, while ***R*-59-Dy-b** showed maxima of the out-of-phase magnetic susceptibility component (χ_M'') in the 1.8 to 6.5 K temperature range and therefore Single Molecule Magnet (SMM) behaviour, Figure 4. 27a). Compound ***R*-57-Dy-a** showed slow relaxation of magnetization just under a H_{dc} of 0.1 T.

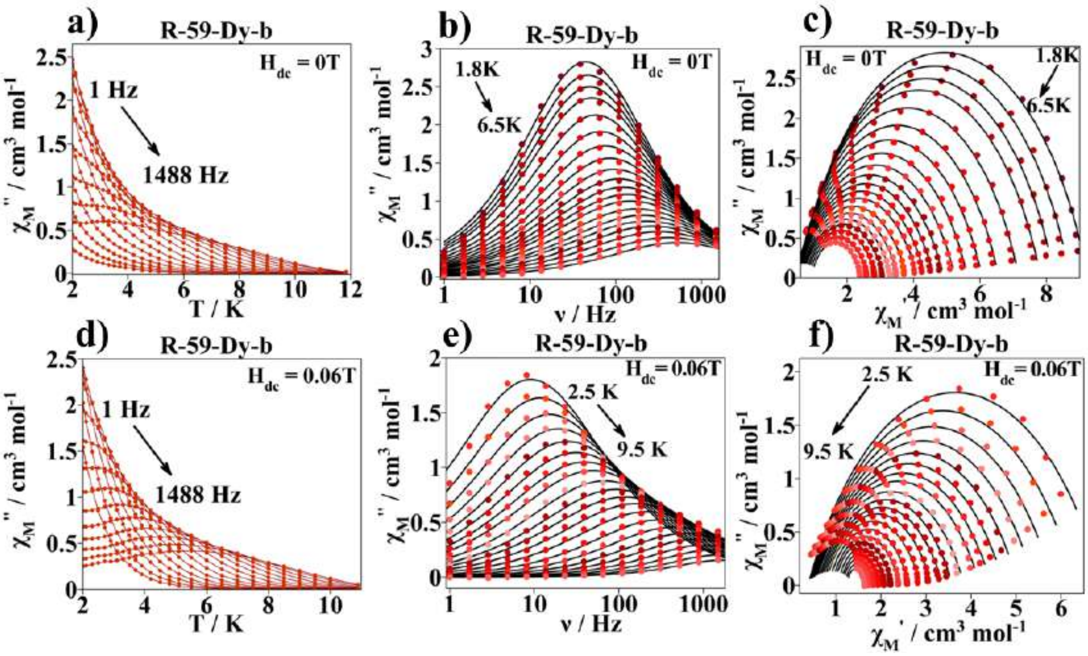

Figure 4. 27 a) and d) χ_M'' *vs* T plots of ***R*-59-Dy-b** measured at a H_{dc} of 0 and of 0.06 T, respectively. The continuous lines are a guide to the eye b) and e) χ_M'' *vs* ν plots of ***R*-59-Dy-b** measured at a H_{dc} of 0 and of 0.06 T, respectively. Continuous black lines are the fitting to the Generalized Debye model and c) and f) are the representation in the Cole-Cole plots of ***R*-59-Dy-b** measured at a H_{dc} of 0 and of 0.06 T, respectively. Continuous black line is the fitting to the Generalized Debye model.

The plot of χ_M'' with the oscillating frequency of ***R*-59-Dy-b** at H_{dc}= 0 T, is presented in Figure 4. 27b). First, on increasing the temperature, χ_M'' maxima remain almost constant. While upon heating the sample until 7 K, the peaks move progressively to higher frequencies. Above this temperature ac response is not observed anymore. The Cole-Cole plot (χ_M' *vs* χ_M'' representation) in Figure 4. 27c) shows non-symmetric semicircles that can be fitted with the one component Generalized Debye model described by the Casimir-Dupré function, Equation 1.32.[33] The fitting leads to α values that remain almost constants along all the temperature range: 0.27 to 0.28. The extracted relaxation times with temperature (ln(τ) *vs* T^{-1}) are depicted in Figure 4. 28. Interestingly, in the ln(τ) *vs* T^{-1} curve no clear linear trend is discerned in the high temperature range suggesting that the spin relaxation of the ***R*-59-Dy-b** system does not take place through the thermally activated Orbach mechanism. The Orbach spin-lattice relaxation takes place through an effective energy barrier from the ground $\pm m_j$ state through a real excited state by a series of phonon absorption and emission processes and it is described by an Arrhenius law, Equation 4.3. Normally, the Orbach process takes place at the higher temperature range since the system needs enough energy to surpass the whole energy barrier.[23]

$$\tau^{-1} = \tau_0^{-1}\exp\left(\frac{-\Delta E}{k_B T}\right)$$ **Equation 4.3**

$$\tau^{-1} = CT^n + AT$$ **Equation 4.4**

$$\tau^{-1} = \tau_0^{-1}\exp\left(\frac{-\Delta E}{k_B T}\right) + AT$$ **Equation 4.5**

By using such equation in the higher temperature range of the ***R*-59-Dy-b** ln(τ) *vs* T^{-1} curve, the obtained activation energy is 9.19 cm^{-1} and $\tau_0 = 4.77 \cdot 10^{-5}$ s, therefore we could stand for the idea that the over barrier mechanism is not prevailing for this relaxation process, Figure APX.X.5.[34] Nonetheless, it could be possible that for ***R*-59-Dy-b** the relaxation of the magnetization is taking place in the low energy vibrational structure (through less energetic acoustic phonons) through the Raman mechanism as already experienced in other Dy-based systems showing slow relaxation of the magnetization.[35,36]

$$\tau^{-1} = CT^n + \tau_{QTM}^{-1}$$ **Equation 4.6**

The best fit of the ln(τ) *vs* T^{-1} curve was obtained when Raman and Quantum Tunnelling of the magnetization (QTM) spin relaxation mechanisms (Equation 4.6) were considered, and the obtained parameters are C = 28.6 $s^{-1}K^{-n}$ with n = 2.4 for Raman and τ_{QTM}= 0.0097 s for QTM processes, Figure 4. 28. A compilation of the fitted parameters obtained from the equations that describe the different relaxation mechanisms for the presented compounds is found in Table 4. 9.

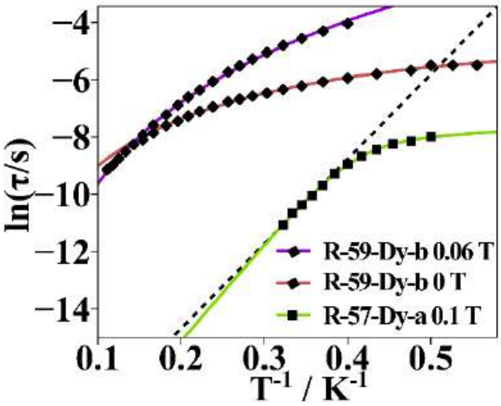

Figure 4. 28 ln(τ) *vs* T^{-1} plots of ***R*-59-Dy-b** obtained at H_{dc} = 0 T, ***R*-59-Dy-b** obtained at H_{dc} = 0.06 T and ***R*-57-Dy-a** obtained at H_{dc} = 0.1 T. Continuous lines represent the best fit according to Raman + QTM equations for ***R*-59-Dy-b** at H_{dc} = 0 T, Raman for ***R*-59-Dy-b** at H_{dc} = 0.06 T and Orbach + Direct equations for ***R*-57-Dy-a** at H_{dc} = 0.1 T.

Furthermore, the field dependence of χ_M'' measured at 3.5 K shows that for ***R*-59-Dy-b** maxima shift to lower oscillating frequencies with the application of a dc magnetic field. The relaxation of the magnetization times with respect to a static magnetic field reach the highest value at the optimal field of 0.06 T, Figure 4. 29a). At H_{dc} = 0.06 T, χ_M''*vs* ν maxima start to appear at lower frequencies compared to the H_{dc} = 0 G measurement, Figure 4. 27e). Also, the temperature range in which χ_{AC} signal appears is higher (2.5-9 K) than in the 0 T magnetic measurement. The χ_M'' peaks move progressively to higher oscillating frequencies on increasing the temperature suggesting that spin relaxation of ***R*-59-Dy-b**, at H_{dc} =0.06 T, takes place through a thermal dependent mechanism along all the temperature range and that by applying the external H_{dc}, the fast QTM is reduced or even removed. The Cole-Cole plots were fitted with the one component Generalized Debye model, Figure 4. 27f). The α parameter remains in a range of smaller values compared to the H_{dc} = 0 G measurement and it also stays constant along all the temperature range varying from 0.011 to 0.014, indicating that the width distribution of the relaxation times diminishes on applying a dc magnetic field for the SMM Dy^{3+} compound. The ln(τ) *vs* T^{-1} plot is represented in Figure 4. 28. By fitting the higher temperature range data with the Arrhenius law that describes the Orbach mechanism, the energy barrier slightly increased to 12.2 cm^{-1} (τ_0=4.98·10^{-6}s) compared to the H_{dc}=0 T measurement, Figure APX.X.5. However, the best fit of the curve is obtained when only the equation corresponding to the Raman relaxation mechanism (first part of Equation 4.6) is used and the obtained parameters are C = 1.2 s^{-1}K^{-n} with n

= 4, Figure 4. 28. The fast QTM is removed by applying the external magnetic field. α values obtained from the Cole-Cole magnetic data are practically 0. Thus, the narrow distribution of relaxation times agrees with the fact that at H_{dc} = 0.06 T relaxation of the magnetization of compound ***R*-59-Dy-b** is mainly governed by one process with one mechanism, Raman in this case.

Table 4. 9 Compilation of the fitted parameters obtained from the different equations that describe the different relaxation of the magnetization mechanisms for compounds presenting slow relaxation of the magnetization: ***R*-47-Nd-a**, ***R*-57-Dy-a**, ***R*-59-Dy-b** and ***R*-63-Yb-b**.

	Orbach		Raman		Direct	QTM
	ΔE/cm^{-1}(K)	τ_0/s	C/s^{-1}K^{-n}	n	A/s^{-1}K^{-1}	τ_{QTM}
R-47-Nd-a			0.8	6.4	435.9	
R-57-Dy-a	23.5 (33.7)	$3.2\cdot10^{-10}$			1425.0	
R-59-Dy-b **H_{dc}=0G**			28.6	2.4		0.0097
R-59-Dy-b **H_{dc}=500G**			1.2	4.1		
R-63-Yb-b			1.26	5.7	126.5	

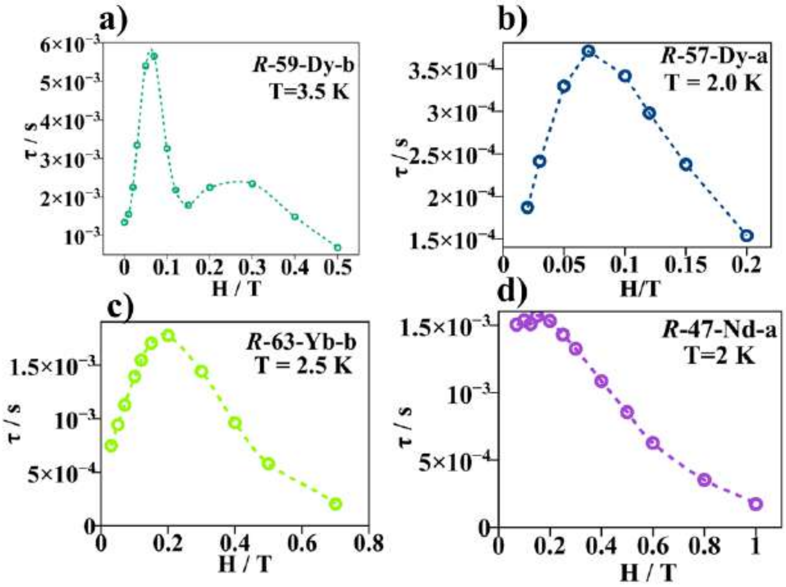

Figure 4. 29 Relaxation of the magnetization times dependency with static magnetic field measured at a) 3.5 b) 2.0 c) 2.5 and d) 2.0 K for ***R*-59-Dy-b**, ***R*-57-Dy-a**, ***R*-63-Yb-b** and ***R*-47-Nd-a**, respectively.

Furthermore, as previously mentioned, compound ***R*-57-Dy-a** showed slow relaxation of the magnetization under an external magnetic dc field. Field dependent measurements at 2 K showed that τ is the greatest when the H_{dc} field is 0.07 T, Figure 4. 29b). The in-phase and out-of-phase magnetic susceptibility measurements of ***R*-57-Dy-a** were monitored at a H_{dc} of 0.1 T. ***R*-57-Dy-a** showed maxima of the χ_M'' component in a small temperature range of 2-3.1 K, Figure 4. 30a). Cole-Cole plots (χ_M'' with χ_M' representation), Figure 4. 30b), show non-symmetric semicircles that become incomplete on increasing the temperature. The plots were successfully fitted to the one component generalized Debye model, leading to α values in the range of 0.008 (at 2 K) to 0.2 (at 3.1 K) indicating that the width of distribution of magnetization relaxation times increases with increasing temperature. The semi-log representation of τ with T^{-1} is showed in Figure 4. 28. At the higher temperature range, few points follow a linear trend. The ln(τ) *vs* T^{-1} curve of ***R*-57-Dy-a** compound was fitted considering only the Orbach mechanism in the higher temperature range thus leading to an effective energy barrier of 18.9 cm^{-1} (27.2 K) and a pre-exponential factor (τ_0) of $2.59\cdot10^{-9}$ s. However, the linear trend is not followed in all the temperature range. The equation that fit best the magnetic data of ***R*-57-Dy-a** are the ones that combines the Orbach (followed in the higher temperature range) and Direct (appears on cooling the sample) relaxation of the magnetization mechanisms, Equation 4.5. The values from the fit are ΔE = 23.5 cm^{-1} (33.7 K) and τ_0 of $3.2e^{-10}$ s for Orbach and A = 1425.0 $s^{-1}K^{-1}$ for Direct. Though ΔE of ***R*-57-Dy-a** system is larger compared to the one calculated for ***R*-59-Dy-b**, still, it is quite low. To verify if ***R*-57-Dy-a** magnetization is relaxing through the Orbach mechanism, ab initio calculation should be performed to know the energy difference between $\pm m_j$ ground and excited states in ***R*-59-Dy-b**. With such low energy barrier, Raman relaxation could be prevailing in the relaxation mechanism though, in this case, no successful fit could be obtained by using the equation describing only this mechanism. Moreover, the temperature range in which ***R*-57-Dy-a** is showing ac response is very short (around 1 K) therefore it is difficult to interpret τ tendency with temperature since few empirical data are obtained.

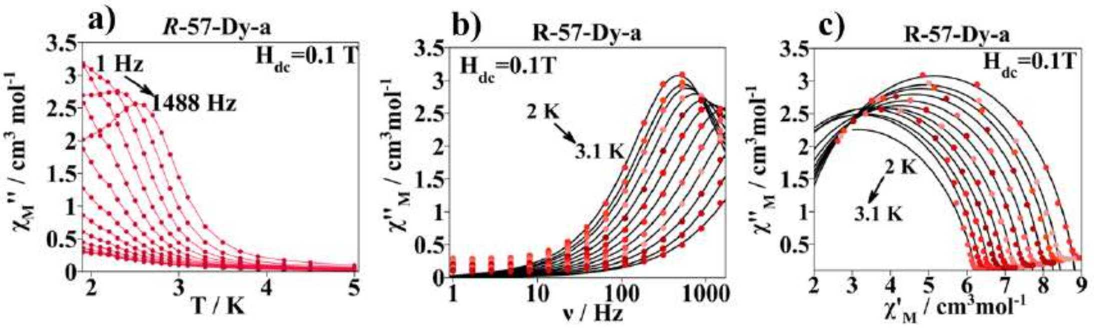

Figure 4. 30 *a)* χ_M'' *vs* T plot of ***R*-57-Dy-a** measured at a H_{dc} of 0.1 T. The red continuous line is a guide to the eye b) χ_M'' *vs* ν plots of ***R*-57-Dy-a** measured at a H_{dc} of 0.1 T. Continuous black line is the fitting to the Generalized Debye model and c) representation of the Cole-Cole plots of ***R*-57-Dy-a** measured at a H_{dc} of 0.1 T. Continuous black line corresponds to the fitting to the Generalized Debye model.

Regarding compounds ***R*-47-Nd-a** and ***R*-63-Yb-b**, at 0 T dc magnetic field, none of them showed magnetic response under the alternating current field indicating that the relaxation of the magnetization goes through the fast QTM relaxation mechanism. A small magnetic field of 0.1 T is enough for both compounds to show χ_M'' maxima. Thus, field dependence measurements at a constant temperature of 2 and 2.5 K were performed for ***R*-47-Nd-a** and ***R*-63-Yb-b** respectively. Relaxation of the magnetization times with the magnetic field reach the highest value at the optimal field of 0.15 T for ***R*-47-Nd-a** and of 0.2 T for ***R*-63-Yb-b**, Figure 4. 29c) and d).

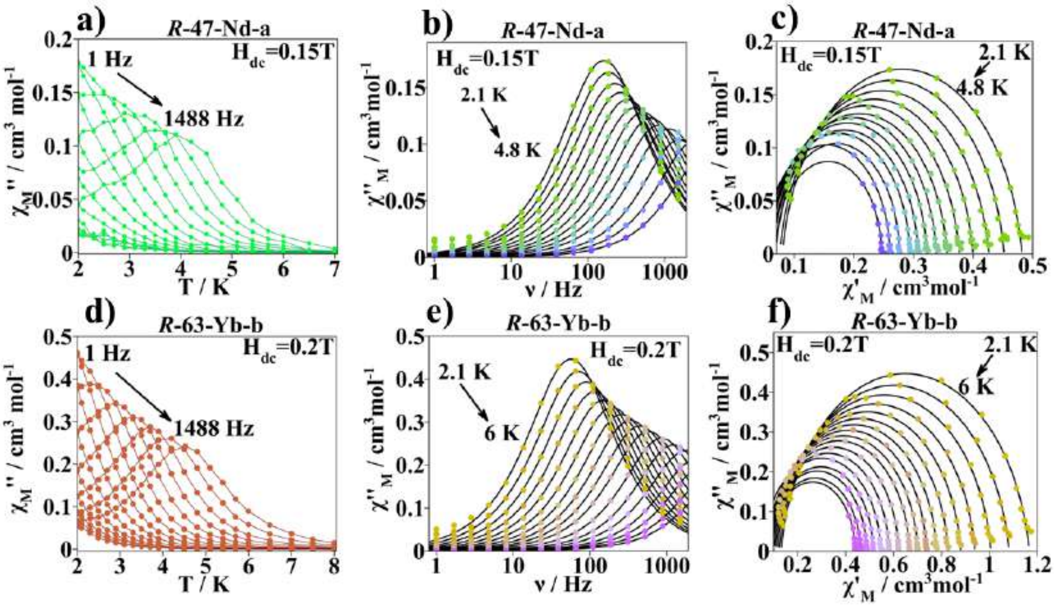

Figure 4. 31 a) and b) χ_M'' *vs* T plot of ***R*-47-Nd-a** and ***R*-63-Yb-b** measured at a H_{dc} of 0.15 and 0.2 T respectively. The continuous lines are guide to the eye b) χ_M'' *vs* ν plots ***R*-47-Nd-a** and ***R*-63-Yb-b** measured at H_{dc} of 0.15 and 0.2 T, respectively. Continuous black line is the fitting to the Generalized Debye model and c) Cole-Cole plot of ***R*-47-Nd-a** and ***R*-63-Yb-b** measured at a H_{dc} of 0.15 and 0.2 T respectively. Continuous black line is the fitting to the Generalized Debye model.

Then, ac measurements at the respective optimal dc magnetic field were carried out for each compound. ***R*-47-Nd-a** showed maxima of the imaginary magnetic susceptibility component in the 2.1 to 4.8 K temperature range while the ac signal appeared in a wider temperature range of 2.1-6 K for ***R*-63-Yb-b,** Figure 4. 31a) and d). For both lanthanide compounds, χ_M'' *vs* ν maxima move progressively to higher frequencies on increasing temperature as showed in Figure 4. 31b) and e). Cole-Cole plot representation shows semicircles that can be well fitted with the one component Debye model, Figure 4. 31c) and f). The collected α parameters range from 0.0035 to 0.0103 for ***R*-47-Nd-a** and from 0.094 to 0.01 for ***R*-63-Yb-b**. α values remain close to 0 in both cases, indicating a narrow distribution of magnetization relaxation times.

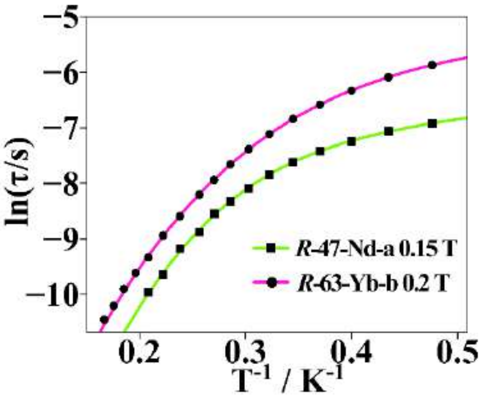

Figure 4. 32 ln(τ) *vs* 1/T plot of ***R*-47-Nd-a** obtained at H_{dc} = 0.15 T and ***R*-63-Yb-b** obtained at H_{dc} = 0.2 T. Continuous lines represent to the best fit according to Raman and Direct equations for both compounds.

Next, the semi-log curve representation of the extracted relaxation times with temperature (ln(τ) *vs* T^{-1}) successfully fit to the sum of both contributions, Raman and Direct mechanisms with Equation 4.4, Figure 4. 32. The values of the parameters obtained from the best fit yielded C = 0.8 $s^{-1}K^{-n}$ with n = 6.4 for Raman and A = 435.9 $s^{-1}K^{-1}$ for Direct for ***R*-47-Nd-a** and C = 1.26 $s^{-1}K^{-n}$ with n = 5.74 for Raman and A = 26.3 $s^{-1}K^{-1}$ for Direct for ***R*-63-Yb-b**. Certainly, at the higher temperature range a linear trend might appear, though by fitting those data points using the Arrhenius law the obtained energy barrier is rather low with values of 18.2 and 18.1 cm^{-1} and τ_0 of $2.0 \cdot 10^{-7}$ and $3.8 \cdot 10^{-7}$ s for ***R*-47-Nd-a** and ***R*-63-Yb-b**, respectively, Figure APX.X.6. Moreover, this linear trend is just followed in a few experimental points thus leading to a better fit when the equations including other relaxation mechanisms are used, in this case Raman and Direct. Other Yb^{3+} and Nd^{3+} compounds with slow relaxation of the magnetization under an external dc magnetic field showed similar behavior.[34,37]

Finally, ***R*-49-Sm-a**, ***R*-53-Tb-a**, ***R*-55-Tb-b** and ***R*-61-Tm-b** polycrystalline powders didn't show χ_M'' dependence with neither temperature nor frequency under the oscillating magnetic field.

4.3 Conclusions

In *Chapter 4*, thirty-two enantiomerically pure lanthanide coordination compounds have been successfully isolated and structurally characterized. Moreover, luminescence, chiroptical and magnetic studies were conducted. Two different families of chiral compounds are presented herein: first, coordination compounds derived from the enantiomerically pure (*R/S*)-(-/+)-α-Methoxyphenylacetic acid (*R/S*-HMPA) and 1,10-phenantroline (phen) and second, coordination compounds derived from the enantiomerically pure (*R/S*)-(-/+)-2-Phenylbutyric acid (*R/S*-2-HPhBut) and the 4,7-Diphenyl-1,10-phenanthroline (bathophen).

From the first family presented in *Section 4.1* of this *Chapter*, the synthetized chiral compounds consist of 1D polymers that expands along the *a* crystallographic axis. The compounds present the $[\mathrm{Ln}(\mu\text{-R/S-MPA})(\mathrm{R/S\text{-}MPA})_2(\mathrm{phen})]_n$ formula where Ln is Ce^{3+} (**_R_-33-Ce** and **_S_-34-Ce**), Nd^{3+} (**_R_-35-Nd** and **_S_-36-Nd**), Eu^{3+} (**_R_-37-Eu** and **_S_-38-Eu**), Tb^{3+} (**_R_-39-Tb** and **_S_-40-Tb**), Dy^{3+} (**_R_-41-Dy** and **_S_-42-Dy**), Sm^{3+} (**_R_-43-Sm** and **_S_-44-Sm**) and Er^{3+} (**_R_-45-Er** and **_S_-46-Er**). From Single Crystal X-Ray diffraction, the crystal structures of **_R_-37-Eu** and **_S_-38-Eu**, **_R_-39-Tb** and **_S_-40-Tb**, **_S_-42-Dy** and **_S_-44-Sm** were obtained. The lanthanide ions present a coordination number of 9 with the O and N donor atoms forming a distorted Spherical tricapped trigonal prism (D$_{3h}$) polyhedron around the Ln^{3+} cation.

On the other hand, from the second group presented in *Section 4.2* of this *Chapter*, the new compounds consist of chiral dinuclear coordination complexes with formula $[\mathrm{Ln}_2(\mu\text{-}\mathit{R/S}\text{-2-PhBut})_4(\mathit{R/S}\text{-2-PhBu})_2(\mathrm{bathohen})_2]$ where Ln is Nd^{3+} (**_R_-47-Nd-a** and **_S_-48-Nd-a**), Sm^{3+} (**_R_-49-Sm-a** and **_S_-50-Sm-a**), Eu^{3+} (**_R_-51-Eu-a** and **_S_-52-Eu-a**), Tb^{3+} (**_R_-53-Tb-a** and **_S_-54-Tb-a**, **_R_-55-Tb-b** and **_S_-56-Tb-b**), Dy^{3+} (**_R_-57-Dy-a** and **_S_-58-Dy-a**, **_R_-59-Dy-b** and **_S_-60-Dy-b**), Tm^{3+} (**_R_-61-Tm-b** and **_S_-62-Tm-b**) and Yb^{3+} (**_R_-63-Yb-b** and **_S_-64-Yb-a**). Two different structural motifs (*structure a* and *structure b*) have been found in this family of compounds. The molecular formula of *structure a* and *b* is the same, the difference is found in the coordination modes of the bridging ligands that connect both metals in each dinuclear unit. The coordination number decreases form 9 in *structure a*, to 8 in *structure b*. This change in coordination number causes the *S/R*-2-PhBut and bathophen ligands to reorganize in the crystal lattice, thereby altering the geometry of the coordination polyhedra which consists of a Muffing-like polyhedron in *structure a* whereas the polyhedron is better described as a triangular dodecahedron in *structure b*, Table 4. 10. Powder X-Ray diffraction data of all compounds revealed that the fact of presenting structural motif *a* or *b* depends on the Ln^{3+} ionic radius along the lanthanide series.

Table 4. 10 Compilation of molecular formula, coordination number and coordination polyhedron and Identification code of compounds ***R***- or ***S***-, ***R*-33-Ce** to ***S*-64-Yb-b**.

Formula	Coordination number and coordination polyhedron	Identification code
[Ln(μ-*R/S*-MPA)(*R/S*-MPA)$_2$(phen)]$_n$	9 TCTPR-9 (D$_3$h)	***R*-33-Ce**, ***S*-34-Ce**, ***R*-35-Nd,** ***S*-36-Nd**, ***R*-37-Eu,** ***S*-38-Eu**, ***R*-39-Tb,** ***S*-40-Tb**, ***R*-41-Dy,** ***S*-42-Dy**, ***R*-43-Sm,** ***S*-44-Sm,** ***R*-45-Er** and ***S*-46-Er**.
[Ln$_2$(μ-*R/S*-2-PhBut)$_4$(*R/S*-2-PhBut)$_4$(bathophen)$_2$] *structure a*	9 MFF-9 (C$_s$)	***R*-47-Nd-a**, ***S*-48-Nd-a**, ***R*-49-Sm-a**, ***S*-50-Sm-b**, ***R*-51-Eu-a,** ***S*-52-Eu-b,** ***R*-53-Tb-a,** ***S*-54-Tb-a,** ***R*-57-Dy-a** and ***S*-58-Dy-a**
[Ln$_2$(μ-*R/S*-2-PhBut)$_4$(*R/S*-2-PhBut)$_4$(bathophen)$_2$] *structure b*	8 TDD-8 (D$_2$d)	***R*-55-Tb-b**, ***S*-56-Tb-b,** ***R*-59-Dy-b**, ***S*-60-Dy-b,** ***R*-61-Tm-b**, ***S*-62-Tm-b** and ***R*-63-Yb-b,** ***S*-64-Yb-b**

Moreover, luminescence studies were carried out for all polycrystalline samples, as well as for the 1 mM DCM solutions only for the dinuclear [Ln$_2$(μ-*R/S*-2-PhBut)$_4$(*R/S*-2-PhBut)$_4$(bathophen)$_2$] series. For the 1D chiral chain complexes, all the compounds presented sensitized luminescence associated to the expected *f-f* transitions. As for the dinuclear *R/S*-2-PhBut derived compounds, excitation at the ligand absorption wavelengths resulted in the expected emission bands corresponding to the *f-f* transitions from each lanthanide ion for the Eu^{3+}, Tb^{3+}, Nd^{3+} and Yb^{3+} polycrystalline samples, both in solid and DCM solutions. However, the excited triplet state of the ligand moieties is not in resonance with ***S*-Dy-a**, ***S*-Dy**-b and ***S*-Tm-b** emitting energy levels, leading to ligand emission and poor luminescence from the *f-f* symmetry forbidden transitions of the Dy^{3+} analogues. All europium and terbium compounds presented rather good luminescence intensities with measurable Quantum Yields. Moreover, difference of the emission intensities is discerned for ***S*-53-Tb-a** and ***S*-55-Tb-b**. The Muffin-like (C_s) coordination polyhedron presented in ***S*-53-Tb-a** induces more distortion around the Tb^{3+} cation due to the lower symmetry of the geometry presented by this polyhedron in comparison with the Triangular dodecahedron (D_2d) presented in ***S*-55-Tb-b**. Lower symmetry around the emitting lanthanide centre is related to more emission intensity since it produces the intrinsic *f-f* transitions to be less prohibited by Laporte's rule explaining the lower Quantum yield measured for ***S*-53-Tb-a** compound compared to ***S*-56-Tb-b.** Quantum yields as well as luminescence lifetimes of the Eu^{3+} and Tb^{3+} derivatives of both chiral families are compiled in Table 4. 11.

Table 4. 11 Photoluminescent parameters compilation of all Eu and Tb analogues of the lanthanide chiral compounds presented in *Chapter 4.*

	τ_{obs} / ms	ϕ^{L}_{Ln}	τ_{rad} / ms	ϕ^{Ln}_{Ln}	η_{sens}
***R*-37-Eu**	1.77	0.14	3.05	0.58	0.24
***R*-39-Tb**	1.50	0.33			
***S*-51-Eu-a solid**	1.80	0.71	2.29	0.82	0.86
***S*-51-Eu-a 1mM DCM**	0.40	0.31	3.40	0.52	0.60
***S*-53-Tb-a solid**	0.40	0.10			
***S*-53-Tb-a 1mM DCM**	[a]	0.015			
***S*-56-Tb-b solid**	0.30	0.05			
***S*-56-Tb-b 1mM DCM**	[a]	0.015			

As for chiroptical properties, Circular Dichroism and Circular Polarized Luminescence were measured for the Europium and Terbium derivatives of both chiral families.

For the first lanthanide family presented in *Section 4.1*, measurements were only performed in the solid state due to its polymer nature. For the europium enantiomeric pair (***R*-37-Eu** and ***S*-38-Eu**), mirror image spectra could be obtained where the different *f-f* transitions can be discerned. On the other hand, for the Tb^{3+} analogues (***R*-39-Tb** and ***S*-40-Tb**) the intensity in the CPL spectra was too low and no reliable conclusions could be extracted from it.

For the dinuclear $[Ln_2(\mu\text{-}R/S\text{-2-PhBut})_4(R/S\text{-2-PhBut})_4(bathophen)_2]$ family, CD and CPL measurements of ***R*-51-Eu-a** and **S-52-Eu-a, *R*-53-Tb-a** and ***S*-54-Tb-a**, ***R*-55-Tb-b** and ***S*-56-Tb-b** revealed rather poor chiroptical properties in the solid state, though for the 1mM DCM solutions clearer mirror image and more intense spectra were obtained. Further comparation of luminescence, CD and CPL studies of such compounds in solid and in 1mM DCM solutions reveals that the dinuclear coordination compound goes through a deep structural change on dissolving each polycrystalline sample into solution.

Magnetic studies were conducted for both chiral lanthanide families. For the polymeric $[Ln(\mu\text{-R/S-MPA})(R/S\text{-MPA})_2(phen)]_n$ derivatives, compounds ***S*-34-Ce**, ***S*-36-Nd**, ***S*-42-Dy** and ***S*-46-Er** showed slow relaxation of the magnetization under an external magnetic field. Slow relaxation of the magnetization was best described by an underbarrier process (Raman and Direct) for compounds ***S*-34-Ce**, ***S*-36-Nd** and ***S*-42-Dy** whereas, $\ln(\tau)$ *vs* T^{-1} curve of ***S*-46-Er** presented an Orbach contribution, however the calculated energy value was low. Further magnetic measurements of the chiral dinuclear compounds, revealed Single Molecular Magnet behaviour for ***R*-59-Dy-b** while slow relaxation in the isomeric ***R*-57-Dy-a** compound was only observed under an external magnetic dc field of 0.1 T. The mechanism prevailing in the relaxation of the magnetization of the SMM compound was the Raman process. In addition, compounds ***R*-47-Nd-a** and ***R*-63-Yb-b** showed slow relaxation of the magnetization under an external DC magnetic field of 0.15 and 0.20 T respectively. Both compounds show quite similar magnetic behaviour with relaxation best described by the contribution of Raman and Direct mechanisms. The difference of magnetic behaviour between compounds ***R*-57-Dy-a** and ***R*-59-Dy-b** may be associated with the higher symmetry around the coordination environment found in *structure b* motifs (TDD-8, T_2d), that enhance axiality around the oblate Dy^{3+} ground state conferring SMM character compared to ***R*-57-Dy-a** (MFF-9, C_s).

4.4 References

[1] A. Beghidja, G. Rogez, P. Rabu, R. Welter and M. Drillon, An approach to chiral magnets using α-hydroxycarboxylates, *J. Mater. Chem*., 2006, **16**, 2715-2728.

[2] H.R. Wen, X.R. Xie, S.J. Liu, J. Bao, F.F. Wang, C.M. Liu, J.-S. Liao, Homochiral luminescent lanthanide dinuclear complexes derived from a chiral carboxylate, *RSC Adv.*, 2015, **5**, 98097.

[3] M.A. Subhan, T. Suzuki, A. Fuyuhiro, S. Kaizaki, Synthesis, X-ray structures and NIR chiroptical properties of a series of dinuclear lanthanide(III) complexes $[Ln_2\{\mu-(-S \text{ or } RS\text{-pba})\}_4(HBpz_3)_2]$; novel configurational chirality due to non-bonding Ln---O interactions, *Dalton Trans*., 2003, **19**, 3785-3791.

[4] E.J. Gao, Q. Yao, M.C. Zhu, D. Zhang, M.Y. Li, H. Fu, M.P. Jiang, H.L. Yan, X.Y. Xun, L. Zhan, H. Wang, Synthesis, crystal structure, solid-state fluorescence and interaction with DNA of mononuclear La(III) complex: $La(Phen)_2L_2(NO_3)$, *J. Coord. Chem*., 2014, **67**, 2086-2095.

[5] W.J. Evans, D.G. Giarikos, J.W. Ziller, Lanthanide Carboxylate Precursors for Diene Polymerization Catalysis: Syntheses, Structures and Reactivity with Et_2AlCl, *Organometallics*, 2001, **20**, 5751-5758.

[6] a) M. Llunell, D. Casanova, J. Cirera, P. Alemany, S. Alvarez, Shape Program. version 2. Universitat de Barcelona: Barcelona, Spain 2010. b) P. Alemany, D. Casanova, S. Alvarez, C. Dryzun, D. Avnir, *Reviews in Computational Chemistry*, 2017, **30**, 289-352.

[7] a) D. A. Atwood, Editor. *The Rare Earth Elements, Fundamentals and Applications*. John Wiley& Sons Ltd. 2012 b) *Luminescence of Lanthanide Ions in Coordination Compounds and Nanomaterials*, ed. A. de Bettencourt-Dias, John Wiley & Sons Ltd, 2014.

[8] K. Binnemans, *Coord. Chem. Rev.*, 2015, **295**, 1-45

[9] A. Aebischer, F. Gumy and J.-C. G. Bünzli., Intrinsic quantum yields and radiative lifetimes of lanthanide tris(dipicolinates), *Phys. Chem. Chem. Phys*., 2009, **11**, 1346-1353.

[10] a) B Casanovas, F. Zinna, L. Di Bari, M. S, El Fallah, M. Font-Bardía and R. Vicente, Circularly polarized luminescence on dinuclear Tb (III) and Eu (III) complexes with (S-) and (R-) 2-phenylpropionate *Dalton Trans*., 2017, **46**, 6349-6357 b) B. Casanovas, S. Speed, M. S. El Fallah, R. Vicente, M. Font-Bardía, F. Zinna and L. Di Bari, Chiral dinuclear Ln (III) complexes derived from S-and R-2-(6-methoxy-2-naphthyl) propionate. Optical and magnetic properties *Dalton Trans*., 2019, **48**, 2059-2067.

[11] C. A. Mattei, K. Dhbaibi, B. Lefeuvre, V. Dorcet, G. Argouarch, O. Cador, B. Le Guennic, O. Maury, C. Lalli, S. Guy, A. Bensalah-Ledoux, F. Riobé, B. Baguenard, F. Pointillart, Circularly polarized luminescence of Eu (III) complexes with chiral 1, 1′-bi-2-naphtol-derived bisphosphate ligands, *Chirality*, 2022, **34**, 34-47.

[12] a) H.-Y. Wong, W.-S. Lo, K.-H, Yim and G.-L. Law, Chirality and chiroptics of lanthanide molecular and supramolecular assemblies, *Chem.*, 2019, **5**, 3058-3095. b) X.-Z. Li, C.-B. Tian and Q.-F. Sun, Coordination-directed self-assembly of functional polynuclear lanthanide supramolecular architectures *Chem. Rev.* 2022, **122**, 6374-6458 c) Y. Kitagawa, M. Tsurui and Y. Hasegawa, Steric and electronic control of chiral Eu (III) complexes for effective circularly polarized luminescence *ACS Omega*, 2020, **5**, 3786-3791.

[13] Y. Hasegawa, Y. Miura, Y. Kitagawa, S. Wada, T. Nakanishi, K. Fushimi, T. Seki, H. Ito, T. Iwasa, T. Taketsugu, M. Gon, K. Tanaka, Y. Chujo, S. Hattori, M. Karasawa and K. Ishii, Spiral Eu (III) coordination polymers with circularly polarized luminescence *Chem. Commun*., 2018, **54**, 10695-10697.

[14] J. Legendziewicz, V. Tsaryuk, V. Zolin, E. Lebedeva, M. Borzechowska and M. Karbowiak, Optical spectroscopy and magnetic studies of dimeric europium capronate with 1, 10-phenanthroline, *New J. Chem.*, 2001, **25**, 1037-1042.

[15] A. Arauzo, A. Lazarescu, S. Shova, E. Bartolomé, R. Cases, J. Luzón, J. Bartolomé and C. Turta, Structural and magnetic properties of some lanthanide (Ln = Eu(iii), Gd(iii) and Nd(iii)) cyanoacetate polymers: field-induced slow magnetic relaxation in the Gd and Nd substitutions *Dalton Trans.,* 2014, **43**, 12342-12356.

[16] M. Andruh, E. Bakalbassis, O. Kahn, J. C. Trombe and P. Porcher, Structure, spectroscopic and magnetic properties of rare earth metal (III) derivatives with the 2-formyl-4-methyl-6-(N-(2-pyridylethyl) formimidoyl) phenol ligand *Inorg. Chem.* 1993, **32**, 1616-1622.

[17] O. Kahn, *Molecular Magnetism*, VHC Publishers, Inc., USA, 1993.

[18] H.-R. Tu, W.-B. Sun, H.-F. Li, P. Chen, Y.-M. Tian, W.-Y. Zhang, Y.-Q. Zhang and P.-F. Yan, Complementation and joint contribution of appropriate intramolecular coupling and local ion symmetry to improve magnetic relaxation in a series of dinuclear Dy_2 single-molecule magnets *Inorg. Chem. Front.*, 2017, **4**, 499-508.

[19] Daniel N. Woodruff, Richard E. P. Winpenny, and Richard A. Layfield, Lanthanide Single-Molecule Magnets *Chem. Rev*. 2013, **113**, 5110–5148

[20] A. Zabala-Lekuona, J. Cepeda, I. Oyarzabal, A. Rodríguez-Diéguez, J. A. García, J. M. Seco and E. Colacio, Rational design of triple-bridged dinuclear Zn II Ln III-based complexes: a structural, magnetic and luminescence study, *Cryst Eng Comm*., 2017, **19**, 256-264.

[21] P. Antal, B. Drahoš, R. Herchel and Z. Trávníček, Muffin-like lanthanide complexes with an N 5 O 2-donor macrocyclic ligand showing field-induced single-molecule magnet behaviour, *Dalton Trans*., 2016, **45**, 15114-15121.

[22] a) L. Gu and R. Wu, Origin of the anomalously low Raman exponents in single molecule magnets, *Phys. Rev. B,* 2021, **103**, 014401 b) G. Handzlik, M Magott, M. Arczyński, A. M. Sheveleva, F. Tuna, S. Baranc and D. Pinkowicza, Identical anomalous Raman relaxation exponent in a family of single ion magnets: towards reliable Raman relaxation determination? *Dalton Trans.*, 2020, **49**, 11942-11949.

[23] K.N. Shrivastava, Theory of spin–lattice relaxation *Phys. Stat. sol. (b),* 1983, **117**, 437-458.

[24] M. Briganti, F. Santanni, L. Tesi, F. Totti, R. Sessoli and A. Lunghi, *J. Am. Chem. Soc.*, A Complete Ab Initio View of Orbach and Raman Spin–

Lattice Relaxation in a Dysprosium Coordination Compound 2021, **143**, 13633-13645.

[25] D. Aravena and E. Ruiz, Spin dynamics in single-molecule magnets and molecular qubits, *Dalton Trans.*, 2020, **49**, 9916-9928.

[26] R. A. Coxall, S. G. Harris, D. K. Henderson, S. Parsons, P. A. Tasker, R. E. P. Winpenny, Inter-ligand reactions: in situ formation of new polydentate ligands, *J. Chem. Soc., Dalton Trans.* **2000**, 2349-2356

[27] J. A. Peters, K. Djanashvili, C. F.G.C. Geraldes, C. Platas-Iglesias, The chemical consequences of the gradual decrease of the ionic radius along the Ln-series, *Coord. Chem. Rev.*, 2020, **406**, 213146.

[28] a) A. M. Kaczmarek, K. V. Hecke and R. V. Deun, Enhanced Luminescence in Ln^{3+}-Doped Y_2WO_6 (Sm, Eu, Dy) 3D Microstructures through Gd^{3+} Codoping *Inorg. Chem.*, 2014, **53,** 9498-9508. b) S. Chemingui, M. Ferhi, K. Horchani-Naifer and M. Férid, Synthesis and luminescence characteristics of Dy^{3+} doped KLa $(PO_3)_4$ *Journal of Luminescence*, 2015, **166,** 82-87.

[29] Martinus H. V. Werts, Ronald T. F. Jukes and Jan W. Verhoeven, The emission spectrum and the radiative lifetime of Eu^{3+} in luminescent lanthanide complexes *Phys. Chem. Chem. Phys.*, 2002, **4**, 1542–1548.

[30] a) B Casanovas, F. Zinna, L. Di Bari, M. S, El Fallah, M. Font-Bardía and R. Vicente, Circularly polarized luminescence on dinuclear Tb (iii) and Eu (iii) complexes with (S-) and (R-) 2-phenylpropionate, *Dalton Trans*., 2017, **46**, 6349.-6357 b) B. Casanovas, S. Speed, M. S. El Fallah, R. Vicente, M. Font-Bardía, F. Zinna and L. Di Bari, Chiral dinuclear Ln (III) complexes derived from S-and R-2-(6-methoxy-2-naphthyl) propionate. Optical and magnetic properties, *Dalton Trans*., 2019, **48**, 2059-2067 c) A. Tubau, F. Zinna, L. Di Bari, M. Font-Bardía and R. Vicente, Luminescence, CPL and magnetic properties of 1D enantiopure Ln^{3+} complexes with (S-) and (R-) α-methoxyphenylacetate ligand, *Dalton Trans.,* 2023, **52**, 1122-1132.

[31] S.Ruggieri, S. Mizzoni, C. Nardon, E. Cavalli, C. Sissa, M. Anselmi, P. Giorgio Cozzi, A. Gualandi, M. Sanadar, A. Melchior, F. Zinna, O. G. Willis, L. Di Bari and F. Piccinelli, Circularly Polarized Luminescence from New Heteroleptic Eu (III) and Tb (III) Complexes, *Inorg. Chem*. 2023, **62**, 8812-8822.

[32] a) J. Tang, I. Hewitt, N.T. Madhu, G. Chastanet, W. Wernsdorfer, C. E. Anson, C. Benelli, R. Sessoli and A. K. Powell, Dysprosium Triangles Showing Single-Molecule Magnet Behavior of Thermally Excited Spin States, *Angew. Chem. Int. Ed*. 2006, **45**, 1729-1733. b) P.-H. Lin, W.-B. Sun, M.-F. Yu, G.-M. Li, P.-F. Yan and M. Murugesu, An unsymmetrical coordination environment leading to relaxation in a Dy_2 single-molecule magnet, *Chem. Commun*., 2011, **47**, 10993-10995.

[33] H.B.G. Casimir, D. Bijl and F.K. Du Pré, Measurememts on paramagnetic relaxation in chromium potassium alum, *Physica.* 1941, **8**, 449-460

[34] F. S. Santana, M. Perfetti, M. Briganti, F. Sacco, G. Poneti, E. Ravera, J. F. Soares and R. Sessoli, A dysprosium single molecule magnet outperforming current pseudocontact shift agents, *Chem. Sci*., 2022, **13**, 5860-5871 b) S. Mondal and A. Lunghi, Unraveling the contributions to spin–lattice relaxation in kramers single-molecule magnets, *J. Am. Chem. Soc*. 2022, **144**, 22965-22975 c) M. Briganti, F. Santanni, L. Tesi, F. Totti, R. Sessoli and A. Lunghi, A Complete Ab Initio View of Orbach and Raman Spin–Lattice Relaxation in a Dysprosium Coordination Compound, *J. Am. Chem. Soc.* 2021, **143**, 13633-13645

[35] J. Long, B. G. Shestakov, D. Liu, L. F. Chibotaru, Y. Guari, A. V. Cherkasov, G. K. Fukin, A. A. Trifonov and J. Larionova, An organolanthanide (III) single-molecule magnet with an axial crystal-field: influence of the Raman process over the slow relaxation *Chem. Commun.,* 2017, **53**, 4706-4709.

[36] E. Rousset, M. Piccardo, M.-E. Boulon, R. W. Gable, A. Soncini, L. Sorace and C. Boskovic, Slow magnetic relaxation in lanthanoid crown ether complexes: interplay of Raman and anomalous phonon bottleneck processes, *Chem. Eur. J.* 2018, **24,** 14768-14785

[37] a) F. Guégan, J. Jung, B. L. Guennic, F. Riobé, O. Maury, B. Gillon, J. F. Jacquot, Y. Guyot, C. Morell, D. Luneau, Evidencing under-barrier phenomena in a Yb (III) SMM: a joint luminescence/neutron diffraction/SQUID study, *Inorg. Chem. Front.*, 2019, **6**, 3152-3157 b) K. S. Pedersen, J. Dreiser, H. Weihe, R. Sibille, H. V. Johannesen, M. A. Sørensen, B. E. Nielsen, M. Sigrist, H. Mutka, S. Rols, J. Bendix, S. Piligkos, Design of single-molecule magnets: insufficiency of the anisotropy barrier as the sole criterion, *Inorg. Chem.*, 2015, **54**, 7600-7606 c) D. Q. Wu, D. Shao, X. Q. Wei, F. X. Shen, L. Shi, Y. Q. Zhang, X. Y. Wang, Single-ion magnetism in seven-

coordinate Yb III complexes with distorted D_{5h} coordination geometry *Dalton Trans.*, 2017, **46**, 12884-12892 d) W. Zhao, H. Cui, X.-Y. Chen, G. Yi, L. Chen, A. Yuan, C. L. Luo, An eight-coordinate ytterbium complex with a hexagonal bipyramid geometry exhibiting field-induced single-ion magnet behaviour *Dalton Trans*., 2019, **48**, 5621-5626.

5. Abstract

5. Abstract

The main goal of this *Thesis* work is the obtention of new lanthanide(III) coordination compounds presenting luminescence and magnetic properties, hence presenting multiproperty behavior. Moreover, by inducing chirality to the compounds, a third property is added to two families of lanthanide complexes presented herein. The chiroptical properties are studied by means of Circular Dichroism (CD) and Circular Polarized Luminescence (CPL) measurements. This *Thesis* is organized in four main chapters. First the introduction part, where a fundamental knowledge about lanthanides, luminescence phenomena, chiroptical properties and molecular magnetism is untangled as well as the research objectives are presented. The second, third and fourth chapters consists of the presentation and further discussion of the obtained results.

To obtain compounds **1-H_2O** to ***S*-64-Yb-b**, different molecules are used as ligands to achieve different range of nuclearities. Additionally, some of these ligands will serve as sensitizers due to their potential chromophore properties. The molecules used to prepare the anionic forms of the main ligands along this *Thesis* work are 4,4,4-Trifluoro-1-phenyl-1,3-butanedione (HBtfa), 2-fluorobenzoic acid (2-HFBz), 2,6-difluorobenzoic acid (2,6-HF2Bz) and the enantiopure *R*- and *S*-α-methoxyphenylacetic acids (*R*- and *S*-HMPA) and *R* and *S*-2-phenylbutanoic acids (*R* and *S*-2-HPhBut). All syntheses are conducted in basic medium to deprotonate the ligands and facilitate their coordination to the lanthanide ion. Moreover, the molecules used as auxiliary ligands are 4,4'-dinonyl-2,2'-bipyridine (4,4,'-dinonyl-bipy), 1,10-phenanthroline (phen), 2,2'-bipyridil (bipy), 2,2';6',2''-terpyridine (terpy) and 4,7-Diphenyl-1,10-phenanthroline (bathophen).

In *Chapter 2*, ternary 4,4,4-trifluoro-1-phenyl-1,3-butanedione mononuclear lanthanide compounds are obtained by displacement reactions from the $[Ln(Btfa_3)(H_2O)_2]$ precursor with the respective N,N- and N,N,N-polypyridyl ligands. *Chapter 2.2* presents a cerium(III) family with general formula $[Ln(Btfa_3)(L)]$, where L is phen, bipy, terpy and bathophen. In this family the magnetic properties are studied, with the goal of expanding the knowledge about the slow relaxation of magnetization behavior of Cerium, which is rather scarce in the literature. The

magnetic characterization of the Ce^{3+} compounds was supported by Ab-initio calculations which showed that the Orbach mechanism is not involved in relaxation of the magnetization. Otherwise, the relaxation processes are mainly governed by Raman, Direct and Local-Mode mechanisms. For the second Btfa family, presented in *Chapter 2.3* with the current $[Ln(Btfa_3)(4,4\text{-dinonyl-}2,2'\text{-bipy})]$ general formula, luminescence in the solid state as well as in 1 mM chloroform solutions were studied. Form the spectroscopic analysis, no significant structural change is observed when dissolving the polycrystalline powders into chloroform solutions, accounting to a great stability of the compounds in the solvent medium. Due to the outstanding luminescence properties as well as great thermal stability presented for the Eu (**2-Eu**) and Yb (**6-Yb**) derivatives, these two compounds could be successfully used in the emissive layer of two different Organic Light Emitting Diode (OLED) devices. Moreover, the Dysprosium analogue of this family (**5-Dy**) showed Single Ion Magnet (SIM) behavior and sensitized luminescence, hence multiproperty characteristics.

In *Chapter 3*, four families of lanthanide fluorobenzoates derived from the 2-FBz and 2,6-F2Bz ligands are obtained. For these compounds, the main goal is to increase emission quantum yields of the Eu and Tb derivatives by designing new synthetic routes in order to completely remove the coordinating H_2O molecules from the Ln^{3+} chemical environment. Using the 2-FBz and 2,6-F2Bz ligands, four different families of dinuclear compounds were obtained. Compound **4-Ce** with 2-FBz ligand, is an exception and it crystallized into a 2D layer-like structure. Water molecules could not be totally removed from the Ln^{3+} coordination sphere in structures containing 2-FBz ligand with the general formula $[Ln_2(\mu\text{-2FBz})_4(2FBz)_2(H\text{-2FBz})_2(H_2O)_2]$ (**9-Sm** to **15-Yb**) and $(PPh_4)_2[Ln_2(\mu\text{-2-FBz})_2(2\text{-FBz})_6(H_2O)_2]$ (**16-Ce** to **22-Sm). ** Whereas in compounds derived from 2,6-F2Bz ligand, two different dinuclear anhydrous structures with the general formula $(HPy)_2[Ln_2(\mu\text{-2,6-2FBz})_4(NO_3)_4]$ (**23-Eu** to **27-Yb**) and $(HPy)_2[Ln_2(\mu\text{-2,6-2FBz})_4(2,6\text{-2FBz})_4]$ (**28-Eu** to **32-Gd**) were obtained. The Eu and Tb compounds of these flurorobenzoate families presented good luminescence properties. Moreover, synthesis with Ce, Nd, Dy, Er and Yb where also synthetized to study both properties, luminescence and slow relaxation of the magnetization. The dinuclear Dysprosium compounds derived from 2,6-F2Bz ligand (**25-Dy** and **30-Dy**), showed Single Molecular Magnet (SMM) behavior. However the sensitized luminescence was rather weak for these two SMM compounds.

Finally, in *Chapter 4*, the chirality property is added to the luminescent and magnetic characteristics of the final compounds. This is accomplished by using the *R*- and *S*-HMPA and *R* and *S*-2-HPhBut enantiomerically pure ligands. To improve the luminescence properties, the auxiliary chromophore ligands, phen and bathophen are also used for these chiral families.

In the synthesis of lanthanide coordination compounds derived from the enantiomerically pure *R/S*-HMPA acids and phen chromophore ligand, 1D chiral polymeric chains were obtained with the general formula $[\mathrm{Ln}(\mu\text{-}R/S\text{-MPA})(R/S\text{-MPA})_2(\mathrm{phen})]_n$. Circular Polarized Luminescence and Circular Dichroism spectra are measured for the Eu and Tb analogues in the solid state. Moreover, the Ce, Nd, Dy and Er, 1D chiral chains present slow relaxation of the magnetization added to the sensitized luminescence of the Nd, Dy and Er compounds.

With the enantiomerically pure *R/S*-HPhBut acid and the bathophen chromophore ligand, dincuclear lanthanide coordination compounds with the general formula $[\mathrm{Ln}_2(\mu\text{-}R\text{-2-PhBut})_4(R\text{-2PhBut})_2(\mathrm{Bphen})_2]$ were obtained. The compounds undergo a structural change (from *structure a* to *structure b*) on increasing the atomic number along the lanthanide series (Nd to Yb). The change in the structural motif results from a variance in the coordination number producing a special rearrange between the coordinating ligands, altering the crystal structure form *a* to *b*. For the Eu and Tb enantiomeric pairs, CD and CPL spectra were measured in solid state as well as in 1mM DCM solutions with improved chiroptical properties for the solution samples. The significant difference seen in the CD and CPL spectra from solid to solution samples, account to a structural change when dissolving the compounds into the DCM solutions. Moreover, the Nd, Dy, Yb, Sm compounds were synthetized and all present luminescence (ligand based fluorescence in the case of the Dy compounds) as well as slow relaxation (for Nd, Dy and Yb) and SMM behaviour, for the Dy compound.

6. Conclusions

6. Conclusions

- From the structural characterization as well as from the luminescence and magnetic studies of compounds **1-H$_2$O** to ***S*-64-Yb-b** presented along this work the following final remarks can be concluded:
- -4,4,4-trifluoro-1-phenyl-1,3-butanedionate (Btfa) mononuclear lanthanide compounds (**1-H$_2$O** to **7-Gd**) were obtained by displacement reactions from the [Ln(Btfa)$_3$(H$_2$O)$_2$] precursor with the respective N,N- and N,N,N-polypyridyl ligands.
- -Dinuclear compounds were obtained using 2-Fluorobenzoate (2-FBz) (**9-Sm** to **21-Yb**) and 2,6-Difluorobenzoate (2,6-F2Bz) (**23-Eu** to **32-Gd**) ligands. Compound **8-Ce** crystallized into a 2D layer-like structure. Coordinating H$_2$O molecules could not be totally removed from the Ln^{3+} coordination sphere in structures containing 2-FBz whereas in compounds derived from 2,6-F2Bz, two different dinuclear anhydrous structures with general formula (HPy)$_2$[Ln$_2$(μ-2,6-F2Bz)$_4$(NO$_3$)$_4$] and (HPy)$_2$[Ln$_2$(μ-2,6-F2Bz)$_4$(2,6-F2Bz)$_4$], were obtained.
- -Lanthanide contraction effect is revealed in compounds **16-Ce** to **20-Yb** of the 2-FBz family where the **16-Ce** present a higher coordination number compared to the rest of the lanthanide compounds.
- -For all 2-FBz and 2,6-F2Bz compounds **8-Ce** to **32-Gd**, the Ln-O bond lengths decrease on increasing the atomic number along the lanthanide series as a consequence of the lanthanide contraction effect.
- -In the synthesis of lanthanide coordination compounds derived from the enantiomerically pure *R*- or *S*-α-methoxyphenylacetic acids (*R*- or *S*-HMPA) and the 1,10-phenanthroline (phen) chromophore ligand, 1D chiral polymeric chains were obtained. Lanthanide contraction effect is also observed in Ln-O and Ln-N bond distances of ***R*-** or ***S*- 33-46** which decrease on increasing the atomic number along the 6th period.
- -With the enantiomerically pure *R* or *S*-2-phenylbutanoic acids (*R* or *S*-2-HPhBut). and the Diphenyl-1,10-phenanthroline (bathophen) chromophore ligand, dinuclear lanthanide coordination compounds were obtained. The compounds undergo a structural change (from *structure a* to *structure b*) on

increasing the atomic number along the lanthanide series (Nd to Yb). The change in the structural motif results from a change in the coordination number (from 9 to 8) producing a rearrangement between the coordinating ligands in space, altering the crystal structure form *a* to *b*. This change is newly, a result of the lanthanide contraction effect.

- -From the Ce-Btfa family (**1-H_2O** to **5-bathophen**), magnetic characterization supported by ab-initio calculations showed that the Orbach mechanism is not involved in relaxation of the magnetization of these Ce^{3+} compounds. Otherwise, the relaxation processes are mainly governed by Raman, Direct or Local-Mode mechanisms.
- -A different approach for fitting the magnetic data of the Ce-Btfa family is presented. This method involves first, obtaining the field-dependent parameters form the τ *vs* H curve and then fix these parameters into the temperature-dependent τ *vs* T curve. As for the remaining compounds presented in this *Thesis* (from **1-Sm** to **S-64-Yb-b**) that exhibit slow relaxation of the magnetization, the relaxation mechanisms are derived from the temperature dependent magnetic data, while the field dependent data are only used to determine the optimal field in which the compounds show best χ_{AC} performance.
- -Compounds **1-Sm**, **2-Eu**, **3-Tb**, **4-Dy**, **6-Yb**, **9-Sm**, **10-Eu**, **12-Tb**, **13-Dy**, **17-Eu**, **18-Tb**, **19-Dy**, **23-Eu**, **24-Tb**, **25-Dy**, **28-Eu**, **29-Tb**, **30-Dy**, ***R*-37-Eu**, ***R*-39-Tb**, ***R*-42-Sm**, ***R*-41-Dy**, ***R*-35-Nd**, ***S*-50-Sm-a**, ***S*-52-Eu-a**, ***S*-54-Tb-a**, ***S*-56-Tb-b**, ***S*-48-Nda-a** and ***S*-64-Yb-b** showed sensitized luminescence in the solid state.
- For a Er^{3+} coordination compound, showing sensitized luminescence is more unlikely due to the energy gap law and the facility of luminescence quenching due to presence of C-H oscillators. Even so, the Erbium analogues, **5-Er** and **R-42-Er** showed sensitized luminescence.
- -Compounds **26-Nd** and **27-Yb** showed luminescence after excitation at the wavelengths corresponding to intraconfigurational *f-f* absorption transitions.
- -From the absorption and phosphorescence (the latter at 77 K) spectra of the gadolinium analogues **7-Gd**, **11-Gd** and **32-Gd**, the lowest energy singlet and triplet states of each system were measured.
- -Luminescence properties in solution were measured for the Btfa derivatives **1-Sm** to **6-Yb** compounds, for the 2-FBz derivatives **10-Eu** and **12-Tb** compounds

and for the chiral ***S*-50-Nd-a** to ***S*-64-Yb-b** compounds. The **1-Sm**, **2-Eu**, **3-Tb**, **6-Yb** showed sensitized luminescence in 1mM $CHCl_3$ solutions and from the spectroscopic measurements, no evident structural change is observed on dissolving the samples. On the other hand, compounds **10-Eu** and **12-Tb** and the chiral ***S*-50-Sm-a** to ***S*-64-Yb-b** (except for the chiral Dy^{3+} analogues) showed sensitized luminescence in aqueous media and in 1mM DCM solutions, respectively. However, for the latter two groups, the dinuclear structures collapse in solution, suggesting a fluxional equilibrium between different structural arrangements in these media.

- Totally removing the H_2O coordination molecules in the 2,6-2FBz derivatives don't improve emission quantum yields compared to compounds **10-Eu** and **12-Tb** (with 2-FBz ligand) due to poorer sensitization effect and higher symmetry provided by the symmetric 2,6-F2Bz compared to the 2-FBz.
- -Emission quantum yields were measured for all Tb^{3+} and Eu^{3+} compounds. The highest quantum yields were 0.76 for **12-Tb** and 0.71 for ***S*-51-Eu-a**.
- -Luminescence lifetimes were measured for all Eu and Tb compounds, except for **3-Tb** due to low emission intensity. All the measured curves followed a monoexponential law with a single τ_{obs}.
- -Compounds **2-Eu** and **6-Yb** could be successfully used in the emissive layer of two different organic light-emitting diodes (OLED) devices. Both devices showed electroluminescence, in the red range for **2-Eu** and in the nIR range for the **6-Yb** derived devices, after application of a voltage.
- -Solid state Circular Dichroism (CD) spectra of compounds ***R*-37-Eu**, ***S*-38-Eu**, ***R*-39-Tb**, ***S*-40-Tb**, ***R*-41-Dy**, ***S*-42-Dy**, ***R*-43-Sm** and ***S*-44-Sm** are weak indicating that ligand arrangement provided by *R/S*-MPA and phen ligands confers low dissymmetry around the metal ion.
- The enantiomeric pair of compounds ***R*-37-Eu** and ***S*-38-Eu** showed good Circular Polarized Luminescence (CPL) properties in the solid state.
- -Meaningful solid state CD spectra of the [Ln_2(μ-*R/S*-2-PhBut)$_4$(*R/S*-2-PhBut)$_2$(Bphen)$_2$] family could only be obtained for ***R*-55-Tb-b** and ***S*-56-Tb-b** enantiomeric pair due to the weak signal. However, for the 1mM DCM solutions of ***R*-51-Eu-a**, ***S*-52-Eu-a**, ***R*-53-Tb-a**, ***S*-54-Tb-a**, ***R*-55-Tb-b**, ***S*-56-Tb-b**, ***R*-57-Dy-a**, ***S*-58-Dy-b**, ***R*-59-Dy-b** and ***S*-60-Dy-b** mirror images in the Bphen

absorption range are observed indicating that the specie formed in solution shows higher dissymmetry compared to the structure in solid state.

- -Solid state CPL measurements of ***R*-51-Eu-a**/***S*-52-Eu-a** and ***R*-55-Tb-b**/***S*-56-Tb-b** enantiomeric pairs turned out to be weak, however for the 1mM DCM solutions well resolved mirror image with quantifiable g_{lum} values were obtained. This again demonstrates that the species formed in solution exhibit higher dissymmetry compared to the structures in the solid state.
- -Compound **4-Dy** is a SIM operating above 15 K. Moreover, the 2,6-F2Bz derivatives **25-Dy** and **30-Dy** are SMMs in the 1.9-3.7 K and in the 1.9-3.5 K temperature ranges, respectively. For the three compounds, relaxation of the magnetization is governed by the Orbach, Raman and QTM mechanisms under a $H_{dc} = 0$ T. However, magneto-luminescence correlation of **4-Dy** indicates that the relaxation might be taking place through the first excited mj state, therefore through thermal assisted-QTM. Whereas the chiral ***R*-59-Dy-b** compound is a SMM showing χ_{AC} signal in the 1.8 to 6.5 K temperature range, the spin relaxation is mainly governed by Raman and QTM under a $H_{dc} = 0$ T. In all dysprosium(III) compounds, the QTM is removed upon the application of an external magnetic field.
- -Compounds **3-Tb**, **5-Er**, **6-Yb**, **8-Ce**, **13-Dy**, **15-Yb**, **14-Er**, **16-Ce**, **21-Yb**, **26-Nd**, **27-Yb**, **S-34a-Ce**, **S-36-Nd**, **S-42-Dy**, ***S*-46-Er**, ***R*-57-Dy-a**, ***R*-47-Nd-a** and ***R*-63-Yb-b** showed slow relaxation of the magnetization only when an external direct current magnetic field was applied.
- -Relaxation of the magnetization of the terbium compound **3-Tb**, of the cerium compounds **8-Ce, 16-Ce** and ***S*-34a-Ce** as well as the dysprosium **13-Dy** and ***S*-42-Dy** compounds was best described by Raman and Direct relaxation mechanisms.
- All the neodymium **26-Nd, S-36-Nd** and ***R*-47-Nd-a** compounds as well as all the ytterbium compounds **15-Yb, 21-Yb, 27-Yb** and ***R*-63-Yb-b** presented in this *Thesis* work exhibit relaxation of the magnetization under a H_{dc} and the spin dynamics under the applied dc magnetic field are best described with Raman and Direct mechanisms. Presence of underbarrier mechanisms may be explained because of a lack of axial symmetry around the oblate Nd^{3+} and prolate Yb^{3+} cations.

- -The Erbium compounds **5-Er**, **14-Er** and **S-46-Er** presented slow relaxation of the magnetization under a H_{dc} and the relaxation mechanisms describing the spin dynamics were Orbach and Raman for **5-Er** and **_S_-46-Er** and Orbach and Direct for **14-Er**, with relatively low effective energy barriers pointing out a lack of axial symmetry around the prolate ions.
- -Slow relaxation of the magnetization was measured for the isotropic **7-Gd**.
- -Compound **4-Dy** presents multiproperty characteristics: it shows sensitized luminescence and it is a Single Ion Magnet above 15 K. The magneto-optical correlation has been performed for **4-Dy**. Moreover, the dinuclear compounds **25-Dy** and **30-Dy** and the chiral **_R_-59-Dy-b** are SMM operating at lower temperatures compared to **4-Dy**, however their luminescence is mainly dominated by ligand emission due to weak sensitization effect.

7. Appendices

7. Appendices

APPENDIX I

$$\chi_{AC}(\omega) = \chi_S + \frac{\chi_T - \chi_S}{1+(i\omega\tau)^{1-\alpha}}$$ **Equation APX.I.1**

The generalized Debye model described by the Casimir-Du Pré function split into the real and imaginary components χ’ and χ”, Equation APX.I.2 and Equation APX.I.3:

$$\chi'(\omega) = \chi_S + (\chi_T - \chi_S) + \frac{1+(\omega\tau)^{1-\alpha}\sin\left(\frac{\pi}{2}\alpha\right)}{1+2(\omega\tau)^{1-\alpha}\sin\left(\frac{\pi}{2}\alpha\right)+(\omega\tau)^{2-2\alpha}}$$ **Equation APX.I.2**

$$\chi''(\omega) = (\chi_T - \chi_S)\frac{(\omega\tau)^{1-\alpha}\cos\left(\frac{\pi}{2}\alpha\right)}{1+2(\omega\tau)^{1-\alpha}\sin\left(\frac{\pi}{2}\alpha\right)+(\omega\tau)^{2-2\alpha}}$$ **Equation APX.I.3**

The two step relaxation model described by the sum of the two modified Debye functions is described by Equation APX.I.4:

$$\chi_{AC}(\omega) = \chi_{S,TOT} + \frac{\Delta\chi_1}{1+(i\omega\tau_1)^{1-\alpha_1}} + \frac{\Delta\chi_2}{1+(i\omega\tau_2)^{1-\alpha_2}}$$ **Equation APX.I.4**

Furthermore, Equation APX.I.4 splits into the real and imaginary part χ’ and χ” as seen in Equations APX.I.5 and APX.I.6:

$$\chi'(\omega) = \chi_{S,TOT} + \Delta\chi_1\frac{1+(\omega\tau_1)^{1-\alpha_1}\sin\left(\frac{\pi}{2}\alpha_1\right)}{1+2(\omega\tau_1)^{1-\alpha_1}\sin\left(\frac{\pi}{2}\alpha_1\right)+(\omega\tau_1)^{2-2\alpha_1}} +$$

$$\Delta\chi_2\frac{1+(\omega\tau_2)^{1-\alpha_2}\sin\left(\frac{\pi}{2}\alpha_2\right)}{1+2(\omega\tau_2)^{1-\alpha_2}\sin\left(\frac{\pi}{2}\alpha_2\right)+(\omega\tau_2)^{2-2\alpha_2}}$$ **Equation APX.I.5**

$$\chi''(\omega) = \Delta\chi_1\frac{1+(\omega\tau_1)^{1-\alpha_1}\cos\left(\frac{\pi}{2}\alpha_1\right)}{1+2(\omega\tau_1)^{1-\alpha_1}\sin\left(\frac{\pi}{2}\alpha_1\right)+(\omega\tau_1)^{2-2\alpha_1}} +$$

$$\Delta\chi_2\frac{1+(\omega\tau_2)^{1-\alpha_2}\cos\left(\frac{\pi}{2}\alpha_2\right)}{1+2(\omega\tau_2)^{1-\alpha_2}\sin\left(\frac{\pi}{2}\alpha_2\right)+(\omega\tau_2)^{2-2\alpha_2}}$$ **Equation APX.I.6**

APPENDIX II

Elemental analyses of compounds **1-H$_2$O** to ***S*-64-Yb-b** were performed in *Centres Científics i Tecnològics de la Universitat de Barcelona.*

Attenuated Total Reflectance (ATR) Infrared Spectroscopy spectra of all compounds were measured in a FT-IR Specac® instrument equipped with a Golden Gate® plates.

Single crystal X-Ray Diffraction of good quality crystals of compounds **1-H$_2$O**, **2-phen**, **3-bipy-EtOH**, **3-bipy**, **4-terpy**, **5-bathophen**, **2-Eu, 4-Dy**, **6-Yb**, **3-Tb**, **8-Ce**, **10-Eu**, **14-Er**, **15-Yb**, **16-Ce**, **18-Tb**, **21-Yb**, **23-Eu**, **24-Tb**, **29-Tb**, **30-Dy**, ***R*-37-Eu**, ***S*-38-Eu**, ***R*-39-Tb**, ***S*-40-Tb**, ***S*-42-Dy**, ***S*-44-Sm**, ***S*-52-Eu-a** and ***S*-62-Tm-b** were mounted on a D8VENTURE (Bruker) diffractometer with CMOS detector. All the structures were refined by the least-squares method. Intensities were collected with a multilayer monochromated Mo-Kα radiation. Lorentz polarization and absorption corrections were made for all the crystal measurements. The structures were solved by direct methods, using the SHELXS-97 computer program[1] and refined by full-matrix least-squares method, using the SHELXL-2014 computer program.[2] The non-hydrogen atoms were located in successive difference Fourier syntheses and refined with anisotropic thermal parameters on F^2. For hydrogen atoms isotropic temperature factors have been assigned as 1.2 respective of the C atom in which the H is attached. Additional software, Mercury[3] and PLATON[4] were used to obtain the figures of the structures and to obtain the crystallographic tables, respectively.

Powder X-ray diffraction (PDRX) was measured at room temperature for all polycrystalline samples. The data were recorded at the *Serveis Científics i Tecnològics* of the *Universitat de Barcelona* with *PANalytical X'Pert PRO MPD θ/θ* powder diffractometer of 240 millimeters of radius, in a configuration of convergent beam and a focalizing mirror and a transmission geometry. The samples were sandwiched between to films with low absorption Cu Kα radiation (λ=1.5418 Å). The work power is set in 45 kV and 40 mA. The slits of the incident beam define a beam height of 0.4 milli-meters. The detector of the incident and diffracted beam is a 0.02 radians *Soller slits PIXcel* with an active length of 3.347º. The 2*θ*/*θ* scans are from 2 to 70º 2*θ* with a step size of 0.026º 2*θ*. The measuring time is set at 298 seconds per step.

Thermogravimetric analyses (TGA) were measured in the *Serveis Científics i Tecnològics* of the *Universitat de Barcelona.* The TGA measurements were carried out under a N$_2$

atmosphere in a Mettler TG 50 instrument at a heating rate of 10 °C min^{-1}. The TGA measurement were performed in the temperature range between 30 and 600 °C.

Solid and solution state **luminescence spectra** of all compounds were recorded on a Horiba Jobin Yvon SPEX Nanolog fluorescence spectrophotometer (Fluorolog-3 v3.2, HORIBA Jobin Yvon, Cedex, France) equipped with a three slit double grating excitation and emission monochromator with dispersions of 2.1 nm/mm (1200 grooves/mm) at room temperature. The steady-state luminescence was excited by unpolarized light from a 450 W xenon CW lamp and detected at an angle of 22.5° for solid state and at an angle of 90° for solution measurement, by a red-sensitive Hamamatsu R928 photomultiplier tube. The equipment was adjusted to obtain the highest background-to-noise ratio. Spectra were corrected for both the excitation source light intensity variation (lamp and grating) and the emission response (detector and grating).

The **luminescence lifetimes curves** were measured in the same instrument in the phosphorescence mode using a 450 W xenon pulsed lamp (at the corresponding λ_{exc} and 1.5 ns pulse). The measured decays were analyzed using the Origin software package. All the decay curves fitted monoexponentially: $I(t) = I_0 \exp\left(-\frac{t}{\tau_{obs}}\right)$. The fit quality was determined by the χ^2 method of Pearson.

Absolute **Quantum Yield** (ϕ_{Ln}^{L}) measurements were acquired in the G8 Quantum Integrating Sphere from GMP with an interior reflective coating made of Spectralon®. Then the $\phi_{Ln}^{L}$was calculated following:

$$\phi = \frac{E_c - E_c(blank)}{L_a - L_c}$$

L_a is the calculated area of the outgoing amount of light without interaction with a sample (blank) at the used λ_{exc} and L_c is the calculated area after interaction with the sample. E_c refers to the calculated area from the emission spectrum of the sample and E_c(blank) from the emission spectrum of the blank. The lowest possible band pass was employed in both, ϕ_{Ln}^{L} and luminescence lifetime measurements to not surpass the 10^6 CPS to make sure that we are not measuring in the non-linear optic zone, otherwise the results would not be correct.

The assembly of the **OLED devices** and their characterization were realized by Professors Piotr Pander and Fernando B. Dias at the *Physics Department of Durham University, Sound Road, Durham, DH1 3LE, UK*. To assemble the OLED device, pre-cleaned indium-tin-oxide (ITO) coated glass substrates with a sheet resistance of 20 Ω/sq and ITO thickness of 100 nm, were used. The substrates were first washed with distilled water, acetone and then sonicated in acetone and isopropanol, for 15 min each time. Substrates were dried with compressed air and transferred into an oxygen plasma generator for 6 min at full power. Thermally deposited layers were obtained using Kurt J. Lesker Spectros II deposition system at 10^{-6} mbar base pressure. All organic materials and aluminium were deposited at a rate of 1 Å s^{-1}. The LiF layer was deposited at a rate of 0.1–0.2 Å s^{-1}. Characterisation of OLED devices was conducted in a 10 inch integrating sphere (Labsphere) connected to a Source Measure Unit (SMU, Keithley) and coupled with a spectrometer USB4000 or QePro (Ocean Optics). Further details are available in reference.[5] Devices of 4×2 mm pixel size were fabricated.

Electronic Circular Dichroism spectra were recorded with a Jasco J-1500 spectropolarimeter on the polycrystalline samples dispersed in a KBr matrix. In order to check for and minimize contributions from linear dichroism/linear birefringence, for each sample, different spectra were recorded rotating the sample by 180º around the optical axis and then all the spectra were averaged. Solution spectra were recorded in DCM solution (1 mM) in a 1 cm cell.

The **Circularly Polarized Luminescence** experiments of the chiral compounds presented herein were carried out with a home-built CPL spectrofluoropolarimeter[6] that acquires simultaneously the luminescence and CPL data, under UV irradiation (λ_{max} = 254 nm) on quartz plate depositions and on 1 mM DCM solutions. The depositions of the complexes were obtained from n-pentane dispersions. N-pentane was chosen as a dispersant as it does not dissolve the studied compounds and in this way the complexes are deposited as a microcrystalline powder film. Spectra were acquired rotating the sample by ±90º around the optical axis and by flipping the sample by 180º around the axis perpendicular to the collection beam. At least 2 spectra were recorded for each configuration. All the spectra were then averaged to give the final spectra. Acquisition parameters were slit width 0.5 mm, scan speed 0.5 nm/sec, integration time 2 sec, PMT voltage 680/700 V.

Magnetic measurements were performed on solid polycrystalline samples with a Quantum Design MPMS-XL SQUID magnetometer at the Magnetic Measurements Unit from Scientific and Technological Centers (CCiTUB) of the University of Barcelona.

Data were collected for powder microcrystalline samples or for crushed polycrystalline samples of all compounds. The samples were mounted in a gelatin capsule. Direct current (dc) susceptibility measurements were acquired in a 2-300 K temperature range and under an external magnetic field of 0.3 T. Blank measurements were also performed for the capsule and holder and their diamagnetic contributions were corrected. Alternating current (ac) susceptibility measurements were carried out by applying an oscillating ac field of 4 Oe with ac frequencies between 1 and 1500 Hz or between 10 to 1500 Hz at different temperatures and different dc applied fields as indicated along all the magnetic properties discussion of this *Thesis* work.

Ab initio calculations were performed using crystallographic structures and Orca software, version 5.0.3. The def2-TZVP basis set was used. NEVPT2 calculations were not performed to include dynamic correlations as it was previously demonstrated for Ce complexes that it is not essential due to the large ionic character of the Ln-O and Ln-N bonds.[7] The selected active space was (1,7), considering the six doublets. The SINGLE_ANISO module, as implemented in Orca was employed.[8]

To evaluate the vibrational frequencies, the experimental geometries were optimized with Gaussian09,[9] B3LYP functional[10] and using the Stuttgart pseudo/basis set[11] for Ce and a TZV basis set[12] for lighter atoms.

APPENDIX III

Crystallographic data from Chapter 2.2

Table APX.III.1. Crystallographic information from the Single Crystal X-Ray Diffraction measurements of compounds **1-H_2O**, **2-phen** and **3-bipy-EtOH**

Complex	**$[Ce(Btfa)_3(H_2O)_2]$ (1-H_2O)**	**$[Ce(Btfa)_3(H_2O)_2]$ (1-H_2O) r.t.**	**$[Ce(Btfa)_3(phen)]$ (2-phen)**	**$[Ce(Btfa)_3(bipy)(EtOH)]$ (3-bipy-EtOH)**
Formula	$C_{30}H_{22}CeF_9O_8$	$C_{30}H_{22}CeF_9O_8$	$C_{42}H_{26}CeF_9N_2O_6$	$C_{42}H_{31}CeF_9N_2O_7$
FW [g/mol]	821.59	821.59	965.77	986.81
Crystal System	orthorhombic	orthorhombic	monoclinic	triclinic
Space Group	$P2_12_12_1$	$P2_12_12_1$	$P\ 2_1/c$	P-1
a [Å]	10.8091(3)	10.8548(16)	9.6048(7)	10.8841(8)
b [Å]	14.0772(5)	13.219(2)	36.456(3)	12.3497(9)
c [Å]	21.0790(7)	23.317(4)	10.9642(7)	17.1066(12)
α[º]	90	90	90	88.341(3)
β [º]	90	90	93.010(3)	76.600(3)
γ [º]	90	90	90	66.494(3)
V [$Å^3$]	3207.42(18)	3345.8(9)	3833.9(5)	2046.0(3)
Z	4	4	4	2
T[K]	100	294	100	100
λ(Mo kα) [Å]	0.71073	0.71073	0.71073	0.71073
D_{calc} [g cm^{-3}]	1.701	1.631	1.673	1.602
μ(Mo Kα) [mm^{-1}]	1.519	1.457	1.283	1.206
R	0.0307	0.0527	0.0332	0.0491
wR_2	0.0633	0.1523	0.0617	0.1253

Table APX.III.2. Crystallographic information from the Single Crystal X-Ray Diffraction measurements of compounds **3-bipy**, **4-terpy** and **5-bathophen**

Complex	**[Ce(Btfa)$_3$(bipy)] (3-bipy)**	**[Ce(Btfa)$_3$(terpy)] (4-terpy)**	**[Ce(Btfa)$_3$(batophen)(DMSO)] (5-bathophen)**
Formula	$C_{40}H_{26}CeF_9N_2O_6$	$C_{45}H_{29}CeF_9N_3O_6$	$C_{57}H_{41}CeF_9N_3O_7$
FW [g/mol]	941.75	1018.83	1191.05
Crystal System	Monoclinic	Tetragonal	monoclinic
Space Group	$P2_{1/n}$	$P4_3$	$P2_1/c$
a [Å]	11.1505(8)	10.5626(6)	15.4985(6)
b [Å]	22.8068(15)	10.5626(6)	17.0389(7)
c [Å]	15.0009(12)	38.185(2)	20.7744(9)
α[º]	90	90	90
β [º]	99.925(3)	90	107.757(2)
γ [º]	90	90	66.494(3)
V [Å^3]	3757.8(5)	4260.3(5)	90
Z	4	4	4
T[K]	100	100	100
λ(Mo kα) [Å]	0.71073	0.71073	0.71073
D_{calc} [g cm^{-3}]	1.701	1.673	1.602
μ(Mo Kα) [mm^{-1}]	1.519	1.283	1.206
R	0.0307	0.0332	0.0491
wR$_2$	0.0633	0.0617	0.1253

Magnetic data from Chapter 2.2

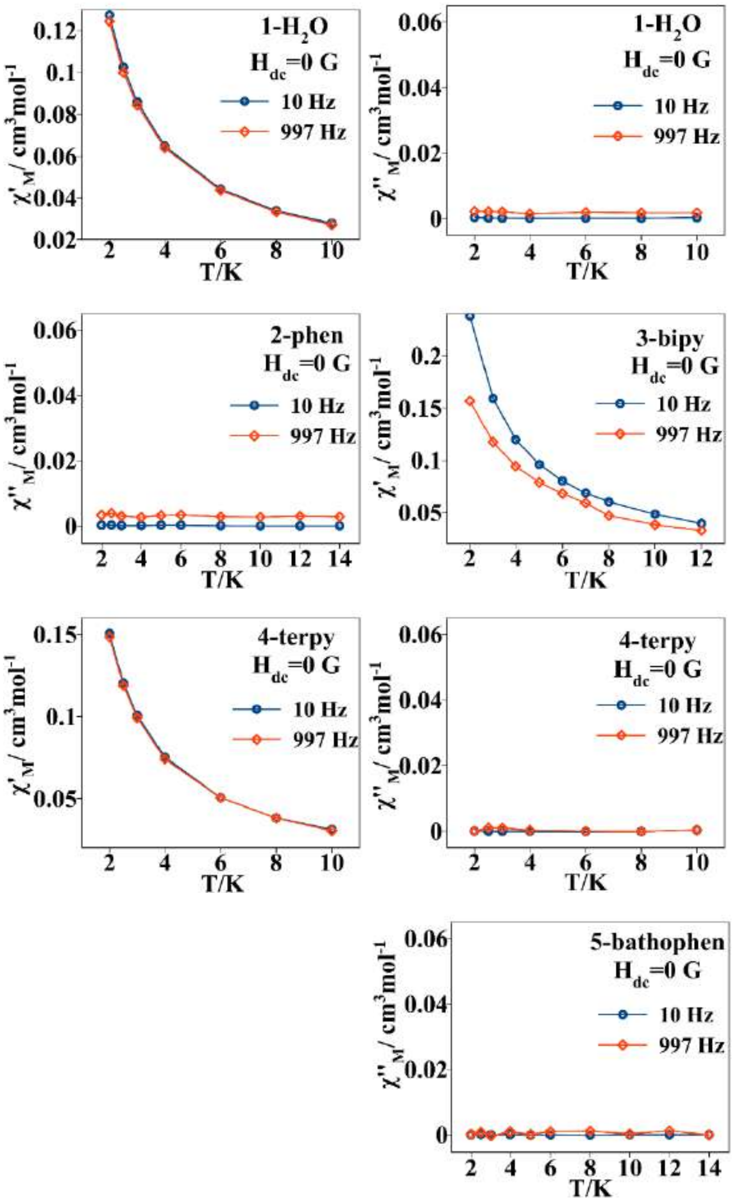

Figure APX.III.1. Dynamic magnetic measurements for compounds **1-H$_2$O** to **5-bathophen** under no external magnetic field (H$_{dc}$=0G). The measurements were performed in an altern current magnetic field of 4 G oscillating between 10 and 997 Hz. The in-phase χ_M’ (left column) and out-of-phase χ_M’’ (right column) magnetic susceptibility components are presented.

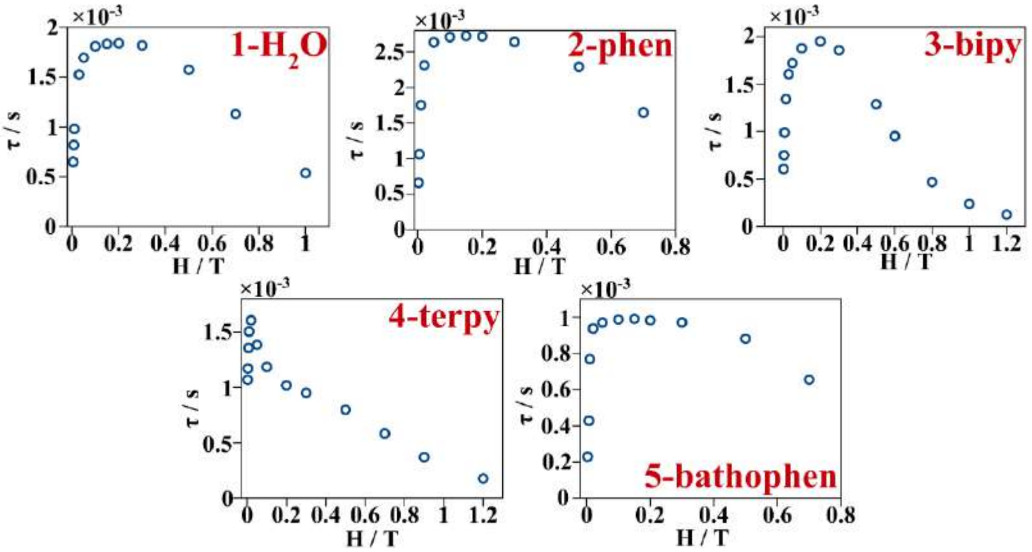

Figure APX.III.2. Relaxation of the magnetization times in front of the H$_{dc}$ measured at a constant temperature of 2.5 K for 1-H$_2$O, 3-bipy and 5-bathophen, of 3.5 K **for 2-phen** and 2 K for **4-terpy** at an oscillating frequency of 1-1488 Hz.

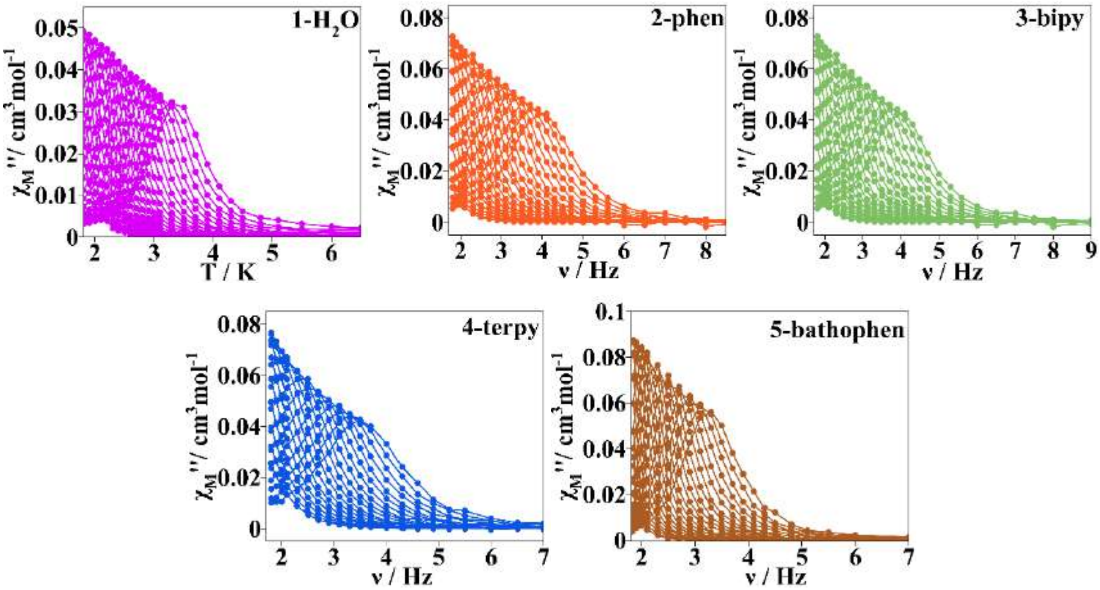

Figure APX.III.3. Magnetic susceptibility out-of-phase component (χ_M'') with temperature plots of compounds **1-H$_2$O** to **5-bathophen**. The altern current measurements are recorded at different temperatures and at the optimal external magnetic field of 0.1 T for **1-H$_2$O to 3-bipy** and of 0.02 T for **4-terpy** and **5-bathophen**.

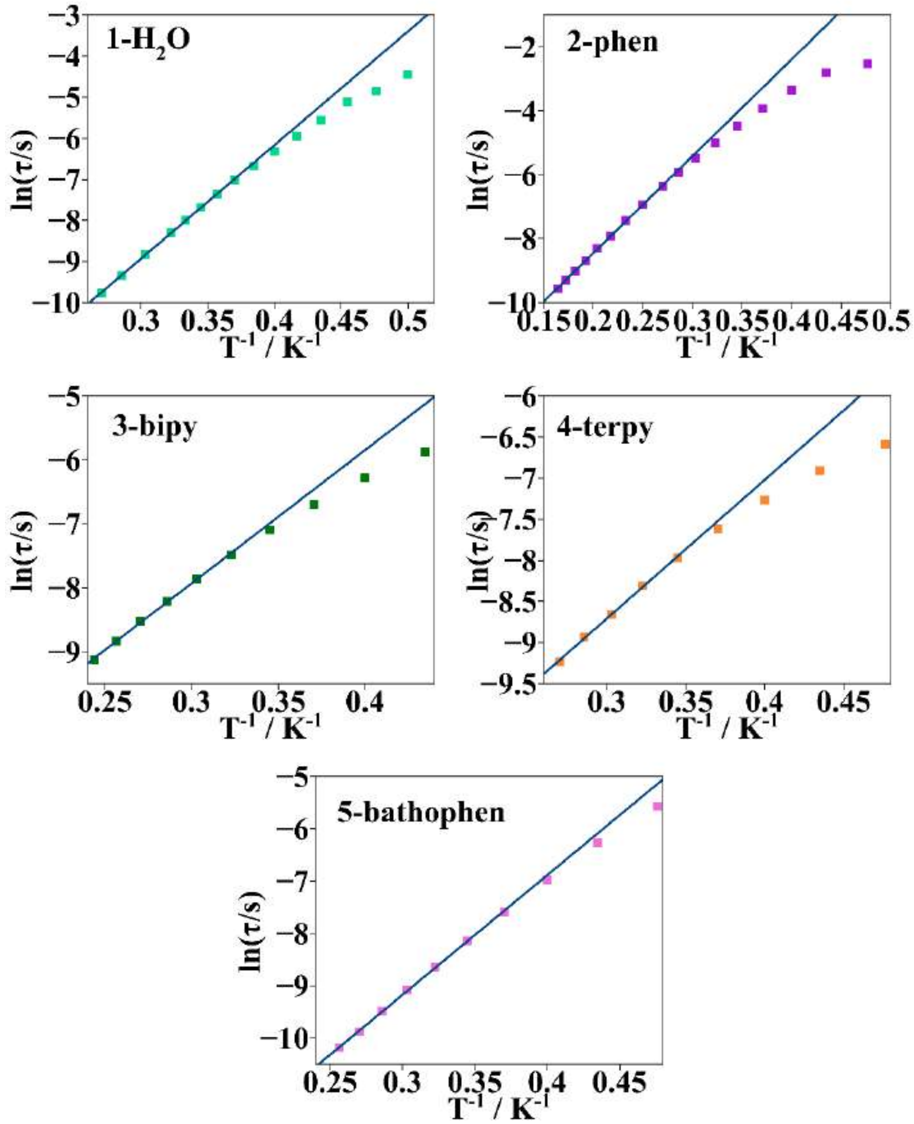

Figure APX.III.4. ln(τ) vs. 1/T plot of compounds **1-H_2O** to **5-bathophen**. Continuous blue line corresponds to the fit using the Arrhenius law that describes the Orbach relaxation of the magnetization process: $\ln(\tau) = \ln(\tau_0)\exp\left(\frac{-\Delta E}{k_B T}\right)$

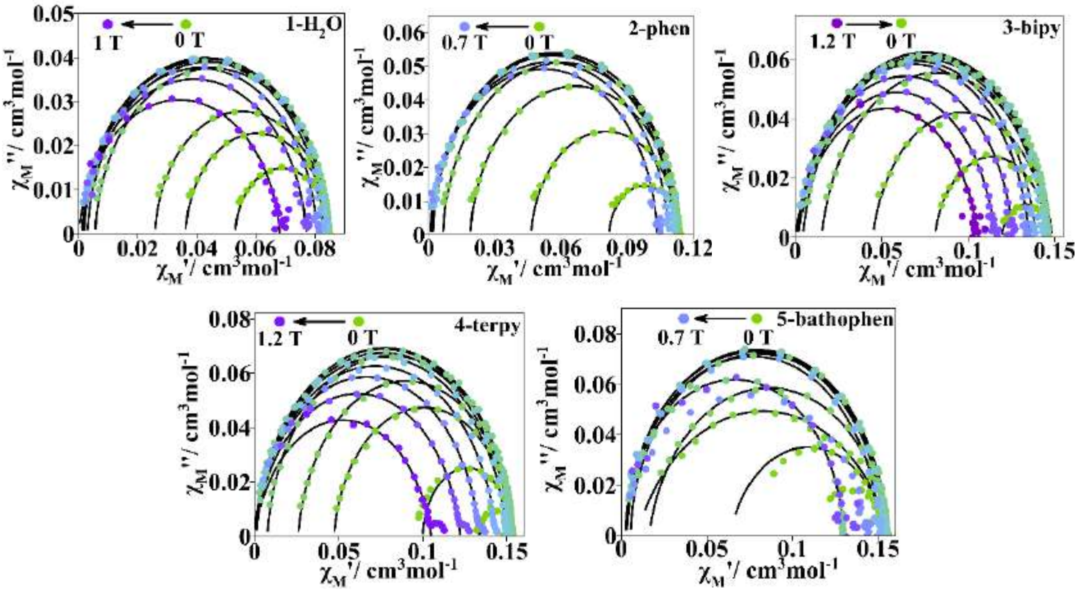

Figure APX.III.5 Cole-Cole plots of compounds **1-H$_2$O** to **5-bathophen** of the alternating current magnetic data measured at different H$_{dc}$ and at a constant temperature of 2.5 K for **1-H$_2$O**, **3-bipy** and **5-bathophen**, of 3.5 K for **2-phen** and 2 K for **4-terpy,** continuous black lines correspond to the fitting with the Generalized Debye model.

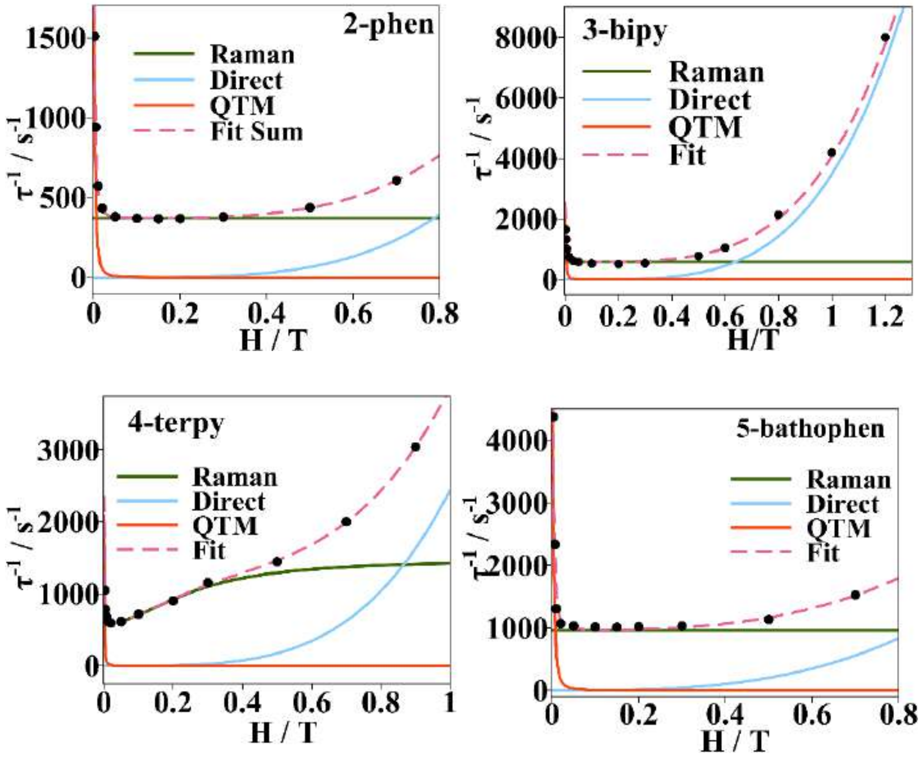

Figure APX.III.6. Contribution of Raman, Direct and QTM mechanism to the τ^{-1} vs. H of compounds **2-phen** to **5-bathophen**. Discontinuous pink line refers to the fit of magnetic data to Eq.2.3.

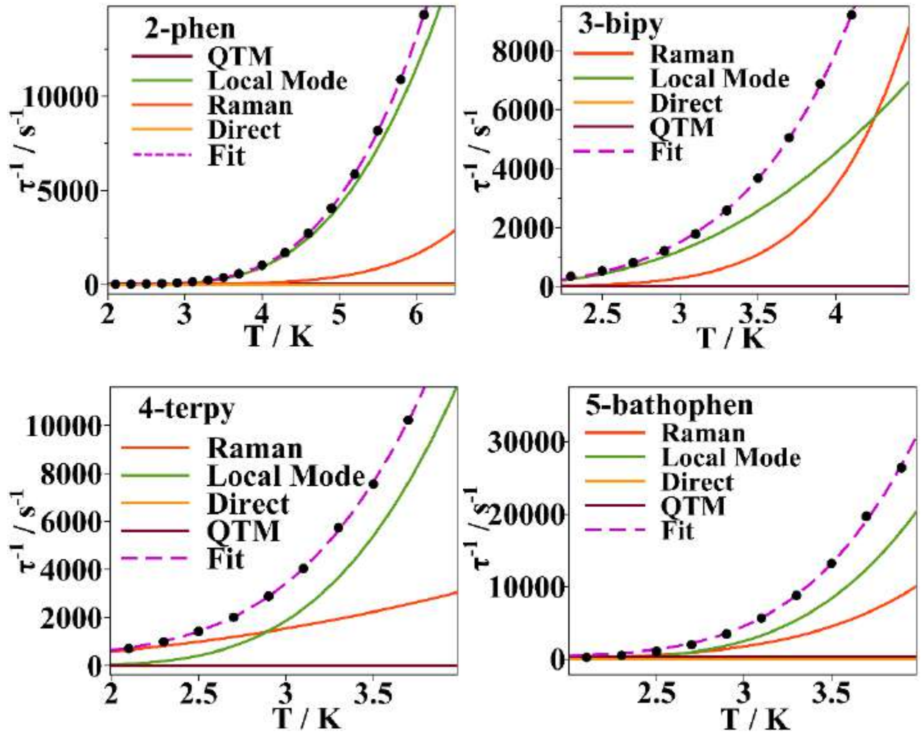

Figure APX.III.7. Contribution of Raman, Local Mode, Direct and QTM mechanism to the τ^{-1} vs. H of compounds **2-phen** to **5-bathophen**. Discontinuous pink line refers to the fit of magnetic data to Eq.2.4.

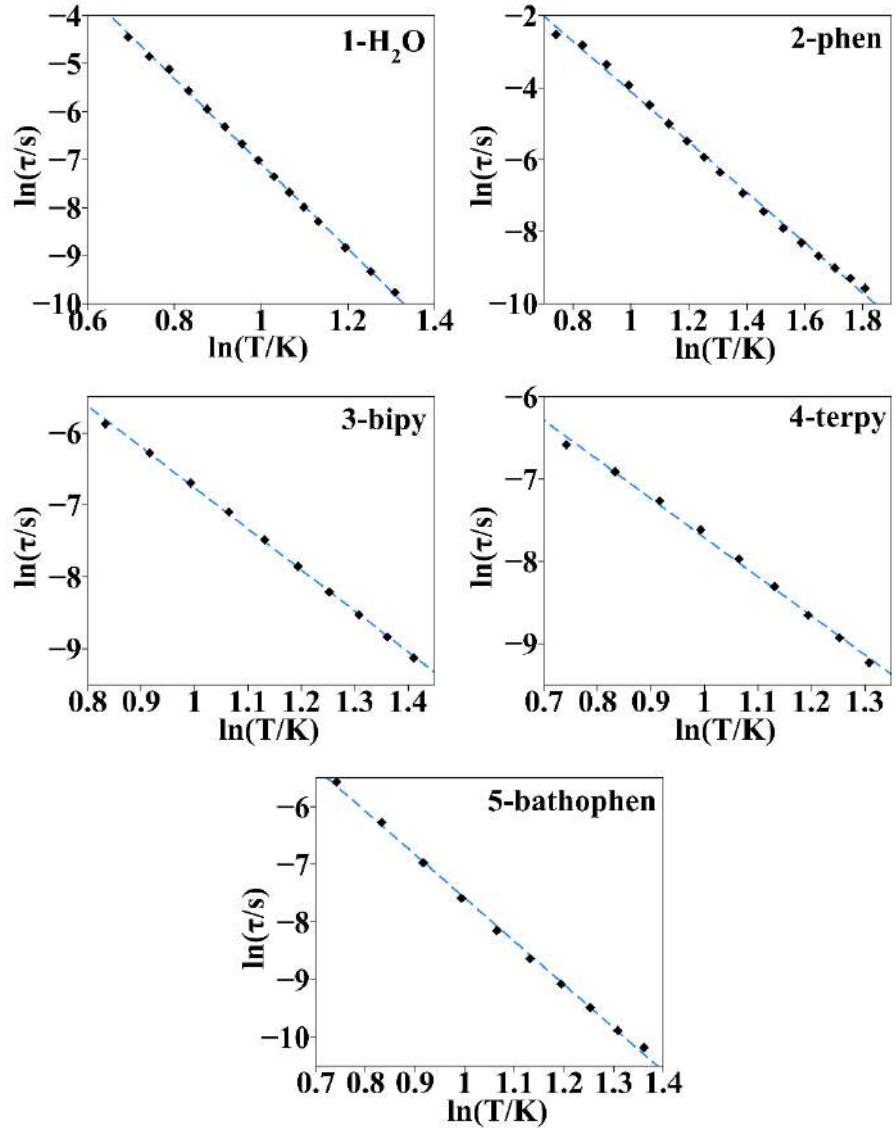

Figure APX.III.8. Ln(τ) vs ln(T) plots of compounds **1-H$_2$O** to **5-bathophen**. Discontinuous blue lines correspond to the fit considering $\ln(\tau) = -n\cdot\ln(T) + \ln(C)$ which describes only the Raman relaxation of the magnetization mechanism.

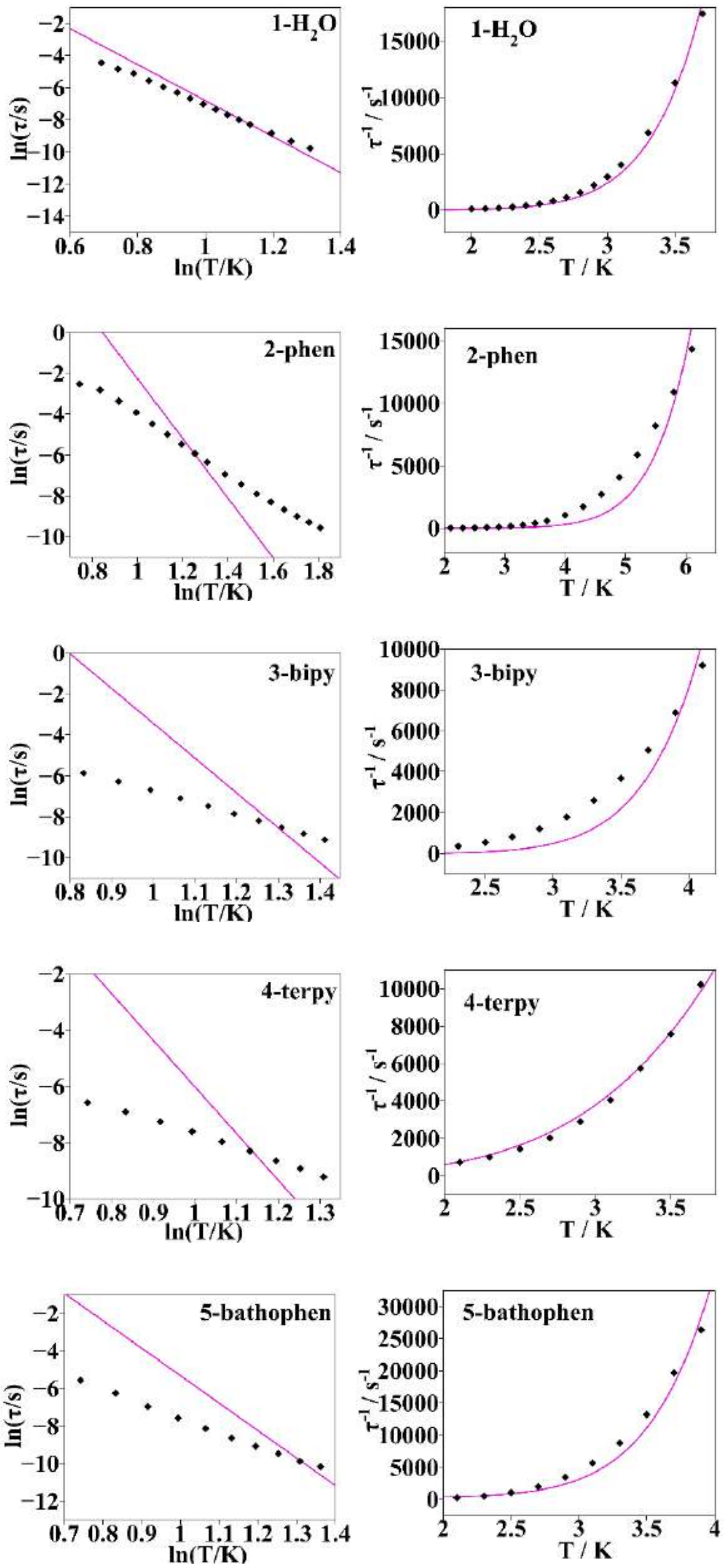

Figure APX.III.9. Ln(τ) vs ln(T) plots of compounds **1-H$_2$O** to **5-bathophen**. Continuous pink line refers to the fit with Eq.2.4 without considering the Local Mode part.

Table APX.III.3. Energy of the lowest 30 vibrational frequencies calculated with DFT for **1**, **2** and **4**.

Frequency	**1**	**2**	**4**
1	6.9	13.0	5.5
2	10.1	15.0	10.7
3	10.2	16.3	12.7
4	12.3	18.1	14.9
5	14.3	21.3	17.5
6	17.9	24.6	19.6
7	18.7	26.8	21.6
8	21.1	34.7	23.7
9	25.3	35.1	25.4
10	26.7	37.7	27.1
11	41.4	38.9	28.6
12	45.6	40.8	34.5
13	46.2	48.1	36.3
14	52.2	51.9	37.6
15	57.3	71.6	38.7
16	64.2	74.9	41.6
17	68.1	84.6	52.7
18	69.0	89.8	56.7
19	75.1	94.4	61.4
20	78.1	99.9	66.7
21	82.2	107.1	67.1
22	85.8	112.6	74.5
23	93.0	122.4	79.4
24	95.5	127.0	79.6
25	106.3	136.6	82.4
26	110.4	139.9	86.4
27	118.7	153.3	88.7
28	126.0	158.9	100.4
29	139.6	164.2	109.1
30	156.9	173.0	118.4

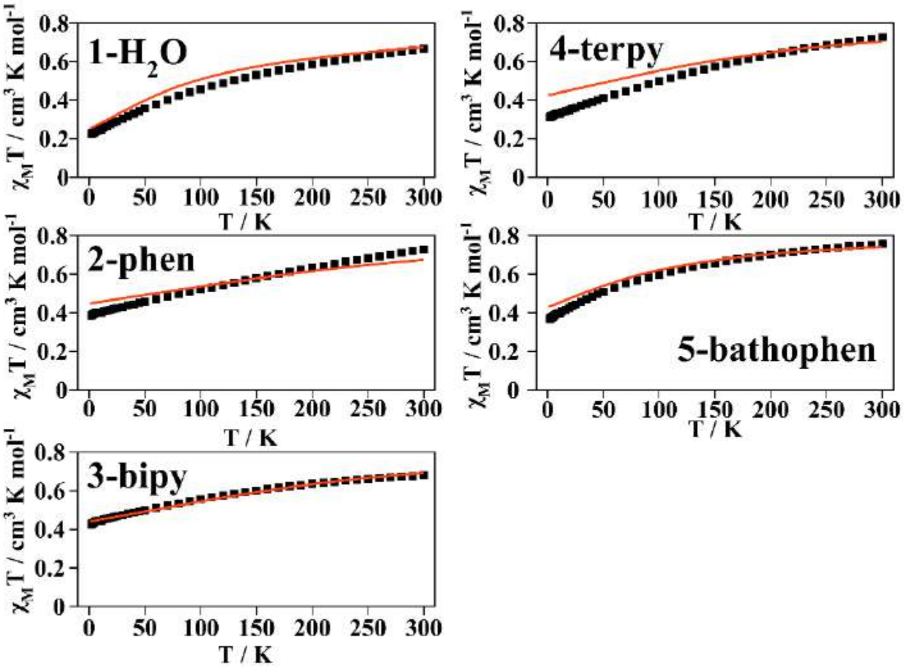

Figure APX.III.10. Experimental (symbols) and calculated (lines) of $\chi_M T$ vs T plots of compounds **1-H$_2$O** to **5-bathophen**.

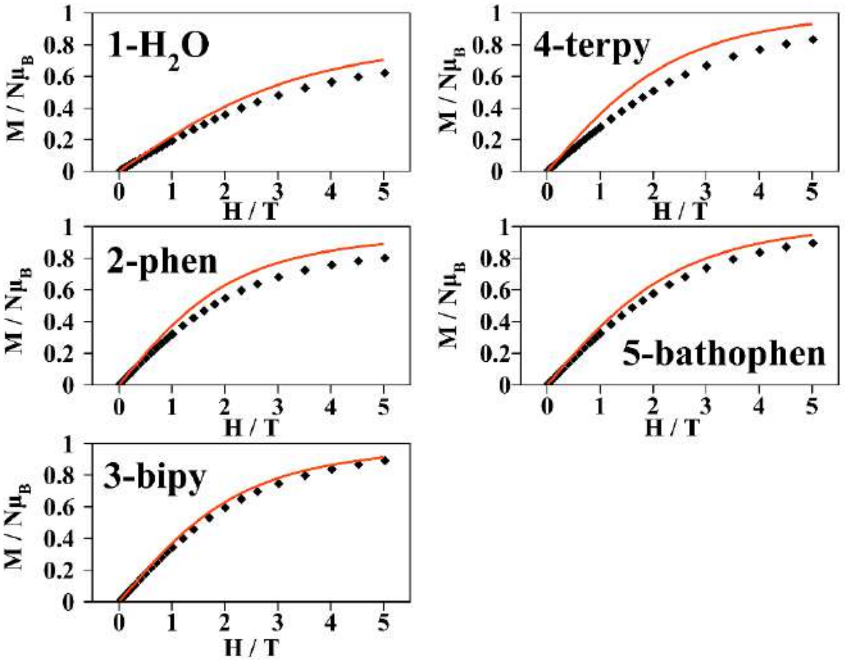

Figure APX.III.11. Experimental (symbols) and calculated (lines) of M vs H of compounds **1-H$_2$O** to **5-bathophen**.

APPENDIX IV

Crystallographic data from Chapter 2.2

Table APX.IV.1. Crystallographic information from the Single Crystal X-Ray Diffraction measurements of compounds **2-Eu**, **4-Dy** and **5-Yb**

Complex	**2-Eu**	**4-Dy**	**6-Yb**	**3-Tb r.t**
Formula	$C_{58}H_{62}EuF_9N_2O_6$	$C_{58}H_{62}DyF_9N_2O_6$	$C_{58}H_{62}F_9N_2O_6Yb$	$C_{58}H_{62}F_9N_2O_6Tb$
FW [g/mol]	1206.05	1216.59	1227.14	1213.01
Crystal System	triclinic	triclinic	triclinic	Triclinic
Space Group	P-1	P-1	P-1	P-1
a [Å]	12.8601(5)	12.8613(12)	12.8760(8)	12.8570(6)
b [Å]	14.0622(7)	14.1376(14)	14.2205(9)	14.9805(7)
c [Å]	16.1521(7)	16.0565(15)	15.9478(10)	16.1248(8)
α[º]	106.558(2)	106.879(4)	107.041(2)	107.762(2)
β [º]	94.495(2)	94.113(4)	93.862(2)	93.451(2)
γ [º]	94.606(2)	94.906(4)	94.880(2)	93.871(2)
V [Å^3]	2775.1(2)	2769.2(5)	2768.7(3)	2940.2(2)
Z	2	2	2	2
T[K]	100	100	100	304(2)
λ(Mo kα) [Å]	0.71073	0.71073	0.71073	0.71073
D_{calc} [g cm^{-3}]	1.443	1.459	1.472	1.370
μ(Mo Kα) [mm^{-1}]	1.211	1.430	1.770	1.279
R	0.0410	0.0421	0.0373	0.0761
wR_2	0.0817	0.1076	0.0863	0.2564

Optical properties from Chapter 2.2

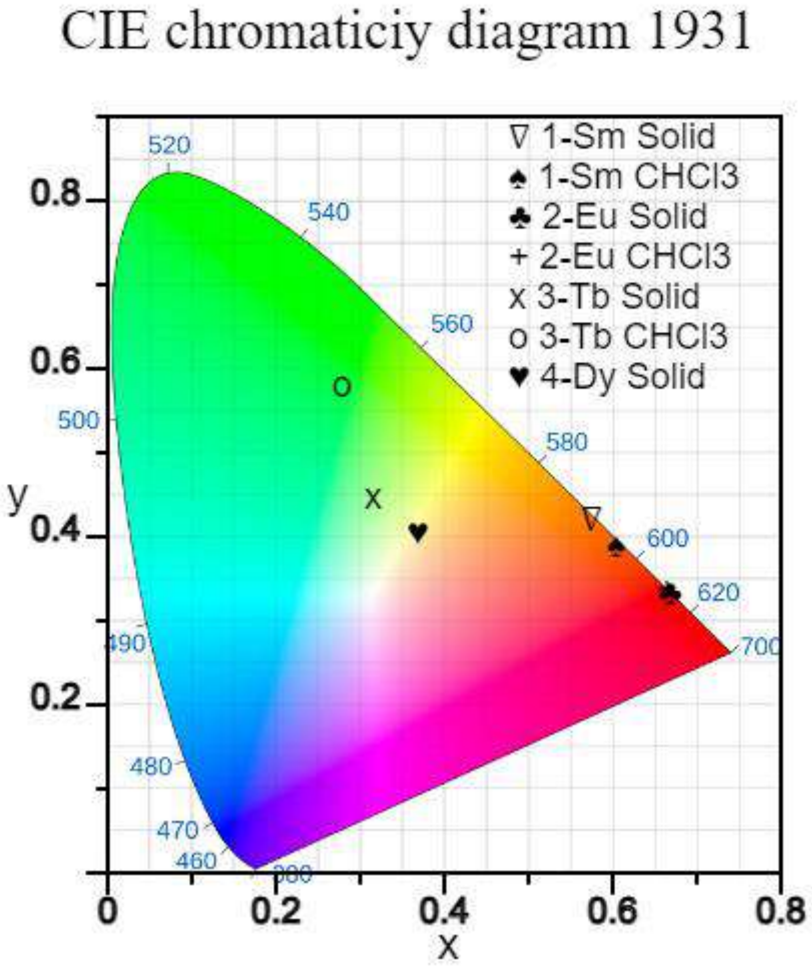

Figure APX.IV.1 CIE chromaticity diagram 1931 color coordinates, calculated for all emission spectra recorded in solid and solution state. CIE chromaticity coordinates for compounds **1-Sm** to **4-Dy** are **1-Sm:** polycrystalline (0.574, 0.420) and solution (0.608, 0.391), **2-Eu:** polycrystalline (0.667, 0.332) and solution (0.664, 0.332), **3-Tb:** polycrystalline (0.317, 0.445) and solution (0.279, 0.578) and **4-Dy:** polycrystalline (0.368, 0.402).

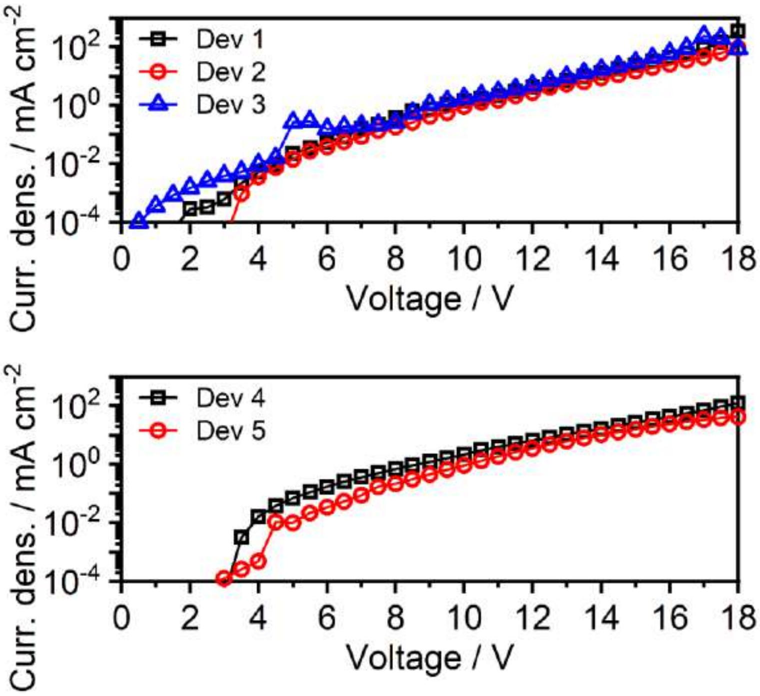

Figure APX.IV.2 Current Density vs. Voltage bias for devices **1-5**. Devices **1**, **2** and **3** are derived from compound **2-Eu** and Devices **4**, **5** derived from compound **6-Yb**.

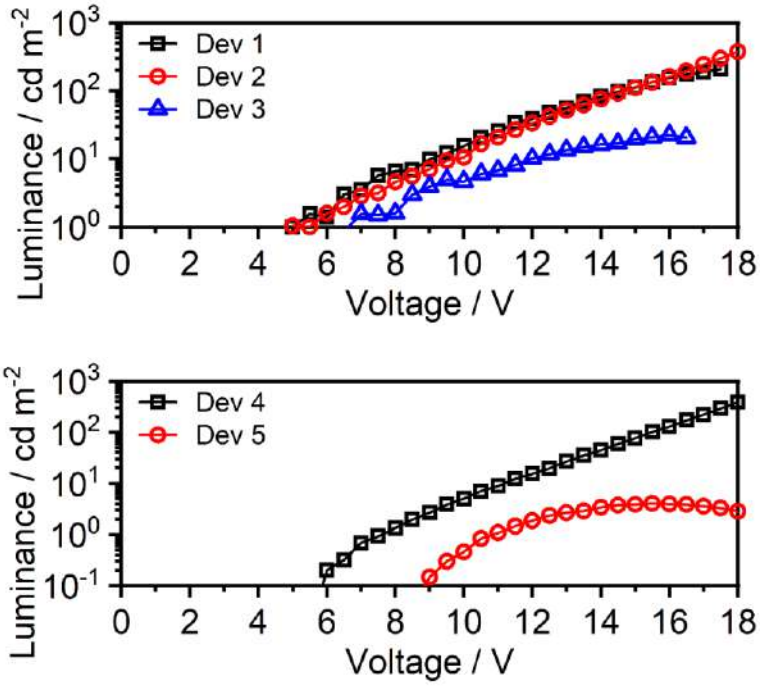

Figure APX.IV.3 Luminance vs. Voltage bias for devices **1-5.** Devices **1**, **2** and **3** are derived from compound **2-Eu** and Devices **4**, **5** derived from compound **6-Yb**.

APPENDIX V

Crystallographic data from Chapter 3.1.1

Table APX.V.1 Crystallographic information from the Single Crystal X-Ray Diffraction measurements of compounds **8-Ce**, **10-Eu**, **14-Er** and **15-Yb**.

Crystal Data	8-Ce	10-Eu	14-Er	15-Yb
Formula	$C_{42}H_{32}Ce_2F_6O_{16}$	$C_{56}H_{38}Eu_2F_8O_{18}$	$C_{56}H_{38}Er_2F_8O_{18}$	$C_{56}H_{38}F_8O_{18}Yb_2$
FW [g/mol]	1186.91	1454.78	1485.75	1496.94
Crystal System	Triclinic	Triclinic	Triclinic	Triclinic
Space Group	P-1	P-1	P-1	P-1
a [Å]	8.9805(5)	9.095(8)	8.9912(17)	8.9457(6)
b [Å]	14.6476(8)	11.378(10)	11.362(2)	11.4051(8)
c [Å]	16.5224(8)	13.659(12)	13.688(3)	13.6544(10)
α[deg]	74.604(2)	110.68(3)	111.062(7)	110.971(2)
β [deg]	89.840(2)	93.12(3)	92.805(7)	92.919(2)
γ [deg]	85.666(2)	92.45(3)	91.732(7)	91.365(2)
V [Å^3]	2089.08(19)	1317.6(2)	1301.6(4)	1297.83(16)
Z	2	1	1	1
T(K)	100	100	100	100
λ(Mo kα) (Å)	0.71073	0.71073	0.71073	0.71073
D_{calc} [g cm^{-3}]	1.887	1.833	1.895	1.915
μ(Mo Kα) [mm^{-1}]	2.253	2.464	3.309	3.688
R	0.0229	0.0199	0.0178	0.0124
wR_2	0.0585	0.0467	0.0429	0.0309

Magnetic Properties from Chapter 3.1.1

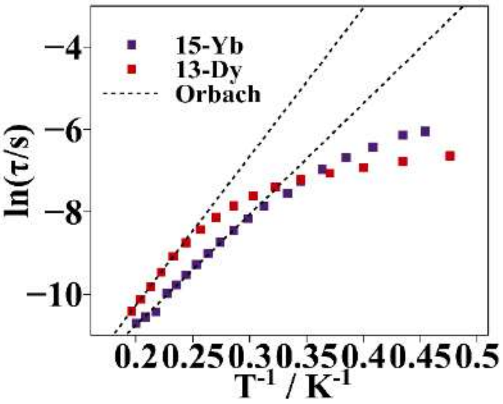

Figure APX.V.1 ln(τ) vs T^{-1} plots of compounds **13-Dy** and **15-Yb.** The curves are fitted considering the Arrhenius law that describes the Orbach mechanism.

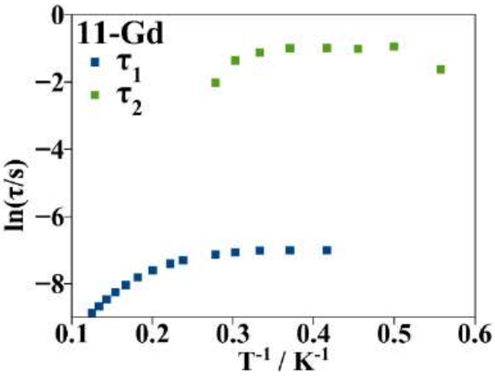

Figure APX.V.2 ln(τ) vs T^{-1} plots of compound **11-Gd**. From the fit of the two component Debye model, two relaxations of the magnetization times were extracted. τ_1 follows a dependency with temperature that could be fitted with Raman and QTM relaxation of the magnetization mechanisms. However, τ_2 refers to the relaxation time obtained form the χ_M'' tails observed at lower temperatures and lower oscillating frequencies. As observed, τ_2 does not exhibit a dependency with temperature that can be fitted with the known equations of the relaxation of magnetization.

APPENDIX VI

Crystallographic data from Chapter 3.1.2

Table APX.VI.1 Crystallographic information from the Single Crystal X-Ray Diffraction measurements of compounds **16-Ce**, **17-Eu** and **21-Yb**.

Crystal Data	16-Ce	18-Tb	21-Yb
Formula	$C_{56}H_{36}Ce_2F_8 O_{18}$,2($C_{24}H_{20}P$),2($H_2O$)	$C_{56}H_{36}F_8O_{18}Tb_2$, 2($C_{24}H_{20}P$)	C_{56} $H_{36.51}$ $F_{8.51}$ O_{18} Yb_2, 2(C_{24} H_{20} P)
FW [g/mol]	2143.86	2145.45	2183.77
Crystal System	monoclinic	monoclinic	monoclinic
Space Group	P21/c	P21/n	P21/n
a [Å]	12.0135(9)	12.3043(11)	12.3281(5)
b [Å]	13.2434(9)	27.324(2)	27.2854(10)
c [Å]	28.780(2)	13.1918(9)	13.1939(5)
α[deg]	90	90	90
β [deg]	99.079(3)	95.038(3)	95.118(1)
γ [deg]	90	90	90
V [Å^3]	4521.5(6)	4418.0(6)	4420.4(3)
Z	2	2	2
T(K)	100	100	100
λ(Mo kα) (Å)	0.71073	0.71073	0.71073
D_{calc} [g cm^{-3}]	1.575	1.613	1.641
μ(Mo Kα) [mm^{-1}]	1.120	1.714	2.230
R	0.0405	0.0351	0.0212
wR_2	0.1075	0.0721	0.0476

Magnetic properties from Chapter 3.1.2

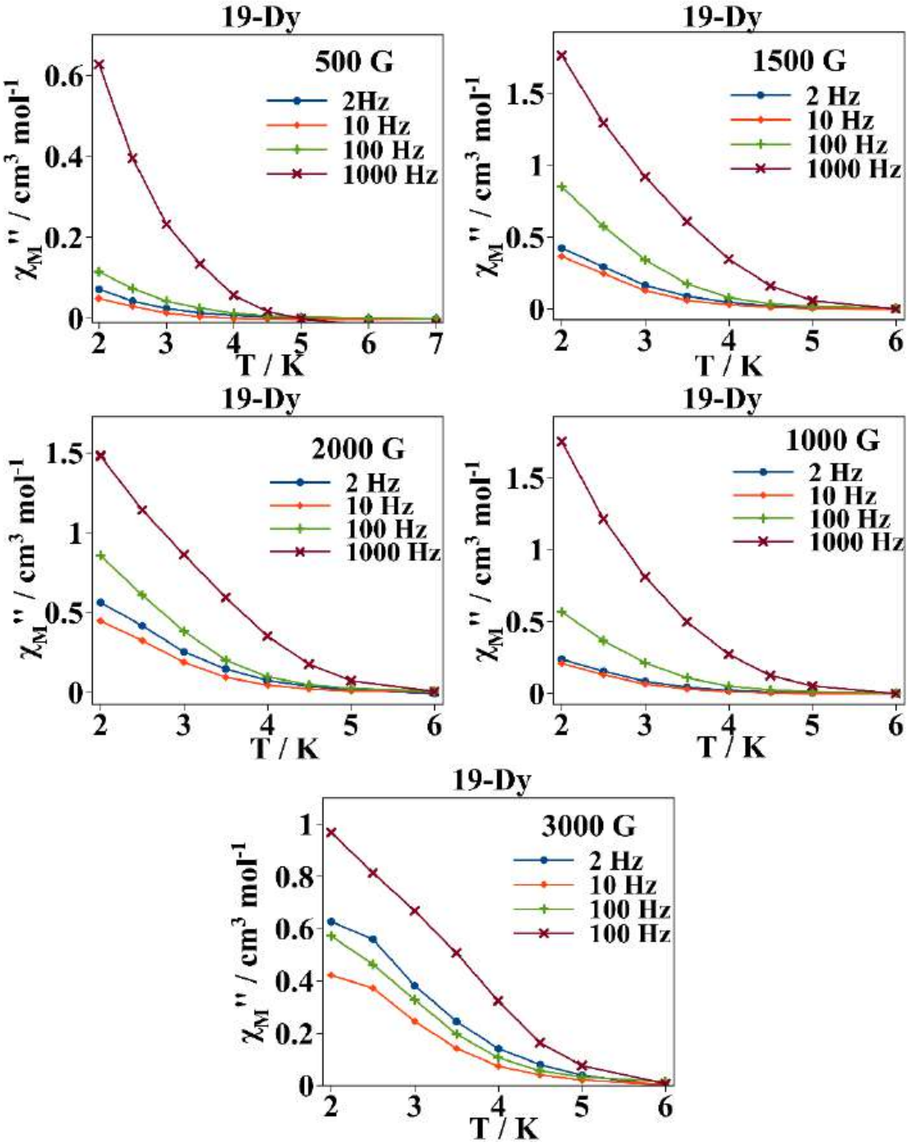

Figure APX.VI.1 Compound **19-Dy** χ_M'' *vs* T plots measured at an external direct current magnetic field of 500 G, 1500 G, 2000 G, 1000 G and 3000 G and an oscillation frequency of 2, 10, 100 and 1000 Hz.

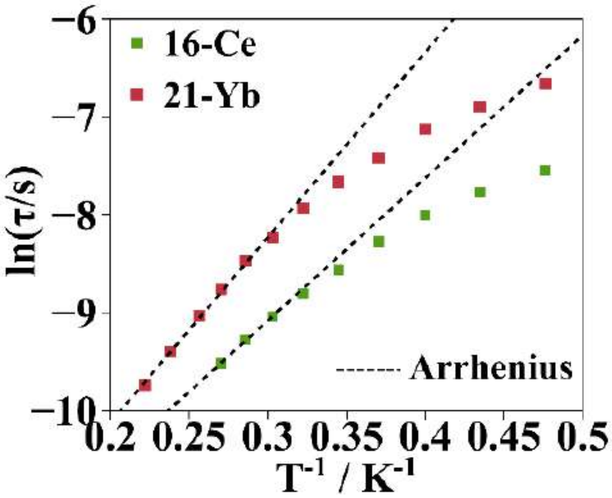

Figure APX.VI.2 ln(τ) vs T^{-1} plots of compounds **16-Ce** and **21-Yb**. The dotted black line corresponds to the fit with the Arrhenius law yielding values of ΔE =10.13 cm^{-1} and τ_0= $1.44\cdot10^{-6}$ for **16-Ce** and ΔE =13.52 cm^{-1} and τ_0= $9.14\cdot10^{-7}$ for **21-Yb**

APPENDIX VII

Crystallographic data from Chapter 3.2.1

Table APX.VII. 1 Crystallographic information from the Single Crystal X-Ray Diffraction measurements of compounds of compounds **23-Eu** and **24-Tb**.

Complex	**23-Eu**	**24-Tb**
Formula	$C_{28}H_{12}Eu_2F_8N_4O_{20}$, $2(C_5H_6N)$	$C_{28}H_{12}Tb_2F_8N_4O_{20}$, $2(C_5H_6N)$
FW [g/mol]	1340.55	1354.49
Crystal System	Monoclinic	Monoclinic
Space Group	P21/n	P21/n
a [Å]	11.0802(7)	11.0785(4)
b [Å]	11.4591(7)	11.4260(5)
c [Å]	16.8755(10)	16.8331(6)
α[º]	90	90
β [º]	93.137(2)	93.126(1)
γ [º]	90	90
V [Å^3]	2139.5(2)	2127.61(14)
Z	2	2
T[K]	100	100
λ(Mo kα) ([Å)	0.71073	0.71073
D$_{calc}$ (g cm^{-3})	2.081	2.114
μ(Mo Kα) (mm^{-1})	3.032	3.425
R	0.0124	0.0149
wR$_2$	0.0297	0.0359

Magnetic properties from Chapter 3.2.1

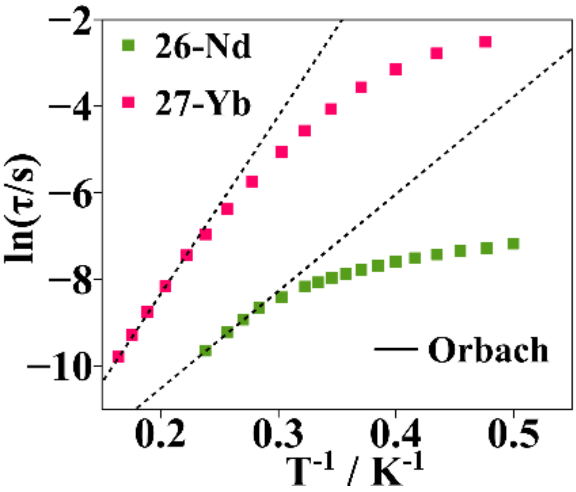

Figure APX.VII.1 ln(τ) vs T^{-1} plots of compounds **26-Nd** and **27-Yb**. The dotted black line corresponds to the fit with the Arrhenius law yielding values of ΔE =15.61 cm^{-1} and τ_0= 0.03·10^{-7} for **26-Nd** and ΔE =27.7 cm^{-1} and τ_0= 8.17·10^{-8} for **27-Yb**

APPENDIX VIII

Crystallographic data from Chapter 3.2.2

Table APX.VIII. 1 Crystallographic information from the Single Crystal X-Ray Diffraction measurements of compounds of compounds **29-Tb** and **30-Dy**.

Complex	**29-Tb**	**30-Dy**
Formula	$C_{56}H_{24}F_{16}O_{16}Tb_2$, 2($C_5H_6N$)	$C_{56}H_{24}Dy_2F_{16}O_{16}$, 2($C_5H_6N$), 2($H_2O$)
FW [g/mol]	1734.83	1778.00
Crystal System	monoclinic	triclinic
Space Group	P21/n	P-1
a [Å]	15.5938(8)	11.0756(7)
b [Å]	19.7954(10)	15.7099(10)
c [Å]	20.2664(11)	18.4939(11)
α[º]	90	93.549(2)
β [º]	92.846(2)	94.867(2)
γ [º]	90	98.898(2)
V [Å^3]	6248.2(6)	3158.5(3)
Z	4	2
T[K]	100	100
λ(Mo kα) (Å)	0.71073	0.71073
D_{calc} (g cm^{-3})	1.844	1.870
μ(Mo Kα) (mm^{-1})	2.366	2.472
R	0.0261	0.0266
wR$_2$	0.0592	0.0753

APPENDIX IX

Table APX.IX.1 Selected bands (cm^{-1}) of **R-** or **S- 33-46** s=strong, m=medium and w=weak, br=broad obtained in ATR-IR spectroscopy

***R*-33-Ce**	3081-2815 (w), 1606 (m), 1553 (s), 1508 (m), 1305 (s), 1325 (w), 1194 (m), 1098 (m), 1063 (m), 985 (m), 837 (m), 711 (s, split), 632(m)
***S*-34-Ce**	3081-2815 (w), 1606 (m), 1553 (s), 1508 (m), 1305 (s), 1325 (w), 1194 (m), 1098 (m), 1063 (m), 985 (m), 838 (m), 711 (s, split), 632(m)
***R*-35-Nd**	3082-2817 (w), 1607 (m), 1554 (s), 1509 (m), 1306 (s), 1326 (w), 1195 (m), 1099 (m), 1066 (m), 987 (m), 839 (m), 709 (s, split), 633(m)
***S*-36-Nd**	3082-2817 (w), 1607 (m), 1554 (s), 1509 (m), 1306 (s), 1326 (w), 1195 (m), 1099 (m), 1066 (m), 987 (m), 839 (m), 709 (s, split), 633(m)
***R*-37-Eu**	3083-2817 (w), 1608 (m), 1552 (s), 1509 (m), 1400 (s), 1326 (w), 1196 (m), 1100 (m), 1065 (m), 987 (m), 839 (m), 713 (s, split), 635(m)
***S*-38-Eu**	3086-2817 (w), 1613 (m), 1557 (s), 1509 (m), 1404 (s), 1317 (w), 1200 (m), 1096 (m), 1065 (m), 983 (m), 839 (m), 713 (s, split), 635 (m)
***R*-39-Tb**	3091-2817 (w), 1613 (m), 1561 (s), 1509 (m), 1404 (s), 1330 (w), 1200 (m), 1096 (m), 1070 (m), 983 (m), 839 (m), 717 (s, split), 635 (m)
***S*-40-Tb**	3091-2817 (w), 1613 (m), 1557 (s), 1509 (m), 1404 (s), 1330 (w), 1200 (m), 114 (m), 1065 (m), 991 (m), 839 (m), 717 (s, split), 635 (m)
***R*-41-Dy**	3087-2817 (w), 1617 (m), 1569 (s), 1513 (m), 1396 (s), 1326 (w), 1204 (m), 1096 (m), 1065 (m), 983 (m), 839 (m), 717 (s, split), 635 (m)
***S*-41-Dy**	3087-2817 (w), 1617 (m), 1569 (s), 1513 (m), 1396 (s), 1326 (w), 1204 (m), 1096 (m), 1065 (m), 983 (m), 839 (m), 717 (s, split), 635 (m)
***R*-43-Sm**	3091-2817 (w), 1609 (m), 1552 (s), 1509 (m), 1396 (s), 1326 (w), 1200 (m), 1100 (m), 165 (m), 983 (m), 843 (m), 713 (s, split), 635 (m)
***S*-44-Sm**	3091-2813 (w), 1609 (m), 1574 (s), 1509 (m), 1396 (s), 1322 (w), 1196 (m), 1104 (m), 1065 (m), 991 (m), 839 (m), 713 (s, split), 635 (m)
***R*-45-Er**	3095-2821 (w), 1611 (m), 1554 (s), 1510 (m), 1408(s), 1340 (w), 1210 (m), 1101 (m), 167 (m), 985 (m), 844 (m), 715 (s, split), 637 (m)
***S*-46-Er**	3095-2821 (w), 1611 (m), 1554 (s), 1510 (m), 1408(s), 1340 (w), 1210 (m), 1101 (m), 167 (m), 985 (m), 844 (m), 715 (s, split), 637 (m)

Crystallographic data from Chapter 4.1

Table APX.IX.2 Crystallographic information from the single crystal X-Ray Diffraction measurements of compounds **R-37-Eu**, ***S*-38-Eu**, ***R*-39-Tb, *S*-40-Tb**, ***S*-42-Dy** and ***S*-44-Sm.**

Crystal Data	**R-37-Eu**	***S*-38-Eu**	***R*-39-Tb**	***S*-40-Tb**	***S*-42-Dy**	***S*-44-Sm**
Formula	$C_{39}H_{35}EuN_2O_9$	$C_{39}H_{35}EuN_2O_9$	$C_{39}H_{35}N_2O_9Tb$	$C_{39}H_{35}N_2O_9Tb$	$C_{39}H_{35}DyN_2O_9$	$C_{39}H_{35}N_2O_9Sm$
FW [g/mol]	827.65	827.65	834.61	834.61	838.19	826.04
Crystal System	monoclinic	monoclinic	monoclinic	monoclinic	monoclinic	Monoclinic
Space Group	P21	P21	P21	P21	P21	P21
a [Å]	6.0481(3)	6.0472(3)	6.0348(3)	6.0361(3)	6.0246(2)	6.0523(2)
b [Å]	23.7053(12)	23.7026(11)	23.6379(12)	23.618(1)	23.5732(10)	23.7820(9)
c [Å]	12.2981(6)	12.3102(6)	12.3125(7)	12.3265(5)	12.3531(5)	12.2968(4)
α[deg]	90	90	90	90	90	90
β [deg]	100.971(2)	100.945(2)	101.130(2)	100.962(2)	101.095(2)	101.027(1)
γ [deg]	90	90	90	90	90	90
V [Å^3]	1730.98(15)	1732.38(15)	1723.34(16)	1725.21(13)	1721.59(12)	1737.27(10)
Z	2	2	2	2	2	2
T(K)	100	100	100	100	100	100
λ(Mo kα) (Å)	0.71073	0.71073	0.71073	0.71073	0.71073	0.71073
D_{calc} [g cm^{-3}]	1.588	1.587	1.608	1.607	1.617	1.579
μ(Mo Kα) [mm^{-1}]	1.872	1.870	2.112	2.110	2.231	1.750
R	0.0394	0.0320	0.0118	0.0259	0.0308	0.0179
wR_2	0.0817	0.0614	0.0281	0.0575	0.0736	0.0405
Flack x	-0.002(7)	0.006(4)	0.002(3)	0.019(9)	0.018(15)	0.008(3)

Circular Polarized Luminescence measurements of Chapter 4.1

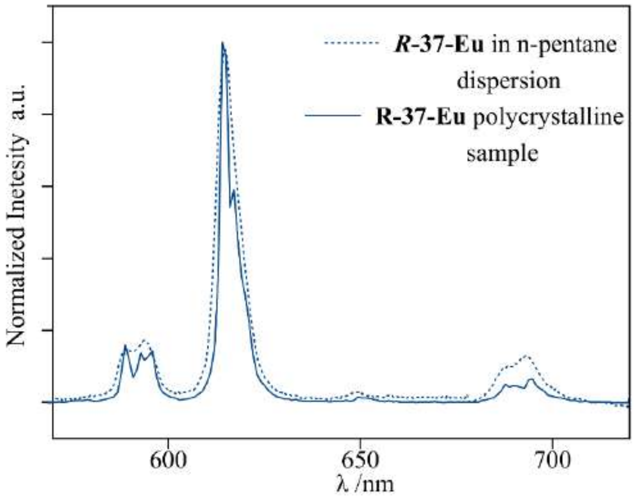

Figure APX.IX.1 Emission spectra of compound ***R*-37-Eu** measured from the polycrystalline sample in a quartz plate (solid line) and the same polycrystalline sample dispersed in n-pentane in the quartz plate deposition (dashed line). The difference in the crystal field splitting that is differentiated in the polycrystalline sample is because the slits used in the different measurements where different and therefore, a change in the resolution of the spectra is observed. In the n-pentane dispersion the slits were 1mm and in the polycrystalline sample, the splits used where 0.3 nm.

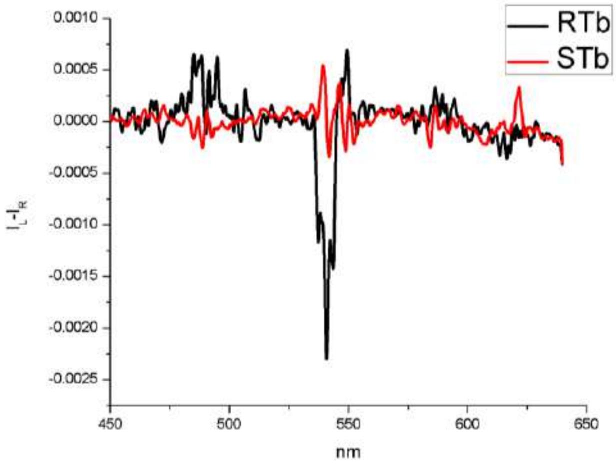

Figure APX.IX.2 CPL spectra of the ***R*-39-Tb** (black) and ***S*-40-Tb** (red) enantiomeric pair.

Magnetic properties of Chapter 4.1

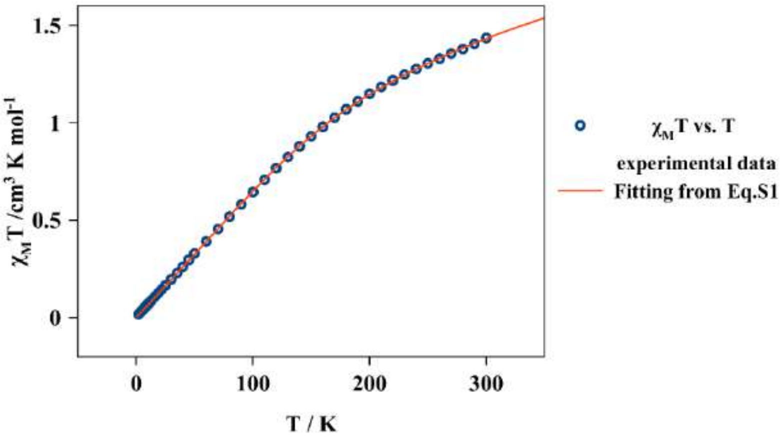

Figure APX.IX.3 χ_MT vs T plot of compound ***S*-38-Eu**. Red line correspont̄s to the best fitting using Equation 4.2.

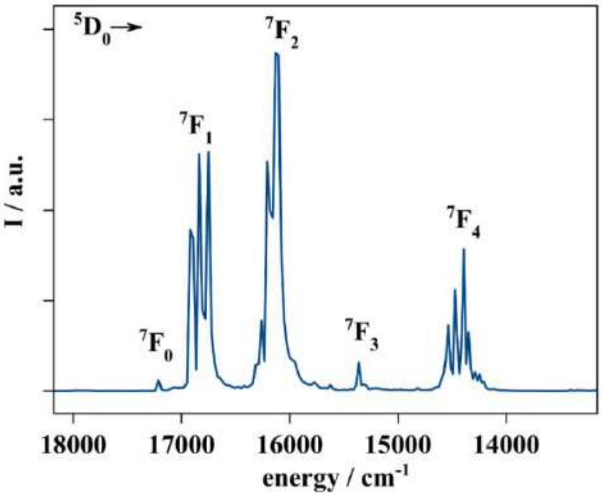

Figure APX.IX.4 Emission spectra of compound ***S*-38-Eu** measured at 77K. The transition energies to $^7F_0$ and $^7F_1$ are depicted in **Table APX.IX.3**.

Table APX.IX.3 The spin-orbit coupling parameter (λ) is the energy gap between the $^7F_0$ and $^7F_1$ states. The three components arising from $^7F_1$ transition due to crystal field are averaged. The resulting λ parameter is 377 cm^{-1} in agreement with the calculated from the magnetic data. The transition energies are in cm^{-1}.

$^5D_0 \rightarrow {}^7F_0$	17212
$^5D_0 \rightarrow {}^7F_1$	16920 16835 16750

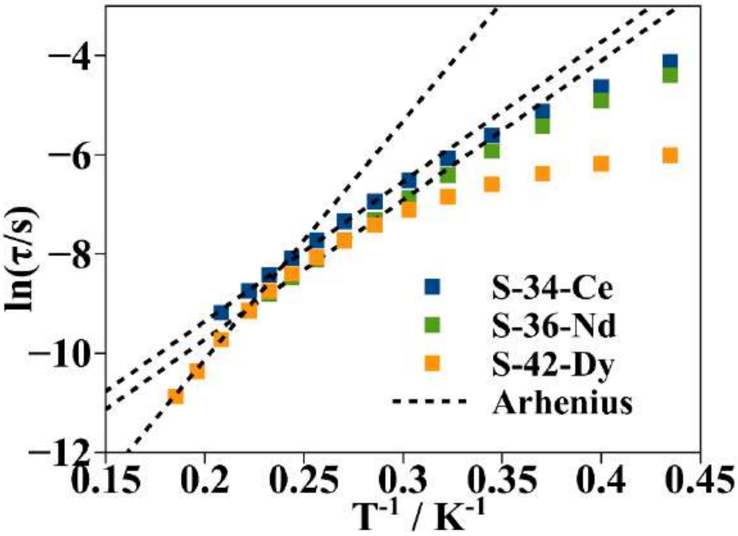

Figure APX.IX.5 ln(τ) vs T^{-1} plots of compounds **S-34-Ce**, **S-36-Nd** and **S-42-Dy**. Continuous black lines correspond to the fit with the Arrhenius law that describes the Orbach relaxation of the magnetization mechanism.

APPENDIX X

Table APX.X.1 Selected bands (cm^{-1}) of ***R*-47-Nd-a** to ***R*-63-Yb-b** s=strong, m=medium and w=weak, br=broad obtained in ATR-IR spectroscopy.

***R*-47-Nd-a**	3056.8(w), 3020.3(w), 2960.5(w), 2927.3(w), 2867.5(w), 1595.6(s), 1555.7(m), 1539.1(s), 1519.2(m), 1492.6(m), 1449.4(m), 1402.9(s), 1296.7(w), 1230.3(w), 1084.1(w), 854.9(w), 831.7(w), 801.8(w), 692.3(s), 625.8(w), 569.4(w), 542.80(w)
***R*-49-Sm-a**	3053.5(w), 3026.9(w), 2957.2(w), 2927.3(w), 2870.9(w), 1595.6(s), 1578.9(m), 1545.8(s), 1519.2(m), 1489.3(w), 1452.8(w), 1409.6(s), 1300.0(w), 1230.2(w), 1087.4(w), 851.7(w), 835.1(w), 805.2(w), 742.1(m), 695.6(s), 625.8(m), 576.0(m), 542.8(m)
***R*-51-Eu-a**	3053.5(w), 3020(w), 2957.2(w), 2930.6(w), 2870.8(w), 1598.9(s), 1575.7(m), 1549.1(s), 1518.2(m), 1489.3(m), 1449.4(m), 1406.2(s), 1296.7(w), 1230.2(w), 1087.4(w), 851.7(w), 831.7(w), 801.9(w), 738.7(m), 692.3(s), 629.2(m), 572.7(m), 542.8(m)
***R*-53-Tb-a**	3053.5(w), 3021.0(w), 2960.2(w), 2931.9(w), 2872.5(w), 1601.4(s), 1579.2(m), 1553.8(s), 1522,3(m), 1493.4(m), 1453.6(m), 1409.7(s), 1299.5(w), 1235.2(w), 1094.3(w), 864.3(w), 835.3(w), 804.2(w), 740.7(m), 694.1(s), 635.8(m), 572.7(m), 541.8(m)
***R*-55-Tb-b**	3098.4(w), 3057.3(w), 3021.7(w), 2962.6(w), 2929.3(w), 2875.3(w), 1650.7(s), 1587.9(m), 1545.8(s), 1525.4(w), 1500.4(w), 1447.7(m), 1421.8(s), 1379.3(w), 1237.3(w), 1096.9(w), 860.5(w), 837.3(w), 805.3(w), 776.4(m), 747.7(m), 700.7(s), 630.7(w), 590.8(w), 554.6(w)
***R*-57-Dy-a**	3051.4(w), 3019.4(w), 2955.6(w), 2925.3(w), 2865.3(w), 1595.6(s), 1573.1(m), 1543.5(s), 1515.3(m), 1482.5(m), 1441.1(m), 1401.9(s), 1293.4(w), 1226.0(w), 1083.7(w), 848.7(w), 825.9(w), 799.3(w), 730.1(m), 691.4(s), 619.5(m), 571.3(m), 540.6(m)
***R*-59-Dy-b**	3086.3(w), 3056.5(w), 3022.6(w), 2962.3(w), 2928.6(w), 2873.1(w), 1648.6(s), 1579.3(m), 1542.7(s), 1522.6(w), 1498.5(w), 1440.3(m), 1415.6(s), 1301.8(w), 1234.8(w), 1093.6(w), 855.3(w), 833.6(w), 802.3(w), 769.4(m), 743.6(m), 699.4(s), 627.2(w), 576.1(w), 547.5(w)

_R_-61-Tm-b	3086.7(w), 3053.5(w), 3023.6(w), 2960.5(w), 2924.0(w), 2870.1(w), 1645.4(s), 1575.7(m), 1545.8(s), 1519.2(w), 1489.3(w), 1439.48(m), 1412.9(s), 1300(w), 1230.3(w), 1090.8(w), 851.7(w), 831.7(w), 801.9(w), 768.6(m), 742.1(m), 695.6(s), 625.8(w), 576.0(w), 546.1(w)
_R_-63-Yb-b	3083.4(w), 3060.2(w), 3023.6(w), 2957.2(w), 2924.0(w), 2870.9(w), 1645.4(s), 1598.9(w), 1578.9(m), 1545.8(s), 1519.2(w), 1489.3(w), 1409.6(s), 1296.7(w), 1233.6(w), 1087.5(w), 851.7(w), 835.1(w), 808.5(w), 771.9(s), 742.1(s), 692.3(s), 625.8(w), 572.7(w), 542.8(w)

Crystallographic data from Chapter 4.2

TableAPX.X.2. Crystallographic information from the Single Crystal X-Ray Diffraction measurements of compounds **_S_-52-Eu-a** and **_S_-62-Tm-b.**

Complex	**_S_-52-Eu-a**	**_S_-62-Tm-b**
Formula	$C_{108}H_{98}Eu_2N_4O_{12}$	$C_{108}H_{98}N_4O_{12}Tm_2$
FW [g/mol]	1947.82	1981.76
Crystal System	Triclinic	Monoclinic
Space Group	P1	C2
a [Å]	11.5491(5)	29.7283(12)
b [Å]	13.4718(5)	12.0158(5)
c [Å]	15.6226(5)	27.0234(12)
α[º]	103.639(1)	90
β [º]	109.404(1)	110.874(2)
γ [º]	93.014(2)	90
V [Å^3]	2205.12(15)	9019.5(7)
Z	1	4
T[K]	100	100
λ(Mo kα) [Å]	0.71073	0.71073
D_{calc} [g cm^{-3}]	1.467	1.459
μ(Mo Kα) [mm^{-1}]	1.477	2.021
R	0.0258	0.71073
wR_2	0.0556	0.1333

Luminescence and Chiroptical properties from Chapter 4.2

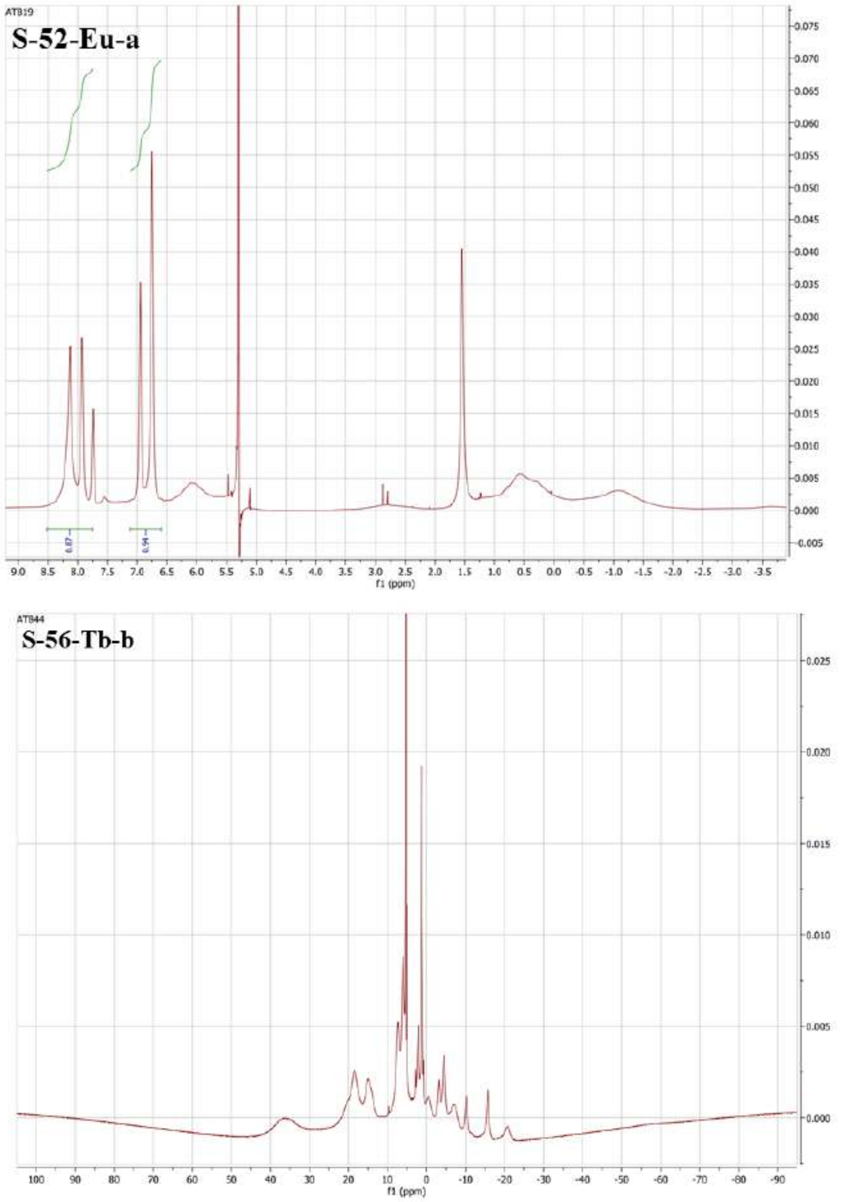

Figure APX.X.1 ^{1}H-NMR spectra of compounds ***S*-52-Eu-a** (down) and ***S*-56-Tb-b** (bottom).

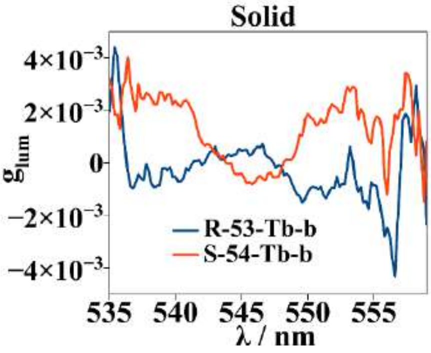

Figure APX.X.2 Dissymmetry factor (g_{lum}) with wavelength plot for ***R*-55-Tb-b** and ***S*-56-Tb-b** enantiomeric pair extracted from the CPL measurement of the polycrystalline samples.

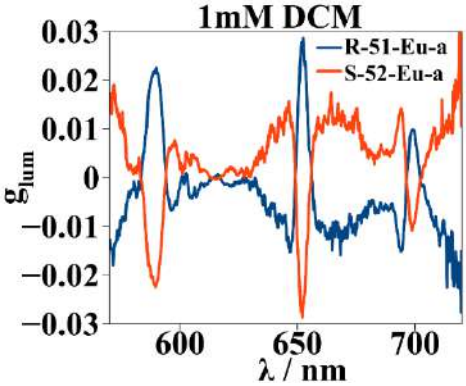

Figure APX.X.3 Dissymmetry factor (g_{lum}) with wavelength plot for ***R*-51-Eu-a** and **S-52-Eu-a** enantiomeric pair extracted from the CPL measurement of the 1mM DCM solutions.

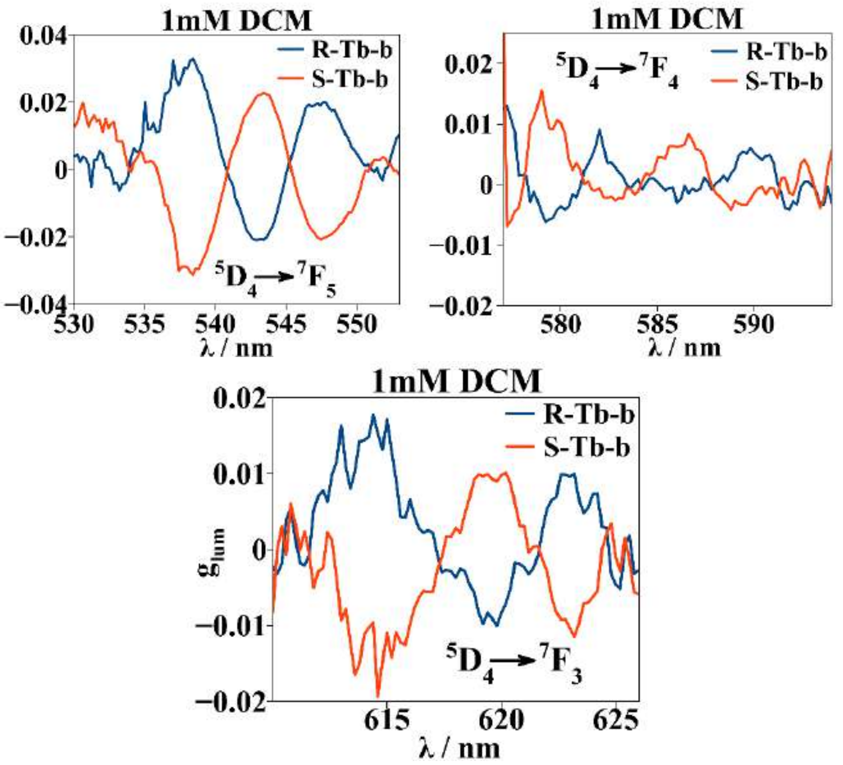

Figure APX.X.4 Dissymmetry factor (g_{lum}) with wavelength plot for ***R*-55-Tb-b** and ***S*-56-Tb-b** enantiomeric pair extracted from the CPL measurement of the 1mM DCM solutions obtained for each Tb^{3+} $^5D_4$→^7F_J transitions. For transition $^5D_4$→$^7F_6$, CPL bands are very weak therefore consistent g_{lum} values could not be extracted

Magnetic properties from Chapter 4.2

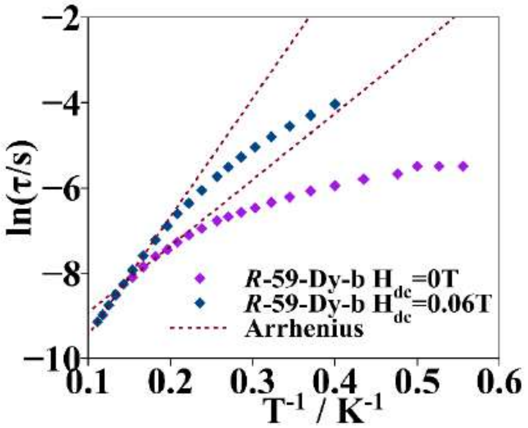

Figure APX.X.5 ln(τ) vs T^{-1} plots of compound ***R*-59-Dy-b** measured at a H_{dc} of 0 and 0.06T. The dotted purple line corresponds to the fit with the Arrhenius law at the higher temperature range.

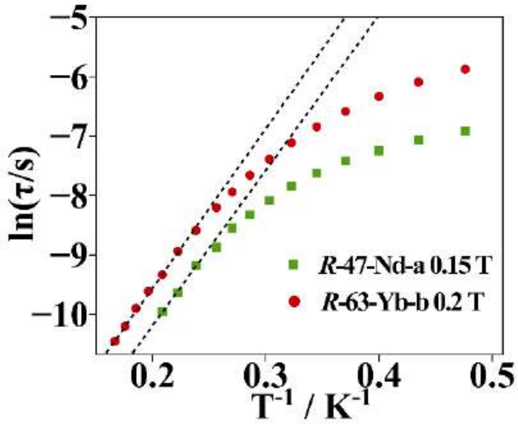

Figure APX.X.6 ln(τ) vs T^{-1} plots of compound ***R*-47-Nd-a** and ***R*-63-Yb-b** measured at a H_{dc} of 0.15 and 0.2 T, respectively. The dotted black line corresponds to the fit with the Arrhenius law at the higher temperature range.

APPENDIX XI

[1] G.M. Sheldrick, *Acta Crystallogr., Sect. A: Fundam. Crystallogr.*, 2008, **64**, 112.

[2] G.M. Sheldrick, *Acta Crystallogr., sect.C: Cryst. Struct. Commun.*, 2015, **71**, 3.

[3] C. F. Macrae, P. R. Edington, P. McCabe, E. Pidcock, G. P. Shields, R. Taylor, T. Towler and J. J. van de Streek, Mercury: Visualization and analysis of crystal structures. *Appl. Cryst.* 2006, **39**, 453–457.

[4] A. L. Spek, PLATON, a Multipurpose Crystallographic Tool; Utrecht University: Utrecht, The Netherlands, 1999.

[5] D. de Sa Pereira, A. P. Monkman and P. Data, Productio[]n and Characterization of Vacuum Deposited Organic Light Emitting Diodes, J. Vis. Exp., 2018, 141, e56593.

[6] F. Zinna, T. Bruhn, C. A. Guido, J. Ahrens, M. Bröring, L. Di Bari and G. Pescitelli, *Chem. Eur. J.*, 2016, **22**, 16089-16098.

[7] S. K. Singh, T. Gupta, L. Ungur, G. Rajaraman, Magnetic Relaxation in Single-Electron Single-Ion Cerium(III) Magnets: Insights from Ab Initio Calculations. *Chem. - A Eur. J.*, 2015, **21** 13812–13819.

[8] a) L. F. Chibotaru, L. Ungur, A. Soncini, The Origin of Nonmagnetic Kramers Doublets in the Ground State of Dysprosium Triangles: Evidence for a Toroidal Magnetic Moment. *Angew. Chemie - Int. Ed.*, 2008, **47**, 4126–4129. b) L. F. Chibotaru, L. Ungur, C. Aronica, H. Elmoll, G. Pilet, D. Luneau, Structure, Magnetism, and Theoretical Study of a Mixed-Valence CoII3CoIII4 Heptanuclear Wheel: Lack of SMM Behavior despite Negative Magnetic Anisotropy. *J. Am. Chem. Soc.*, 2008, **130** 12445–12455.

[9] M. J. Frisch, G. W. Trucks, H. B. Schlegel, G. E. Scuseria, M. A. Robb, J. R. Cheeseman, G. Scalmani, V. Barone, B. Mennucci, G. A. Petersson, H. Nakatsuji, M. Caricato, X. Li, H. P. Hratchian, A. F. Izmaylov, J. Bloino, G. Zheng, J. L. Sonnenberg, M. Hada, M. Ehara, K. Toyota, R. Fukuda, J. Hasegawa, M. Ishida, T. Nakajima, Y. Honda, O. Kitao, H. Nakai, T. Vreven, J. A. J. Montgomery, J. E. Peralta, F. Ogliaro, M. Bearpark, J. J. Heyd, E. Brothers, K. N. Kudin, V. N. Staroverov, R. Kobayashi, J. Normand, K. Raghavachari, A. Rendell, J. C. Burant, S. S. Iyengar, J. Tomasi, M. Cossi, N. Rega, N. J. Millam, M. Klene, J. E. Knox, J. B. Cross, V. Bakken, C. Adamo, J. Jaramillo, R. Gomperts, R. E. Stratmann, O. Yazyev, A. J. Austin, R. Cammi, C. Pomelli, J. W. Ochterski, R. L. Martin, K. Morokuma, V. G. Zakrzewski, G. A. Voth, P. Salvador,

J. J. Dannenberg, S. Dapprich, A. D. Daniels, Ö. Farkas, J. B. Foresman, J. V. Ortiz, J. Cioslowski, D. J. Fox, Gaussian 09 (Revision D.01). Wallingford, CT 2016.

[10] A. D. Becke, Density-functional Thermochemistry. III. The Role of Exact Exchange. *J. Chem. Phys.*, 1993, **98**, 5648–5652.

[11] M. Dolg, H. Stoll, H. Preuss, Energy-Adjusted Ab Initio Pseudopotentials for the Rare Earth Elements. *J. Chem. Phys.*, 1989, **90**, 1730–1734.

[12] A. Schäfer, H. Horn, R. Ahlrichs, Fully Optimized Contracted Gaussian Basis Sets for Atoms Li to Kr. *J. Chem. Phys.*, 1994, **100**, 5829–5835.

(40) (a) M. Llunell, D. Casanova, J. Cirera, P. Alemany, S. Alvarez, Shape Program., version 2, Universitat de Barcelona, Barcelona, Spain, 2010; (b) P. Alemany, D. Casanova, S. Alvarez, C. Dryzum, D. Avnir, Continuous Symmetry Measures: A New Tool in Quantum Chemistry, *Rev. Comput. Chem.*, 2017, **30**, 289-352.

8. Peer-reviewed publications

NJC

PAPER

View Article Online
View Journal | View Issue

Cite this: *New J. Chem.*, 2021, **45**, 22208

Received 9th September 2021,
Accepted 28th October 2021

DOI: 10.1039/d1nj04335h

rsc.li/njc

Improving the emission quantum yield in dinuclear Eu(III) and Tb(III) complexes with 2-fluorobenzoate†

Ànnia Tubau,[ab] Laura Rodríguez,[ab] Ariadna Lázaro,[ab] Ramon Vicente *[ab] and Mercè Font-Bardía[c]

The reaction of $Ln(NO_3)_2 \cdot 6H_2O$ salts (Ln = Eu and Tb) with an excess of 2-fluorobenzoic acid (H-2FBz) in an ethanol/water mixture allows the isolation of dinuclear compounds with the formula $[Ln_2(\mu_2\text{-}2FBz)_4(2FBz)_2(H\text{-}2FBz)_2(H_2O)_2]$ (Ln = Eu (**1**) and Tb (**2**), 2FBz = 2-fluorobenzoate). A solid-state photoluminescence study of complexes **1** and **2** shows the 4f–4f lanthanide transitions in the visible range with improved emission quantum yields. **1** and **2** are water soluble and photoluminescence studies have also been performed in water and D_2O solutions, showing that the emission due to the 4f–4f electronic transitions is still present. The magnetic behaviors of **1** and **2** are also reported.

Introduction

Usually lanthanide(III) (Ln(III)) coordination compounds show luminescence from 4f–4f electronic transitions within the closed shell of individual ions (responsible for the light emission). The energy bands generated from these transitions are narrow and characteristic of each Ln(III) and the emitting excited states are long-lived. Since the f–f transitions are parity-forbidden, free Ln(III) ions have extremely low molar extinction coefficients (ε_λ) for direct excitation leading to a low luminescence intensity. To overcome this problem, the presence of light-harvesting ligands coordinated to Ln(III) can enhance the metal luminescence *via* an energy transfer process, commonly known as the antenna effect.[1–3] On the other hand, luminescent lanthanide complexes are of interest due to their wide range of applications in materials science and biosciences.[1–14]

For the synthesis of Ln(III) coordination compounds, R-benzoate anions have been widely used as ligands due to the strong interaction between the Ln(III) ions and the oxygen atoms from the carboxylate group and also because of the luminescence properties generated from the strongly absorbing chromophore group of the organic fragment.[1,15,16]

Recently, S. Bräse *et al.* have published a thorough study of lanthanide fluorobenzoate coordination compounds searching for the optimal lanthanide and optimal ligand fluorination degree to obtain photostable, non-toxic and luminescent compounds suitable for use as bio-probes.[17] As a conclusion of the study, europium 2-fluorobenzoate (2FBz) dihydrate of formula $[Eu_2(2FBz)_6(H_2O)_4]$ combined the best properties with a polycrystalline quantum yield (QY) of 15%.

The quenching of luminescence is due to high-energy vibrations (namely OH stretching for water).[1,3] In Eu(III) the gap between the $^5D_0$ and $^7F_6$ states is approximately 12 000 cm^{-1}. It follows that the quenching of the emissive state is easily accomplished through three vibrational quanta of the O–H bond, with a vibrational energy of 3600 cm^{-1}.[1b] Taking into account the experience of our research group in the syntheses and luminescence study of 2-fluorobenzoate lanthanide(III) coordination compounds[18,19] we have considered the preparation of a new europium 2-fluorobenzoate monohydrate compound of the formula $[Eu_2(\mu_2\text{-}2FBz)_4(2FBz)_2(H\text{-}2FBz)_2(H_2O)_2]$ (H-2FBz is 2-fluorobenzoic acid) with the aim of increasing the emission quantum yield taking into account that the number of quenching water molecules in the new compound is a half with respect to $[Eu_2(2FBz)_6(H_2O)_4]$.

In this work we present the synthesis and structure of a new dinuclear compound, $[Eu_2(\mu_2\text{-}2FBz)_4(2FBz)_2(H\text{-}2FBz)_2(H_2O)_2]$ (**1**), which is isostructural to the previously reported $[Tb_2(\mu_2\text{-}2FBz)_4(2FBz)_2(H\text{-}2FBz)_2(H_2O)_2]$ (**2**) compound.[20] **1** and **2** have been prepared by us using a new straightforward room temperature synthetic method. The coordination number of

---

[a] *Departament de Química Inorgànica i Orgànica, Secció de Química Inorgànica, Universitat de Barcelona, Martí i Franquès 1-11, 08028 Barcelona, Spain. E-mail: rvicente@ub.edu*

[b] *Institut de Nanociència i Nanotecnologia (IN2UB), Universitat de Barcelona, 08028 Barcelona, Spain*

[c] *Departament de Mineralogia, Cristallografia i Dipòsits Minerals and Unitat de Difracció de R-X, Centre Científic i Tecnològic de la Universitat de Barcelona (CCiTUB), Universitat de Barcelona, Solé i Sabarís 1-3, 08028 Barcelona, Spain*

† Electronic supplementary information (ESI) available: Tables S1 and S2; Fig. S1–S6. CCDC 2097703 (**1**). For ESI and crystallographic data in CIF or other electronic format see DOI: 10.1039/d1nj04335h

the lanthanide ions is 9 for **1** and **2**. Suitable single crystals for single crystal X-ray diffraction were obtained for compound **1**. The obtained powders of **1** and **2** were characterized by infrared spectroscopy by attenuated total reflectance, elemental analysis, powder X-ray diffraction and thermogravimetry. Furthermore, for **1** and **2**, the magnetic behaviour and luminescence properties including the emission quantum yield in solid and in water and D_2O solutions are reported.

Results and discussion

Syntheses

In our experiment, we have used a straightforward room temperature synthetic procedure that is different from the refluxing procedure used to prepare the already published complexes $[Tb_2(\mu_2\text{-}2FBz)_4(2FBz)_2(H\text{-}2FBz)_2(H_2O)_2]$[20] or $[Nd_2(\mu_2\text{-}2FBz)_4(2FBz)_2(H\text{-}2FBz)_2(H_2O)_2]$.[21] We have successfully obtained with our new synthetic procedure a new dinuclear europium(III) compound $[Eu_2(\mu_2\text{-}2FBz)_4(2FBz)_2(H\text{-}2FBz)_2(H_2O)_2]$ (**1**) and the yet structurally published $[Tb_2(\mu_2\text{-}2FBz)_4(2FBz)_2(H\text{-}2FBz)_2(H_2O)_2]$ (**2**). The key of our straightforward room temperature synthetic method is the addition of a big excess of 2-fluorobenzoic acid which occupies two coordination water positions with respect to the previously reported $[Ln_2(2FBz)_6(H_2O)_4]$.

Infrared spectra

The characteristic bands observed for the 2-fluorobenzoic acid (H-2FBz) molecule and compounds **1** and **2** are summarized in Table 1. For the Eu(III) and Tb(III) compounds, the characteristic $\nu_{C=O}$ stretching vibration at 1684 cm^{-1} from the free ligand, H-2FBz, disappears in the IR spectra while the asymmetric ($\nu_{as(COO^-)}$) and symmetric ($\nu_{s(COO^-)}$) absorption peaks of the COO^- group at around 1602–104 and 1383–1381 cm^{-1}, respectively, appear, indicating the coordination of the ligands to the lanthanide ions by oxygen donor atoms. Furthermore, the broad band corresponding to the ν_{O-H} of compounds **1** and **2** is different from the band corresponding to the ν_{O-H} stretching of the free ligand. The free ligand O–H stretching mainly arises from the COOH group while in the complexes this vibration is assigned to the H_2O molecules that are coordinated to Ln^{3+} atoms.

X-Ray crystal structure

Structural motif of $[Eu_2(\mu_2\text{-}2FBz)_4(2FBz)_2(H\text{-}2FBz)_2(H_2O)_2]$ 1

Compound **1** crystallizes in a triclinic crystal system with a *P*-1 space group. A partially labelled molecular plot and the coordination geometry figure are shown in Fig. 1. The crystallographic data and selected bond lengths and angles are listed in Tables S1 and S2 (ESI†), respectively.

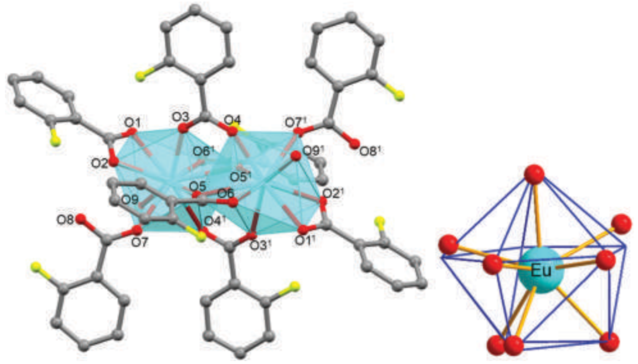

Fig. 1 (Right) Partially labelled plot of compound **1**. H atoms are omitted for clarity. The symmetry transformation used to generate equivalent atoms is^1 $-x + 1$, $-y + 1$, $-z + 2$. Colour code: grey = C, red = oxygen, green = fluorine and blue = Eu. (Left) Coordination polyhedron of the Eu(III) ions in compound **1**. The blue line shows the ideal Muffin (MFF-9) polyhedron.

Table 1 Assignment of selected IR spectra bands for the free ligand and the complexes (cm^{-1})

	$\nu_{C=O}$	ν_{H-O}	$\nu_{as(COO^-)}$	$\nu_{s(COO^-)}$
H-2FBz	1685	2870	—	—
1 (Eu)	—	3428	1588	1394
2 (Tb)	—	3419	1602	1383

The calculation of the distortion degree of the EuO_9 coordination polyhedron for **1** (Fig. 1b) with respect to the ideal nine-vertex polyhedra, using the continuous shape measure theory and SHAPE software,[22,23] shows an intermediate distortion between various coordination polyhedra. The lowest continuous shape measure (CShM) values for compound **1** correspond to Muffin (MFF-9, C_s), spherical capped square antiprism (CSAPR-9, C_{4v}) and spherical tricapped trigonal prism (TCTPR-9, D_{3h}) with values of 1.233, 1.475, 1.999 and 2.617, respectively (Fig. 1b).

The crystal structure of **2** was previously published by Xia Li *et al.*[20] Powder X-ray diffraction measurements (Fig. S1, ESI†) have been realized for both synthesized compounds (**1** and **2**), confirming that they are isostructural and that all the products obtained from the reactions are the desired products with the formula $[Ln_2(\mu_2\text{-}2FBz)_4(2FBz)_2(H\text{-}2FBz)_2(H_2O)_2]$. The calculation of the degree of distortion of the TbO_9 coordination polyhedron for **2** (Fig. 2) with respect to the ideal nine-vertex polyhedra, using the continuous shape measure theory and SHAPE software,[22,23] shows an intermediate distortion between various coordination polyhedra. The lowest continuous shape measure (CShM) values for compound **2** correspond to the spherical capped square antiprism (CSAPR-9, C_{4v}), spherical tricapped trigonal prism (TCTPR-9, D_{3h}) and tricapped trigonal prism (JTCTPR-9, D_{3h}) with values of 2.337, 2.820 and 2.926, respectively.

The coordination sphere of each Eu(III) is formed by O1 and O2 from a 2FBz ligand in the bidentate chelating coordination mode (Fig. 3a) and O7 from an H-2FBz (Fig. 3d). There are two ligands in the bidentate bridging coordination mode (Fig. 3b) that are bonded to the Eu(III) atoms through O3 and O4_a and two 2FBz ligands that are in the bidentate chelating bridging coordination mode (Fig. 3c) bonded to the lanthanide atom through the O5, O6_a and O5_a atoms. The latest O atom is doubly bridging both Eu(III) centres of the structure.

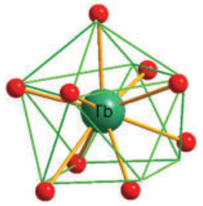

Fig. 2 Coordination polyhedron of the Tb(III) ions in compound **2**. The green line shows the ideal spherical capped square antiprism (CSAPR-9) polyhedron.

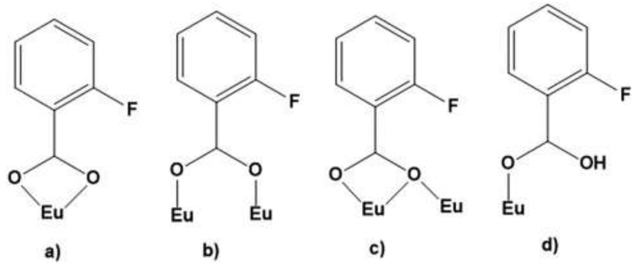

Fig. 3 Representation of the different coordination modes of 2-FBz and H-the 2-FBz ligand: (a) chelating bridge, (b) *syn–syn* bridge, (c) chelating-bridge, and (d) monodentate for the H-2-FBz acid.

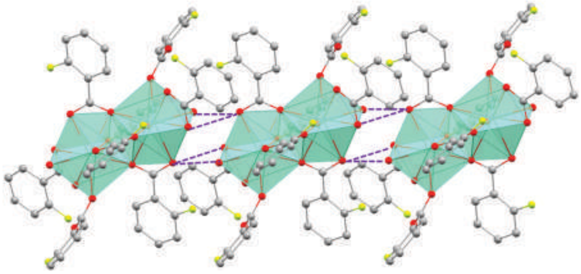

Fig. 4 Supramolecular arrangement representation of compound **1** in the [100] direction. In blue: H–O···H intermolecular hydrogen bonds.

The symmetry transformation used to generate equivalent atoms is _a: −*x* + 1, −*y* + 1, −*z* + 2. Finally, the coordination sphere is completed by O9 from an H_2O molecule. The Eu–O bond length is in the range of 2.348(2) to 2.638(2) Å, the Eu···Eu intramolecular distance is 3.964(3) Å and the O1–Eu–O2 bite angle of the 2FBz ligand in the bidentate chelating coordination mode is 51.69(4)°.

Intermolecular interactions to consider are the O–H···O H-bond from the H_2O molecule and O1 and O6 of two carboxylate groups in the bidentate chelating and bidentate chelating bridging coordination modes, respectively. The H9OA/H9OB···O1/O6 distance is 2.020 Å and the O9–H9OA···O1 and O9–H9OB···O6 angles are 154.06° and 149.34°. This arrangement propagates along the [100] direction of the crystal lattice, and thus the final supramolecular structure consists of a 1D chain Fig. 4.

Thermal stability

Compounds **1** and **2** are thermally stable until 100 °C. In the interval 100–250 °C, **1** and **2** lose the two H-2FBz and the two water molecules: found 21.79% (21.73% expected for **1**); found 21.48 (21.63% expected for **2**). Fig. S2a and b (ESI†) for **1** and **2** respectively.

Photophysical properties of 1 and 2

Photoluminescence properties have been studied in the solid state at room temperature for both lanthanide compounds. As stated before, highly luminescent lanthanide(III) coordination compounds can be potentially used as bio-probes. For this, it is important to study the solubility in aqueous solution. For compounds **1** and **2** the solubility values in deionized water were 7.98 and 6.2 mmol L^{-1}, respectively. Furthermore, photophysical measurements were performed in H_2O and in D_2O solutions at their respective solubility concentrations, in order to study the possible structural changes and the optical properties of **1** and **2** in these media.

Europium compound. Excitation spectra collected at a maximum emission wavelength (λ_{em}) of 617 nm ($^5D_0 \rightarrow {}^7F_2$) showed an intense band at 274 nm for the solid state sample (Eu–s), and at 298 nm for the H_2O (Eu–H_2O) and D_2O (Eu–D_2O) solutions. This band corresponds to the $\pi \rightarrow \pi^*$ transitions centered on the ligand molecules.[17] In addition, for the three excitation spectra, direct f–f transitions of Eu(III) could be discerned: $^5D_4 \leftarrow {}^7F_0$ at 361 nm and $^5L_6 \leftarrow {}^7F_0$ at 394 nm, Fig. S3 (ESI†).

Emission spectra were recorded upon excitation of the samples at a wavelength (λ_{ex}) of 274 nm for the Eu–s sample and at 298 nm for the solution samples Eu–H_2O and Eu–D_2O, which correspond to the ligand absorption maxima. For the three samples, excitation at the ligand wavelength induced the emission of Eu(III), Fig. 5. The bands that arise from the f–f transitions were assigned to $^5D_0 \rightarrow {}^7F_0$ at 580 nm, $^5D_0 \rightarrow {}^7F_1$ at 593 nm, $^5D_0 \rightarrow {}^7F_2$ at 617 nm, $^5D_0 \rightarrow {}^7F_3$ at 651 nm and $^5D_0 \rightarrow {}^7F_4$ at 698 nm. For the Eu–D_2O and Eu–H_2O samples,

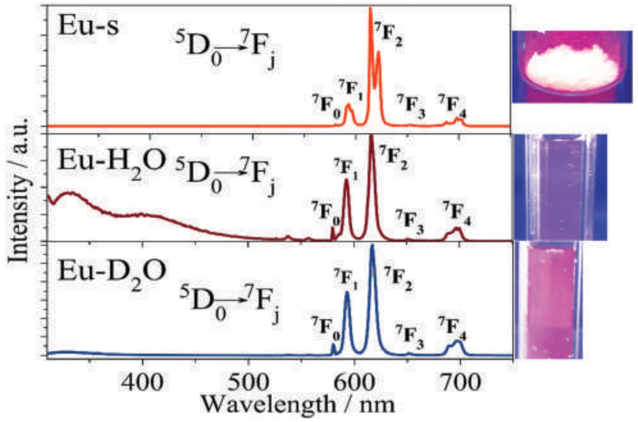

Fig. 5 Emission spectra of compound **1** in the microcrystalline sample (Eu–s), dissolved in water (Eu–H_2O) and in deuterium oxide (Eu–D_2O). To the right of the spectra is shown the naked eye luminescence of each sample.

residual ligand emission could be seen in the 300–500 nm range, though for the Eu–D_2O sample, the emission from the lanthanide ion was clearly more intense. For the Eu–s sample, no emission from the ligand was seen, proposing an effective antenna effect. The emission wavelengths of the f–f transitions were the same in both the solid sample and the solution samples. Also, the $^5D_0 \rightarrow {}^7F_0$ transition appears as a single band for the three samples; therefore, we could assume that the lanthanide ion presents only one type of coordination sphere though high-resolution emission spectra recorded at low temperatures are required in order to confirm this statement. Since the degeneracy of the electronic ground state $(2J + 1)$ caused by the ligand field effect is one for an Eu(III) ion, any splitting that we can see in the $0 \rightarrow 0$ transition will be due to the presence of compounds with different coordination environments.[24] However, several changes in the band shape and intensity, that are related to a change in the coordination environment of Eu(III) ions, were seen when dissolving the compounds into aqueous solutions. The $^5D_0 \rightarrow {}^7F_2$ hypersensitive band is responsible for the red emission of europium and it is sensitive to the Eu(III) surroundings. The red emission colour can be seen in the naked eye for the three europium samples, Fig. 5 (right). For the Eu–s sample, this band is split, indicating that the lanthanide cation is not placed in a position with inversion symmetry inside the structure, but no splitting is seen for the Eu–H_2O and Eu–D_2O systems. In addition, the intensity ratio of the $^5D_0 \rightarrow {}^7F_2$ and $^5D_0 \rightarrow {}^7F_1$ transitions ($0 \rightarrow 2/0 \rightarrow 1$ ratio) gives us information about the symmetry of the coordination environment and hence an increase of this ratio is attributed to an increase of the asymmetry around the Eu(III) surroundings.[25,26] For **1** the $0 \rightarrow 2/0 \rightarrow 1$ ratio is 5 in the solid state and 2 in water and deuterated oxide solutions, respectively, indicating higher symmetry around the Eu(III) ions in the solution samples. This fact indicates a significant change in the coordination environment of the lanthanide anion and therefore a structural change of the $[Eu_2(\mu_2\text{-}2FBz)_4(2FBz)_2(H\text{-}2FBz)_2(H_2O)_2]$ arrangement when the microcrystalline sample is dissolved in water solution. The suggested structural changes account for the solvation of the lanthanide ions and in order to know how many H_2O molecules coordinate to the Eu(III) center, the photoluminescence lifetimes (τ_{obs}) in H_2O and D_2O solution were obtained, Fig. S4 (ESI†). The emission decays, monitored at a λ_{em} of 617 nm, were fitted monoexponentially ($I(t) = I_0 \exp(-t/\tau_{obs})$), confirming the presence of single emitting species, and the τ_{obs} values were 0.14 ms for the Eu–H_2O sample and 2.68 ms for the Eu–D_2O sample. The number of $H_2O(q)$ molecules in the first coordination sphere was calculated using the equation presented by Horrocks and Sudnick (eqn (1)):[27]

$$q = A\left(\frac{1}{\tau_{obs(H_2O)}} - \frac{1}{\tau_{obs(D_2O)}}\right) \qquad (1)$$

where $\tau_{obs(H_2O)}$ and $\tau_{obs(D_2O)}$ are the lifetimes in ms of Eu(III) dissolved in H_2O and D_2O, respectively, and A is 1.05 for Eu(III). With this equation, q was 7.1.

Using the revised equation presented by Supkowski and Horrocks[28] (eqn (2)), which also takes into account the H_2O molecules in the second coordination sphere, the q value was also 7.1. In the refined equation, A is 1.11 and B is 0.31 for Eu(III).

$$q = A\left(\frac{1}{\tau_{obs(H_2O)}} - \frac{1}{\tau_{obs(D_2O)}} - B\right) \qquad (2)$$

Thus, the europium compound when solved in water solvates to 7 H_2O molecules, probably breaking the dinuclear system, leading to mononuclear europium species with water and 2-fluorobenzoate ligands coordinated to the metal.

In order to study the luminescence and sensitization efficiency of both europium solid and aqueous systems further, the overall quantum yields (QYs) were measured and the corresponding photophysical parameters were calculated, Table 2. The QY can be defined as a result of multiplying the intrinsic quantum yield (ϕ_{Ln}) by the sensitization efficiency (η_{sens}) as follows in eqn (3):

$$QY = \eta_{sens} \cdot \phi_{Ln} \qquad (3)$$

ϕ_{Ln} describes the efficiency of direct absorption and emission of lanthanide f–f transitions and η_{sens} indicates the ligand to lanthanide energy transfer efficiency. In addition, the intrinsic quantum yield can be calculated using eqn (4):

$$\phi_{Ln} = \frac{\tau_{obs}}{\tau_{rad}} \qquad (4)$$

where τ_{rad} refers to the radiative lifetime which corresponds to the lifetime in the absence of non-radiative deactivations. Because of the pure magnetic dipole character of the $^5D_0 \rightarrow {}^7F_1$ transition, this band is almost independent of the local symmetry around Eu(III). Therefore, the τ_{rad} parameter can be calculated from the corrected emission spectrum of the europium compound by means of eqn (5)[24,29,30]

$$\frac{1}{\tau_{rad}} = A_{MD,0} \cdot n^3 \left(\frac{I_{TOT}}{I_{MD}}\right) \qquad (5)$$

where $A_{MD,0}$ is a constant (14.65 cm^{-1}), n is the refractive index (1.517 for the microcrystalline sample and 1.334 for water) and $\frac{I_{TOT}}{I_{MD}}$ is the ratio between the total integrated area measured from the corrected Eu(III) emission spectrum (I_{TOT}) to the integrated area of the pure magnetic dipole transition $^5D_0 \rightarrow {}^7F_1$ (I_{MD}).[31]

Upon the λ_{ex} of 274 nm, the QY for the polycrystalline sample (Eu–s) was 27%. Also the photoluminescence decay

Table 2 Lifetimes (τ_{obs}), overall quantum yields (QYs) and the calculated photoluminescence parameters: radiative lifetimes (τ_{rad}), intrinsic quantum yield (ϕ_{Ln}) and sensitization efficiency (η_{sens}) of compound **1** in the microcrystalline sample (Eu–s), dissolved in water (Eu–H_2O) and in deuterium oxide (Eu–D_2O)

	τ_{obs} (ms)	QY (%)	τ_{rad} (ms)	ϕ_{Ln} (%)	η_{sens} (%)
Eu–s	0.72	27	2.58	28	96
Eu–H_2O 7.9 mmol L^{-1}	0.14	0.6	7.48	2	30
Eu–D_2O 7.9 mmol L^{-1}	2.68	30	7.86	34	88

time could be fitted monoexponentially for the solid sample leading to a τ_{obs} value of 0.72 ms. The ϕ_{Ln} and η_{sens} values were 28% and 96%, respectively, indicating a very good sensitization efficiency of the europium compound in the solid sample. The values of QY and τ_{obs} for Eu–s are significantly larger than the previously published values for the $[Eu_2(2FBz)_6(H_2O)_4]$ compound which are 15% and 0.52 ms, respectively,[17] thus verifying the effect of the highest number of coordinated water molecules in the quantum yield. By dissolving the solid sample of **1** into a 6.2 mmol L^{-1} aqueous solution, the QY was 30% for the Eu–D_2O sample and it decreased drastically down to 0.6% for the Eu–H_2O sample. The ϕ_{Ln} and η_{sens} values were 2% and 30%, respectively, for the Eu–H_2O sample.

The lower quantum yield of the Eu–H_2O sample indicates the presence of more favored non-radiative pathways, because of the high energy bond vibrations that are present in the europium ion environment due to the seven inner sphere water molecules. The Eu–D_2O sample yields larger values of ϕ_{Ln} and η_{sens} (34% and 88%, respectively).

Terbium compound. Excitation spectra recorded at a maximum emission wavelength (λ_{em}) of 543 nm for the polycrystalline sample (Tb–s) and at 548 nm ($^5D_4 \rightarrow {}^7F_5$) for the aqueous solutions in H_2O (Tb–H_2O) and D_2O (Tb–D_2O) showed an intense band at 290 nm, for Tb–s, and at 297 nm for Tb–H_2O and Tb–D_2O corresponding to the $\pi \rightarrow \pi^*$ excitation transitions from the ligand moieties, Fig. S5 (ESI†). Emission spectra under the respective ligand excitation wavelength (λ_{ex} = 290 nm for Tb–s and 297 nm for Tb–H_2O and D_2O) gave rise to characteristic bands from the f–f transitions of the Tb(III) ion, Fig. 6. For the three samples, the first band at 490 nm is assigned to $^5D_4 \rightarrow {}^7F_6$ whereas the most intense bands centered at 544 nm for the Tb–s sample and at 546 nm for the Tb–H_2O and Tb–D_2O samples correspond to the $^5D_4 \rightarrow {}^7F_5$ transition, responsible for the green emission colour that can be seen through the naked eye under excitation of UV light for the three different samples of compound **2** (Fig. 6, right). Furthermore, the weaker intense bands at 586 and 622 nm were assigned to the $^5D_4 \rightarrow {}^7F_4$ and $^5D_4 \rightarrow {}^7F_3$ transitions, respectively.[32]

A compilation of the measured photoluminescence parameters of compound **2** is presented in Table 3. The measured lifetime for the Tb–H_2O sample was also in the millisecond range (0.50 ms), higher than the τ_{obs} observed for the Eu–H_2O compound (0.14 ms). Compound **2** dissolved in D_2O (Tb–D_2O) reached a τ_{obs} of 1.86 ms. The outcome number of coordination water molecules, q, for the terbium compound was 6.1 taking into account the first coordination sphere (eqn (1))[27] (A = 4.2 for Tb(III)) and 7 using the developed equation that considers also the second coordination sphere contribution, (eqn (2), where A is 5 and B is 0.06 for the Tb(III) ion).[33] The Tb(III) ion coordinates to 5 more molecules of H_2O when dissolved in aqueous solution, shifting 2 nm to the red range of the $^5D_4 \rightarrow {}^7F_5$ emission transition. Therefore, structural changes also take place when dissolving the Tb(III) polycrystalline sample in H_2O solution. The QYs in solution for compound **2** were 4% (Tb–H_2O) and 26% (Tb–D_2O). Furthermore, for the Tb(III) solid sample the τ_{obs} was 1.43 ms and the compound showed a rather high sensitization quantum yield of 76%. The decay times recorded for the three Tb(III) samples were fitted monoexponentially in agreement with a single emitting species, Fig. S6 (ESI†).

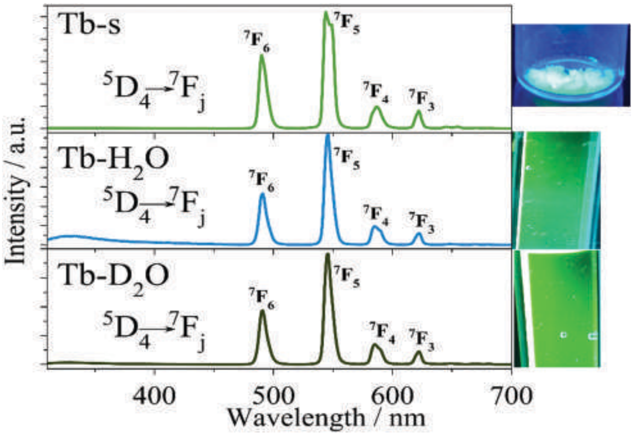

Fig. 6 Emission spectra of compound **2** in the microcrystalline sample (Tb–s) and dissolved in water solution (Tb–H_2O) and in deuterium oxide (Tb–D_2O). To the right of the spectra is shown the naked eye luminescence of each sample.

Table 3 Lifetimes (τ_{obs}) and overall quantum yields (QYs) of compound **2** in the microcrystalline sample (Tb–s), dissolved in water (Tb–H_2O) and in deuterium oxide (Tb–D_2O)

	τ_{obs} (ms)	QY (%)
Tb–s	1.43	76
Tb–H_2O 6.2 mmol L^{-1}	0.50	4
Tb–D_2O 6.2 mmol L^{-1}	1.86	26

All in all, the emission and sensitization efficiency decreases considerably when compounds **1** and **2** are dissolved in water because of the luminescence quenching produced by the high O–H vibrating bonds from the water molecules that promote energy loss by non-radiative processes.[1,3] However, the photoluminescence properties are still present in water solution taking into account that their luminescence can be seen through the naked eye for compounds **1** and **2**, making them an ideal choice as candidates for bioanalytical applications.

Magnetic properties

Direct current (dc) magnetic susceptibility and magnetization measurements were performed for compounds **1** and **2** on polycrystalline samples. $\chi_M T$ *versus* temperature plots in the 2–300 K temperature range under a dc magnetic field of 0.3 T are depicted in Fig. 7. At room temperature (300 K) the $\chi_M T$ values are 2.8 and 24.3 cm^3 mol^{-1} K for **1** and **2**, respectively. For **2**, the room temperature $\chi_M T$ value is close to the one expected for two isolated Tb(III) ions in the ground state ($^7F_6$, $S = 3$, $L = 3$, $J = 6$, $g_J = 3/2$) which is 23.64 cm^3 mol^{-1} K.[1] However, for **1** the room temperature $\chi_M T$ value is not 0, revealing the presence of populated excited J states ($^7F_1$) that are very close in energy to the ground state ($^7F_0$, $S = 3$, $L = 3$, $J = 0$, $g_J = 0$).

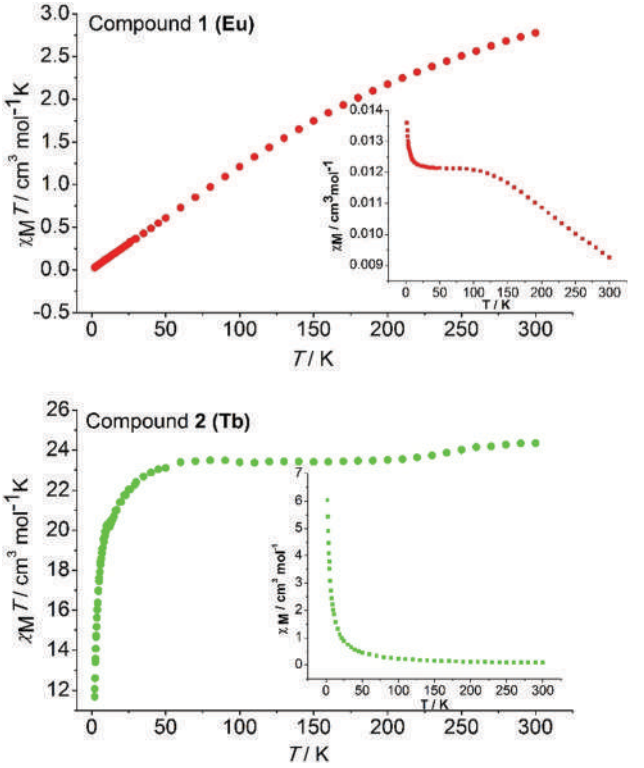

Fig. 7 $\chi_M T$ *vs.* T plots for compounds **1** and **2**.

On cooling the samples, for **1**, the $\chi_M T$ values decrease gradually up to 0.03 cm^3 mol^{-1} K. This value is very close to 0 and it suggests that the ground state at this temperature (2 K) agrees with $m_j = 0$. The susceptibility values of compound **2** are almost independent *versus* temperature until ~50 K where they decrease suddenly to a finite value of 12.1 cm^3 mol^{-1} K. This fact may be attributed to the depopulation of m_j states (split levels form the crystal field) in the ground state.

Magnetization dependence on an applied magnetic field measured at 2 K, Fig. S7 (ESI†), reveals no saturation in a high magnetic field (5 T) with a magnetization value of 0.10 Nμ_B for **1**. Compound **2** in a high applied magnetic field presents a saturation magnetization value of 10.2 Nμ_B.

The χ_M *versus* T plot (inset Fig. 7) of **1** shows a smooth increase of χ_M values. Below 125 K, χ_M reaches a constant value of 0.012 cm^3 mol^{-1} K, confirming the thermal depopulation of the mixed $^7F_1$ excited state, and only the $^7F_0$ ground state is populated at this point. At very low temperatures of ~4 K, the europium compound shows a small increase of χ_M values because of the presence of some remnant paramagnetic species. For an europium ion, the energy difference between the ground state term ($^7F_0$) with the first ($^7F_1$) and second ($^7F_2$) excited levels is small and mixing of these J levels can occur because of the crystal field effect or Zeeman effect. The χ_M *versus* T plot of **2** results in a typical paramagnetic behavior.

The plot of $1/\chi_M$ *versus* T resulted in a linear tendency for compound **2** (Fig. 8), in the whole measured temperature range, confirming that the terbium compound obeys the Curie Weiss law $\left(\chi_M = \dfrac{C}{T-\theta}\right)$. The Curie constant ($C$) and Weiss temperature (θ) were determined to be 24.2 cm^3 mol^{-1} and 2.6 K, respectively.

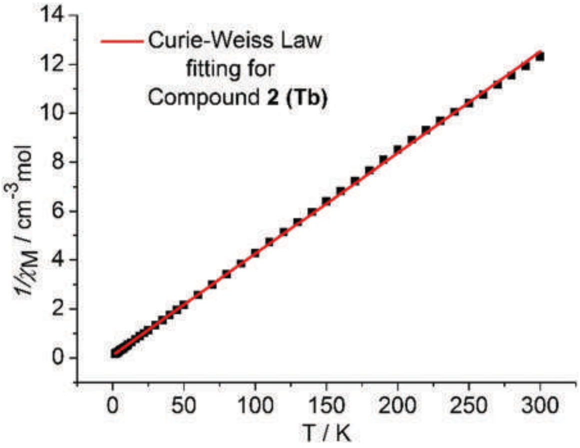

Fig. 8 $1/\chi_M$ *vs.* T plot for compound **2**.

The obtained magnetic results of **1** and **2** are in agreement with other Eu(III) and Tb(III) compounds.[1,32,34–38]

Conclusions

With the aim of studying the effects of the reduction of the number of water molecules on the photoluminescence properties with respect to the previously published compounds of formula $[Ln_2(2FBz)_6(H_2O)_4]$, we have presented structural, magnetic and luminescence studies of two homodinuclear lanthanide compounds of formula $[Ln_2(\mu_2\text{-}2FBz)_4(2FBz)_2(H\text{-}2FBz)_2(H_2O)_2]$ Ln = Eu (**1**) and Tb (**2**), which show a diminution of half the number of coordinated water molecules. From a synthetic point of view, we have used a new straightforward room temperature synthetic procedure to avoid the refluxing step used to prepare the previously published $[Tb_2(\mu_2\text{-}2FBz)_4(2FBz)_2(H\text{-}2FBz)_2(H_2O)_2]$ compound.

A solid-state photoluminescence study of complexes **1** and **2** shows the 4f–4f lanthanide transitions in the visible range. The overall quantum yield has values of 27 and 76% for **1** and **2**, respectively. For the previously published compounds of formula $[Ln_2(2FBz)_6(H_2O)_4]$ the quantum yields were 15 and 50% for the corresponding Eu and Tb derivatives, respectively.[17] Compounds **1** and **2** are water soluble, with solubility values of 7.98 and 6.2 mmol L^{-1} for **1** and **2**, respectively. The QYs decrease to 0.23% and 3.8% for **1** and **2**, respectively when dissolved in water. Photoluminescence lifetimes are 0.13 and 0.42 ms for **1** and **2**, respectively. In addition, the radiative lifetime, intrinsic quantum yield and sensitization efficiency of **1** in water solution are 7.48 ms, 2% and 30%, respectively. In **1** and **2** the photoluminescence properties are still present in water solution, making them an ideal choice as candidates for bioanalytical applications.

A magnetic study of **1** and **2** shows no SMM behavior and is in agreement with other Eu(III) and Tb(III) compounds.[1,32,34–38]

Experimental section

Starting materials

Ln(NO$_3$)$_3$·xH$_2$O salts (Strem Chemicals) and 2-fluorobenzoic acid (Aldrich) were used as received.

Spectral and magnetic measurements

The elemental analyses of the compounds were performed at the Serveis Científics i Tecnològics of the Universitat de Barcelona. Infrared spectra (4000–400 cm^{-1}) were recorded by KBr pellets using a PerkinElmer 380-B spectrophotometer. Solid state fluorescence spectra were recorded using a Horiba Jobin Yvon SPEX Nanolog fluorescence spectrophotometer at room temperature. Lifetimes were recorded using a DeltaPro TCSPC equipment from Horiba Scientific upon excitation of the samples with a 283 nm nanoLED. Luminescence quantum yields were recorded using an Absolute PL quantum yield spectrometer from Hamamatsu Photonics upon excitation of the samples at 274 and 290 nm for **1** and **2**, respectively.

Thermal analyses were carried out using an STA 409 PC Luxx thermoanalyzer (NETZSCH, Germany) in the temperature range of 30–600 °C under a N$_2$ atmosphere, with a heating rate of 10 °C min^{-1}.

Magnetic measurements were performed on solid polycrystalline samples using a Quantum Design MPMS-XL SQUID magnetometer at the Magnetic Measurements Unit of the Universitat de Barcelona. Pascal constants were used to estimate the diamagnetic corrections, which were subtracted from the experimental susceptibilities to give the corrected molar magnetic susceptibilities.

Solubility

Water solubility of **1** and **2** was measured by refluxing a suspension of 150 mg of the respective lanthanide compound in 5 mL of deionized water for 1 h. Then the mixture was allowed to cool at room temperature. After this, 3 mL of clear solution was placed in a crystallizer of known mass and allowed to evaporate. The variance in the mass of the crystallizer corresponds to the product mass that was dissolved in 3 mL of deionized water.

X-Ray crystallography

A colorless prism-like specimen of **1**, with approximate dimensions of 0.046 mm × 0.055 mm × 0.181 mm, was used for X-ray crystallographic analysis. The X-ray intensity data was measured using a D8 Venture system equipped with a multilayer monochromator and a Mo microfocus (λ = 0.71073 Å).

The frames were integrated with the Bruker SAINT software package[39] using a narrow-frame algorithm. The integration of the data using a triclinic unit cell yielded a total of 48 286 reflections to a maximum θ angle of 30.58° (0.70 Å resolution), of which 8053 were independent (average redundancy 5.996, completeness = 99.4%, R_{int} = 3.37%, R_{sig} = 2.32%) and 7500 (93.13%) were greater than $2\sigma(F^2)$. The final cell constants of a = 9.0953(8) Å, b = 11.3783(10) Å, and c = 13.6591(12) Å, α = 110.681(3)°, β = 93.121(3)°, γ = 92.453(3)°, and volume = 1317.6(2) Å^3 are based upon the refinement of the XYZ-centroids of reflections above $20\sigma(I)$. Data were corrected for absorption effects using the Multi-Scan method (SADABS).[40] The calculated minimum and maximum transmission coefficients (based on crystal size) are 0.6698 and 0.7461.

The structure was solved and refined using the Bruker SHELXTL Software Package,[41] using the space group $P\bar{1}$, with Z = 1 for the formula unit, C56H38Eu2F8O18. The final anisotropic full-matrix least-squares refinement on F2 with 385 variables converged at R_1 = 1.99%, for the observed data and wR_2 = 4.67% for all data. The goodness-of-fit was 1.104. The largest peak in the final difference electron density synthesis was 0.998 e$^-$ Å^{-3} and the largest hole was −0.754 e$^-$ Å^{-3} with an RMS deviation of 0.097 e$^-$ Å^{-3}. On the basis of the final model, the calculated density was 1.833 g cm^{-3} and F(000), 716 e$^-$.

Molecular plots were obtained using the MERCURY program.

Synthesis of the [Ln$_2$(2FBz)$_4$(2FBz)$_2$(H-2FBz)$_2$(H$_2$O)$_2$] complexes

An ethanol solution (20 mL) containing Ln(NO$_3$)$_3$·nH$_2$O (0.9 mmol) was added to an ethanol/H$_2$O (1 : 1) solution (20 mL) containing 2-fluorobenzoic acid (540.40 mg, 4 mmol) and pyridine (355.95 mg, 4.5 mmol). After the reagents were dissolved, 2-fluorobenzoic acid (270.2 mg, 2 mmol) was added. The solution was stirred for 30 minutes and then allowed to stand at room temperature. Single crystals suitable for X-ray diffraction were obtained within two weeks. The crystals were obtained by filtration and washed with ethanol.

[Eu$_2$(μ$_2$-2FBz)$_4$(2FBz)$_2$(H-2FBz)$_2$(H$_2$O)$_2$]. White crystals. Yield (%) 33. IR: 3418(br), 1666(w), 1604(s, split), 1565(m), 1528(m), 1488(w), 1454(m), 1422(m), 1381(s), 1293(m), 1250(w), 1210(m), 1164(w), 873(m) 856(m), 841(m), 808(m), 789(w), 748(s), 693(w), 655(m), 569(m) cm^{-1}. Anal. calcd (found) for C$_{56}$H$_{38}$Eu$_2$F$_8$O$_{18}$: C (%) 46.23 (46.07), H (%) 2.63 (2.39).

[Tb$_2$(μ$_2$-2FBz)$_4$(2FBz)$_2$(H-2FBz)$_2$(H$_2$O)$_2$]. White crystals. Yield (%) 55. IR: 3419(br), 1669(w), 1602(s, split), 1562(m), 1529(m), 1483(w), 1446(m), 1423(m), 1383(s), 1293(m), 1247(w), 1234(m), 1157(w), 1131(w), 1097(m), 1031(w), 951(w), 875(m), 855(m), 842(m), 808(m), 789(w), 749(s), 689(w), 649(m), 563(m) cm^{-1}. Anal. calcd (found) for C$_{56}$H$_{38}$Tb$_2$F$_8$O$_{18}$: C (%) 45.80 (45.23), H (%) 2.60 (2.50).

Conflicts of interest

The authors declare no conflicts of interest.

Acknowledgements

R. V. and A. T. acknowledge the financial support from the Ministerio de Ciencia, Innovación y Universidades (Spain), Project PGC2018-094031-B-100. L. R. and A. L. acknowledge the financial support from the Ministerio de Ciencia, Innovación y Universidades (Spain), PID2019-104121GB-I00.

References

1 (*a*) *The Rare Earth Elements: Fundamentals and Applications*, ed. D. A. Atwood, John Wiley & Sons Ltd, 2012; (*b*) *Luminescence of Lanthanide Ions in Coordination Compounds and Nanomaterials*, ed. A. de Bettencourt-Dias, John Wiley & Sons Ltd, 2014.

2 E. G. Moore, A. P. S. Samuel and K. N. Raymond, *Acc. Chem. Res.*, 2009, **42**, 542–552.

3 J.-C. G. Bünzli, *Coord. Chem. Rev.*, 2015, **19**, 293–294.

4 (*a*) Z. Xia, Z. Xu, M. Chen and Q. Liu, *Dalton Trans.*, 2016, **45**, 11214–11232; (*b*) J.-C. G. Bünzli and C. Piguet, *Chem. Soc. Rev.*, 2005, **34**, 1048–1077.

5 (*a*) J.-C. G. Bünzli, *Acc. Chem. Res.*, 2006, **39**, 53–61; (*b*) S. Swavey and R. Swavey, *Coord. Chem. Rev.*, 2009, **253**, 2627–2638.

6 S. V. Eliseeva and J.-C. G. Bünzli, *Chem. Soc. Rev.*, 2010, **39**, 189–227.

7 E. G. Moore, A. P. S. Samuel and K. N. Raymond, *Acc. Chem. Res.*, 2009, **42**, 542–552.

8 C. P. Montgomery, B. S. Murray, E. J. New, R. Pal and D. Parker, *Acc. Chem. Res.*, 2009, **42**, 925–937.

9 S. J. Butler, M. Delbianco, L. Lamarque, B. K. McMahon, E. R. Neil, R. Pal, D. Parker, J. W. Walton and J. M. Zwier, *Dalton Trans.*, 2015, **44**, 4791–4803.

10 E. J. New, D. Parker, D. G. Smith and J. W. Walton, *Curr. Opin. Chem. Biol.*, 2010, **14**, 238–246.

11 S. V. Eliseeva and J.-C. G. Bünzli, *Chem. Soc. Rev.*, 2010, **39**, 189–227.

12 A. D'Aléo, L. Ouahab, C. Andraud, F. Pointillart and O. Maury, *Coord. Chem. Rev.*, 2012, **256**, 1604–1620.

13 M. Sy, A. Nonat, N. Hildebrandt and L. J. Charbonnière, *Chem. Commun.*, 2016, **52**, 5080–5095.

14 G.-Q. Jin, Y. Ning, J.-X. Geng, Z.-F. Jiang, Y. Wang and J.-L. Zhang, *Inorg. Chem. Front.*, 2020, **7**, 289–299.

15 L. Li, X. Zhao, N. Xiao, Y. Wang, Z. Wang, S. Yang and X. Zhou, *Inorg. Chim. Acta*, 2015, **426**, 107–112.

16 V. V. Utochnikova, A. S. Kalyakina, N. N. Solodukhin and A. N. Aslandukov, *Eur. J. Inorg. Chem.*, 2019, 2320–2332.

17 A. S. Kalyakina, V. V. Utochnikova, I. S. Bushmarinov, I. M. Le-Deygen, D. Volz, P. Weis, U. Schepers, N. P. Kuzmina and S. Bräse, *Chem. – Eur. J.*, 2017, **23**, 14944–14953.

18 B. Casanovas, M. Font-Bardía, S. Speed, M. S. El Fallah and R. Vicente, *Eur. J. Inorg. Chem.*, 2018, 1928–1937.

19 B. Casanovas, S. Speed, R. Vicente and M. Font-Bardía, *Polyhedron*, 2019, **173**, 114113.

20 X. Li, Z.-Y. Zhang and Y.-Q. Zou, *Eur. J. Inorg. Chem.*, 2005, 2909–2918.

21 X. Li, Y.-Q. Zou and H.-B. Song, *J. Chem. Crystallogr.*, 2007, **37**, 555–559.

22 S. Alvarez, P. Alemany, D. Casanova, J. Cirera, M. Llunell and D. Avnir, *Chem. Soc. Rev.*, 2005, **249**, 1693–1708.

23 J. Cirera and S. Alvarez, *Dalton Trans.*, 2013, **42**, 7002–7008.

24 K. Binnemans, *Coord. Chem. Rev.*, 2015, **295**, 1–45.

25 J. W. de Oliveira Maciel, M. A. Lemes, A. K. Valdo, R. Rabelo, F. Terra Martins, L. J. Queiroz Maia, R. Costa de Santana, F. Lloret, M. Julve and D. Cangussu, *Inorg. Chem.*, 2021, **60**, 6176–6190.

26 L. Zur, *J. Mol. Struct.*, 2013, **1041**, 50–54.

27 W. D. Horrocks Jr. and D. R. Sudnick, *J. Am. Chem. Soc.*, 1979, **101**, 334–340.

28 R. M. Supkowski and W. D. W. Horrocks Jr., *Inorg. Chim. Acta*, 2002, **340**, 44–48.

29 M. H. V. Werts, R. T. F. Jukes and J. W. Verhoeven, *Phys. Chem. Chem. Phys.*, 2002, **4**, 1542–1548.

30 A. Aebischer, F. Gumy and J. C. G. Bünzli, *Phys. Chem. Chem. Phys.*, 2009, **11**, 1346–1353.

31 S. Petoud, S. M. Cohen, J.-C. G. Bünzli and K. N. Raymond, *J. Am. Chem. Soc.*, 2003, **125**, 13324–13325.

32 A. J. Kanimozhi and V. Alexander, *Dalton Trans.*, 2017, **46**, 8562–8571.

33 A. Beeby, I. M. Clarkson and R. J. Dickins, *J. Chem. Soc., Perkin Trans. 2*, 1999, 493–504.

34 J. Tang and P. Zhang, *Lanthanide Single Molecule Magnets*, New York Dordrecht London, Spring-Verlag Berlin Heidelberg, 2015.

35 B. Barja, P. Aramendia, R. Baggio, M. T. Garland, O. Peña and M. Perec, *Inorg. Chim. Acta*, 2003, **355**, 183–190.

36 A. Arauzo, A. Lazarescu, S. Shova, E. Bartolomé, R. Cases, J. Luzón, J. Bartolomé and C. Turta, *Dalton Trans.*, 2014, **43**, 12342–12356.

37 J. Legendziewicz, V. Tsaryuk, V. Zolin, E. Lebedeva, M. Borzechowska and M. Karbowiak, *New J. Chem.*, 2001, **25**, 1037–1042.

38 E. Bartolomé, A. Arauzo, J. Luzón, S. Melnic, S. Shova, D. Prodius, I. C. Nlebedim, F. Bartolomé and J. Bartolomé, *Dalton Trans.*, 2019, **48**, 5022–5034.

39 SAINT Version 7.68A, Bruker AXS Inc., 2009.

40 SADABS Version 2008/1, Sheldrick, Bruker AXS Inc.

41 SHELXT, LG. M. Sheldrick, *Acta Crystallogr., Sect. A: Found. Adv.*, 2008, **64**, 112–122.

Dalton Transactions

ROYAL SOCIETY OF CHEMISTRY

PAPER

View Article Online
View Journal | View Issue

Cite this: *Dalton Trans.*, 2023, **52**, 1122

Luminescence, CPL and magnetic properties of 1D enantiopure Ln^{3+} complexes with (*S*-) and (*R*-) α-methoxyphenylacetate ligand†

Ànnia Tubau,[a] Francesco Zinna, [b] Lorenzo Di Bari, *[b] Mercè Font-Bardía[c] and Ramon Vicente *[a]

Received 17th October 2022,
Accepted 12th December 2022

DOI: 10.1039/d2dt03356a

rsc.li/dalton

The reaction of $Ln(NO_3)_2 \cdot 6H_2O$ (Ln = Eu, Tb, Dy and Sm) with (*R*)-(−)-α-methoxyphenylacetic acid (***R*-HMPA**) and 1,10-phenanthroline (phen) in EtOH/H_2O allows the isolation of 1D chiral compounds of formula $[Ln(\mu\text{-}R\text{-MPA})(R\text{-MPA})_2(\text{phen})]_n$ in which Ln = Eu (***R*-Eu**), Tb (***R*-Tb**), Dy (***R*-Dy**) and Sm (***R*-Sm**). The same synthesis by using (*S*)-(+)-α-methoxyphenylacetic acid (***S*-HMPA**) instead of (*R*)-(−)-α-methoxyphenylacetic acid allows the isolation of the enantiomeric compounds with formula $[Ln(\mu\text{-}S\text{-MPA})(S\text{-MPA})_2(\text{phen})]_n$ where Ln = Eu (***S*-Eu**), Tb (***S*-Tb**), Dy (***S*-Dy**) and Sm (***S*-Sm**). Single crystal X-Ray diffraction measurements were performed for compounds ***R*/*S*-Eu**, ***R*/*S*-Tb**, ***S*-Dy** and ***S*-Sm**. The luminescence and the circular dichroism measured in the solid state are reported. All compounds show sensitized luminescence, notably the Eu^{3+} and Tb^{3+} ones, whose emission color can be perceived by the naked eye. For the Eu^{3+} and Tb^{3+} derivatives the quantum yield and the circular polarized luminescence have been measured. For the magnetic allowed transition $^5D_0 \rightarrow {}^7F_1$ of the Eu^{3+} compound, the anisotropy factor g_{lum} is ±0.013 (+for ***S*-Eu**). Also, magnetic properties of all compounds were studied with the Dy^{3+} analogue showing slow relaxation of the magnetization under a direct current magnetic field of 1000 Oe.

Introduction

Lanthanide(III) compounds are currently mainly studied for their peculiar magnetic and luminescent properties derived from their partially filled 4f valence shell. Regarding magnetic properties, since the discovery of the first mononuclear lanthanide complexes of formula $[Pc_2Ln]^- \cdot TBA^+$ (Ln = Tb, Dy; Pc = dianion of phthalocyanine; TBA$^+$ = tetrabutylammonium) showing slow magnetization relaxation and acting as single molecule magnets (SMMs),[1] a plethora of mono and polynuclear SMMs complexes derived from lanthanide ions with large orbital momentum and strong magnetic anisotropy have been reported.[2] On the other hand, lanthanide(III) complexes with luminescence properties are of interest due to their applications in materials and biosciences.[3] The preparation of chiral lanthanide(III) coordination compounds is of high current interest to achieve circularly polarized luminescence (CPL)[4] for applications in circularly polarized organic light-emitting diodes (CP-OLEDs),[5] biological sensing[6] and anti-counterfeiting devices.[7] Moreover, CPL active lanthanide complexes are studied in the context of molecular magnetism.[8]

The chiral ligands naturally induce a dissymmetric environment around the Ln^{3+} ion, which determines the onset of chiroptical properties allied to the f–f transitions of the ion. In emission this is sensitively monitored through CPL, which can be conveniently quantified by means of the dissymmetry factor g_{lum}, eqn (1):

$$g_{\text{lum}} = 2\frac{I_L - I_R}{I_L + I_R} = 2\frac{\Delta I}{I} \quad (1)$$

where I_L and I_R are the left and right circularly polarized components of the emission of the compound.

Usually, non-aggregated organic molecules or d-metal complexes display g_{lum} factors of the order of 10^{-4}–10^{-3},[9] while lanthanide complexes may show much higher values (10^{-1}–1.4).[10] Usually, CPL is measured for mononuclear Eu^{3+} com-

---

[a] *Departament de Química Inorgànica i Orgànica, Secció de Química Inorgànica, Universitat de Barcelona, Martí i Franquès 1-11, 08028 Barcelona, Spain. E-mail: rvicente@ub.edu*

[b] *Dipartimento di Chimica e Chimica Industriale, Università di Pisa, via Moruzzi 13, I 56124 Pisa, Italy. E-mail: lorenzo.dibari@unipi.it*

[c] *Departament de Mineralogia, Cristal lografia i Dipòsits Minerals and Unitat de Difracció de Raigs X. Centres Científics i Tecnològics de la Universitat de Barcelona (CCiTUB). Universitat de Barcelona, Solé i Sabarís 1-3, 08028 Barcelona, Spain*

† Electronic supplementary information (ESI) available. CCDC 2191286 (***S*-Dy**), 2191287 (***R*-Eu**), 2191288 (***R*-Tb**), 2191289 (***S*-Tb**), 2191290 (***S*-Sm**) and 2191291 (***S*-Eu**). For ESI and crystallographic data in CIF or other electronic format see DOI: https://doi.org/10.1039/d2dt03356a

plexes, while it is more rarely investigated for complexes with higher nuclearity, such as binuclear helicates[11] or trinuclear[12] and heptanuclear[13] systems.

Recently[14] we have used the chiral bidentate bridging carboxylate ligands generated from (*S*)-(+)- or (*R*)-(−)-2-phenylpropionic acid and *S*-(+)- and *R*-(−)-2-(6-methoxy-2-naphthyl)propionic acid to synthesize two series of enantiomeric pure dinuclear 4f-metal ion complexes of formula [Ln_2(*S*-L)$_6$(phen)$_2$] or [Ln_2(*R*-L)$_6$(phen)$_2$] (HL = chiral carboxylic acid) by adding simultaneously neutral chelating 1,10-phenanthroline (phen) ligands which block two coordination sites per Ln^{3+} ion and terminate further aggregation. The 1,10-phenanthroline ligands have also the role to sensitize the luminescence of the lanthanide ion, through the so-called antenna effect. In fact, because of the weak f–f absorption of trivalent lanthanide ions, a suitable chromophoric organic ligand should be employed to populate the lanthanide emitting states through an energy transfer process.[15]

For the published *R* and *S* complexes of formula [Eu_2(2-phenylpropionate)$_6$(phen)$_2$] and [Eu_2([2-(6-methoxy-2-naphthyl) propionate])$_6$(phen)$_2$], the analysis of the data yielded values of g_{lum} factors for $^5D_0 \rightarrow {}^7F_1/{}^7F_2$ transitions around $g_{\text{lum}} = \pm 1 \times 10^{-2}$ and $g_{\text{lum}} = \pm 1 \times 10^{-3}$ respectively.[14]

With the aim to obtain new lanthanide compounds in which luminescent, chiroptical and magnetic properties could coexist, and therefore, obtain multifunctional materials, we present herein the structural, magnetic and optical studies of eight new chiral lanthanide coordination complexes derived from the use of the pure enantiomeric *R*- or *S*-species of the α-methoxyphenylacetic acid (***R***- and ***S*-HMPA** respectively, (Scheme 1)) and the auxiliary ligand 1,10-phenanthroline. The reaction of the above ligands with the respective nitrate lanthanide salts lead to new 1D complexes with the formula [Ln(μ-*R*-MPA)(*R*-MPA)$_2$(phen)]$_n$ or [Ln(μ-*S*-MPA)(*S*-MPA)$_2$(phen)]$_n$ for ***R***- or ***S*-HMPA** respectively (Ln = Eu, Tb, Dy and Sm). The presence of the methoxy group in the α-methoxyphenylacetate ligand induces the formation of a 1D polymeric chain along the *a* axis instead of the dinuclear compounds of formula [Ln_2(*R*/*S*-L)$_6$(phen)$_2$] found for the previous chiral compounds published by our group where *R*/*S*-L = *R*/*S*-2-phenylpropionic acid and *R*/*S*-2-(6-methoxy-2-naphthyl)propionic acid.[14]

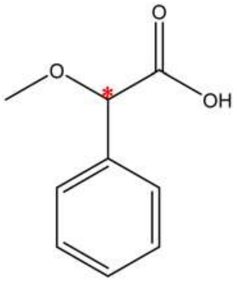

Scheme 1 *R*/*S*-α-Methoxyphenylacetic acid (***R*/*S*-HMPA**).

Experimental section

Starting materials

$Ln(NO_3)_3 \cdot 6H_2O$ salts, (*S*)-(+)- or (*R*)-(−)-α-methoxyphenylacetic acid and 1,10-phenantroline (Aldrich) were used as received.

Synthesis of 1D complexes [Ln(μ-*R*/*S*-MPA)(*R*/*S*-MPA)$_2$(phen)]$_n$. Into 20 mL of an ethanol/water solution in the 1 : 1 ratio, the respective *R*/*S*-α-methoxyphenilacetic acid (1.5 mmol, 249 mg) and KOH (1.5 mmol, 84.2 mg) were dissolved. Then, 1,10-phenantroline (0.3 mmol, 54 mg) dissolved in 5 mL of ethanol/water (1 : 1) was added. Afterward, a solution (5 mL) in the same ethanol/water ratio with the $Ln(NO_3)_3 \cdot nH_2O$ salt (0.22 mmol) was added dropwise into the reaction mixture. The colorless solution was magnetically stirred for 1 h and then left to stand at room temperature. After 1 week, needle shaped white single crystals suitable for monocrystal X-Ray diffraction appeared. Anal. Calc. (%) for ***R*-Eu** C, 56.6; H, 4.3; N, 3.4, found: C, 57,0; H, 4.4; N, 3.4. Calc(%) for ***S*-Eu** C, 56.6; H, 4.3; N, 3.4, found: C, 56.6; H, 4.6; N, 3.4. Calc. (%) for ***R*-Tb** C, 56.1; H, 4.2; N, 3.4, found: C, 56.5; H, 4.4; N, 3.4. Calc(%) for ***S*-Tb** C, 56.1; H, 4.2; N, 3.4, found: C, 56.2; H, 4.3; N, 3.4. Calc. (%) for ***R*-Sm** C, 56.7; H, 4.3; N, 3.4, found: C, 57,0; H, 4.3; N, 3.4. Calc(%) for ***S*-Sm** C, 56.7; H, 4.3; N, 3.4, found: C, 56.5; H, 4.4; N, 3.4. Calc. (%) for ***R*-Dy** C, 55.9; H, 4.2; N, 3.3, found: C, 56.2; H, 4.2; N, 3.3. Calc(%) for ***S*-Dy** C, 55.9; H, 4.2; N, 3.3, found: C, 56.2; H, 4.2; N, 3.3. Selected IR bands (KBr pellet, cm^{-1}, Fig. S1†) 3083–2817 (w), 1608 (m), 1552 (s), 1509 (m), 1400 (s), 1326 (w), 1196 (m), 1100 (m), 1065 (m), 987 (m), 839 (m), 713 (s, split), 635(m) for ***R*-Eu**, 3086–2817 (w), 1613 (m), 1557 (s), 1509 (m), 1404 (s), 1317 (w), 1200 (m), 1096 (m), 1065 (m), 983 (m), 839 (m), 713 (s, split), 635 (m) for ***S*-Eu**, 3091–2817 (w), 1613 (m), 1561 (s), 1509 (m), 1404 (s), 1330 (w), 1200 (m), 1096 (m), 1070 (m), 983 (m), 839 (m), 717 (s, split), 635 (m) for ***R*-Tb**, 3091–2817 (w), 1613 (m), 1557 (s), 1509 (m), 1404 (s), 1330 (w), 1200 (m), 114 (m), 1065 (m), 991 (m), 839 (m), 717 (s, split), 635 (m) for ***S*-Tb**, 3091–2817 (w), 1609 (m), 1552 (s), 1509 (m), 1396 (s), 1326 (w), 1200 (m), 1100 (m), 165 (m), 983 (m), 843 (m), 713 (s, split), 635 (m) for ***R*-Sm**, 3091–2813 (w), 1609 (m), 1574 (s), 1509 (m), 1396 (s), 1322 (w), 1196 (m), 1104 (m), 1065 (m), 991 (m), 839 (m), 713 (s, split), 635 (m) for ***S*-Sm**, 3087–2817 (w), 1617 (m), 1569 (s), 1513 (m), 1396 (s), 1326 (w), 1204 (m), 1096 (m), 1065 (m), 983 (m), 839 (m), 717 (s, split), 635 (m) for ***R*-Dy** and 3087–2817 (w), 1617 (m), 1569 (s), 1513 (m), 1396 (s), 1326 (w), 1204 (m), 1096 (m), 1065 (m), 983 (m), 839 (m), 717 (s, split), 635 (m) for ***S*-Dy**.

IR and magnetic measurements

Infrared spectra (4000–400 cm^{-1}) were recorded from KBr pellets on a PerkinElmer 380-B spectrophotometer.

Magnetic measurements were performed on solid polycrystalline samples with a Quantum Design MPMS-XL SQUID magnetometer at the Magnetic Measurements Unit of the University of Barcelona. Pascal's constants were used to estimate the diamagnetic corrections, which were subtracted from the experimental susceptibilities to give the corrected molar magnetic susceptibilities.

Luminescence properties

Solid state fluorescence spectra of compounds were recorded on a Horiba Jobin Yvon SPEX Nanolog fluorescence spectrophotometer (Fluorolog-3 v3.2, HORIBA Jobin Yvon, Cedex, France) equipped with a three slit double grating excitation and emission monochromator with dispersions of 2.1 nm mm^{-1} (1200 grooves per mm) at room temperature. The steady-state luminescence was excited by unpolarized light from a 450 W xenon CW lamp and detected at an angle of 22.5° for solid state measurement by a red-sensitive Hamamatsu R928 photomultiplier tube. The equipment was adjusted to obtain the highest background-to-noise ratio. Spectra were corrected for both the excitation source light intensity variation (lamp and grating) and the emission spectral response (detector and grating).

The excited state decay curves were measured in the same instrument in the phosphorescence mode using a 450 W xenon pulsed lamp (λ = 371 nm, 1.5 ns pulse). The measured decays were analyzed using the Origin software package. Both decay curves fitted monoexponentially: $I(t) = I_0 \exp\left(-\frac{t}{\tau_{\mathrm{obs}}}\right)$. The fit quality was determined by the χ^2 method of Pearson. Absolute quantum yield (Φ_{TOT}) measurements were acquired in the G8 Quantum Integrating Sphere from GMP with an interior reflective coating made of Spectralon®. Then the Φ_{TOT} was calculated following eqn (2):

$$\Phi = \frac{E_{\mathrm{c}} - E_{\mathrm{c}}(\mathrm{blank})}{L_{\mathrm{a}} - L_{\mathrm{c}}} \tag{2}$$

L_{a} is the calculated area of the outgoing amount of light without interaction with a sample (blank) at the used λ_{exc} and L_{c} after interaction with the sample. E_{c} refers to the calculated area from the emission spectrum of the sample and E_{c} (blank) from the emission spectrum of the blank. Band pass of 0.3 nm for the QY measurements and of 0.5 nm for lifetime measurements were employed in order to not surpass the 10^6 CPS to make sure that we are not measuring in the non-linear optic zone, otherwise the results would not be correct.

Chiroptical spectroscopy measurements

ECD spectra. ECD spectra were recorded with a Jasco J-1500 spectropolarimeter on the polycrystalline samples dispersed in a KBr matrix. In order to check for and minimize contributions from linear dichroism/linear birefringence, for each sample, different spectra were recorded rotating the sample by 180° around the optical axis and then all the spectra were averaged.

CPL spectra. The circularly polarized luminescence experiments for compounds ***S*/*R*-Eu** and ***S*/*R*-Tb** were carried out with a home-built CPL spectrofluoropolarimeter[16] that acquires simultaneously the luminescence and CPL data, under UV irradiation ($\lambda_{\max}$ = 254 nm) on quartz plate depositions. The depositions of the complexes were obtained from *n*-pentane dispersions. *N*-pentane was chosen as a dispersant as it does not dissolve the compounds and in this way the complexes are deposited as a microcrystalline powder film. Several spectra were acquired rotating the sample by ±45° around the optical axis and by flipping the sample by 180° around the axis perpendicular to the collection beam.

X-ray crystallography. Good quality crystals of ***R*/*S*-Eu**, ***R*/*S*-Tb**, ***S*-Dy** and ***S*-Sm** were selected and mounted on a D8VENTURE (Bruker) diffractometer with CMOS detector. The crystallographic data, conditions retained for the intensity data collection, and some features of the structure refinements are listed in Table S1.† All the structures were refined by the least-squares method. Intensities were collected with a multilayer monochromated Mo-Kα radiation. Lorentz polarization and absorption corrections were made for the ***R*/*S*-Eu**, ***R*/*S*-Tb**, ***S*-Dy** and ***S*-Sm** crystal measurements. The structures were solved by direct methods, using the SHELXS-97 computer program[17] and refined by full-matrix least-squares method, using the SHELXL-2014 computer program.[18] The non-hydrogen atoms were located in successive difference Fourier syntheses and refined with anisotropic thermal parameters on F^2. For hydrogen atoms isotropic temperature factors have been assigned as 1.2 respective of the C atom in which the H is attached.

Results and discussion

General syntheses

A straightforward room temperature synthetic route using the *R*/*S*-α-methoxyphenylacetic acid (HMPA), 1,10-phenantroline (phen) and $\mathrm{Ln(NO_3)_3{\cdot}H_2O}$ (Ln = Eu ***R*/*S*-Eu**, Tb ***R*/*S*-Tb**, Dy ***R*/*S*-Dy** and Sm ***R*/*S*-Sm**) with further slow evaporation of the solvent, lead to enantiopure chiral *R*/*S*-$[\mathrm{Ln}(\mu\text{-MPA})(\mathrm{MPA})_2(\mathrm{phen})]_n$ 1D chain compounds. Several trials were carried out before concluding that the best conditions for obtaining single crystals suitable for monocrystal X-Ray diffraction were by using an excess of the ***R*/*S*-HMPA** ligand with $\mathrm{H_2O}$/EtOH in a 1 : 1 (v/v) proportion as the solvent.

Molecular structures of the *R*/*S*-[Ln(μ-MPA)(MPA)$_2$(phen)]$_n$ compounds. Single crystal X-Ray diffraction measurements were performed for compounds ***R*/*S*-Eu**, ***R*/*S*-Tb**, ***S*-Dy** and ***S*-Sm**. All the compounds crystallize in the monoclinic $P2_1$ space group. The asymmetric unit of ***R*/*S*-Ln** consists of a unit formed by one Ln^{3+} ion, two chelating *R*/*S*-α-methoxyphenylacetate (*R*/*S*-MPA) ligands, one *R*/*S*-MPA bridging ligand and one phen molecule. The asymmetric unit is expanded in space forming a 1D polymeric chain along the crystallographic *a* axis.

All the Ln^{3+} compounds are isostructural as it is seen in the powder X-Ray diffraction spectra (Fig. S2†), also, affirming the pure phase and crystallinity of the compounds. Therefore, only the new compound ***R*-Eu** will be discussed.

A partially labelled plot of the structure of compound ***R*-Eu** is shown in Fig. 1 and the mirror image of ***R*/*S*-Eu** compounds is depicted in Fig. 2. Selected bond distances of ***R*/*S*-Eu**, ***R*/*S*-Tb**, ***S*-Dy** and ***S*-Sm** and crystallographic information are listed in Table 1 and Table S1† respectively.

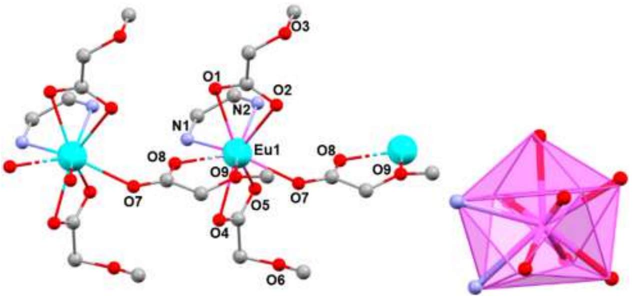

Fig. 1 Left, partially labeled plot of compound ***R*-Eu**. Phenyl groups and H atoms have been omitted for a better view of the 1D structure. Right, idealized coordination polyhedron (spherical tricapped trigonal prism) compared with the real positions of the coordinating atoms of compound ***R*-Eu**.

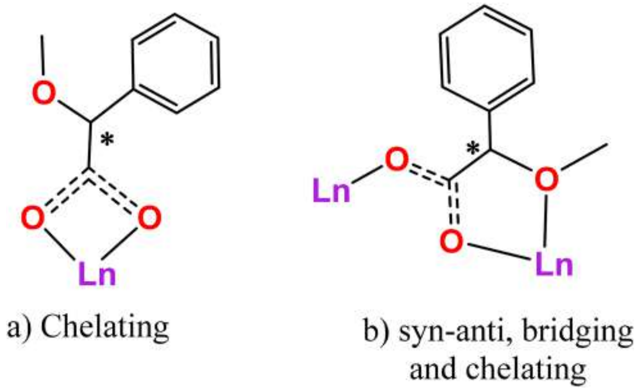

a) Chelating

b) syn-anti, bridging and chelating

Scheme 2 Coordination modes of *R*/*S*-α-methoxyphenylacetate.

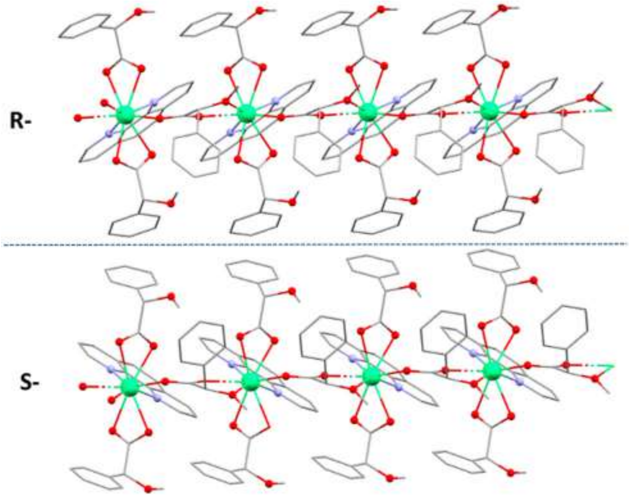

Fig. 2 Compounds ***R*-** and ***S*-Eu** presented as the mirror image of each other.

The structure consists of a polymeric 1D chain of formula [Eu(μ-*R*-MPA)(*R*-MPA)$_2$(phen)]n where each Eu^{3+} is nonacoordinated. The polymeric chain extends along the [1 0 0] direction. The EuO$_7$N$_2$ coordination sphere encompasses two *R*-MPA ligands that are coordinated in the bidentate carboxylate chelating coordination mode (Scheme 2a) to Eu1 by the O1, O2 and O7, O8 atoms, with Eu–O distances in the range of 2.450–2.500 Å. Another *R*-MPA ligand is bridging two Eu^{3+} through the O7 and O8 atoms from the carboxylate group in the syn-anti conformation (Scheme 2b). The O9 oxygen atom from the methoxy group of this *R*-MPA ligand coordinates also to the neighbouring europium atom. The Eu–O7, Eu–O8 and Eu–O9 distances are 2.396, 2.388 and 2.539 Å respectively. Finally, the coordination sphere of the lanthanide ion is completed by two N atoms (N1 and N2) from the 1,10-phenantroline molecule in the chelating coordination mode with Eu–N distances of 2.569 and 2.558 Å for Eu–N1 and Eu–N2 respectively. The Eu1⋯Eu1_a intrachain distance is 6.048 Å and the shortest interchain distance is 12.298 Å. The crystal structure of ***S*-Eu** is very similar to ***R*-Eu** but its configuration is mirror symmetrical with ***R*-Eu**. Symmetry operators for generating equivalent positions are: (a) $-1 + x, y, z$.

The SHAPE software,[19] was used to determine the degree of distortion of the coordination polyhedron in compound ***R*-Eu**. It consists of a distorted polyhedron between the spherical tricapped trigonal prism (D_{3h}), spherical capped square antiprism (C_{4v}) and muffing (C_s) geometries with Continuous Shape measurements (CShM) of 1.821, 2.084 and 2.075 respectively (Fig. 1, right). The degree of distortion of the coordination geometry of the other compounds is shown in Table S2.†

Table 1 Selected bond distances (Å) for ***R*/*S*-Eu**, ***R*/*S*-Tb**, ***S*-Dy** and ***S*-Sm**

Bond distance (Å)	*R*-Eu	*S*-Eu	*R*-Tb	*S*-Tb	*S*-Dy	*S*-Sm
Ln–O1	2.500(5)	2.478(3)	2.417(2)	2.461(3)	2.456(6)	2.461(2)
LnO2	2.489(5)	2.445(4)	2.4601(18)	2.416(3)	2.464(5)	2.4891(19)
Ln–O4	2.450(6)	2.489(3)	2.4740(18)	2.470(3)	2.395(6)	2.510(2)
Ln–O5	2.476(5)	2.498(3)	2.4674(19)	2.475(3)	2.453(5)	2.4988(18)
Ln–O7	2.396(5)	2.394(3)	2.3688(18)	2.371(2)	2.364(4)	2.4050(19)
Ln–O8	2.388(4)	2.395(2)	2.3639(13)	2.365(2)	2.356(5)	2.4039(19)
Ln–O9	2.539(5)	2.540(3)	2.525(19)	2.521(3)	2.513(5)	2.557(2)
Ln–N1	2.569(5)	2.564(4)	2.545(2)	2.537(3)	2.527(7)	2.583(2)
Ln–N2	2.558(6)	2.567(4)	2.538(2)	2.545(4)	2.523(6)	2.582(2)
Ln⋯Ln (intrachain)	6.048(5)	6.047(4)	6.054(8)	6.036(4)	6.025(4)	6.052(3)
Ln⋯Ln shortest interchain distance	12.298	12.310	12.312	12.326	12.353	12.297

The Ln–O and Ln–N bond lengths diminish following $Sm^{3+} > Eu^{3+} > Tb^{3+} > Dy^{3+}$, confirming the lanthanide(III) contraction tendency along the 6th period.[20]

Luminescence properties

Luminescence properties of all compounds were studied and measured in the solid state at room temperature. Since each enantiomer pair shows the same luminescence properties, only the *R*-enantiomer of each lanthanide is discussed in this section. The excitation and absorbance spectra measured in the solid state of the enantiomers of each compound are displayed in Fig. S3 and S4.†

Excitation spectra were recorded at the emission wavelength (λ_{em}) of 614 nm ($^5D_0 \rightarrow {}^7F_2$) for ***R*-Eu**, at 546 nm ($^5D_4 \rightarrow {}^7F_5$) for ***R*-Tb**, at 572 nm ($^4F_{9/2} \rightarrow {}^6H_{13/2}$) for ***R*-Dy** and at 644 nm ($^4G_{5/2} \rightarrow {}^6H_{9/2}$) for ***R*-Sm**. The four spectra show an intense and broad band around 300 to 360 nm corresponding to the $\pi \rightarrow \pi^*$ and $n \rightarrow \pi^*$ ligand centred excitation transitions from the *R*-MPA and phen ligands. Only for compound ***R*-Eu**, excitation arising from Eu f–f transitions could be discerned at 375, 395 and 464 nm corresponding to $^5D_4 \rightarrow {}^7F_0$, $^5L_6 \rightarrow {}^7F_0$ and $^5D_2 \rightarrow {}^7F_0$ respectively. Room temperature emission spectra of ***R*-Eu**, **Tb**, **Dy** and **Sm**, were obtained by employing an excitation wavelength (λ_{exc}) of 330 nm.

In the emission spectra of ***R*-Eu**, (Fig. 3a) different bands can be observed at 580, 595, 614, 650 and 691 nm corresponding to the $^5D_0 \rightarrow {}^7F_{J=0-4}$ transitions. $^5D_0 \rightarrow {}^7F_0$ corresponds to a forbidden transition ($\Delta J = 0$), therefore its intensity is very low and in this case is almost imperceptible. The magnetically allowed $^5D_0 \rightarrow {}^7F_1$ transition, with intensity independent of the environment, is split due to the crystal field. For a coordination geometry with symmetry lower than cubic, hexagonal, trigonal and tetragonal (meaning D_{2h}, D_2, C_{2v}, C_{2h}, C_2, C_s, S_2 or C_1), the degeneracy is lifted up to $2J + 1$ m_j components due to crystal field splitting. For the $^7F_1$ state, m_j values are $2J + 1 = 3$ and for the presented Eu^{3+} compound, all the three components can be discerned in the emission spectra. This result is consistent with the structural characterization of ***R*-Eu** since the calculated ideal coordination polyhedron with less distortion with respect to the experimental, presents a distortion between the D_{3h}, C_{4v} but also with the low symmetry *Cs* point group. Furthermore, $^5D_0 \rightarrow {}^7F_2$ is the most intense band located in the red range and responsible for the red-orange emission colour that could be seen by the naked eye for ***S*-Eu**, Fig. S5.† This band is a hypersensitive transition,

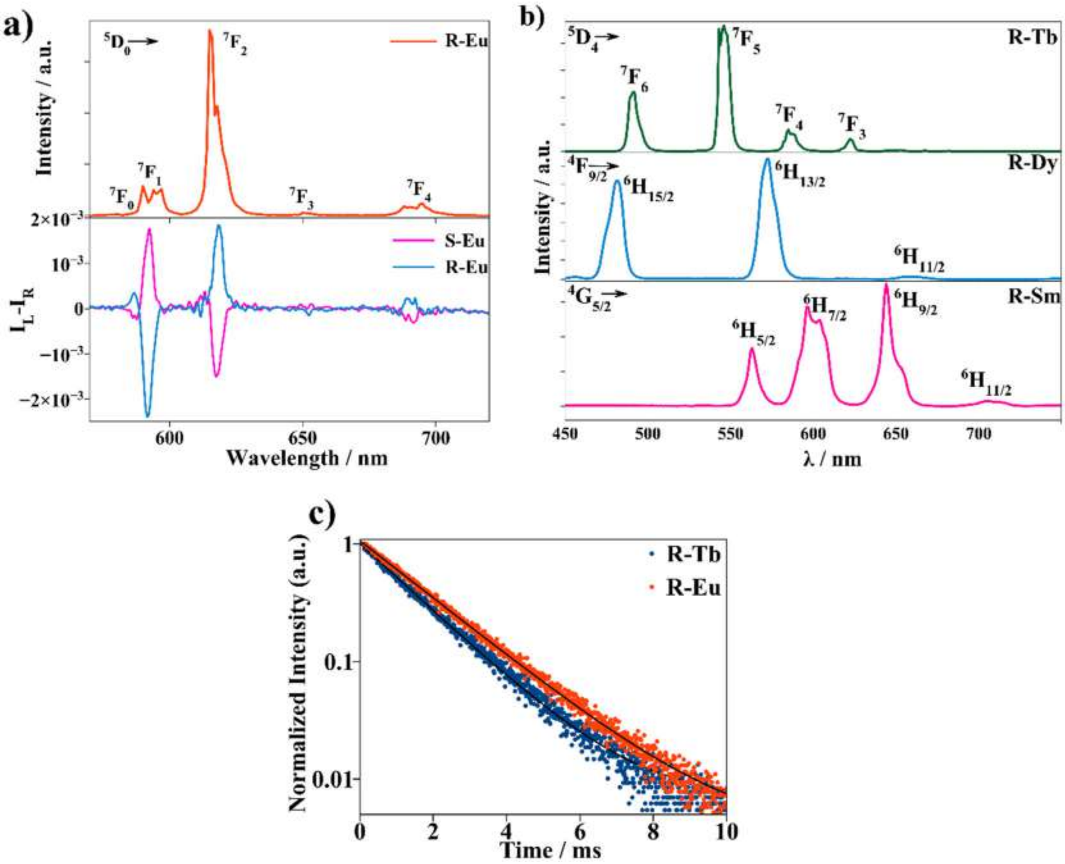

Fig. 3 (a) Emission spectra of compound ***R*-Eu** (λ_{exc} = 330 nm). Bottom, CPL spectra of ***S***- and ***R*-Eu** enantiomers. (b) Emission spectra for complexes ***R*-Tb**, ***R*-Dy** and ***R*-Sm** recorded at λ_{exc} = 330 nm. (c) Lifetimes curves for compounds ***R*-Tb** and ***R*-Eu**. Solid lines represents mono-exponential fittings.

and in the case of ***S*-Eu**, its splitting indicates that the lanthanide ion is not occupying an inversion symmetry site inside the structure.[21]

The ***R*-Tb** compound shows green emission that could be seen by the naked eye (Fig. S5†). The bands arising from the f–f Tb^{3+} transitions can be differentiated at 491, 546, 585 and 623 nm corresponding to the $^5D_4 \rightarrow {}^7F_{J\,=\,6\text{–}3}$ transitions (Fig. 3b).

In the visible range, the bands arising from the ***R*-Dy** compounds can be observed at 481 nm, corresponding to the magnetically allowed $^4F_{9/2} \rightarrow {}^6H_{15/2}$ transition, at 572 nm, corresponding to the $^4F_{9/2} \rightarrow {}^6H_{13/2}$ transition and at 659 nm (weak band) corresponding to the $^4F_{9/2} \rightarrow {}^6H_{11/2}$ transition. Furthermore, in the near infrared (NIR) range, two bands can be observed at 996 and 1144 nm (Fig. S6†), which are assigned to the transitions from the $^4F_{9/2}$ energy level to $^6F_{7/2}$ and $^6F_{5/2}$ respectively.

For the ***R*-Sm** compound, four bands are identified at 563, 600, 644 and 705 nm in the visible range and assigned to the $^4G_{5/2} \rightarrow {}^6H_{5/2\text{–}11/2}$ transitions (Fig. 3b), furthermore, in the NIR range, the $^4G_{5/2} \rightarrow {}^6H_{15/2}$ transition can be seen as a shoulder at 896 nm. The f–f emission transitions arising from the $^4G_{5/2}$ emitting level to the $^6F_{5/2\text{–}9/2}$ energy states are found at 940, 1016 and 1166 nm respectively (Fig. S7†).[3a,20]

The excitation at the ligand absorption wavelengths for all compounds induced the expected emission bands corresponding to the characteristic f–f transitions from each lanthanide ion. Also, below 450 nm, no emission from the ligands is detected, indicating that energy transfer from the excited states of the organic moieties to the emitting energy level of the respective lanthanide (the antenna effect) takes place for these compounds.[20] Nonetheless, the overall quantum yield (ϕ^{L}_{Ln}), that is the ratio of the photons emitted by the lanthanide to the photons absorbed by the ligand, was measured with an integrating sphere with the intention to better understand the luminescent efficiency of the presented compounds. For ***S*-Eu** the absolute quantum yield resulted to be 0.14. The photoluminescence time decay was recorded at the λ_{ex} of 330 nm and collecting the measurement at 614 nm, corresponding to the $^5D_0 \rightarrow {}^7F_2$ transition. The curve of the intensity against time (ms), showed in Fig. 3c, was fitted using a mono-exponential equation (see Experimental section) with a decay time (τ_{obs}) of 1.77 ms for the Eu^{3+} compound, confirming that the red emission of ***S*-Eu** comes from a single emitting centre and a single radiative deactivation process. In addition, more information about the sensitization mechanism that takes place for this system can be determined for the Eu^{3+} compound. The sensitization efficiency (η_{sens}) accounts to the percentage of energy absorbed by the chromophore ligands transferred to the excited state of the lanthanide ion and it is an important factor in the overall quantum yield that can be defined as: $\phi^{L}_{Ln} = \eta_{sens}\cdot\phi^{Ln}_{Ln}$. The other step that elucidates the ϕ^{L}_{Ln} is the intrinsic quantum yield (ϕ^{Ln}_{Ln}) that refers to the quantum yield once the emitting level of the Ln^{3+} ion is populated. The intrinsic quantum yield is described as the ratio between the measured time decay and the radiative lifetime $\phi^{Ln}_{Ln} = \dfrac{k_{rad}}{k_{rad} + k_{non\text{-}rad}} = \dfrac{\tau_{obs}}{\tau_{rad}}$. Due to the pure magnetic dipole character of the $^5D_0 \rightarrow {}^7F_1$ transition, a simplified equation can be used to calculate the τ_{rad} from Eu^{3+} $^5D_0$ excited state, corresponding to the lifetime in absence of non-radiative deactivations (eqn (S1)†).[21] For ***S*-Eu**, τ_{rad} is 3.05 ms. Therefore, the ϕ^{Ln}_{Ln} is 0.58. As expected, it is higher than the measured ϕ^{L}_{Ln}, because the intrinsic quantum yield do not depend on the efficiency of the ligand to Ln energy transfer, however, it takes into account deactivation mechanisms such as back-transfer energy or other quenching effects. Finally, the calculated η_{sens} results of 0.24 evidencing a sensitization effect that is rather low, nevertheless it is enough for ***S*-Eu** to present the desired optical properties.[21,22]

On the other hand, the measured ϕ^{L}_{Ln} for the ***S*-Tb** sample was higher than the Eu^{3+} analogue, yielding 0.33. Moreover, the luminescence lifetime was measured by monitoring the emission decay at 546 nm, corresponding to the more intense emission band $^5D_4 \rightarrow {}^7F_5$, Fig. 3c. The τ_{obs} calculated from the monoexponential fitting is 1.50 ms, confirming also the presence of one type of emitting specie and emission mechanism.

For ***R*-Dy** and ***R*-Sm**, the QY and the luminescent time decay were not measured due to the low emission intensity of the compounds.

Circular dichroism (CD) and circular polarized luminescence (CPL) measurements. The Circular Dichroism (CD) measurements were carried out in solid state on pellets containing the sample dispersed in a KBr matrix. The complexes show rather weak Cotton effects (Fig. 4). The bands around 200–460 nm are assigned mainly to the absorption of the phen ligand, with contributions from the $\pi \rightarrow \pi^*$ transition of MPA. Spectra of the free ligand are found in Fig. S8.† For these 1D lanthanide chains the ligand arrangement formed by the MPA and phen ligands are organized in the space around the metal ion conferring low dissymmetry to the complex and leading to the weak CD associated to the ligand-centered electronic transitions.

Circular Polarized Luminescence (CPL) measurements were performed for ***R*/*S*-Eu** and ***R*/*S*-Tb**. The samples were deposited in a quartz plate, from a suspension in *n*-pentane, which acts only as a dispersing agent, considering that the compounds are not soluble in this solvent. The emission spectra recorded simultaneously with CPL spectra were not significantly different from those measured on the polycrystalline samples (see above). This suggests that *n*-pentane does not induce any change to the complexes (Fig. S9†). The CPL spectra of compounds ***R*/*S*-Eu** recorded at the excitation wavelength of 254 nm are depicted in Fig. 3a, bottom. The Eu^{3+} enantiomeric pairs show low intensity CPL signal, nevertheless, the mirror image bands corresponding to $^5D_0 \rightarrow {}^7F_1$, $^7F_2$ and $^7F_4$ Eu(III) f–f transitions can be clearly discerned. The magnetic dipole transition, $^5D_0 \rightarrow {}^7F_1$, at 595 nm is the most intense one. Two well resolved components due to crystal field can be observed. The m_J component located in the higher energy region of the transition shows a splitting that appears as a bifid structure revealing the three crystal field splitting components. Next, at

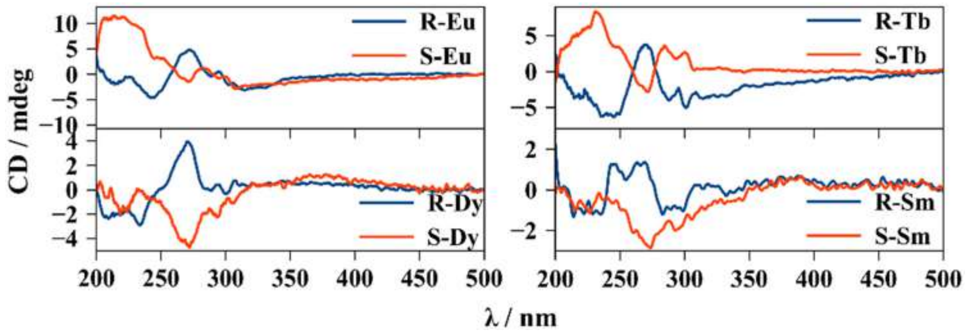

Fig. 4 Circular dichroism spectra of compounds ***R***/***S*-Eu**, ***R***/***S*-Tb**, ***R***/***S*-Dy** and ***R***/***S*-Sm** measured in the solid state.

614 nm the $^5D_0 \rightarrow {}^7F_2$ transition shows lower intensity and only one component is well differentiated. Finally, at 691 nm, the $^5D_0 \rightarrow {}^7F_4$ transition appears with very low intensity, though at least two m_j components can be differentiated. The dissymmetry factor could be quantified (Eq.1) for the $^5D_0 \rightarrow {}^7F_1$ and $^5D_0 \rightarrow {}^7F_2$ transitions leading to a $g_{\text{lum}} = \Delta I/I$ of ±0.013 (+for ***S*-Eu**) for the $^5D_0 \rightarrow {}^7F_1$ transition and ±0.003 (+for the ***R*-Eu** enantiomer) for the hypersensitive transition (Table 2). The presented g_{lum} values are similar to other reported Eu^{3+} coordination compounds with carboxylate ligands and to other Eu^{3+} polymeric chain complexes measured in the solid state.[14,23] CPL measurements were performed for the ***S***/***R*-Tb** compounds as well, but the intensity of the obtained spectra is too low to extract meaningful information (Fig. S10†). CPL studies in polymeric Lanthanide chains and measured in the solid state remains rare.[24] Y. Hasegawa *et al.*[25] presented a polymeric chain complex with g_{lum} values for the magnetic dipole transition up to 0.17 measured in the solid state.

Due to low luminescence, the CPL of ***R***/***S*-Dy** and ***R***/***S*-Sm** could not be measured.

Magnetic properties

DC magnetic susceptibility studies. Since *S*- and *R*-enantiomers are expected to show the same magnetic properties, direct current (dc) magnetic susceptibility (χ_M) and magnetization (M) measurements were performed for the *S*-enantiomers on the polycrystalline samples. The χ_M measurements were carried out under a dc field of 0.3 T in the 2–300 K temperature range. The $\chi_M T$ dependence with T plots are presented in Fig. 5. At room temperature (300 K) the $\chi_M T$ values are 1.43, 11.41, 13.82 and 0.40 $cm^3\ mol^{-1}$ K for ***S*-Eu**, ***S*-Tb**, ***S*-Dy** and ***S*-Sm** respectively. For one isolated Ln^{3+} cation, the calculated $\chi_M T$ values are: 0 $cm^3\ mol^{-1}$ K for Eu^{3+} ground state $^7F_0$; 11.82 $cm^3\ mol^{-1}$ K for Tb^{3+} ground state $^7F_6$ and g_j = 3/2; 14.17 $cm^3\ mol^{-1}$ K for Dy^{3+} ground state $^6H_{15/2}$ and g_j = 4/3, 0.09 $cm^3\ mol^{-1}$ K for Sm^{3+} ground state $^6H_{5/2}$ and g_j = 2/7.[3a]

Table 2 g_{lum} values of the ***R***/***S*-Eu** enantiomeric pair for the $^5D_0 \rightarrow {}^7F_1$ and the $^5D_0 \rightarrow {}^7F_2$ transitions

R/***S*-Eu**	$^5D_0 \rightarrow {}^7F_1$	$^5D_0 \rightarrow {}^7F_2$
g_{lum}	±0.013 (+for ***S*-Eu**)	±0.003 (+for ***R*-Eu**)

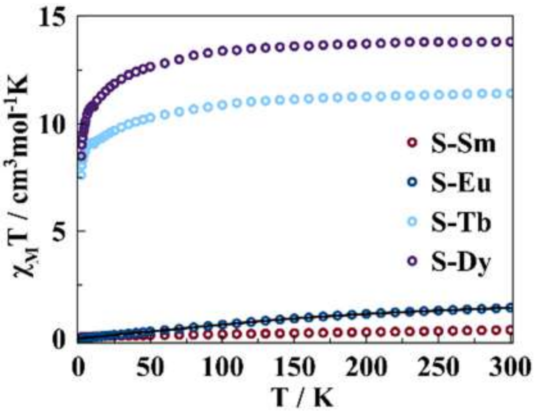

Fig. 5 $\chi_M T$ temperature dependence measured at an external static field of 0.3 T. Continuous black line corresponds to the fitting of the $\chi_M T$ *versus T* data using eqn (S2)† for compound ***S*-Eu**.

The experimental $\chi_M T$ value at room temperature for compound ***S*-Eu** is higher than 0. Due to the rather small spin–orbit coupling parameter (λ) between the $^7F_{(0-1)}$ states, at room temperature the higher energy ^7F_J states closer to the ground state are thermally populated (mainly the $^7F_1$ state). Then the $\chi_M T$ values decrease gradually on cooling the sample due to the thermal depopulation of the ^7F_J excited states. At 2 K, $\chi_M T$ is 0.017 $cm^3\ mol^{-1}$ K confirming that at low temperature the non-magnetic ground state (J = 0) is stabilized. The χ_M *vs.* T plot for compound ***S*-Eu** (Fig. S11†) shows an increase of the χ_M values when approaching to 2 K due to remnant paramagnetic rare earth impurities. If we consider the presented polymeric chain formed by non-magnetically coupled Eu^{3+} ions, the λ value can be calculated from $\chi_M T$ *vs.* T data considering Eu^{3+} as a free ion by using eqn (S2)†[26,27] (the plot of the $\chi_M T$ *vs.* T data only for ***S*-Eu** is shown in Fig. S12†). From the best fitting the λ value is 335 cm^{-1}. From the spectroscopic data, the energy gap between the $^7F_0$ and $^7F_1$ should correspond to the λ parameter. The λ value has been calculated from the emission spectra of ***S*-Eu** measured at 77 K, Fig. S13 and Table S3.† This value is 377 cm^{-1} for ***S*-Eu**. This result is similar to other Europium compounds.[28,29]

On cooling the samples, for ***S*-Tb** and ***S*-Dy**, the $\chi_M T$ values remain almost constant till ~50 K and below this temperature, the susceptibility values decrease up to 7.80 cm^3 mol^{-1} K for ***S*-Tb** and to 8.49 cm^3 mol^{-1} K for ***S*-Dy** due to thermal depopulation of the m_j states. The possibility of magnetic coupling between the Ln^{3+} ions has not been considered for these compounds due to: (i) the well shielded nature of electrons in the $4f^n$ orbitals (ii) the Ln–Ln intra and inter-molecular shortest distances are too long (6.04 ± 0.01 and 12.32 ± 0.02 Å respectively).

For the ***S*-Sm** compound, the $\chi_M T$ value at room temperature is also higher than the one calculated for a free ion. For a Sm^{3+} ion, the ^6H ground state is split due to spin–orbit coupling by $^6H_{J\,=\,5/2–15/2}$ with a λ parameter around 200 cm^{-1}. Therefore, at room temperature, the excited ^6H_J states are thermally populated. The diminution of $\chi_M T$ on cooling the sample is due to the thermal depopulation of the J states.[26,27] ***S*-Sm** magnetic data could not be fitted successfully under the free ion approximation.

Magnetization dependence with an applied magnetic field at 2 K for all compounds are depicted in Fig. S14.† None of the presented compounds show saturation of the magnetization.

AC magnetic susceptibility studies

In order to study the dynamic magnetic properties of the *R*/*S*-[Ln(μ-MPA)(MPA)$_2$(phen)]$_n$ compounds, ac magnetic susceptibility measurements in a 4 × 10^{-4} T oscillating field were recorded for compounds ***S*-Tb**, ***S*-Dy** and ***S*-Sm**.

At a 0 Oe dc external magnetic field, the in-face (χ'_M) and out-of-face (χ''_M) magnetic susceptibility components were measured in an oscillating field at 10 and 1000 Hz and in the 2 to 12 K temperature range. Only for compound ***S*-Dy**, a temperature dependence for the χ'_M component was observed, where it increases on decreasing the temperature without reaching a maximum point above 2 K. Nevertheless, no χ''_M dependence with temperature and frequency was observed at all, Fig. S15.† This fact suggests that the relaxation of the magnetization goes through a shortcut path between the two bistable $\pm m_j$ states, the so called quantum tunneling of the magnetization (QTM). In order to suppress the fast QTM, two different dc fields (10 and 1000 Oe) at different temperatures where applied to the samples. Then, maxima in the χ'_M and χ''_M components were discerned below 8 K only for the ***S*-Dy** compound. In order to establish the optimum dc magnetic field, measurements of the χ'_M and χ''_M with frequency, at a constant temperature of 3 K, and applying dc fields from 0 to 3000 Oe, were performed for ***S*-Dy**. A plot of τ $(1/2\pi\omega)$ with the dc field shows that the relaxation time is the greatest when the applied external magnetic field is 1000 Oe. Then this dc field is chosen as the optimal one (Fig. S16†).

On performing the measurements with a 1000 Oe dc field, a dependence of the χ''_M with temperature and frequencies is clearly observed and maximum points are discerned for the magnetic susceptibility components below 8 K (Fig. 6, left). Nevertheless, at 2 K in the $\chi''_M(T)$ plot, a second maximum is perceived suggesting a faster relaxation process differentiated from the one occurring at higher temperatures (Fig. S17†). This faster mechanism probably accounts for the QTM, which is not totally removed on applying the external dc field.[30]

The representation of the ac data in the Cole–Cole plots, Fig. 6, middle, shows semicircles that are not perfectly symmetric. Furthermore, a shoulder can be discerned corresponding to the χ'_M *vs.* χ''_M points obtained at lower temperatures and lower frequencies accounting to the faster mechanism differentiated in the $\chi''_M(T)$ plot. The fit was not successful using a two component generalized Debye model because of the lack of a sufficient number of experimental data points corresponding to the faster mechanism. Nevertheless, a good fit was obtained for the slower process using the one-component generalized Debye model (eqn (S3) and Table S4†).[31] The fitting of the Cole–Cole curves were obtained using the CCFit software.[32] The representation of ln(τ) *vs.* 1/T is depicted in Fig. 6, right. The linear trend in the slope in the low temperature region was fitted by an Arrhenius law. This model describes the relaxation of the magnetization by the thermally assisted Orbach mechanism that occurs between the $\pm m_j$ degenerate states in the ground state *via* the highest energy excited m_j state of the Dy^{3+} ion. The calculated energy barrier (Δ) is 31.6 cm^{-1} and the pre-exponential factor (τ_0) of the Arrhenius law is 4.9 × 10^{-9} s. But linearity is followed only for few points, suggesting that at higher temperature more than one relaxation mechanism is active. Also the distribution of

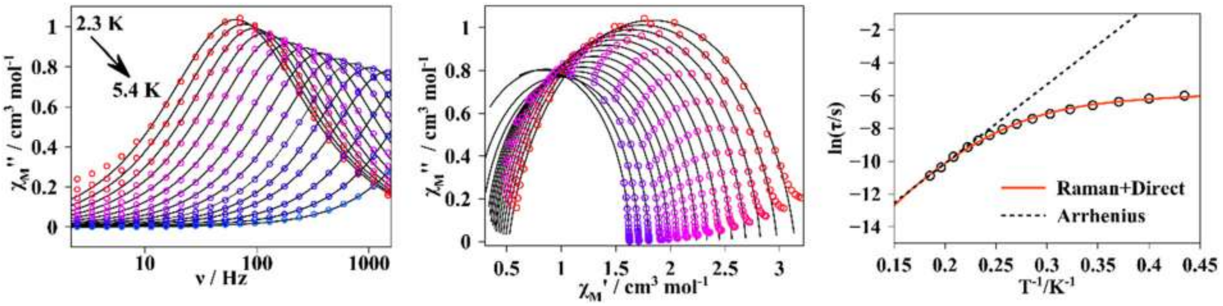

Fig. 6 Left, χ''_M *vs.* frequency plot for compound ***S*-Dy** and middle, Cole–Cole plot. Black lines correspond to the fitting with the one component Debye model for both graphics. Right, ln(τ) *vs.* 1/T plot, dashed line represents the fitting with the Arrhenius law and orange line with eqn (3).

the coefficient values (α) obtained in the fitting by using the generalized Debye model in the Cole–Cole plots, that are in the 0.150–0.002 range, suggest the presence of other relaxation mechanisms such as the QTM, Direct and Raman other than just the Orbach. Thus, the $\ln(\tau)$ *vs.* $1/T$ curve was adjusted taking into account all of the above mechanisms. The best fit was obtained when the spin–lattice relaxation mechanism, Raman and Direct equations are considered, eqn (3).

$$\tau^{-1} = CT^n + AH^4T \tag{3}$$

The obtained parameters from the best fit where $C = 0.011$ s^{-1} $K^{-9.07}$, $n = 9.07$ and $A = 183.29$ s^{-1} T^{-4} K^{-1}. For a Kramer ion such as Dy^{3+}, the dependence of τ with T should follow the power law $\tau \propto T^9$ when the relaxation of the magnetization goes through the two phonon relaxation Raman process. Nevertheless, n with values in the interval 1–6 has been claimed to be reasonable when the acoustic phonons are also considered in the spin–lattice relaxation of Raman. Important care has to be taken when fitting the ac data with the different relaxation of the magnetization mechanisms due to over parametrization when using such equations.[33–37]

Similar behaviour has been reported for other carboxylate bridged Dy^{3+} complexes and polymeric chains[38–40] and nine coordinate Dy^{3+} compounds with similar coordination geometry as the presented compound.[30,41–43]

For compounds ***S*-Tb** and ***S*-Sm**, no dependence of either magnetic susceptibility components (χ'_M and χ''_M) was observed neither at a 0 dc field nor at higher dc applied fields.

Conclusion

In this work, eight enantiomerically pure lanthanide coordination compounds have been successfully isolated. The lanthanide compounds consist of a chiral coordination 1D polymer that expands along the *a* crystallographic axis. The compounds have the $[Ln(\mu\text{-}R/S\text{-MPA})(R/S\text{-MPA})_2(phen)]_n$ formula where ***R*/*S*-HMPA** stands for (*R*/*S*)-(±)-α-methoxyphenylacetic acid and Ln = Eu^{3+}, Tb^{3+}, Dy^{3+} and Sm^{3+}. Single crystal X-Ray diffraction measurements were performed for compounds ***R*/*S*-Eu**, ***R*/*S*-Tb**, ***S*-Dy** and ***S*-Sm**. ***R*/*S*-Eu**, ***R*/*S*-Tb**, ***R*/*S*-Dy** and ***R*/*S*-Sm** coordination compounds have been characterized by means of Powder X-Ray Diffraction and Infrared spectroscopy. Moreover, luminescence studies have been carried out, as all the compounds presented sensitized luminescence associated to the expected f–f transitions. The ***S*-Eu** and ***S*-Tb** compounds showed rather good luminescence properties with measured Quantum Yields of 0.14 and 0.33 respectively. Also, the luminescence lifetime was measured and from the monoexponential curves, a τ_{obs} of 1.77 ms for ***R*-Eu** and of 1.50 ms for ***R*-Tb** analogue were extracted. Furthermore, a chiroptical study was performed on these coordination polymers in the solid state. Circular dichroism spectra were recorded and CPL measurements were performed for the most luminescent analogues (***R*/*S*-Eu** and ***R*/*S*-Tb**). For the europium compounds, mirror image spectra could be obtained where the different f–f transitions can be discerned. On the other hand, for the Tb^{3+} analogue the intensity in the CPL spectra was too low and no reliable conclusions could be extracted from it. Finally, magnetic studies were performed for all the *S*-enantiomers. Only the ***S*-Dy** compound shows slow relaxation of the magnetization under an external magnetic field. Thus, the ***S*-Dy** compound displays luminescent, chiral and field-induced SMM properties and can be considered as a multifunctional complex. All luminescence, chirooptical and magnetic measurements were carried out in the solid state since the compounds presented here consist of chiral polymeric chains, which would be disrupted by dissolution into any solvent.

Conflicts of interest

There are no conflicts to declare.

Acknowledgements

R. V. and A. T. acknowledge the financial support from Ministerio de Ciencia, Innovación y Universidades (Spain), project PGC2018-094031-B-100.

References

1 N. Ishikawa, M. Sugita, T. Ishikawa, S. Y. Koshihara and Y. Kaizu, *J. Am. Chem. Soc.*, 2003, **125**, 8694.

2 (*a*) J. Tang and P. Zhang, *Lanthanide Single Molecule Magnets*, Springer-Verlag, Berlin Heidelberg, 2015; (*b*) H. L. C. Feltham and S. Brooker, *Coord. Chem. Rev.*, 2014, **276**, 1; (*c*) D. N. Woodruff, R. E. P. Winpenny and R. A. Layfield, *Chem. Rev.*, 2013, **113**, 5110; (*d*) A. Zabala-lekuona, J. M. Seco and E. Colacio, *Coord. Chem. Rev.*, 2021, **441**, 213984; (*e*) A. Borah and R. Murugavel, *Coord. Chem. Rev.*, 2022, **453**, 214288.

3 (*a*) *The Rare Earth Elements, Fundamentals and Applications*, ed. D. A. Atwood, John Wiley& Sons Ltd, 2012; (*b*) Z. Xia, Z. Xu, M. Chen and Q. Liu, *Dalton Trans.*, 2016, **45**, 11214; (*c*) J.-C. G. Bünzli and C. Piguet, *Chem. Soc. Rev.*, 2005, **34**, 1048; (*d*) J.-C. G. Bünzli, *Acc. Chem. Res.*, 2006, **39**, 53; (*e*) S. Swavey and R. Swavey, *Coord. Chem. Rev.*, 2009, **253**, 2627; (*f*) S. V. Eliseeva and J.-C. G. Bünzli, *Chem. Soc. Rev.*, 2010, **39**, 189; (*g*) E. G. Moore, A. P. S. Samuel and K. N. Raymond, *Acc. Chem. Res.*, 2009, **42**, 542; (*h*) C. P. Montgomery, B. S. Murray, E. J. New, R. Pal and D. Parker, *Acc. Chem. Res.*, 2009, **42**, 925; (*i*) S. J. Butler, M. Delbianco, L. Lamarque, B. K. McMahon, E. R. Neil, R. Pal, D. Parker, J. W. Walton and J. M. Zwier, *Dalton Trans.*, 2015, **44**, 4791; (*j*) J. C. Bünzli, *Coord. Chem. Rev.*, 2015, **293–294**, 19; (*k*) Q. Zhang, W. Ge, X. Zhang and X. Chen, *Dalton Trans.*, 2022, **51**, 8714; (*l*) P. Pradhan, S. Priya, M. Rajendran, K. Singh and S. Vaidyanathan, *Dalton Trans.*, 2022, **51**, 715.

4 (*a*) G. Koeckelberghs, S. Sioncke, T. Verbiest, A. Persoons and C. Samyn, *Chem. Mater.*, 2003, **15**, 2870; (*b*) S. Dang, J.-H. Zhang, Z.-M. Sun and H.-J. Zhang, *Chem. Commun.*, 2012, **48**, 11139; (*c*) E. Peeters, M. P. T. Christiaans, R. A. J. Janssen, H. F. M. Schoo, H. P. J. M. Dekkers and E. W. Meijer, *J. Am. Chem. Soc.*, 1997, **119**, 9909; (*d*) J. P. Leonard, P. Jensen, T. McCabe, J. E. O'Brien, R. D. Peacock, P. E. Kruger and T. Gunnlaugsson, *J. Am. Chem. Soc.*, 2007, **129**, 10986; (*e*) F. Stomeo, C. Lincheneau, J. P. Leonard, J. E. O'Brien, R. D. Peacock, C. P. McCoy and T. Gunnlaugsson, *J. Am. Chem. Soc.*, 2009, **131**, 9636.

5 (*a*) F. Zinna, U. Giovanella and L. Di Bari, *Adv. Mater.*, 2015, **27**, 1791; (*b*) F. Zinna, M. Pasini, F. Galeotti, C. Botta, L. Di Bari and U. Giovanella, *Adv. Funct. Mater.*, 2017, **27**, 1603719; (*c*) F. Zinna, L. Arrico, T. Funaioli, L. di Bari, M. Pasini, C. Botta and U. Giovanella, *J. Mater. Chem. C*, 2022, **10**, 463.

6 (*a*) S. Shuvaev, E. A. Suturina, K. Mason and D. Parker, *Chem. Sci.*, 2018, **9**, 2296; (*b*) M. Leonzio, A. Melchior, G. Faura, M. Tolazzi, M. Bettinelli, F. Zinna, L. Arrico, L. Di Bari and F. Piccinelli, *New J. Chem.*, 2018, **42**, 7931; (*c*) J. Yuasa, T. Ohno, H. Tsumatori, R. Shiba, H. Kamikubo, M. Kataoka, Y. Hasegawa and T. Kawai, *Chem. Commun.*, 2013, **49**, 4604; (*d*) K. M. Ayers, N. D. Schley and G. Ung, *Inorg. Chem.*, 2020, **59**, 7657; (*e*) J. Gong and X. Zang, *Coord. Chem. Rev.*, 2022, **453**, 214329; (*f*) N. F. M. Mukthar, N. D. Schley and G. Ung, *J. Am. Chem. Soc.*, 2022, **144**, 6148; (*g*) P. Stachelek, L. MacKenzie, D. Parker and R. Pal, *Nat. Commun.*, 2022, **13**, 553; (*h*) A. T. Frawley, R. Pal and D. Parker, *Chem. Commun.*, 2016, **52**, 13349.

7 (*a*) M. Górecki, L. Carpita, L. Arrico, F. Zinna and L. Di Bari, *Dalton Trans.*, 2018, **47**, 7166; (*b*) L. E. MacKenzie and R. Pal, *Nat. Rev. Chem.*, 2021, **5**, 109–124.

8 (*a*) F. Gendron, S. Di Pietro, L. Abad Galán, F. Riobé, V. Placide, L. Guy, F. Zinna, L. Di Bari, A. Bensalah-Ledoux, Y. Guyot, G. Pilet, F. Pointillard, B. Baguenard, S. Guy, O. Cador, O. Maury and B. Le Guennic, *Inorg. Chem. Front.*, 2021, **8**, 914; (*b*) B. Lefeuvre, C. A. Mattei, J. Flores Gonzalez, F. Gendron, V. Dorcet, F. Riobé, C. Lalli, B. Le Guennic, O. Cador, O. Maury, S. Guy, A. Bensalh-Ledoux, B. Baguenard and F. Pointillard, *Chem. – Eur. J.*, 2021, **27**, 7362.

9 E. M. Sánchez-Carnerero, A. R. Agarrabeitia, F. Moreno, B. L. Maroto, G. Muller, M. J. Ortiz and S. de la Moya, *Chem. – Eur. J.*, 2015, **21**, 13488.

10 (*a*) F. Zinna and L. Di Bari, *Chirality*, 2015, **27**, 1; (*b*) J. L. Lunkley, D. Shirotani, K. Yamanari, S. Kaizaki and G. Muller, *Inorg. Chem.*, 2011, **50**, 12724; (*c*) F. Zinna, C. Resta, S. Abbate, E. Castiglioni, G. Longhi, P. Mineo and L. Di Bari, *Chem. Commun.*, 2015, **51**, 11903.

11 (*a*) M. Cantuel, G. Bernardinelli, G. Muller, J. P. Riehl and C. Piguet, *Inorg. Chem.*, 2004, **43**, 1840; (*b*) F. Stomeo, C. Lincheneau, J. P. Leonard, J. E. Obrien, R. D. Peacock, C. P. McCoy and T. Gunnlaugsson, *J. Am. Chem. Soc.*, 2009, **31**, 9636.

12 (*a*) O. Mamula, M. Lama, S. G. Telfer, A. Nakamura, R. Kuroda, H. Stoeckli-Evans and R. Scopelitti, *Angew. Chem.*, 2005, **117**, 2583; (*b*) M. Lama, O. Mamula, G. S. Kottas, F. Rizzo, L. De Cola, A. Nakamura, R. Kuroda and H. Stoeckli-Evans, *Chem. – Eur. J.*, 2007, **13**, 7358.

13 G. Bozoklu, C. Gateau, D. Imbert, J. Pecaut, K. Robeyns, Y. Filinchuk, F. Memon, G. Muller and M. Mazzanti, *J. Am. Chem. Soc.*, 2012, **134**, 8372.

14 (*a*) B. Casanovas, F. Zinna, L. Di Bari, M. S. El Fallah, M. Font-Bardía and R. Vicente, *Dalton Trans.*, 2017, **46**, 6349; (*b*) B. Casanovas, S. Speed, M. S. El Fallah, R. Vicente, M. Font-Bardía, F. Zinna and L. Di Bari, *Dalton Trans.*, 2019, **48**, 2059.

15 (*a*) K. Miyata, Y. Konno, T. Nakanishi, A. Kobayashi, M. Kato, K. Fushimi and Y. Hasegawa, *Angew. Chem., Int. Ed.*, 2013, **52**, 6413; (*b*) Y. Kuramochi, T. Nakagawa, T. Yokoo, J. Yuasa, T. Kawaia and Y. Hasegawa, *Dalton Trans.*, 2012, **41**, 6634; (*c*) H. Xin, F.-Y. Li, M. Shi, Z.-Q. Bian and C.-H. Huang, *J. Am. Chem. Soc.*, 2003, **125**, 7166; (*d*) A. P. Bassett, S. W. Magennis, P. B. Glover, D. J. Lewis, N. Spencer, S. Parsons, R. M. Williams, L. D. Cola and Z. Pikramenou, *J. Am. Chem. Soc.*, 2004, **126**, 9413; (*e*) X.-P. Yang, R. A. Jones and S.-M. Huang, *Coord. Chem. Rev.*, 2014, **273**, 63; (*f*) M. Tropiano, N. L. Kilah, M. Morten, H. Rahman, J. J. Davis, P. D. Beer and S. Faulkner, *J. Am. Chem. Soc.*, 2011, **133**, 11847; (*g*) J. D. Moore, R. L. Lord, G. A. Cisneros and M. J. Allen, *J. Am. Chem. Soc.*, 2012, **134**, 17372; (*h*) B. Alpha, J.-M. Lehn and G. Mathis, *Angew. Chem., Int. Ed. Engl.*, 1987, **26**, 266; (*i*) C. Bazzicalupi, A. Bencini, A. Bianchi, C. Giorgi, V. Fusi, A. Masotti, B. Valtancoli, A. Roque and F. Pina, *Chem. Commun.*, 2000, 561.

16 F. Zinna, T. Bruhn, C. A. Guido, J. Ahrens, M. Bröring, L. Di Bari and G. Pescitelli, *Chem. – Eur. J.*, 2016, **22**, 16089.

17 G. M. Sheldrick, *Acta Crystallogr., Sect. A: Fundam. Crystallogr.*, 2008, **64**, 112.

18 G. M. Sheldrick, *Acta Crystallogr., Sect. C: Cryst. Struct. Commun.*, 2015, **71**, 3.

19 (*a*) M. Llunell, D. Casanova, J. Cirera, P. Alemany and S. Alvarez, *Shape Program., version 2*, Universitat de Barcelona, Barcelona, Spain, 2010; (*b*) P. Alemany, D. Casanova, S. Alvarez, C. Dryzun and D. Avnir, *Rev. Comput. Chem.*, 2017, **30**, 2892.

20 *Luminescence of Lanthanide Ions in Coordination Compounds and Nanomaterials*, ed. A. de Bettencourt-Dias, John Wiley & Sons Ltd, 2014.

21 K. Binnemans, *Coord. Chem. Rev.*, 2015, **295**, 1.

22 A. Aebischer, F. Gumy and J.-C. G. Bünzli, *Phys. Chem. Chem. Phys.*, 2009, **11**, 1346.

23 C. A. Mattei, K. Dhbaibi, B. Lefeuvre, V. Dorcet, G. Argouarch, O. Cador, B. Le Guennic, O. Maury, C. Lalli, S. Guy, A. Bensalah-Ledoux, F. Riobé, B. Baguenard and F. Pointillart, *Chirality*, 2022, **34**, 34.

24 (*a*) H.-Y. Wong, W.-S. Lo, K.-H. Yim and G.-L. Law, *Chem*, 2019, **5**, 3058; (*b*) X.-Z. Li, C.-B. Tian and Q.-F. Sun, *Chem.*

Rev., 2022, **122**, 6374; (*c*) Y. Kitagawa, M. Tsurui and Y. Hasegawa, *ACS Omega*, 2020, **5**, 3786.

25 Y. Hasegawa, Y. Miura, Y. Kitagawa, S. Wada, T. Nakanishi, K. Fushimi, T. Seki, H. Ito, T. Iwasa, T. Taketsugu, M. Gon, K. Tanaka, Y. Chujo, S. Hattori, M. Karasawa and K. Ishii, *Chem. Commun.*, 2018, **54**, 10695.

26 J. Legendziewicz, V. Tsaryuk, V. Zolin, E. Lebedeva, M. Borzechowska and M. Karbowiak, *New J. Chem.*, 2001, **25**, 1037.

27 A. Arauzo, A. Lazarescu, S. Shova, E. Bartolomé, R. Cases, J. Luzón, J. Bartolomé and C. Turta, *Dalton Trans.*, 2014, **43**, 12342.

28 M. Andruh, E. Bakalbassis, O. Kahn, J. C. Trombe and P. Porcher, *Inorg. Chem.*, 1993, **32**, 1616.

29 O. Kahn, *Molecular Magnetism*, VHC Publishers, Inc., USA, 1993.

30 H.-R. Tu, W.-B. Sun, H.-F. Li, P. Chen, Y.-M. Tian, W.-Y. Zhang, Y.-Q. Zhang and P.-F. Yan, *Inorg. Chem. Front.*, 2017, **4**, 499.

31 Y.-N. Guo, G.-F. Xu, Y. Guo and J. Tang, *Dalton Trans.*, 2011, **40**, 9953.

32 N. F. Chilton, CC-FIT, program/ **https://www.nfchilton.com/software.html**, 2014.

33 G. Handzlik, M. Magott, M. Arczyński, A. M. Sheveleva, F. Tuna, S. Baranc and D. Pinkowicza, *Dalton Trans.*, 2020, **49**, 11942.

34 L. Gu and R. Wu, *Phys. Rev. B*, 2021, **103**, 014401.

35 K. N. Shrivastava, *Phys. Status Solidi B*, 1983, **117**, 437.

36 M. Briganti, F. Santanni, L. Tesi, F. Totti, R. Sessoli and A. Lunghi, *J. Am. Chem. Soc.*, 2021, **143**, 13633.

37 D. Aravena and E. Ruiz, *Dalton Trans.*, 2020, **49**, 9916.

38 M. Fang, J.-J. Li, P.-F. Shi, B. Zhao and P. Cheng, *Dalton Trans.*, 2013, **42**, 6553.

39 J. Tian, B. Li, X. Zhang, X. Li, X. Li and J. Zhang, *Dalton Trans.*, 2013, **42**, 8504.

40 W.-H. Zhu, X. Xiong, C. Gao, S. Li, Y. Zhang, J. Wang, C. Zhang, A. K. Powell and S. Gao, *Dalton Trans.*, 2017, **46**, 14114.

41 D. N. Woodruff, R. E. P. Winpenny and R. A. Layfield, Lanthanide Single-Molecule Magnets, *Chem. Rev.*, 2013, **113**(7), 5110–5148.

42 A. Zabala-Lekuona, J. Cepeda, I. Oyarzabal, A. Rodríguez-Diéguez, J. A. García, J. M. Seco and E. Colacio, *CrystEngComm*, 2017, **19**, 256.

43 P. Antal, B. Drahoš, R. Herchel and Z. Trávníček, *Dalton Trans.*, 2016, **45**, 15114.

Dalton Transactions

ROYAL SOCIETY OF CHEMISTRY

PAPER

View Article Online
View Journal | View Issue

Check for updates

Cite this: *Dalton Trans.*, 2024, **53**, 9387

New series of mononuclear β-diketonate cerium(III) field induced single-molecule magnets†

Ànnia Tubau,[a] Silvia Gómez-Coca, *[a,b] Saskia Speed,[a] Mercè Font-Bardía[c] and Ramon Vicente *[a]

Received 22nd March 2024,
Accepted 4th May 2024

DOI: 10.1039/d4dt00848k

rsc.li/dalton

Five new β-diketonate Ce^{3+} mononuclear complexes, $[Ce(Btfa)_3(H_2O)_2]$ (**1**), $[Ce(Btfa)_3(phen)]$ (**2**), $[Ce(Btfa)_3(bipy)]$ (**3**), $[Ce(Btfa)_3(terpy)]$ (**4**) and $[Ce(Btfa)_3(bathophen)(DMF)]$ (**5**), where $Btfa^-$ = 4,4,4-trifluoro-1-phenyl-1,3-butanedionate, phen = 1,10-phenanthroline, bipy = 2,2′-bipyridyl, terpy = 2,2′:6′,2″-terpyridine and bathophen = 4,7-diphenyl-1,10-phenanthroline, have been synthesized and structurally characterized through X-ray diffraction of single crystals. The central Ce^{3+} atom displays a coordination number of 8 for **1**, **2** and **3** and of 9 for **4** and **5**. Under a 0 T external magnetic field, none of the given compounds exhibits single molecule magnet (SMM) behaviour. However, a small magnetic field, between 0.02 and 0.1 T, is enough for all the compounds to exhibit slow relaxation of the magnetization. A comprehensive magnetic analysis, with experimental magnetic data and *ab initio* calculations, was undertaken for all the complexes, and the study highlights the significance of the different spin relaxation mechanisms that must be considered for a Ce^{3+} lanthanide ion.

Introduction

Magnetically bistable molecules that exhibit slow relaxation of the magnetization below a critical temperature, T_B, are named single molecule magnets (SMMs). The energy barrier separating the two bistable magnetic states is named the effective energy barrier (U_{eff}) and, for transition metal compounds, it is described by the magnetic anisotropy (D) and the square of the overall ground spin state (S): $U_{eff} = |D|\cdot S^2$ or $U_{eff} = |D|\cdot(S^2 - 1/4)$ for integer and non-integer S values respectively. The first molecular system for which single-molecular magnet type behaviour was observed was the mixed valence dodecanuclear Mn_{12} cluster with the formula $[Mn_{12}O_{12}(CH_3COO)_{16}(H_2O)_4]$ in 1993,[1] previously reported in 1980.[2] At the end of the twentieth century, efforts to obtain new SMMs with higher T_B and U_{eff} centred on transition metal clusters.[3] SMM systems show very interesting properties and could be used in many potential applications such as memory storage.[3,4] After a plethora of 3d metal clusters were studied, the field of single molecule magnets moved onto lanthanide(III) ions, starting with the mononuclear Tb(III) phthalocyaninato-based double-decker complex $[TbPc_2]^-$ (Pc = phthalocyanine). It showed SMM behaviour and it was isolated in 2003 by N. Ishikawa *et al.*[5] Due to the shielding of the $4f^n$ electrons by the filled $5s^2$ and $5p^6$ orbitals, the interaction between the lanthanide ion and the donor atoms can be considered as electrostatic in nature. Consequently, lanthanide ions have unquenched orbital angular momentum (L) that leads to strong spin–orbit coupling and therefore, intrinsic magnetic anisotropy; this makes them good candidates for SMMs. Mononuclear SMMs, also called single ion magnets (SIMs), are mononuclear systems that show slow relaxation of the magnetization.[6–13] In lanthanides, the intrinsic magnetic anisotropy that the ions show is a key factor determining the magnetic properties of lanthanide(III) compounds, but the crystal field effect has relevance in the modulation of such anisotropy to tune the magnetic properties depending on the electron density of the m_J ground state. Rinehart and Long[14] revealed that the electron density of the m_J ground state could be oblate (equatorially extended) or prolate (axially extended). For instance, in the $[TbPc_2]^-$ compound, the donor atoms of the ligand are located in the axial positions leading to an axial stressed coordination environment that enhances magnetic anisotropy on the easy axis leading to a good SMM performance of this Tb^{3+} compound with an oblate m_J ground state.[5]

In the design of SMMs, heavy metal lanthanides such as Tb^{3+}, Dy^{3+} and Er^{3+} ions have been extensively used because of

---

[a] *Departament de Química Inorgànica i Orgànica, Universitat de Barcelona, Martí i Franquès 1-11, 08028 Barcelona, Spain. E-mail: rvicente@ub.edu*

[b] *Institut de Química Teòrica i Computacional, Universitat de Barcelona, Diagonal 645, 08028 Barcelona, Spain*

[c] *Departament de Mineralogia, Cristal lografia i Dipòsits Minerals and Unitat de Difracció de R-X. Centre Científic i Tecnològic de la Universitat de Barcelona (CCiTUB), Universitat de Barcelona, Solé i Sabarís 1-3, 08028 Barcelona, Spain*

† Electronic supplementary information (ESI) available: Thermogravimetric curves, elemental analysis and IR data, SCXRD and PXRD data, excitation spectra, emission spectra at 77 K, ac magnetic data. CCDC 2261969–2261974 and 2341701. For ESI and crystallographic data in CIF or other electronic formats see DOI: **https://doi.org/10.1039/d4dt00848k**

their large magnetic and angular momentum J, where $J = L + S$ for half-filled Ln^{3+} ions, and consequently large magnetic anisotropy. Indeed, a rapid overview of the literature on lanthanide-based SMMs shows that most of the scientific production on this subject is related to Dy^{3+}, Tb^{3+} and Er^{3+} based species, with Dy^{3+} being the most popular.[3,6–13] For instance, the mononuclear dysprosium complex $[(Cp^{iPr5})Dy(Cp^*)][B(C_6F_5)_4]$, where $CpiPr_5$ = pentaisopropylcyclopentadienyl and Cp^* = pentamethylcyclopentadienyl, was shown to exhibit the highest reported blocking temperature of 80 K.[10,11,15] Still, the most relevant permanent magnets that are employed in industry are the ones based on light lanthanide ions, including the NdFeB and $SmCo_5$ ferromagnets.[16] In this sense, the number of reported lanthanide-based SMMs of light lanthanides such as Ce^{3+} or Nd^{3+} ions is much smaller than those mentioned above.[17] Focusing on cerium(III), its electronic configuration is $4f^1$ with a $^2F_{5/2}$ ground state and in some Ce^{3+} compounds magnetic relaxation can be observed because the spin–orbit effect of the $4f^1$ electron can create non-negligible magnetic anisotropy.

When the Ce^{3+} ion ($^2F_{5/2}$ ground state) is set in a coordination complex, the spin–orbit coupling component (J) splits into ($2J + 1$) $\pm m_j$ states: $+J$, $+J - 1,\ldots, -J + 1, -J$, due to the crystal field: ± 5/2, ± 3/2 and ±1/2. For Ce^{3+} compounds the goal would be to choose the ideal coordination environment around the lanthanide ion to yield an axial geometry that would stabilize the $m_j = \pm5/2$ Kramers doublet (KD) with an oblate 4f-shell electron density distribution as the ground state and destabilize the prolate electron distribution, $m_j = \pm1/2$ and ±3/2 states. Such systems would lead to a reduced quantum tunneling of magnetization (QTM) effect with anisotropic barriers higher in energy (reduced m_j mixing) and, in principle, improve the SMM performance.[14,18,19] Regarding β-diketonate systems, two series of mononuclear Ce^{3+} β-diketonate complexes with N-donor auxiliary ligands are found in the literature, Table S1.† First, 1,1,1-trifluoro-5,5-dimethyl-2,4-hexadione (Hfdh) led to the $[Ce(fdh)_3(bpy)]$ compound with D_{4d} symmetry.[20] Based on the 4,4,4-trifluoruro-1-(naphthalene-2-yl)butane-1,3-dionato (ntfa) β-diketonate ligand, we recently published a series of compounds: $[Ce(ntfa)_3(MeOH)_2]$, $[Ce(ntfa)_3(5,5'\text{-}Me_2bipy)]$ and $[Ce(ntfa)_3(bipy)_2]$, with field induced SIM behavior and D_{2d}, D_{2d} and C_{2v} point group symmetries, respectively.[21] For these mononuclear Ce^{3+} β-diketonate complexes, *ab initio* calculations at zero field on the electron gyromagnetic ratio (g tensor) for each m_j state were described. Easy axial anisotropy was found (g_{xx} and $g_{yy} < g_{zz}$) through the calculations, which demonstrated that the effective g tensor of the ground doublet presented considerable transverse contributions (g_{xx} and g_{yy}) that led to the ground state wavefunction $|\pm5/2\rangle$ mixed with $|\pm1/2\rangle$ and $|\pm3/2\rangle$ from the other excited m_j doublets.

Otherwise, the only Ce^{3+} compound showing SMM behavior to date is the trinuclear Zn–Ce–Zn compound prepared from an *o*-vanillin Schiff base based ligand.[22] For this heterometallic compound, g_{zz} yielded 4.06 from *ab initio* calculations; this is close to the theoretical value of 4.28 for a pure $m_j = \pm5/2$ Kramers doublet, $g_{zz} = 2g_J m_j$.[23] From the measured high-field electron paramagnetic resonance (HF-EPR) spectrum, g_{zz} is 3.27, which is assigned to the ground state of $m_j = 5/2$ KD with slight mixing of the $m_j = 1/2$ pair. Nevertheless, two mononuclear Ce^{3+} metallocene compounds, $[Ce(Cp^{ttt})_2\{(C_6F_5\text{-}k^1\text{-}F)B(C_6F_5)_3\}]$ and $[Ce(Cp^{ttt})_2Cl]$, are found in the literature where the g_{zz} axial component obtained by multiconfigurational analysis shows even higher values than the trinuclear Zn–Ce–Zn SMM compound, with values up to 4.16 and 4.22, respectively, and a ground state wavefunction of 100% $|\pm5/2\rangle$ for the first compound.[24] The two Cp^{ttt} groups placed in the axial positions of the lanthanide cation and the low equatorial interactions of the $[B(C_6F_5)_4]^-$ and Cl^- anions, led to Ce^{3+} centers in an axial stressed symmetry. Furthermore, for these organometallic compounds, the EPR measurements were recorded and the experimental g^{eff} values were close to the computed ones. However, despite the calculated g_{zz} values being near 4.28, these compounds only showed slow relaxation of the magnetization when applying an external magnetic field of 1000 Oe. The other mononuclear cerium compounds found in the literature showing slow relaxation of the magnetization under an external H_{dc}, according to *ab initio* calculations, resulted from axial symmetry but with a considerable rhombic contribution to the ground state. Their magnetic properties are compiled in Tables S1 and S2.†[25–29] A similar result was found for the dinuclear Ce^{3+} compound $[Ce_2(RR\text{-}L)_2(\mu\text{-}Cl)_6]$, where L is 1,4,7,10-tetrakis(2-pyridylmethyl)-1,4,7,10-tetraaza-cyclododecane, Table S3.†[30] In addition, the natural isotopes of Ce^{3+} do not have nuclear spin; this results in clearer and easier to interpret EPR spectra. Interestingly, in the studies published where EPR was also measured for the Ce^{3+} compounds, the g_{xx}, g_{yy} and g_{zz} experimental values were in good agreement with the computational experiments.[22,24,25,30] At the moment, as far as we know, pure Ising type axial anisotropy ($g_z = 4.28$) has not been found in the computational calculations nor in EPR measurements for any of the Ce^{3+} compounds found in the literature. It is worth noting that slow relaxation of the magnetization under relatively small H_{dc} fields was measured for some Ce^{3+} coordination complexes where multiconfigurational CASSCF calculations indicated easy plane magnetic anisotropy that led to larger contributions of the $|\pm1/2\rangle$ and $|\pm3/2\rangle$ wavefunctions in the ground state $\pm m_j$ KD.[25–29] Even though there was a transverse contribution to the ground state, the compounds showed similar magnetic behavior to those compounds with more axially strained coordination geometries. We attempted to compile the magnetic characteristics of the Ce^{3+} compounds found in the literature in Tables S1–S5.†

More examples of Ce^{3+} SMM compounds are needed to further understand their spin relaxation and so that we can control and manipulate it to be able to design compounds with better SMM performance. With the aim of increasing this limited family of compounds and providing new insights into the understanding of cerium(III) spin relaxation, five new β-diketonate Ce^{3+} coordination compounds are presented. The presented complexes are derived from the β-diketonate ligand

$Btfa^-$ = 4,4,4-trifluoro-1-phenyl-1,3-butanedionate with polypyridyl molecules as ancillary ligands and they have the formulae $[Ce(Btfa)_3(H_2O)_2]$ (**1**), $[Ce(Btfa)_3(phen)]$ (**2**), $[Ce(Btfa)_3(bipy)]$ (**3**), $[Ce(Btfa)_3(terpy)]$ (**4**) and $[Ce(Btfa)_3(bathophen)(DMF)]$ (**5**), where phen = 1,10-phenanthroline, bipy = 2,2′-bipyridyl, terpy = 2,2′:6′,2″-terpyridine and bathophen = bathophenanthroline. For this purpose, the nitrogen donor N,N-L and N,N,N-L auxiliary ligands could be placed in the equatorial positions of the Ce^{3+} metallic center while the β-diketonates could be fixed in the axial positions, thus, in this way, stressing an axial geometry. Moreover, the five compounds were structurally and magnetically characterized and a thorough investigation of the experimental magnetic data and *ab initio* calculations was conducted to gain deeper insights into the spin dynamics involved in the magnetization relaxation of these compounds.

Experimental section

Starting materials

4,4,4-Trifluoro-1-phenyl-1,3-butanedione (HBtfa), 2,2′-bipyridyl (bipy), 1,10-phenanthroline (phen), 2,2′:6′,2′-terpyridine (terpy) and bathophenanthroline (bathophen) were purchased from Sigma-Aldrich. Cerium(III) chloride hexahydrate was obtained from Strem Chemicals and the other chemicals used were of analytical grade.

$[Ce(Btfa)_3(H_2O)_2]$ (1). A methanol solution (5 mL) containing $CeCl_3·6H_2O$ (2 mmol, 0.745 mg) was added to a previously mixed methanol solution (10 mL) composed of NaOH (6 mmol, 240 mg) and HBtfa (6 mmol, 1296.96 mg). The solution was stirred for 1 hour at room temperature. Then 80 mL of deionized water was added to the reaction mixture and it was allowed to stir overnight. The orange precipitate was filtered and dried under vacuum (yield: 75%). Anal. Calc. for $C_{30}H_{22}CeF_9O_8$ (821.59 g mol^{-1}): C, 43.9; H, 2.7%. Found: C, 43.2; H, 2.7%. Selected IR bands (ATR-IR, cm^{-1}): 3648(m), 3363(br), 1608(s), 1571(s), 1530(m), 1483(m), 1457(m), 1308(m), 1281(s), 1243(m), 1182(m), 1133(s), 1075(m), 943(m), 771(m), 700(m), 629(m) cm^{-1}.

$[Ce(Btfa)_3(1,10\text{-}phen)]$ (2). An ethanol solution (15 mL) containing phen (1 mmol, 180.21 mg) was added to another ethanol solution (15 mL) containing $[Ce(Btfa)_3(H_2O)_2]$ (1 mmol, 824.6 mg). The solution was stirred for 30 minutes and then left to stand undisturbed at room temperature. Orange single crystals suitable for X-ray diffraction were obtained within a week (yield: 56%). Anal. Calc. for $C_{42}H_{26}CeF_9N_2O_6$ (965.77 g mol^{-1}): C, 52.2; N, 2.9; H, 2.7%. Found: C, 52.0; N, 2.9; H, 2.6%. Selected IR bands (ATR-IR, cm^{-1}): 1609(s), 1576(s), 1521(s), 1486(m), 1470(m), 1320(m), 1287(s), 1241(m), 1180(s), 1133(s), 945(m), 844(m), 746(s), 699(s), 628(m), 578(m).

$[Ce(Btfa)_3(bipy)(EtOH)]/[Ce(Btfa)_3(bipy)]$ (3a/3). An ethanol solution (15 mL) containing bipy (1 mmol, 156.2 mg) was added to another ethanol solution (15 mL) containing $[Ce(Btfa)_3(H_2O)_2]$ (1 mmol, 824.6 mg). The solution was stirred for 30 minutes and then left to stand at room temperature. Orange single crystals suitable for X-ray diffraction were obtained within a week (yield: 82%). X-ray diffraction analysis of several single crystals of the sample showed that the bulk compound was a mixture of two compounds: $[Ce(Btfa)_3(bipy)(EtOH)]$ (**3a**) and $[Ce(Btfa)_3(bipy)]$ (**3**). Compound **3** can be obtained in two different ways: after exposure of the single crystals from the bulk sample to the open air for three months or by heating the bulk sample in the oven for 1 h at 100 °C. Anal. Calc. for $C_{40}H_{26}CeF_9N_2O_6$ (941.7 g mol^{-1}) (**3**): C, 51.0; N, 3.0; H, 2.8%. Found: C, 51.2; N, 2.8; H, 2.8%. Selected IR bands (ATR-IR, cm^{-1}): for compound **3a** 3054(m, broad), 1635(m), 1606(s, split), 1572(s), 1523(m), 1483(m), 1466(m), 1433(m), 1313(m, split), 1280(s), 1240(m), 1170(m), 1123(s, split), 1071(s), 1011(m), 941(m), 755(s, split), 699(s), 626(s), 573(s), for compound **3** 1635(m), 1606(s, split), 1572(s), 1523(m), 1483(m), 1466(m), 1433(m), 1313(m, split), 1280(s), 1240(m), 1170(m), 1123(s, split), 1071(s), 1011(m), 941(m), 755 (s, split), 699(s), 626(s), 573(s).

$[Ce(Btfa)_3(terpy)]$ (4). An ethanol solution (15 mL) containing terpy (1 mmol, 233.3 mg) was added to another ethanol solution (15 mL) containing $[Ce(Btfa)_3(H_2O)_2]$ (1 mmol, 824.6 mg). The solution was stirred for 30 minutes and then left to stand at room temperature. Orange single crystals suitable for X-ray diffraction were obtained within a week (yield: 21%). Anal. Calc. for $C_{45}H_{29}CeF_9N_3O_6$ (1018.8 g mol^{-1}): C, 53.0; N 4.1, H 2.9%. Found: C, 52.6; N, 3.4; H, 2.6%. Selected IR bands (ATR-IR, cm^{-1}): 1609(s, split), 1576(s), 1526(m), 1469(s), 1439(m), 1313(m), 1277(s), 1237(m), 1170(s), 1123(s), 1071(m), 1004(m), 938(m), 759(s), 716(s), 696(s), 652(m), 629(s), 573(m).

$[Ce(Btfa)_3(bathophen)(DMF)]$ (5). An *N*,*N*-dimethylformamide (DMF) solution (10 mL) of bathophen (1 mmol, 332.40) was added to an ethanol solution (20 mL) containing $[Ce(Btfa)_3(H_2O)_2]$ (1 mmol, 824.6 mg). The orange solution was stirred for 30 min at 80 °C, filtered and left to stand undisturbed at room temperature. Orange single crystals suitable for X-ray diffraction were obtained within a month (yield: 24%). Anal. Calc. for $C_{57}H_{41}CeF_9N_3O_7$ (1191.1 g mol^{-1}): C, 57.5; N, 3.5; H, 3.5%. Found: C, 57.1; N, 3.5; H, 3.4%. Selected IR bands (ATR-IR, cm^{-1}): 1662(w), 1612(s, split), 1572(m), 1526(m), 1466(m), 1433(w), 1310(m), 1277(s), 1234(m), 1180(s), 1123(s), 1067(m), 1021(m), 938(m), 762(s, split), 696(s), 669(m), 626(s), 573(s).

IR and elemental analyses

Infrared spectra of solid complexes were recorded on a Bruker Alpha P (platinum-ATR-cap) spectrometer. Elemental microanalyses were carried out with an Elementar Vario EN3 analyser.

Magnetic measurements

Magnetic measurements were performed on solid polycrystalline samples with a Quantum Design MPMS-XL SQUID magnetometer at the Magnetic Measurements Unit of the Scientific and Technological Center (CCiTUB) of the University of Barcelona. Data were collected for powdered microcrystalline samples or for crushed polycrystalline samples of compounds **1** to **5**, the purity and structural integrity of which were analyzed by powder X-ray diffraction (see Molecular structure section of the Results and discussion). The samples were mounted in a gelatin capsule. Direct current (dc) susceptibility measurements were made over the 2–300 K temperature range and under an external magnetic field of 0.3 T. Blank measurements were also recorded for the capsule and holder and their diamagnetic contributions were corrected. Pascal's constants were used to estimate the diamagnetic corrections, which were subtracted from the experimental susceptibilities to give the corrected molar magnetic susceptibilities. Alternating current (ac) susceptibility measurements were carried out by applying an oscillating ac field of 4 Oe with ac frequencies between 1 and 1500 Hz for **1**, **3** and **5** and between 10 and 1500 Hz for compounds **2** and **4** at different temperatures and different dc applied fields indicated in the text.

X-ray crystallography

Crystals of **1–5** were mounted in air on a D8VENTURE (Bruker) diffractometer with a CMOS detector. Crystallographic data, conditions required for intensity data collection and some features of the structure refinements are listed in Tables S6 and S7.† All the structures were refined by the least-squares method. Intensities were collected with multilayer monochromated Mo-Kα radiation. Lorentz polarization and absorption corrections were made for all samples. The structures were solved by direct methods, using the SHELXS-97 computer program[31] and refined by the full-matrix least-squares method, using the SHELXL-2018 computer program.[32] The non-hydrogen atoms were located in successive difference Fourier transformations and refined with anisotropic thermal parameters on F^2. For hydrogen atoms, isotropic temperature factors were assigned to be 1.2 or 1.5 times the respective parent.

Powder X-ray diffraction (PXRD) measurements (see Fig. S1–S5†) were used to check the bulk phase purity. The powder patterns were recorded on a Bruker D8 Advance diffractometer (Bruker AXS, Madison, WI, USA) with a LynxEye detector in Bragg–Brentano θ/θ geometry, with the sample dispersed thinly on a zero-background Si sample holder, λ(CuKα) = 1.54060 Å, scanning from 2θ = 5° to 50°, with a step size of 0.02°.

Computational details

Ab initio calculations were performed using crystallographic structures and Orca software, version 5.0.3. The def2-TZVP basis set was used.[33] NEVPT2 calculations did not include dynamic correlations as it was previously demonstrated for Ce complexes that this was not essential due to the large ionic character of the Ln–O and Ln–N bonds.[34] The selected active space was (1,7), considering the seven doublets. The SINGLE_ANISO module, as implemented in Orca, was employed.[35]

To evaluate the vibrational frequencies, the experimental geometries were optimized with Gaussian09,[36] the B3LYP functional[37] and using the Stuttgart pseudo/basis set[38] for Ce and a TZV basis set[39] for lighter atoms.

Results and discussion

General syntheses

Deprotonation of the β-diketone 4,4,4-trifluoro-1-phenyl-1,3-butanedione (HBtfa; Scheme 1a) in a basic medium and further addition of cerium(III) chloride led to the precipitation of the neutral [Ce(Btfa)$_3$(H$_2$O)$_2$] (**1**) aqua complex. Compound **1** was used as the precursor in subsequent reactions. Compounds **2–5** were obtained through the displacement of the H$_2$O molecules of **1** by different polypyridyl ligands. The nitrogen containing molecules used for this family of cerium(III) compounds were: 1,10-phenanthroline (phen; Scheme 1b), 2,2′-bipyridyl (bipy; Scheme 1c), 2,2′;6′,2″-terpyridine (terpy; Scheme 1d) and bathophenanthroline (bathophen; Scheme 1e). The reaction of precursor compound **1** with chelating N,N-L and N,N,N-L ligands in a 1 : 1 ratio and in an ethanolic solution (DMF/ethanol in the case of complex **5**) led to the mononuclear Ce^{3+} coordination complexes [Ce(Btfa)$_3$(phen)] (**2**), [Ce(Btfa)$_3$(bipy)] (**3**), [Ce(Btfa)$_3$(terpy)] (**4**) and [Ce(Btfa)$_3$(bathophen)(DMF)] (**5**).

In the case of compounds **3a** and **3**, after the reaction of precursor **1** with the 2,2′-bipyridyl (bipy) ligand in ethanol as a solvent, structure determination by single crystal X-ray diffraction by using one chosen crystal from the bulk product indicated that the compound was [Ce(Btfa)$_3$(bipy)(EtOH)], **3a.** Powder X-ray diffraction (PXRD) of the whole powder sample, Fig. S3,† indicates the presence of two phases. After various recrystallization processes of the product, the PXRD spectra

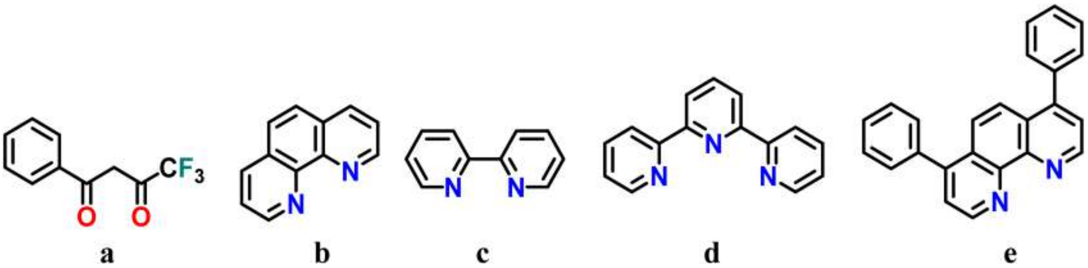

Scheme 1 Molecular representations of (a) 4,4,4-trifluoro-1-phenyl-1,3-butanedionate (HBtfa), (b) 1,10-phenanthroline (phen), (c) 2,2′-bipyridyl (bipy), (d) 2,2′;6′,2″-terpyridine (terpy) and (e) bathophenanthroline (bathophen).

were still the same. At that point, by choosing another single crystal of the bulk compound, SCXRD afforded a different structure with the formula [Ce(Btfa)$_3$(bipy)] (**3**).

Complex **3** can be isolated by removing all the coordinated EtOH molecules present in the bulk product from [Ce(Btfa)$_3$(bipy)(EtOH)] (**3a**). We found two different ways to do so. First, by leaving the obtained product in the open air for 3 months. The second method was to keep sample **3a** in the oven for 1 h at 100 °C, Fig. S3e.† Moreover, TGA measurements were performed on a freshly prepared sample, which probably predominantly contained compound **3a**. As can be observed in Fig. S6,† at around 100 °C there is a weight decrease corresponding to the loss of 4.9% of the sample content. This percentage corresponds to one EtOH molecule; the decrease of the curve starts at 29.56 °C and finishes at 175.17 °C. Then complex **3** was isolated as can be seen by PXRD, Fig. S1.†

Molecular structures of the compounds

The structures of compounds **1–5** and **3a** are presented here. A partially labelled plot of the Ce^{3+} mononuclear complexes, coordination polyhedra and intermolecular interaction arrangements are presented in Fig. 1–8 and Fig. S7–S10.† Crystallographic data are collected in Tables S6 and S7.† Selected bond lengths of compounds **1–5** are listed in Table 1.

[Ce(Btfa)$_3$(H$_2$O)$_2$] (1). Complex **1**, with the formula [Ce(Btfa)$_3$(H$_2$O)$_2$], crystallizes in an orthorhombic crystal system, $P2_12_12_1$ space group. The structure of **1** consists of mononuclear molecules in which each Ce^{3+} ion is octa-coordinated in a CeO$_8$ coordination environment (Fig. 1a). The central ion is coordinated to six oxygen atoms from three different Btfa$^-$ ligands, with Ce–O distances in the 2.390(3)–2.505(3) Å range. In addition, the other two coordination sites around the central atom are occupied by the O7 and O8 atoms of two water molecules, with Ce–O(water) distances of 2.535(4) and 2.520(3) Å, respectively. The estimation of the distortion coefficients of the CeO$_8$ coordination polyhedron for **1** with reference to the ideal eight vertex polyhedron was performed by employing the continuous shape measure theory and SHAPE software,[40] as for all the other compounds presented herein, showing that the O$_8$ disposition for **1** was intermediate between different coordination polyhedra. The best SHAPE estimation led to the triangular dodecahedron (TDD-8, D_{2d}) geometry with a continuous shape measurement (CShM) value of 0.416, Fig. 1b.

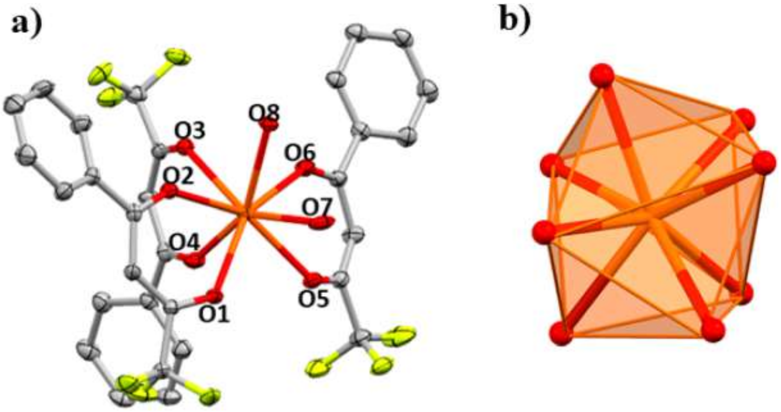

Fig. 1 (a) Partially labelled structure of **1** where hydrogen atoms have been omitted for clarity. (b) Idealized coordination polyhedron (triangular dodecahedron; TDD-8, D_{2d}) compared with the real positions of the coordinating atoms of compound **1**.

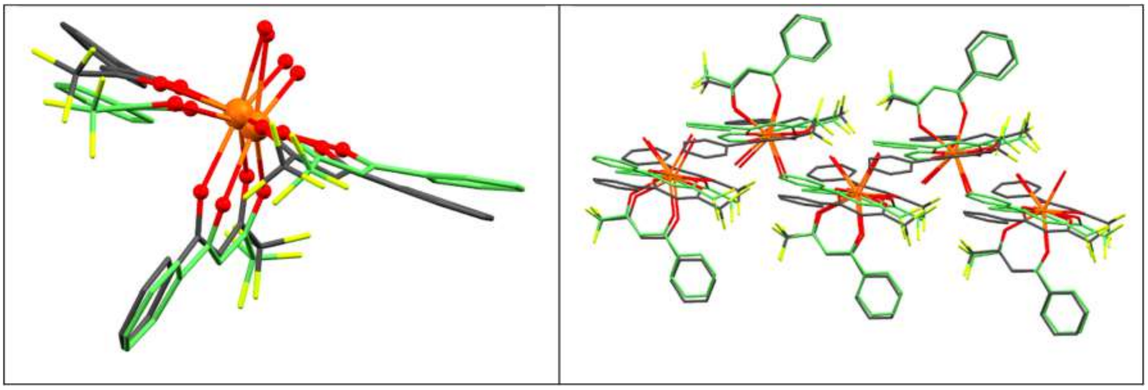

Fig. 2 Superimposed crystal structures of compound **1** obtained by single crystal XRD. The structure in default colours is the structure measured at 100 K and in green is the structure measured at 294 K.

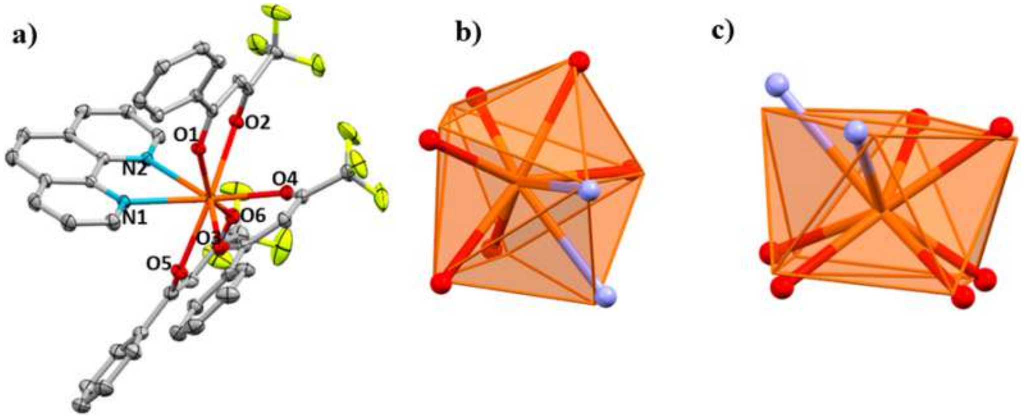

Fig. 3 (a) Partially labelled structure of **2**. The hydrogen atoms have been omitted for clarity. (b) Idealized coordination polyhedron (triangular dodecahedron; TDD-8, D_{2d}) compared with the real positions of the coordinating atoms of compound **2**. (c) Idealized coordination polyhedron (square antiprism; SAPR-8, D_{4d}) compared with the real positions of the coordinating atoms of compound **2**.

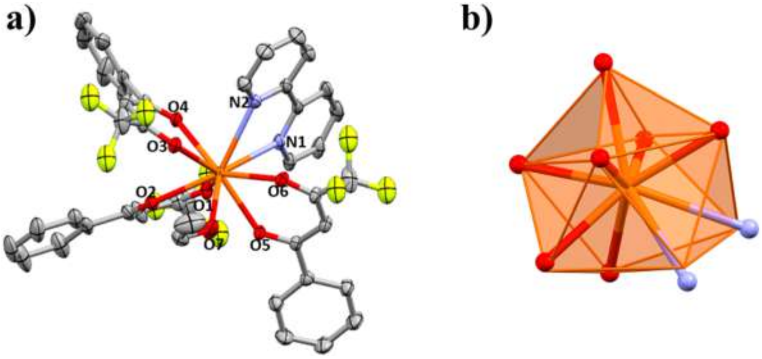

Fig. 4 (a) Partially labelled structure of **3a** where hydrogen atoms have been omitted for clarity. (b) Idealized coordination polyhedron (tricapped trigonal prism; TCTPR-9, D_{3h}) compared with the real positions of the coordinating atoms of compound **3a**.

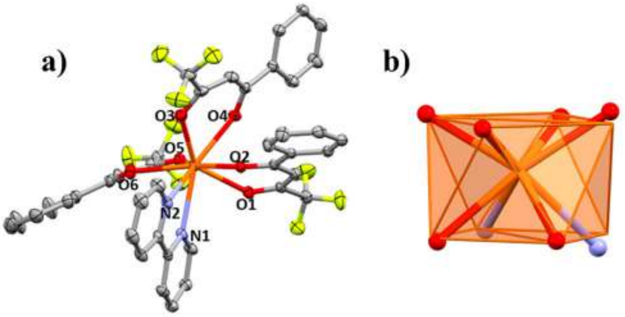

Fig. 5 (a) Partially labelled structure of **3** where hydrogen atoms have been omitted for clarity. (b) Idealized coordination polyhedron (square antiprism; SAPR-8, D_{4d}) compared with the real positions of the coordinating atoms of compound **3**.

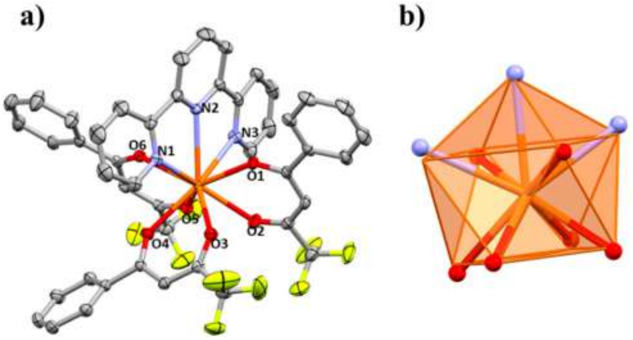

Fig. 6 (a) Partially labelled structure of **4** where hydrogen atoms have been omitted for clarity. (b) Idealized coordination polyhedron (capped square antiprism; CSAPR-9, C_{4v}) compared with the real positions of the coordinating atoms of compound **4**.

Molecules of **1** are arranged in space through hydrogen bonds forming an infinite 1D chain in the [1 0 0] direction, Fig. S7.† The atoms contributing to these intermolecular interactions are the hydrogens from the two water molecules coordinated to the cerium(III) atoms. On one hand, the H atoms from O8 interact with O1 and O5 from two different β-diketonates of the neighbouring coordination complex with donor (D)⋯acceptor (A) distances of 2.777 and 2.761 Å. On the other hand, the H atoms from the other O7 water molecule are connected through H-bonding with the O3 and F34 atoms

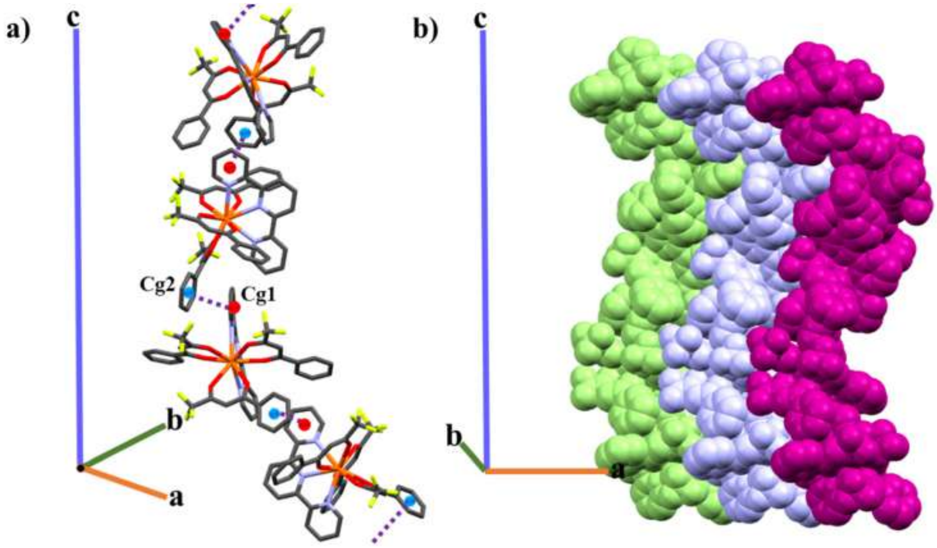

Fig. 7 (a) Helical chain formed by the intermolecular interactions of compound **4**. The π–π stacking interactions are represented by the purple dotted lines and (b) helical chains along the 4_3 screw axis.

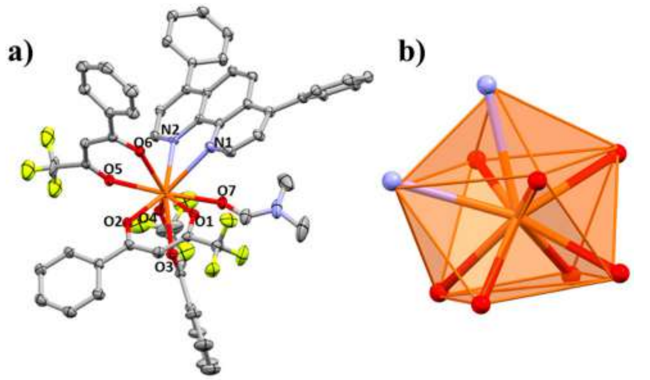

Fig. 8 (a) Partially labelled structure of **5** where hydrogen atoms have been omitted for clarity. (b) Idealized coordination polyhedron (capped square antiprism; CSAPR-9, C_{4v}) compared with the real positions of the coordinating atoms of compound **5**.

from the nearby complex with D–A distances of 2.868 and 3.026 Å respectively. The shortest Ce–Ce intermolecular distance is 6.105 Å.

PXRD for **1** was measured at 294 K, and the resulting spectrum was compared with the calculated one for the single crystal measured at 100 K to verify that the entire polycrystalline product was the same as the structure obtained by single crystal X-ray diffraction, Fig. S1.† However, the spectra do not match very well. Not even after several recrystallizations of the product. Then, one single crystal was measured by XRD at room temperature (300 K). The calculated spectrum for this new structure determination matches the spectrum of the powder one measured at 294 K, Fig. S1.† Comparing the crystallographic data for compound **1** at 100 K and at room temperature (Table S6†), we can see that, on decreasing the temperature, there is a slight structural change. The crystal system and space group are still the same (orthorhombic, $\alpha = \beta = \gamma = 90°$ and $P2_12_12_1$), but the cell parameters change from a = 10.854, b = 13.219 and c = 23.317 Å at room temperature to a = 10.809, b = 14.77 and c = 21.079 Å at 100 K. The structure at room temperature (294 K) shows Ce–O distances and angles that are slightly different from those measured at 100 K, Table 1. At room temperature, the coordination polyhedral geometry is still close to an ideal triangular dodecahedron

Table 1 Selected bond lengths (Å) of compounds **1–5**

	1	**1 r.t.**	**2**	**3a**	**3b**	**5**	**6**
Ce–O1	2.455(3)	2.438(7)	2.453(2)	2.443(3)	2.421(2)	2.450(2)	2.448(3)
Ce–O2	2.427(4)	2.474(6)	2.467(2)	2.481(2)	2.467(1)	2.454(2)	2.461(3)
Ce–O3	2.505(3)	2.522(6)	2.425(2)	2.460(3)	2.405(2)	2.531(2)	2.511(4)
Ce–O4	2.390(3)	2.379(7)	2.419(1)	2.496(3)	2.459(2)	2.490(2)	2.470(3)
Ce–O5	2.471(3)	2.422(7)	2.434(2)	2.464(3)	2.417(2)	2.428(2)	2.476(3)
Ce–O6	2.402(4)	2.473(7)	2.416(2)	2.490(2)	2.446(2)	2.461(2)	2.479(3)
Ce–O7	2.535(4)	2.509(7)	—	2.570(3)	—	—	2.541(3)
Ce–O8	2.520(3)	2.553(7)	—	—	—	—	
Ce–N1	—		2.659(2)	2.713(3)	2.660(2)	2.688(3)	2.701(4)
Ce–N2	—		2.697(2)	2.730(3)	2.668(2)	2.717(2)	2.701(4)
Ce–N3	—		—	—	—	2.680(3)	—

(TDD-8, D_{2d}) with a CShM value of 0.327, whereas the CShM value for **1** at 100 K is 0.416.

In Fig. 2 the structures obtained at 300 K and 100 K are superimposed. The slight difference between the distances and angles is enough to change the cell parameters when cooling the single crystal resulting in different powder XRD patterns.

[Ce(Btfa)$_3$(phen)] (2). Complex **2** with the formula [Ce(Btfa)$_3$(phen)] crystallizes in the monoclinic crystal system, $P2_1/c$ space group. In **2** each Ce^{3+} ion is octacoordinated with a CeN_2O_6 coordination environment formed by one phen and three $Btfa^-$ ligands, Fig. 3a. Two of the coordination sites around the central Ce^{3+} ion are occupied by the N1 and N2 atoms of the phen ligand, with Ce–N distances of 2.659(2) and 2.697(2) Å, respectively. In addition, the Ce(III) ion is also coordinated to six oxygen atoms from three different $Btfa^-$ chelating ligands, with Ce–O distances in the 2.416(2)–2.467(2) Å range.

The CeN_2O_6 disposition for **2** is intermediate between different coordination polyhedra. The lowest CShM values for **2** correspond to the triangular dodecahedron (TDD-8, D_{2d}) and square antiprism (SAPR-8, D_{4d}) geometries with CShM values of 1.700 and 1.835, respectively, Fig. 3b and c. The PXRD spectrum of the powder sample of **2** compared to the one calculated for the single crystal structure matchs perfectly indicating the purity of the bulk product, Fig. S2.†

The [Ce(Btfa)$_3$(phen)] molecules are arranged in the crystal lattice through π–π stacking interactions between the ring formed by C5–C10 from one $Btfa^-$ ligand (Cg3) and the three rings with delocalized electron density from the phen ligand (Cg9). The intermolecular distance between the two centroids (Cg3⋯Cg9) is 3.921 Å and the interaction grows along the [0 0 1] base vector as an infinite 1D chain Fig. S8.† The shortest Ce–Ce intermolecular distance is 8.806 Å.

[Ce(Btfa)$_3$(bpy)(EtOH)] (3a). Complex **3a**, [Ce(Btfa)$_3$(bpy)(EtOH)], crystallizes in the triclinic crystal system, with the $P\bar{1}$ space group, Fig. 4a. The structure of **3a** consists of mononuclear molecules in which each Ce^{3+} ion is nonacoordinated with a CeN_2O_7 coordination environment formed by six O atoms from the three deprotonated β-diketonate ligands with Ce–O distances in the 2.496–2.443 Å range, two N atoms from the bipy ancillary ligand with Ce–N distances of 2.713 and 2.730 Å and the O atom from the ethanol molecule with a Ce–O distance of 2.570 Å. The fluorine atoms from the $-CF_3$ group of the substituted β-diketone molecule show disorder. The CeN_2O_7 nine coordination polyhedron has a coordination geometry close to that of a tricapped trigonal prism (TCTPR-9, D_{3h}), Fig. 4b, with a CShM value of 0.562.

Powder X-ray diffraction was performed and the result was compared with the calculated PXRD spectrum of the single crystal structure of **3a**, but the spectra did not properly match, Fig. S3b.† As mentioned before, this is because, after the reaction of the [Ce(Btfa)$_3$(H_2O)$_2$] precursor with bipy, a mixture of structures [Ce(Btfa)$_3$(bipy)(EtOH)] (**3a**) and [Ce(Btfa)$_3$(bipy)] (**3**) crystallizes. Unlike **3**, compound **3a** cannot be isolated.

[Ce(Btfa)$_3$(bipy)] (3). Complex [Ce(Btfa)$_3$(bipy)] (**3**) crystallizes in the monoclinic crystal system, with the $P2_1/n$ space group. The structure of **3** consists of molecules in which each Ce^{3+} ion is octacoordinated with a CeO_6N_2 coordination environment formed by six O atoms from the three $Btfa^-$ molecules with Ce–O distances in the range of 2.467–2.405 Å and by two N atoms from the bipy ligand with Ce–N distances of 2.660 and 2.668 Å, Fig. 5a, Table 1. In this mononuclear complex the Ce–O and Ce–N distances are slightly shorter compared to the ones found in [Ce(Btfa)$_3$(bpy)(EtOH)] (**3a**). The CeO_6N_2 octacoordinated polyhedron has a coordination geometry that is close to an ideal square antiprism (SAPR-8, D_{4d}) with a CShM value of 1.058, Fig. 5b. As explained in the General syntheses section, compound **3** can be isolated from the mixture of **3a** and **3** that is obtained after the reaction by heating the sample in an oven for 1 h at 100 °C.

The intermolecular interactions to consider for both structures, **3a** and **3**, are the π–π stacking interactions between the rings from the bipy ligands with Cg1–Cg2 distances of 3.687 Å for **3a** and of 3.999 Å for **3**. Moreover, other weak intermolecular interactions such as π–H build up a three-dimensional supramolecular structure, see Fig. S9a and S9b.† The shortest Ce–Ce intermolecular distance is 8.647 Å.

[Ce(Btfa)$_3$(terpy)] (4). Complex **4** crystallizes in a tetragonal crystal system in the Sohncke $P4_3$ space group. The Sohncke space groups are formed of 65 space groups, which contain only rotation and translation symmetry operations (operations of the first kind) and where the reflection, glide reflection, rotoinversion and inversion mirror operations are restricted. Some of the molecular structures containing these non-enantiogenic space groups, 22 out of 65, result in chiral crystal structures (which are different from chiral molecules). For example, proteins generally crystallize in Sohncke space groups.[41] The structure of **4** consists of molecules in which each Ce^{3+} ion is nonacoordinated with a CeO_6N_3 coordination environment, Fig. 6a. The CeO_6N_3 coordination sphere is generated by six O atoms from the three $Btfa^-$ ligands with Ce–O distances ranging from 2.428 to 2.531 Å and the three N atoms from the terpy ligand with Ce–N distances ranging from 2.680 to 2.717 Å. The CeN_3O_6 nine coordination polyhedron has a coordination geometry close to an ideal capped square antiprism (CSAPR-9, C_4v) with a CShM value of 0.751, Fig. 6b.

Each asymmetric unit is formed by one mononuclear entity. For **4**, the asymmetric unit grows in space forming a laevorotatory 4_3-helical chain through the *c* axis (left-handed chain) and, therefore, homo-chiral packing of helices in the crystal is induced. The helix is formed around the crystallographic 4_3 screw axis *via* the π–π stacking interaction between two different rings with delocalized electron density, one from the terpy ligand (Cg1) and the other from one $Btfa^-$ β-diketone molecule (Cg2) with an intermolecular distance of 3.767 Å, Fig. 7a. The helices align themselves along the *a* and *b* axis through weak Van der Waals interactions, resulting in the formation of a chiral crystal structure, Fig. 7b. The shortest Ce⋯Ce intermolecular distance is 10.563 Å.

The enantiomeric pair for this Sohncke space group is $P4_1$ in which the helix would be dextrorotatory. To find a crystal with the enantiomeric $P4_1$ Sohncke space group, a second single crystal was measured. For this second measurement, the same $P4_3$ space group was found. Though both crystals presented the same chirality, we cannot assert that the final product is purely chiral and neglect the idea that it could be a racemic mixture. The powder XRD results presented in Fig. S4† support one single phase for the whole powder product of **4**.

[Ce(Btfa)$_3$(bathophen)(DMF)] (5). Complex [Ce(Btfa)$_3$(bathophen)(DMF)] (**5**) crystallizes in the monoclinic crystal system, $P2_1/c$ space group. The structure of **5** consists of mononuclear molecules in which each Ce^{3+} ion is nonacoordinated with a CeN_2O_7 coordination environment, Fig. 8a. The coordination sphere encompasses six O atoms from three $Btfa^-$ ligands with Ce–O distances in the 2.448 to 2.511 Å range, two N atoms from the bathophen ligand with Ce–N distances of 2.724 and 2.701 Å and a DMF molecule through the O atom with a Ce–O distance of 2.541 Å. The N_2O_7 vertexes are established around the Ce^{3+} metal in a polyhedral geometry that is close to an ideal capped square antiprism (CSAPR-9, C_4v) with a CShM value of 0.316, Fig. 8b. The mononuclear complexes are arranged in space through π–π stacking interactions between one of the aromatic rings from the bathophen ligand (Cg1) and one phenyl ring from a $Btfa^-$ ligand. The Cg(1)–Cg(2) intermolecular distance is 3.818 Å and it grows along the *c* axis as shown in Fig. S4.† The shortest Ce–Ce intermolecular distance is 10.770 Å. Moreover, PXRD measurements were performed on the powder product. The calculated PXRD spectrum from the single crystal structure was compared with the experimental one, which affirmed a single phase throughout the sample, Fig. S5.†

Magnetic properties

Static magnetic properties

Direct current (dc) magnetic susceptibility and magnetization measurements were performed on polycrystalline samples of compounds **1–5**. Since compound **3a** was not isolated as a pure compound, the magnetic study was not performed for this sample. The $\chi_M T$ *vs.* T plots in the 2–300 K temperature range under a dc magnetic field of 0.3 T are shown in Fig. 9 (left). At room temperature (300 K) the $\chi_M T$ values for compounds **1–5** are 0.67, 0.73, 0.68, 0.73 and 0.76 cm^3 mol^{-1} K respectively. These $\chi_M T$ values are close to the calculated value for an isolated Ce^{3+} cation in the ground state, $^2F_{5/2}$ ($S = 1/2$, $L = 3$, $J = 5/2$, $g_J = 6/7$), which is 0.8 cm^3 mol^{-1} K.[8] On cooling the samples, the $\chi_M T$ values decrease gradually due to the progressive thermal depopulation of the m_j states to finite values at 2 K of 0.23, 0.40, 0.44, 0.32 and 0.38 cm^3 mol^{-1} K for compounds **1–5** respectively. Other mononuclear Ce^{3+} coordination compounds show similar $\chi_M T$ *vs.* T curves.[21,42,43] The field dependence of the magnetization (M) recorded at 2 K is depicted in Fig. 9 (right). On increasing the external magnetic field up to 5 T, the magnetization values increase to 0.62, 0.84, 0.89, 0.83 and 0.89 $N_A\mu_B$ for **1–5** respectively without stabilization of the M values, showing no evidence of saturation of the magnetization ($g_J J$). Similar behavior is found for other Ce^{3+} compounds showing significant magnetic anisotropy.[17,21,30]

Dynamic magnetic properties

No frequency dependence of the out-of-phase magnetic susceptibility component (χ_M'') was found under a 0 T external magnetic dc field for complexes **1–5** (Fig. S11†), suggesting the lack of a pure axial Ising type geometry, which sets $m_j = \pm 5/2$ as the ground doublet, and makes the reorientation of the magnetization occur through the fast quantum tunneling of magnetization (QTM) mechanism preventing the SMM behavior.[23] Nevertheless, by applying a small direct current (dc) magnetic field (H_{dc}), the QTM was suppressed enough so that all the above compounds showed slow relaxation of the magnetization.

To decide which external dc magnetic field was optimal for each compound, ac measurements were performed at a constant temperature of 2.5 K for **1**, **3** and **5**, of 3.5 K for **2**, and of 2 K for **4** at oscillating frequencies between 1 and 1488 Hz and under different H_{dc} fields. The measurements of χ_M' and χ_M'' with frequency (ν) plots, at a constant temperature, are depicted in Fig. S12† for samples **1–5**. When applying low H_{dc} (0.002–0.01 T), χ_M'' shows maximum values at higher frequencies. On increasing H_{dc}, the peaks increase in intensity, reach-

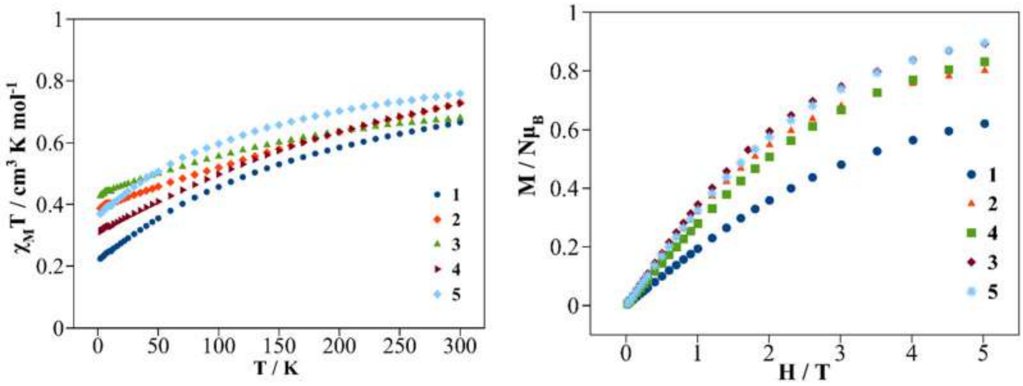

Fig. 9 $\chi_M T$ *vs.* T plot (left) and M *vs.* magnetic field plot (right) for compounds **1–5**.

ing their maximum values and shifting to the 96–177 Hz frequency zone, then staying constant until higher H_{dc} is applied. Then χ_M'' shifts again to higher frequencies, diminishing its intensity. The optimal H_{dc} was 0.1 T for **1** and **3**, 0.05 T for **2** and 0.02 T for **4** and **5**, Fig. S13.† Given the shorter Ce⋯Ce intermolecular distance of 6.105 Å, compound **1** might require a greater external H_{dc}. The shortest Ce⋯Ce intermolecular distances found for structures **2–5** are 8.806, 8.647, 10.563 and 10.770 Å respectively.

This behavior is represented as τ^{-1} based on the H_{dc} plots, Fig. 10. At low magnetic fields, τ^{-1} values decrease, corresponding to suppression of the QTM mechanism by the external magnetic field. After 0.3 T for **1–3** and **5**, the τ^{-1} values remain almost constant, accounting for the predominancy of Raman and other thermally dependent relaxation processes. For compound **4**, the constant trend at intermediate H_{dc} is rather poor and it is not as well differentiated as for the other compounds. When surpassing the specific H_{dc}, this constant tendency is broken, and τ^{-1} values increase exponentially following the H^4 power law, showing that the direct process is taking place at higher magnetic fields. ($\tau^{-1} = AH^4T$ for relaxation of the magnetization through a direct process.)

Under the chosen dc external magnetic field, dynamic measurements were performed under an oscillating ac field of 4×10^{-4} T in the 1–1488 Hz frequency range for **1**, **3** and **5**, and of 10–1488 Hz for **2** and **4**. Maximum values of the out of phase magnetic susceptibility component can be seen below 5 K for **1–5**, Fig. S14.† All the samples show slow relaxation of the magnetization over a similar temperature range; compound **2** is the one for which the χ_M'' dependence extends to higher temperature (5.7 K).

The χ_M'' *vs.* oscillating frequency plots at different temperatures are depicted in Fig. 11 and χ_M' *vs.* ν plots at different temperatures are found in Fig. S15.† For complexes **1–5**, the χ_M'' peaks shift progressively to higher frequencies as the temperature increases, demonstrating the thermal dependence of magnetization relaxation. Therefore, we could assume that the QTM relaxation process would be considerably reduced after the application of an external dc field.[3] When comparing compounds **1–5**, **2** shows χ_M'' dependence on T at lower frequencies, whereas **3** shows a dependence at higher ones.

The Cole–Cole plots for **1–5** (Fig. 12) are not perfectly symmetrical semicircles. The curves could be fitted using the generalized Debye model described with the Casimir–Du Pré function (eqn (S1)†)[44] from which the relaxation times for magnetization can be extracted. The resulting parameters obtained from the fitting are presented in Tables S8–S12.† The distribution of relaxation times (α) is narrow for the presented compounds mostly for **1**, **4** and **5** in which α values are 0.077–0.0041, 0.0529–0.0031 and 0.05–0.0118 respectively while for **2** and **3** α values are over a slightly wider range of 0.1804–0.0018 and 0.1335–0.0146 respectively.

For a spin system, magnetization relaxation can occur through different relaxation mechanisms. The dependence of τ on temperature (T) and the applied external magnetic field (H) is expressed in eqn (1).

$$\tau^{-1} = aH^4T + d\left(\frac{1+eH^2}{1+fH^2}\right)T^n + \frac{B_1}{1+B_2H^2} + \tau_0{}^{-1}\exp\left(\frac{-\Delta E}{k_BT}\right) \quad (1)$$

The first term is the field dependent direct process, which involves one phonon, the second term refers to the Raman process that occurs through a virtual state involving two phonons. Here it is represented as a field dependent term using the Brons–Van Vleck equation, which has a coefficient field dependence and exponential dependence on temperature. The d parameter represents zero-field relaxation, e is related to the paramagnetic center concentration and the f parameter reports the effect of the external field on suppres-

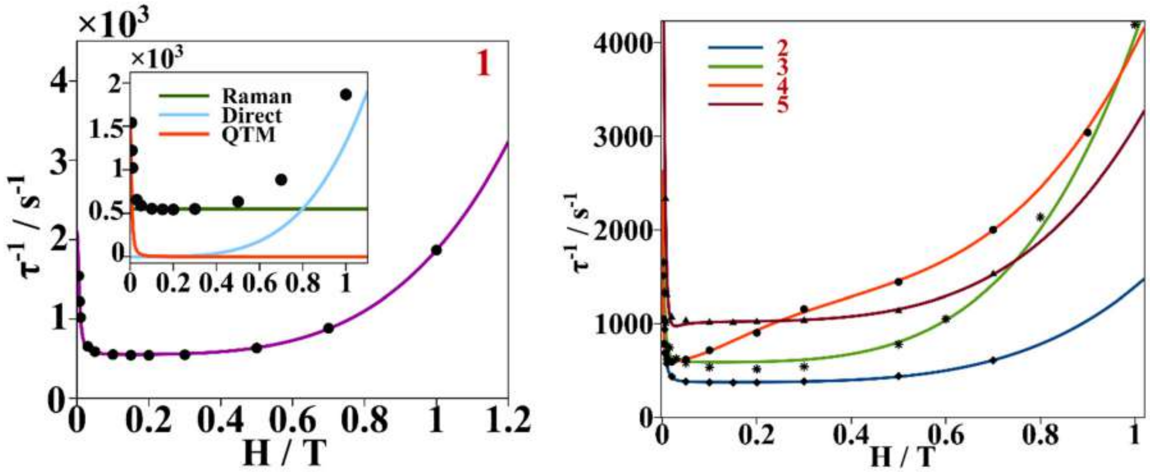

Fig. 10 Left, dependence of τ^{-1} on a static magnetic field (black dots) for compound **1**, continuous purple line accounts for the fitting using field dependent eqn (3). Inset shows the contribution of Raman, direct and QTM mechanisms to τ^{-1} *vs.* H for compound **1**. Right, dependence of τ^{-1} on a static magnetic field for compounds **2–5**. The continuous blue, green, orange and red lines correspond to the fitting of the experimental magnetic data (discrete dots) of compounds **2** to **5** respectively with eqn (3).

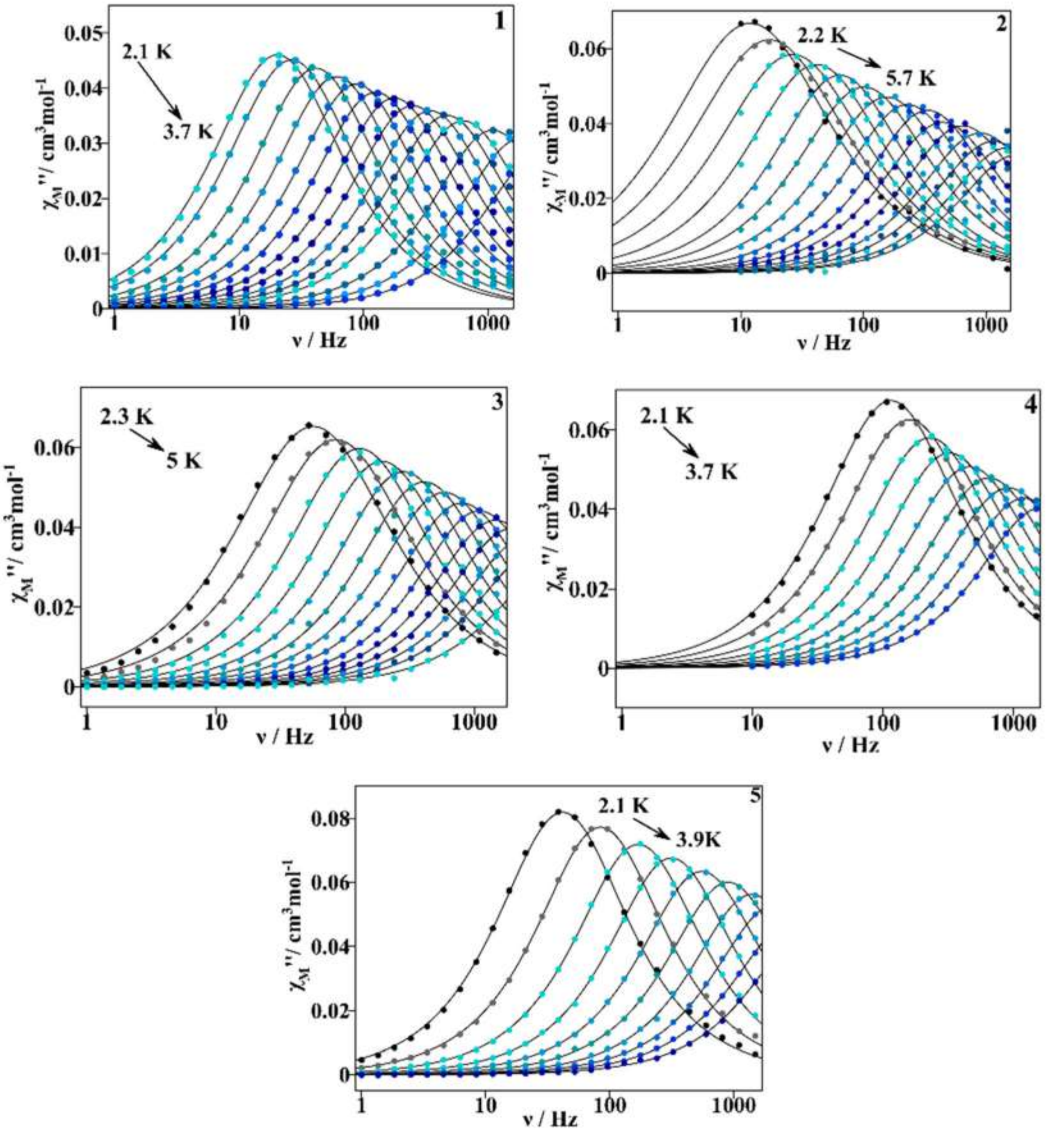

Fig. 11 χ_M'' *vs.* frequency plots for compounds **1–5** measured at an oscillating ac field of 4×10^{-4} T, and at a H_{dc} of 0.1 T for **1–3**, and of 0.02 T for **4** and **5**. The continuous lines correspond to the fitting with eqn (S1).†

sing spin relaxation. The third term of eqn (1) describes the fast QTM and, finally, the last term relates to the so called thermally assisted relaxation process, the Orbach process. It follows the Arrhenius law and experimentally, when the Orbach process takes place, a linear trend of log(τ) with temperature is expected. This spin–lattice mechanism involves two phonons, and relaxation occurs through an effective energy barrier from the ground state $\pm m_j$ through a real excited state. Normally, the Orbach process takes place at a higher temperature range since the system needs enough energy to surpass the whole energy barrier between the $\pm m_j$ ground states.[45,46]

For the title compounds a linear slope appears to be followed in the higher temperature range. We fit the experimental τ values of **1–5** using the Arrhenius law, and the values obtained for the activation energy barrier are in the range of 12.2–19.8 cm^{-1} with τ_0 values between 10^{-7} and 10^{-8} s, Table S13 and Fig. S16.† This linear trend could indicate that the relaxation of magnetization is taking place through an over-barrier Orbach mechanism for **1–5** or a thermally assisted tunneling process through the first $\pm m_j$ excited state. Nevertheless, for all the cerium(III) compounds found in the literature where *ab initio* calculations were performed, the energy differences between the $\pm m_j$ ground Kramers doublet (KD) and the first excited $\pm m_j$ KD are in the range of 258–339 cm^{-1} for mononuclear Ce^{3+}–β-diketonate complexes,[20,21] 220–787 cm^{-1} for other Ce^{3+}–mononuclear compounds,[23–28,47,48] 303–348 cm^{-1} for Ce^{3+}–polynuclear compounds[30,49] and 180–303 cm^{-1} for Ce^{3+}–heterometallic compounds.[29,34,50,51] Interestingly, the activation energy barrier calculated from experimental data (ΔE_{exp}), with the

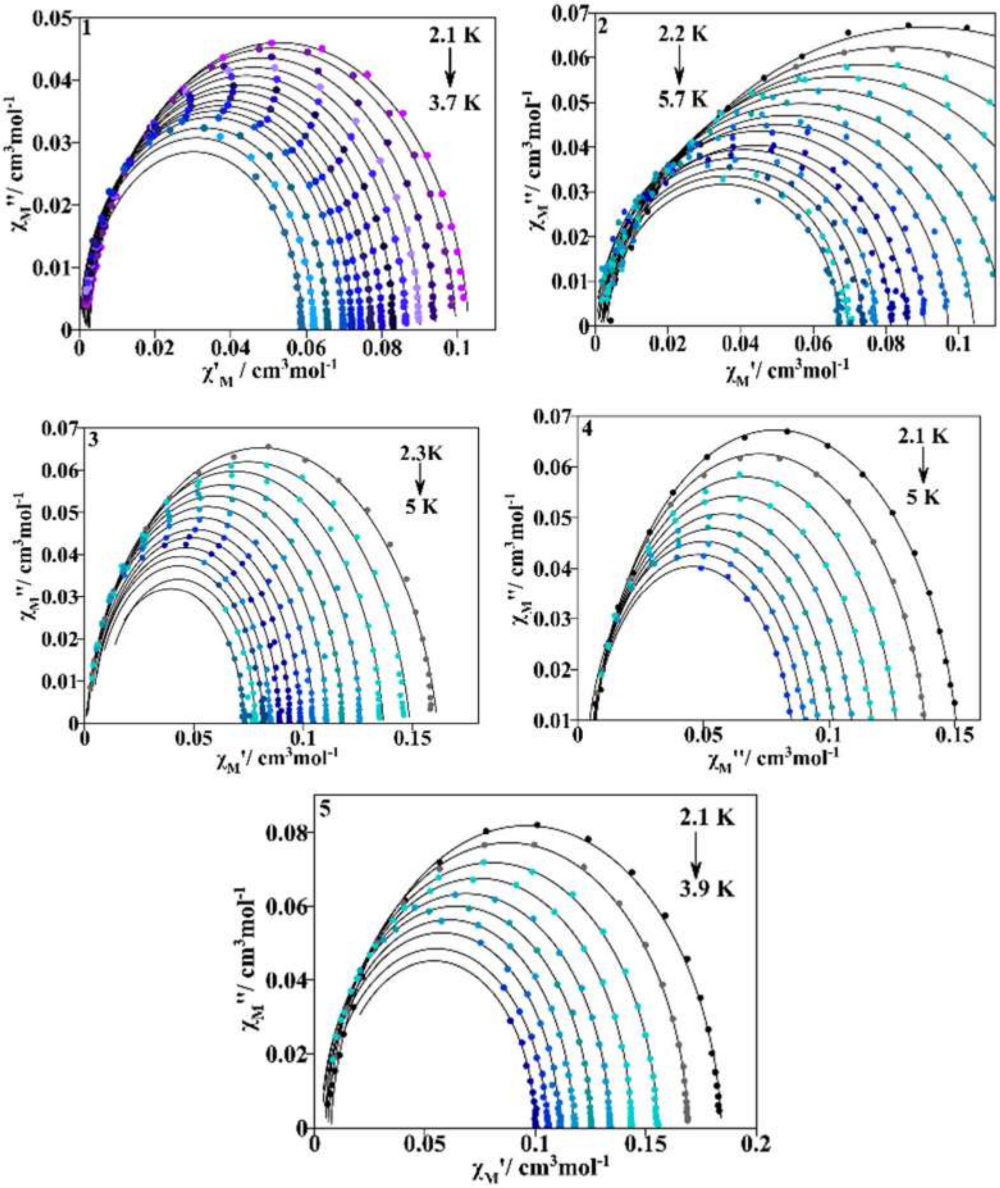

Fig. 12 Cole–Cole plots for compounds **1–5**. The continuous black lines refer to the fitting with the generalized Debye model.

Arrhenius law, considering an Orbach mechanism, led to very similar values for all the previous Ce^{3+} compounds. The maximum value reported is 38 cm^{-1},[28] but the ΔE_{exp} values for the vast majority of published Ce^{3+} complexes lie in the 20–30 cm^{-1} range and it appears that there is no difference between compounds presenting easy axial or easy plane symmetry.[20,21,26,27,29,43,47,50,52,53] Besides, *ab initio* calculations (see the Computational results section) of the former cerium (III) systems result in an energy difference between the ground and first excited m_j states much higher in energy (151.9–372.6 cm^{-1}, see Table S14†) than the energy barrier obtained from experimental data using the Arrhenius law that describes the Orbach process.

The lack of a linear trend in the log(τ) *vs.* T plots throughout the temperature range could be explained by considering the presence of other magnetization relaxation mechanisms occurring at the same time as the Orbach process or taking into consideration that the Orbach process is not taking place at all, as a comparison of experimental data with *ab initio* calculations appears to indicate. Furthermore, hyperfine interactions between the electronic spin and the nuclear spin of a lanthanide ion can split the electronic doublet into different manifolds making new pathways for magnetization that could explain the linear trend with temperature. But the natural isotopes of cerium do not possess nuclear spin. Another proposed spin–lattice relaxation mechanism is the local mode, and it is referred to as a thermally dependent process, which considers that spin relaxation goes through a higher energy state that is a local vibration from the same m_j ground state following eqn (2). Then Δ_{loc} can be extracted and is referred to as the local mode energy (cm^{-1}).[54] Δ_{loc} could be experimentally assigned from vibrational spectroscopic techniques.[55,56]

$$\tau^{-1} = A_{\text{loc}}\left(\frac{e^{-\frac{\Delta_{\text{loc}}}{k_{\text{B}}T}}}{\left(e^{-\frac{\Delta_{\text{loc}}}{k_{\text{B}}T}}-1\right)^{2}}\right) \tag{2}$$

With the above exposed considerations, we tried to fit the magnetic data with the thermally dependent components of eqn (1) but by adding the local mode function instead of the Orbach one. Given that the temperature ranges over which there is a magnetic response for **1–5** are small and the risk of over-parametrization when many parameters are used in the equation, we first proceed to fit the dependence of τ^{-1} on the magnetic field so in this way we can extract the parameters from the equations that are field dependent: dT^n, e and f for Raman, B_1 and B_2 for the QTM and a for the direct process (eqn (3)) and then the parameters corresponding to these equations can be fixed in the temperature dependent function.

The Cole–Cole plots of the field dependent experimental magnetic data measured at a constant temperature were fitted using the generalized Debye model, Fig. S17 and Tables S15–S19.† The field dependent magnetic data could be fitted following eqn (3), for all the compounds, Fig. 10. In the τ^{-1} *vs* H plot, the different tendencies from the predominant QTM, Raman and direct mechanisms are well differentiated, first, each part is fitted independently with the corresponding mechanism and the fitted parameters are used as the starting point for the whole set. The obtained parameters from the field dependent fitting of compounds **1–5** are compiled in Table 2. The inset in Fig. 10 and Fig. S18† show the contributions of each relaxation mechanism to magnetization relaxation along the magnetic fields of compounds **1–5**.

$$\tau^{-1} = aH^4T + \frac{B_1}{1+B_2H^2} + d\left(\frac{1+eH^2}{1+fH^2}\right)T^n + K(T) \tag{3}$$

Then the temperature dependent experimental magnetic data were fitted with eqn (4) and the parameters n from the Raman process and c and ω from the local mode spin relaxation mechanism were obtained for **1–5**. The τ^{-1} dependence on T plots are depicted in Fig. 13 and the obtained parameters from the best fit are compiled in Table 3. The contribution of each relaxation mechanism to τ^{-1} with temperature is shown in the inset of Fig. 13 and in Fig. S19.†

$$\tau^{-1} = A(H)T + K(H) + D(H)T^n + A_{\text{loc}}\left(\frac{e^{-\frac{\Delta_{\text{loc}}}{k_{\text{B}}T}}}{\left(e^{-\frac{\Delta_{\text{loc}}}{k_{\text{B}}T}}-1\right)^{2}}\right) \tag{4}$$

When looking at the dependence of τ^{-1} on the field, for all the compounds under low external bias dc magnetic fields, the QTM mechanism is the one dominating magnetization relaxation. Under high external dc fields for **1** and **3** the direct

Table 2 Values obtained from the fitting of τ^{-1} *vs.* *H* curves with the field dependent curve function: $\tau^{-1} = AH^4T + \frac{B_1}{1+B_2H^2} + d\left(\frac{1+eH^2}{1+fH^2}\right)T^n + K(T)$

	Raman		Direct		QTM	
Compound	dT^n (s^{-1})	e (T^{-2})	f (T^{-2})	a ($\text{s}^{-1}\ \text{T}^{-4}$)	B_1 (s^{-1})	B_2 (T^{-2})
1	549.21	82.78	22 760.23	526.71	1549.17	22 760.21
2	370.07	214.49	77 778.39	291.57	1691.25	77 778.40
3	575.89	1279.27	87 007.58	1394.18	2054.14	87 010.40
4	585.82	23.25	15.40	1270.65	2055.59	556 254.6
5	197.48	14 891.10	3561.34	832.12	5754.71	42 402.08

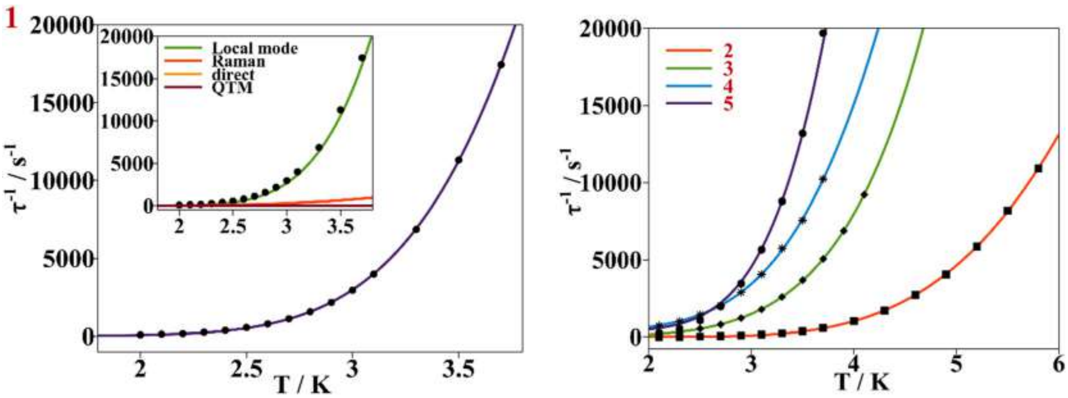

Fig. 13 Dependence of τ^{-1} on temperature obtained from the experimental magnetic data measured at an external magnetic field of 0.1 T for **1** and **3**, of 0.05 for **2** and of 0.02 T for **4** and **5**. Left, the plot of compound **1**. Inset shows the contributions of each magnetization relaxation mechanism separately. Right, the plots for compounds **2–5**.

Table 3 Values obtained from the fitting of τ^{-1} *vs.* *H* curves with the field dependent curve function: $\tau^{-1} = C\left(\frac{e^{-\frac{\omega}{T}}}{\left(e^{-\frac{\omega}{T}}-1\right)^2}\right)T^n + D(H)T^n + A(H)T + K(H)$

Compound	Raman	Local mode	
	n	C (s^{-1})	ω (cm^{-1})/(K)
1	4.82	4.03×10^7	19.95/28.71
2	7.20	1.7×10^7	20.89/30.07
3	8.27	3.16×10^5	11.55/16.61
4	2.40	3.05×10^6	15.42/22.19
5	6.16	1.20×10^7	17.70/25.47

process is the dominant one while for **2**, **4** and **5** the Raman process is still relevant, Fig. 10 and Fig. S18.†

From the global fit the obtained local mode energy values for the different compounds are in the range of 11.55–20.90 cm^{-1} (16.61–30.07 K). With this approach, the spin relaxation of compound **1** appears to be governed by the local mode mechanism, Fig. 13 inset. While for **2**, **4** and **5** spin relaxation over the temperature range is best described by both the Raman and local mode mechanisms, Fig. S19.† In fact for compound **4** it is well discerned that the Raman mechanism prevails in the lower temperature range while the local mode mechanism plays an important role in the higher temperature range, Fig. S19(4).† Moreover, compound **3** shows a smaller contribution of the local mode (ω), which is the smallest of the presented compounds with a value of 11.55 cm^{-1} (16.61 K), but there is a higher contribution from the n parameter from the Raman process (n = 8.2) and the direct mechanism (it has the highest $A(H)$ value). This suggests that for **3**, spin relaxation is mostly taking place through the Raman and direct processes.

Additionally, the temperature dependence of τ could also be fitted with only the Raman term as the ln(τ) *vs.* ln(T) plots lead to straight lines for the magnetic data for all compounds, Fig. S20.† A fitting of these plots taking into account just Raman relaxation of the magnetization mechanism described by the $\ln(\tau) = -n \cdot \ln(T) + \ln(C)$ equation leads to good values of n and C, which are n = 8.9 and C = 5.9 for **1**, n = 7.0 and C = 17.8 for **2**, n = 5.7 and C = 0.3 for **3**, n = 4.7 and C = 0.0519 for **4** and n = 7.5 and C = 0.9 for **5**. This leads us to consider that the Raman process may actually be the relevant mechanism for the magnetic relaxation of these cerium(III) compounds. However, a fitting of temperature dependent data with eqn (3) without considering the local mode but taking into account the contribution of all the field dependence terms, leads to unsuccessful fitting of the data, Fig. S21.† Therefore, two different approaches are presented to explain the spin dynamics of **1**–**4**.

The first is that, when considering the contributions of QTM and direct processes to magnetic relaxation, this would lead to overparametrization, so the parameters for those mechanisms are first obtained from the field dependent magnetic data and fixed in the temperature dependent fitting. In this approach, the local mode has to be considered to obtain a good fitting of magnetization relaxation times with temperature since only considering the Raman process leads to unsuccessful fitting. The second approach is just to consider the Raman relaxation mechanism and neglect the contribution that direct and QTM mechanisms may have on spin relaxation; this also leads to reasonable results. Still the contributions of the QTM and direct mechanisms to spin relaxation should not be overlooked, especially the direct mechanism, if an external magnetic field is applied to measure the alternating current magnetic susceptibility.

The existence of multiple potential explanations to describe the spin dynamics phenomenon of compounds **1**–**5**, once again, highlights the need for continued investigation into the magnetic behavior, at the molecular level, of Ce(III) coordination compounds.

Geometry optimization and calculation of the DFT vibrational frequencies were performed for **1**, **2** and **4**. The analysis of the frequencies shows a large amount of low energy vibrational frequencies (Table S20†) that can contribute to spin relaxation through the local-mode process; however, a spin–phonon calculation of these frequencies to verify their contribution is out of the scope of this paper.

Computational results

Ab initio calculations were performed on the crystallographic structures, see the Computational details section. CASSCF calculations incorporating spin–orbit effects *via* the RASSI approach were conducted to delve into the magnetic characteristics of compounds **1**–**5**. Cerium(III) complexes exhibit a 4f^1 and a $^2F_{5/2}$ ground state. The simulated magnetic susceptibility and magnetization profiles are similar to the experimentally observed curves, see Fig. S22 and S23,† indicating good agreement between theoretical predictions and actual experimental results.

Except compound **1**, the remaining systems studied show a large g_z component, see Table 4, indicating large axial anisotropy. The values are similar to those for other previously

Table 4 Calculated components of the *g* tensor and wavefunction analysis of the ground Kramers doublet state at the CASSCF-RASSI level

Compound	g_x	g_y	g_z	Wavefunction
1	0.563	1.391	2.392	$0.28|\pm 5/2\rangle + 0.42|\pm 3/2\rangle + 0.30|\pm 1/2\rangle$
2	0.108	0.481	3.754	$0.90|\pm 5/2\rangle + 0.005|\pm 3/2\rangle + 0.09|\pm 1/2\rangle$
3	0.460	0.940	3.600	$0.87|\pm 5/2\rangle + 0.04|\pm 3/2\rangle + 0.09|\pm 1/2\rangle$
4	0.775	1.255	3.379	$0.89|\pm 5/2\rangle + 0.08|\pm 3/2\rangle + 0.03|\pm 1/2\rangle$
5	0.501	1.500	3.350	$0.82|\pm 5/2\rangle + 0.04|\pm 3/2\rangle + 0.14|\pm 1/2\rangle$

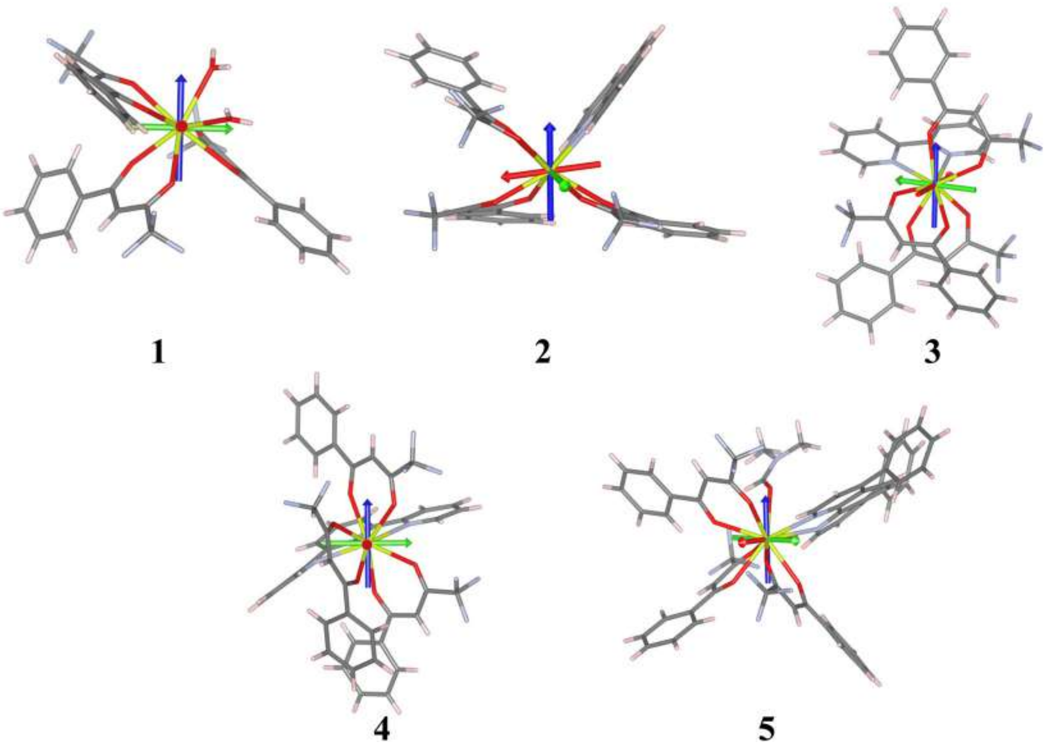

Fig. 14 Calculated orientations of the g tensor of the ground Kramers doublet, where g_z, g_y and g_x components are represented by blue, green and red arrows, respectively. Cerium, fluorine, oxygen, nitrogen, carbon and hydrogen are represented in yellow, light blue, red, blue, gray and pink.

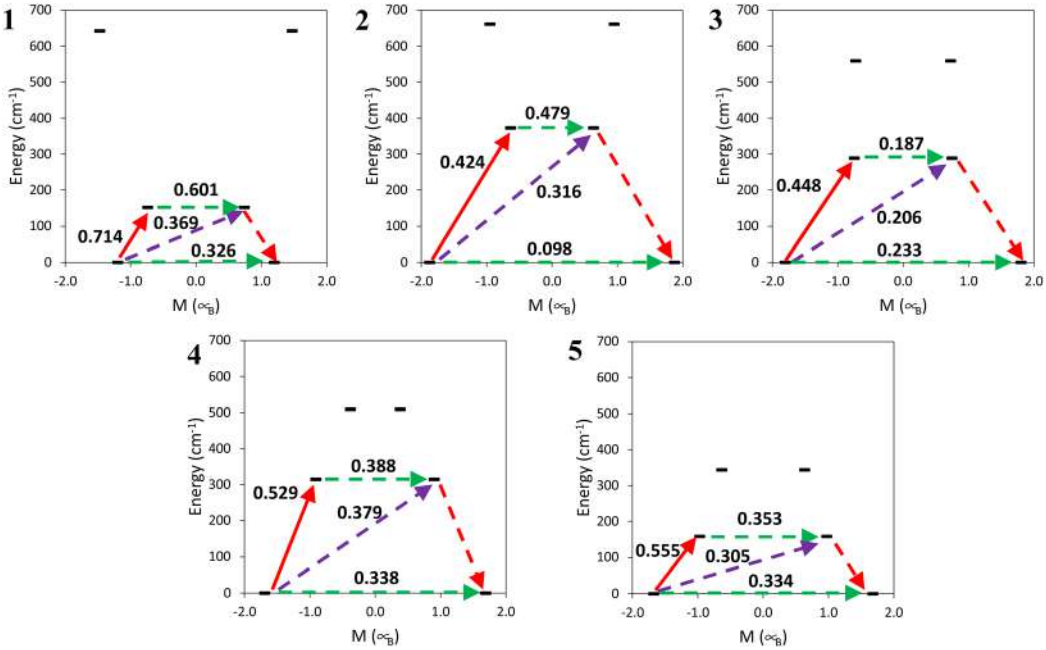

Fig. 15 Calculated state energies as a function of their magnetic moment, M_z, along the main anisotropy axis. The arrows correspond to the quantum tunneling mechanism of ground and first excited states (green), the hypothetical Orbach relaxation process (purple) and the transition between the ground and first Kramers doublets (red). The values close to the arrows indicate the matrix elements of the transition magnetic moments (efficient spin relaxation mechanism is expected above 0.1).

reported Ce systems (see Tables S1–S5†); however, for a perfectly axial Ce^{3+} complex the value should be 4.19 (30/7). Compounds **2–4** with values in the range of 3.3–3.8 are consistent with an $m_J = \pm 5/2$ ground state with a contribution from $m_J = \pm 3/2$ states. The orientation of the calculated g_z is quite different for the compounds (see Fig. 14). The coordination numbers are also different, eight for **1–3**, and nine for **4** and **5**. In the case of an $m_J = \pm 5/2$ ground state an oblate f electron density, with a perpendicular g_z orientation, is expected. The g_z tensor would be oriented in a way that the metal–ligand electrostatic repulsion would be reduced. It can be achieved by (i) the alignment of g_z with the shortest Ce–O distances, in a way that the f electron density disc stays perpendicular to that direction or (ii) the location of the f electron density disc in the plane containing the longest Ce–L distances. In this family of compounds in general g_z is located in a way that it is not pointing to any ligand and the electron density disc tries to avoid all the ligands. This happens for **1**, **2**, **4** and **5**. However, for **3** it is mainly oriented with one of the Ce–O bonds (Ce1–O5) and with the f electron density disc oriented close to the Ce–N bonds. In the case of **4** g_z is oriented in a way that the f electron density disc avoids most of the ligands but is in the same plane as some of the Ce–N bonds of the terpyridine ligand.

The analysis of the decomposition of the RASSI wavefunction of the ground Kramers doublet can be found in Table 4. It shows, as expected, a different contribution for **1**, where a large mixture of the three components is observed; this correlates with smaller g_z and larger g_x and g_y components. For the other compounds a larger contribution from the wave function $|\pm 5/2\rangle$ (80–90%) mixed with $|\pm 1/2\rangle$ and $|\pm 3/2\rangle$ from the other excited m_J doublets is found; this also explains the larger anisotropy of these Ce complexes.

The energy of the Kramers doublet and transition probabilities between the states were calculated, see Fig. 15. The first excited Kramers doublet is around 150 cm^{-1} in **1** and **5** and around 300 cm^{-1} or more for the other complexes, see also Table S14.† In all the cases, as commented on before, the energy difference is much larger than the energy barrier that can be obtained from the fit of the dependence of relaxation times on temperature with the Arrhenius equation, 12–20 cm^{-1}. All the complexes show a large tunnelling probability in the ground state, with complex **2** having the smallest one, of 0.1. This agrees with the necessity to apply an external dc field to show an out-of-phase magnetic susceptibility signal (χ_M''). Besides **2** having the smallest tunnelling probability in this family of compounds the optimal field needed is not the smallest one. This is probably also related to the shorter Ce⋯Ce distance in **2** in comparison with **4** and **5**.

Conclusions

As a continuation of our interest in the less studied lanthanide (III) SIM compounds derived from Ce^{3+} ions,[21] in this paper we have presented five new β-diketonate–Ce^{3+} coordination compounds with the aim of providing new insights into understanding the cerium spin relaxation. The five structurally characterized new Ce^{3+} complexes are derived from the β-diketone HBtfa = 4,4,4-trifluoro-1-phenyl-1,3-butanedione with polypyridyl molecules as ancillary ligands: $[Ce(Btfa)_3(H_2O)_2]$ (**1**), $[Ce(Btfa)_3(phen)]$ (**2**), [Ce(Btfa)3(bipy)] (**3**), $[Ce(Btfa)_3(terpy)]$ (**4**) and $[Ce(Btfa)_3(bathophen)(DMF)]$ (**5**), where phen = 1,10-phenanthroline, bipy = 2,2′-bipyridine, terpy = 2,2′:6′,2″-terpyridine and bathophen = 4,7-diphenyl-1,10-phenanthroline. In the new reported compounds, Ce^{3+} displays a coordination number of 8 for **1**, **2** and **3** and a coordination number of 9 for **4** and **5**. Moreover, the five compounds have been magnetically characterized and a meticulous study has been carried out to further understand the spin dynamics in the magnetization relaxation of these new field induced SMM compounds. Furthermore, *ab initio* calculations were performed for the former compounds. For all the compounds, the Orbach mechanism was disregarded in light of the published literature and the obtained *ab initio* results. The local mode mechanism was used instead. The calculations also show the axiality of the compounds and corroborate the presence of low energy vibrational modes that could contribute to spin relaxation through the local mode. Finally, a compilation of the cerium(III) coordination complexes found in the literature before 2023 and showing slow magnetization relaxation is given in Tables S1–S5.† From the published experimental data and *ab initio* calculations, we can infer that the stabilization of m_J with the highest value as the ground state does not imply the presence of SMM behavior for the previously magnetically studied Ce^{3+} coordination compounds.

Conflicts of interest

There are no conflicts to declare.

Acknowledgements

À. T., S. S. and R. V. acknowledge financial support from the Ministerio de Ciencia, Innovación y Universidades (Spain), Project PGC2018-094031-B-100. S. G.-C. acknowledges financial support from the Ministerio de Ciencia, Innovación y Universidades (Spain), Projects PID2021-122464NB-I00, TED2021-129593B-I00 and Maria de Maeztu CEX2021-001202-M. S. G.-C. acknowledges the CSUC and BSC supercomputer centers for computational resources.

References

1 R. Sessoli, D. Gatteschi, A. Caneschi and M. A. Novak, Magnetic bistability in metal-ion cluster, *Nature*, 1993, **365**, 141–143.

2 T. Lis, Preparation, Structure, and Magnetic Properties of a Dodeeanuelear Mixed-Valence Manganese Carboxylate,

Acta Crystallogr., Sect. B: Struct. Crystallogr. Cryst. Chem., 1980, **36**, 2042–2046.

3 A. Zabala-Lekuona, J. M. Seco and E. Colacio, Single-Molecule Magnets: From Mn12-ac to dysprosium metallocenes, a travel in time, *Coord. Chem. Rev.*, 2021, **441**, 213984.

4 (*a*) M. Mannini, F. Pineider, P. Sainctavit, C. Danieli, E. Otero, C. Sciancalepore, A. M. Talarico, M.-A. Arrio, A. Cornia, D. Gatteschi and R. Sessoli, Magnetic memory of a single-molecule quantum magnet wired to a gold surface, *Nat. Mater.*, 2009, **8**, 194–197; (*b*) M. Urdampilleta, S. Klyatskaya, J. P. Cleuziou, M. Ruben and W. Wernsdorfer, Supramolecular spin valves, *Nat. Mater.*, 2011, **10**, 502–506; (*c*) S. G. McAdams, A.-M. Ariciu, A. K. Kostopoulos, J. P. S. Walsh and F. Tuna, Molecular single-ion magnets based on lanthanides and actinides: Design considerations and new advances in the context of quantum technologies, *Coord. Chem. Rev.*, 2017, **346**, 216–239.

5 N. Ishikawa, M. Sugita, T. Ishikawa, S.-Y. Koshihara and Y. Kaizu, Lanthanide Double-Decker Complexes Functioning as Magnets at the Single-Molecular Level, *J. Am. Chem. Soc.*, 2003, **125**, 8694–8695.

6 J. J. Le Roy, I. Korobkov and M. Murugesu, A sandwich complex with axial symmetry for harnessing the anisotropy in a prolate erbium(III) ion, *Chem. Commun.*, 2014, **50**, 1602–1604.

7 (*a*) D. N. Woodruff, R. E. P. Winpenny and R. A. Layfield, Lanthanide Single-Molecule Magnets, *Chem. Rev.*, 2013, **113**, 5110–5148; (*b*) M. Jeletic, P.-H. Lin, J. J. Le Roy, I. Korobkov, S. I. Gorelsky and M. Murugesu, An Organometallic Sandwich Lanthanide Single-Ion Magnet with an Unusual Multiple Relaxation Mechanism, *J. Am. Chem. Soc.*, 2011, **133**, 19286–19289.

8 *The Rare Earth Elements: Fundamentals and Applications*, ed. D. A. Atwood, John Wiley & Sons Ltd, 2005.

9 J. Tang and P. Zhang, *Lanthanide Single Molecule Magnets*, Springer Berlin Heidelberg, Berlin, Heidelberg, 2015.

10 F. S. Guo, B. M. Day, Y. C. Chen, M. L. Tong, A. Mansikkamäki and R. A. Layfield, A Dysprosium Metallocene Single-Molecule Magnet Functioning at the Axial Limit, *Angew. Chem., Int. Ed.*, 2017, **56**, 11445–11449.

11 C. A. P. Goodwin, F. Ortu, D. Reta, N. F. Chilton and D. P. Mills, Molecular magnetic hysteresis at 60 kelvin in dysprosocenium, *Nature*, 2017, **548**, 439–442.

12 S.-D. Jiang, B.-W. Wang, H.-L. Sun, Z.-M. Wang and S. Gao, An Organometallic Single-Ion Magnet, *J. Am. Chem. Soc.*, 2011, **133**, 4730–4733.

13 J. Y. Ge, L. Cui, J. Li, F. Yu, Y. Song, Y. Q. Zhang, J. L. Zuo and M. Kurmoo, Modulating Single-Molecule Magnetic Behavior of a Dinuclear Erbium(III) Complex by Solvent Exchange, *Inorg. Chem.*, 2017, **56**, 336–343.

14 J. Rinehart and J. Long, Exploiting single-ion anisotropy in the design of f-element single-molecule magnets, *Chem. Sci.*, 2011, **2**, 2078–2085.

15 F.-S. Guo, B. M. Day, Y.-C. Chen, M.-L. Tong, A. Mansikkamäki and R. A. Layfield, Magnetic hysteresis up to 80 kelvin in a dysprosium metallocene single-molecule magnet, *Science*, 2018, **362**, 1400–1403.

16 (*a*) J. F. Herbst, $R_2Fe_{14}B$ materials: Intrinsic properties and technological aspects, *Rev. Mod. Phys.*, 1991, **63**, 819–898; (*b*) Y. Li, X. L. Zhang, R. Qiu and Y. S. Kang, Synthesis and investigation of $SmCo_5$ magnetic nanoparticles, *Colloids Surf., A*, 2008, **313–314**, 621–624; (*c*) P. K. Deheri, V. Swaminathan, S. D. Bhame, Z. Liu and R. V. Ramanujan, Sol–Gel Based Chemical Synthesis of $Nd_2Fe_{14}B$ Hard Magnetic Nanoparticles, *Chem. Mater.*, 2010, **22**, 6509–6517.

17 (*a*) F. Pointillart, O. Cador, B. Le Guennic and L. Ouahab, Uncommon lanthanide ions in purely 4f Single Molecule Magnets, *Coord. Chem. Rev.*, 2017, **346**, 150–175; (*b*) A. Borah and R. Murugavel, Magnetic Relaxation in Single-Ion Magnets Formed by Less-Studied Lanthanide Ions Ce(III), Nd(III), Gd(III), Ho(III), Tm(II/III) and Yb(III), *Coord. Chem. Rev.*, 2022, **453**, 214288.

18 S. T. Liddle and J. van Slageren, Improving f-element single molecule magnets, *Chem. Soc. Rev.*, 2015, **44**, 6655–6669.

19 J.-L. Liu, Y.-C. Chen and M.-L. Tong, Symmetry strategies for high performance lanthanide-based single-molecule magnets, *Chem. Soc. Rev.*, 2018, **47**, 2431–2453.

20 M.-X. Xu, Y.-S. Meng, J. Xiong, B.-W. Wang, S.-D. Jiang and S. Gao, Magnetic anisotropy investigation on light lanthanide complexes, *Dalton Trans.*, 2018, **47**, 1966–1971.

21 F. A. Mautner, F. Bierbaumer, R. C. Fischer, À. Tubau, S. Speed, E. Ruiz, S. S. Massoud, R. Vicente and S. Gómez-Coca, Insights into the Spin Dynamics of Mononuclear Cerium(III) Single-Molecule Magnets, *Inorg. Chem.*, 2022, **61**, 11124–11136.

22 S. Hino, M. Maeda, K. Yamashita, Y. Kataoka, M. Nakano, T. Yamamura, H. Nojiri, M. Kofu, O. Yamamuro and T. Kajiwara, Linear trinuclear Zn(II)-Ce(III)-Zn(II) complex which behaves as a single-molecule magnet, *Dalton Trans.*, 2013, **42**, 2683–2686.

23 S. K. Singh, T. Gupta, L. Ungur and G. Rajaraman, Magnetic Relaxation in Single-Electron Single-Ion Cerium (III) Magnets: Insights from Ab Initio Calculations, *Chem. – Eur. J.*, 2015, **21**, 13812–13819.

24 J. Liu, D. Reta, J. A. Cleghorn, Y. X. Yeoh, F. Ortu, C. A. P. Goodwin, N. F. Chilton and D. P. Mills, Light lanthanide Metallocenium cations exhibiting weak equatorial anion Interactions, *Chem. – Eur. J.*, 2019, **25**, 7749–7758.

25 E. Rousset, M. Piccardo, M.-E. Boulon, R. W. Gable, A. Soncini, L. Sorace and C. Boskovic, Slow magnetic relaxation in Lanthanoid Crown Ether Complexes: interlay of Raman and Anomalous Phonon Bottleneck Process, *Chem. – Eur. J.*, 2018, **24**, 14768–14785.

26 A. Upadhyay, K. R. Vignesh, C. Das, S. K. Singh, G. Rajaraman and M. Shanmugam, Influence of the ligand field on the slow relaxation of magnetization of unsymmetrical monomeric lanthanide complexes: synthesis and theoretical studies, *Inorg. Chem.*, 2017, **56**, 14260–14276.

27 E. Regincós-Martí, A. B. Canaj, T. Sharma, A. Celmina, C. Wilson, G. Rajaraman and M. Murrie, Importance on an

Axial LnIII-F Bond across the lanthanide series and Single-Molecule Magnet Behavior in the Ce and Nd analogues, *Inorg. Chem.*, 2022, **61**, 9906–9917.

28 J.-D. Leng, Q.-Y. Hua, W.-T. Liu, Z.-X. Tao, N.-W. Tan, Y.-F. Wang and W.-Q. Lin, Slow magnetic relaxation of mononuclear complexes based on uncommon Kramers lanthanoide ions CeIII, SmIII and YbII, *Dalton Trans.*, 2022, **51**, 12661–12669.

29 N. Ahmed and K. U. Ansaria, Zero-field slow magnetic relaxation behavior of Zn2Dy in a family of trinuclear near-linear Zn2Ln complexes: synthesis, experimental and theoretical investigations, *Dalton Trans.*, 2022, **51**, 8766–8776.

30 J. Mayans, L. Tesi, M. Briganti, M.-E. Boulon, M. Font-Bardía, A. Escuer and L. Sorace, Single-ion anisotropy and Intramolecular interactions in Ce^{3+} and Nd^{3+} dimers, *Inorg. Chem.*, 2021, **60**, 8692–8703.

31 G. M. Sheldrick, A short history of SHELX, *Acta Crystallogr., Sect. A: Fundam. Crystallogr.*, 2008, **64**, 112–122.

32 G. M. Sheldrick, Crystal structure refinement with SHELXL, *Acta Crystallogr., Sect. C: Cryst. Struct. Commun.*, 2015, **71**, 3–8.

33 (*a*) M. Dolg, H. Stoll and H. Preuss, Energy–adjusted ab initio pseudopotentials for the rare earth elements, *J. Chem. Phys.*, 1989, **90**, 1730–1734; (*b*) M. Dolg, H. Stoll, A. Savin and H. Preuss, Energy-adjusted pseudopotentials for the rare earth elements, *Theor. Chim. Acta*, 1989, **75**, 173–194; (*c*) M. Dolg, H. Stoll and H. Preuss, A combination of quasirelativistic pseudopotential and ligand field calculations for lanthanoid compounds, *Theor. Chim. Acta*, 1993, **85**, 441–450; (*d*) F. Weigend and R. Ahlrichs, Balanced basis sets of split valence, triple zeta valence and quadruple zeta valence quality for H to Rn: Design and assessment of accuracy, *Phys. Chem. Chem. Phys.*, 2005, **7**, 3297–3305; (*e*) F. Weigend, Accurate Coulomb-fitting basis sets for H to Rn, *Phys. Chem. Chem. Phys.*, 2006, **8**, 1057–1065; (*f*) A. Hellweg, C. Hattig, S. Hofener and W. Klopper, Optimized accurate auxiliary basis sets for RI-MP2 and RI-CC2 calculations for the atoms Rb to Rn, *Theor. Chem. Acc.*, 2007, **117**, 587–597; (*g*) J. Chmela and M. E. Harding, Optimized auxiliary basis sets for density fitted post-Hartree–Fock calculations of lanthanide containing molecules, *Mol. Phys.*, 2018, **116**, 1523–1538.

34 S. K. Singh, T. Gupta, L. Ungur and G. Rajaraman, Magnetic Relaxation in Single-Electron Single-Ion Cerium (III) Magnets: Insights from Ab Initio Calculations, *Chem. – Eur. J.*, 2015, **21**, 13812–13819.

35 (*a*) L. F. Chibotaru, L. Ungur and A. Soncini, The Origin of Nonmagnetic Kramers Doublets in the Ground State of Dysprosium Triangles: Evidence for a Toroidal Magnetic Moment, *Angew. Chem., Int. Ed.*, 2008, **47**, 4126–4129; (*b*) L. F. Chibotaru, L. Ungur, C. Aronica, H. Elmoll, G. Pilet and D. Luneau, Structure, Magnetism, and Theoretical Study of a Mixed-Valence CoII3CoIII4 Heptanuclear Wheel: Lack of SMM Behavior despite Negative Magnetic Anisotropy, *J. Am. Chem. Soc.*, 2008, **130**, 12445–12455.

36 M. J. Frisch, G. W. Trucks, H. B. Schlegel, G. E. Scuseria, M. A. Robb, J. R. Cheeseman, G. Scalmani, V. Barone, B. Mennucci, G. A. Petersson, H. Nakatsuji, M. Caricato, X. Li, H. P. Hratchian, A. F. Izmaylov, J. Bloino, G. Zheng, J. L. Sonnenberg, M. Hada, M. Ehara, K. Toyota, R. Fukuda, J. Hasegawa, M. Ishida, T. Nakajima, Y. Honda, O. Kitao, H. Nakai, T. Vreven, J. A. J. Montgomery, J. E. Peralta, F. Ogliaro, M. Bearpark, J. J. Heyd, E. Brothers, K. N. Kudin, V. N. Staroverov, R. Kobayashi, J. Normand, K. Raghavachari, A. Rendell, J. C. Burant, S. S. Iyengar, J. Tomasi, M. Cossi, N. Rega, N. J. Millam, M. Klene, J. E. Knox, J. B. Cross, V. Bakken, C. Adamo, J. Jaramillo, R. Gomperts, R. E. Stratmann, O. Yazyev, A. J. Austin, R. Cammi, C. Pomelli, J. W. Ochterski, R. L. Martin, K. Morokuma, V. G. Zakrzewski, G. A. Voth, P. Salvador, J. J. Dannenberg, S. Dapprich, A. D. Daniels, Ö. Farkas, J. B. Foresman, J. V. Ortiz, J. Cioslowski and D. J. Fox, *Gaussian 09 (Revision D.01)*, Wallingford, CT, 2016.

37 A. D. Becke, Density–functional Thermochemistry. III. The Role of Exact Exchange, *J. Chem. Phys.*, 1993, **98**, 5648–5652.

38 M. Dolg, H. Stoll and H. Preuss, Energy-Adjusted Ab Initio Pseudopotentials for the Rare Earth Elements, *J. Chem. Phys.*, 1989, **90**, 1730–1734.

39 A. Schäfer, H. Horn and R. Ahlrichs, Fully Optimized Contracted Gaussian Basis Sets for Atoms Li to Kr, *J. Chem. Phys.*, 1994, **100**, 5829–5835.

40 (*a*) M. Llunell, D. Casanova, J. Cirera, P. Alemany and S. Alvarez, *Shape Program., version 2*, Universitat de Barcelona, Barcelona, Spain, 2010; (*b*) P. Alemany, D. Casanova, S. Alvarez, C. Dryzum and D. Avnir, Continuous Symmetry Measures: A New Tool in Quantum Chemistry, *Rev. Comput. Chem.*, 2017, **30**, 289–352.

41 (*a*) C. Dryzum and D. Avnir, On the abundance of chiral crystals, *Chem. Commun.*, 2012, **48**, 5874–5876; (*b*) K. Chulvi, A. M. Costero, L. E. Ochando and P. Gaviña, Racemic Triarylmethanol Derivative Crystallizes as a Chiral Crystal Structure with Enantiomeric Disorder, in the Sohncke Space Group $P2_1$, *Cryst. Growth Des.*, 2015, **15**, 3452–3456; (*c*) M. Nespolo, M. I. Aroyo and B. Souvignier, Crystallographic shelves: space-group hierarchy explained, *J. Appl. Crystallogr.*, 2018, **51**, 1481–1491.

42 A. Ben Khélifa, M. S. Belkhiria, G. Huang, S. Freslon, O. Guillou and K. Bernot, Single-molecule magnet behavior in polynuclear assembly of trivalent cerium ions with polyoxomolybdates, *Dalton Trans.*, 2015, **44**, 16458–16464.

43 C. Takehara, P. L. Then, Y. Kataoka, M. Nakano, T. Yamamura and T. Kajiwara, Slow magnetic relaxation of light lanthanide-based linear LnZn2 trinuclear complexes, *Dalton Trans.*, 2015, **44**, 18276–18283.

44 H. B. G. Casimir, D. Bijl and F. K. Du Pré, Measurememts on paramagnetic relaxation in chromium potassium alum, *Physica*, 1941, **8**, 449–460.

45 C. E. Jackson, I. P. Moseley, R. Martinez, S. Sung and J. M. Zadrozny, A reaction-coordinate perspective of magnetic relaxation, *Chem. Soc. Rev.*, 2021, **50**, 6684–6699.

46 D. Aravena and E. Ruiz, Spin dynamics in single-molecule magnets and molecular qubits, *Dalton Trans.*, 2020, **49**, 9916–9928.

47 J. J. Le Roy, I. Korobkov, J. E. Kim, E. J. Schelter and M. Murugesu, Structural and magnetic conformation of cerocene $[\mathrm{Ce(COT'')_2}]^-$ exhibiting a uniconfigurational f^1 ground state and slow-magnetic relaxation, *Dalton Trans.*, 2014, **43**, 2737–2740.

48 S. K. Gupta, S. Shanmugan, T. Rajeshkumar, A. Borah, M. Damjanović, M. Schulze, W. Wernsdorfer, G. Rajaraman and R. Murugavel, A single-ion single-electron cerrous magnets, *Dalton Trans.*, 2019, **48**, 15928–15938.

49 (*a*) M. V. Marinho, D. O. Reis, W. X. C. Oliveira, L. F. Marques, H. O. Stumpf, M. Déniz, J. Pasán, C. Ruiz-Pérez, J. Cano, F. Lloret and M. Julve, Photoluminescent and Slow Magnetic Relaxation Studies on Lanthanide(III)-2,5-pyrazinedicarboxylate Frameworks, *Inorg. Chem.*, 2017, **56**, 2108–2123; (*b*) A. López, C. Cruz, V. Paredes-García, V. Veiga, F. Lloret, J. Torres and R. Chiozzone, Field-induced magnetic relaxation in heteropolynuclear LnIII/ZnII metal organic frameworks: cerium and dysprosium cases, *New J. Chem.*, 2023, **47**, 21781–21789.

50 Q.-W. Li, R.-C. Wan, Y.-C. Chen, J.-L. Liu, L.-F. Wang, J.-H. Jia, N. F. Chilton and M.-L. Tong, Unprecedent hexagonal bipyramidal single-ion magnets based on metallacrows, *Chem. Commun.*, 2016, **52**, 13365–13368.

51 E. Pilichos, M. Font-Bardia, A. Escuer and J. Mayans, Structural and magnetic studies of mononuclear lanthanide complexes derived from N-rich chiral Schiff bases, *Dalton Trans.*, 2021, **50**, 1746–1753.

52 S. Hiro, M. Maeda, Y. Kataoka, M. Nakano, T. Yamamura and T. Kajiwara, SMM behavior observed in Ce(III)Zn(II)2 linear trinuclear complex, *Chem. Lett.*, 2013, **42**, 1276–1278.

53 H. Wada, S. Ooka, T. Yamamura and T. Kajiwara, Light lanthanide Complexes with crown ether and its aza derivative which show slow magnetic relaxation behaviors, *Inorg. Chem.*, 2017, **56**, 147–155.

54 (*a*) P. G. Klemens, *Phys. Rev.*, 1961, **122**, 443; (*b*) D. W. Feldman, J. G. Castle and J. Murphy, spin relaxation of atomic hydrogen in CaF2-evidence for local mode, *Phys. Rev.*, 1965, **138**, A1208–A1216; (*c*) Y. Zhou, B. E. Bowler, G. R. Eaton and S. S. Eaton, Electron Spin Lattice Relaxation Rates for S = 12 Molecular Species in Glassy Matrices or Magnetically Dilute Solids at Temperatures between 10 and 300 K, *J. Magn. Reson.*, 1999, **139**, 165–174.

55 C. B. Harris, R. M. Shelby and P. A. Cornelius, Effects of Energy Exchange on Vibrational Dephasing Times in Raman Scattering, *Phys. Rev. Lett.*, 1977, **38**, 1415–1419.

56 N. V. Vugman and M. Rothier Amaral Jr., Influence of localized anharmonic vibrations on electron paramagnetic resonance spectroscopy, *Phys. Rev. B*, 1990, **42**, 9837–9872.

Journal of
Materials Chemistry C

ROYAL SOCIETY
OF CHEMISTRY

PAPER

View Article Online
View Journal | View Issue

Cite this: *J. Mater. Chem. C*, 2024, **12**, 8127

Slow magnetic relaxation and luminescence properties in β-diketonate lanthanide(III) complexes. Preparation of Eu(III) and Yb(III) OLED devices†

Ànnia Tubau,[a] Laura Rodríguez,[a] Piotr Pander,[bcd] Lucy Weatherill,[d] Fernando B. Dias,[d] Mercè Font-Bardía[e] and Ramon Vicente *[a]

The reaction of [Ln(btfa)$_3$(H$_2$O)$_2$] (btfa$^-$ = 4,4,4-trifluoro-1-phenyl-1,3-butanedionate) with 4,4′-dinonyl-2,2′-bipyridyl (4,4′-dinonylbipy) in ethanol allows isolation of mononuclear complexes [Ln(btfa)$_3$(4,4′-dinonylbipy)] Ln = Sm (**1-Sm**), Eu (**2-Eu**), Tb (**3-Tb**), Dy (**4-Dy**), Er (**5-Er**) and Yb (**6-Yb**). The solid state luminescence emission in the visible region for **1-Sm**, **2-Eu**, **3-Tb** and **4-Dy** and in the NIR region for **1-Sm**, **5-Er** and **6-Yb** shows efficient energy transfer from the 4,4,4-trifluoro-1-phenyl-1,3-butanedionate ligands to the central Ln^{3+} ion for all the compounds. Finally, complexes **2-Eu** and **6-Yb** were successfully used as emitters in multilayer vacuum-deposited OLEDs. The electroluminescence quantum efficiency (EQE) of the corresponding devices reached 2.1% and ∼0.1–0.2% for **2-Eu** (λ_{EL} = 614 nm) and **6-Yb** (λ_{EL} = 977 nm), respectively. Maximum radiant emittance recorded for the Ln-associated emission achieved 135 μW cm^{-2} for **2-Eu** and 121 μW cm^{-2} for **6-Yb**. These values for efficiency and radiant emittance are unusually high for such type of emitters. Moreover, magnetic studies were performed on all compounds. Alternating current (AC) dynamic measurements indicated Single Molecular Magnet (SMM) behaviour for **4-Dy** and field-induced slow relaxation of the magnetization for complexes **3-Tb**, **5-Er** and **6-Yb**. The anisotropy energy barriers and pre-exponential factors are 91.1 cm^{-1}, τ_0 = 7.2 × 10^{-9} s (under zero magnetic field) and ΔE = 109.3 cm^{-1}, τ_0 = 9.3 × 10^{-10} s under 0.1 T magnetic field for **4-Dy** and ΔE = 24.6 cm^{-1}, τ_0 = 8.7 × 10^{-8} s (under 0.07 T) for **5-Er**. Besides, we observe that for compounds **3-Tb** and **6-Yb** the relaxation of the magnetization does not occur through the Orbach process.

Received 5th March 2024,
Accepted 14th May 2024

DOI: 10.1039/d4tc00902a

rsc.li/materials-c

1. Introduction

Single-molecule magnets (SMMs) refer to magnetically bistable molecules that exhibit slow relaxation of the magnetization below a critical temperature, T_B, while U_{eff} is the energy barrier separating the two spin ground states. By the end of the twentieth century, the effort to obtain SMMs with the highest T_B and U_{eff} focused on transition metal clusters. The first mononuclear lanthanide complexes ([Pc$_2$Ln]$^-$·TBA$^+$ with Ln = Tb, Dy; Pc^{2-} = phthalocyanine dianion; and TBA$^+$ = tetrabutylammonium) showing slow relaxation of the magnetization were published in 2003.[1] Consequently, the research effort in the field of SMMs with higher T_B and/or U_{eff} was shifted to complexes derived from lanthanide ions with large orbital momentum and strong magnetic anisotropy.[2] Due to the shielding of the 4f^n electrons, the interaction between the lanthanide ion and the donor atoms of the ligands can be considered as electrostatic in nature. Consequently, lanthanide ions have unquenched orbital angular momentum (L) that leads to strong spin–orbit coupling interactions and therefore intrinsic magnetic anisotropy, which make them good candidates for SMMs. Single Ion Magnets (SIMs) are thus mononuclear lanthanide systems that show slow relaxation of the magnetization. A notable example of SIMs are Dy(III)

---

[a] *Departament de Química Inorgànica i Orgànica, Universitat de Barcelona, Martí i Franquès 1-11, E-31321 Barcelona, Spain. E-mail: rvicente@ub.edu*
[b] *Faculty of Chemistry, Silesian University of Technology, Strzody 9, 44-100 Gliwice, Poland*
[c] *Centre for Organic and Nanohybrid Electronics, Silesian University of Technology, Konarskiego 22B, 44-100 Gliwice, Poland*
[d] *Physics Department, Durham University, South Road, Durham, DH1 3LE, UK*
[e] *Departament de Mineralogia, Cristal·lografia i Dipòsits Minerals and Unitat de Difracció de R-X, Centre Científic i Tecnològic de la Universitat de Barcelona (CCiTUB), Universitat de Barcelona, Solé i Sabarís 1-3, 08028 Barcelona, Spain*

† Electronic supplementary information (ESI) available: Thermogravimetric curves, elemental analysis and IR data, SCXRD and PXRD data, excitation spectra, emission spectra at 77 K, ac magnetic data. CCDC 2298951–2298953. For ESI and crystallographic data in CIF or other electronic format see DOI: **https://doi.org/10.1039/d4tc00902a**

compounds exhibiting an anisotropy barrier, U_{eff}, of 1837 cm^{-1} [3] with T_B = 80 K above that of liquid nitrogen.[4]

In addition to the magnetic properties, the lanthanide(III) ions also display intrinsic photoluminescent properties due to the 4f–4f electronic transitions, which result in long-lived and narrowband photoluminescence. The lanthanide(III) ions have an incompletely filled 4f subshell, which is protected from the coordinating atoms due to the filled $5s^2$ and $5p^6$ orbitals and thus the transitions yield sharp emissive lines characteristics of each central ion. However, the electronic 4f–4f transitions are Laporte forbidden due to the parity selection rule, leading to low molar extinction coefficients ($\varepsilon < 10\ \text{M}^{-1}\ \text{cm}^{-1}$) for direct photoexcitation of Ln(III) ions. To address this problem, it is necessary to use organic chromophores that absorb energy and subsequently transfer it to the Ln(III) ion. This sensitization mechanism is commonly known as the "antenna effect".[5,6]

The characteristic narrow emission bands and long emission lifetimes of lanthanide(III) coordination compounds over a wide wavelength range (vis/near-IR)[7–14] makes these compounds interesting for potential applications in telecommunications and biological imaging.[15–17] Particular attention has been drawn towards complexes of Nd^{3+}, Er^{3+} and Yb^{3+} cations as they exhibit near infrared (NIR) emission.[6–9,12–14] In this regard, β-diketones are among the most important "antenna ligands" owing to the following merits: (1) they show intense absorption from their conjugated π–π* transitions within a wide wavelength range; (2) they show efficient $S_1 \rightarrow T_1$ intersystem crossing; (3) several β-diketone systems have shown to exhibit optimal triplet state energy, above the emitting level of the lanthanide ion, therefore providing adequate sensitization of the central atom (specially Eu^{3+}); (4) they can form stable adducts with Ln(III) ions through O,O bidentate chelating modes.[18]

The interest in luminescent multifunctional materials that can act as SMMs is increasing.[7,8,19] We have previously published a series of multifunctional Nd(III) coordination complexes[20] derived from the β-diketonate ligand 4,4,4-trifluoro-1-(2-naphthyl)butane-1,3-dionato (ntfa^-) of the form $[\text{Nd(ntfa)}_3(\text{ANCL})]$, (ANCL = ancillary ligand). More recently we published a new series of luminescent multifunctional SMM materials derived from the 4,4,4-trifluoro-1-phenyl-1,3-butanedionate anion (btfa^-) of the form $\text{HAcr}[\text{Ln(btfa)}_4]$, Ln = Nd(III), Dy(III), and Yb(III); HAcr = acridinium cation, with the aim of studying their photophysical and magnetic behaviour.[21]

To extend the number of multifunctional complexes derived from the β-diketonate anion 4,4,4-trifluoro-1-phenyl-1,3-butanedionate (btfa^-), we report here a series of compounds of the form $[\text{Ln(btfa)}_3(4,4'\text{-dinonylbipy})]$, Ln = Sm (**1-Sm**), Eu (**2-Eu**), Tb (**3-Tb**), Dy (**4-Dy**), Er (**5-Er**) and Yb (**6-Yb**); 4,4′-dinonylbipy = 4,4′-dinonyl-2,2′-bipyridyl. Alternating current (AC) dynamic measurements of **3-Tb**, **5-Er** and **6-Yb** indicated field-induced slow relaxation of the magnetization under the application of a 0.1, 0.07 and 0.1 T magnetic field, respectively. Besides that, **4-Dy** compound shows SMM behaviour with an anisotropy energy barrier and pre-exponential factor yielding 91.1 cm^{-1} and $\tau_0 = 7.2 \times 10^{-9}$ s respectively. The solid state luminescence in the visible region for **1-Sm**, **2-Eu**, **3-Tb** and **4-Dy** and in the NIR region for **1-Sm**, **4-Dy**, **5-Er** and **6-Yb** upon excitation of ligand-centred absorption bands demonstrate efficient energy transfer from the 4,4,4-trifluoro-1-phenyl-1,3-butanedionate ligands to the central Ln^{3+} ion in all these compounds.

On the other hand, lanthanide(III) complexes show potential as emitters in organic light-emitting diodes (OLEDs). For instance, the Eu^{3+} complexes display high colour purity in red emission. Eu^{3+} complexes provided with an asymmetrical ligand field facilitate the $^5\text{D}_0 \rightarrow {}^7\text{F}_2$ transition to yield essentially monochromatic single-band red emission at around 612 nm. Similarly, Yb^{3+} complexes displaying photoluminescence at ∼1000 nm are ideal candidates for use in NIR OLEDs. Kido *et al.* reported in 1994[22] a ternary Eu^{3+} complex $[\text{Eu(DBM)}_3\text{Phen}]$ (DBM^- = 1,3-diphenylpropane-1,3-dionate and Phen = 1,10-phenanthroline) showing maximum luminance of 460 cd m^{-2} in an OLED.[23] Since this work β-diketonate ligands have been profusely used in luminescent Ln(III) complexes for application in OLEDs. In this work, we present new OLEDs built by using complexes of the form $[\text{Ln(btfa)}_3(4,4'\text{-dinonylbipy})]$, where Ln = Eu(III) in **2-Eu** and Ln = Yb(III) in **6-Yb**. The electroluminescence quantum efficiency (EQE) of the corresponding devices reached 2.1% for **2-Eu** (λ_{EL} = 614 nm) and ∼0.1–0.2% for **6-Yb** (λ_{EL} = 977 nm). Maximum radiant emittance recorded for the Ln-associated emission achieved 135 μW cm^{-2} for **2-Eu** and 121 μW cm^{-2} for **6-Yb**. These efficiency and radiant emittance figures are unusually high for such type of emitters.[23]

2. Experimental

2.1. Materials and physicochemical measurements

4,4,4-Trifluoro-1-phenyl-1,3-butanedione and 4,4′-dinonyl-2,2′-bipyridyl were purchased from Sigma-Aldrich. Lanthanide chloride hexahydrates and lanthanide(III) nitrate hexahydrates were obtained from Strem Chemicals. Materials used for OLED fabrication have been purchased from suppliers indicated in parentheses: HAT-CN – dipyrazino[2,3-*f*:2′,3′-*h*]quinoxaline-2,3,6,7,10,11-hexacarbonitrile (sublimed, LUMTEC); TSBPA – 4,4′-(diphenylsilanediyl)bis(*N*,*N*-diphenylaniline) (LUMTEC); mCP – 1,3-bis(carbazol-9-yl)benzene (sublimed, LUMTEC); TPBi – 1,3,5-tris(1-phenyl-1*H*-benzimidazol-2-yl)benzene (Sublimed, LUMTEC); PO-T2T – 2,4,6-tris[3-(diphenylphosphinyl)phenyl]-1,3,5-triazine (LUMTEC); LiF (99.995%, Sigma Aldrich); Al pellets (99.9995%, Lesker).

Infrared spectra (4000–400 cm^{-1}) were recorded in KBr pellets using a PerkinElmer 380-B spectrophotometer. Infrared spectra and a compilation of the most significant bands of all compounds are depicted in Fig. S1 in the ESI.†

The elemental analyses of all compounds were performed at the Serveis Científics i Tecnològics of the Universitat de Barcelona.

2.2. Crystal structure analysis

Crystallographic data for the structures of **2-Eu**, **4-Dy** and **6-Yb** were collected at 100(2) K on a Bruker D8 Venture diffractometer using Mo-Kα radiation. These data showed that **2-Eu**, **4-Dy** and **6-Yb** were isostructural. Crystallographic data for the structure of **3-Tb** were collected at room temperature (304 K). Crystallographic data of the four complexes are summarized in Table S1 (ESI†). Following data reduction, Lp and absorption corrections (programs APEX and SADABS[24,25] and solution by direct methods, the structures were refined against F^2 with full-matrix least-squares method using the program SHELX-2014).[26] Anisotropic displacement parameters were employed for non-hydrogen atoms. Hydrogen atoms were added at calculated positions and refined by use of a riding model with isotropic displacement parameters based on those of the parent atom. Additional software: Mercury[27] and PLATON.[28] The full crystallographic data for the structures of complexes **2-Eu**, **4-Dy** and **6-Yb** have been deposited at the Cambridge Structural Database (CSD).

Powder X-ray diffraction (PXRD) room temperature measurements were used to verify bulk phase purity. PXRD data were recorded at the Serveis Científics i Tecnològics of the Universitat de Barcelona with *PANalytical X'Pert PRO MPD θ/θ* powder diffractometer of 240 millimetres of radius, in a configuration of convergent beam with a focalizing mirror and a transmission geometry with flat samples sandwiched between low absorbing films Cu Kα radiation (λ = 1.5418 Å). Work power: 45 kV – 40 mA. Incident beam slits defining a beam height of 0.4 millimetres. Incident and diffracted beam 0.02 radians *Soller* slits *PIXcel* detector: Active length = 3.347°. $2\theta/\theta$ scans from 2 to 70° 2θ with a step size of 0.026° 2θ and a measuring time of 298 seconds per step. The alert found in structures **4-Dy** and **6-Yb** were mainly due to the fact that there is a q peak that is not assigned to any element. However, when observed closely the electron density appears close to the lanthanide ion. For **4-Dy** the more intense q peaks appear at a distance of 0.970 and of 0.996 Å from the Dy^{3+} ion. For **6-Yb** the more intense q peak appear at a distance of 1.75 Å from the last sp^3 C atom of one of the aliphatic chains. Hence, due to the inconsistent distance, it is unlikely that such residual density originates form unaccounted atom types since this residual density peak challenges any chemical interpretation. Moreover, powder X-ray diffraction analysis matches the pattern calculated from both single crystal structures. This alert probably arises from strong absorption effects that could not be fully corrected.

2.3. Magnetic measurements

Magnetic measurements were performed by the Mesures Magnètiques Unit from Scientific and Technological Centers (CCiTUB), Universitat de Barcelona, using a Quantum Design MPMS-XL SQUID magnetometer. Pascal's constants were used to estimate the diamagnetic corrections, which were subtracted from the experimental susceptibilities to give the corrected molar magnetic susceptibilities.

2.4. Thermogravimetric measurements

Thermogravimetric analysis (TGA) measurements were carried out under N_2 atmosphere in a Mettler TG 50 instrument at a heating rate of 10 °C min^{-1}. For compounds **2-Eu** and **6-Yb**, TGA measurement were performed in the temperature range between 30 and 600 °C. The sample weight stays steady up until 250–300 °C where it loses 75.2% of its weight. Decomposition of the compounds is observed at temperatures above 300 °C (Fig. S2, ESI†).

2.5. Luminescence measurements

Solid state and solution fluorescence spectra were recorded on a Horiva Jobin Yvon SPEX Nanolog fluorescence spectrophotometer equipped with a three slit double grating excitation and emission monochromator with dispersions of 2.1 nm mm^{-1} (1200 grooves per mm) at room temperature. The steady-state luminescence was excited by unpolarized light from a 450 W xenon CW lamp and detected at an angle of 22° for solid state and of 90° for the solution measurements by a red-sensitive Hamamatsu R928 photomultiplier tube. Spectra were reference corrected for both the excitation source light intensity variation (lamp and grating) and the emission spectral response (detector and grating). Near infra-red spectra were recorded at an angle of 22° using a liquid nitrogen cooled, solid indium/gallium/arsenic detector (850–1600 nm). To measure the emission spectra, samples were excited at the excitation wavelength (λ_{exc}) of 306 nm for **1-Sm** and **2-Eu**, of 320 nm for **3-Tb** and of 360 nm for **6-Yb**, for solution samples. Solution samples **4-Dy** and **5-Er** were excited at the emission wavelength of 320 nm according to the absorption spectra since no reliably excitation spectra could be obtained. Polycrystalline samples were excited at the λ_{exc} of 359 nm for **1-Sm** to **6-Yb**.

The excited state decay curves were measured in the same instrument in the phosphorescence mode using a 450 W xenon pulsed lamp (1.5 ns pulse). Experiments were monitored at the respective λ_{exc} and at the emission wavelength (λ_{em}) of 651 nm ($^4G_{5/2} \rightarrow {}^6H_{9/2}$) for **1-Sm** and of 614 nm ($^5D_0 \rightarrow {}^7F_2$) for **2-Eu**. The measured decays were analyzed using the Origin software package. Both decay curves fitted monoexponentially: $\ln(I) = \ln(I_0) - \frac{1}{\tau_{obs}}$. The fit quality was determined by Pearson's χ^2 test. Luminescence quantum yields (ϕ_{Ln}^{L}) were recorded using an Absolute PL quantum yield spectrometer from Hamamatsu Photonics upon excitation of samples at the respective λ_{exc}.

2.6. OLED characterization

We used pre-cleaned indium-tin-oxide (ITO) coated glass substrates with a sheet resistance of 20 Ω sq^{-1} and ITO thickness of 100 nm. The substrates were first washed with distilled water, acetone and then sonicated in acetone and isopropanol, for 15 min each time. Substrates were dried with compressed air and transferred into an oxygen plasma generator for 6 min at full power. Thermally deposited layers were obtained using Kurt J. Lesker Spectros II deposition system at 10^{-6} mbar base pressure. All organic materials and aluminium were deposited at a rate of 1 Å s^{-1}. The LiF layer was deposited at a rate of 0.1–0.2 Å s^{-1}. Characterisation of OLED devices was conducted in a 10 inch integrating sphere (Labsphere) connected to a Source Measure Unit (SMU, Keithley) and coupled with a spectrometer

USB4000 or QePro (Ocean Optics). Further details are available in reference.29 Devices of 4 × 2 mm pixel size were fabricated.

2.7. Syntheses of the complexes

Synthesis of [Ln(Btfa)$_3$(H$_2$O)$_2$]. A methanol solution (10 mL) containing NaOH (6 mmol, 240 mg), HBtfa (6 mmol, 1296.9 mg) and LnCl$_3$·nH$_2$O (2 mmol) was stirred for 1 hour at room temperature. Then 80 mL of deionized water were added to the reaction mixture and it was allowed to stir overnight. The pale precipitate (light pink for the Er^{3+} compound) was filtrated and dried under vacuum (yield: 70–80%).[21]

Synthesis of [Ln(Btfa)$_3$(4,4′-dinonyl-2,2′-bipy)]. An ethanol solution (15 mL) containing 4,4′-dinonyl-2,2′-bipy (1 mmol, 408.7 mg) was added to another ethanol solution (15 mL) containing the corresponding [Ln(Btfa)$_3$(H$_2$O)$_2$] (1 mmol). The solution was stirred for 30 minutes and then left to stand at room temperature. Block like single crystals suitable for X-ray diffraction were obtained within a week (yield: 60–70%).

3. Structural characterization

3.1. Monocrystalline X-ray diffraction

Addition of the 4,4′-dinonyl-2,2′-bipyridyl ligand to the [Ln(Btfa)$_3$(H$_2$O)$_2$] precursor, yielded neutral mononuclear compounds with formula [Ln(Btfa)$_3$(4,4′-dinonyl-2,2′-bipy)]: Ln = Sm^{3+}(**1-Sm**), Eu^{3+} (**2-Eu**), Tb^{3+} (**3-Tb**), Dy^{3+} (**4-Dy**), Er^{3+} (**5-Er**) and Yb^{3+} (**6-Yb**). The single crystal X-ray diffraction structure at 100 K was obtained for compounds **2-Eu**, **4-Dy** and **6-Yb**. Crystallographic details from the measurement and selected bond distances and angles are compiled in Tables S1 and S2 (ESI†) respectively. Compounds **1-Sm** to **6-Yb** are isostructural, therefore only the structure of compound **2-Eu** will be described, Fig. 1(left).

Compound **2-Eu** crystallizes in a triclinic crystal system and a P$\bar{1}$ space group. The Eu^{3+} metal ion is octacoordinated and the EuO$_6$N$_2$ polyhedron is made up of six O atoms from three β-diketonate ligands with Eu–O bond distances in the range of 2.343–2.389 Å and two N atoms from one polypyridyl ancillary ligand with Eu–N distances of 2.559 and 2.575 Å. The closest Eu···Eu intermolecular distance is 8.968 Å. The six oxygen and two nitrogen atoms are gathered around the Eu^{3+} central ion, forming a geometrical polyhedron that is close to an ideal square antiprism (SAPR-8, D_{4d} symmetry) Fig. 1(right). One of the basal planes is made up of the O1, O2, N1 and N2 atoms and the other one of O3, O4, O5 and O6. The geometry has been calculated with the SHAPE program.[30,31] For compound **2-Eu** the deviation from the optimal polyhedron accounted by the continuous shape measurement (CShM) values for the SAPR-8 geometry is 1.040. For compounds **4-Dy** and **6-Yb** the CShM values for the SAPR-8 geometry are 0.902 and 0.790 respectively.

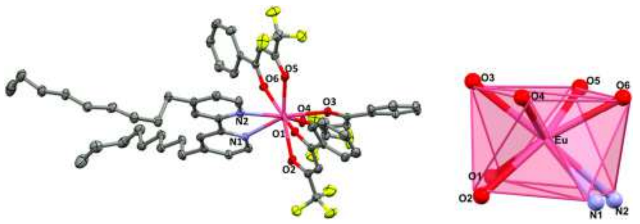

Fig. 1 Left: Crystal structure of complex **2-Eu** with labels for atoms coordinating the central ion. Hydrogen atoms have been omitted for clarity. Right: Ideal coordination polyhedron superimposed on the coordination sphere around the Eu^{3+} ion.

The crystal packing in **2-Eu** is built up through weak intermolecular interactions. Fig. S3 (ESI†) therefore, we can consider that the mononuclear complexes are isolated one from the other through the crystal lattice.

3.2. Powder X-ray diffraction

To verify the crystallinity and phase purity in bulk, Powder X-ray Diffraction (PXRD) were recorded at room temperature for **1-Sm** to **6-Yb** complexes. The measured PXRD were compared to the calculated pattern obtained from the single crystal structure of **2-Eu**, **4-Dy** and **6-Yb** recorded at 100 K, Fig. S4 (ESI†). Interestingly, we observed that the experimental and calculated patterns did not match. Therefore, we then perform a single crystal measurement at room temperature (304 K) using **3-Tb** crystals (Fig. S5 and Table S1, ESI†). The calculated powder pattern obtained from this measurement matches the powder diffractograms of the other complexes, Fig. S6 (ESI†). From these results we conclude that upon changing the temperature from 300 K to 100 K, there is a slight change in the atomic coordinates of the crystals which results in a noticeable difference in some cell parameters (*i.e.* parameter b is greater compared to the 100 K measurements), thus leading to a different PXRD pattern, but the crystal cell and space group remain the same, Table S1 (ESI†).

4. Optical properties

Absorption spectra were recorded for all complexes in chloroform solutions ($c = 10^{-6}$ M), Fig. 2a. Spectra of complexes **1-Sm** to **6-Yb** show similar absorption pattern in the 235–370 nm range. As a means of assigning the absorption bands shown by the coordination complexes, absorption spectra were also recorded for the free ligands separately. The 4,4′-dinonyl-2,2′-bipy ligand was diluted in chloroform solution ($c = 10^{-6}$ M) and HBtfa was diluted in a 1 mM NaOH chloroform solution to measure absorption of respective β-diketone salt, Fig. 2b. Absorption spectrum of the free 4,4′-dinonyl-2,2′-bipy show two bands at 242 and 282 nm while Btfa shows an intense band at 325 nm and less intense bands at 220–248 nm corresponding to the π → π* and n → π* singlet state transitions. The UV-Vis absorption spectra of **1-Sm** to **6-Yb** correlate with those of the constituent ligands. The band corresponding to coordinated Btfa absorption appears slightly blue shifted, compared to the free ligand, about 6 nm. Whereas the absorption bands of 4,4′-dinonyl-2,2′-bipy where red-shifted, compared to the free ligand, about 25 nm nm upon coordination. The band appearing at 282 nm in the free 4,4′-dinonyl-2,2′-bipy spectra appears as a shoulder around 310 nm in the complexes spectra

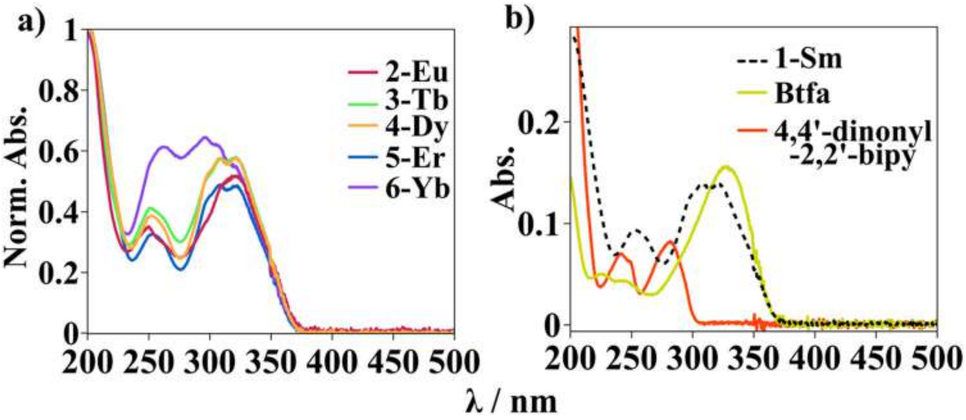

Fig. 2 Absorption spectra of (a) the Ln^{3+} compounds in chloroform solutions $c = 10^{-6}$ M; and (b) spectra of the free 4,4′-dinonyl-2,2′-bipy ligand in $CHCl_3$ solution and spectra of Btfa salt in a 1 mM NaOH, $CHCl_3$ solution. The free ligand absorption spectra has been superimposed onto **1-Sm** spectra for sake of wavelength shift comparison.

superimposing to the Btfa associated absorption band. This may explain the intense and broader band appearing at 277–370 nm. Similar UV-Vis absorption spectra are obtained for previous published [Ln(β-diketonate)$_3$(L)] systems, where L is the ancillary ligand based on *N*,*N*-donor polypyridyl molecules.[18g,h]

The emission spectra of all complexes in the series **1-Sm** to **6-Yb** were recorded in $CHCl_3$ solutions and in polycrystalline samples. The measurements were monitored by exciting the samples at the respective absorption maxima (Fig. 2(left) and Fig. S7, ESI†) giving rise to the emission of the respective lanthanide f–f transitions in the visible (400–700 nm) and NIR range (800–1600 nm) (Fig. 3). The expected emission profiles are recorded in all cases (with slightly better resolution in the polycrystalline samples) except for **4-Dy** and **6-Er** where no significant emission was observed in solution. Emission bands displayed by the aforementioned lanthanide compounds are assigned in Fig. 3 and a compilation of the obtained wavelengths with the assignation of each transition can be found in Table S3 (ESI†). The characteristic red, green, and yellowish photoluminescence emission color of the **1-Sm**, **2-Eu**, **3-Tb** and **4-Dy** samples in solid state and in solution, were sufficiently intense to be observed with the naked eye, Figs. S8 and S9 (ESI†). Color coordinates were calculated for all emission spectra recorded in solid and solution state and are shown in the CIE chromaticity diagram 1931 in Fig. S10 (ESI†).

The characteristic emission originated from the f–f transitions of each lanthanide ion can be observed for **1-Sm**, **2-Eu**, **3-Tb**, and **5-Yb** with no residual emission of the ligand in the 300–500 nm range. This indicates an efficient energy transfer from the excited state of the ligand to the lanthanide emitting energy levels, the so-called antenna effect. This is also confirmed by the corresponding excitation spectra which shows the broad and intense band corresponding to the ligand while excitation transitions corresponding to the f–f lanthanide(III) ions are not observed.[32] The emission bands at 564, 608, 647 and 707 nm found in the **1-Sm** spectrum are assigned to the transitions from the $^4G_{5/2}$ energy level to the $^6H_{5/2}$, $^6H_{7/2}$, $^6H_{9/2}$ and $^6H_{11/2}$ levels of the ^6H_J ground state respectively, Fig. 3a. Additional bands are found in the NIR range, at 953 nm assigned to the $^4G_{5/2} \rightarrow {}^6F_{5/2}$ transition overlapped with the $^4G_{5/2} \rightarrow {}^6F_{1/2}$, $^4G_{5/2} \rightarrow {}^6H_{15/2}$ and $^4G_{5/2} \rightarrow {}^6F_{3/2}$ transitions. The less intense bands found at 1033, 1188 and 1300 nm are assigned to $^4G_{5/2} \rightarrow {}^6F_{7/2}$, $^4G_{5/2} \rightarrow {}^6F_{9/2}$ and $^4G_{5/2} \rightarrow {}^6F_{11/2}$ transitions respectively. A better defined NIR emission spectrum was observed for **1-Sm** polycrystalline sample than in $CHCl_3$ solution.

The emission spectrum of **2-Eu** displays several bands at 579, 592 and 611 nm (most intense) that are assigned to the $^5D_0 \rightarrow {}^7F_0$ ($\Delta J = 0$), $^5D_0 \rightarrow {}^7F_1$ (split due to the crystal field) and $^5D_0 \rightarrow {}^7F_2$ transitions respectively, Fig. 3b. While the band at 592 nm is a pure magnetic dipole transition in which the intensity is practically independent of the Eu^{3+} environment, the signal at 611 nm is assigned to the hypersensitive band since it accounts for an electric dipole transition. From the latter, the structure of the band is distinguished where at least three components, ascribed to the $^5D_0 \rightarrow {}^7F_2$ transition, can be discerned. Differentiation of $^5D_0 \rightarrow {}^7F_2$ components may indicate that the Eu^{3+} ion is not occupying an inversion symmetry site inside the structure which agrees with the coordination geometry obtained from the SHAPE calculations (square antiprism, D_{4d} symmetry). The less intense bands at 651 and at 703 nm are assigned to $^5D_0 \rightarrow {}^7F_3$ and $^5D_0 \rightarrow {}^7F_4$ transitions, respectively.

For compound **3-Tb**, the bands found at 489, 545, 581 and 619 nm are assigned to the transitions from the $^5D_4$ emissive state to the ground state $^7F_6$, $^7F_5$, $^7F_4$ and $^7F_3$ energy levels, respectively. As for **4-Dy**, emission of the $CHCl_3$ solution, is mainly dominated by the ligand in the 300–400 nm range instead of the transitions centered at the Dy^{3+} ion. While for the polycrystalline sample, three intense emission bands originating from the dysprosium(III) $^7F_{9/2}$ emissive energy level are differentiated at 481, 577, and 664 nm, Fig. 3d. The bands are assigned to $^7F_{9/2} \rightarrow {}^6H_{15/2}$, $^7F_{9/2} \rightarrow {}^6H_{13/2}$ and $^7F_{9/2} \rightarrow {}^6H_{11/2}$ transitions, respectively. In addition, a very low intense signal at 454 nm is observed. This signal is assigned to the forbidden

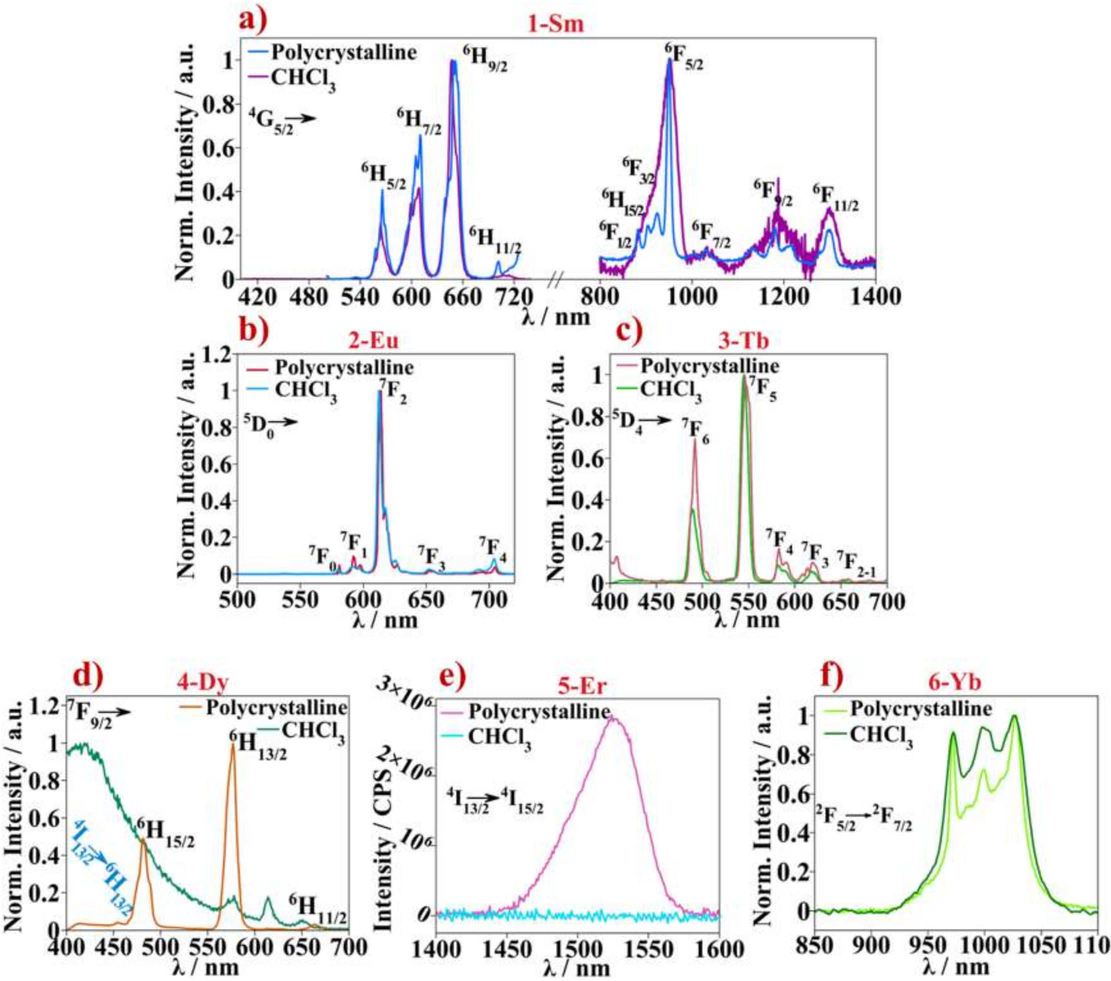

Fig. 3 Luminescence emission spectra of compounds **1-Sm** to **6-Yb** measured in polycrystalline samples and in a $1{\cdot}10^{-6}$ M $CHCl_3$ solution. To measure the emission spectra, samples were excited at the excitation wavelength (λ_{exc}) of 306 nm for **1-Sm** and **2-Eu**, 320 nm for **3-Tb** and 360 nm for **6-Yb**, for solution samples. Moreover, solution samples of **4-Dy** and **5-Er** were excited at the emission wavelength of 320 nm according to the absorption profile since no reliably excitation spectra could be obtained. Polycrystalline samples were excited at the λ_{exc} of 359 nm for **1-Sm** to **6-Yb**.

magnetic dipole transition ($\Delta J = 0$) $^4I_{13/2} \rightarrow {}^6H_{13/2}$, such as in the case of $^5D_0 \rightarrow {}^7F_0$ in the Eu^{3+} ion.[33] Furthermore, for the NIR Er^{3+} emitter (**5-Er**), emission is totally quenched when the compound is found in the $CHCl_3$ solution. However, in the solid-state sample, Er^{3+} centered emission is observed at 1526 nm which is assigned to the $^4I_{13/2} \rightarrow {}^4I_{15/2}$ transition, Fig. 3e. Finally, sample **6-Yb** displays the expected Yb^{3+} band corresponding to the $^5F_{5/2} \rightarrow {}^2F_{7/2}$ transition appearing at 1000 nm, Fig. 3f. The band splitting due to crystal field effects is clearly visible.[32,34]

Emission spectra of the polycrystalline samples were also recorded at 77 K (Fig. S11, ESI†). Under these conditions, the crystal field splitting of the emission bands acquires better resolution in all the polycrystalline samples except for the **5-Er** compound (not shown) where the emission spectrum remains unchanged from the luminescence observed at room temperature. For compounds **1-Sm**, **4-Dy** and **6-Yb** the splitting into $J + \frac{1}{2}$ component (for Kramer ions) due to crystal field can be clearly observed. However, for compounds **2-Eu** and **3-Tb**, the $2J + 1$ (non-Kramer ions) splitting of each emission band is not clearly resolved. Perhaps even lower temperatures than 77 K are necessary to obtain high-resolution spectra in this case.[32]

Interestingly, the NIR spectra of the **4-Dy** compound, for which emission has not been observed at room temperature, could be recorded at 77 K, Fig. S11e (ESI†). Clear bands are now discerned at 964 and 1154 nm which are assigned to the $^4F_{9/2} \rightarrow {}^6F_{7/2}$ and $^4F_{9/2} \rightarrow {}^6F_{5/2}$ f–f Dy^{3+} transitions, respectively. Furthermore, the third band found at 1018 nm is attributed to the $^6H_{5/2} + {}^6F_{7/2} \rightarrow {}^6H_{15/2}$ transition.[35]

4.1. Photoluminescence quantum yield (ϕ^{L}_{Ln}) and luminescence decay time (τ_{obs})

The overall photoluminescence quantum yields (ϕ^{L}_{Ln}) and luminescence decay times (τ_{obs}) were measured in both, $CHCl_3$ solution and polycrystalline samples at room temperature, and the results are presented in Table 1.

2-Eu is the complex showing the highest ϕ^{L}_{Ln} and longest luminescence lifetime that is at least one order of magnitude

Table 1 Overall quantum yields and luminescence lifetime of compounds **1-Sm** to **4-Dy** measured in polycrystalline samples ($\phi^{L}_{\mathrm{Ln\,polycryst}}$ and $\tau_{\mathrm{obs\,polycryst}}$) and CHCl3 solutions ($\phi^{L}_{\mathrm{Ln\,solution}}$ and $\tau_{\mathrm{obs\,solution}}$). Samples were excited at the respective absorption maxima (see Section 2.7 of the Experimental section)

	$\phi^{L}_{\mathrm{Ln\,polycryst}}$	$\phi^{L}_{\mathrm{Ln\,solution}}$	$\tau_{\mathrm{obs\,polycryst}}$ (ms)	$\tau_{\mathrm{obs\,solution}}$ (ms)
1-Sm	0.03	0.03	0.06	0.07
2-Eu	0.68	0.42	0.90	0.65
3-Tb	0.01	0.006	[a]	[a]
4-Dy	0.005	[a]	[a]	[a]

[a] Value not recorded due to limitations in the equipment.

larger compared to the values recorded for the other compounds. The ϕ^{L}_{Ln}values recorded for **2-Eu**, **3-Tb** and **4-Dy** are about 2-fold higher in the polycrystalline samples than in chloroform solution. Lifetimes are in order of ~60–70 µs (**1-Sm**) to ~1 ms (**2-Eu**) while all samples display monoexponential luminescence decay (Fig. 4). The presence of a single decay time component, τ_{obs}, for **1-Sm** and **2-Eu** is suggestive of a single radiative deactivation process, both in the solid state and in solution.[34]

The low ϕ^{L}_{Ln} values observed in **3-Tb** are consistent with other reported in the literature. For these compounds, low luminescence ϕ^{L}_{Ln} are related to back energy transfer due to the low energy gap between the lowest triplet state of the ligands and terbium(III) $^{5}D_{4}$ (20 400 cm^{-1}) emitting energy level. Latva *et al.*[36] concluded that the back transfer energy (studied for a large group of Tb^{3+} coordination compounds) usually occurred when this energy difference was below 1850 cm^{-1}. In this regard, the gadolinium analogue of compounds **1-Sm** to **6-Yb**, [Gd(Btfa)$_3$(4,4′-dinonyl-2,2′-bipy)] **7-Gd**, was synthetized. From the edge of the UV absorption spectrum the singlet state (S_1) energy was obtained, 27 137 cm^{-1} (376 nm), Fig. S12 (ESI†) bottom left. The triplet state energy can be deduced from the 0-phonon band of the Gd^{3+} analogue phosphorescence spectrum measured at 77 K which appeared at 21 229 cm^{-1} (471 nm), Fig. S12 (ESI†) bottom right. The energy separating the S_1 and T_1 state is 5908 cm^{-1}. Such small singlet–triplet energy difference (below 7000 cm^{-1}) favors intersystem crossing ($S_1 \rightarrow T_1$) leaving behind other competitive processes such as relaxation back to the S_0 ground state.[37a] Moreover, the energy difference between the lowest triplet state and the emissive Tb^{3+} energy level, is 829 cm^{-1}. Thus, following Latva's rule, compound **3-Tb** shows a low quantum yield due to back energy transfer taking place as a result of the low energy difference between T_1 and terbium's $^{5}D_{4}$ emitting level.[37]

Additionally, the narrow energy gap of the Sm(III) cation promotes nonradiative relaxation processes, shortening luminescence decay and reducing luminescence efficiency. This also explains the low values of ϕ^{L}_{Ln} and τ_{obs} obtained for **1-Sm** which are common in other Sm-β-diketone systems.[38] For **5-Yb** and **6-Er** samples, the QY could not be measured as being too low to be recorded accurately.

Additional parameters regarding the sensitization mechanism of **2-Eu** system can be calculated. Owing to the pure magnetic dipole character of $^{5}D_{0} \rightarrow {}^{7}F_{1}$ transition, the radiative lifetime (τ_{rad}) from the $^{5}D_{0}$ emissive level, of **2-Eu** compound can be calculated from the corrected emission spectrum, eqn (S2) (ESI†).[39] For the Eu^{3+} polycrystalline sample τ_{rad} is 1.26 ms and 1.23 ms for the $CHCl_3$ solution. Then the intrinsic quantum yield (ϕ^{L}_{Ln}) is 0.71 and 0.53 for the solid and solution samples, respectively (see Section 1.3 of ESI†). Moreover, the amount of energy absorbed by the chromophore ligands that is transferred to the excited state of the lanthanide ion is known as the sensitization efficiency (η_{sens}), and it plays a significant role in the overall quantum yield, which is defined as: $\phi^{L}_{\mathrm{Ln}} = \eta_{\mathrm{sens}} \cdot \phi^{\mathrm{Ln}}_{\mathrm{Ln}}$. Thus, the η_{sens} figures of 0.95 in polycrystalline powder and of 0.79 in $CHCl_3$ solution, show a nearly 100% efficient sensitization of the [Eu$_2$(Btfa)$_3$(4,4′-dinonyl-2,2′-bipy)] (**2-Eu**) system in solid state.[34,37a]

4.2. Stability of the coordination sphere in CHCl$_3$ solutions

If the corresponding normalized emission profiles in $CHCl_3$ and polycrystalline samples are superimposed and observable changes are differentiated, a change in the lanthanide coordination environment due to solvation effects may be considered and therefore a lack of stability in solution of the coordination compound. However, emission spectra of the aforementioned

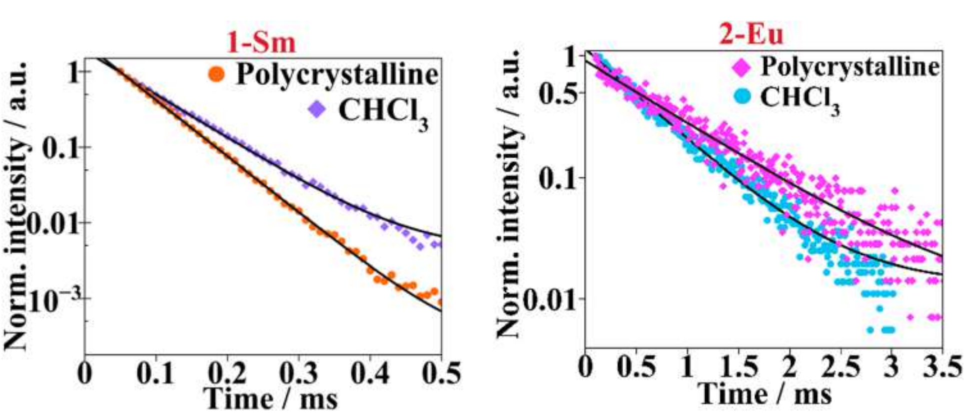

Fig. 4 Luminescence lifetime curves are presented in semi-log plots for complexes **1-Sm** and **2-Eu**. The solid black lines represent the mono-exponential fitting with $I(t) = I_0 e^{-\frac{t}{\tau_{\mathrm{obs}}}} + C$.

compounds have similar shape, hinting that the coordination compound are still present in the $CHCl_3$ solution.

Moreover, spectroscopic–structure correlation (from solid state and $CHCl_3$ solution) can be derived from the corrected emission spectra of **1-Sm** and **2-Eu** compounds owing to the distinctive emission bands exhibited by these lanthanide ions. The crystal field splitting of the hypersensitive band ($^5D_0 \rightarrow {}^7F_2$) recorded for Eu^{3+} compound is the same in both solid and solution. Also, the integrated area of the magnetic dipole transition ($^5D_0 \rightarrow {}^7F_1$) to the electric dipole ratio ($0 \rightarrow 1/0 \rightarrow 2$) gives information about the asymmetry factor being 0.09 for the polycrystalline sample and 0.07 in chloroform. The ratio between these two bands is minor, evidencing that there is no significant change around the Eu^{3+} environment when dissolving the **2-Eu** sample into chloroform. Same reasoning can be done for the **1-Sm** compound since $^4G_{5/2} \rightarrow {}^6H_{9/2}$ transition also has a hypersensitive character (yet not as strong as in Eu^{3+}) and $^4G_{5/2} \rightarrow {}^6H_{5/2}$ is predominantly magnetic dipole in nature. Then for the polycrystalline sample the $(5/2 \rightarrow 5/2)/(5/2 \rightarrow 9/2)$ ratio is 0.26 and for the $CHCl_3$ is 0.22. The difference of the asymmetric factor of **1-Sm** is similar on changing the phase from solid to solution as well, therefore, suggesting that structural changes in the samarium(III) environment are the slightest due to solvating effects.[34,38a]

By comparing the QY and η_{sens} values for the polycrystalline and solution samples we reach similar conclusions. Both diminish on dissolving the samples in $CHCl_3$. There are more degrees of freedom in solution media (*i.e.* vibrations and rotations), hence escalating the non-radiative decay. In this way, **4-Dy** and **5-Er** solution samples are virtually non-emissive.

4.3. Organic light-emitting diodes (OLEDs)

Despite their large molecular weight, complexes **2-Eu** and **6-Yb** sublime at relatively low temperatures, around 140–150 °C (significantly below the decomposition temperature at ~290 °C) at $\sim 10^{-6}$ mbar pressure. This may be due to their ball-like geometry and the peripheral alkyl and $-CF_3$ ligand groups that reduce intermolecular interactions and increase the volatility of the material. This type of design is highly desirable in materials used in the emissive layer of OLEDs. Vacuum-deposited devices were produced as a proof-of-concept with this group of luminescent materials. OLED electroluminescence and electrical characteristics are shown in Fig. 5 and Fig. S13–S15 (ESI†) as well as in Table 2.

The complex **2-Eu** displays high photoluminescence quantum yield (PLQY) both in neat film and in powder, indicating that photoluminescence quenching is negligible in the solid state. As **2-Eu** can be used at higher loads in the emissive layer, OLEDs incorporating **2-Eu** at 20% load in the hole-transporting host mCP were produced {**Device 1:** ITO|HAT-CN (10 nm)|TSBPA (40 nm)|mCP (2 nm)|mCP co 20% **2-Eu** (20 nm)|PO-T2T (5 nm)|TPBi (40 nm)|LiF (0.8 nm)|Al (100 nm)} or in the blend host mCP : TPBi {**Device 2:** ITO|HAT-CN (10 nm)|TSBPA (40 nm)|mCP (2 nm)|mCP : TPBi (60 : 40) co 20% **2-Eu** (20 nm)|TPBi (50 nm)|LiF (0.8 nm)|Al (100 nm)}. As **2-Eu** does not significantly absorb light above 400 nm and its absorbance in the 350–400 nm region is limited, a non-negligible level of host luminescence contaminating the EL spectrum is observed. An alternative approach to **Devices 1** and **2** was to use a 5 nm thick neat emissive layer of **2-Eu** sandwiched between electron-blocking and hole-blocking materials {**Device 3:** ITO|HAT-CN (10 nm)|TSBPA (40 nm)|**2-Eu** (5 nm)|PO-T2T (20 nm)|TPBi (30 nm)|LiF (0.8 nm)|Al (100 nm)}. This strategy led to the host emission being eliminated and colour purity improved. However, the maximum luminance of this OLED was significantly reduced.

All three OLED structures (OLEDs **1–3**) display similar EL spectra typical of luminescence originating from Eu^{3+}complexes with visibly narrowband emission peak at 614 nm. Significantly less intense emission bands in the region 530–710 nm are also observed. These EL spectra are significantly narrowband with FWHM of 6–8 nm leading to high colour purity, with potential for good colour rendering in displays. The modest maximum external quantum efficiency (EQE) of 2.0–2.1% and luminance ~200–600 cd m^{-2} is most likely a result of

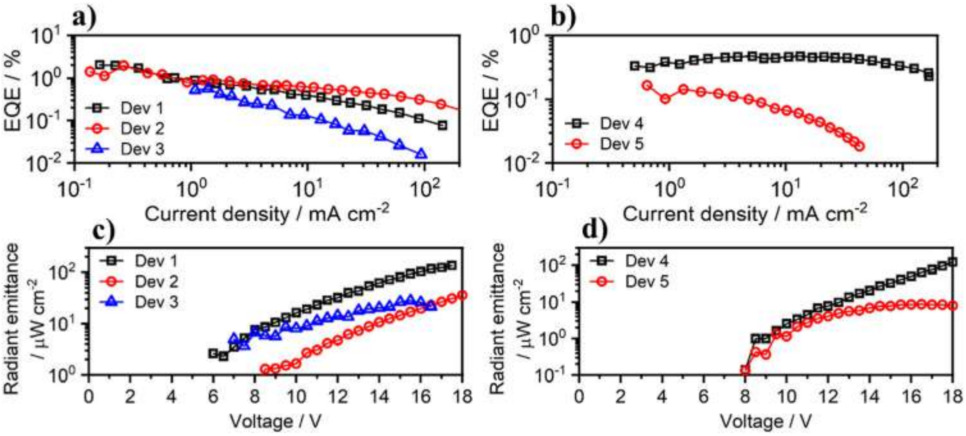

Fig. 5 External quantum efficiency (EQE) *vs.* current density characteristics of devices **1–5** from compounds (a) **1-Eu** and (b) **6-Yb**. Radiant emittance *vs.* voltage bias for devices **1–5** from compounds (c) **1-Eu** and (d) **6-Yb**.

Table 2 Electroluminescent properties of OLED devices **1–5**

	Dev 1	**Dev 2**	**Dev 3**	**Dev 4**	**Dev 5**
Emitter	**2-Eu**	**2-Eu**	**2-Eu**	**6-Yb**	**6-Yb**
V_{ON}/V^a	4.5	5.0	4.0	4.0	4.5
L_{max}/cd m^b	210	590	20	477	4
R_{max}/μW cm^c	135[h]	36[h]	28[h]	121[i]	9[i]
λ_{EL}/nm^d	581, 593, 614, 655, 694, 704[h]	581, 593, 614, 655, 694, 704[h]	581, 593, 614, 655, 694, 704[h]	977, 1005, 1031[i]	977, 1005, 1031[i]
CIE 1931 $(x; y)^e$	(0.51; 0.30)	(0.52; 0.28)	(0.60; 0.30)	—	—
CE_{max}/cd A^f	2.6	2.6	0.4	—	—
EQE_{max}/%^{g}	2.1	2.0	0.6	0.46/0.10[i]	0.17

[a] Turn-on voltage at 10^{-2} mA cm^{-2}. [b] Maximum luminance (visible spectrum). [c] Maximum radiant emittance for the EL bands associated with the emitter. [d] EL maxima associated with the emitter emission. [e] Colour coordinates of electroluminescence spectrum in colour space CIE 1931 as defined by the International Commission on Illumination. [f] Maximum current efficiency. [g] Maximum external quantum efficiency. [h] For wavelength range $\lambda > 550$ nm. [i] For wavelength range $\lambda > 900$ nm.

the long photoluminescence lifetime characteristic of Eu^{3+}complexes.

Similarly to **2-Eu**, complex **6-Yb** also offers attractive luminescent properties, but this time in the near infra-red region. OLEDs with the similar structure of **Device 2** but using **6-Yb** as the emitter were produced (**Device 4**). A significant electroluminescence contribution from the host material is visible in this device, mostly due to the relatively small PLQY of the **6-Yb** complex. However, the electroluminescence originating from the **6-Yb** emitter appears at relatively longer wavelengths in the near infra-red region, and hence is attractive for various potential practical applications. The ∼1000 nm electroluminescence band on its own reaches a maximum radiant emittance of 121 μW cm^{-2} and 0.1% EQE, which is comparable with other emitters in this wavelength range. In order to eliminate the electroluminescence from the host material, we used complex **6-Yb** in neat film, reproducing the structure of **Device 3**. However, the thickness of 5 nm was found to be insufficient and a significant electroluminescence from a through-space TSBPA:PO-T2T exciplex was observed. Hence, **Device 5** features an emissive layer of 10 nm **6-Yb** neat film. This device produces a relatively strong near infra-red electroluminescence at ∼1000 nm, but a weak contribution from the TSBPA:PO-T2T exciplex is still present.

Magnetic properties

DC measurements. Direct current (DC) magnetic susceptibility (χ_M) and magnetization (M) measurements were performed on polycrystalline samples **1-Sm** to **6-Yb**. The χ_M measurements were carried out under a DC field of 0.3 T in the 2–300 K temperature range. The temperature dependence of $\chi_M T$ is shown in Fig. 6. $\chi_M T$ values at room temperature (300 K) are 0, 1.3, 11.8, 15.0, 11.2 and 2.6 cm^3 mol^{-1} K for **1-Sm**, **2-Eu**, **3-Tb**, **4-Dy**, **5-Er**, and **6-Yb** respectively. For one isolated Ln^{3+} cation, the calculated $\chi_M T$ values are: 0.09 cm^3 mol^{-1} K for Sm^{3+} ground state $^6H_{5/2}$ and $g_j = 2/7$; 0 cm^3 mol^{-1} K for Eu^{3+} ground state $^7F_0$; 11.82 cm^3 mol^{-1} K for Tb^{3+} ground state $^7F_6$ and $g_j = 3/2$; 14.17 cm^3 mol^{-1} K for Dy^{3+} ground state $^6H_{15/2}$ and $g_j = 4/3$, 11.48 cm^3 mol^{-1} K for Er^{3+} ground state $^4I_{15/2}$ and 2.57 cm^3 mol^{-1} K for Yb^{3+} ground state $^2F_{7/2}$ and $g_j = 8.7$.[32a]

Owing to the relatively small spin–orbit coupling parameter (λ) splitting the ^6H_J (for Sm^{3+}) and ^7F_J (for Eu^{3+}) states, the J states higher in energy are found to be electronically populated at room temperature. This may explain why room temperature $\chi_M T$ values of **1-Sm** and **2-Eu** determined experimentally are larger than the calculated values. Upon cooling both samples, $\chi_M T$ curves decrease due to thermal depopulation of the excited J states of Sm^{3+} and Eu^{3+} ions respectively.[40]

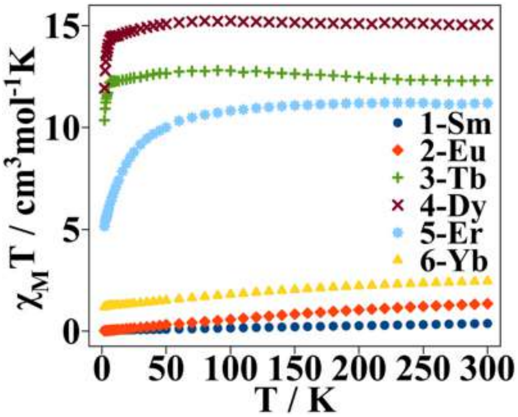

Fig. 6 Temperature dependence of $\chi_M T$ measured at an external static field of 0.3 T, for compounds **1-Sm** to **6-Yb**.

Room temperature $\chi_M T$ of **3-Tb**, **4-Dy**, **5-Er** and **6-Yb** agree with the calculated parameters for an isolated Ln^{3+} ion. Upon decreasing the temperature, the $\chi_M T$ curves of the four compounds remain nearly constant until ∼50 K. Below this temperature, $\chi_M T$ values decrease suddenly to 10.3, 11.9, 5.1 and 1.2 cm^3 mol^{-1} K, for **3-Tb**, **4-Dy**, **5-Er** and **6-Yb** respectively, due to thermal depopulation of the crystal field m_j states. For the presented compounds, magnetic coupling between the lanthanide ions has not been considered due to (i) the mononuclear nature of such compounds that lead to extensive Ln⋯Ln intermolecular distances and (ii) the well shielded nature of electrons in the $4f^n$ orbitals.[41]

The curves of the magnetization dependence with an external magnetic field, measured at a constant temperature of 2 K, are depicted in Fig. 7. None of the presented compounds shows saturation of the magnetization at 5 T ($g_j \cdot J$).[32]

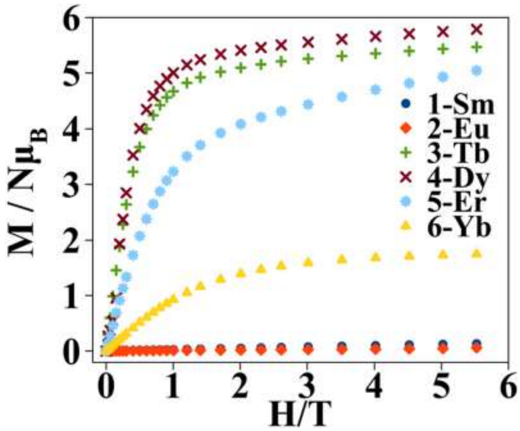

Fig. 7 Magnetization dependence with an external magnetic field measured at 2 K for compounds **1-Sm** to **6-Yb**.

Alternating current measurements. Moreover, alternating current (AC) magnetic susceptibility measurements were performed for all lanthanide samples except for **1-Eu**. Under a direct current external magnetic field (H_{dc}) of 0 T, only **4-Dy** showed slow relaxation of the magnetization and therefore single ion magnet (SIM) behaviour. Magnetic susceptibility imaginary component (χ_M'') shows maxima in the 2–18 K temperature range Fig. 8a. When cooling the sample down to 2 K, the χ_M'' values increase again, though a second peak is not observed. This is probably due to the Quantum Tunnelling of the Magnetization (QTM) mechanism that is taking place at such low temperatures.[41] The AC magnetic data were measured under an oscillating magnetic field of 4×10^{-4} T in the 1–1488 Hz frequency range Fig. 8b. χ_M'' maxima from the low temperature curves remain constant until a certain temperature where they move to higher frequencies upon increasing the temperature. This suggests that at low temperature the relaxation of the magnetization occurs *via* a temperature independent mechanism such as QTM whereas at the higher temperature range, thermally activated mechanisms, such as Orbach and/or Raman, are taking place.[42] In-phase and out-of-phase magnetic susceptibility representation (χ_M' *vs.* χ_M'') in the so called Cole–Cole plot show semicircles that are not perfectly symmetric, Fig. 8c.

The Cole–Cole plot can be fitted using the one component Generalized Debye model in the 2.5–13.5 K temperature range, eqn (S3) (ESI†)[43] The fits of the Cole–Cole curves of the different magnetic data were obtained using the CCFit software[44] (Table S4, ESI†). The α parameter quantifies the width distribution of the relaxation times of magnetization. For **4-Dy** α varies from 0.24 at 2.5 K to 0.03 at 13.5 K.

The semi-log representation of the relaxation of the magnetization times as function of temperature (ln(τ) *vs.* 1/*T*) is depicted in Fig. 9a. In the high temperature range a clear linear trend is observed. The linear segment is fitted following an Arrhenius type law, eqn (1). This model describes the thermally assisted Orbach relaxation of the magnetization mechanism taking place between the degenerate $\pm m_J$ ground state levels *via*

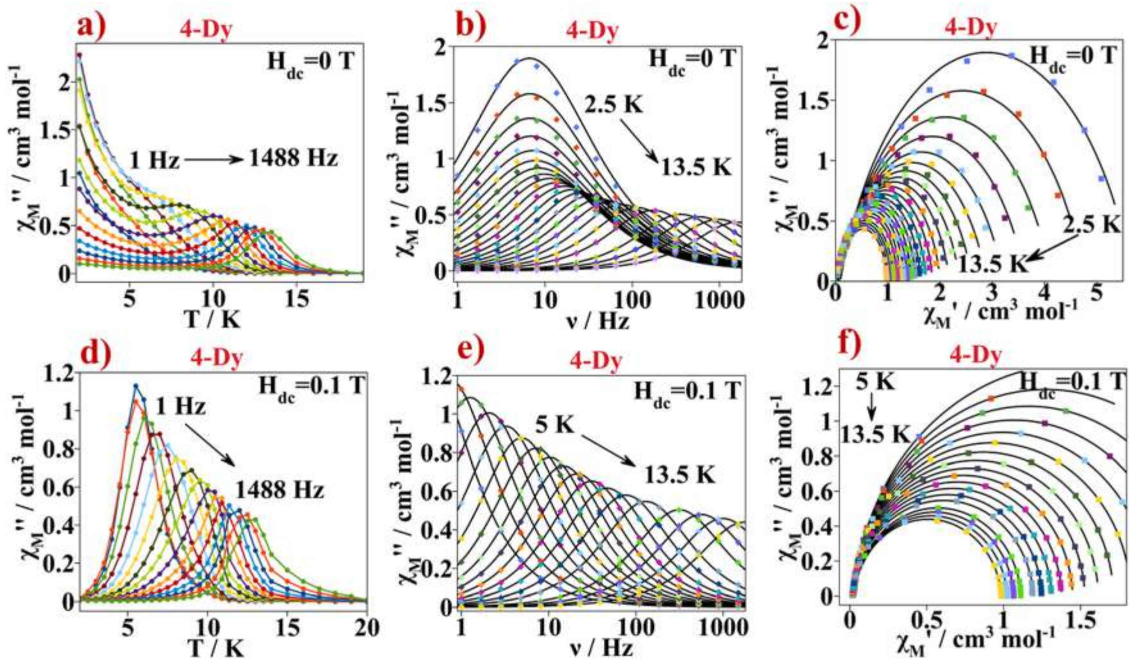

Fig. 8 (a) χ_M'' *versus* temperature plot obtained at a H_{dc} = 0 T for **4-Dy**. Continuous lines serve as an eye guide, (b) χ_M'' *versus* frequency plot obtained at a H_{dc} = 0 T for **4-Dy**. Continuous black lines correspond to the best fit according to eqn (S3) (ESI†), (c) Cole–Cole plot for **4-Dy** from the AC data recorded at a H_{dc} = 0 T. Continuous black line corresponds to the best fit according to eqn (S3) (ESI†), (d) χ_M'' *versus* temperature plot obtained at a H_{dc} = 0.1 T for **4-Dy**. Continuous lines serve as an eye guide, (e) χ_M'' *versus* frequency plot obtained at a H_{dc} = 0.1 T for **4-Dy**. Continuous black line corresponds to the best fit according to eqn (S3) (ESI†) and (f) Cole–Cole plot for **4-Dy** from the AC data measured at a H_{dc} = 0.1 T. Continuous black line corresponds to the best fit according to eqn S3 (ESI†).

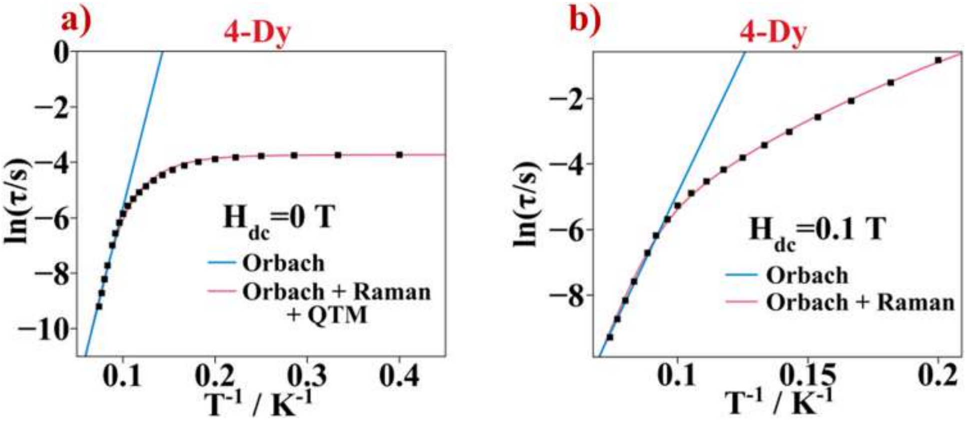

Fig. 9 (a) ln(τ) *vs.* 1/*T* plot of **5-Dy** obtained in the H_{dc} = 0 T. (b) ln(τ) *vs.* 1/*T* plot of **5-Dy** obtained in the H_{dc} = 0.1 T. In both figures, continuous lines represent the best fit using the stated equations of the relaxation of magnetization mechanisms.

an energetically higher excited m_j state of the Dy^{3+} ion.

$$\tau^{-1} = {\tau_0}^{-1}\exp\left(\frac{-\Delta E}{k_B T}\right) \quad (1)$$

By fitting the magnetic data in the 10–13.5 K temperature range using eqn (1), the effective energy barrier (ΔE) yielded 91.1 cm^{-1} and the pre-exponential factor (τ_0) was 7.2×10^{-9} s. However, the linear fashion is not followed along all the temperatures. This indicates the presence of another mechanism responsible for the relaxation of the magnetization under 13.5 K. On cooling the sample, the ln(τ) *vs.* T^{-1} curve enters a plateau region indicating that the spin of the lanthanide ion returns to the equilibrium phase *via* the faster QTM process. Consequently, the ln(τ) *vs.* T^{-1} curve was fitted with eqn (2) considering the three relaxation mechanisms. The best fit was obtained with ΔE = 103.7 cm^{-1} and $\tau_0 = 2.53 \times 10^{-9}$ s for Orbach, $C = 8.18 \times 10^{-4}$ s^{-1} K^{-n} and n = 5.5 for Raman and τ_{QTM} = 0.03 s for the QTM processes.

$$\tau^{-1} = CT^n + {\tau_0}^{-1}\exp\left(\frac{-\Delta E}{k_B T}\right) + {\tau_{QMT}}^{-1} \quad (2)$$

To remove the QTM in the relaxation of the magnetization process of **4-Dy**, an external magnetic field can be applied while measuring the AC magnetic susceptibility response. An external magnetic field breaks the degeneracy between the $\pm m_j$ states so the fast QTM between the m_j levels is reduced or even eliminated.[41]

To establish the optimal H_{dc} for the Dy^{3+} sample, χ_M' and χ_M'' components were measured at constant temperature (11 K) and by applying different external magnetic fields, from 0 to 1.8 T. A plot of τ (1/2πω) *vs.* H_{dc} shows that the relaxation time is the greatest when the applied external magnetic field is 0.1 T. This DC field was found to be optimal, Fig. S17 (ESI†).

Fig. 8d and e show the AC measurement of **4-Dy** at H_{dc} of 0.1 T. Now, on cooling the sample, no increase of the χ_M'' component with temperature is observed, suggesting that the fastest relaxation mechanism observed at low temperatures in the H_{dc} = 0 experiments, QTM, is not present. The magnetic data were analysed in the temperature range where the χ_M'' *vs.* *T* peaks appear between 5 and 13.5 K. The χ_M'' *versus* the oscillating frequency relationship shows maxima that move progressively from lower frequency to higher frequency values as temperature increases, indicating a temperature dependent relaxation mechanism. The curves from the Cole–Cole plots, Fig. 8f, were fitted using the one component Generalized Debye model, and the obtained α values are in the range 0.02–0.05, Table S5 (ESI†).

The ln(τ) *versus* T^{-1} plot for H_{dc} = 0.1 T measurement is shown in Fig. 9b. A linear trend appears in the high temperature range corresponding to the Orbach relaxation mechanism. The linear part was fitted using the Arrhenius law giving ΔE = 109.3 cm^{-1} and $\tau_0 = 9.3 \times 10^{-10}$ s. The trend of the ln(τ) *vs.* T^{-1} curve changes as the temperature decreases. Moreover, the plateau at low temperature seen in the ln(τ) *vs.* T^{-1} curve of the H_{dc} = 0 T measurement, corresponding to the QTM, is not seen anymore. Thus, the fitting was done taking out the QTM part of eqn (2). The best fit gave ΔE = 140.5 cm^{-1} and $\tau_0 = 3.6 \times 10^{-11}$ s values for the Orbach mechanism and $C = 1.10 \times 10^{-4}$ s^{-1} K^{-n} and n = 6.2 values for the Raman mechanism.

The magnetic behaviour of the former compound is similar to other β-diketonate compounds with the DyO_6N_2 coordination environment. The ΔE value presented herein is similar to that obtained in other systems with the Btfa$^-$ β-diketonate ligand found in the literature.[45] The mononuclear compound with formula [Dy(Btfa)(bipy)][45a] shows SIM behaviour, but just a few maxima are found in the high frequency range. When applying an external magnetic field of 0.12 T, the QTM is reduced, and the SIM performance is improved with a ΔE of 62.9 cm^{-1}. Changing the polypyridyl ligand from bipy to 4,4′-dinonyl-2,2′-bipy (**6-Dy**) in the presented work, the SIM performance improves with a ΔE of 91.1 cm^{-1} at a 0 DC external magnetic field and it is enhanced to 109 cm^{-1} when a H_{dc} of 0.1 T is applied.

The magnetic anisotropy axis of the $m_j = \pm 15/2$ state can be calculated using a simple electrostatic model presented by the Chilton Group.[46] To enhance the SMM behavior, the $\pm m_j$ ground state stabilized by the crystal field should be the one

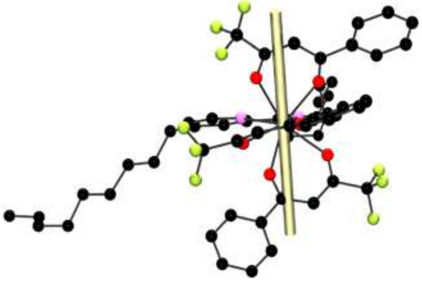

Fig. 10 Orientation of the magnetic anisotropy axis of the $m_j = \pm 15/2$ state (yellow rod) of compound **4-Dy**.

with the greatest value: ±15/2, for a Dy^{3+} ion, which has an oblate electron density. Therefore, to stabilize this m_j state, an axially stressed coordination environment should be induced. The more electron-rich atoms (O atoms from the β-diketonate ligands in this case) should be in the axial positions. Generally, the atoms with highly electron-rich atoms will form the shortest Dy-donor atom bond distances. Therefore, by calculating the anisotropy axis, if it passes through the shortest Dy–O bond distances of the more electronegative atoms, this will indicate that the m_j ground state is in its major contribution of ±15/2 (the largest m_j value). To calculate the anisotropic axis from the crystallographic data, the Magellan program, which can only be used for Dy^{3+} ions, was used. Fig. 10 shows the magnetic axis in yellow, and it goes along the Dy–O bonds formed by Dy–O2 and Dy–O5 with the shortest bond distances which are 2.311 and 2.320 Å, respectively. We can conclude that the stabilized m_j ground state of compound **4-Dy** is ±15/2.

The remaining lanthanide compounds, **3-Tb**, **5-Er** and **6-Yb**, showed slow relaxation of the magnetization just when an external magnetic field was applied. The magnetic response of such complexes was measured under the optimal H_{dc} = 0.1 T for **3-Tb** and **6-Yb** and 0.05 T for **5-Er**, Fig. S16 and S17 (ESI†). The plots of the out-of-phase magnetic susceptibility components varying with temperature and frequency are depicted in Fig. 11 for **3-Tb**, **5-Er** and **7-Yb.**

For **3-Tb**, the maximum values of χ_M'' appear upon cooling the sample down to the liquid helium temperature and at high oscillating frequencies. Nevertheless, the Cole–Cole plots for **3-Tb** are uncompleted asymmetric semicircles that can be fitted

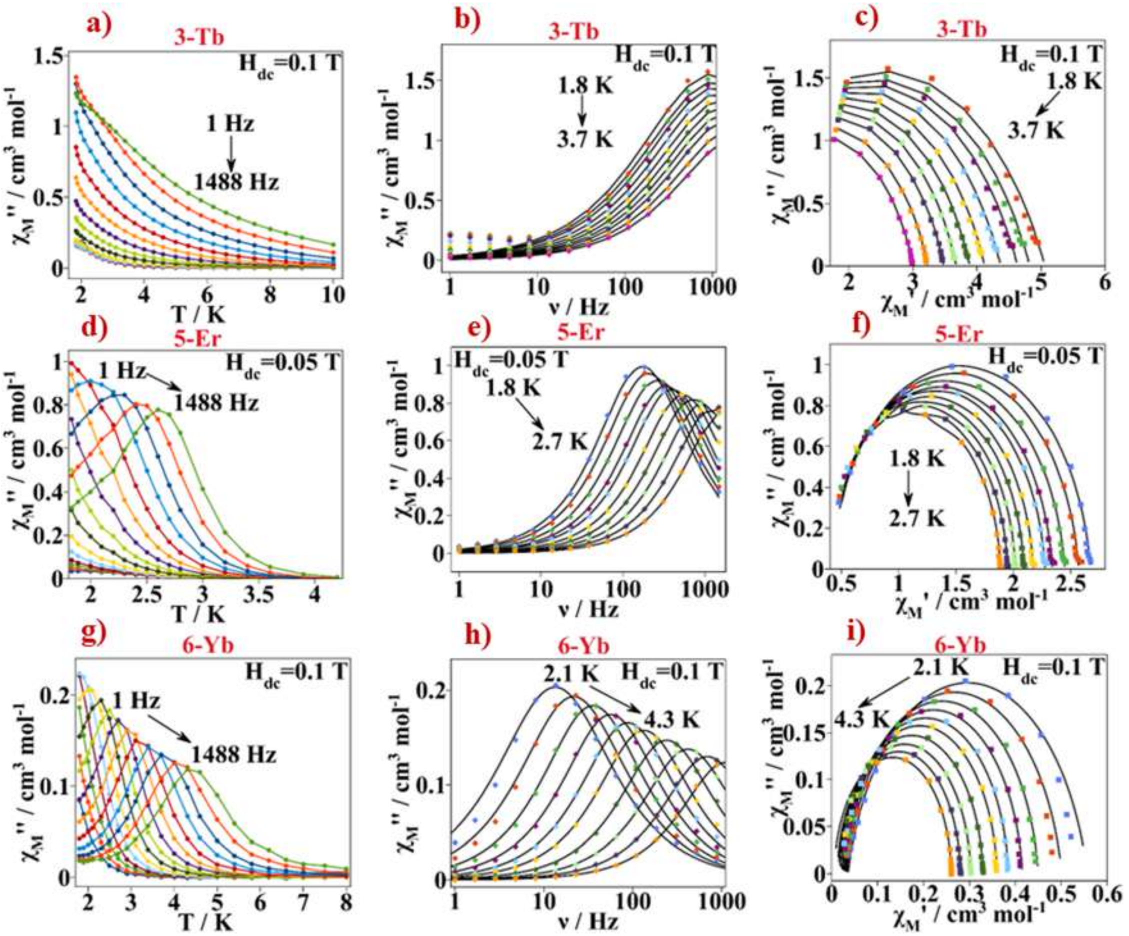

Fig. 11 (a), (d) and (g) temperature dependence of χ_M'' for **3-Tb**, **5-Er** and **6-Yb** respectively. Continuous lines serve as an eye guide. (b), (e) and (h) χ_M'' *versus* frequency characteristics for **3-Tb**, **5-Er** and **6-Yb** respectively. Continuous black lines correspond to the best fit according to eqn (S3) (ESI†). (c), (f), (i) Cole–Cole plots for compounds **3-Tb**, **5-Er** and **6-Yb** respectively. Continuous black lines correspond to the best fit according to eqn (S3) (ESI†). The AC data were recorded with H_{dc} = 0.1 T for **3-Tb** and **6-Yb** and 0.05 T for **5-Er**.

using the one component Debye model with α values of 0.3 to 0.23 on increasing temperature, Table S6 (ESI†). The ln(τ) *vs.* T^{-1} plot is shown in Fig. 12a. No linear trend is followed along the temperature axes, indicating that the relaxation of the magnetization of the Tb^{3+} compound does not occur through the Orbach process. Clearly, a temperature dependence of the relaxation times is observed, therefore the Raman process can be considered. The best fit of the magnetic data of **3-Tb** is obtained when both, Raman and Direct mechanism, are considered with values of $C = 0.93\ s^{-1}\ K^{-n}$ and $n = 5.21$ for the Raman and of $A = 3275.1\ s^{-1}\ K^{-1}$ for the Direct process. The terbium(III) ion has a ${}^7F_6$ ground state. When the Tb^{3+} ion is coordinated to ligand molecules forming a coordination compound, J splits into $2J + 1$ $\pm m_J$ states due to the crystal field effect. For J equal to 6, that would be 13 m_J sublevels comprised between +6 to −6. Due to the non-Kramer nature of the Tb^{3+} ion, a certain crystal field can stabilize the m_J ground state with the lower value which in this case would be $m_J = 0$. If this occurred, then no relaxation of the magnetization nor SMM behaviour could be seen at all. For a Tb^{3+} compound showing SMM behaviour, the crystal field should optimize the oblate shaped electron density m_J state with larger value ($m_J = 6$). Therefore, the crystal field of compound **3-Tb** stabilizes a ground state different than $m_J = 0$, though there is transverse contribution in the ground state wavefunction because of QTM presence at $H_{dc} = 0$ T and even applying an optimal external magnetic field, slow relaxation of the magnetization is recorded but in a very narrow temperature range.[47]

Compounds **5-Er** and **6-Yb** show clear maxima of the χ_M'' component in a rather low temperature range (1.8–2.7 K for **5-Er** and of 2.1–4.3 K for **6-Yb**). For **5-Er** and **6-Yb**, in the plots of the out-of-phase magnetic susceptibility components *versus* temperature and frequency, the χ_M'' peaks move progressively to higher frequencies upon increasing the temperature. The Cole–Cole plots show non-symmetric semicircles, Fig. 11c, f and i. For **5-Er** and **6-Yb**, Cole–Cole curves could be fitted with the one component Generalized Debye model equation, eqn (S3) and Tables S7 and S8 (ESI†). The α values obtained from the fit are in the range of 0.08 to 0.03 (for **5-Er**) and of 0.16 to 0.02 (for **6-Yb**) on increasing temperature. Relaxation of magnetization times with temperature characteristics are plotted in Fig. 12b and c.

For the **5-Er** compound, the Arrhenius law is used to fit the linear segment in the higher temperature range. The obtained effective energy barrier is 13.0 cm^{-1} and the pre-exponential factor is 8.75×10^{-8} s. The linear trend is not followed along the curve, therefore a function with the equation including the Orbach and Raman relaxation mechanisms (first two components in eqn (2)) gives the best fit. The obtained parameters are $\Delta E = 24.6\ cm^{-1}$, $\tau_0 = 8.75 \times 10^{-8}$ s, $C = 96.1\ s^{-1}\ K^{-n}$ and $n = 4.05$. Finally, for compound **6-Yb**, the magnetic data cannot be fitted using the Arrhenius law since there is no clear linear trend in the higher temperature range and therefore the relaxation of the magnetization by the Orbach process is excluded. The best fit of the ln(τ) *vs.* T^{-1} curves is acquired when equations describing the Raman and Direct relaxation of the magnetization processes are considered, eqn (3), and the obtained parameters are $C = 0.51\ s^{-1}\ K^{-n}$, $n = 6.5$ and $A = 8.58\ s^{-1}\ K^{-1}$. Other Yb^{3+} coordination compounds where the slow relaxation of the magnetization process is dominated by Raman and Direct mechanisms rather than Orbach, are found in the literature.[48] A compilation of the fitted parameters for all compounds is found in Table S9 (ESI†).

$$\tau^{-1} = CT^n + AT \tag{3}$$

It is important to consider that the low temperature range in which the **3-Tb**, **5-Er** and **6-Yb** compounds show slow relaxation of the magnetization is very narrow and therefore not many values of τ can be extracted. Added to the over-parametrization when using the different combinations of the equations (Raman, Direct, Orbach, QTM, Local mode) to acknowledge the relaxation of the magnetization mechanisms, it becomes difficult to extract accurate conclusions.

4.4. Correlation between magnetic and spectroscopic data

The relaxation of magnetization energy barrier described by the Orbach mechanism of **4-Dy** calculated by means of the magnetic data can be compared with the energy barrier calculated through the spectroscopic data. The emission spectrum of **4-Dy**

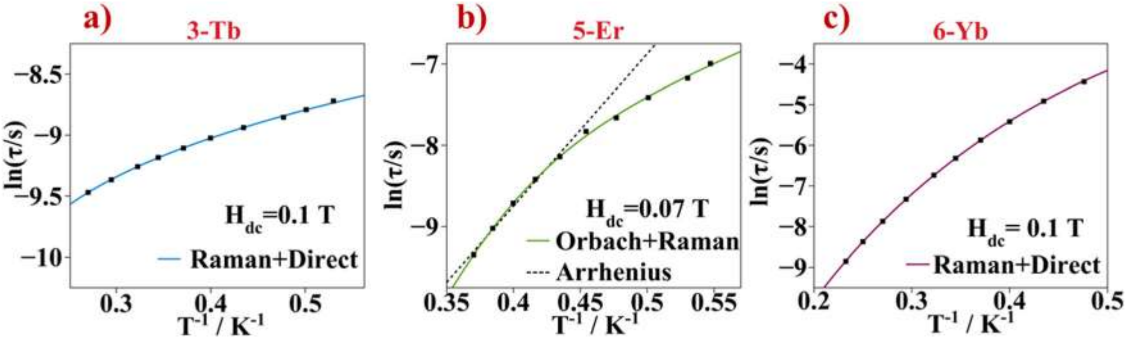

Fig. 12 (a) ln(τ) *vs.* 1/T plot of (a) **3-Tb**, (b) **5-Er** and (c) **6-Yb** obtained at the H_{dc} = 0.1, 0.07 and 0.1 T respectively. In the three figures, continuous lines represent the best fit using the stated equations of the relaxation of magnetization mechanisms. The black dotted line in (b) represents the fit in the high temperature range following an Arrhenius law.

was obtained at $T = 77$ K configuring the experiment to use a slower acquisition time. By measuring the emission spectrum at such low temperature, the corresponding $\pm m_j$ energy levels formed by the crystal field splitting can be distinguished. Assuming that only the first m_j state of the $^4F_{9/2}$ emitting level is populated and that at such low temperature we can reduce, as much as possible, the presence of hot bands and vibronic side bands, the $^6H_{15/2}$ ground state of the Dy^{3+} Kramer ion splits due to the crystal field effect by $J + 1/2$ states: $\pm m_j = \pm 15/2$, $\pm 13/2$, $\pm 11/2$, $\pm 9/2$, $\pm 7/2$, $\pm 5/2$, $\pm 3/2$, $\pm 1/2$.

A multi-Gaussian function fit is performed for the $^7F_{9/2} \rightarrow {}^6H_{15/2}$ emission band, Fig. S18 (ESI†). Different trials with more than eight Gaussian functions were performed to include the 'hot bands'. A good fit is obtained when 9 Gaussian functions are used. The ninth Gaussian function covers the small shoulder at the low energy range. This indicates that even at low temperatures the side emission bands such as the 'hot bands' are still present. They can appear even at lower temperatures as demonstrated in other published studies.[49] Thus, the first two bands that are higher in energy are assigned to the zero phonon $0' \rightarrow 0$ and $0' \rightarrow 1$ transitions. The energy difference between the peaks of the two first Gaussian functions is 93.8 cm^{-1}. Attending to the calculated ΔE value from the magnetic data (91 cm^{-1}), the Orbach relaxation process occurs only through the first $\pm m_j$ excited state. This could consider the fact that the thermally activated relaxation of the magnetization process (Orbach) does not take place through the whole energy barrier composed by all the $\pm m_j$ states of the Dy^{3+} ion but only *via* the first $\pm m_j$ excited state.

Moreover, the emission spectra of the **6-Yb** compounds measured, also, at 77 K show that the $^2F_{5/2} \rightarrow {}^2F_{7/2}$ emission transition is split due to crystal field into four well distinguished peaks. The Yb^{3+} $^2F_{7/2}$ ground state break of the degeneracy due to crystal field splitting, should lead to four $\pm m_j$ states ($\pm 7/2$, $\pm 5/2$, $\pm 3/2$, $\pm 1/2$). A multi-Gaussian fit of the emission spectra is performed successfully with four Gaussian functions, Fig. S19 (ESI†). The splitting between the peaks is as follows: 25.1 (1st–2nd), 13.6 (2nd–3rd) and 17.7 cm^{-1} (3rd–4th). The dynamic magnetic data for **6-Yb** show that the magnetization does not relax through an effective energy barrier *via* the Orbach process.

5. Conclusions

Six new β-diketonate lanthanide coordination compounds have been synthesized and fully characterized spectroscopically and magnetically. The new mononuclear compounds with formula $[Ln(btfa)_3(4,4'\text{-dinonylbipy})]$ Ln = Sm (**1-Sm**), Eu (**2-Eu**), Tb (**3-Tb**), Dy (**4-Dy**), Er (**5-Er**) and Yb (**6-Yb**) have been isolated through the reaction of $[Ln(btfa)_3(H_2O)_2]$ ($btfa^-$ = 4,4,4-trifluoro-1-phenyl-1,3-butanedionate) with 4,4′-dinonyl-2,2′-bipyridyl (4,4′-dinonylbipy) in ethanol. The structural characterization has been carried out by single crystal X-ray diffraction and by X-ray powder diffraction.

Photoluminescence studies were performed for all complexes in $CHCl_3$ solution and in solid state. Furthermore the solid samples were also measured at the liquid nitrogen temperature (77 K). All polycrystalline samples show sensitized luminescence when exciting the samples at the ligand excitation band indicating an effective antenna effect.

Luminescence quantum yield could be measured for the visible light emitters **1-Sm**, **2-Eu**, **3-Tb**, and **4-Dy** in chloroform solution and in solid state, with the europium compound yielding the highest value of 0.68 in polycrystalline sample and of 0.42 in solution. Moreover, luminescence decay lifetime was measured for the **1-Sm** and **2-Eu** compounds with the **2-Eu** polycrystalline sample showing the greatest $\tau_{obs} = 0.90$ ms.

Owing to the peripheral alkyl and $-CF_3$ groups of the 4,4′-dinonyl-2,2′-bipy and $btfa^-$ ligands, the **2-Eu** and **6-Yb** complexes showed a relatively low sublimation temperature, around 140–150 °C at $\sim 10^{-6}$ mbar, hence they are promising materials for OLEDs. Considering the good luminescence properties of the **2-Eu** complex and intriguing long wavelength PL of **6-Yb** they were selected to produce vacuum deposited OLEDs. The **2-Eu** based OLED showed an external quantum efficiency of 2.0–2.1% and luminance in a range $\sim$200–600 cd m^{-2}. Using **6-Yb** as the emitter gave a near infrared electroluminescence at $\sim$1000 nm with an EQE of 0.1–0.17%.

From the magnetic study of this series of compounds, dynamic magnetic measurements proved that **5-Dy** display SIM behaviour at relatively high temperatures showing maximum values of the χ_M'' component up to 14 K. The phonon lattice mechanism dominating in the high temperature range is the Orbach process with an effective energy barrier of 91.1 cm^{-1}. Moreover, at intermediate temperatures the Raman mechanism is present and the process of quantum nature, QTM, governs the relaxation of the magnetization at the low temperature range. By applying an optimal DC magnetic field of 0.1 T the QTM is removed, and the magnetic relaxation is still dominated by the Orbach process at high temperatures with a greater ΔE value of 109.3 cm^{-1} than that found at $H_{dc} = 0$ T. The Raman mechanism is involved while cooling the sample. Magnetic and spectroscopic studies of **5-Dy** showed that the thermal activated relaxation of the magnetization process (Orbach) does not take place through the whole energy barrier composed of all the $\pm m_j$ states of the Dy^{3+} ion but only *via* the first $\pm m_j$ excited state. In addition, **3-Tb**, **5-Er** and **6-Yb** show slow relaxation of the magnetization under an external applied magnetic field. The mechanisms that best describe the relaxation of the magnetization of these three compounds resulted in a combination of Raman and Direct for **3-Tb** and **6-Yb** and Orbach and Raman for the **5-Er** analogue.

Conflicts of interest

There are no conflicts to declare.

Acknowledgements

R. V. and A. T. acknowledge the financial support from Ministerio de Ciencia, Innovación y Universidades (Spain), Project PGC2018-094031-B-100.

References

1 N. Ishikawa, M. Sugita, T. Ishikawa, S. Y. Koshihara and Y. Kaizu, Lanthanide Double-Decker Complexes Functioning as Magnets at the Single-Molecular Level, *J. Am. Chem. Soc.*, 2003, **125**, 8694–8695.

2 (*a*) J. Tang and P. Zhang, *Lanthanide Single Molecule Magnets*, Springer-Verlag, Berlin Heidelberg, 2015; (*b*) H. L. C. Feltham and S. Brooker, Review of purely 4f and mixed-metal nd-4f single-molecule magnets containing only one lanthanide ion, *Coord. Chem. Rev.*, 2014, **276**, 1–33; (*c*) D. N. Woodruff, R. E. P. Winpenny and R. A. Layfield, Lanthanide Single-Molecule Magnets, *Chem. Rev.*, 2013, **113**, 5110–5148; (*d*) A. Borah and R. Murugavel, Magnetic relaxation in single-ion magnets formed by less-studied lanthanide ions Ce(III), Nd(III), Gd(III), Ho(III), Tm(II/III) and Yb(III), *Coord. Chem. Rev.*, 2022, **453**, 214288; (*e*) D. N. Woodruff, F. Tuna, M. Bodensteiner, R. E. P. Winpenny and R. A. Layfield, Single-Molecule Magnetism in Tetrametallic Terbium and Dysprosium Thiolate Cages, *Organometallics*, 2013, **32**, 1224–1229; (*f*) S. Zhang, H. Ke, Q. Shi, J. Zhang, Q. Yang, Q. Wei, G. Xie, W. Wang, D. Yang and S. Chen, Dysprosium(III) complexes with a square-antiprism configuration featuring mononuclear single molecule magnetic behaviours based on diferent β-diketonate ligands and auxiliary ligands, *Dalton Trans.*, 2016, **45**, 5310–5320; (*g*) L. Razquin-Bobillo, O. Pajuelo-Corral, A. Zabala-Lekuona, A. Rodríguez-Diéguez and J. Cepeda, An experimental and theoretical study of the.magnetic relaxation in heterometallic coordination polymers based on 6-methyl-2-oxonicotinate and lanthanide(III) ions with square antiprismatic environament, *Dalton Trans.*, 2022, **51**, 16243–16255.

3 (*a*) F.-S. Guo, B. M. Day, Y.-C. Chen, M.-L. Tong, A. Mansikkamäki and R. A. Layfield, A Dysprosium Metallocene Single-Molecule Magnet Functioning at the Axial Limit, *Angew. Chem., Int. Ed.*, 2017, **56**, 11445–11449; (*b*) C. A. P. Goodwin, F. Ortu, D. Reta, N. F. Chilton and D. P. Mills, Molecular magnetic hysteresis at 60 kelvin in dysprosocenium, *Nature*, 2017, **548**, 439–442.

4 F.-S. Guo, B. Day, Y.-C. Chen, M. L. Tong, A. Mansikkamäki and R. A. Layfield, Magnetic hysteresis up to 80 kelvin in a dysprosium metallocene single-molecule magnet, *Science*, 2018, **362**, 1400–1403.

5 Y. Hasegawa, Y. Kitagawa and T. Nakanish, Effective photosensitized, electrosensitized, and mechanosensitized luminescence of lanthanide complexes, *NPG Asia Mater.*, 2018, **10**, 52–70.

6 (*a*) J.-C. G. Bünzli, On the design of highly luminescent lanthanide complexes, *Coord. Chem. Rev.*, 2015, **293–294**, 19–47; (*b*) G. F. de Sá, O. L. Malta, C. de Mello Donegá, A. M. Simas, R. L. Longo and P. A. Santa-Cruz, Spectroscopic Properties and Design of Highly Luminescent Lanthanide Coordination Complexes, *Coord. Chem. Rev.*, 2000, **196**, 165–195.

7 G. Huang, G. Calvez, Y. Suffren, C. Daiguebonne, S. Freslon, O. Guillou and K. Bernot, Closing the Circle of the Lanthanide-Murexide Series: Single-Molecule Magnet Behavior and Near-Infrared Emission of the Nd^{III} Derivative, *Magnetochemistry*, 2018, **4**, 44, DOI: 10.3390/magnetochemistry4040044.

8 B. Casanovas, M. Font-Bardía, S. Speed, M. S. El Fallah and R. Vicente, Field Induced SMM and Visible/NIR-luminescence behaviour for dinuclear Ln(III) complexes with 2-fluorobenzoate, *Eur. J. Inorg. Chem.*, 2018, 1928–1937.

9 (*a*) H.-Y. Chen, W.-M. Wang, H.-L. Gao and J.-Z. Cui, *RSC Adv.*, 2016, **6**, 34165–34174; (*b*) S. Bala, M. S. Bishwas, B. Pramanik, S. Khanra, K. M. Fromm, P. Poddar and R. Mondal, Construction of Polynuclear Lanthanide (Ln = DyIII, TbIII, and NdIII) Cage Complexes Using Pyridine–Pyrazole-Based Ligands: Versatile Molecular Topologies and SMM Behavior, *Inorg. Chem.*, 2015, **54**, 8197–8206.

10 L. A. Galán, S. Wada, L. Cameron, A. N. Sobolev, Y. Hasegawa, E. Zysman-Colman, M. I. Ogden and M. Massi, Photophysical investigation of near infrared emitting lanthanoid complexes incorporating tris(2-naphthoyl) methane as a new antenna ligand, *Dalton Trans.*, 2019, **48**, 3768–3776.

11 C. Yang, L. M. Fu, Y. Wang, J. P. Zhang, W. T. Wong, X.-C. Ai, F. Y. Qiao, B. S. Zou and L.-L. Gui, A Highly Luminescent Europium Complex Showing Visible-Light-Sensitized Red Emission: Direct Observation of the Singlet Pathway, *Angew. Chem., Int. Ed.*, 2004, **116**, 5120–5123.

12 (*a*) D. Imbert, M. Cantuel, J.-C. G. Bunzli, G. Bernardinelli and C. Piguet, Extending Lifetimes of Lanthanide-Based Near-Infrared Emitters (Nd, Yb) in the Millisecond Range through Cr(III) Sensitization in Discrete Bimetallic Edifices, *J. Am. Chem. Soc.*, 2003, **125**, 15698–15699; (*b*) A. Beeby, B. P. Burton-Pye, S. Faulkner, G. R. Motson, J. C. Jeffery, J. A. McCleverty and M. D. Ward, Synthesis and near-IR luminescence properties of neodymium(III) and ytterbium(III) complexes with poly(pyrazolyl)borate ligands, *J. Chem. Soc., Dalton Trans.*, 2002, 1923–1928.

13 (*a*) W. Li, J. Li, H. Li, P. Yan, G. Hou and G. Li, NIR luminescence of 2-(2,2,2-trifluoroethyl)-1-indone (TFI) neodymium and ytterbium complexes, *J. Lumin.*, 2014, **146**, 205–210; (*b*) X. Wang, L. Wang, Y. Luo, W. Wu, X. Tian, Q. Zhang and B. Chen, NIR luminescence of a visible-light-sensitized neodymium complex with large experimental fluorescence branching ratio for 4F3/2 → 4I11/2 in PMMA, *J. Mater. Res.*, 2011, **26**, 1517–1523.

14 (*a*) S. D. Bennett, S. J. A. Pope and B. D. Ward, Near-IR luminescent neodymium complexes: spectroscopic probes for hydroamination catalysis, *Chem. Commun.*, 2013, **49**, 6072–6074; (*b*) N. M. Shavaleev, R. Scopelliti, F. Gumy and J.-C. G. Bünzli, Near-Infrared Luminescence of Nine-Coordinate Neodymium Complexes with Benzimidazole-Substituted 8-Hydroxyquinolines, *Inorg. Chem.*, 2008, **47**, 9055–9068.

15 (*a*) S. Comby and J.-C. G. Bünzli, Lanthanide Near-Infrared Luminescence in Molecular Probes and Devices, *Handbook on the Physics and Chemistry of Rare Earths*, Elsevier, Amsterdam, The Netherlands, 2007, vol. 37, pp. 217–470;

(*b*) Y. Hasegawa and T. Nakanishi, Luminescent lanthanide coordination polymers for photonic applications, *RSC Adv.*, 2015, **5**, 338–353; (*c*) Y. Hasegawa, Photofunctional Lanthanoid Complexes, Coordination Polymers, and Nanocrystals for Future Photonic Applications, *Bull. Chem. Soc. Jpn.*, 2014, **87**, 1029–1057.

16 (*a*) J.-L. Liu, Y.-C. Chen and M.-L. Tong, Symmetry strategies for high performance lanthanide-based single-molecule magnets, *Chem. Soc. Rev.*, 2018, **47**, 2431–2453; (*b*) S. V. Eliseeva and J.-C. G. Bünzli, Lanthanide luminescence for functional materials and bio-sciences, *Chem. Soc. Rev.*, 2010, **39**, 189–227.

17 J.-C. G. Bünzli, Luminescence Bioimaging with Lanthanide Complexes, in *Luminescence of Lanthanide Ions in Coordination Compounds and Nanomaterials*, ed. A. De Bettencourt-Dias, John Wiley & Sons, Chichester, 2014, ch. 4, pp. 125–196.

18 (*a*) Y. Ding, Y. Wang, H. Li, Z. Duan, H. Zhang and Y. Zheng, Photostable and efficient red-emitters based on zeolite L crystals, *J. Mater. Chem.*, 2011, **21**, 14755–14759; (*b*) R. Ilmi, S. Kanslz, N. Dege and M. S. Khan, Synthesis, structure, Hirshfeld surface analysis and photophysical studies of red emitting europium acetylacetonate complex incorporating a phenanthroline derivative, *J. Photochem. Photobiol., A*, 2019, **377**, 268–281; (*c*) P. P. F. da Rosa, Y. Kitagawa and Y. Hasegawa, Luminescent lanthanide complex with seven-coordination geometry, *Coord. Chem. Rev.*, 2020, **406**, 213153; (*d*) Z. Ahmed and K. Iftikhar, Red, orange-red and near-infrared light emitting ternary lanthanide tris β-diketonate complexes with distorted C_{4v} geometrical structures, *Dalton Trans.*, 2019, **48**, 4973–4986; (*e*) J. Li, H. Li, P. Yan, P. Chen, G. Hou and G. Li, Synthesis, Crystal Structure, and Luminescent Properties of 2-(2,2,2-Trifluoroethyl)-1-indone Lanthanide Complexes, *Inorg. Chem.*, 2012, **51**, 5050–5057; (*f*) R. Ilmi, M. S. Khan, Z. Li, L. Zhou, W.-Y. Wong, F. Marken and P. R. Raithby, Utilization of Ternary Europium Complex for Organic Electroluminescent Devices and as a Sensitizer to Improve Electroluminescence of Red-Emitting Iridium Complex, *Inorg. Chem.*, 2019, **58**, 8316–8331; (*g*) R. Ishimatsu, E. Kunisawa, K. Nakano, C. Adach and T. Imato, Electrogenerated Chemiluminescence and Electronic States of Several Organometallic Eu(III) and Tb(III) Complexes: Effects of the Ligands, *ChemistrySelect*, 2019, **4**, 2815–2831; (*h*) L. Arrué, J. Santoyo-Flores, N. Pizarro, X. Zarate, D. Páez-Hernández and E. Schott, The role played by structural and energy parameters of β-Diketones derivatives as antenna ligands in Eu(III) complexes, *Chem. Phys. Lett.*, 2021, **773**, 138600.

19 J. Long, Y. Guari, R. A. S. Ferreira, L. D. Carlos and J. Larionova, Recent advances in luminescent lanthanide based Single-Molecule Magnets, *Coord. Chem. Rev.*, 2018, **363**, 57–70.

20 R. Vicente, À. Tubau, S. Speed, F. A. Mautner, F. Bierbaumer, R. C. Fischer and S. S. Massoud, Slow magnetic relaxation and luminescence properties in neodymium(III) 4,4,4-trifluoro-1-(2-naphthyl)butane-1,3-dionato complexes incorporating bipyridyl ligands, *New J. Chem.*, 2021, **45**, 14713–14723.

21 S. Speed, À. Tubau, R. Vicente, E. Castro and M. Font-Bardía, Slow Magnetic Relaxation and Luminescence Properties in Tetra β-diketonate Lanthanide(III) Complexes, *Magnetochemistry*, 2023, **9**, 131–145.

22 J. Kido, H. Hayase, K. Hongawa, K. Nagai and K. Okuyama, *Appl. Phys. Lett.*, 1994, **65**, 2124–2126.

23 (*a*) H. Xua, Q. Sun, Z. An, Y. Wei and X. Liu, Electroluminescence from europium(III) complexes, *Coord. Chem. Rev.*, 2015, **293–264**, 228–249; (*b*) R. Ilmi, X. Li, N. K. Al Rasbi, L. Zhou, W.-Y. Wong, P. R. Raithby and M. S. Khan, Two new red-emitting ternary europium(III) complexes with high photoluminescence quantum yields and excepcional performance in OLED devices, *Dalton Trans.*, 2023, **52**, 12885–12891.

24 Bruker APEX, *SAINT v. 8.37A*, Bruker AXS Inc., Madison, WI, USA, 2015.

25 G. M. Sheldrick, *SADABS v. 2*, University of Goettingen, Goettingen, Germany, 2001.

26 G. M. Sheldrick, Crystal structure refinement with SHELXL, *Acta Crystallogr., Sect. C: Struct. Chem.*, 2015, **71**, 3–8.

27 C. F. Macrae, P. R. Edington, P. McCabe, E. Pidcock, G. P. Shields, R. Taylor, T. Towler and J. J. van de Streek, Mercury: Visualization and analysis of crystal structures. *Appl. Cryst*. 2006, **39**, 453–457.

28 A. L. Spek, *PLATON, a Multipurpose Crystallographic Tool; Utrecht University: Utrecht*, The Netherlands, 1999.

29 D. de Sa Pereira, A. P. Monkman and P. Data, Production and Characterization of Vacuum Deposited Organic Light Emitting Diodes, *J. Vis. Exp.*, 2018, **141**, e56593, DOI: 10.3791/56593.

30 M. Llunell, D. Casanova, J. Cirera, P. Alemany and S. Alvarez, Shape Program. version 2, Universitat de Barcelona, Barcelona, Spain, 2010.

31 P. Alemany, D. Casanova, S. Alvarez, C. Dryzun and D. Avnir, Continuous Symmetry Measures: A New Tool in Quantum Chemistry, *Rev. Comput. Chem.*, 2017, **30**, 289–352, DOI: 10.1002/9781119356059.ch7.

32 (*a*) *The Rare Earth Elements: Fundamentals and Applications*, ed. D. A. Atwood, John Wiley & Sons Ltd, 2012; (*b*) *Luminescence of Lanthanide Ions in Coordination Compounds and Nanomaterials*, ed. A. de Bettencourt-Dias, John Wiley & Sons Ltd, 2014.

33 C. M. Reddy, B. D. P. Raju, N. J. Sushma, N. S. Dhoble and S. J. Dhoble, *Renewable Sustainable Energy Rev.*, 2015, **5**, 566–584.

34 K. Binnemans, Interpretation of europium(III) spectra, *Coord. Chem. Rev.*, 2015, **295**, 1.

35 (*a*) W. T. Carnall, P. R. Fields and K. Rajnak, Electronic Energy Levels in the Trivalent Lanthanide Aquo Ions. I. Pr^{3+}, Nd^{3+}, Pm^{3+}, Sm^{3+}, Dy^{3+}, Ho^{3+}, Er^{3+}, and Tm^{3+}, *J. Chem. Phys.*, 1968, **49**, 4424–4442; (*b*) X. Yu, J. Peng, Z. Shi, Y. Shen, Z. Zhang and G. Li, Tubular solids of lanthanide-doped polyoxometalates in micrometer-scale: synthesis and NIR-

luminescent properties, *J. Lumin.*, 2015, **160**, 289–292; (*c*) À. Tubau, F. Zinna, L. Di Bari, M. Font-Bardía and R. Vicente, Luminescence, CPL and magnetic properties of 1D enantiopure Ln^{3+} complexes with (S-) and (R-) α-methoxyphenylacetate ligand, *Dalton Trans.*, 2023, **52**, 1122–1132; (*d*) J. Feng, L. Zhou, S.-Y. Song, A.-F. Li, W.-F. Li, W.-Q. Fan, L.-N. Sun, Y.-N. Yu and H.-J. Zhang, A study on the near-infrared luminescent properties of xerogel materials doped with dysprosium complexes, *Dalton Trans.*, 2009, 6593–6598; (*e*) M. Pan, B.-B. Du, Y.-X. Zhu, M.-Q. Yue, Z.-W. Wei and C.-Y. Su, Highly Efficient Visible-to-NIR Luminescence of Lanthanide(III) Complexes with Zwitterionic Ligands Bearing, *Chem. – Eur. J.*, 2016, **22**, 2440–2451; (*f*) S. Biju, N. Gopakumar, J.-C. G. Bünzli, R. Scopelliti, H. K. Kim and M. L. P. Reddy, Brilliant Photoluminescence and Triboluminescence from Ternary Complexes of DyIII and TbIII with 3-Phenyl-4-propanol-5-isoxazolonate and a Bidentate Phosphine Oxide Coligand, *Inorg. Chem.*, 2013, **52**, 8750–8758.

36 M. Latva, H. Takalo, V.-M. Mukkala, C. Matachescu, J. C. Rodríguez-Ubis and J. Kankare, Correlation between the lowest triplet state energy level of the ligand and lanthanide(III) luminescence quantum yield, *J. Lumin.*, 1997, **75**, 149–169.

37 (*a*) A. Aebischer, F. Gumy and J.-C. G. Bünzli, Intrinsic quantum yields and radiative lifetimes of lanthanide tris(dipicolinates), *Phys. Chem. Chem. Phys.*, 2009, **11**, 1346–1353; (*b*) S. Sato and M. Wada, Relations between Intramolecular Energy Transfer Efficiencies and Triplet State Energies in Rare Earth β-diketone Chelates, *Bull. Chem. Soc. Jpn.*, 1970, **43**, 1955–1962; (*c*) C. R. De Silva, J. Li, Z. Zheng and L. R. Corrales, Correlation of calculated excited-state energies and experimental quantum yields of luminescent Tb(III) β-diketonates, *J. Phys. Chem. A*, 2008, **112**(20), 4527–4530.

38 (*a*) S. Biju, Y. K. Eom, J.-C. G. Bünzli and H. K. Kim, A new tetrakis β-diketone ligand for NIR emitting Ln III ions: Luminescent doped PMMA films and flexible resins for advanced photonic applications, *J. Mater. Chem. C*, 2013, **1**, 6935–6944; (*b*) J. Bolton, New NIR emission from Sm^{3+} in Yb^{3+}-Sm^{3+} co-doped tellurite glass, *J. Lumin.*, 2021, **231**, 117717; (*c*) H. F. Brito, O. L. Malta, M. C. F. C. Felinto, E. E. S. Teotonio, J. F. S. Menezes, C. F. B. Silva, C. S. Tomiyama and C. A. A. Carvalho, Luminescence investigation of the Sm(III)-β-diketonates with sulfoxides, phosphine oxides and amides ligands, *J. Alloys Compd.*, 2002, **344**, 293–297; (*d*) L.-N. Sun, J.-B. Yu, H.-J. Zhang, Q.-G. Meng, E. Ma, C.-Y. Peng and K.-Y. Yang, Near-infrared luminescent mesoporous materials covalently bonded with ternary lanthanide [Er(III), Nd(III), Yb(III), Sm(III), Pr(III)] complexes, *Microporous Mesoporous Mater.*, 2007, **98**, 156–165.

39 M. H. V. Werts, R. T. F. Jukes and J. W. Verhoeven, The emission spectrum and the radiative lifetime of Eu^{3+} in luminescent lanthanide complexes, *Phys. Chem. Chem. Phys.*, 2002, **4**, 1542–1548.

40 (*a*) M. Andruh, E. Bakalbassis, O. Kahn, J. C. Trombe and P. Porcher, Structure, spectroscopic and magnetic properties of rare earth metal(III) derivatives with the 2-formyl-4-methyl-6-(N-(2-pyridylethyl)formimidoyl)phenol ligand, *Inorg. Chem.*, 1993, **32**, 1616–1622; (*b*) O. Kahn, *Molecular Magnetism*, VHC Publishers, Inc., USA, 1993.

41 A. Zabala-Lekuona, J. M. Seco and E. Colacio, Single-Molecule Magnets: From Mn12-ac to dysprosium metallocenes, a travel in time, *Coord. Chem. Rev.*, 2021, **441**, 213984.

42 (*a*) K. N. Shrivastava, Theory of Spin–Lattice Relaxation, *Phys. Status Solidi B*, 1983, **117**, 437–458; (*b*) R. Orbach, On the theory of spin-lattice relaxation in paramagnetic salts, *Proc. Phys. Soc.*, 1961, **77**, 821–826; (*c*) H. B. G. Casimir and F. K. Du Pré, Note on the thermodynamic interpretation of paramagnetic relaxation phenomena, *Physica*, 1938, **5**, 507–511.

43 Y.-N. Guo, G.-F. Xu, Y. Guo and J. Tang, Relaxation dynamics of dysprosium(III) single molecule magnets, *Dalton Trans.*, 2011, **40**, 9953–9963.

44 N. F. Chilton, CC-FIT, program, **https://www.nfchilton.com/software.html**, 2014.

45 (*a*) P. P. Cen, S. Zhang, X. Y. Liu, W. M. Song, Y. Q. Zhang, G. Xie and S. P. Chen, Electrostatic potential determined magnetic dynamics observed in two mononuclear β-diketone dysprosium(III) single-molecule magnets, *Inorg. Chem.*, 2017, **56**, 3644–3656; (*b*) Z. G. Wang, J. Lu, C. Y. Gao, C. Wang, J. L. Tian, W. Gu, X. Liu and S. P. Yan, Single-ion magnet behavior of a new mononuclear dysprosium complex, *Inorg. Chem. Commun.*, 2013, **27**, 127–130; (*c*) X. L. Li, A. Wang, M. Cui, C. Gao, X. Yu, B. Su, L. Zhou, C. M. Liu, H. P. Xiao and Y. Q. Zhang, Modulating Two Pairs of Chiral DyIII Enantiomers by Distinct β-Diketone Ligands to Show Giant Differences in Single-Ion Magnet Performance and Nonlinear Optical Response, *Inorg. Chem.*, 2022, **61**, 9283–9294; (*d*) X. L. Li, C. Zhu, Q. Rong, J. Wei, R. Li, C. M. Liu, X.-L. Li, C. Zhu, Q. Rong, J. Wei, R. Li and C.-M. Liu, A pair of mononuclear Dy(III) enantiomers showing single-ion magnetic and ferroelectric properties, *New J. Chem.*, 2018, **42**, 10906–10911.

46 N. F. Chilton, D. Collison, E. J. L. McInnes, R. E. P. Winpenny and A. Soncini, An electrostatic model for the determination of magnetic anisotropy in dysprosium complexes, *Nat. Commun.*, 2013, **4**, 2551, DOI: **10.1038/ncomms3551**.

47 S. Kapurwan, A. Mondal, P. K. Sahu and S. Konar, *Inorg. Chem.*, 2022, **61**(44), 17459–17468.

48 (*a*) F. Guégan, J. Jung, B. L. Guennic, F. Riobé, O. Maury, B. Gillon, J. F. Jacquot, Y. Guyot, C. Morell and D. Luneau, Evidencing under-barrier phenomena in a Yb(III) SMM: a joint luminescence/neutron diffraction/SQUID study, *Inorg. Chem. Front.*, 2019, **6**, 3152–3157; (*b*) K. S. Pedersen, J. Dreiser, H. Weihe, R. Sibille, H. V. Johannesen, M. A. Sørensen, B. E. Nielsen, M. Sigrist, H. Mutka, S. Rols, J. Bendix and S. Piligkos, Design of Single-Molecule Magnets: Insufficiency of the Anisotropy Barrier as the Sole Criterion, *Inorg. Chem.*, 2015, **54**, 7600–7606; (*c*) D. Q. Wu, D. Shao, X. Q. Wei, F. X. Shen, L. Shi, Y. Q. Zhang and X. Y. Wang, Single-ion magnetism in seven-coordinate YbIII

complexes with distorted D5h coordination geometry, *Dalton Trans.*, 2017, **46**, 12884–12892; (*d*) W. Zhao, H. Cui, X.-Y. Chen, G. Yi, L. Chen, A. Yuan and C. L. Luo, An eight-coordinate ytterbium complex with a hexagonal bipyramid geometry exhibiting fieldinduced single-ion magnet behaviour, *Dalton Trans.*, 2019, **48**, 5621–5626.

49 (*a*) G. Cucinotta and J. Luzón, Magnetic anisotropy in a dysprosium/DOTA single-molecule magnet: Beyond simple magneto-structural correlations, *Angew. Chem., Int. Ed.*, 2012, **51**, 1606–1610; (*b*) D. Errulat, R. Marin, D. A. Gálico, K. L. M. Harriman, A. Pialat, B. Gabidullin, F. Iikawa, O. D. D. Couto Jr., J. O. Moilanen, E. Hemmer, F. A. Sigoli and M. Mugurescu, A Luminescent Thermometer Exhibiting Slow Relaxation of the Magnetization: Toward Self-Monitored Building Blocks for Next-Generation Optomagnetic Devices, *ACS Cent. Sci.*, 2019, **5**, 1187–1198; (*c*) J. Long, J. Rouquette, J.-M. Thibaud, R. A. S. Ferreira, L. D. Carlos, B. Donnadieu, V. Vieru, L. F. Chibotaru, L. Konczewicz, J. Haines, Y. Guari and J. Larionova, A High-Temperature Molecular Ferroelectric Zn/Dy Complex Exhibiting Single-Ion-Magnet Behavior and Lanthanide Luminescence, *Angew. Chem., Int. Ed.*, 2015, **54**, 2236–2240; (*d*) Y. Bi, C. Chen, Y.-F. Zhao, Y.-Q. Zhang, S.-D. Jiang, B.-W. Wang, J.-B. Han, J.-L. Sun, Z.-Q. Bian, Z.-M. Wanga and S. Gao, Thermostability and photoluminescence of Dy(III) single-molecule magnets under a magnetic field, *Chem. Sci.*, 2016, **7**, 5020–5031.